UNIVERSITY OF CALIFORNIA, IRVINE

Reaction-driven non-equilibrium molecular self-assembly

DISSERTATION

submitted in partial satisfaction of the requirements
for the degree of

DOCTOR OF PHILOSOPHY
in Chemistry

by

Paul Joshua Hurst

Dissertation Committee:
Assistant Professor Joseph Patterson, Chair
Professor Zhibin Guan
Assistant Professor Seunghyun Sim
Assistant Professor Stacy Copp

2023

DEDICATION

To my dear wife Morgan.

You have fully supported me and our family through the ups and downs.

To my daughters, Beatrice and Clara.

You have been my biggest source of joy.

Table of Contents

LIST OF FIGURES

LIST OF TABLES

ACKNOWLEDGEMENTS

I want to first acknowledge my advisor Professor Joe Patterson for his mentorship throughout my PhD. Joe gave me scientific freedom to ask my own questions and develop my own experiments while providing me with expertise in polymer chemistry, self-assembly, and electron microscopy.

I would like to acknowledge all my colleagues in the Patterson lab for their assistance. I have had the opportunity to work with many of them. Some of the research contained in this dissertation was made possible by their work.

I also want to thank all professors and students I have collaborated with including (but not limited to) the groups of Zhibin Guan, James Nowick, Brent Sumerlin, Seunghyun Sim, and Stacy Copp.

This work was largely supported by start-up funds as my advisor, Joe Patterson started at UCI at the same time as me. It has also been supported by the UC Irvine Center for Complex and Active Materials (DMR-2011967). I have also been honored to be the recipient of the Allergan Fellowship (Fall 2021) and the Rowland Fellowship (2022-2023 academic year) which have allowed me to focus my efforts more fully on my research. I also acknowledge the use of facilities and instrumentation at the UC Irvine Materials Research Institute (IMRI) supported in part by the National Science Foundation Materials Research Science and Engineering Center program through the UC Irvine Center for Complex and Active Materials (DMR-2011967).

Chapter 2 in this dissertation is an adaptation of the material Hurst, P.J., Rakowski, A.M. & Patterson, J.P. "Ring-opening polymerization-induced crystallization-driven self-assembly of poly-L-lactide-*block*-polyethylene glycol block copolymers (ROPI-CDSA)",

Nature Communications, **2020**, *11* (1), 4690, used with permission from Springer Nature. The co-authors listed in this publication are Alexander M. Rakowski and Joseph P. Patterson.

Chapter 3 in this dissertation is an adaptation of the material Hurst, P.J., Graham, A.A., Patterson, J.P. “Gaining Structural Control by Modification of Polymerization Rate in Ring-Opening Polymerization-Induced Crystallization-Driven Self-Assembly”, *ACS Polymer Au*, **2022**, *2* (6), 501, used with permission from the American Chemical Society. The co-authors listed in this publication are Annissa A. Graham and Joseph P. Patterson

Chapter 7 in this dissertation is an adaptation of the material Hurst et al., “Visualizing Teixobactin Supramolecular Assemblies and Cell Wall Damage in *B. Subtilis* Using CryoEM”, *ACS Omega*, **2021**, *6* (41), 27412, used with permission from the American Chemical Society. The co-authors listed in this publication are Michael A. Morris, Annissa A. Graham, James S. Nowick, and Joseph P. Patterson.

VITA

Paul Joshua Hurst

EDUCATION

Doctor of Philosophy, Chemistry
2023
University of California, Irvine — Irvine, CA

Bachelor of Science, Chemistry — 2018
Brigham Young University — Provo, UT

RESEARCH

Graduate Research Assistant — 2018-2023
University of California, Irvine — Irvine, CA

Undergraduate Research Assistant — 2015-2018
Brigham Young University — Provo, UT

PUBLICATIONS

1. "Waste-Free Fully Electrically Fueled Dissipative Self-Assembly System." Dipankar Barpuzary, Paul J Hurst, Joseph P Patterson, Zhibin Guan, JACS., 2023, 145 [6] 3727-3735
2. "Facile Synthesis of Multifunctional Bioreducible Polymers For mRNA Delivery." James C Hickey, Paul J Hurst, Joseph P Patterson, Zhibin Guan, Eur. J. Chem., 2022, 29 [12] e202203393
3. "Gaining Structural Control by Modification of Polymerization Rate in Ring-Opening Polymerization-Induced Crystallization-Driven Self-Assembly." Paul Joshua Hurst, Annissa A Graham, Joseph P Patterson, ACS Polymer Au, 2022, 2 [6], 501-509
4. "Visualizing Teixobactin Supramolecular Assemblies and Cell Wall Damage in B. Subtilis Using CryoEM." Paul Joshua Hurst, Michael A Morris, Annissa A Graham, James S Nowick, Joseph P Patterson, ACS Omega, 2021, 6 [41] 27412-27417
5. "Solvent selectivity governs the emergence of temperature responsiveness in block copolymer self-assembly." Alessandro Ianiro, Marco MRM Hendrix, Paul Joshua Hurst, Joseph P Patterson, Mark Vis, Michael Sztucki, A Catarina C Esteves, Remco Tuinier, Macromol., 2021, 54 [6] 2912-2920
6. "Ring-opening polymerization-induced crystallization-driven self-assembly of poly-L-lactide-block-polyethylene glycol block copolymers (ROPI-CDSA)." Paul J Hurst, Alexander M Rakowski, Joseph P Patterson, Nat. Comm. 2020, 11 [1] 4690
7. "Nonionic block copolymer coacervates." Aoon Rizvi, Urja Patel, Alessandro Ianiro, Paul J Hurst, Jovany G Merham, Joseph P Patterson, Macromol., 2020, 53 [14] 6078-6086

8. “Ultrahigh molecular weight hydrophobic acrylic and styrenic polymers through organic-phase photoiniferter-mediated polymerization.” R Nicholas Carmean, Michael B Sims, C Adrian Figg, Paul J Hurst, Joseph P Patterson, Brent S Sumerlin, ACS Macro Lett., 2020, 9 [4] 613-618
9. “Direct observation of amorphous precursor phases in the nucleation of protein–metal–organic frameworks.” Alana F Ogata, Alexander M Rakowski, Brooke P Carpenter, Dmitry A Fishman, Jovany G Merham, Paul J Hurst, Joseph P Patterson, JACS., 2020, 142 [3] 1433-1442

ABSTRACT OF THE DISSERTATION

Reaction-driven non-equilibrium molecular self-assembly

by

Paul Joshua Hurst

Doctor of Philosophy in Chemistry

University of California, Irvine, 2023

Professor Joseph Patterson, Chair

Molecular self-assembly is the spontaneous organization of molecules into higher-ordered nano or microstructures. Considering the free energy landscape, self-assembly can be highly pathway dependent, leading to the formation of structures not at the free energy minimum or non-equilibrium. Some non-equilibrium systems arise through chemical reaction-induced assembly. Living organisms rely on reaction-driven non-equilibrium assemblies for growth and adaptability. Thus, to develop biomimetic materials, we will have to gain a better mechanistic understanding of non-equilibrium self-assembly. The focus of this dissertation is on the development and mechanistic analysis of two classes of reaction-driven non-equilibrium systems: polymerization-induced self-assembly and transient or dissipative supramolecular assembly.

In the first part of the dissertation, I developed a one pot scalable and reproducible synthesis for polyester-based block copolymer nanostructures coined ring-opening polymerization-induced crystallization-driven self-assembly (ROPI-CDSA). In ROPI-CDSA, mPEG is chain-extended by L-lactide in toluene with the assistance of an organocatalyst forming semicrystalline poly-(L)-lactide-*block*-polyethylene glycol (PLLA-

b-PEG) block copolymers. As the polymer chain grows, it becomes increasingly solvophobic, leading to self-assembly. The resulting nanomorphology can be controlled by modifying the polymer concentration or PLLA chain length. Additionally, through catalyst selection, both the onset and rate of self-assembly can be controlled. Fast polymerizations result in a rate of polymerization faster than a rate of self-assembly leading to non-equilibrium assembly. A consequence of this disparity is that through catalyst choice, we can access different morphologies without any variation in molecular structure. Next, in ROPI-CDSA, traditional organocatalytic catalysts are swapped for antibiotics with similar functional groups. The resulting drug-embedded polymer nanoparticles retain antibacterial activity. I postulate that this drug-catalyst strategy can be extended to other examples of polymerization-induced self-assembly for the scalable one pot production of drug-loaded polymer suspensions. A hybrid photoiniferter ROPI-CDSA system is also developed expanding ROPI-CDSA to a variety of biocompatible polyacrylamido-*b*-polyesters.

The second part of the dissertation focuses on the investigation of two transient supramolecular systems. One system is the antibiotic teixobactin which forms sheet-like assemblies. At higher concentrations, these assemblies selectively act upon gram positive bacterial cell walls, whereas at lower concentrations aggregates are either formed transiently or sparingly at the cell surface. The other system is a chemically-fueled redox system, where oxidation of a thiol into a disulfide hydrogelator leads to nanofiber assembly. As the fuel depletes, the disulfide is reduced back to the thiol precursor, leading to disassembly. I study the assembly and disassembly processes sequentially and synchronously using time-resolved cryoEM. I show that a thermodynamically unstable

stacked nanorod phase observed transiently in the sequential process is sustained throughout the synchronous process showing that energy input drives non-equilibrium self-assembly.

As the systems studied in this dissertation mirror biological processes, further understanding of non-equilibrium molecular self-assembly is key to the development of the next generation of robust, adaptable, and active materials as well as unlocking the origins of life.

“How much better is it to get wisdom than gold! And to get understanding rather to be chosen than silver!” (Proverbs 16:16)

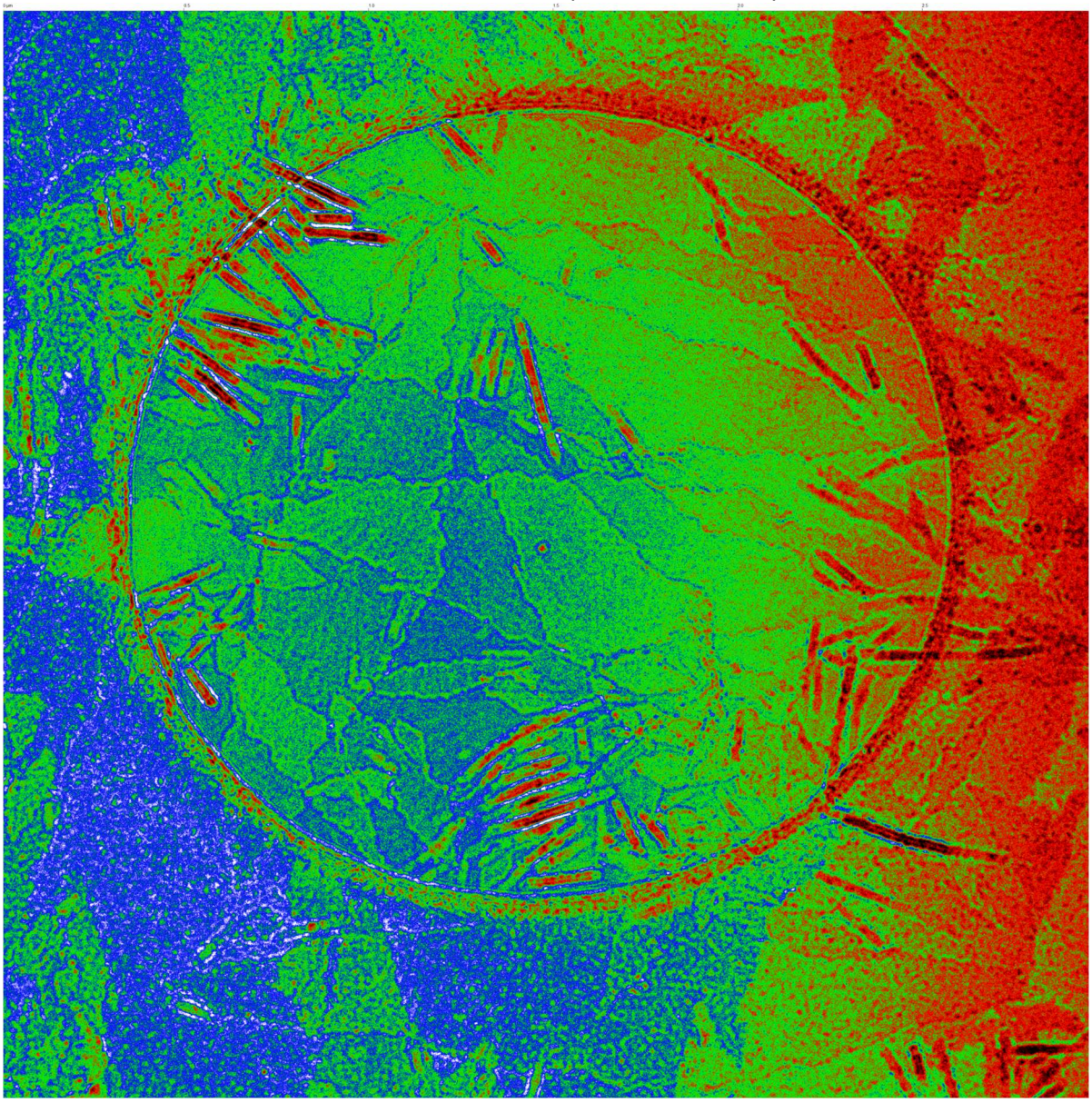

Figure 0.1: “Primordial Soup” by Paul Joshua Hurst. False colored cryogenic electron micrograph of block copolymer lamellae and rods.

Chapter 1: Non-equilibrium Solution-Phase Molecular Self-Assembly

1.0. Significance

Molecular self-assembly is the spontaneous organization of molecules into higher-ordered structures. According to the energetics and the pathway, a self-assembly process can be categorized by one of three frameworks: thermodynamic control, kinetic control, or dissipative (energy-driven). The latter two are pathway dependent and are considered non-equilibrium processes. This chapter will introduce solution-based systems that are prone to undergo non-equilibrium self-assembly. Currently, non-equilibrium systems that have been developed are quite rudimentary and simple when compared to their biological counterparts. Through a better understanding of non-equilibrium self-assembly, we will be able to develop the next generation of biomimetic materials endowed with adaptability and robustness.

1.1. Introduction

Molecular self-assembly is the spontaneous organization of molecules into higher-ordered structures.[1,2] This organization is generally driven by non-covalent interactions such as hydrogen bonding, hydrophobic effects, and electrostatic interactions. On the free energy landscape, these interactions are much weaker than covalent bonds which for complex systems can lead to a variety of pathways or states of assembly.[3,4] Some of these pathways may be kinetically favorable (lower energy barrier) but not reach the lowest free energy configuration. Therefore, to fully understand a self-assembly process, we need to consider the final and initial states as well as the pathway in which these states are connected. In doing so, we can understand the characteristics of various types of molecular self-assemblies. As the complexity of synthetic systems begins to match those of biological systems, we need to define a series of generalized frameworks. For purposes of characterization, self-assembled systems can either be considered at equilibrium or non-equilibrium. Additionally, they can be dependent on an input of energy or not. Systems that reach equilibrium or the lowest free energy configuration are said to be thermodynamically controlled.[4,5] Alternatively, systems in which the kinetics affect the outcome, but which reach a stable state are said to be kinetically controlled, existing in either a metastable or kinetically-trapped state.[4–7] Finally, systems in which an input of fuel is necessary to maintain assembly are referred to as dissipative systems. Dissipative self-assemblies exist transiently in a metastable state, but disassemble upon depletion of the energy source. [7–11] Both kinetically controlled and dissipative processes are therefore considered to be non-equilibrium processes. As non-equilibrium processes provide access to energy-driven structures, the development of these processes will lead to the realization of biomimetic systems that meet or exceed biological systems.[12] In this

chapter, I will discuss these molecular self-assembly frameworks in the solution phase, drawing from common classes of solution-based soft matter such as supramolecular aggregates/polymers, lipids, and amphiphilic block copolymers. This chapter is not meant to provide a detailed characterization of these systems, but to provide the reader with a framework for non-equilibrium molecular self-assembly with key examples and methods in enabling non-equilibrium states.

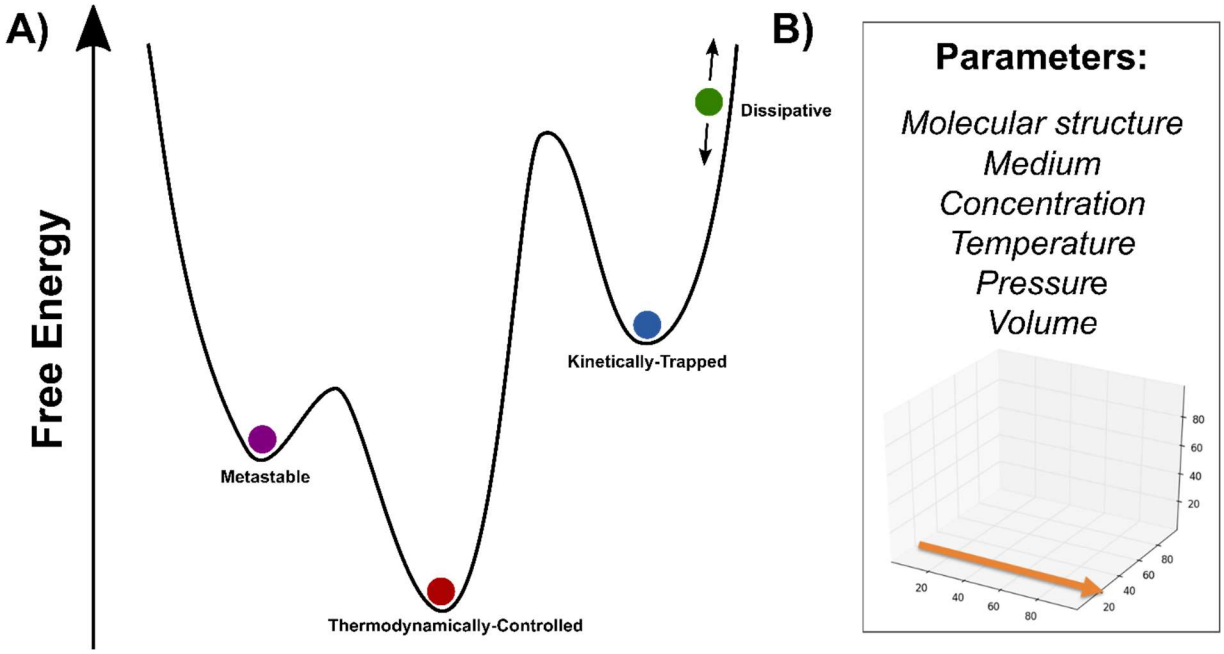

Figure 1.1: Molecular self-assembly frameworks and high dimensional phase. A) Relative free energies of the self-assembly frameworks discussed in this chapter. Thermodynamically controlled processes occupy the lowest energy, with metastable and kinetically-trapped existing in stable but non-equilibrium configurations. Dissipative processes are driven out-of-equilibrium through the input of energy. B) When studying molecular self-assemblies, from "limitless" parameters, a few are selected to determine the effect of a parameter on the energetics of the system.

1.2. Defining the high dimensional phase space

Unlike the relatively few frameworks for molecular self-assembly (Figure 1.1A), the variables or dimensions of self-assembly processes can be infinite. For simplification, these "limitless" number of dimensions can be categorized into six fundamental types: 1) the molecular structure of the building blocks, 2) the medium, 3) the concentration(s) of

the building blocks, 4) the temperature, 5) the pressure, and 6) the volume (Figure 1.1B). Some of these parameters can then be further subdivided, for example one could study the pH and ionic strength, both of which concern the medium. In defining the phase space, we need to first determine the dimensions of interest. For example, in conventional solvent switch assembly, variation in molecular structure, the ratio of selective and non-selective solvent(s), and the concentration of molecules are varied which gives a three-dimensional phase space. Other factors, such as temperature, volume, and pressure are all constant. Next, we need to differentiate between the pathway and the final state. The pathway is dependent on the phase space and the direction and is not a state function, unlike the final free energy state, and is sensitive to the procedure used to initiate assembly. For example, the pathway can proceed through a non-equilibrium mechanism but still arrive at a thermodynamic equilibrium in the final state. When there are competing pathways, the pathway(s) that leads to the thermodynamic route is called on-pathway, whereas the pathway(s) that leads to a metastable or kinetically-trapped route is called off-pathway. An example is illustrated by a study by Korevaar et. al.[13] into the supramolecular polymerization kinetics of *S*-chiral oligo(p-phenylenevinylene) (*S*-OPV). Here the assembly of *S*-OPV is able to initially self-assemble into either stable left-handed (on-pathway) or less stable right-handed helical aggregates (off-pathway). However, the right-handed helical aggregates are later converted to more stable left-handed aggregates. When considering both pathways and end-states, we have three possible combinations: (i) an equilibrium pathway (on-pathway assembly) and final state, (ii) a non-equilibrium pathway (metastable off-pathway assembly) but an equilibrium final state, and (iii) a non-equilibrium pathway and a non-equilibrium final state (Figure 1.2). Generally,

when referring to thermodynamically controlled or kinetically controlled self-assembly, we refer to the final state. Thus, thermodynamic assemblies can arise from situation (i) or (ii) as shown in Figure 1.2 but kinetic assemblies must arise from a non-equilibrium pathway, (iii). In contrast, dissipative self-assembly is pathway-defined as it can only proceed through an input of energy. Now that I have defined self-assembly frameworks, phase space, and pathways, I will move on to discuss characteristics of the different frameworks. One sidenote is that some of these terms discussed have slightly different definitions within the field of molecular self-assembly as well as in other fields that study non-equilibrium assembly.

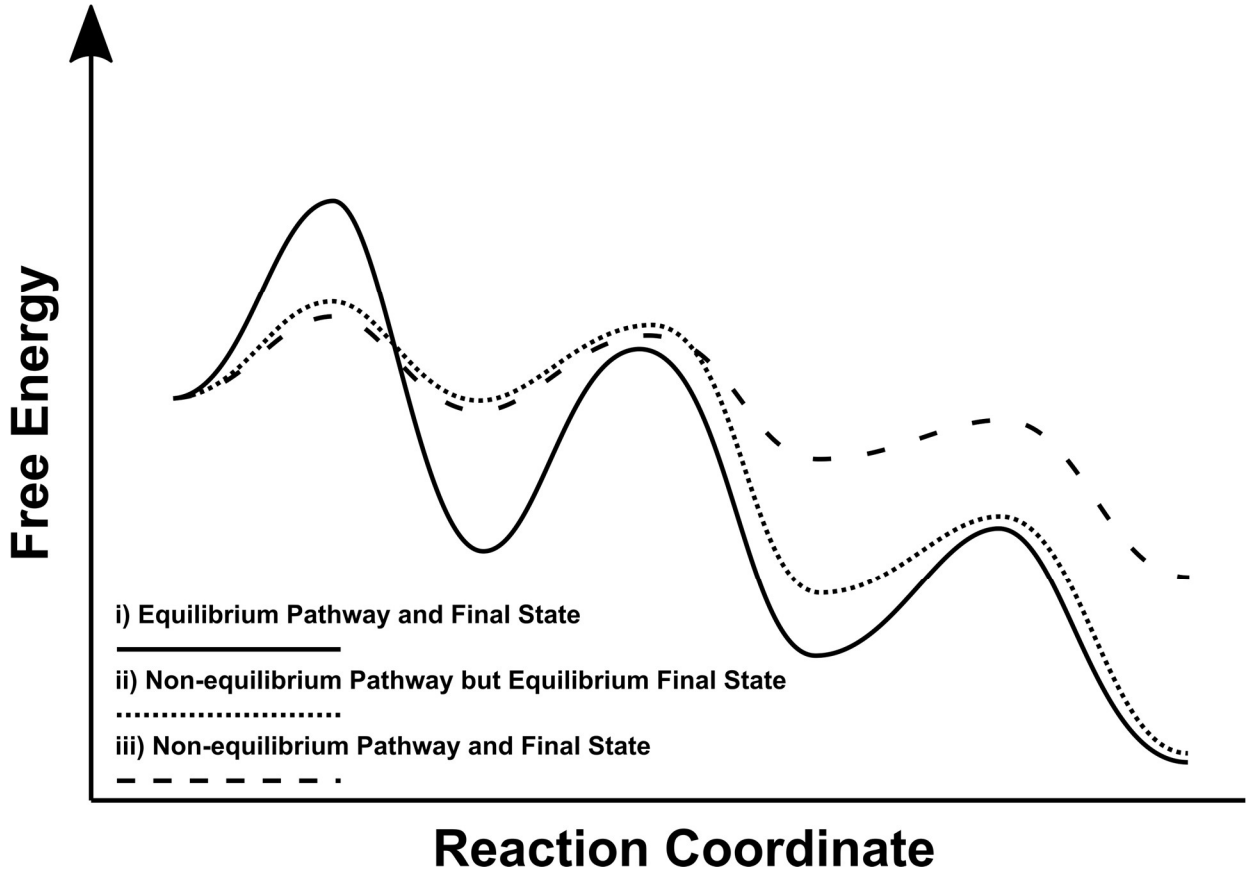

Figure 1.2: Simple theoretical pathway complexity in equilibrium and non-equilibrium assembly processes. (i) represents an equilibrium pathway (on-pathway) leading to an equilibrated state. (ii) represents a non-equilibrium pathway (off-pathway) that still leads to an equilibrium pathway. (iii) represents a non-equilibrium pathway that leads to a non-equilibrium end-state.

1.3. Thermodynamic Control

A thermodynamically controlled system is one in which the system reaches equilibrium or one in which an absolute free energy minimum is reached. In reaching a thermodynamic end state, the pathway is irrelevant as long as it leads to equilibrium as previously discussed (Figure 1.2). Therefore, control over a thermodynamic state involves changing the dimensions of self-assembly, such as switching the pH, increasing the temperature, or concentration and solvent composition. In a study by Stupp et al.,[14] the self-assembly of a peptide amphiphile was very sensitive to ionic strength. At low ionic strength the peptide amphiphiles assembled into short fibrils with random coil structure but at higher ionic strength, the fibrils were much longer and had an ordered beta-sheet structure. As shown in Figure 1.3, the circular dichroism (CD) signal at 202 nm was highly sensitive to both the salt and peptide amphiphile concentrations. These discrete changes are indicative of a thermodynamically controlled system where the end state is highly dependent on the phase space. In thermodynamic systems, monomer/unimer exchange must be able to readily occur. Here monomer is used for small molecule (supramolecular) systems and unimer for amphiphilic polymers and lipids. Following, the onset of self-assembly, the kinetics monomer/unimer exchange can be described through a sequence of association and dissociation steps of the building block.[7,15] Generally, simple and short building blocks such as those of small molecule amphiphiles including surfactants, lipids, and select supramolecular systems readily can exchange with each other.[1] As the

building blocks become larger and more complex, the likelihood that the resulting assemblies will adopt the lowest possible energy configuration decreases.[5,6,16]

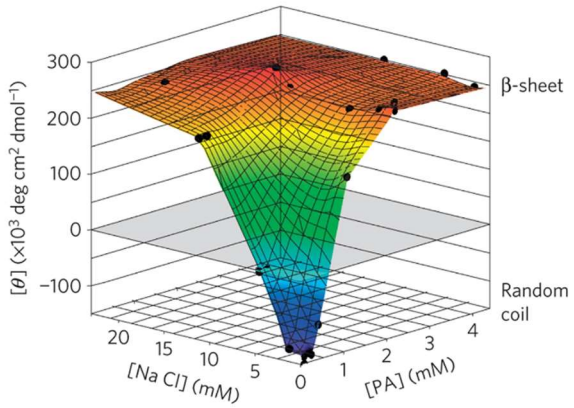

Figure 1.3: Circular Dichroism signal at 202 nm spectra plotted as a function of PA (peptide amphiphiles) and salt concentrations. Negative CD intensities denote a random coil structure; positive values correspond to a β-sheet signal. Reproduced from ref. 14 with permission from Springer Nature, copyright 2016.

Thermodynamic systems have proven to be useful. The dynamic nature of thermodynamic assemblies has allowed for the development of switchable assemblies where a trigger alters the energy landscape leading to a change in the assembly morphology.[17] These types of systems are needed in future materials development, but these systems often lack adaptability if the desired conditions change. Thermodynamic systems are programmed to match static conditions or at most a trigger. However, in real world conditions, the environmental conditions are always changing. For example, synthetic lipid assemblies typically exist under equilibrium conditions in an isolated vial. In contrast, cellular lipid membranes exist in non-equilibrium conditions from the constant removal and addition of lipids and proteins by the intracellular medium.[18] Therefore, we also need to turn our attention to more complex non-equilibrium systems in our quest to master molecular self-assembly to the extent nature has. Additionally, fundamental non-equilibrium systems present key advantages over their equilibrium counterparts. For example, kinetically controlled systems provide access to unique more ordered structures. And energy-driven, or dissipative systems are able to drive function

or change through the addition of energy (fuel, light, etc.) rather than through environmental alterations.

1.4. Kinetic control

Kinetic control is generally used to describe a final condition that is not at dynamic equilibrium. Kinetically-controlled systems exist in a non-equilibrium state but exhibit stable morphologies in contrast to dissipative systems which exist in a dynamic non-equilibrium or out-of-equilibrium state. Kinetically-controlled systems can either be classified as metastable or kinetically-trapped, where metastable systems will eventually move into an equilibrium state (the kinetics are slow) or kinetically-trapped where the energy barrier to equilibrium is too high to overcome.[4,7]

In contrast to thermodynamic control, a key feature of kinetically-controlled systems is that the free energy landscape is highly dependent on the pathway. Thus, different methods for preparing kinetically-controlled systems can yield different morphologies. Therefore, factors like the rate of solvent addition, mixing speed, presence of additives, among others affect the outcome. In this section, I will discuss factors of thermodynamic and kinetic control for both micellar and supramolecular systems.

1.4.1. Amphiphilic micellar self-assembly (lipids and block copolymers)

Amphiphilic molecules such as surfactants, lipids, and select block copolymers possess both a solvophillic corona-forming and solvophobic core-forming end. Under the proper conditions, these molecules prefer to aggregate, typically via nucleation and growth to lower the unfavorable interactions of the solvophobic core segment with the solvent.[19] Accounting for the free energy and the geometry, this type of self-assembly can generally be predicted by the critical packing parameter (CPP).[20–23]

$$CPP = \frac{V}{a_0 l_c}$$

Where V is the molecular volume, a_0 is the optimal surface area, and l_c is the critical chain length. Generally, self-assembly is thermodynamically-controlled from the presence of unimer exchange between the growing particle and solution, though other mechanisms allow exchange such as fission of a micelle or collision of two micelles.[5,15,20,24] Here, taking the CPP into account, lipid morphology can be tuned to obtain different structures.[25] Generally, a CPP of <1/3 favors spherical micelles, between 1/3 and ½ favors cylindrical micelles or worms, 0.5-1 favors bilayer vesicles, and >1 it favors inverse micelles (Figure 1.4).[25,26] These inverse micelles arrange in ordered liquid crystalline states. For amphiphilic block copolymers, the polymer-polymer interaction parameter (χ_{AB}) and the individual polymer-solvent interaction parameters χ_{AS} and χ_{BS} must also be taken into account.[27] These parameters, like CPP, are affected by relative volume fractions of each block, the solvophobicity, and the degree of polymerization of each block.[28] It should be noted that the CPP and the interaction parameters are based off a minimization of free energy and only account for structures at a thermodynamic equilibrium.

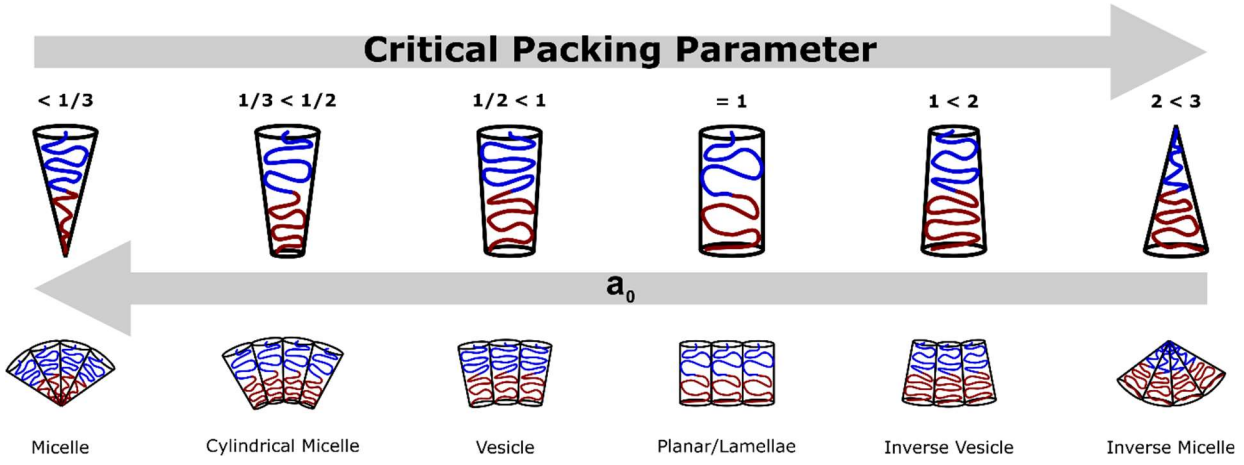

Figure 1.4: Values of critical packing parameter with the corresponding molecular shapes of the molecules and the structures they assemble into. The lines inside the shapes represent block copolymers with blue being the solvophilic block and red the solvophobic block. a_0 the optimal surface area decreases with increasing critical packing parameter.

Amphiphilic block copolymers, including blends, have a tendency to yield kinetically-controlled structures.[5,15,29–31] Polymer chains are prone to a high degree of entanglement which prevents them from adopting the most stable geometric configurations in accordance with the critical packing parameter. The energy barrier for unimer exchange is often too high due the limited chain mobility, particular at room temperature. [5,29,31] On the other hand, higher chain mobility is typically achieved in shorter chain polymers, polymers with low glass transition temperatures (T_g), and/or polymers with low solvophobicity of the core block.[5,19,29] For instance, in two studies, no unimer exchange was observed for two poly(styrene) based block copolymers at room temperature, while very slow exchange was found at 60 °C in shorter chain polymers (close to bulk T_g of polystyrene).[32,33] Therefore, to achieve thermodynamic control in block copolymer systems, factors that influence the free energy of the system such as polymer type and composition, concentration, nature of the solvent(s) and the presence of additives are employed.[34]

Kinetic considerations such as the preparation technique need to also be considered. Typical methods for the self-assembly of block copolymers include thin film hydration, direct dissolution, and solvent switch. In thin film hydration, a common solvent is used to dissolve polymer powders to make a thin film that is subsequently hydrated. In direct dissolution, a dry polymer is added to a selective solvent. In solvent switch, a polymer is dissolved in a common solvent and a selective solvent is added, triggering

self-assembly.[29] The latter preparation technique is arguably the most common.[5] In solvent switch the speed of water addition has been shown to affect the morphological outcome.[5,35,36]

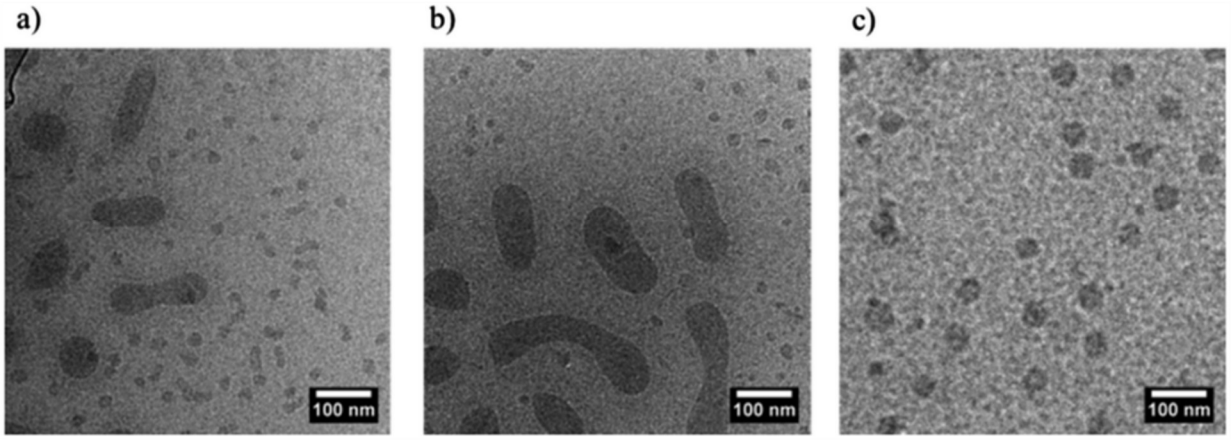

Figure 1.5: Cryo-TEM micrographs of P(EHA-co-DMA)-b-PDMA blends prepared by multiple preparation techniques: (A) Prepared by direct dissolution (B) Prepared by thin film rehydration (C) Prepared by solvent switch. The presence of different structures and sizes between the samples suggest that the pathway plays an important role in the morphological outcome. Reproduced from ref. 29 from the Royal Society of Chemistry, copyright 2016.

Experimentally, determining if a block copolymer system is under thermodynamic control is challenging. If variation of the preparation technique occurs and the structures change, it is a sign of kinetic control. In a study by Wright et. al.[29] a range of assembly conditions were probed for a blending method of block-random copolymers. Direct dissolution, thin film hydration, and solvent switch were all used in the assembly block-random poly(*N,N*- dimethyl acrylamide) based copolymers (P(EHA-co-DMA)-b-PDMA). All preparation techniques yielded different final states; evidence that unimer exchange was not fast enough at room temperature for this system (Figure 1.5). The resulting assemblies were then heated to 75 °C for 5 h and reanalyzed. All systems but the solvent switch method changed, indicating that in this particular case, the solvent switch method

operated under thermodynamic control. This example highlights the importance of preparation technique and temperature in the formation of non-equilibrium systems.

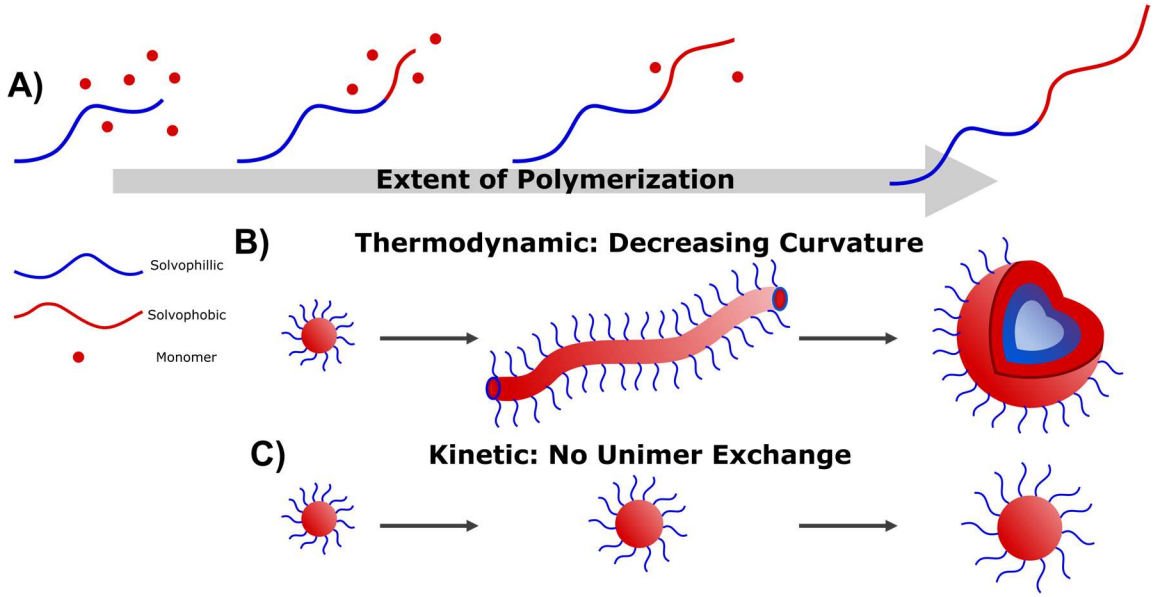

Figure 1.6: Polymerization-induced self-assembly (PISA). A) In PISA, a macro stabilizing block (blue) is chain-extended with monomer (red) to a fully formed block copolymer. B) Under thermodynamic control, as the polymer chain lengthens, assembly is triggered and may undergo phase transitions from spheres to worms to vesicles, corresponding with decreasing curvature. C) Under kinetic control, unimer exchange is arrested making morphological transitions highly unlikely. In these cases, micelles may increase in size, but morphology will not change.

1.4.2. Polymerization-induced self-assembly

The traditional methods of block copolymer self-assembly (solvent switch, etc.) are typically conducted in dilute solution conditions (<1 % w/w). In contrast, a newer technique coined polymerization-induced self-assembly (PISA) has been developed as an alternative route for the in situ scalable production of block copolymer nanoparticles at high concentrations (up to 50% w/w).[28,37–39] In PISA, the stabilizing block is chain extended with a monomer which will form the solvophobic block (Figure 1.6A). The monomer can either be soluble (dispersion PISA) or present in an emulsion (emulsion PISA). In PISA, control over polymer block length and concentration has afforded some control over the resulting morphology. Most examples of PISA have been developed from

reversible addition-fragmentation chain-transfer (RAFT) polymerization, however PISA has been developed for a wide variety of polymerization techniques,[39–43] including ring-opening polymerization,[44] which I will discuss in Chapters 2-5.

Notable examples of RAFT-PISA, such as the polymerization of 2-hydroxypropyl methacrylate (HPMA) using a water-soluble poly(glycerol monomethacrylate) (PGMA) shows the development of spheres to worms to vesicles corresponding with increasing PHPMA block length as the polymerization progresses.[45] Such evolution is said to follow a thermodynamic pathway as higher-ordered self-assemblies result from increasing degree of polymerization of the solvophobic block (Figure 1.6B). For PHPMA core block copolymers, the CCP is generally observed, indicating thermodynamic control.[38] However, it is both difficult to measure the CCP or difficult to accurately state if this pathway is the true thermodynamic pathway or some metastable analog. Conversely, if no particle evolution is observed as the chain length increases appreciably, the resulting assemblies are likely kinetically-trapped (Figure 1.6C). For example, in a PISA study by Yuan et. al.[46] the chain extension of poly(*N,N*-dimethylaminoethyl methacrylate) by the polymerization of benzyl methacrylate (BzMA) results in spherical morphology. However, this kinetic barrier is overcome through the copolymerization of BzMA with solvophilic 3-(triethoxysilyl)propyl methacrylate (TESPMA). Other factors of controlling morphology include switching from photoinitiated vs thermally initiated processes,[47,48] changes in initiator concentration,[49,50] solvent composition,[50,51] monomer types,[52] and Z-group substitution, in the case of RAFT-PISA.[53] In these cases, differences in morphology can be attributed to changes in the rate of polymerization, a kinetic effect. However, in each of these cases, thermodynamic parameters (phase space) are also modified making it

more difficult to discern the true effect polymerization rate has on morphological outcome. Luo et al.[47] compared photoinitiated and thermal initiated PISA using diacetone acrylamide monomer (DAAM) with a 3-(benzylthiocarbonothioylthio)propanoic acid, PDMA based macro-RAFT yielding [PDMA$_m$-PDAAM$_n$-BTPA]$_2$ block copolymers. Under identical temperatures, photoinitiation led to the production of spherical micelles whereas thermal initiation led to the production of vesicles (Figure 1.7). The primary reason for this observation is that the polymerization rate of photoinitiation was much faster. Faster polymerization likely leads to kinetically-trapped structures as unimer exchange is likely to be arrested at higher conversions than in a slower polymerization. However, in this case, the initiation mechanism between photoinitiation and thermal initiation are inherently different. In Chapter 3, I will introduce the first example of PISA that controls rates without environmental changes or changes to the polymer structure. Polymerization rate control has the potential to allow for a wide range of nanostructures to be produced from block copolymers with identical chemical structures.

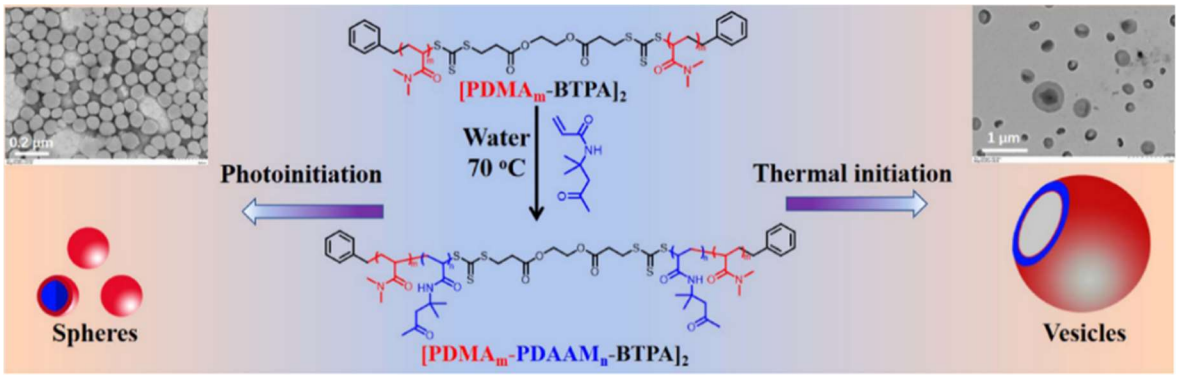

Figure 1.7: Scheme for the preparation of [PDMA$_m$-PDAAM$_n$-BTPA]$_2$ block copolymer assemblies by either photoinitiated PISA or thermally initiated PISA of DAAM in water at 70 °C with cryoEM insets showing spherical micelles for photoinitiated PISA and vesicles for thermal initiated PISA. Reproduced from ref. 47 with permission from American Chemical Society, copyright 2021.

1.4.3. Supramolecular polymers

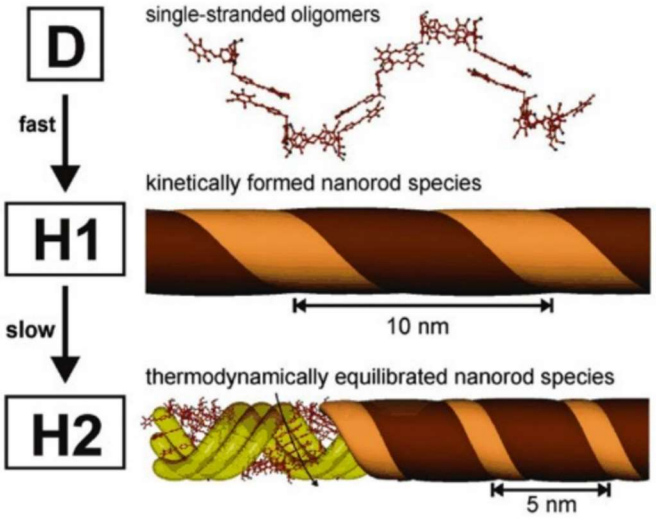

Figure 1.8: Schematic representation of self-assembly sequence involving simple supramolecular polymers **D** formed by the antiparallel aggregation of merocyanines, kinetically formed **H1** aggregates, and thermodynamically equilibrated **H2** aggregates, distinguished by their differing helical pitches. Reproduced from ref. 57 with permission from John Wiley and Sons [Israel Journal of Chemistry], copyright 2011.

Another polymerization process, like PISA, termed supramolecular polymerization can also lead to molecular self-assemblies. Supramolecular polymers consist of monomers bound together in a directional non-covalent fashion. Generally, supramolecular polymerization proceeds through thermodynamic control due to the strength of the interactions spontaneous and fast equilibration nature of intermolecular interactions used.[6,54,55] Kinetic control can be made possible through the use of strong or multiple non-covalent interactions. Kinetic control can also occur through the use of additives, poor solvents, external stimuli, etc.[6,7,54] In a study by Würthner et. al.[56,57] the addition of a poor solvent methylcyclohexane to a solution of bis(merocyanine) dye monomer (D) in a good solvent of tetrahydrofuran yielded two different nanorod products, distinguished by their different helical pitches (H1 and H2). Through increasing the amount of methylcyclohexane, the kinetic metastable product, H1, was trapped for days before reverting to the thermodynamic product, H2 (Figure 1.8).

Building off kinetic control is the development of chain growth supramolecular polymerization. Analogous to the polymerization of covalent polymers, supramolecular polymers typically either organize via an isodesmic (step-growth like) mechanism where all monomers are able to react with each other or a cooperative (chain-growth) mechanism where a chain is grown off an initiating species (Figure 1.9).[4,7,54] Cooperative growth is initiated through addition of small aggregate fragments or seeds as well as the addition of initiator.[54,55,58] If the growth solely proceeds through the active ends as in a chain growth manner, it can further be labelled as a living supramolecular polymerization. The occurrence of this mechanism leads to supramolecular polymers with low dispersity. In a seminal example of initiator-based living supramolecular polymerization, Aida et. al.[58] developed metastable corannulene-based chiral monomers with a shape-promoted intramolecular hydrogen bonding network promoting a cagelike conformation with low propensity for polymerization. Upon interacting with tailored corannulene-based initiators with an open structure, the cagelike structure is opened, able to react with another closed cagelike structure. Growth was only achieved through the growing chain end, thereby the process was truly living.

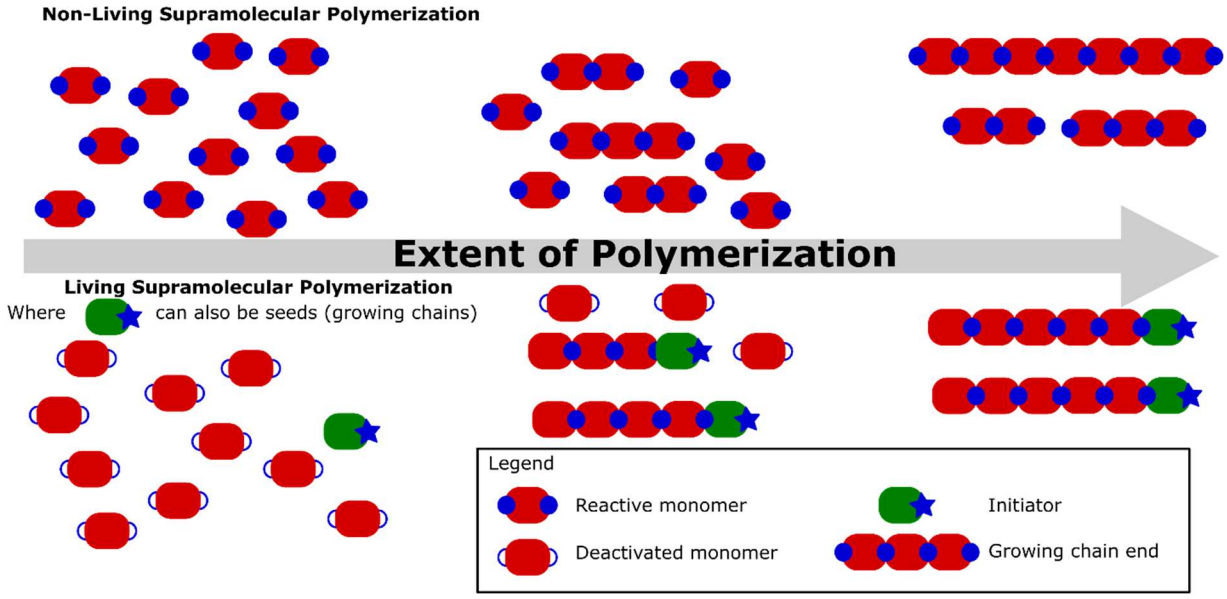

Figure 1.9: Simple depiction of non-living (top) and living supramolecular polymerization (bottom). Living supramolecular polymerization can occur from an initiator or from a seed. Living supramolecular polymerization yields polymers with lower dispersity due to the controlled growth. Furthermore, some polymerizations are kinetically controlled but are not living due to the presence of some uncontrolled growth. This would be depicted with a mixture of the two processes shown above.

1.4.4. Crystallization-driven self-assembly

Block copolymer self-assembly takes upon a new dimension if the core-forming block is crystalline or semi-crystalline. In this case, crystallization drives the self-assembly away from spheres to 1D cylindrical and 2D platelet structures.[59] This process, coined crystallization-driven self-assembly (CDSA) is a type of supramolecular polymerization where individual polymer unimers act as the monomer and the driving force is polymer crystallization.[54] CDSA can also be deemed "living" when growth is controlled, typically through seeding.[59,60] CDSA can be fairly complicated due to the various interrelated self-assembly parameters such as solvent interaction, crystallization temperature, rate of undercooling (when applicable), and often results in kinetically trapped structures.[59] With the core block achieving crystallinity or semi crystallinity in a confined environment, the barrier for unimer exchange becomes too high. Despite the final state of CDSA systems

being in a trapped state, the CDSA process can be altered to achieve different end states. The rate of crystallization can determine if the system resembles more kinetic control or thermodynamic control. In a living CDSA study by Manners et. al.[61] polyferrocenyldimethylsilane (PFDMS) based block copolymers either formed branched structures through rapid deposition and epitaxial crystallization or they formed linear structures under less rapid formation. The Manners group was also the first to develop a synchronous polymerization and crystallization process coined polymerization-induced crystallization-driven self-assembly (PI-CDSA),[41] of which more will be discussed in Chapter 2 with my development of a PI-CDSA for ring-opening polymerization.

1.5. Dissipative: Pumping of energy to sustain out-of-equilibrium process

Lastly, an assembly can be considered dissipative if an input of energy is necessary to be maintained. These systems can receive energy in the form of chemical fuel, light, or electricity.[7,8,62–77] As previously mentioned, a dissipative system is defined by the process rather than the end point as in thermodynamic and kinetic processes. Although dissipative systems are critical in living systems, only recently have we seen the development of synthetic dissipative self-assembly. And unlike the kinetic-systems, molecular dissipative self-assembly has largely been developed for supramolecular systems, although there are some exceptions.[78]

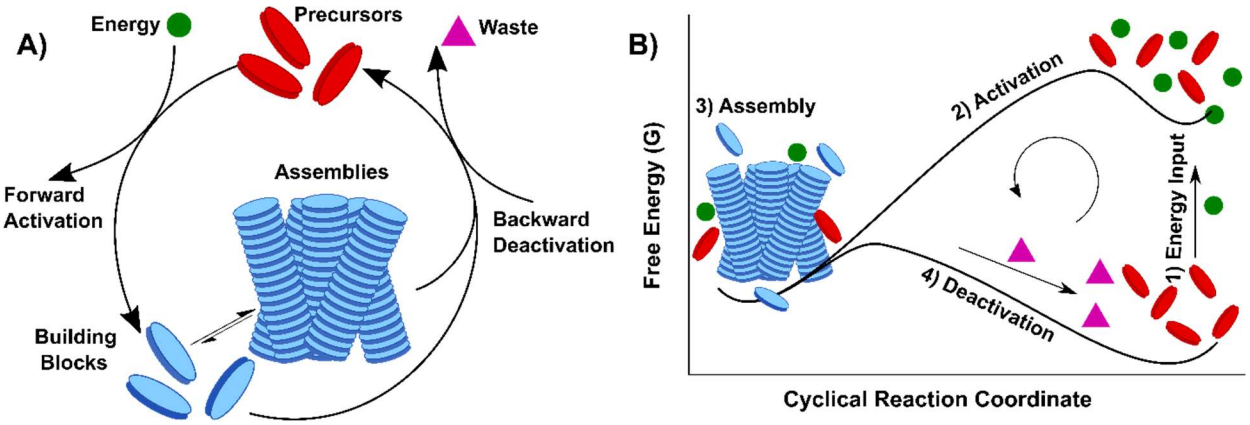

Figure 1.10: Dissipative self-assembly. A) Molecular dissipative self-assembly cyclic reaction scheme. B) Free energy cyclical reaction coordinate for a generic fuel-driven dissipative system. The steps are the order events occur although the event of activation, assembly, and deactivation continue until the energy is depleted. For a system to driven out-of-equilibrium, there must be an input of energy (chemical fuel, light, electricity, etc.).

1.5.1. Design of active material systems

In dissipative molecular self-assembly, at least two competing reactions are necessary to drive the formation of structure: a forward reaction assembling the precursor and a backward reaction dismantling it (Figure 1.10A).[9] From a chemical point of view, the precursor acts as a catalyst, catalyzing the conversion of fuel into waste products. In fact, the system is only out-of-equilibrium because of the input of chemical fuel (Figure 1.10B). Self-assembly is transient because when the energy dissipates, the system deactivates and disassembles. For the assembly to occur, the forward reaction is initially faster than the backward reaction to build up enough assembling species. As the fuel depletes, the backward reaction dominates, leading to disassembly. The system must have kinetic asymmetry where the forward reaction preferentially activates non-assembling precursors and the backward reaction preferentially deactivates the assembled or aggregated state.[11] This asymmetry allows for a high concentration of assembling species to build up allowing for dissipative assembly to occur. In addition to

kinetic asymmetry, active material systems must undergo a change in solubility when the precursor is activated, triggering assembly. This can either occur through a direct reaction between the precursor and the energy source or indirectly through the energy source creating an environment change (e.g. pH switch).[10]

These changes in solubility are ultimately related to a molecular change in the precursor. Based off this change, Boekhoven et. al.[9] characterized dissipative molecular self-assembly into three categories: 1) The chemical reaction cycle eliminates an electrostatic charge in the precursor. 2) The chemical reaction network forms a bond between two non-assembling building blocks. 3) The precursor undergoes a conformational change. Many different systems have been developed demonstrating these concepts. Elimination of electrostatic charge was among the first synthetic dissipative self-assembly systems developed. Boekhoven et. al.[63,64] developed a charge neutralizing system in which dibenzoyl L-cystine is activated through the methylation of one its two anionic carboxylate groups (Figure 1.11). Over time, the resulting esters hydrolyze reverting the dibenzoyl L-cystine back to its original state. Functional groups that easily change charge due to pH switches or some substitution reactions are commonly used in this strategy.

The second category of bond formation between two precursors generally leads to the removal of hydrogen bonding or favorable orientations that lead to self-assembly. In some cases, this change is due to dimerization, which then leads to assembly. For example, in a dissipative system developed by Guan et. al. that is fueled by either chemical energy[74] or electricity,[75,76] upon activation a cysteine-derivative (thiol) is oxidized and dimerizes into its cystine form (disulfide). Assembly can also be achieved

by using a fuel that is key to the assembly. Prins et. al.[65] developed a dissipative chemical reaction cycle fueled by ATP. Here, ATP is a fuel and an amphiphilic headgroup, forming a complex with three surfactant tails that results in vesicle formation.

Lastly, the last design category is to induce a conformational change that leads to self-assembly. Most of the reactions used in this category are photoisomerizations. For example, Sleiman et. al.[79] used an azobenzene derivative as a precursor which is able to photoisomerize from the thermodynamic trans conformation to the cis conformation upon exposure to UV light. In this and other examples,[79–81] the thermodynamically unfavored isomer must spontaneously isomerize back to the thermodynamically favorable state. Similar to these examples are dissipative liquid crystal systems. In a system developed by Takeda et. al.[82] noncovalent thin crystalline assemblies of oleic acid and azobenzene derivatives exhibited directional bending motion upon continuous exposure to blue light that is driven by trans to cis photoisomerization. Upon a buildup of cis isomer, the assemblies rearranged which ultimately led to a decrease in cis isomer from a change in photoisomerization quantum yield. This allowed for a buildup of trans isomer that reverted the system to its original state.

This chapter has only highlighted a small example of molecular dissipative systems. This field is still operating with minimal complexity. Future design of dissipative processes may include systems that produce fuel, possess multiple sources of energy, and have multiple dissipative cycles occurring. These systems would mirror biological reality better, but to aid designing more complex dissipative systems will require understanding the basic principles of dissipative assembly and making direct comparisons between dissipative and non-dissipative processes.

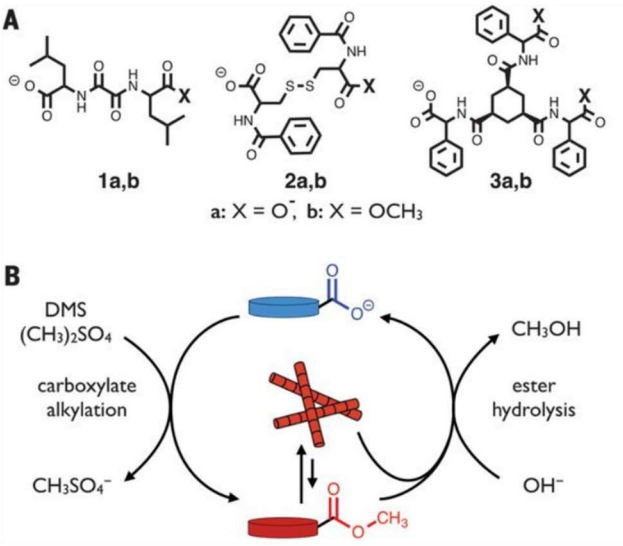

Figure 1.11: A) Chemical structures of tested molecular gelators **1**, **2**, and **3**. B) In a typical reaction cycle, carboxylate groups on the inactive self-assembling building blocks (**1a**, **2a**, and **3a**) react with the fuel, DMS, to produce methyl esters **1b**, **2b**, and **3b.** These activated building blocks self-assemble into fibrous structures. Methyl esters can hydrolyze both in the assembled and free states to revert to the original inactive building block. One full cycle produces CH_3OH (methanol) and $CH_3SO_4^-$ (MMS) as waste products. Reproduced from ref. 64 with permission from The American Association for the Advancement of Science, copyright 2015.

1.5.2. Principles of dissipative self-assembly

A central tenet of dissipative self-assembly is that fluxes of energy and material can form unique structures, with dynamic behaviors capable of useful functions.[10,74,83–86] Dissipative self-assembly of supramolecular structures dissipates both energy and matter through repeated execution of the assembly and disassembly reactions making the process out-of-equilibrium. These features allow for the ability to endow control over assembly. The control of energy over space and time can allow for responsive and adaptive materials. Temporal resolution can be achieved through altering fuel concentration and release. A greater challenge is achieving spatial resolution as it generally requires energy to be released to a localized area. Spatial resolution has been achievable both using light and electricity as energy sources. For example, when energized electrochemically, the aforementioned cysteine-derivate electrochemical redox system assembles by the electrode.[75,76] Therefore, careful design of the electrode and control of electrical input allows for a high degree of spatiotemporal resolution. The applicability of the current synthetic systems of dissipative molecular

assembly is very limited as the cyclical process is not linked to an adjacent process or function. Further development of molecular dissipative self-assembly should aim to transfer out-of-equilibrium self-assembly into work as done in biology.[77]

Theoretically, dissipative self-assembly systems should possess properties different from non-dissipative processes, enabling them to perform useful functions. However, few examples have been able to directly make comparisons between the two processes as it is difficult to decouple the forward and backward reaction, as one or more of the steps is often dependent on the solvent, or the fuel source participates in both the forward and backward reaction.[63,64] For example, Rizzuto et. al.[87] developed a supramolecular DNA fiber system where annealing by slow proton dissipation selects for morphologies otherwise inaccessible by conventional self-assembly. Comparison of the forward reaction to the coupled dissipative reaction was key to showing that a coupled process can lead to the formation of higher order structures, suggesting a coupled reaction is more dissipative than a sequential reaction. However, with this system, it was not possible to isolate the backward reaction from the dissipative process as the forward assembly reaction cannot be “turned off”. In Chapter 6 I will demonstrate a system I developed and studied with the help of collaborators, where we compare a dissipative process with a process in which the forward and backward reactions are performed sequentially. I will make comparisons between the two using time resolved cryoEM to show that the dissipative process forms and maintains unique structures when compared to the sequential process.

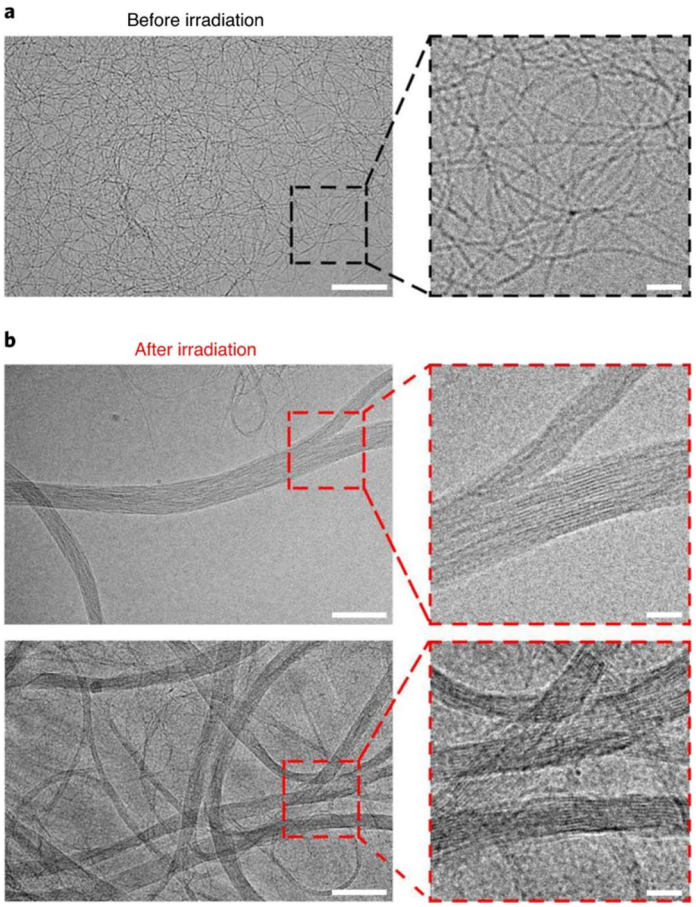

Figure 1.12: Cryo-EM images of supramolecular DNA fibers before and after proton dissipation. Representative micrographs of fibers (87) before proton dissipation (A), wherein fibers are observed to bundle, and after proton dissipation (B), wherein individual fibers are observed to aggregate parallel to one another, along the axis of fiber polymerization. Scale bars, 100 nm (left) and 25 nm (right). Reproduced from ref. 87 with permission from Springer Nature, copyright 2021.

1.6. Outlook

The thorough development of lipid self-assembly has allowed for the development of an increasing list of pharmaceutical interventions.[88] For example, lipid nanoparticles have been used in the delivery of chemotherapy, reducing side-effects and increasing efficacy. Recently, lipid nanoparticles have been used to encapsulate and thereby protect mRNA in the delivery of COVID spike protein mRNA. These advances have saved countless lives, but they only represent a small fraction of the possibilities of soft matter self-assembled materials. Lipid nanoparticles are generally at a thermodynamic equilibrium due to their small size and charge being both stable and at a minimum on the energy landscape. Block copolymers could soon replace or supplement lipid-based drug and RNA delivery.[89,90] These systems could show increased stability due to kinetic trapping and more synthetic variation. Supramolecular materials also represent a new class of materials that can be used in multiple applications ranging from optoelectronics to biomedical devices.[4,7] Additionally,

we need to expand our horizons beyond static systems into dissipative systems. We are currently at the frontiers of molecular dissipative self-assembly. Through new developments and mechanistic insight, dissipative systems will be engineered to perform adaptive functions. Unlocking these secrets will help us understand the origin of life,[91] allowing us to develop synthetic materials that mimic biology with excellent adaptability and unique function.

1.7. References

(1) Mattia, E.; Otto, S. Supramolecular Systems Chemistry. *Nature Nanotechnology* **2015**, *10* (2), 111–119. https://doi.org/10.1038/nnano.2014.337.

(1) Mattia, E.; Otto, S. Supramolecular Systems Chemistry. *Nat. Nanotechnol.* **2015**, *10* (2), 111–119. https://doi.org/10.1038/nnano.2014.337.

(2) Rizvi, A.; Mulvey, J. T.; Carpenter, B. P.; Talosig, R.; Patterson, J. P. A Close Look at Molecular Self-Assembly with the Transmission Electron Microscope. *Chem. Rev.* **2021**, *121* (22), 14232–14280. https://doi.org/10.1021/acs.chemrev.1c00189.

(3) Wu, H.; Ting, J. M.; Werba, O.; Meng, S.; Tirrell, M. V. Non-Equilibrium Phenomena and Kinetic Pathways in Self-Assembled Polyelectrolyte Complexes. *J. Chem. Phys.* **2018**, *149* (16), 163330. https://doi.org/10.1063/1.5039621.

(4) Matern, J.; Dorca, Y.; Sánchez, L.; Fernández, G. Revising Complex Supramolecular Polymerization under Kinetic and Thermodynamic Control. *Angew. Chem. Int. Ed.* **2019**, *58* (47), 16730–16740. https://doi.org/10.1002/anie.201905724.

(5) Mai, Y.; Eisenberg, A. Self-Assembly of Block Copolymers. *Chem. Soc. Rev.* **2012**, *41* (18), 5969–5985. https://doi.org/10.1039/C2CS35115C.

(6) Hendricks, M. P.; Sato, K.; Palmer, L. C.; Stupp, S. I. Supramolecular Assembly of Peptide Amphiphiles. *Acc. Chem. Res.* **2017**, *50* (10), 2440–2448. https://doi.org/10.1021/acs.accounts.7b00297.

(7) Sorrenti, A.; Leira-Iglesias, J.; J. Markvoort, A.; Greef, T. F. A. de; M. Hermans, T. Non-Equilibrium Supramolecular Polymerization. *Chem. Soc. Rev.* **2017**, *46* (18), 5476–5490. https://doi.org/10.1039/C7CS00121E.

(8) Tena-Solsona, M.; Rieß, B.; Grötsch, R. K.; Löhrer, F. C.; Wanzke, C.; Käsdorf, B.; Bausch, A. R.; Müller-Buschbaum, P.; Lieleg, O.; Boekhoven, J. Non-Equilibrium Dissipative Supramolecular Materials with a Tunable Lifetime. *Nat. Commun.* **2017**, *8* (1), 15895. https://doi.org/10.1038/ncomms15895.

(9) Rieß, B.; Grötsch, R. K.; Boekhoven, J. The Design of Dissipative Molecular Assemblies Driven by Chemical Reaction Cycles. *Chem* **2020**, *6* (3), 552–578. https://doi.org/10.1016/j.chempr.2019.11.008.

(10) Rossum, S. A. P. van; Tena-Solsona, M.; Esch, J. H. van; Eelkema, R.; Boekhoven, J. Dissipative Out-of-Equilibrium Assembly of Man-Made Supramolecular Materials. *Chem. Soc. Rev.* **2017**, *46* (18), 5519–5535. https://doi.org/10.1039/C7CS00246G.

(11) Ragazzon, G.; Prins, L. J. Energy Consumption in Chemical Fuel-Driven Self-Assembly. *Nat. Nanotechnol.* **2018**, *13* (10), 882–889. https://doi.org/10.1038/s41565-018-0250-8.

(12) Zhu, Q.; Tree, D. R. Simulations of Morphology Control of Self-Assembled Amphiphilic Surfactants. *J. Polym. Sci. n/a* (n/a). https://doi.org/10.1002/pol.20220771.

(13) Korevaar, P. A.; George, S. J.; Markvoort, A. J.; Smulders, M. M. J.; Hilbers, P. A. J.; Schenning, A. P. H. J.; De Greef, T. F. A.; Meijer, E. W. Pathway Complexity in Supramolecular Polymerization. *Nature* **2012**, *481* (7382), 492–496. https://doi.org/10.1038/nature10720.

(14) Tantakitti, F.; Boekhoven, J.; Wang, X.; Kazantsev, R. V.; Yu, T.; Li, J.; Zhuang, E.; Zandi, R.; Ortony, J. H.; Newcomb, C. J.; Palmer, L. C.; Shekhawat, G. S.; de la Cruz, M. O.; Schatz, G. C.; Stupp, S. I. Energy Landscapes and Functions of

Supramolecular Systems. *Nat. Mater.* **2016**, *15* (4), 469–476. https://doi.org/10.1038/nmat4538.
(15) Lodge, T. P.; Seitzinger, C. L.; Seeger, S. C.; Yang, S.; Gupta, S.; Dorfman, K. D. Dynamics and Equilibration Mechanisms in Block Copolymer Particles. *ACS Polym. Au* **2022**, *2* (6), 397–416. https://doi.org/10.1021/acspolymersau.2c00033.
(16) Yan, Y.; Huang, J.; Tang, B. Z. Kinetic Trapping – a Strategy for Directing the Self-Assembly of Unique Functional Nanostructures. *Chem. Commun.* **2016**, *52* (80), 11870–11884. https://doi.org/10.1039/C6CC03620A.
(17) Heinen, L.; Walther, A. Celebrating Soft Matter ’s 10th Anniversary: Approaches to Program the Time Domain of Self-Assemblies. *Soft Matter* **2015**, *11* (40), 7857–7866. https://doi.org/10.1039/C5SM01660F.
(18) Simons, K.; Vaz, W. L. C. Model Systems, Lipid Rafts, and Cell Membranes. *Annu. Rev. Biophys. Biomol. Struct.* **2004**, *33* (1), 269–295. https://doi.org/10.1146/annurev.biophys.32.110601.141803.
(19) Nicolai, T.; Colombani, O.; Chassenieux, C. Dynamic Polymeric Micelles versus Frozen Nanoparticles Formed by Block Copolymers. *Soft Matter* **2010**, *6* (14), 3111–3118. https://doi.org/10.1039/B925666K.
(20) Kobierski, J.; Wnętrzak, A.; Chachaj-Brekiesz, A.; Dynarowicz-Latka, P. Predicting the Packing Parameter for Lipids in Monolayers with the Use of Molecular Dynamics. *Colloids Surf. B Biointerfaces* **2022**, *211*, 112298. https://doi.org/10.1016/j.colsurfb.2021.112298.
(21) Israelachvili, J. N. *Intermolecular and Surface Forces*; Academic Press, 2011.
(22) Kumar, V. V. Complementary Molecular Shapes and Additivity of the Packing Parameter of Lipids. *Proc. Natl. Acad. Sci.* **1991**, *88* (2), 444–448. https://doi.org/10.1073/pnas.88.2.444.
(23) Israelachvili, J. N.; Mitchell, D. J.; Ninham, B. W. Theory of Self-Assembly of Lipid Bilayers and Vesicles. *Biochim. Biophys. Acta BBA - Biomembr.* **1977**, *470* (2), 185–201. https://doi.org/10.1016/0005-2736(77)90099-2.
(24) Hibino, M.; Takata, S.; Hiroi, K.; Aoki, H.; Terashima, T. Dynamic Exchange of Amphiphilic Random Copolymers between Micelles in Water: Kinetics and Mechanism Analyzed by TR-SANS. *Macromolecules* **2023**. https://doi.org/10.1021/acs.macromol.2c02408.
(25) Tan, A.; Hong, L.; Du, J. D.; Boyd, B. J. Self-Assembled Nanostructured Lipid Systems: Is There a Link between Structure and Cytotoxicity? *Adv. Sci.* **2019**, *6* (3), 1801223. https://doi.org/10.1002/advs.201801223.
(26) Mouritsen, O. G. Lipids, Curvature, and Nano-Medicine. *Eur. J. Lipid Sci. Technol.* **2011**, *113* (10), 1174–1187. https://doi.org/10.1002/ejlt.201100050.
(27) B. Doncom, K. E.; D. Blackman, L.; B. Wright, D.; I. Gibson, M.; K. O’Reilly, R. Dispersity Effects in Polymer Self-Assemblies: A Matter of Hierarchical Control. *Chem. Soc. Rev.* **2017**, *46* (14), 4119–4134. https://doi.org/10.1039/C6CS00818F.
(28) Karayianni, M.; Pispas, S. Block Copolymer Solution Self-Assembly: Recent Advances, Emerging Trends, and Applications. *J. Polym. Sci.* **2021**, *59* (17), 1874–1898. https://doi.org/10.1002/pol.20210430.
(29) B. Wright, D.; P. Patterson, J.; C. Gianneschi, N.; Chassenieux, C.; Colombani, O.; K. O’Reilly, R. Blending Block Copolymer Micelles in Solution; Obstacles of

Blending. *Polym. Chem.* **2016**, *7* (8), 1577–1583. https://doi.org/10.1039/C5PY02006A.
(30) Blanazs, A.; Ryan, A. J.; Armes, S. P. Predictive Phase Diagrams for RAFT Aqueous Dispersion Polymerization: Effect of Block Copolymer Composition, Molecular Weight, and Copolymer Concentration. *Macromolecules* **2012**, *45* (12), 5099–5107. https://doi.org/10.1021/ma301059r.
(31) Patterson, J. P.; Robin, M. P.; Chassenieux, C.; Colombani, O.; O'Reilly, R. K. The Analysis of Solution Self-Assembled Polymeric Nanomaterials. *Chem. Soc. Rev.* **2014**, *43* (8), 2412–2425. https://doi.org/10.1039/C3CS60454C.
(32) van Stam, J.; Creutz, S.; De Schryver, F. C.; Jérôme, R. Tuning of the Exchange Dynamics of Unimers between Block Copolymer Micelles with Temperature, Cosolvents, and Cosurfactants. *Macromolecules* **2000**, *33* (17), 6388–6395. https://doi.org/10.1021/ma992174a.
(33) Wang, Y.; Balaji, R.; Quirk, R. P.; Mattice, W. L. Detection of the Rate of Exchange of Chains between Micelles Formed by Diblock Copolymers in Aqueous Solution. *Polym. Bull.* **1992**, *28* (3), 333–338. https://doi.org/10.1007/BF00294831.
(34) Zhang, L.; Eisenberg, A. Multiple Morphologies and Characteristics of "Crew-Cut" Micelle-like Aggregates of Polystyrene-b-Poly(Acrylic Acid) Diblock Copolymers in Aqueous Solutions. *J. Am. Chem. Soc.* **1996**, *118* (13), 3168–3181. https://doi.org/10.1021/ja953709s.
(35) Zhang, L.; Eisenberg, A. Thermodynamic vs Kinetic Aspects in the Formation and Morphological Transitions of Crew-Cut Aggregates Produced by Self-Assembly of Polystyrene-b-Poly(Acrylic Acid) Block Copolymers in Dilute Solution. *Macromolecules* **1999**, *32* (7), 2239–2249. https://doi.org/10.1021/ma981039f.
(36) Shen, H.; Eisenberg, A. Morphological Phase Diagram for a Ternary System of Block Copolymer PS310-b-PAA52/Dioxane/H2O. *J. Phys. Chem. B* **1999**, *103* (44), 9473–9487. https://doi.org/10.1021/jp991365c.
(37) Canning, S. L.; Smith, G. N.; Armes, S. P. A Critical Appraisal of RAFT-Mediated Polymerization-Induced Self-Assembly. *Macromolecules* **2016**, *49* (6), 1985–2001. https://doi.org/10.1021/acs.macromol.5b02602.
(38) Warren, N. J.; Armes, S. P. Polymerization-Induced Self-Assembly of Block Copolymer Nano-Objects via RAFT Aqueous Dispersion Polymerization. *J. Am. Chem. Soc.* **2014**, *136* (29), 10174–10185. https://doi.org/10.1021/ja502843f.
(39) Penfold, N. J. W.; Yeow, J.; Boyer, C.; Armes, S. P. Emerging Trends in Polymerization-Induced Self-Assembly. *ACS Macro Lett.* **2019**, *8* (8), 1029–1054. https://doi.org/10.1021/acsmacrolett.9b00464.
(40) Varlas, S.; Foster, J. C.; O'Reilly, R. K. Ring-Opening Metathesis Polymerization-Induced Self-Assembly (ROMPISA). *Chem. Commun.* **2019**, *55* (62), 9066–9071. https://doi.org/10.1039/C9CC04445K.
(41) Boott, C. E.; Gwyther, J.; Harniman, R. L.; Hayward, D. W.; Manners, I. Scalable and Uniform 1D Nanoparticles by Synchronous Polymerization, Crystallization and Self-Assembly. *Nat. Chem.* **2017**, *9*, 785. https://doi.org/10.1038/nchem.2721.
(42) Grazon, C.; Salas-Ambrosio, P.; Ibarboure, E.; Buol, A.; Garanger, E.; Grinstaff, M. W.; Lecommandoux, S.; Bonduelle, C. Aqueous Ring-Opening Polymerization-Induced Self-Assembly (ROPISA) of N-Carboxyanhydrides. *Angew. Chem. Int. Ed.* **2020**, *59* (2), 622–626. https://doi.org/10.1002/anie.201912028.

(43) Cao, J.; Tan, Y.; Chen, Y.; Zhang, L.; Tan, J. Expanding the Scope of Polymerization-Induced Self-Assembly: Recent Advances and New Horizons. *Macromol. Rapid Commun.* **2021**, *42* (23), 2100498. https://doi.org/10.1002/marc.202100498.
(44) Hurst, P. J.; Rakowski, A. M.; Patterson, J. P. Ring-Opening Polymerization-Induced Crystallization-Driven Self-Assembly of Poly-L-Lactide-Block-Polyethylene Glycol Block Copolymers (ROPI-CDSA). *Nat. Commun.* **2020**, *11* (1), 4690. https://doi.org/10.1038/s41467-020-18460-2.
(45) Blanazs, A.; Madsen, J.; Battaglia, G.; Ryan, A. J.; Armes, S. P. Mechanistic Insights for Block Copolymer Morphologies: How Do Worms Form Vesicles? *J. Am. Chem. Soc.* **2011**, *133* (41), 16581–16587. https://doi.org/10.1021/ja206301a.
(46) Li, D.; Huo, M.; Liu, L.; Zeng, M.; Chen, X.; Wang, X.; Yuan, J. Overcoming Kinetic Trapping for Morphology Evolution during Polymerization-Induced Self-Assembly. *Macromol. Rapid Commun.* **2019**, *40* (16), 1900202. https://doi.org/10.1002/marc.201900202.
(47) Luo, X.; Zhao, S.; Chen, Y.; Zhang, L.; Tan, J. Switching between Thermal Initiation and Photoinitiation Redirects RAFT-Mediated Polymerization-Induced Self-Assembly. *Macromolecules* **2021**, *54* (6), 2948–2959. https://doi.org/10.1021/acs.macromol.1c00038.
(48) Blackman, L. D.; Doncom, K. E. B.; Gibson, M. I.; O'Reilly, R. K. Comparison of Photo- and Thermally Initiated Polymerization-Induced Self-Assembly: A Lack of End Group Fidelity Drives the Formation of Higher Order Morphologies. *Polym. Chem.* **2017**, *8* (18), 2860–2871. https://doi.org/10.1039/C7PY00407A.
(49) D'Agosto, F.; Rieger, J.; Lansalot, M. RAFT-Mediated Polymerization-Induced Self-Assembly. *Angew. Chem. Int. Ed.* **2020**, *59* (22), 8368–8392. https://doi.org/10.1002/anie.201911758.
(50) Khor, S. Y.; Quinn, J. F.; Whittaker, M. R.; Truong, N. P.; Davis, T. P. Controlling Nanomaterial Size and Shape for Biomedical Applications via Polymerization-Induced Self-Assembly. *Macromol Rapid Commun* **2019**, *40* (2), e1800438. https://doi.org/10.1002/marc.201800438.
(51) R. Jones, E.; Semsarilar, M.; Wyman, P.; Boerakker, M.; P. Armes, S. Addition of Water to an Alcoholic RAFT PISA Formulation Leads to Faster Kinetics but Limits the Evolution of Copolymer Morphology. *Polym. Chem.* **2016**, *7* (4), 851–859. https://doi.org/10.1039/C5PY01795E.
(52) Hwang, S.-H.; Kang, S.-Y.; Yang, S.; Lee, J.; Choi, T.-L. Synchronous Preparation of Length-Controllable 1D Nanoparticles via Crystallization-Driven In Situ Nanoparticlization of Conjugated Polymers. *J. Am. Chem. Soc.* **2022**, *144* (13), 5921–5929. https://doi.org/10.1021/jacs.1c13385.
(53) R. Guimarães, T.; Loong Bong, Y.; W. Thompson, S.; Moad, G.; Perrier, S.; B. Zetterlund, P. Polymerization-Induced Self-Assembly via RAFT in Emulsion: Effect of Z-Group on the Nucleation Step. *Polym. Chem.* **2021**, *12* (1), 122–133. https://doi.org/10.1039/D0PY01311K.
(54) Wehner, M.; Würthner, F. Supramolecular Polymerization through Kinetic Pathway Control and Living Chain Growth. *Nat. Rev. Chem.* **2020**, *4* (1), 38–53. https://doi.org/10.1038/s41570-019-0153-8.

(55) Ogi, S.; Sugiyasu, K.; Manna, S.; Samitsu, S.; Takeuchi, M. Living Supramolecular Polymerization Realized through a Biomimetic Approach. *Nat. Chem.* **2014**, *6* (3), 188–195. https://doi.org/10.1038/nchem.1849.
(56) Lohr, A.; Lysetska, M.; Würthner, F. Supramolecular Stereomutation in Kinetic and Thermodynamic Self-Assembly of Helical Merocyanine Dye Nanorods. *Angew. Chem. Int. Ed.* **2005**, *44* (32), 5071–5074. https://doi.org/10.1002/anie.200500640.
(57) Lohr, A.; Würthner, F. Chiral Amplification, Kinetic Pathways, and Morphogenesis of Helical Nanorods upon Self-Assembly of Dipolar Merocyanine Dyes. *Isr. J. Chem.* **2011**, *51* (10), 1052–1066. https://doi.org/10.1002/ijch.201100023.
(58) Kang, J.; Miyajima, D.; Mori, T.; Inoue, Y.; Itoh, Y.; Aida, T. A Rational Strategy for the Realization of Chain-Growth Supramolecular Polymerization. *Science* **2015**, *347* (6222), 646–651. https://doi.org/10.1126/science.aaa4249.
(59) Ganda, S.; Stenzel, M. H. Concepts, Fabrication Methods and Applications of Living Crystallization-Driven Self-Assembly of Block Copolymers. *Prog. Polym. Sci.* **2020**, *101*, 101195. https://doi.org/10.1016/j.progpolymsci.2019.101195.
(60) MacFarlane, L.; Zhao, C.; Cai, J.; Qiu, H.; Manners, I. Emerging Applications for Living Crystallization-Driven Self-Assembly. *Chem. Sci.* **2021**, *12* (13), 4661–4682. https://doi.org/10.1039/D0SC06878K.
(61) Qiu, H.; Gao, Y.; Du, V. A.; Harniman, R.; Winnik, M. A.; Manners, I. Branched Micelles by Living Crystallization-Driven Block Copolymer Self-Assembly under Kinetic Control. *J. Am. Chem. Soc.* **2015**, *137* (6), 2375–2385. https://doi.org/10.1021/ja5126808.
(62) te Brinke, E.; Groen, J.; Herrmann, A.; Heus, H. A.; Rivas, G.; Spruijt, E.; Huck, W. T. S. Dissipative Adaptation in Driven Self-Assembly Leading to Self-Dividing Fibrils. *Nat. Nanotechnol.* **2018**, *13* (9), 849–855. https://doi.org/10.1038/s41565-018-0192-1.
(63) Boekhoven, J.; Brizard, A. M.; Kowlgi, K. N. K.; Koper, G. J. M.; Eelkema, R.; van Esch, J. H. Dissipative Self-Assembly of a Molecular Gelator by Using a Chemical Fuel. *Angew. Chem. Int. Ed.* **2010**, *49* (28), 4825–4828. https://doi.org/10.1002/anie.201001511.
(64) Boekhoven, J.; Hendriksen, W. E.; Koper, G. J. M.; Eelkema, R.; van Esch, J. H. Transient Assembly of Active Materials Fueled by a Chemical Reaction. *Science* **2015**, *349* (6252), 1075. https://doi.org/10.1126/science.aac6103.
(65) Maiti, S.; Fortunati, I.; Ferrante, C.; Scrimin, P.; Prins, L. J. Dissipative Self-Assembly of Vesicular Nanoreactors. *Nat. Chem.* **2016**, *8* (7), 725–731. https://doi.org/10.1038/nchem.2511.
(66) Pezzato, C.; Prins, L. J. Transient Signal Generation in a Self-Assembled Nanosystem Fueled by ATP. *Nat. Commun.* **2015**, *6* (1), 7790. https://doi.org/10.1038/ncomms8790.
(67) Dhiman, S.; Jain, A.; George, S. J. Transient Helicity: Fuel-Driven Temporal Control over Conformational Switching in a Supramolecular Polymer. *Angew. Chem. Int. Ed.* **2017**, *56* (5), 1329–1333. https://doi.org/10.1002/anie.201610946.
(68) Dhiman, S.; Jain, A.; Kumar, M.; George, S. J. Adenosine-Phosphate-Fueled, Temporally Programmed Supramolecular Polymers with Multiple Transient States. *J. Am. Chem. Soc.* **2017**, *139* (46), 16568–16575. https://doi.org/10.1021/jacs.7b07469.

(69) Sorrenti, A.; Leira-Iglesias, J.; Sato, A.; Hermans, T. M. Non-Equilibrium Steady States in Supramolecular Polymerization. *Nat. Commun.* **2017**, *8* (1), 15899. https://doi.org/10.1038/ncomms15899.
(70) della Sala, F.; Maiti, S.; Bonanni, A.; Scrimin, P.; Prins, L. J. Fuel-Selective Transient Activation of Nanosystems for Signal Generation. *Angew. Chem. Int. Ed.* **2018**, *57* (6), 1611–1615. https://doi.org/10.1002/anie.201711964.
(71) Mishra, A.; Korlepara, D. B.; Kumar, M.; Jain, A.; Jonnalagadda, N.; Bejagam, K. K.; Balasubramanian, S.; George, S. J. Biomimetic Temporal Self-Assembly via Fuel-Driven Controlled Supramolecular Polymerization. *Nat. Commun.* **2018**, *9* (1), 1295. https://doi.org/10.1038/s41467-018-03542-z.
(72) Pappas, C. G.; Sasselli, I. R.; Ulijn, R. V. Biocatalytic Pathway Selection in Transient Tripeptide Nanostructures. *Angew. Chem. Int. Ed.* **2015**, *54* (28), 8119–8123. https://doi.org/10.1002/anie.201500867.
(73) De, S.; Klajn, R. Dissipative Self-Assembly Driven by the Consumption of Chemical Fuels. *Adv. Mater.* **2018**, *30* (41), 1706750. https://doi.org/10.1002/adma.201706750.
(74) Ogden, W. A.; Guan, Z. Redox Chemical-Fueled Dissipative Self-Assembly of Active Materials. *ChemSystemsChem* **2020**, *2* (4), e1900030. https://doi.org/10.1002/syst.201900030.
(75) Selmani, S.; Schwartz, E.; Mulvey, J. T.; Wei, H.; Grosvirt-Dramen, A.; Gibson, W.; Hochbaum, A. I.; Patterson, J. P.; Ragan, R.; Guan, Z. Electrically Fueled Active Supramolecular Materials. *J. Am. Chem. Soc.* **2022**, *144* (17), 7844–7851. https://doi.org/10.1021/jacs.2c01884.
(76) Barpuzary, D.; Hurst, P. J.; Patterson, J. P.; Guan, Z. Waste-Free Fully Electrically Fueled Dissipative Self-Assembly System. *J. Am. Chem. Soc.* **2023**, *145* (6), 3727–3735. https://doi.org/10.1021/jacs.2c13140.
(77) Weißenfels, M.; Gemen, J.; Klajn, R. Dissipative Self-Assembly: Fueling with Chemicals versus Light. *Chem* **2021**, *7* (1), 23–37. https://doi.org/10.1016/j.chempr.2020.11.025.
(78) Li, X.; Wang, G.; Zhang, Q.; Liu, Y.; Sun, T.; Liu, S. Dissipative Self-Assembly of a Dual-Responsive Block Copolymer Driven by a Chemical Oscillator. *J. Colloid Interface Sci.* **2022**, *615*, 732–739. https://doi.org/10.1016/j.jcis.2022.01.183.
(79) Rakotondradany, F.; Whitehead, M. A.; Lebuis, A.-M.; Sleiman, H. F. Photoresponsive Supramolecular Systems: Self-Assembly of Azodibenzoic Acid Linear Tapes and Cyclic Tetramers. *Chem. – Eur. J.* **2003**, *9* (19), 4771–4780. https://doi.org/10.1002/chem.200304864.
(80) Jalani, K.; Dhiman, S.; Jain, A.; J. George, S. Temporal Switching of an Amphiphilic Self-Assembly by a Chemical Fuel-Driven Conformational Response. *Chem. Sci.* **2017**, *8* (9), 6030–6036. https://doi.org/10.1039/C7SC01730H.
(81) Fredy, J. W.; Méndez-Ardoy, A.; Kwangmettatam, S.; Bochicchio, D.; Matt, B.; Stuart, M. C. A.; Huskens, J.; Katsonis, N.; Pavan, G. M.; Kudernac, T. Molecular Photoswitches Mediating the Strain-Driven Disassembly of Supramolecular Tubules. *Proc. Natl. Acad. Sci.* **2017**, *114* (45), 11850–11855. https://doi.org/10.1073/pnas.1711184114.
(82) Ikegami, T.; Kageyama, Y.; Obara, K.; Takeda, S. Dissipative and Autonomous Square-Wave Self-Oscillation of a Macroscopic Hybrid Self-Assembly under

Continuous Light Irradiation. *Angew. Chem.* **2016**, *128* (29), 8379–8383. https://doi.org/10.1002/ange.201600218.
(83) Kondepudi, D. K.; De Bari, B.; Dixon, J. A. Dissipative Structures, Organisms and Evolution. *Entropy* **2020**, *22* (11), 1305. https://doi.org/10.3390/e22111305.
(84) Qin, B.; Yin, Z.; Tang, X.; Zhang, S.; Wu, Y.; Xu, J.-F.; Zhang, X. Supramolecular Polymer Chemistry: From Structural Control to Functional Assembly. *Prog. Polym. Sci.* **2020**, *100*, 101167. https://doi.org/10.1016/j.progpolymsci.2019.101167.
(85) Tagliazucchi, M.; Weiss, E. A.; Szleifer, I. Dissipative Self-Assembly of Particles Interacting through Time-Oscillatory Potentials. *Proc. Natl. Acad. Sci.* **2014**, *111* (27), 9751–9756. https://doi.org/10.1073/pnas.1406122111.
(86) Arango-Restrepo, A.; Rubi, J. M.; Barragán, D. The Role of Energy and Matter Dissipation in Determining the Architecture of Self-Assembled Structures. *J. Phys. Chem. B* **2019**, *123* (27), 5902–5908. https://doi.org/10.1021/acs.jpcb.9b02928.
(87) Rizzuto, F. J.; Platnich, C. M.; Luo, X.; Shen, Y.; Dore, M. D.; Lachance-Brais, C.; Guarné, A.; Cosa, G.; Sleiman, H. F. A Dissipative Pathway for the Structural Evolution of DNA Fibres. *Nat. Chem.* **2021**. https://doi.org/10.1038/s41557-021-00751-w.
(88) Xu, L.; Wang, X.; Liu, Y.; Yang, G.; Falconer, R. J.; Zhao, C.-X. Lipid Nanoparticles for Drug Delivery. *Adv. NanoBiomed Res.* **2022**, *2* (2), 2100109. https://doi.org/10.1002/anbr.202100109.
(89) McKinlay, C. J.; Vargas, J. R.; Blake, T. R.; Hardy, J. W.; Kanada, M.; Contag, C. H.; Wender, P. A.; Waymouth, R. M. Charge-Altering Releasable Transporters (CARTs) for the Delivery and Release of MRNA in Living Animals. *Proc. Natl. Acad. Sci.* **2017**, *114* (4), E448–E456. https://doi.org/10.1073/pnas.1614193114.
(90) Phan, H.; Cossutta, M.; Houppe, C.; Le Cœur, C.; Prevost, S.; Cascone, I.; Courty, J.; Penelle, J.; Couturaud, B. Polymerization-Induced Self-Assembly (PISA) for in Situ Drug Encapsulation or Drug Conjugation in Cancer Application. *J. Colloid Interface Sci.* **2022**, *618*, 173–184. https://doi.org/10.1016/j.jcis.2022.03.044.
(91) Cafferty, B. J.; Wong, A. S. Y.; Semenov, S. N.; Belding, L.; Gmür, S.; Huck, W. T. S.; Whitesides, G. M. Robustness, Entrainment, and Hybridization in Dissipative Molecular Networks, and the Origin of Life. *J. Am. Chem. Soc.* **2019**, *141* (20), 8289–8295. https://doi.org/10.1021/jacs.9b02554.

Chapter 2: The initial development of ring-opening polymerization-induced crystallization-driven self-assembly (ROPI-CDSA)

This chapter is adapted from a research article “Ring-opening polymerization-induced crystallization-driven self-assembly of poly-L-lactide-block-polyethylene glycol block copolymers (ROPI-CDSA). Paul J Hurst, Alexander M Rakowski, Joseph P Patterson, Nat. Comm. 2020, 11 [1] 4690.”

2.0. Abstract

The self-assembly of block copolymers into 1D, 2D and 3D nano- and microstructures is of great interest for a wide range of applications. A key challenge in this field is obtaining independent control over molecular structure and hierarchical structure in all dimensions using scalable one-pot chemistry. The development of ring opening polymerization-induced crystallization-driven self-assembly (ROPI-CDSA) of poly-L-lactide-*block*-polyethylene glycol block copolymers into 1D, 2D and 3D nanostructures addresses this challenge. A key feature of ROPI-CDSA is that the polymerization time is much shorter than the self-assembly relaxation time, resulting in a non-equilibrium self-assembly process. The self-assembly mechanism is analyzed by cryo-transmission electron microscopy, wide-angle x-ray scattering, Fourier transform infrared spectroscopy, and turbidity studies. The analysis revealed that the self-assembly mechanism is dependent on both the polymer molecular structure and concentration. Knowledge of the self-assembly mechanism enabled the kinetic trapping of multiple hierarchical structures from a single block copolymer. The work in this chapter guides the development of subsequent ROPI-CDSA processes.

2.1. Introduction

Self-assembly of block copolymers (BCP) in solution has received significant interest in the areas of drug delivery, medical imaging, catalysis, and templated synthesis.[1, 2] The properties and performance of these materials are intrinsically linked to both their molecular and hierarchical structure.[3] Consequently, research in this area has been focused on providing a fundamental understanding of how the molecular structure and assembly environment can be tailored to control the hierarchical assembly process.[4] Without the input of external energy, self-assembly processes can be either thermodynamically or kinetically controlled.[5, 6] Thermodynamically controlled processes will adopt the hierarchical structure with the lowest free energy regardless of the starting conformation of the BCPs. Thermodynamically controlled processes tend to result in predictable and well-defined structures. However, their application is limited by their sensitivity to changes in the environment, which can significantly alter the formed structures.[7, 8] Kinetically controlled processes tend to result in stable structures, but the final structures can be highly sensitive to the assembly method.[5, 7, 9] While the final structural dependence on assembly methodology offers the flexibility to form multiple hierarchical structures from a single BCP, it necessitates strict control of the synthetic conditions.[3, 7, 10]

Typically, BCP self-assembly is achieved via direct dissolution, solvent-switch, and thin-film hydration methods.[11-13] However, with these methods it is challenging to control the formation of anisotropic structures, they involve multi-step processes that are difficult to scale up reproducibly, and result in low concentration BCP solutions (typically ≤1% solids w/w).[14-16] To address these challenges, crystallization-driven self-assembly (CDSA) and polymerization-induced self-assembly (PISA) have emerged as promising

alternatives. CDSA utilizes BCPs with a semi-crystalline core-forming block to form anisotropic 1D and 2D structures with high precision, where crystallization of the BCP core is the dominant driving force of self-assembly.[17-23] Whereas amorphous BCPs typically assemble into spheres, worms, and vesicles,[14, 24] crystalline BCPs will typically result in morphologies with low curvature such as 2D platelet lamellae or 1D nanorods,[15] which introduces anisotropy to the system. In CDSA, the insoluble block is typically crystallized by dissolving the polymer in a selective solvent to facilitate/induce crystallization,[18, 24] often utilizing heat-cool cycles to control the crystallization process.[15, 23, 24] However, as with traditional self-assembly methods, CDSA typically occurs in dilute solutions (~1% solids w/w).[14, 20, 24] The PISA method utilizes controlled polymer chemistry to generate the BCP directly in the selective solvent system.[11, 13, 14, 25-27] Conceptually, a homopolymer is chain-extended with a co-monomer and as the core-forming block grows it becomes increasingly insoluble, triggering self-assembly of the BCP. PISA is a scalable method that affords control over the BCP structure at high concentrations (10-50% solids w/w).[14, 25, 28-30] To date, most PISA processes have been reversible-deactivation radical polymerizations (RDRP),[1, 2, 11, 14] primarily reversible addition-fragmentation chain-transfer polymerization (RAFT-PISA).[11, 14, 31-33] However, PISA can theoretically be extended to all types of living polymerizations and has been demonstrated with living anionic polymerization,[34] ring-opening metathesis (ROMP) of norbornenes,[13, 29] radical ring-opening copolymerization (rROP) of cyclic ketenes,[35] and ring-opening polymerization (ROP) of N-carboxyanhydrides.[36] PISA has also been combined with CDSA, termed polymerization-induced crystallization-driven self-assembly (PI-CDSA), to generate crystalline self-assemblies in high concentrations (10-25% solids w/w).[15, 16, 37]

Currently PI-CDSA has been demonstrated for sequential living anionic polymerization,[15, 16] and the ring-opening metathesis of organometallic polymers.[37] Polylactones, being semi-crystalline in nature, are excellent candidates for the development of a fully organic PI-CDSA to produce biocompatible, biodegradable BCP materials at high concentration in a scalable process. Polylactones, including poly(L-lactide) (PLLA) are the most widely known class of sustainable polymers,[38] and are incorporated into multiple FDA-approved formulas.[39-41] To date, ROP is the only controlled method to synthesize polylactone-based BCPs.[2, 28] Thus, the development of a ring-opening PI-CDSA (ROPI-CDSA), would address the production limitations of polylactone-based crystalline-nanoparticles facilitating their use commercially.

The absence of ring-opening PI-CDSA of lactones is likely due to the stringent requirements for ROP reactions and the limited monomer/polymer/solvent combinations available.[38, 42, 43] Foremost, ROP of lactones cannot occur in protic solvents, as these solvents would compete with initiation species. However, some aprotic organic solvents, including aromatics like toluene, have induced crystallization in PLLA at room temperature.[44] Here, the work in this chapter details the development of ring opening PI-CDSA of poly-(L-lactide)-*block*-polyethylene glycol (PLLA-*b*-PEG) BCPs in toluene. Kinetics studies of the polymerization and self-assembly show that ROPI-CDSA results in a non-equilibrium assembly process. Structural and morphological evolution of self-assembly is tracked with cryogenic transmission electron microscopy (cryo-TEM), wide-angle X-ray scattering (WAXS), UV/Vis spectroscopy, and Fourier transform infrared (FTIR) spectroscopy, revealing a hierarchical (1D → 2D → 3D) growth mechanism. The data reveals that the assembly process and the final meta-stable structures can be

controlled by alterations in both BCP molecular structure and concentration. Knowledge of the mechanism enables the trapping of materials with different structures and dimensionalities.

2.2. Experimental Section

Materials: $mPEG_{45}$ (MW = 2000) (Sigma Aldrich) was azeotropically distilled x2 in toluene and high-vacuumed overnight. L-lactide (TCI) was recrystallized in toluene x3. Anhydrous toluene (99.8%), and triazabicyclodecene (TBD) were purchased from Sigma Aldrich and were used without further purification. Benzoic acid (Fisher Chemical) was used without further purification. Milli-Q water (ρ> 18 MΩ cm) was used as the solvent for all aqueous solutions. Chemicals were stored in a dry-N_2 atmosphere glove box. Reactions were performed in a N_2 glove box.

PLLA-*b*-PEG synthesis and self-assembly: Procedure adapted from Waymouth et. al.[42] L-lactide (64.9 mg, 0.45 mmol, PLLA target DP = 45) was added to a solution of $mPEG_{45}$ (40mg, 20 μmol) in 1.08 mL of toluene (10% solids w/w). 15 μL (0.1% mol) TBD from a toluene stock solution (4.3 mg/mL) was then added. The solution was stirred for 90 seconds and subsequently quenched with 0.05 mL benzoic acid stock solution (100 mg/mL). Thr rate of stirring appeared to influence the self-assembly kinetics and therefore stirring was kept at 400 rpm for reproducibility (For full results see Table A.1, for additional synthetic information see Table A.2). ^{1}H NMR (500 MHz, $CDCl_3$) δ 5.16 (q, *J* = 7.0 Hz, CH, PLLA backbone), 5.03 (q, *J* = 6.7 Hz, CH L-lactide), 3.72 – 3.59 (m, CH_2 PEG backbone), 3.54 (dd, *J* = 5.6, 3.6 Hz, CH_2, PEG), 3.37 (s, 3H, terminal CH_3 PEG), 1.67 (dd, *J* = 6.7, 1.5 Hz, CH_3 L-lactide), 1.58 (d, *J* = 6.7 Hz, CH_3 PLLA backbone), 1.50 (dd, *J* = 14.7, 7.0 Hz, terminal CH_3 PLLA) (See also Figure A.1).

Preparation of aqueous solutions by lyophilization and resuspension or solvent extraction: Lyophilized powders were obtained by freezing the toluene solutions in a round bottom flask with liquid nitrogen followed by sublimation using a vacuum pump. Resuspension of the powders was aided by sonication for 30 minutes in a Branson 3800 Ultrasonic Cleaner. Solvent extractions were performed by dropping a few (5-10) μL of toluene solution into excess water and vortexing for 10 seconds. In both cases aqueous solutions with a concentration of 0.5 mg/mL (0.5% solids w/w) were obtained and cryo-TEM analysis showed similar results for both preparations.

Structural characterization: Proton nuclear magnetic resonance (^{1}H NMR) spectra were collected on a 500 MHz Bruker Avance spectrometer in $CDCl_3$. Chemical shifts are given in ppm, calibrated from residual $CHCl_3$. Gel permeation chromatography (GPC) was performed in DMF using an Agilent 1100 chromatograph equipped with RID detector and a PL gel 5 μm 300x7.5mm mixed column. Samples were calibrated against polystyrene standards (See Figure A.2 for GPC traces).

Turbidity measurements: Self-assembly kinetics were measured with UV/Vis spectroscopy on a Thermo Scientific NanoDrop 2000c. Changes in turbidity were measured at 600 nm every 15 seconds for 720 minutes with a moderate stirring rate. Triplicate runs were taken of each sample (See Figure A.3). Plots shown in chapter 2 are binned by a factor of 20.

Crystallization measurements: Wide-angle x-ray scattering (WAXS) patterns were measured on a Rigaku Smart lab X-ray diffractometer in Bragg-Brentano diffraction mode utilizing x-rays generated at 40kV and 44mA with Cu Kα irradiation (step size 0.2 deg, speed 1.0, IS 2/3 deg, RS1 2/3 deg, RS2 0.3 mm) . Approximately 20mg of a lyophilized

sample was used in measurements. PLLA crystallinity was originally calculated using Smart Lab (Rigaku) software (Figure A.4), but due to the possibility of overlapping PEG peaks, a deconvolution routine was employed to separate PEG and PLLA peaks (Figure A.5). Using Smart Lab software, following background correction, amorphous peak and crystalline peak areas were defined using previous peak assignment of PLLA-*b*-PEG.[45, 46] Additional crystallinity analysis was conducted using a custom peak fitting python script. The area of interest was restricted between 10-30° and a constant background was subtracted. After which a model function was created as the sum of a mixture of Voigt and Gaussian components. The model was subsequently fitted to the experimental data by optimizing the individual component parameters (peak center, amplitude, sigma, and gamma). The quality of the fit was assessed by measuring the mean square error between the model and the experimental data. The parameters and script used to fit the data is discussed further in the SI. In both cases crystallinity was calculated from the area of crystalline peaks as a percentage of the total peak area (For more details on peak assignment see SI). % Crystallinity was normalized by the mass ratio of the PLLA segment. Fourier transform infrared (FTIR) absorbance spectra were collected on a Jasco 4700 FTIR from lyophilized samples.

Cryogenic-transmission electron microscopy (cryo-TEM): Cryo-TEM samples were prepared from resuspended or extracted solutions onto Quantifoil R2/2 (Electron Microscopy Sciences) grids. Grids were glow discharged for 70 seconds to increase hydrophilicity prior to sample loading. Vitrification was carried out by an Automatic Plunge Freezer ME GP2 (Leica Microsystems) with 3 µL of sample. Grid preparation was performed at 95% humidity and the grids were blotted for 3 seconds prior to plunging into

liquid propane. Cryo-TEM samples were then placed on a Gatan Cryo-TEM holder and imaged on a JEOL 2100F TEM using a Schottky type field emission gun operating at 200 keV. Images were recorded using DigitalMicrograph (Gatan) software with a Gatan OneView CMOS camera at 4k x 4k resolution.

Scanning electron microscopy (SEM): Samples were prepared from lyophilized samples which were freeze-cracked in liquid N_2 and coated *ex-situ* with 3 nm of iridium (Quorum, Q150T Plus). Secondary electron images were collected on a FEI, Quanta 3D FEG with Everhart-Thornley detector, using a 5 kV acceleration potential, and a probe current of 200 pA.

2.3. Results

2.3.1. ROPI-CDSA design and synthetic parameters

ROPI-CDSA experiments were performed using L-lactide as the monomer, mono-functional polyethylene glycol ($mPEG_{45}$) as the initiator, toluene as the solvent and triazabicyclodecene (TBD) the catalyst (Figure 2.1a).[43, 47-49] While other organocatalysts can achieve better dispersity (Đ) than TBD, they require high catalyst loading (1-10% mol vs 0.1% mol) and longer reaction times.[49] TBD is a highly active ROP catalyst that can achieve high conversion in seconds.[38, 48] If reaction mixtures are left too long the Đ will broaden from transesterification.[48] Therefore to limit transesterification, reactions were quenched after 90 seconds for concentrations of 10% solids w/w and 60 seconds for concentrations greater than 10% solids w/w. A library of 19 polymers was synthesized with a variation in the degree of polymerization (DP) of the PLLA block and total solids concentration (Table 2.1: **1-19**). For $PLLA_{10}$-*b*-PEG_{45}, **1-4** (5-20% solids w/w), no self-assembly was observed visually (i.e. solutions remain clear/ no observed turbidity) or by

cryo-TEM. At 20% solids w/w (PLLA$_{45}$-*b*-PEG$_{45}$ **10**, PLLA$_{90}$-*b*-PEG$_{45}$ **16**, and PLLA$_{135}$-*b*-PEG$_{45}$ **19**), control over Đ worsens, most likely due to transesterification from higher TBD solution concentrations (see also Table A.1). The 20% solids w/w samples macroscopically phase separate forming distinct solution and gel-like phases.

Table 2.1: Molecular characterization of PLLA-*b*-PEG BCPs synthesized via ROPI-CDSA.

Polymer	DP	% w/w	M_n (Da)[a]	Đ[b]	Polymer	DP	% w/w	M_n (Da)[a]	Đ[b]
1	10	5.0	2700	1.07	**11**	60	10.0	6000	1.15
2	10	7.5	2700	1.07	**12**	75	10.0	6900	1.14
3	10	10.0	2700	1.08	**13**	90	5.0	8000	1.10
4	10	20.0	2700	1.09	**14**	90	7.5	8100	1.16
5	25	10.0	3700	1.11	**15**	90	10.0	8400	1.12
6	25	20.0	3700	1.15	**16**	90	20.0	8400	1.34
7	45	5.0	5200	1.12					
8	45	7.5	5400	1.12	**17**	120	7.5	10400	1.17
9	45	10.0	5300	1.16	**18**	135	10.0	11100	1.10
10	45	20.0	5200	1.25	**19**	135	20.0	11600	1.37

a: ^{1}H NMR b: GPC

Above 20% solids w/w, mPEG$_{45}$ is not fully soluble in toluene. At 20% solids, limited PEG solubility may have also contributed to transesterification. For samples **5-19**, the polymerizations reached >92% (Figure A.1) conversion within 60-90 seconds and resulted in well-defined (Đ < 1.2) block copolymers (Figure A.2). The resulting solutions became turbid at various time points, ranging from during the polymerization for **16** (PLLA$_{90}$-*b*-PEG$_{45}$ 20% solids w/w) and **19** (PLLA$_{135}$-*b*-PEG$_{45}$) to more than 24 hr post-polymerization for **5** (PLLA$_{25}$-*b*-PEG$_{45}$ 10% solids w/w) and **7** (PLLA$_{45}$-*b*-PEG$_{45}$ 5% solids w/w). This indicates that in most instances the relaxation time is significantly longer than

the polymerization time and is dictated by the molecular structure of the BCP. Here, relaxation time refers to the time taken for the assembled structures to reach a low energy configuration and stop reorganizing. Control experiments were performed by synthesizing PLLA homopolymers in dichloromethane (where PLLA is fully soluble) and toluene (where PLLA is partially soluble), using ethanol as an initiator. In dichloromethane, >95% conversion was achieved in 90 seconds, whereas in toluene only 25% and 28% conversion were achieved after 90 seconds for $PLLA_{45}$ and $PLLA_{90}$, respectively (Table A.3). This demonstrates that the PEG chains promote the polymerization by increasing the solubility of the growing PLLA chain in toluene. This is similar to previous PISA reports which have shown that self-assembly during polymerization can enhance the rate of polymerization of the selective block.[14] A second control was performed to determine if the polymerization is required for initiation of the self-assembly process, PLLA-*b*-PEG BCPs synthesized in dichloromethane were purified and re-dispersed directly in toluene. The polymers did not fully dissolve/disperse even when left over a period of months, indicating that direct polymerization in toluene is required to form stable assemblies at room temperature and that the structures formed in ROPI-CDSA are under kinetic control. Heat-cool cycles or a solvent-switch would likely also lead to the formation of stable assemblies, however the purpose of the second control was to determine if the samples are pathway dependent. Pathway dependence indicates that it should be possible to control the ROPI-CDSA structures by modification of both the thermodynamics and kinetics of the process (see discussion section on non-equilibrium PISA).

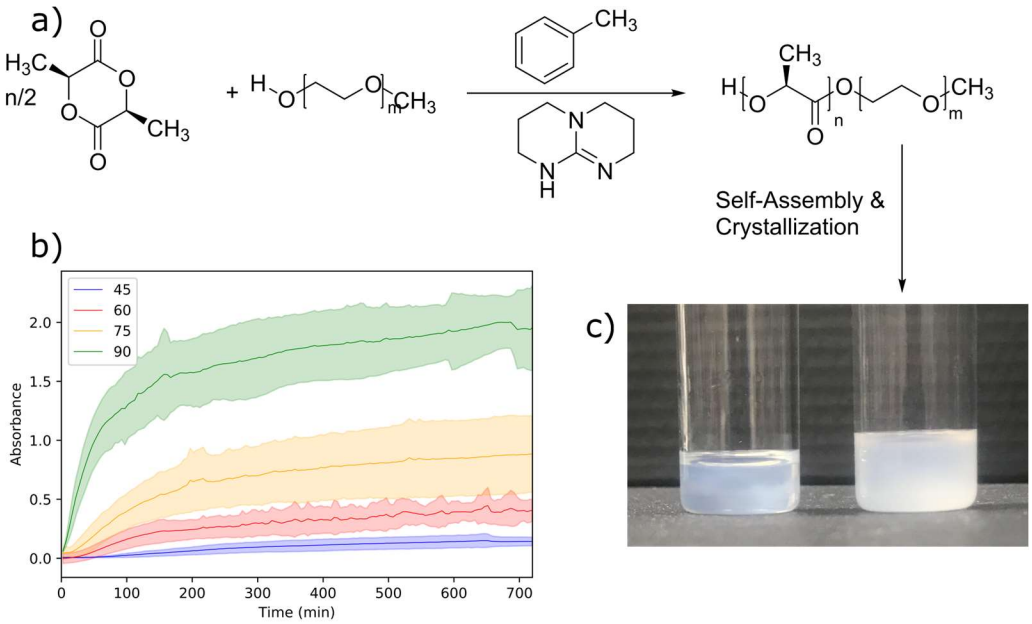

Figure 2.1: ROPI-CDSA scheme and self-assembly kinetics. a) ROPI-CDSA scheme. b) Turbidity measurements (UV/Vis 600 nm) for PLLA DP 45, 60, 75 and 90 at 10% solids w/w, with PEG DP 45 standard error calculated from 3 runs. The data shows that the self-assembly kinetics vary as a function of PLLA DP, where increasing DP results in a faster rate of self-assembly. c) Photographs showing the difference in turbidity for samples 9 (PLLA45-b-PEG45 10% solids w/w left) and 15 (PLLA90-b-PEG45 10% solids w/w right).

2.3.2. Self-assembly and crystallization kinetics

To track how PLLA DP influences the self-assembly kinetics, UV/Vis measurements were performed to track the turbidity changes post polymerization for polymers PLLA$_{45}$-*b*-PEG$_{45}$ **9**, PLLA$_{45}$-*b*-PEG$_{45}$ **11**, PLLA$_{45}$-*b*-PEG$_{45}$ **12**, and PLLA$_{45}$-*b*-PEG$_{45}$ **15**, all at 10% solids w/w. (Figure 2.1b). Measurements were performed at 600 nm, a wavelength in which no molecular species present in ROPI-CDSA absorb. The data showed that with increasing PLLA DP, the initial rate of self-assembly increases and results in more turbid final solutions.

To determine if crystallization of the PLLA block is a driving force in the self-assembly, the solutions for PLLA$_{45}$-*b*-PEG$_{45}$(10% solids w/w **9**) and PLLA$_{90}$-*b*-PEG$_{45}$ (10% solids w/w **15**) were freeze-dried at various time points between 5 minutes and 24 hours post

polymerization. The dried powders were analyzed by WAXS and FTIR spectroscopy to monitor the crystallization behavior (Figure 2.2). Crystallinity is tracked over time by comparing the area of the crystalline peaks to the total area in WAXS patterns (Figure A.4-6, Tables A.4-5 and Appendix A Supplementary Discussion on % crystallinity calculations). In both cases, metastable crystalline intermediates signified by broad peaks were observed at early time points giving way to sharper crystalline peaks at later time points (Figure 2.2). For $PLLA_{45}$-*b*-PEG_{45} (10% solids w/w **9**) , the PLLA crystallinity increased rapidly during the first three hours to 51% crystalline and then increased slowly, to a maximum of approximately 81% crystalline around 24 hours. For $PLLA_{90}$-*b*-PEG_{45} (10% solids w/w **15**), the crystallinity increased at a faster rate, reaching 48% crystallinity within the first hour and then increased slowly to 63% at 24 hours. The WAXS data is consistent with the development of the α crystalline form of PLLA, which is considered the more thermodynamically stable polymorph (Figure 2.2a-b).[45, 50, 51] To compare BCP crystallization to homopolymer crystallization, two PLLA samples with DP = 45 and DP = 90 were crystallized in toluene, which achieved 87% and 86% crystallinity, respectively. This indicates that the presence of the PEG block could inhibit crystallization for longer PLLA blocks. The FTIR spectra show the carbonyl-stretch at 1749 cm^{-1} broadening to form two peaks (1749 cm^{-1} and 1754 cm^{-1}), which is also consistent with the crystallization of PLLA (Figure 2.2c-d).[50-52] Peak ratios of 1754 cm^{-1} to 1749 cm^{-1} indicate significant changes in the carbonyl environment occurring in the early time points in $PLLA_{45}$-*b*-PEG_{45} (10% solids w/w **9**) and $PLLA_{90}$-*b*-PEG_{45} (10% solids w/w **15**), supporting the WAXS data.

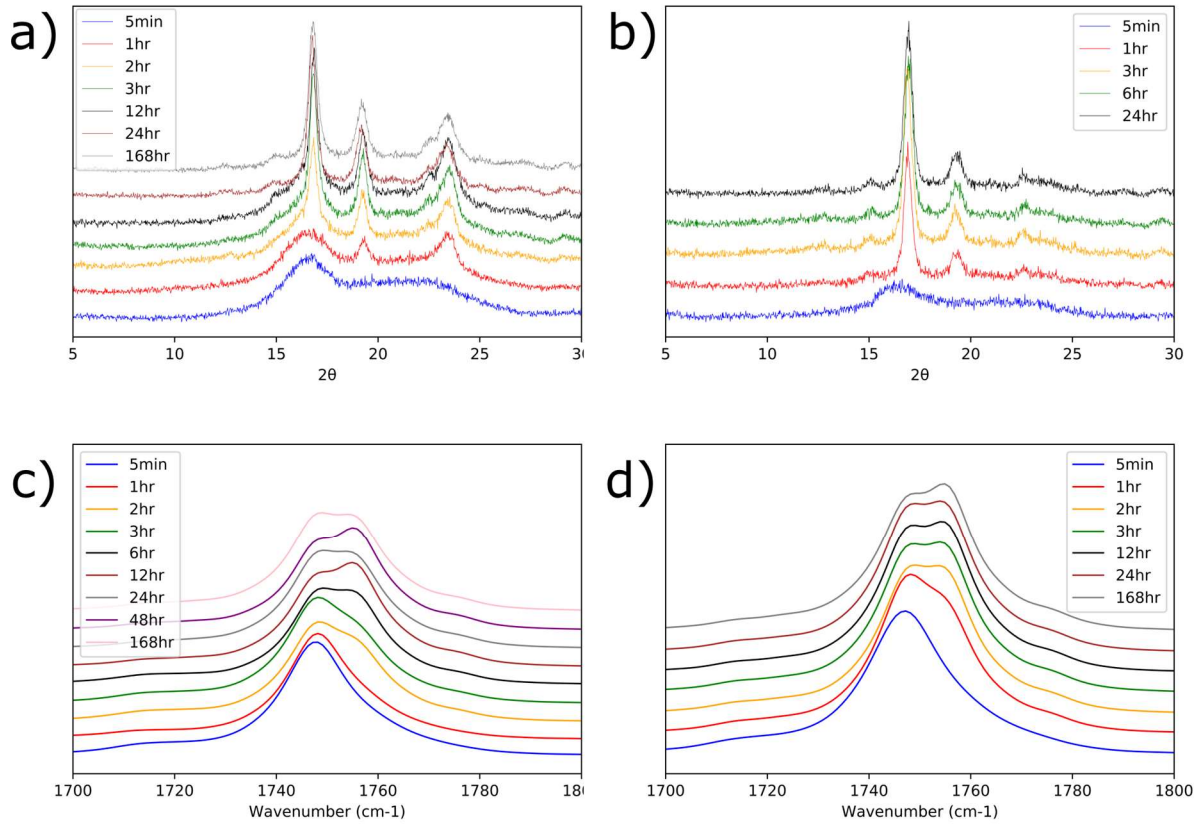

Figure 2.2: Kinetics of PLLA crystallization. a-b: WAXS pattern for PLLA45-b-PEG45 (10% solids w/w 9) (a) and PLLA90-b-PEG45 (10% solids w/w 15) (b) over time and c-d: FTIR spectra of the carbonyl shift for 9 (c) and 15 (d). Note for 2a, from 24hr to 168hr, no significant difference is observed. For 2b, from 3hr to 24hr, no significant difference is observed. Note that for 2a, 5 min and 1 hr, and 2b, 5 min show metastable crystalline intermediates. The data shows a development in the crystallinity over time indicating that the self-assembly process measured in Figure 2.1 is related to the crystallization of the PLLA core forming block.

2.3.3. Self-assembly mechanism

To monitor the morphological evolution, the freeze-dried samples were re-dispersed in water (a non-solvent for PLLA) at 0.5% solids w/w and analyzed by cryo-TEM. Previous examples of CDSA of PLLA-based BCPs in water demonstrate that for self-assembly to occur, solutions must be heated in water (>65°C) and cooled.[20, 21] Thus, at room temperature, PLLA-*b*-PEG nanoparticles should be stable in water. Furthermore, it is well known that crystallinity and nanostructure of PLLA-based block copolymers are stable to

dehydration and resuspension.[53]To confirm that the BCP structures formed in toluene are stable to freeze drying and re-dispersion, several control experiments were performed (see Appendix A and Figures A.7-12). All of these control experiments showed the structures to be stable. Additionally, cryo-TEM analysis of the ROPI-CDSA structures which had been in water several weeks after resuspension, and water resuspensions from dehydrated BCPs aged several months showed stable structures. Which indicates that the BCPs form stable kinetically-trapped structures, consistent with previous literature of PLLA-based BCPs in water (Figure A.13).[19, 20, 22] This also demonstrates that ROPI-CDSA can be used to produce a range of hierarchal PLLA-*b*-PEG structures by kinetically trapping in water at various time points during the self-assembly process.

The cryo-TEM data for $PLLA_{45}$-*b*-PEG_{45} (10% solids w/w **9**, Figure 2.3a-c) shows that the assembly process proceeds via the formation of spheres (t = 1 hour diameter = 14.4±2.6 nm Figure A.14), that evolve into rods (t = 3 hours diameter = 15.8±2.3 nm and length = 56.1±42.4 nm Figures A.15-16), which appear to aggregate and form lamellae (t = 24 hours thickness = 24.7±2.2 nm length = 3212±927 nm width = 859±308 nm Figure A.17). For most time-points, the samples showed a mixture of structures (e.g. spheres and rods or rods and lamellae), which is consistent with a kinetically controlled process.[54, 55] On several occasions the rods appear to be aligned (Figure 2.3b inset) and in some cases they appear to be connected by long fibers (diameter = 10 nm, length > 1 μm, Figure A.18). The distinction between nanorods and nanofibers is typically related to their aspect ratios, where nanorods typically have ratios of 3-15 and fibers typically are >> 15.[56] Here, the fibers appear to act as nucleation sites for the spheres and rods, directing their formation. The cryo-TEM data for sample $PLLA_{90}$-*b*-PEG_{45} (10% solids w/w **15**,

Figure 2.3d-f) shows a different formation pathway. The initial structures appear to be poorly-defined rod-like precursors (diameter = 29±12 nm length = 90±27 nm Figure A.19) which evolve into lamellae (width = 360±250 nm length = 1270±910 nm thickness = 22±2 nm Figure A.20) with a second population of rod-like structures (diameter = 22±6 nm length = 101±35 nm Figure A.21). After 6 hours, the rod-like structures are no longer present, with only lamellae (width = 360±230 nm length = 1300±700 nm thickness = 23±2 nm Figure A.22) and 3D lamellae stacks present, confirmed through a tilt series (Figure A.23).

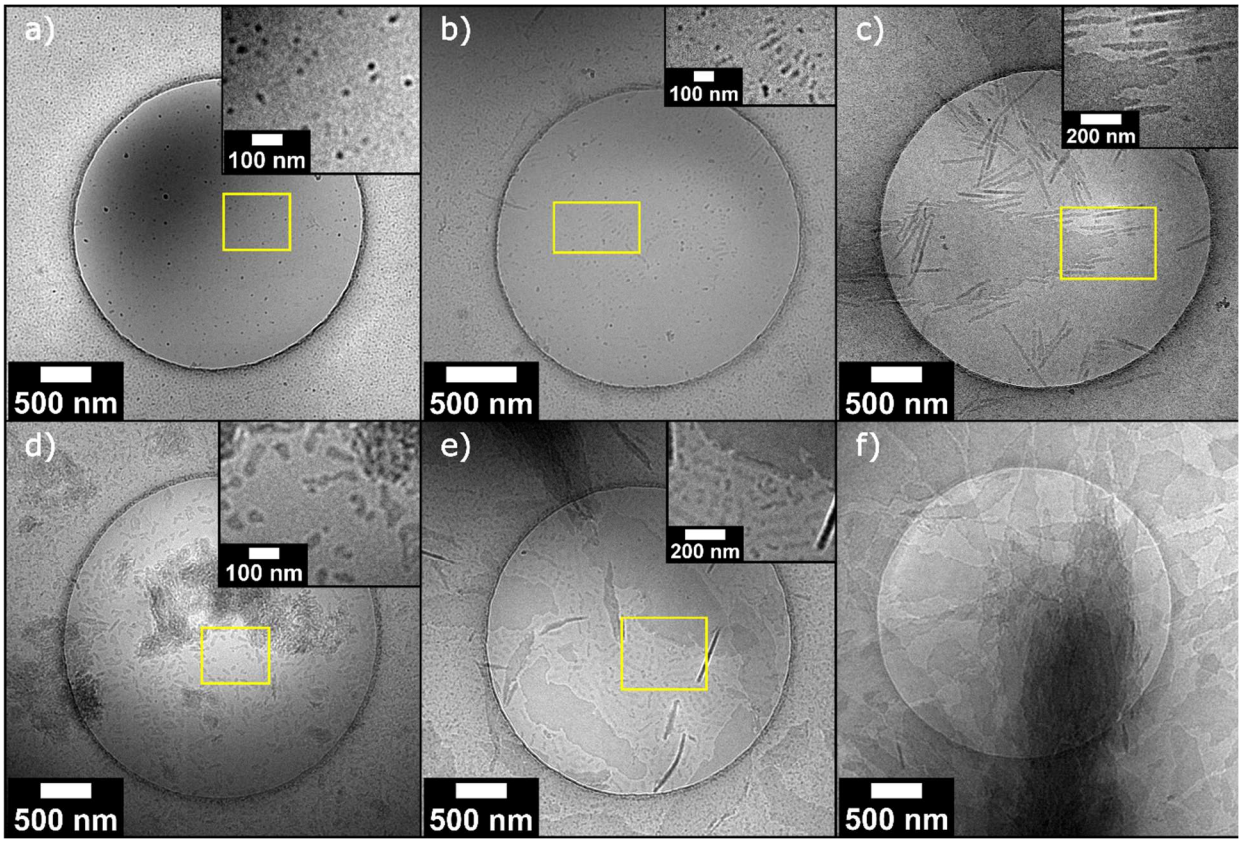

Figure 2.3: Morphological evolution of $PLLA_{45}$-b-PEG_{45} (10% solids w/w **9**) and $PLLA_{90}$-b-PEG_{45} (10% solids w/w **15**). Time-resolved cryo-TEM images a-c: **9**, a=1hr, b=6hr, c=24hr. d-f: **15**, d=5min, e=3hr, f=6hr. The data show two distinct assembly mechanisms that appear to be a result of unimer addition (sample 9) and particle aggregation (sample 15), resulting in lamella with different morphologies.

2.3.1. Phase diagram

The above data show that the structure of the PLLA-*b*-PEG assemblies varies as a function of both molecular structure and time post polymerization. To construct a phase diagram and verify the reproducibility of ROPI-CDSA,[11, 14, 26] samples were left for several days post polymerization. However, it is important to note that each sample will likely have its own self-assembly pathway to reach these relaxed, meta-stable structures. Representative cryo-TEM and SEM images of various morphologies are shown in Figure 2.4. The samples from Table 2.1 are plotted as a function of PLLA DP and % solids w/w and constitute a phase diagram shown in Figure 2.5. Samples **7** and **8** ($PLLA_{45}$-*b*-PEG_{45} 5% and 7.5% solids w/w respectively, Figure 2.4a-b) formed short rods (width 20-30 nm, length 20-70 nm), sample **5** ($PLLA_{25}$-*b*-PEG_{45} 10% solids w/w) (Figure 2.4c) formed fibers (diameter ≈ 10 nm, length > 1 micron) similar to the structure found in Figure 2.3b and Figure A.12, samples **6** ($PLLA_{25}$-*b*-PEG_{45} 20% solids w/w)**, 9-10** ($PLLA_{45}$-*b*-PEG_{45} 10% and 20% solids w/w respectively)**, 11** ($PLLA_{60}$-*b*-PEG_{45} 10% solids w/w) and (Figure 2.4d-f) formed a mixture of rods (width 20-30 nm length 100-1000 nm) and lamellae **12** ($PLLA_{75}$-*b*-PEG_{45} 10% solids w/w) (width 200-1000 nm length 500 nm to 4 μm) , and samples **13** ($PLLA_{90}$-*b*-PEG_{45} 5% solids w/w) and **14** ($PLLA_{90}$-*b*-PEG_{45} 7.5% solids w/w) (Figure 2.4g-h) formed lamellae (width 100-1000 nm length 200 nm to 3.5 μm). Samples **15-16** ($PLLA_{90}$-*b*-PEG_{45} 10% and 20% solids w/w respectively), **17** ($PLLA_{120}$-*b*-PEG_{45} - 7.5% solids w/w), and **18-19** ($PLLA_{135}$-*b*-PEG_{45} 10% and 20% solids w/w respectively) (Figure 2.4i-l) formed organogels in the toluene solution as confirmed by oscillatory

rheology (Figure A.24) which indicated that a 3D network formed in solution.[57] Stacks or aggregates of lamellae were observed by cryo-TEM (Figure 2.4i-j). Freeze drying of the samples and analyzing the bulk powders by SEM revealed the formation of a 3D porous material. Here individual lamellae are not clearly discernable, although it appears that the materials are likely composed of individual lamellae measuring approximately 5 μm in length The SEM images are in good agreement with with cryo-TEM images collected from the gels, both showing the presence of lamellae and an abundance of 3D stacked lamellae with lengths of 500 nm to 5 μm.

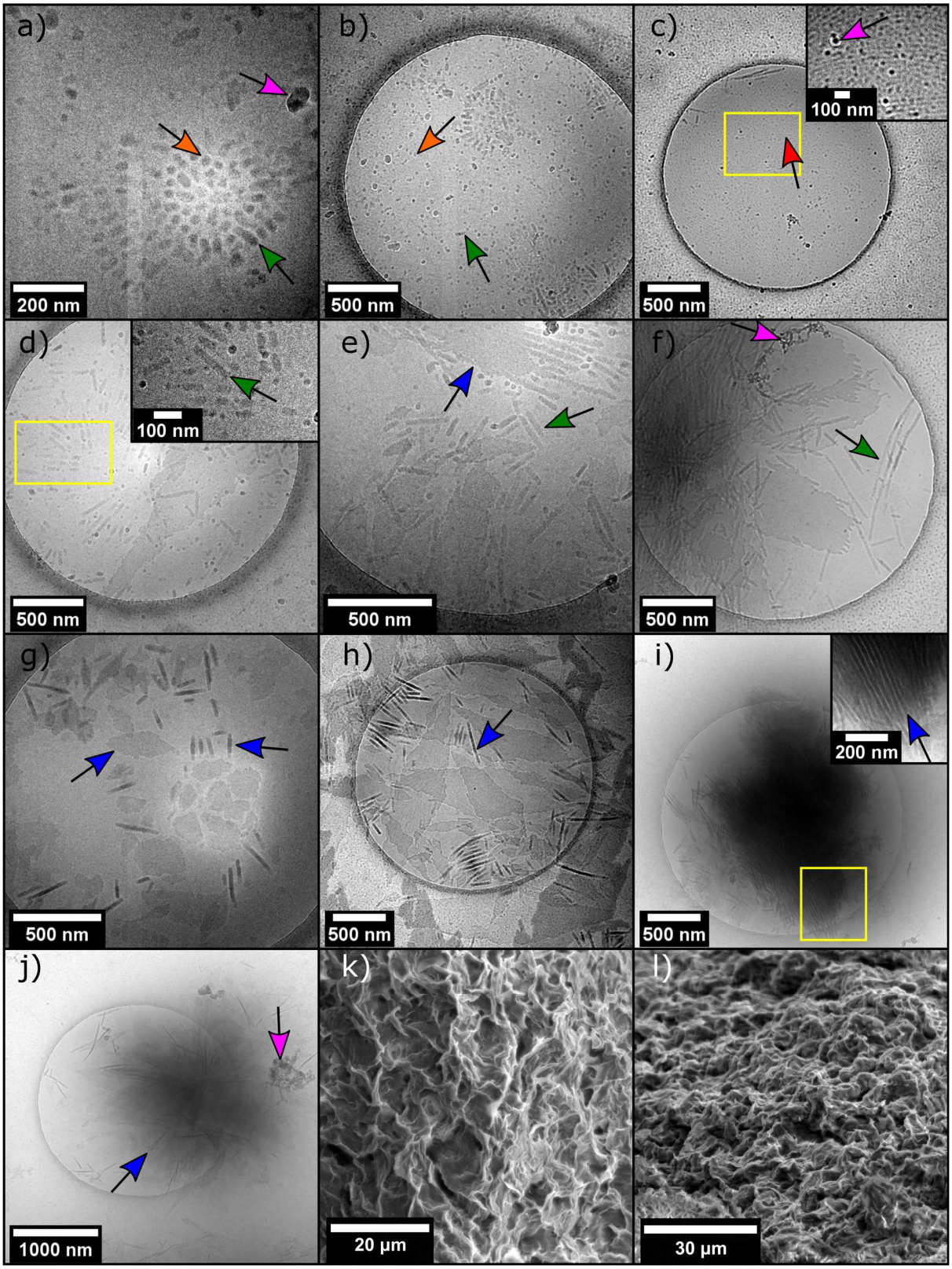
Legend:
Spheres
Rods
Fibers
Lamellae
Ice Contamination
a)
200 nm
b)
500 nm
c)
100 nm
500 nm
d)
100 nm
500 nm
e)
500 nm
f)
500 nm
g)
500 nm
h)
500 nm
i)
200 nm
500 nm
j)
1000 nm
k)
20 µm
l)
30 µm

Figure 2.4: Selected cryo-TEM (a-j) and SEM (k-l) images for representative morphologies of the phase diagram, a-c is for 1-D systems, d-h are for 2-D systems, i-l are for 3-D systems. Images are from the following samples: a-b **7**, c **5**, d-e **9**, f **6**, g-h **13**, i **16**, j **19**, k-l **17**. (See Table 2.1 for a sample guide). The data show that ROPI-CDSA can be used to form block copolymer materials with a wide range of morphologies, dimensions, and length scales.

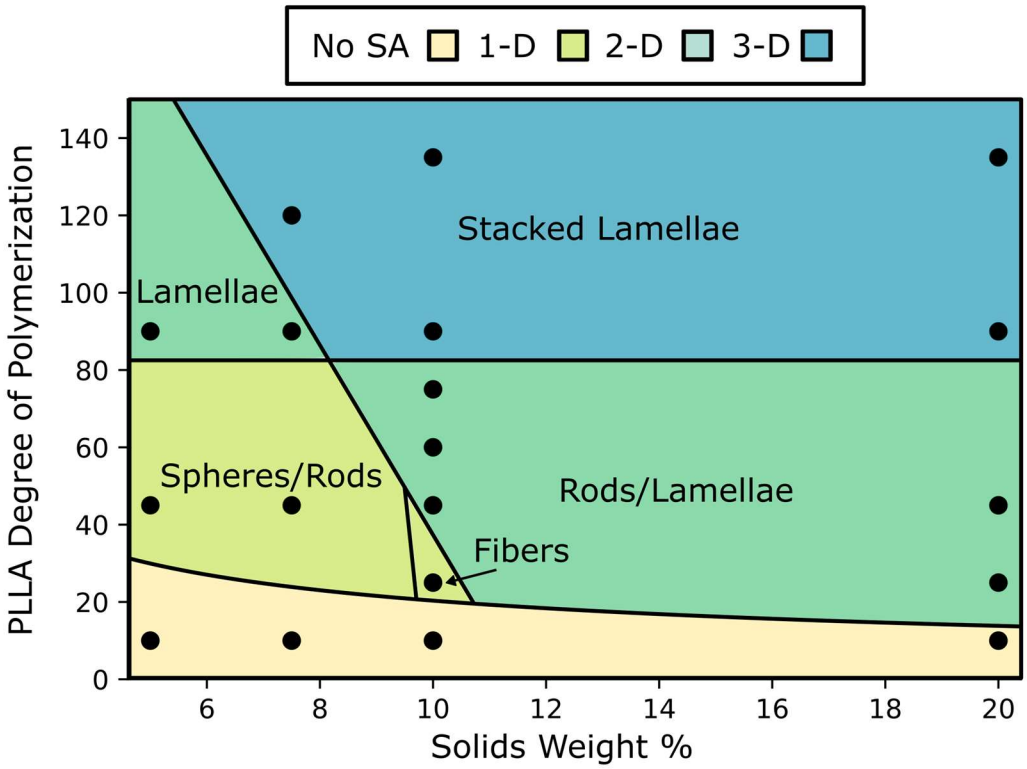

Figure 2.5: Phase diagram showing hierarchical ordering for samples **1-19** (Table 2.1). No SA refers to no self-assembly observed. The phase diagram shows a clear trend where higher dimensional structures are favored at higher solids content and higher PLLA DPs.

2.4. Discussion

2.4.1. Hierarchical growth mechanisms

This work tracks the evolution of PLLA-*b*-PEG morphologies immediately following polymerization, revealing a hierarchical evolution from 0D spheres to 1D rods and fibers to 2D lamellae and, in select cases, to 3D porous networks consisting of stacked or

aggregated lamellae. Lamellae are likely favored as polymer crystallinity tends to promote morphologies with low curvature,[17, 18] while stacking can minimize surface energies.

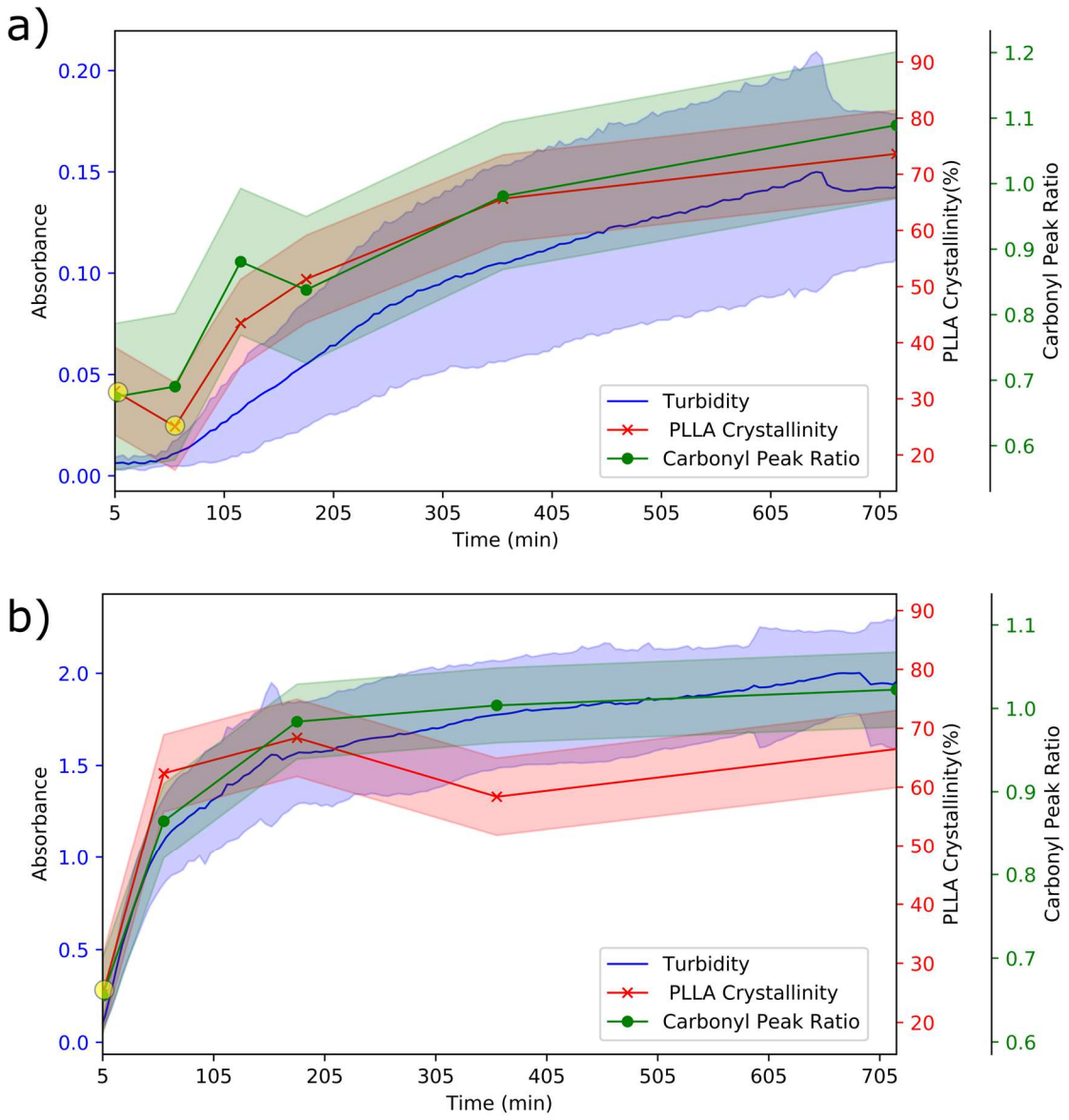

Figure 2.6: Composite graphs showing the change in turbidity (measured at 600 nm), % crystallinity of PLLA block, and carbonyl peak ratio for a) $PLLA_{45}$-b-PEG_{45} (10% solids w/w **9**) and b) $PLLA_{90}$-b-PEG_{45} (10% solids w/w **15**). Standard error of 3 runs is plotted for turbidity measurements and a calculated error is plotted for crystallinity and carbonyl peak ratio values, see Appendix A for more details. For the PLLA crystallinity (%) data, early time point metastable crystalline precursors are highlighted with a yellow circle. The data shows that the self-assembly kinetics are coincident with the crystallinity kinetics.

Comparison of the kinetic data obtained from UV-Vis, WAXS and FTIR shows that crystallization is coincident with self-assembly for both $PLLA_{45}$-*b*-PEG_{45} (10% solids w/w **9**) and $PLLA_{90}$-*b*-PEG_{45} (10% solids w/w **15**), despite the kinetics for both samples being significantly different (Figure 2.6). This suggests that the self-assembly is driven by the crystallization of the PLLA block; although, our control experiments show that polymerization is promoted by the presence of the PEG initiator. Consequently, the assembly process is proposed to be driven by both the amphiphilicity of the BCP, and the crystallization of the PLLA block.[24] The data showed that the length of the PLLA block strongly influences the self-assembly kinetics and morphology, with longer blocks favoring faster self-assembly (Figures 2.1 and 2.6), and the formation of higher dimensional structures (Figure 2.5). This kinetic observation is consistent with previous reports on the CDSA of poly(L-lactide)-*block*-poly(N,N-dimethylacrylamide) (PLLA-*b*-PDMA) diblock copolymers in alcohols, where the kinetic differences were attributed to the difference in solubility of the BCP chain (i.e. more soluble polymers crystallize more slowly).[23, 58] However, the morphological results revealed the more solvophobic PLLA-*b*-PDMA polymers formed lower dimensional structures (1D vs 2D),[23, 58] in contrast to what is reported here. For ROPI-CDSA of PLLA-*b*-PEG there are two fundamentally different assembly mechanisms for $PLLA_{45}$-*b*-PEG_{45} (10% solids w/w **9**) and $PLLA_{90}$-*b*-PEG_{45} (10% solids w/w **15**). $PLLA_{45}$-*b*-PEG_{45} (10% solids w/w **9**) (more soluble polymer) appears

to initially form high aspect ratio fibers that act as nucleation sights for the crystalline rods, directing the growth to occur along the fiber in one dimension. As rod growth occurs during the time period where most of the crystallinity develops, I propose that these rods form by unimer addition from either the solution or by Ostwald ripening of the fibers.[59] At later time points, these rods aggregate, resulting in 2D growth and the formation of the lamellae (Figure 2.7a). $PLLA_{90}$-*b*-PEG_{45} (10% solids w/w **15**) (less soluble polymer) initially appears to form irregularly shaped particles which grow through a particle aggregation mechanism. This results in an initial 2D growth, forming lamellae, and later in 3D growth, forming stacked lamellae and the hierarchical porous network (Figure 2.7b). The morphological difference between the lamellae formed in $PLLA_{45}$-*b*-PEG_{45} (10% solids w/w **9**) and $PLLA_{90}$-*b*-PEG_{45} (10% solids w/w **15**) are also consistent with proposed mechanistic differences (Figure 2.3). Cryo-TEM images of $PLLA_{60}$-*b*-PEG_{45} (10% solids w/w **11**) and $PLLA_{75}$-*b*-PEG_{45} (10% solids w/w **12**) show morphologies that are consistent with both mechanisms acting simultaneously. The lamellae structures formed by **11** and **12** have characteristics of both **9**, as they are composed of aligned rods, and **15,** in that the lamellae are irregularly shaped (See Figure A.25).

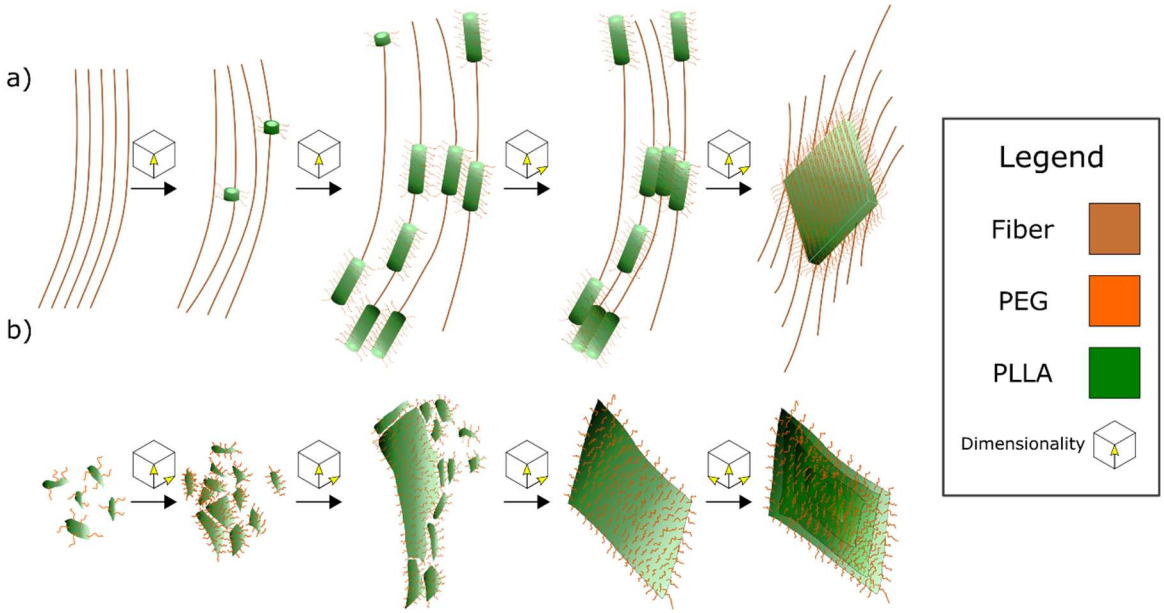

Figure 2.7: ROPI-CDSA growth mechanisms a) Proposed growth mechanism for $PLLA_{45}$-b-PEG_{45} (10% solids w/w **9**), favoring unimer growth. First, fibers form as a template for 1D growth, giving spheres and rods. Later, these rods aggregate to form 2D lamellae. b) Proposed growth mechanism for $PLLA_{90}$-b-PEG_{45} (10% solids w/w **15**), favoring aggregation. First, ill-defined 2D rod-like structures form and grow via aggregation. Later, 2D lamellae aggregate, giving 3D lamella stacks.

These two different initial growth mechanisms (templated unimer addition and particle aggregation) are consistent with growth models previously reported for small molecules and inorganic crystals,[59, 60] where the observed differences in formation pathways are explained by considering the relative energy barriers for either pathway. In our work, the longer PLLA block reduces the energy barrier for crystallization and raises the energy barrier for unimer exchange. However, one important consideration for macromolecular self-assembly that is not present for small molecules or inorganic crystals is the influence of chain stretching.

The dimensions of self-assembled BCP structures are determined by the aggregation number and the stretching or coiling of the polymer chains.[17, 61] For spheres, rods, and lamellae, the degree of polymer chain stretching (ω) can be determined by

comparing the measured radius (*r*) (or half the lamella thickness) to the maximum length of the polymer chain (L_{max}) (Figure 2.8).

$$\omega = \frac{r}{L_{max}}$$

From distance calculations using CrystalMaker® software, the molecular length of a PLLA monomer is 3.69 Å (see Appendix A and Figure A.26). The total fully extended PLLA backbone lengths (L_{max}) are 16.6 nm and 33.2 nm for $PLLA_{45}$-*b*-PEG_{45} (10% solids w/w **9**) and $PLLA_{90}$-*b*-PEG_{45} (10% solids w/w **15**), respectively. This would result in a theoretical maximum fiber/rod diameter and/or lamella thickness of 33.2 nm for $PLLA_{45}$-*b*-PEG_{45} and 66.4 nm for $PLLA_{90}$-*b*-PEG_{45}. For **9**, the fibers have an ω of 0.33 (0.29-0.37); for the rods and lamella, ω changes over time from ω_{1hr} = 0.42 (0.34-0.50) to ω_{24hr} = 0.74 (0.68-0.81), becoming more stretched out during the self-assembly process. (N.B. lamella interdigitation is ruled out as I observed ω > 0.5). For **15**, ω stays relatively constant, at about 0.35 (0.32-0.37). In comparison to $PLLA_{45}$-*b*-PEG_{45} (10% solids w/w **9**), $PLLA_{90}$-*b*-PEG_{45} (10% solids w/w **15**) has a longer PLLA block and a smaller ω. This results in particles of **15** having a substantially lower corona density than **9**. I propose that this promotes particle aggregation events by lowering the barrier to inter-lamellar core-core interactions.[62] This lower corona density also facilitates stacking and the formation of structures in 3D.

2.4.2. Non-equilibrium PISA

An interesting feature of PISA experiments is that the molecular structure of the species assembling changes during the assembly process. As it is well known that the thermodynamics and kinetics of self-assembly change with molecular structure,[8, 63, 64] PISA processes occur as a result of the evolving energy landscape. As the initial homopolymer and monomer are soluble, the system is initially 'in-equilibrium' (and dissolved). Every addition of monomer to the end of the homopolymer chain creates a building block (the growing block copolymer) that is higher in free energy (due to its increasingly amphiphilic nature). The majority of PISA experiments can be categorized as either thermodynamically-controlled[14, 26, 65] or kinetically-trapped,[2, 26, 27, 33, 65-67] which differ based on the type of evolving energy landscape. In the thermodynamically controlled systems, the energy landscape is relatively smooth compared to k_BT, resulting in very short relaxation times. With each monomer addition, the landscape changes and the system relaxes to its thermodynamic minimum. Consequently, the system evolves down a thermodynamic pathway and the design of these systems is based on thermodynamic considerations.[28] In the kinetically-trapped systems, the landscape evolves such that it becomes rough compared to k_BT, at which point the system gets

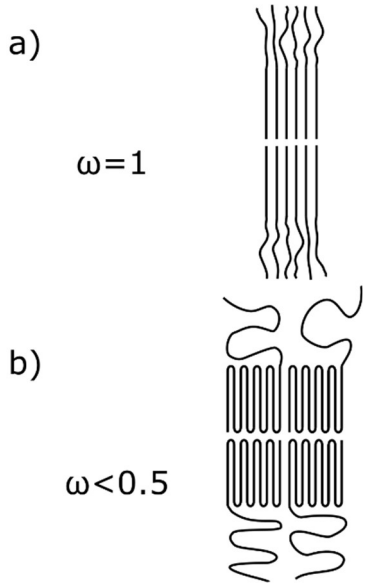

Figure 2.8: Proposed polymer chain stretching in CDSA with differing degree of polymer chain stretching, ω. a) when ω=1 giving a dense corona and b) when ω<0.5 giving significant coiling. In ROPI-CDSA, $PLLA_{45}$-b-PEG_{45} (10% solids w/w **9**) has a denser corona, in-between ω=1 and ω<0.5. In contrast, $PLLA_{90}$-b-PEG_{45} (10% solids w/w **15**) has a ω<0.5 exhibiting more coiling.

trapped in its configuration.[33, 68] In this system, the polymer evolves thermodynamically until the morphology gets locked in place by the changing energy landscape. The key feature of both these types of PISA processes (thermodynamically and kinetically controlled) is that the relaxation time is much faster than the polymerization time.[69] Consequently, after each monomer addition, the system relaxes to a lower energy state and the overall reaction coordinate proceeds downhill (Figure 2.9) and the assembly is finished once the polymerization finishes. In the system described here, the roughness of the energy landscape is on the order of k_BT. The consequence of this is that the relaxation times (driven by the crystallization kinetics) are long (hours to days). As the polymerization times are short (seconds to minutes), this creates a situation where with each monomer addition the system becomes increasingly further from its minimum free energy organization as the system does not have time to relax to a lower energy state (Figure 2.9). Therefore, I propose that during ring-opening polymerization, it is the release of the lactide ring strain which drives a non-equilibrium self-assembly evolution (See supplementary discussion on non-equilibrium assembly in Appendix A).[70, 71] Although not all of the chemical energy stored in the monomer will be converted into free energy to drive self-assembly (some being lost as heat energy), as the growing polymer chain is unstable, it has a higher free energy than the soluble homopolymer. Interestingly, the ring strain release during lactide polymerization (-23 kJ/mol),[72] is similar to the energy stored in GDP-rich microtubules, a classic out-of-equilibrium biological system (-22 kJ/mol).[73, 74] Microtubule assembly is a classic dissipative assembly process. The dissipative nature of the assembly is related to the reversibility of the chemistry, which is common in out-of-equilibrium systems.[74-76] In the presented PLLA-*b*-PEG systems, while the self-assembly

is initiated through a modification of the molecular structure, the chemistry is non-reversible, which is advantageous for using the process to trap the meta-stable structures. Here, this is achieved by re-dispersing the structures in water, where the energy landscape (at room temperature) is rough compared to k_BT. Consequently, we can divide the process into two stages. Stage 1 is the non-equilibrium assembly process that occurs during polymerization (Figure 2.9, stage 1). Stage 2 is the relaxation process that occurs as the high energy structures relax to a lower energy configuration (Figure 2.9, stage 2). In this chapter, only the relaxation process has been studied; however, our control experiments show that the presence of the PEG block is essential for the polymerization to occur efficiently, indicating that some assembly is taking place during stage 1. This is justified from the evidence that kinetically-trapped BCPs structures, are highly dependent on the assembly mechanisms.[62, 77-79] Furthermore, comparing kinetically-trapped structures in water using the same BCP but different methods (solvent switch and CDSA, Figures A.8-11) shows that ROPI-CDSA forms by a different pathway. Our hypothesis is that this pathway is dependent on the non-equilibrium stage of the assembly process (Figure 2.9, stage 1), and can provide access to meta-stable precursors that do not occur during the other assembly methods. Our data show two mechanisms by which meta-stable precursors can direct self-assembly. First, the formation of the highly coiled amorphous fibers which directs the location and dimensionality of the crystallization process. Second, the formation of precursor particles with low corona densities facilitates 2D and 3D growth through particle aggregation. Although more work is needed to investigate the non-equilibrium assembly process, the prospect of controlling PISA assembly mechanisms by changing the relative rates of polymerization and self-assembly

provides an exciting opportunity to create novel polymeric materials based on kinetic considerations (rather than thermodynamic considerations). For example, Khor et. al.[80] demonstrated that changing the rate of polymerization in emulsion RAFT PISA experiments resulted different morphological outcomes. Specifically, that a faster rate of polymerization provides access to polymer vesicles instead of spheres (achieved at slower rates of polymerization). Although not discussed in the text, a plausible explanation for this is that the faster rate of polymerization provides access to a non-equilibrium state that enables relaxation to vesicles. This study is an important example which, in addition to the work presented here, highlights that further study of the non-equilibrium behavior in PISA experiment can provide access to unique assembly processes and potentially to unique structures.

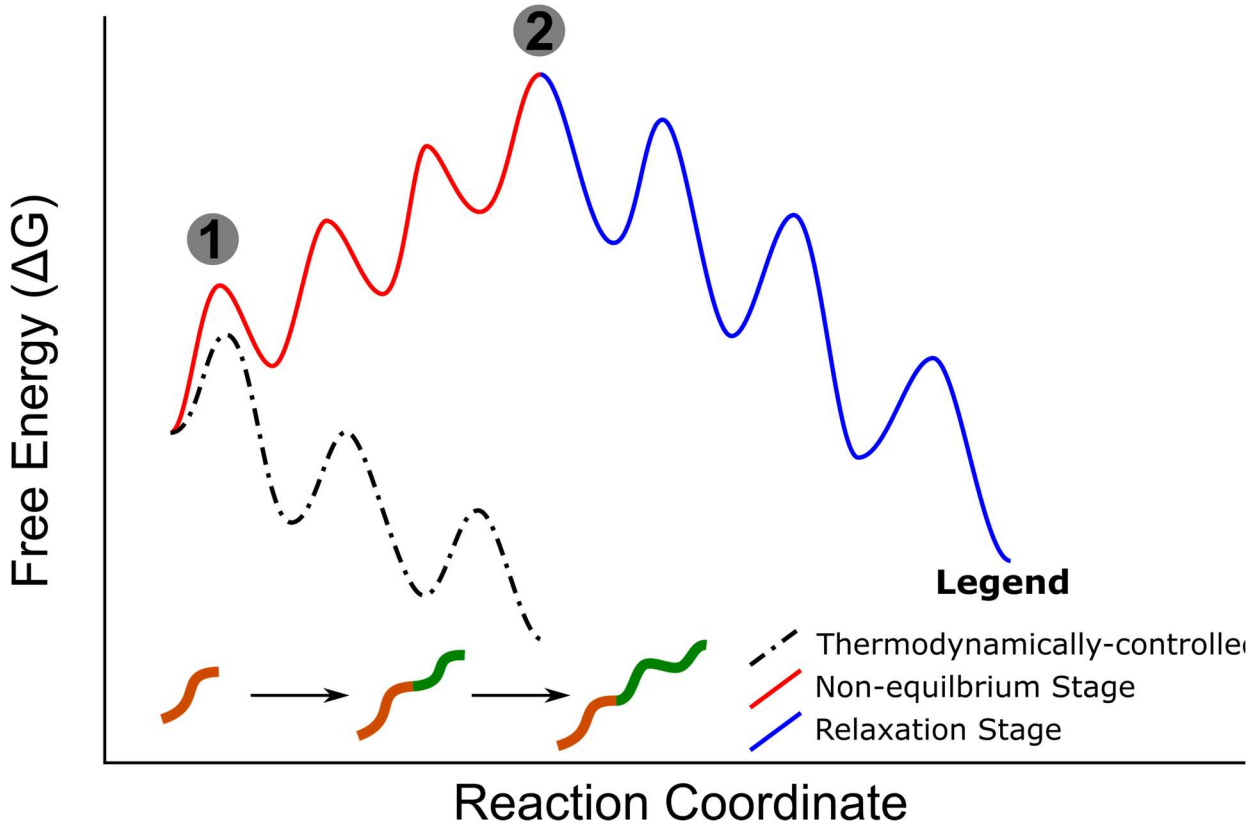

Figure 2.9: Free energy diagram for polymerization-induced self-assembly. The dashed lines represent the situation where the relaxation time is short compared to the polymerization time. Consequently, with each monomer addition, the growing block copolymer relaxes to a lower energy configuration. The result is that the reaction proceeds downhill and finishes when the polymerization terminates. The solid line represents the situation where the polymerization time is much shorter than the relaxation time. Consequently, with each monomer addition, the growing block copolymer cannot fully relax to a lower energy configuration. The result is that the reaction initially proceeds uphill (Stage 1) and then relaxes post polymerization (Stage 2). In Stage 2, the energy barriers represent morphological transitions (e.g. spheres to rods or rods to lamellae).

2.5. Conclusion

ROP of L-lactide in toluene, using a monofunctionalized PEG initiator, and TBD as a catalyst, results in the polymerization-induced crystallization-driven self-assembly of PLLA-*b*-PEG block copolymers. This method, termed ROPI-CDSA, can produce 1D, 2D, and 3D structures with concentrations ranging from 5-20% solids w/w. As the rates of the polymerization are faster than the rates of self-assembly and crystallization, the initial structures generated post polymerization are very far from equilibrium. Over time, driven by crystallization and solvent compatibility, the system relaxes to a lower energy configuration. The hierarchical growth is controlled by three processes operating on different time-scales, polymerization, amphiphilic self-assembly, and crystallization. Polymerization creates an amphiphile which can self-assemble by microphase separation, and a polymer capable of undergoing crystallization driven self-assembly. The interplay between these three processes is complex but provides a rich design space to create block hierarchical copolymer materials. The growth mechanism can occur via a predominantly unimer addition or particle aggregation mechanism. Understanding of the mechanism and kinetics of the relaxation process allows a range of meta-stable structures to be trapped by freeze drying, from a single BCP. The freeze-dried structures can then be stored and redispersed in water as required. This work provides a basis for

the use of ROPI-CDSA to generate hierarchical 1D, 2D, and 3D materials using biocompatible and biodegradable polymers with a scalable one pot strategy. It additionally outlines an approach for utilizing PISA as a method to create non-equilibrium self-assembly processes and trap unique meta-stable structures.

2.6. References

1. Khor, S. Y.; Quinn, J. F.; Whittaker, M. R.; Truong, N. P.; Davis, T. P., Controlling Nanomaterial Size and Shape for Biomedical Applications via Polymerization-Induced Self-Assembly. *Macromol Rapid Commun* **2019,** *40* (2), e1800438.
2. Le, D.; Keller, D.; Delaittre, G., Reactive and Functional Nanoobjects by Polymerization-Induced Self-Assembly. *Macromol Rapid Comm* **2019,** *40* (2), 1800551.
3. Gerbelli, B. B.; Vassiliades, S. V.; Rojas, J. E. U.; Pelin, J. N. B. D.; Mancini, R. S. N.; Pereira, W. S. G.; Aguilar, A. M.; Venanzi, M.; Cavalieri, F.; Giuntini, F.; Alves, W. A., Hierarchical Self-Assembly of Peptides and its Applications in Bionanotechnology. *Macromolecular Chemistry and Physics* **2019,** *220* (14), 1900085.
4. Qiu, H.; Hudson, Z. M.; Winnik, M. A.; Manners, I., Multidimensional hierarchical self-assembly of amphiphilic cylindrical block comicelles. *Science* **2015,** *347* (6228), 1329.
5. Lohr, A.; Lysetska, M.; Würthner, F., Supramolecular Stereomutation in Kinetic and Thermodynamic Self-Assembly of Helical Merocyanine Dye Nanorods. *Angewandte Chemie International Edition* **2005,** *44* (32), 5071-5074.
6. Wang, J.; Liu, K.; Xing, R.; Yan, X., Peptide self-assembly: thermodynamics and kinetics. *Chemical Society Reviews* **2016,** *45* (20), 5589-5604.
7. van Rijt, M. M. J.; Ciaffoni, A.; Ianiro, A.; Moradi, M.-A.; Boyle, A. L.; Kros, A.; Friedrich, H.; Sommerdijk, N. A. J. M.; Patterson, J. P., Designing stable, hierarchical peptide fibers from block co-polypeptide sequences. *Chem Sci* **2019,** *10* (39), 9001-9008.
8. Nicolai, T.; Colombani, O.; Chassenieux, C., Dynamic polymeric micelles versus frozen nanoparticles formed by block copolymers. *Soft Matter* **2010,** *6* (14), 3111-3118.
9. Tanoue, R.; Higuchi, R.; Enoki, N.; Miyasato, Y.; Uemura, S.; Kimizuka, N.; Stieg, A. Z.; Gimzewski, J. K.; Kunitake, M., Thermodynamically Controlled Self-Assembly of Covalent Nanoarchitectures in Aqueous Solution. *Acs Nano* **2011,** *5* (5), 3923-3929.
10. He, X.; He, Y.; Hsiao, M.-S.; Harniman, R. L.; Pearce, S.; Winnik, M. A.; Manners, I., Complex and Hierarchical 2D Assemblies via Crystallization-Driven Self-Assembly of Poly(l-lactide) Homopolymers with Charged Termini. *J Am Chem Soc* **2017,** *139* (27), 9221-9228.
11. Blanazs, A.; Ryan, A. J.; Armes, S. P., Predictive Phase Diagrams for RAFT Aqueous Dispersion Polymerization: Effect of Block Copolymer Composition, Molecular Weight, and Copolymer Concentration. *Macromolecules* **2012,** *45* (12), 5099-5107.
12. Yeow, J.; Boyer, C., Photoinitiated Polymerization-Induced Self-Assembly (Photo-PISA): New Insights and Opportunities. *Advanced Science* **2017,** *4* (7), 1700137.
13. Wright, D. B.; Touve, M. A.; Adamiak, L.; Gianneschi, N. C., ROMPISA: Ring-Opening Metathesis Polymerization-Induced Self-Assembly. *ACS Macro Letters* **2017,** *6* (9), 925-929.
14. Canning, S. L.; Smith, G. N.; Armes, S. P., A Critical Appraisal of RAFT-Mediated Polymerization-Induced Self-Assembly. *Macromolecules* **2016,** *49* (6), 1985-2001.
15. Boott, C. E.; Gwyther, J.; Harniman, R. L.; Hayward, D. W.; Manners, I., Scalable and uniform 1D nanoparticles by synchronous polymerization, crystallization and self-assembly. *Nature Chemistry* **2017,** *9*, 785.

16. Oliver, A. M.; Gwyther, J.; Boott, C. E.; Davis, S.; Pearce, S.; Manners, I., Scalable Fiber-like Micelles and Block Co-micelles by Polymerization-Induced Crystallization-Driven Self-Assembly. *J. Am. Chem. Soc.* **2018,** *140* (51), 18104-18114.
17. Vilgis, T.; Halperin, A., Aggregation of coil-crystalline block copolymers: equilibrium crystallization. *Macromolecules* **1991,** *24* (8), 2090-2095.
18. He, W.-N.; Xu, J.-T., Crystallization assisted self-assembly of semicrystalline block copolymers. *Progress in Polymer Science* **2012,** *37* (10), 1350-1400.
19. Inam, M.; Cambridge, G.; Pitto-Barry, A.; Laker, Z. P. L.; Wilson, N. R.; Mathers, R. T.; Dove, A. P.; O'Reilly, R. K., 1D vs. 2D shape selectivity in the crystallization-driven self-assembly of polylactide block copolymers. *Chem Sci* **2017,** *8* (6), 4223-4230.
20. Petzetakis, N.; Dove, A. P.; O'Reilly, R. K., Cylindrical micelles from the living crystallization-driven self-assembly of poly(lactide)-containing block copolymers. *Chem Sci* **2011,** *2* (5), 955-960.
21. Petzetakis, N.; Walker, D.; Dove, A. P.; O'Reilly, R. K., Crystallization-driven sphere-to-rod transition of poly(lactide)-b-poly(acrylic acid) diblock copolymers: mechanism and kinetics. *Soft Matter* **2012,** *8* (28), 7408-7414.
22. Pitto-Barry, A.; Kirby, N.; Dove, A. P.; O'Reilly, R. K., Expanding the scope of the crystallization-driven self-assembly of polylactide-containing polymers. *Polymer Chemistry* **2014,** *5* (4), 1427-1436.
23. Yu, W.; Inam, M.; Jones, J. R.; Dove, A. P.; O'Reilly, R. K., Understanding the CDSA of poly(lactide) containing triblock copolymers. *Polymer Chemistry* **2017,** *8* (36), 5504-5512.
24. Ganda, S.; Stenzel, M. H., Concepts, fabrication methods and applications of living crystallization-driven self-assembly of block copolymers. *Progress in Polymer Science* **2020,** *101*, 101195.
25. Charleux, B.; Delaittre, G.; Rieger, J.; D'Agosto, F., Polymerization-Induced Self-Assembly: From Soluble Macromolecules to Block Copolymer Nano-Objects in One Step. *Macromolecules* **2012,** *45* (17), 6753-6765.
26. Warren, N. J.; Armes, S. P., Polymerization-Induced Self-Assembly of Block Copolymer Nano-objects via RAFT Aqueous Dispersion Polymerization. *J Am Chem Soc* **2014,** *136* (29), 10174-10185.
27. Sun, J.-T.; Hong, C.-Y.; Pan, C.-Y., Formation of the block copolymer aggregates via polymerization-induced self-assembly and reorganization. *Soft Matter* **2012,** *8* (30), 7753-7767.
28. Penfold, N. J. W.; Yeow, J.; Boyer, C.; Armes, S. P., Emerging Trends in Polymerization-Induced Self-Assembly. *ACS Macro Letters* **2019,** *8* (8), 1029-1054.
29. Varlas, S.; Foster, J. C.; O'Reilly, R. K., Ring-opening metathesis polymerization-induced self-assembly (ROMPISA). *Chem Commun* **2019,** *55* (62), 9066-9071.
30. D'Agosto, F.; Rieger, J.; Lansalot, M., RAFT-mediated polymerization-induced self-assembly. *Angewandte Chemie International Edition n/a* (n/a).
31. Figg, C. A.; Simula, A.; Gebre, K. A.; Tucker, B. S.; Haddleton, D. M.; Sumerlin, B. S., Polymerization-induced thermal self-assembly (PITSA). *Chem Sci* **2015,** *6* (2), 1230-1236.
32. Fu, C.; Xu, J.; Boyer, C., Photoacid-mediated ring opening polymerization driven by visible light. *Chem Commun* **2016,** *52* (44), 7126-7129.

33. Cunningham, V. J.; Alswieleh, A. M.; Thompson, K. L.; Williams, M.; Leggett, G. J.; Armes, S. P.; Musa, O. M., Poly(glycerol monomethacrylate)–Poly(benzyl methacrylate) Diblock Copolymer Nanoparticles via RAFT Emulsion Polymerization: Synthesis, Characterization, and Interfacial Activity. *Macromolecules* **2014,** *47* (16), 5613-5623.
34. Tanaka, H.; Yamauchi, K.; Hasegawa, H.; Miyamoto, N.; Koizumi, S.; Hashimoto, T., In situ and real-time small-angle neutron scattering studies of living anionic polymerization process and polymerization-induced self-assembly of block copolymers. *Physica B: Condensed Matter* **2006,** *385-386*, 742-744.
35. Guégain, E.; Zhu, C.; Giovanardi, E.; Nicolas, J., Radical Ring-Opening Copolymerization-Induced Self-Assembly (rROPISA). *Macromolecules* **2019,** *52* (10), 3612-3624.
36. Grazon, C.; Salas-Ambrosio, P.; Ibarboure, E.; Buol, A.; Garanger, E.; Grinstaff, M. W.; Lecommandoux, S.; Bonduelle, C., Aqueous Ring-Opening Polymerization-Induced Self-Assembly (ROPISA) of N-Carboxyanhydrides. *Angewandte Chemie International Edition* **2020,** *59* (2), 622-626.
37. Sha, Y.; Rahman, M. A.; Zhu, T.; Cha, Y.; McAlister, C. W.; Tang, C., ROMPI-CDSA: ring-opening metathesis polymerization-induced crystallization-driven self-assembly of metallo-block copolymers. *Chem Sci* **2019,** *10* (42), 9782-9787.
38. Dove, A. P., Organic Catalysis for Ring-Opening Polymerization. *ACS Macro Letters* **2012,** *1* (12), 1409-1412.
39. Bobo, D.; Robinson, K. J.; Islam, J.; Thurecht, K. J.; Corrie, S. R., Nanoparticle-Based Medicines: A Review of FDA-Approved Materials and Clinical Trials to Date. *Pharmaceutical Research* **2016,** *33* (10), 2373-2387.
40. He, X.; Li, L.; Su, H.; Zhou, D.; Song, H.; Wang, L.; Jiang, X., Poly(ethylene glycol)-block-poly(ε-caprolactone)-and phospholipid-based stealth nanoparticles with enhanced therapeutic efficacy on murine breast cancer by improved intracellular drug delivery. *Int J Nanomedicine* **2015,** *10*, 1791-1804.
41. Wang, J.; Li, S.; Han, Y.; Guan, J.; Chung, S.; Wang, C.; Li, D., Poly(Ethylene Glycol)-Polylactide Micelles for Cancer Therapy. *Front Pharmacol* **2018,** *9*, 202-202.
42. Lohmeijer, B. G. G.; Pratt, R. C.; Leibfarth, F.; Logan, J. W.; Long, D. A.; Dove, A. P.; Nederberg, F.; Choi, J.; Wade, C.; Waymouth, R. M.; Hedrick, J. L., Guanidine and Amidine Organocatalysts for Ring-Opening Polymerization of Cyclic Esters. *Macromolecules* **2006,** *39* (25), 8574-8583.
43. Kamber, N. E.; Jeong, W.; Waymouth, R. M.; Pratt, R. C.; Lohmeijer, B. G. G.; Hedrick, J. L., Organocatalytic Ring-Opening Polymerization. *Chemical Reviews* **2007,** *107* (12), 5813-5840.
44. Sato, S.; Gondo, D.; Wada, T.; Kanehashi, S.; Nagai, K., Effects of various liquid organic solvents on solvent-induced crystallization of amorphous poly(lactic acid) film. *J Appl Polym Sci* **2013,** *129* (3), 1607-1617.
45. Kricheldorf, H. R.; Meier-Haack, J., Polylactones, 22 ABA triblock copolymers of L-lactide and poly(ethylene glycol). *Die Makromolekulare Chemie* **1993,** *194* (2), 715-725.
46. Aldén, M.; Lydén, M.; Tegenfeldt, J., Effect of counterions on the interactions in solid dispersions between polyethylene glycol, griseofulvin and alkali dodecyl sulphates. *International Journal of Pharmaceutics* **1994,** *110* (3), 267-276.

47. Chuma, A.; Horn, H. W.; Swope, W. C.; Pratt, R. C.; Zhang, L.; Lohmeijer, B. G. G.; Wade, C. G.; Waymouth, R. M.; Hedrick, J. L.; Rice, J. E., The reaction mechanism for the organocatalytic ring-opening polymerization of L-lactide using a guanidine-based catalyst: Hydrogen-bonded or covalently bound? *J Am Chem Soc* **2008,** *130* (21), 6749-6754.
48. Pratt, R. C.; Lohmeijer, B. G.; Long, D. A.; Waymouth, R. M.; Hedrick, J. L., Triazabicyclodecene: a simple bifunctional organocatalyst for acyl transfer and ring-opening polymerization of cyclic esters. *J Am Chem Soc* **2006,** *128* (14), 4556-7.
49. Pratt, R. C.; Lohmeijer, B. G. G.; Long, D. A.; Lundberg, P. N. P.; Dove, A. P.; Li, H.; Wade, C. G.; Waymouth, R. M.; Hedrick, J. L., Exploration, Optimization, and Application of Supramolecular Thiourea−Amine Catalysts for the Synthesis of Lactide (Co)polymers. *Macromolecules* **2006,** *39* (23), 7863-7871.
50. Pan, P.; Inoue, Y., Polymorphism and isomorphism in biodegradable polyesters. *Prog. Polym. Sci.* **2009,** *34* (7), 605-640.
51. Saeidlou, S.; Huneault, M. A.; Li, H.; Park, C. B., Poly(lactic acid) crystallization. *Progress in Polymer Science* **2012,** *37* (12), 1657-1677.
52. Lan, Q.; Li, Y., Mesophase-Mediated Crystallization of Poly(l-lactide): Deterministic Pathways to Nanostructured Morphology and Superstructure Control. *Macromolecules* **2016,** *49* (19), 7387-7399.
53. Petzetakis, N.; Robin, M. P.; Patterson, J. P.; Kelley, E. G.; Cotanda, P.; Bomans, P. H. H.; Sommerdijk, N. A. J. M.; Dove, A. P.; Epps, T. H.; O'Reilly, R. K., Hollow Block Copolymer Nanoparticles through a Spontaneous One-step Structural Reorganization. *Acs Nano* **2013,** *7* (2), 1120-1128.
54. Exploring the energy landscape. *Nature Nanotechnology* **2015,** *10* (2), 101-101.
55. Mattia, E.; Otto, S., Supramolecular systems chemistry. *Nat. Nanotechnol.* **2015,** *10* (2), 111-119.
56. Yu, H.-Y.; Zhang, H.; Song, M.-L.; Zhou, Y.; Yao, J.; Ni, Q.-Q., From Cellulose Nanospheres, Nanorods to Nanofibers: Various Aspect Ratio Induced Nucleation/Reinforcing Effects on Polylactic Acid for Robust-Barrier Food Packaging. *ACS Applied Materials & Interfaces* **2017,** *9* (50), 43920-43938.
57. Suzuki, M.; Hanabusa, K., Polymer organogelators that make supramolecular organogels through physical cross-linking and self-assembly. *Chemical Society Reviews* **2010,** *39* (2), 455-463.
58. Inam, M.; Cambridge, G.; Pitto-Barry, A.; Laker, Z. P. L.; Wilson, N. R.; Mathers, R. T.; Dove, A. P.; O'Reilly, R. K., 1D vs. 2D shape selectivity in the crystallization-driven self-assembly of polylactide block copolymers. *Chem Sci* **2017,** *8* (6), 4223-4230.
59. De Yoreo, J. J.; Gilbert, P. U. P. A.; Sommerdijk, N. A. J. M.; Penn, R. L.; Whitelam, S.; Joester, D.; Zhang, H.; Rimer, J. D.; Navrotsky, A.; Banfield, J. F.; Wallace, A. F.; Michel, F. M.; Meldrum, F. C.; Cölfen, H.; Dove, P. M., Crystallization by particle attachment in synthetic, biogenic, and geologic environments. *Science* **2015,** *349* (6247), aaa6760.
60. De Yoreo, J. J.; Vekilov, P. G., Principles of Crystal Nucleation and Growth. *Rev. Mineral. Geochem.* **2003,** *54* (1), 57-93.
61. Patterson, J. P.; Robin, M. P.; Chassenieux, C.; Colombani, O.; O'Reilly, R. K., The analysis of solution self-assembled polymeric nanomaterials. *Chemical Society Reviews* **2014,** *43* (8), 2412-2425.

62. Parent, L. R.; Bakalis, E.; Ramírez-Hernández, A.; Kammeyer, J. K.; Park, C.; de Pablo, J.; Zerbetto, F.; Patterson, J. P.; Gianneschi, N. C., Directly Observing Micelle Fusion and Growth in Solution by Liquid-Cell Transmission Electron Microscopy. *J Am Chem Soc* **2017,** *139* (47), 17140-17151.
63. Wright, D. B.; Patterson, J. P.; Gianneschi, N. C.; Chassenieux, C.; Colombani, O.; O'Reilly, R. K., Blending block copolymer micelles in solution; obstacles of blending. *Polymer Chemistry* **2016,** *7* (8), 1577-1583.
64. Choi, S.-H.; Lodge, T. P.; Bates, F. S., Mechanism of Molecular Exchange in Diblock Copolymer Micelles: Hypersensitivity to Core Chain Length. *Physical Review Letters* **2010,** *104* (4), 047802.
65. Zhou, W.; Qu, Q.; Xu, Y.; An, Z., Aqueous Polymerization-Induced Self-Assembly for the Synthesis of Ketone-Functionalized Nano-Objects with Low Polydispersity. *ACS Macro Letters* **2015,** *4* (5), 495-499.
66. Lowe, A. B., RAFT alcoholic dispersion polymerization with polymerization-induced self-assembly. *Polymer* **2016,** *106*, 161-181.
67. Truong, N. P.; Dussert, M. V.; Whittaker, M. R.; Quinn, J. F.; Davis, T. P., Rapid synthesis of ultrahigh molecular weight and low polydispersity polystyrene diblock copolymers by RAFT-mediated emulsion polymerization. *Polymer Chemistry* **2015,** *6* (20), 3865-3874.
68. Varlas, S.; Foster, J. C.; O'Reilly, R. K., Ring-opening metathesis polymerization-induced self-assembly (ROMPISA). *Chem Commun (Camb)* **2019,** *55* (62), 9066-9071.
69. Takahashi, R.; Miwa, S.; Sobotta, F. H.; Lee, J. H.; Fujii, S.; Ohta, N.; Brendel, J. C.; Sakurai, K., Unraveling the kinetics of the structural development during polymerization-induced self-assembly: decoupling the polymerization and the micelle structure. *Polymer Chemistry* **2020,** *11* (8), 1514-1524.
70. Marolf, D. M.; Jones, M. R., Measurement Challenges in Dynamic and Nonequilibrium Nanoscale Systems. *Analytical Chemistry* **2019**.
71. Mattia, E.; Otto, S., Supramolecular systems chemistry. *Nat. Nanotechnol.* **2015,** *10* (2), 111-119.
72. Duda, A.; Penczek, S., Thermodynamics of L-lactide polymerization. Equilibrium monomer concentration. *Macromolecules* **1990,** *23* (6), 1636-1639.
73. Desai, A.; Mitchison, T. J., MICROTUBULE POLYMERIZATION DYNAMICS. *Annu. Rev. Cell Dev. Biol.* **1997,** *13* (1), 83-117.
74. Ragazzon, G.; Prins, L. J., Energy consumption in chemical fuel-driven self-assembly. *Nature Nanotechnology* **2018,** *13* (10), 882-889.
75. Tena-Solsona, M.; Boekhoven, J., Dissipative Self-Assembly of Peptides. *Isr. J. Chem.* **2019,** *0* (0).
76. van Rossum, S. A. P.; Tena-Solsona, M.; van Esch, J. H.; Eelkema, R.; Boekhoven, J., Dissipative out-of-equilibrium assembly of man-made supramolecular materials. *Chem. Soc. Rev.* **2017,** *46* (18), 5519-5535.
77. Ianiro, A.; Wu, H.; van Rijt, M. M. J.; Vena, M. P.; Keizer, A. D. A.; Esteves, A. C. C.; Tuinier, R.; Friedrich, H.; Sommerdijk, N. A. J. M.; Patterson, J. P., Liquid–liquid phase separation during amphiphilic self-assembly. *Nature Chemistry* **2019,** *11* (4), 320-328.
78. Cui, H.; Chen, Z.; Zhong, S.; Wooley, K. L.; Pochan, D. J., Block Copolymer Assembly via Kinetic Control. *Science* **2007,** *317* (5838), 647.

79. Yan, Y.; Huang, J.; Tang, B. Z., Kinetic trapping – a strategy for directing the self-assembly of unique functional nanostructures. *Chem Commun* **2016,** *52* (80), 11870-11884.
80. Khor, S. Y.; Truong, N. P.; Quinn, J. F.; Whittaker, M. R.; Davis, T. P., Polymerization-Induced Self-Assembly: The Effect of End Group and Initiator Concentration on Morphology of Nanoparticles Prepared via RAFT Aqueous Emulsion Polymerization. *ACS Macro Letters* **2017,** *6* (9), 1013-1019.

Chapter 3: Gaining Structural Control by Modification of Polymerization Rate in Ring-Opening Polymerization-Induced Crystallization-Driven Self-Assembly

This chapter is adapted from a research article “Gaining Structural Control by Modification of Polymerization Rate in Ring-Opening Polymerization-Induced Crystallization-Driven Self-Assembly. Paul Joshua Hurst, Annissa A Graham, Joseph P Patterson, ACS Polymer Au, 2022, 2 [6], 501-509.”

3.0. Abstract

Polymerization-induced self-assembly (PISA) has become an important one pot method for the preparation of well-defined block copolymer nanoparticles. In PISA, morphology is typically controlled by changing molecular architecture and polymer concentration. However, several computational and experimental studies have suggested that changes in polymerization rate can lead to morphological differences. In this chapter, I demonstrate that catalyst selection can be used to control morphology independent of polymer structure and concentration in ring-opening polymerization-induced crystallization-driven self-assembly (ROPI-CDSA). Slower rates of polymerization give rise to slower rates of self-assembly, resulting in denser lamellae and more 3D structures when compared to faster rates of polymerization. The explanation for this is that the fast samples transiently exist in a non-equilibrium state as self-assembly starts at a higher solvophobic block length when compared to the slow polymerization. Following this work, I expect that subsequent examples of rate variation in PISA will allow for greater control over morphological outcome.

3.1. Introduction

Polymerization-induced self-assembly (PISA) has revolutionized the synthesis of block copolymer self-assemblies as it enables the reproducible scaled-up production of nanoparticles.[37,39,91,92] Compared to traditional self-assembly, which generally yields solutions that are 1% solids w/w, PISA can garner solutions ranging from 10-50% solids w/w and enables easy access to a range of higher-ordered morphologies such as worms and vesicles.[92,93] PISA has been developed for a wide range of polymerization techniques[42,49,50,92,94–97] with the most studied method being reversible addition-fragmentation chain-transfer (RAFT).[49,92,94] In addition, PISA for crystalline and semicrystalline polymers, termed polymerization-induced crystallization-driven self-assembly (PI-CDSA), has been developed to allow for the scaled-up production of anisotropic nanostructures such as rods and lamellae.[41,52,98–101]

As outlined in Chapter 2, prior to the work in this chapter, I developed PISA for the ring-opening polymerization (ROP) of semicrystalline polyesters, termed ring-opening polymerization-induced crystallization-driven self-assembly (ROPI-CDSA).[99] This process occurred by chain extending polyethylene glycol (PEG) with L-lactide in toluene using triazabicyclodecene (TBD) as the catalyst. The resulting poly-(L)-lactide-*block*-polyethylene glycol (PLLA-*b*-PEG) particle morphology could be controlled by changing the polymer structure (degree of polymerization (DP)) and concentration, as is common with other PISA processes.[37,94] In contrast to most PISA examples where self-assembly is fast with respect to polymerization,[102] there was a delay between the polymerization and self-assembly. TBD-catalyzed ROP of L-lactide is very fast (~ 1 minute) whereas the resulting self-assembly, which was driven by crystallization was considerably slower (~ hours). Due to this delay, one could trap different morphologies post polymerization by

freeze drying and redispersing the samples in water where the structures become kinetically trapped. This trapping enables time-post-polymerization to be an additional factor to control morphology in PISA experiments. This strategy is advantageous as it enables different morphologies to be formed from the same polymer and at the same concentration. The interpretation of this data was that during the polymerization, the polymers are in a non-equilibrium state as the chains are temporarily soluble in the selective solvent. Thus, I hypothesize that a modification in the polymerization kinetics would lead to a change in the non-equilibrium state, resulting in a different self-assembly mechanism, allowing access to different morphologies.

Dissipative particle dynamics (DPD) simulations have indicated that polymerization rate can be used to control morphology of poly(4-vinylpyridine)-*b*-polystyrene PISA processes.[103,104] The explanation for the change in morphology was that fast polymerization rates led to larger amounts of exposed solvophobic block resulting in a faster rate of self-assembly. Experimentally, mode of initiation, changes in initiator concentration, solvent composition, monomer types, and Z-group substitution, in the case of RAFT-PISA, have shown differences in morphology, which have been attributed to changes in the rate of polymerization.[47–53] However, there is limited quantitative information on how the rate of polymerization affects morphology because designing experiments to modulate the propagation rate constant, k_p, without affecting thermodynamic parameters or polymerization control are difficult. For example, changing monomer type, temperature or solvent composition will also change the free energy landscape for the assembly process, making it difficult to assign differences in

morphology to kinetic effects alone. Additionally, the relaxation time is typically fast for RAFT-PISA processes limiting mechanistic studies into potential non-equilibrium states.

Generally, in controlled polymerization, k_p depends on the nature of the monomer under a given temperature and solvent, however the presence of a catalyst can modulate k_p without changing the environment. In the ROP of polyesters, a variety of catalytic systems have been developed to allow for the polymerization of one monomer with a range of k_p values.[105,106] Thus, we can use different catalysts in ROPI-CDSA to monitor polymerization kinetics and compare any differences between the resulting self-assemblies.

Here, to test my hypothesis, two ROP catalytic systems (one fast and one slow) are used to alter the polymerization rate of L-lactide and the self-assembly of PLLA-*b*-PEG block copolymers. Kinetic studies of polymerization and self-assembly were conducted using ^{1}H NMR and UV/Vis spectroscopy, respectively. Rheology was used to probe the mechanical properties of the resulting organogels. Wide-angle X-ray scattering (WAXS) and Fourier-transform infrared spectroscopy (FTIR) were used to determine crystallization properties. Dry cryoTEM, SEM, and AFM were used to determine the nanoscale morphology.

3.2. Results

3.2.1. Synthetic Parameters and Polymerization and Assembly Kinetics

Testing the hypothesis that polymerization kinetics affects the morphology of ROPI-CDSA reactions requires two systems with almost identical thermodynamics and significantly different kinetics (fast or slow). Therefore, all ROPI-CDSA reactions were performed in the same solvent (toluene), at the same temperature and concentration,

forming PLLA-*b*-PEG block copolymers with the same molecular weight and dispersity. The polymerization kinetics were controlled by catalyst selection. TBD was not used as a catalyst due to reports of potential transesterification at higher degrees of polymerization.[99,107] Hedrick and Waymouth et. al.[108,109] developed a dual catalytic system for the polymerization of cyclic esters which utilizes a thiourea (TU), derived from cyclohexylamine and 3,5-bis(trifluoromethyl)phenyl isothiocyanate, paired with a tertiary amine or diazabicycloundecene (DBU). The amidine DBU (1% mol) was paired with TU (7.5% mol) for the fast reaction and the tertiary amine (-)-sparteine (7.5% mol) was paired with TU (7.5% mol) for the slow reaction (Figure 3.1A-B). DBU can catalyze the ROP of L-lactide without TU due to its higher basicity but to control environmental conditions, 7.5% mol TU was used in both the slow and fast reactions. A series of fast and slow polymerizations were carried out, varying PLLA DP (200, 400) and solids content (10, 15, 20 w/w%). The PLLA DP 200, 10% systems were repeated three times for reproducibility.

Table 3.1: Polymerization table of $PLLA_n$-*b*-PEG_{45} block copolymers synthesized in this study.

ID	Co-catalyst	PLLA DP	Solids w/w%	Đ	Gel (Y/N)
1	DBU	200	10	1.06	N
2	DBU	200	10	1.16	N
3	DBU	200	10	1.12	N
4	DBU	200	15	1.14	N
5	DBU	200	20	1.17	Y
6	DBU	400	10	1.14	N
7	(-)-sparteine	200	10	1.16	Y
8	(-)-sparteine	200	10	1.10	Y
9	(-)-sparteine	200	10	1.17	Y
10	(-)-sparteine	200	15	1.16	Y
11	(-)-sparteine	200	20	1.13	Y
12	(-)-sparteine	400	10	1.15	Y

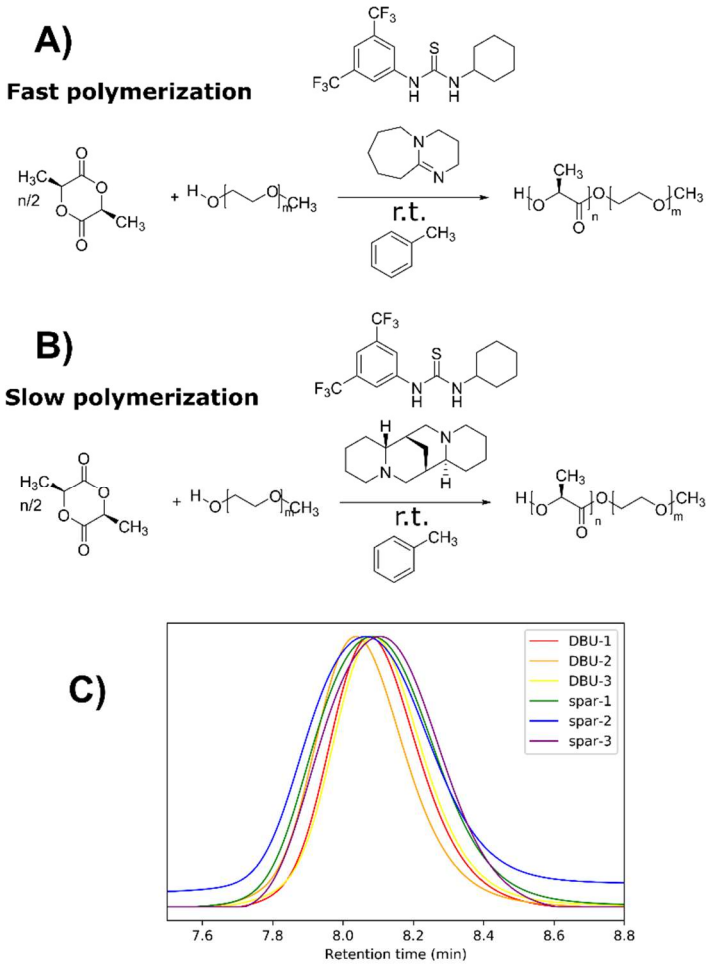

Figure 3.1: Polymerization schemes and SEC data. ROP of L-lactide to produce PLLA-b-PEG catalyzed by TU and A) DBU or B) (-)-sparteine. C) Triplicate SEC data for $PLLA_{200}$-b-PEG_{45} for polymers **1-3** and **7-9**. All Đ ≈ 1.1 indicating a controlled polymerization.

The resulting polymers were analyzed by size exclusion chromatography (SEC) and ^{1}H NMR spectroscopy. Both catalytic systems reached >95% conversion with Đ < 1.2, indicating a controlled polymerization (Figure 3.1C, Table 3.1, Table B.1, Figures B.1-3). The polymerization kinetics of PLLA DP = 200, 10% solids w/w, reactions (**1-3**, **7-9**) were studied using ^{1}H NMR spectroscopy. The rate equation for a di-catalytic ROP system depends on the concentration of both active catalytic species (TU and cocat), the initiator (I) and the monomer (LA) (Equation 3.1).[109]

$$-\frac{d[LA]}{dt} = -k_p K_1 K_2 [TU][cocat][I][LA] = -k_{app}[LA] \quad (3.1)$$

As only the monomer concentration changes, the system can be modeled as a pseudo-first order reaction. Because finding the propagation rate constant (k_p) would require thermodynamic knowledge of the catalyst-monomer association constants,[109] the apparent propagation rate constant (k_{app}) was found. ^{1}H NMR kinetic studies show two

k_{app} values for both polymerization processes (1st k_{app}: fast k_{app} = 19 ± 2 h^{-1}, slow k_{app} = 0.16 ± 0.02 h^{-1}) with an increase in k_{app} that corresponds to the onset of turbidity of the self-assembly (2nd k_{app}: fast k_{app} = 40 ± 3 h^{-1}, slow k_{app} = 0.54 ± 0.12 h^{-1}) (Figure 3.2, Table 3.2, Figures B.4-5) consistent with previous PISA literature.[37,47,110,111] There is a three-fold increase in k_{app} for the slow polymerization compared to a two-fold increase for the fast polymerization. Increases in the propagation rate are usually explained by a high local concentration of monomer in or near the self-assembled phase. Differences in the local environment or growth mechanism could explain the difference in the percent increase of k_{app} although further research would be needed to verify this hypothesis. The self-assembly kinetics were probed using UV/Vis spectroscopy performed at 600 nm to measure turbidity (Figure 3.2, Figures B.6-7). The turbidity studies confirm that self-assembly starts at approximately the same time as the change in k_{app}, indicating that the onset of self-assembly increases k_{app}. The (-)-sparteine co-catalyzed slow polymerization system became turbid around 70% (PLLA DP = 140) conversion compared to 85% conversion (PLLA DP = 170) for the fast DBU co-catalyzed polymerization system. Additionally, the time to maximum turbidity is substantially different for the fast polymerization and slow polymerization samples taking ~ 0.15 and 12 h respectively. The turbidity data appears to be sigmoidal, which has been observed in a variety of self-assembly processes.[33–36] Therefore, the data was modelled as a logistic function (Equation 3.2).

$$f(x) = \frac{L}{1+e^{-k(x-x_0)}} + m \tag{3.2}$$

Where L is the maximum value of the function, m is the intercept, x_0 is the x value of the steepness point of the curve, and k quantifies the steepness of the sigmodal curve. Here

k can then be used as a numerical quantification of the rate of turbidity, which is an estimate for the rate of self-assembly. Fitting the data to the logistic function gives $k_{turbidity}$ of 70.2 and 0.98 h^{-1} for the fast and slow polymerization systems respectively. Thus, both the rate of polymerization (k_{app}) and the rate of self-assembly ($k_{turbidity}$) are much greater in the fast polymerization than the slow polymerization.

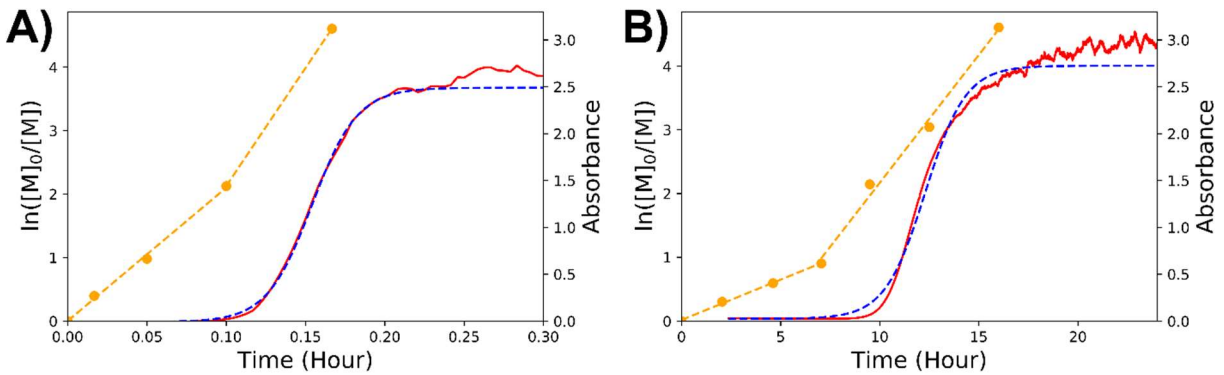

Figure 3.2: Polymerization and self-assembly kinetics for the A) fast and B) slow polymerizations of $PLLA_{200}$-b-PEG_{45}. The orange markers are the measured values of $ln[M]_0/[M]$ with the dotted line representing the linear fit. The red line is the measured absorbance at 600 nm using UV/Vis spectroscopy with the blue line being the logistic fit.

Table 3.2: Polymerization kinetics studies of $PLLA_{200}$-*b*-PEG_{45}.
All trendlines used to get k values had R^2>0.95.

ID	Co-catalyst	1st k_{app} h^{-1}	2nd k_{app} h^{-1}
1	DBU	17	42
2	DBU	18	40
3	DBU	21	37
Average	DBU	19 ± 2	40 ± 3
7	(-)-sparteine	0.18	0.60
8	(-)-sparteine	0.17	0.63
9	(-)-sparteine	0.13	0.40
Average	(-)-sparteine	0.16 ± 0.02	0.54 ± 0.12

3.2.2. Structural and Morphological Studies

In addition to the variable polymerization and self-assembly kinetics, structural and morphological differences were observed between the fast and slow polymerization samples. The slow polymerizations, co-catalyzed by (-)-sparteine (**7-12**), led to the formation of organogels as defined by a gel-inversion test and oscillatory rheology (Figure 3.3, Figure B.8). Only sample **5** for the fast

reactions, co-catalyzed by DBU, formed a gel while the rest of the samples remained liquid (Figure 3.3). At 20% solids w/w, the storage modulus of the slow polymerization sample, **11**, was about an order of magnitude higher (10^4 Pa) than the fast polymerization sample (10^3 Pa), **5**. As a control experiment, to determine if co-catalyst differences were responsible for the rheological differences, polymerizations were carried out using (-)-sparteine or DBU ($PLLA_{200}$-*b*-PEG_{45}, 10% solids w/w) and upon quenching with benzoic acid, the other co-catalyst was added (DBU to (-)-sparteine polymerized solutions and (-)-sparteine to DBU polymerized solutions). No appreciable differences in the storage modulus were detected by oscillatory rheology in organogel samples between the control and the non-control for the slow polymerization samples (Figure B.8). Both fast polymerization samples remained liquids.

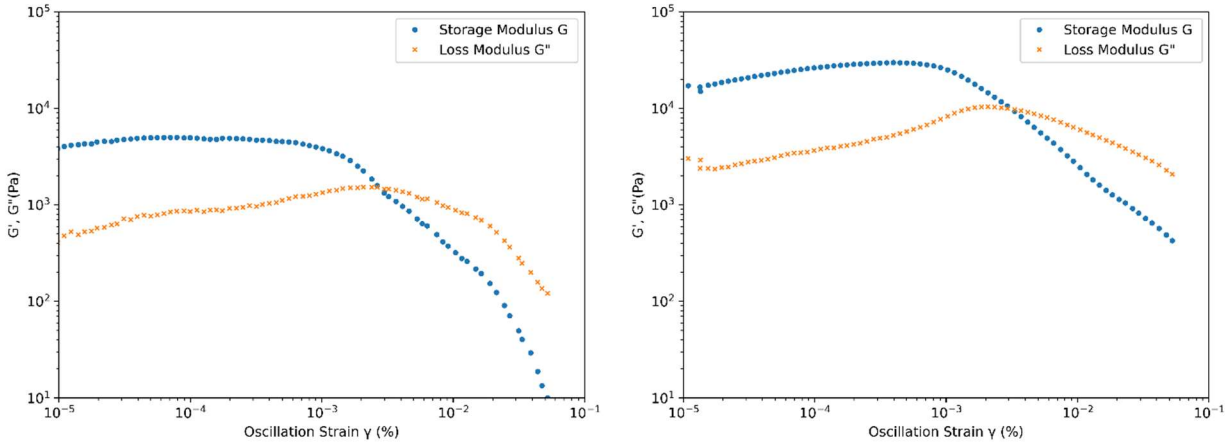

Figure 3.3: Oscillatory rheology for organogels **5** (left, DBU co-catalyst) and **11** (right, (-)-sparteine co-catalyst) for $PLLA_{200}$-b-PEG_{45} at 20% solids w/w. **11** has a storage modulus nearly one order of magnitude higher than **5** indicating it is the stronger gel.

WAXS and FTIR were then performed on freeze-dried powders of **1**-**12** to elucidate if structural differences were a result of differences in crystallization behavior (Figure 3.4, Figure B.9). WAXS shows that the crystallinity between the catalytic groups is very similar (Figure 3.4A-B). The calculated % crystallinity ranges for all samples are around 23%,

indicating that both systems crystallized to a similar extent (Table B.2). WAXS data show no evidence of TU crystallization suggesting that the TU is well integrated into the polymer matrix (Figure B.10). At 2θ 16.7 and 19.1, there are some small differences in peak positions (< 0.03), however triplicate runs of **7**-**9** show that peak values between the same sample have a standard deviation of 0.03 (Figure B.11), indicating these differences are statistically insignificant. FTIR shows that the carbonyl environment is similar in all samples and suggests supramolecular interactions between the TU and the PLLA ester (Figure 3.4C-D). In this work, the PLLA C=O stretches have two peaks at 1748 cm^{-1} and 1756 cm^{-1} (Figure 3.4D). In the first example of ROPI-CDSA, the C=O shifts were 1749 cm^{-1} and 1754 cm^{-1}, indicating differences in the carbonyl environment from the exclusion of TU.[15] Furthermore, a lack of N-H stretches is an indication that the N-H groups in the TU are hydrogen bonding with C=O (Figure S12).[37] Moreover, other TU stretches are offset from their original values indicating that the TU is well integrated into the polymer structure (Figure 3.4C).

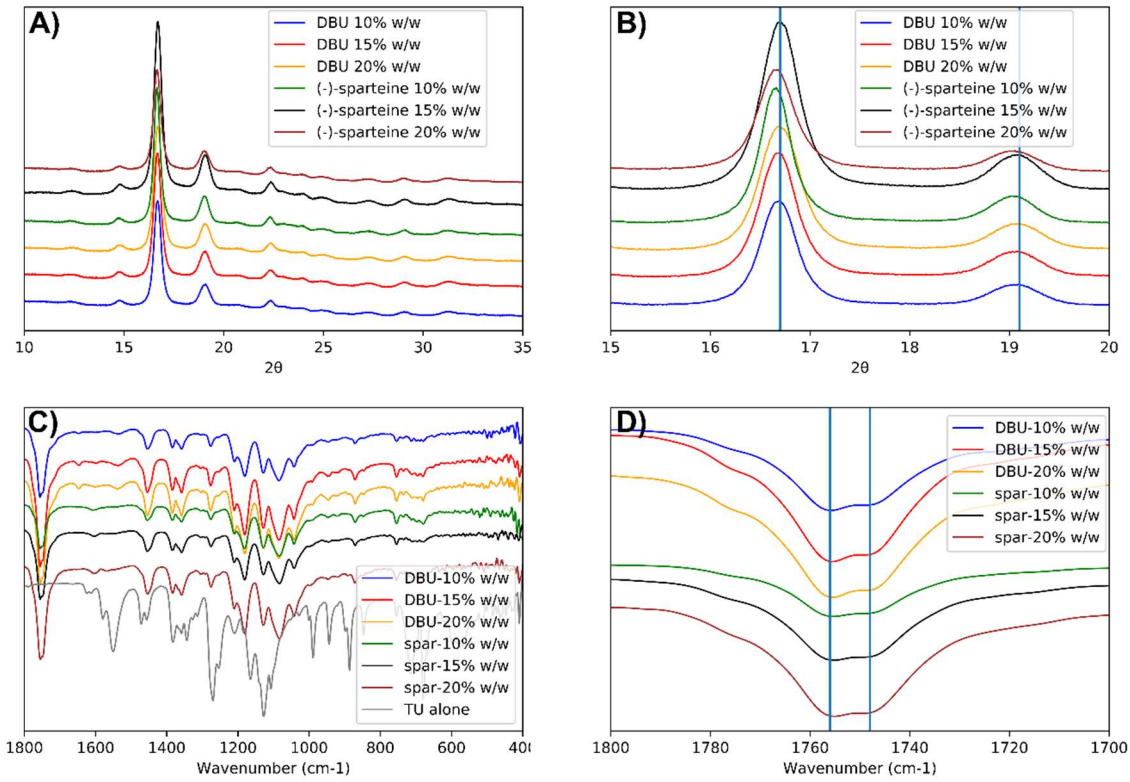

Figure 3.4: WAXS patterns and FTIR spectra for $PLLA_{200}$-b-PEG_{45} freeze-dried samples. A) WAXS overview. B) Close up on the two major peaks reveal slight offsets between the (-)-sparteine and DBU co-catalyzed samples. C) FTIR spectra of fingerprint and carbonyl region. D) FTIR of carbonyl with lines at 1748 cm^{-1} and 1756 cm^{-1}.

To determine the structure of the resulting self-assemblies and organogels, dry-CryoTEM, SEM, and AFM were performed on **1** and **7** (Figure 3.5). In contrast to our previous study,[15] the polymer toluene solutions could not be resuspended or extracted into water without precipitation. This is likely due to the hydrophobicity of the TU which is incorporated into the block copolymer self-assemblies. Therefore, a dry sample was imaged under cryogenic conditions (dry-cryoTEM) to minimize beam damage to the sample.[38] CryoTEM images of the fast polymerization sample, **1**, revealed a planar 2D aggregates (Figure 3.5A-B, Figure B.13) whereas the slow polymerization sample, **7**, revealed complex 3D aggregates (Figure 3.5E-F). AFM revealed that the lamellae thickness of **1**, the fast polymerization sample, was significantly thicker (Figure 3.5D, I,

5.6 ± 1.2 nm, n=21) than **7**, the slow polymerization sample (Figure 3.5H-I, 3.0 ± 0.2 nm, n=23). These values are thin compared to our previous paper and other relevant examples of PLLA-based block copolymer assemblies and further work is needed to understand the exact folding.[15,39,40] It should also be noted that the fast polymerization sample AFM micrograph showed the presence of double-stacked lamellae (10.2 ± 1.1 nm, n=14) as well as higher ordered stacks whereas the slow polymerization only showed single lamellae (Figures B.14-15). Due to the fact that the PEG block will contribute to this measurement, it is not possible to determine the folding factor for the PLLA block.[15] However, considering that both samples have the same molecular structure and assuming that drying artefacts are similar, this indicates that the PLLA blocks in the fast reaction are significantly less folded than in the slow reaction. This lower degree of folding can explain why 2D aggregates are favored over 3D aggregates.

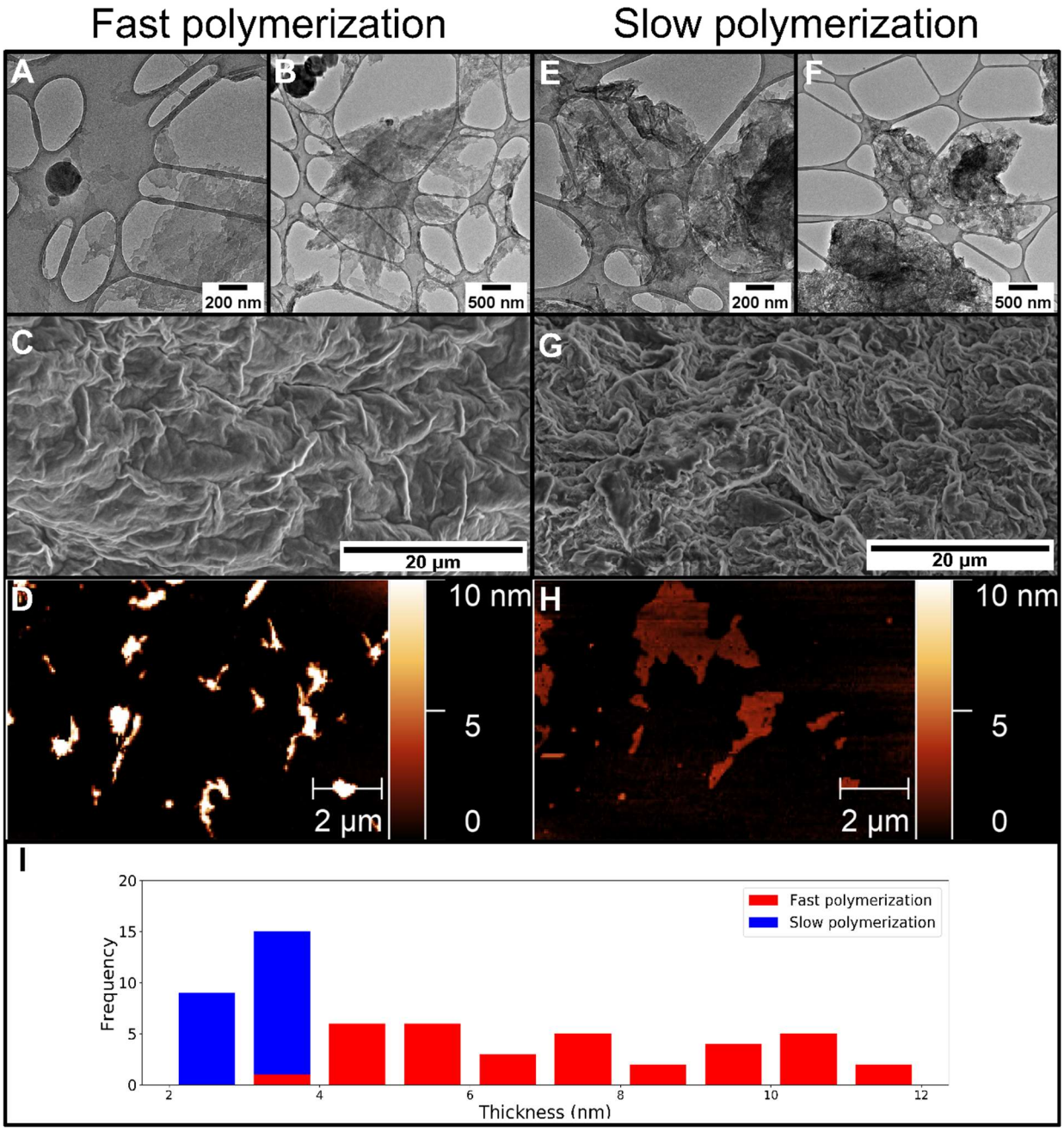

Figure 3.5: Dry cryoTEM, SEM, and AFM micrographs and histogram of $PLLA_{200}$-b-PEG_{45} assemblies resulting from a fast polymerization with co-catalyst DBU (A-D) and slow polymerization with with-cocatalyst (-)-sparteine (E-H). The stacked histogram (I) shows measurements for the fast polymerization in red and the slow polymerization in blue. The slow polymerization yields denser structures as shown in E-G, but the individual lamellae are thinner (H-I) than the fast polymerization (D, I).

3.3. Discussion

3.3.1. Slower polymerization kinetics lead to dense 3D networks

The combined SEC, ^{1}H-NMR, WAXS, and FTIR data reveal that the PLLA$_{200}$-*b*-PEG$_{45}$, polymers have the same molecular structure and crystallization behavior regardless of co-catalyst. Despite these similarities, the rheology, CryoTEM, SEM, and AFM data reveal that the fast and slow reactions form different structures in solution. The fast reactions favor the formation of 2D lamellae, resulting in solutions or weak gels, whereas the slow reactions favor the formation of 3D networks and stronger gels. The ^{1}H-NMR and turbidity kinetics studies show that the slow reactions become turbid at lower conversions and have a slower rate of self-assembly. Our previous paper studied the mechanism of ROPI-CDSA and revealed that the 3D networks can form through a particle aggregation-based mechanism.[15] I hypothesized that this was facilitated by forming structures with a low corona density as this would lower the energy barrier to aggregation.[41] The data here is consistent with this hypothesis as the AFM lamellae thickness measurements show that that the PLLA block in the slow reactions are much more folded than in the fast reactions. Given that both the fast and slow reactions form polymer with the same degree of polymerization, this would result in the assemblies in the slow reactions having lower corona densities that favor aggregation and the formation of 3D networks.

3.3.2. Non-equilibrium self-assembly

In the previous chapter, the polymerization time was much shorter (seconds to minutes) than the self-assembly relaxation time (hours to days). From a thermodynamic perspective we interpreted this as forming a non-equilibrium state as the system does not have sufficient time to relax with each monomer addition. Here, the polymerization is

sufficiently slow such that self-assembly begins before polymerization is complete. The fast DBU-catalyzed polymerization becomes turbid at higher conversions than the slow (-)-sparteine-catalyzed polymerization. In discussing the relative free energy of these two systems, we can divide the free energy diagram into three stages: early polymerization, late polymerization, and post-polymerization (Figure 3.6). In the early polymerization stage, the polymer chains are not sufficiently solvophobic to assemble or crystallize and consequently the free energy decreases as the polymerization progresses for both the fast and slow polymerizations. In the late polymerization state, the polymer chains are sufficiently solvophobic to initiate self-assembly and crystallization.

For the slow reaction, the free energy continues to decrease because the chains are able to undergo self-assembly and crystallization. For the fast reaction the polymer chains do not undergo assembly or crystallization and therefore, transiently exist in a non-equilibrium state until the onset of self-assembly. When the fast polymerization system begins to self-assemble, it does so with a greater exposed surface-area of solvophobic PLLA blocks, leading to enhanced self-assembly kinetics and more aggregation. A consequence of this is that the fast polymerization system becomes kinetically trapped at

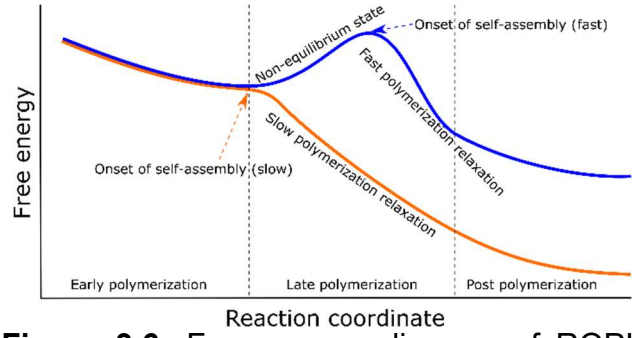

Figure 3.6: Free energy diagram of ROPI-CDSA resulting from fast polymerization (blue) and slow polymerization (orange). The polymerization is divided into three stages: Early polymerization where the polymers do not have a thermodynamic driving force to assemble, late polymerizations where the polymers have a thermodynamic driving force to assembly, and post polymerizations. Due to the relative rates of polymerization and self-assembly the fast polymerization temporarily accesses a non-equilibrium state leading to differences in the final kinetically trapped morphology.

a higher free energy relative to the slow polymerization system. Lastly, in the post-polymerization stage, additional increases in turbidity are observed in both systems, highlighting a lag in self-assembly kinetics with respect to polymerization.

3.4 Conclusion

In conclusion, I have demonstrated that polymerization rate has a significant effect on the self-assembly rate, morphological outcome, and structural properties in the ROPI-CDSA of PLLA-*b*-PEG block copolymers (Figure 3.7). In this specific case, slow polymerizations result in more folded PLLA chains, earlier stage self-assembly, slower self-assembly kinetics and the formation of 3D networks. In contrast, fast polymerizations form less-folded PLLA blocks, later stage self-assembly, faster self-assembly kinetics, and 2D structures. The differences in morphology are attributed to differences in the assembly mechanism, which is driven by non-equilibrium chemistry in the fast reaction. Therefore, in addition to the variables of polymer architecture, solution concentration, and time post-polymerization, changing the rate of polymerization can be used to control polymer morphology. Thus, the rate of polymerization can be utilized to gain structural control without the modification of molecular structure. As additional polymerization methods and catalysts are developed, we anticipate that polymerization rate will be commonly used to manipulate morphology. Furthermore, I anticipate that the phenomena described here is applicable to all PISA processes if the relative rates of polymerization and self-assembly can be appropriately controlled.

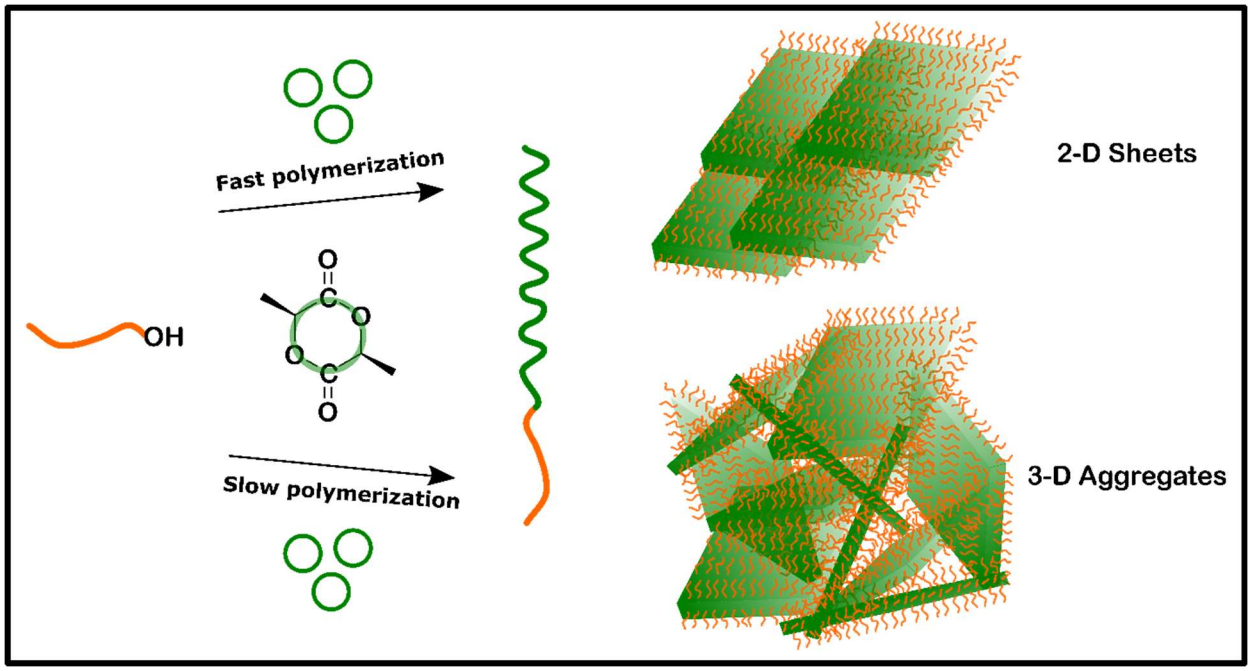

Figure 3.7: Summary of Chapter 3. A fast polymerization (top) led to 2-D sheets whereas a slow polymerization led to 3-D aggregates which formed an organogel.

3.5. Experimental Section

Materials: mPEG45 (MW = 2000) (Sigma Aldrich) was azeotropically distilled ×2 in toluene and high-vacuumed overnight. L-lactide (TCI) was recrystallized in toluene ×3. Anhydrous toluene (99.8%), DBU, and (-)-sparteine were obtained from Sigma Aldrich and stored under 4Å molecular sieves. Benzoic acid (Fisher Chemical) was used without further purification. Thiourea (TU) derived from cyclohexylamine (Sigma Aldrich) and 3,5-bis(trifluoromethyl)phenyl isothiocyanate (TCI) was synthesized following established literature procedures.[29] Chemicals were stored in a dry-N_2 atmosphere glove box. Reactions were performed in a N_2 glove box.

DBU and TU catalyzed (fast polymerization) PLLA-*b*-PEG synthesis and self-assembly: Procedure adapted from Hedrick and Waymouth et al.[29,30] L-lactide (288 mg, 2 mmol, PLLA target DP = 200) was added to a solution of mPEG45 (40 mg, 20 µmol) and 7.5%

mol TU (51 mg, 150 μmol) in 4.0 mL of toluene (10% solids w/w). 1% mol DBU (3 μL, 30 μmol) was added. The solution was stirred for 16 m and subsequently quenched with 0.05 mL of saturated benzoic acid toluene solution. Stirring was kept at 400 rpm for reproducibility and solutions were stirred for at least 24 h post-polymerization. ^{1}H NMR (500 MHz, $CDCl_3$) δ 5.16 (q, J = 7.0 Hz, CH, PLLA backbone), 3.72–3.59 (m, CH_2 PEG backbone), 3.54 (dd, J = 5.6, 3.6 Hz, CH2, PEG), 3.37 (s, 3H, terminal CH_3 PEG), 1.58 (d, J = 6.7 Hz, CH_3 PLLA backbone), 1.50 (dd, J = 14.7, 7.0 Hz, terminal CH_3 PLLA).

(-)-sparteine and TU catalyzed (slow polymerization) PLLA-*b*-PEG synthesis and self-assembly: Procedure adapted from Hedrick and Waymouth et al.[29] L-lactide (288 mg, 2 mmol, PLLA target DP = 200) was added to a solution of mPEG45 (60 mg, 30 μmol) and 7.5% mol TU (51 mg, 150 μmol) in 4.3 mL of toluene (10% solids w/w). 7.5% mol (-)-sparteine (35 μL, 150 μmol) was added. The solution was stirred for 24 h and subsequently quenched with 0.05 mL of saturated benzoic acid toluene solution. Stirring was kept at 400 rpm for reproducibility and solutions were stirred for at least 24 h post-polymerization. ^{1}H NMR (500 MHz, $CDCl_3$) δ 5.16 (q, J = 7.0 Hz, CH, PLLA backbone), 3.72–3.59 (m, CH_2 PEG backbone), 3.54 (dd, J = 5.6, 3.6 Hz, CH_2, PEG), 3.37 (s, 3H, terminal CH_3 PEG), 1.58 (d, J = 6.7 Hz, CH_3 PLLA backbone), 1.50 (dd, J = 14.7, 7.0 Hz, terminal CH_3 PLLA).

Lyophilization: Lyophilized powders were obtained by freezing the toluene solutions in a round bottom flask with liquid nitrogen followed by sublimation using a vacuum pump.

Structural characterization and polymerization kinetics: Proton nuclear magnetic resonance (^{1}H NMR) spectra were collected on a 500 MHz Bruker Avance spectrometer in $CDCl_3$. Chemical shifts are given in ppm, calibrated from residual $CHCl_3$.

Polymerization kinetics were collected by dropping 0.1 mL of reaction mixture into a vial with a drop of saturated benzoic acid solution and diluting in $CDCl_3$. Conversion was calculated from comparing the peak area of the PLLA peak at 5.16 to the L-lactide monomer peak at 5.03.[15] Size exclusion chromatography (SEC) was performed in THF using an Agilent 1100 chromatograph equipped with RID detector and a PL gel 5 µm 300 × 7.5 mm mixed column. Samples were calibrated against polystyrene standards.

Turbidity measurements: Self-assembly kinetics were measured on an Agilent Technologies Cary 60 UV-Vis spectrometer in a N_2 atmosphere in a glovebox using a 1 cm pathlength quartz cuvette. Changes in turbidity were measured at 600 nm every 15 s until the measurement plateaued with a moderate stirring rate.

Rheology: Oscillatory rheology was collected from organogels on a TA DHR 2 rheometer. Gels were loaded using a 20 mm steel Peltier plate. Measurements were taken from $1.0e^{-3}$ to 100.0 strain % at 25 °C.

Crystallinity characterization: Wide-angle X-ray scattering (WAXS) patterns were measured on a Rigaku Smart lab X-ray diffractometer in Bragg-Brentano diffraction mode utilizing X-rays generated at 40 kV and 44 mA with Cu Kα irradiation (step size 0.02 deg, speed 1.0, IS 0.5 deg, RS1 4.0 deg, RS2 13 mm). Approximately 20 mg of a lyophilized sample was used in measurements. Crystallinity was estimated using the Smart lab software after peaks were assigned to PLLA-*b*-PEG. Fourier transform infrared (FTIR) absorbance spectra were collected on a Jasco 4700 FTIR from lyophilized samples.

Morphological characterization: Dry cryogenic-transmission electron microscopy (cryo-TEM) samples were prepared from toluene samples that were freshly diluted x100 onto Lacey Carbon (Electron Microscopy Sciences) grids. Vitrification was carried out by an

Automatic Plunge Freezer ME GP2 (Leica Microsystems) with 3 µL of sample. Grid preparation was performed at ambient humidity and the grids were blotted for 3 s prior to plunging into liquid nitrogen. Cryo-TEM samples were then placed on a Gatan Cryo-TEM holder and imaged on a JEOL 2100F TEM using a Schottky type field emission gun operating at 200 keV. Images were recorded using SerialEM software in low dose imaging mode with a Gatan OneView CMOS camera at 4k × 4k resolution.

Scanning electron microscopy (SEM) samples were prepared from lyophilized samples which were freeze-cracked in liquid N_2 and coated ex-situ with 3 nm of iridium (Quorum, Q150T Plus). Secondary electron images were collected on a FEI Magellan 400 SEM, Quanta 3D FEG with Everhart-Thornley detector, using a 5 kV acceleration potential, and a probe current of 200 pA.

Atomic force microscopy (AFM) micrographs were collected on a Anton Paar AFM in tapping mode using Arrow^{TM} silicon non-contact tapping mode reflex coating tips (Nanoworld) . Samples were dropcasted from toluene samples that were freshly diluted by x100 on silicon nitride chips. Micrographs were processed using Gwyddion. The images were leveled by mean plane subtraction and rows were aligned using matching . The polynomial background was removed (degree = 3) and horizontal scars were corrected. The lower and upper percentiles in each image were limited by 0.2% to remove noise artefacts.

3.6. References

(1) Charleux, B.; Delaittre, G.; Rieger, J.; D'Agosto, F. Polymerization-Induced Self-Assembly: From Soluble Macromolecules to Block Copolymer Nano-Objects in One Step. *Macromolecules* **2012**, *45* (17), 6753–6765. https://doi.org/10.1021/ma300713f.

(2) Canning, S. L.; Smith, G. N.; Armes, S. P. A Critical Appraisal of RAFT-Mediated Polymerization-Induced Self-Assembly. *Macromolecules* **2016**, *49* (6), 1985–2001. https://doi.org/10.1021/acs.macromol.5b02602.

(3) Penfold, N. J. W.; Yeow, J.; Boyer, C.; Armes, S. P. Emerging Trends in Polymerization-Induced Self-Assembly. *ACS Macro Lett.* **2019**, *8* (8), 1029–1054. https://doi.org/10.1021/acsmacrolett.9b00464.

(4) Yeow, J.; Boyer, C. Photoinitiated Polymerization-Induced Self-Assembly (Photo-PISA): New Insights and Opportunities. *Adv. Sci.* **2017**, *4* (7), 1700137. https://doi.org/10.1002/advs.201700137.

(5) Zhang, W.-J.; Hong, C.-Y.; Pan, C.-Y. Polymerization-Induced Self-Assembly of Functionalized Block Copolymer Nanoparticles and Their Application in Drug Delivery. *Macromol. Rapid Commun.* **2019**, *40* (2), 1800279. https://doi.org/10.1002/marc.201800279.

(6) D'Agosto, F.; Rieger, J.; Lansalot, M. RAFT-Mediated Polymerization-Induced Self-Assembly. *Angew. Chem. Int. Ed.* **2020**, *59* (22), 8368–8392. https://doi.org/10.1002/anie.201911758.

(7) Derry, M. J.; Fielding, L. A.; Armes, S. P. Polymerization-Induced Self-Assembly of Block Copolymer Nanoparticles via RAFT Non-Aqueous Dispersion Polymerization. *Prog. Polym. Sci.* **2016**, *52*, 1–18. https://doi.org/10.1016/j.progpolymsci.2015.10.002.

(8) Wright, D. B.; Touve, M. A.; Adamiak, L.; Gianneschi, N. C. ROMPISA: Ring-Opening Metathesis Polymerization-Induced Self-Assembly. *ACS Macro Lett.* **2017**, *6* (9), 925–929. https://doi.org/10.1021/acsmacrolett.7b00408.

(9) Khor, S. Y.; Quinn, J. F.; Whittaker, M. R.; Truong, N. P.; Davis, T. P. Controlling Nanomaterial Size and Shape for Biomedical Applications via Polymerization-Induced Self-Assembly. *Macromol Rapid Commun* **2019**, *40* (2), e1800438. https://doi.org/10.1002/marc.201800438.

(10) Guégain, E.; Zhu, C.; Giovanardi, E.; Nicolas, J. Radical Ring-Opening Copolymerization-Induced Self-Assembly (RROPISA). *Macromolecules* **2019**, *52* (10), 3612–3624. https://doi.org/10.1021/acs.macromol.9b00161.

(11) Grazon, C.; Salas-Ambrosio, P.; Ibarboure, E.; Buol, A.; Garanger, E.; Grinstaff, M. W.; Lecommandoux, S.; Bonduelle, C. Aqueous Ring-Opening Polymerization-Induced Self-Assembly (ROPISA) of N-Carboxyanhydrides. *Angew. Chem. Int. Ed.* **2020**, *59* (2), 622–626. https://doi.org/10.1002/anie.201912028.

(12) Liu, C.; Hong, C.-Y.; Pan, C.-Y. Polymerization Techniques in Polymerization-Induced Self-Assembly (PISA). *Polym. Chem.* **2020**, *11* (22), 3673–3689. https://doi.org/10.1039/D0PY00455C.

(13) Boott, C. E.; Gwyther, J.; Harniman, R. L.; Hayward, D. W.; Manners, I. Scalable and Uniform 1D Nanoparticles by Synchronous Polymerization, Crystallization and Self-Assembly. *Nat. Chem.* **2017**, *9*, 785. https://doi.org/10.1038/nchem.2721.

(14) Sha, Y.; Rahman, M. A.; Zhu, T.; Cha, Y.; McAlister, C. W.; Tang, C. ROMPI-CDSA: Ring-Opening Metathesis Polymerization-Induced Crystallization-Driven Self-Assembly of Metallo-Block Copolymers. *Chem. Sci.* **2019**, *10* (42), 9782–9787. https://doi.org/10.1039/C9SC03056E.
(15) Hurst, P. J.; Rakowski, A. M.; Patterson, J. P. Ring-Opening Polymerization-Induced Crystallization-Driven Self-Assembly of Poly-L-Lactide-Block-Polyethylene Glycol Block Copolymers (ROPI-CDSA). *Nat. Commun.* **2020**, *11* (1), 4690. https://doi.org/10.1038/s41467-020-18460-2.
(16) I. Peterson, G.; Yang, S.; Choi, T.-L. Direct Formation of Nano-Objects via in Situ Self-Assembly of Conjugated Polymers. *Polym. Chem.* **2021**, *12* (10), 1393–1403. https://doi.org/10.1039/D0PY01389G.
(17) Hwang, S.-H.; Kang, S.-Y.; Yang, S.; Lee, J.; Choi, T.-L. Synchronous Preparation of Length-Controllable 1D Nanoparticles via Crystallization-Driven In Situ Nanoparticlization of Conjugated Polymers. *J. Am. Chem. Soc.* **2022**, *144* (13), 5921–5929. https://doi.org/10.1021/jacs.1c13385.
(18) Guan, S.; Chen, A. One-Pot Synthesis of Cross-Linked Block Copolymer Nanowires via Polymerization-Induced Hierarchical Self-Assembly and Photodimerization. *ACS Macro Lett.* **2020**, *9* (1), 14–19. https://doi.org/10.1021/acsmacrolett.9b00868.
(19) Takahashi, R.; Miwa, S.; Sobotta, F. H.; Lee, J. H.; Fujii, S.; Ohta, N.; Brendel, J. C.; Sakurai, K. Unraveling the Kinetics of the Structural Development during Polymerization-Induced Self-Assembly: Decoupling the Polymerization and the Micelle Structure. *Polym. Chem.* **2020**, *11* (8), 1514–1524. https://doi.org/10.1039/C9PY01810G.
(20) Wang, J. Tuning Polymerization Rate Program Block Copolymer Assemblies in PISA: A Simulation Study. *IOP Conf. Ser. Mater. Sci. Eng.* **2020**, *859*, 012007. https://doi.org/10.1088/1757-899x/859/1/012007.
(21) Wang, J.; Fang, T.; Li, J.; Yan, Y.; Li, Z.; Zhang, J. Precise Mesoscopic Model Providing Insights into Polymerization-Induced Self-Assembly. *Langmuir* **2020**, *36* (27), 8009–8016. https://doi.org/10.1021/acs.langmuir.0c01404.
(22) Luo, X.; Zhao, S.; Chen, Y.; Zhang, L.; Tan, J. Switching between Thermal Initiation and Photoinitiation Redirects RAFT-Mediated Polymerization-Induced Self-Assembly. *Macromolecules* **2021**, *54* (6), 2948–2959. https://doi.org/10.1021/acs.macromol.1c00038.
(23) Blackman, L. D.; Doncom, K. E. B.; Gibson, M. I.; O'Reilly, R. K. Comparison of Photo- and Thermally Initiated Polymerization-Induced Self-Assembly: A Lack of End Group Fidelity Drives the Formation of Higher Order Morphologies. *Polym. Chem.* **2017**, *8* (18), 2860–2871. https://doi.org/10.1039/C7PY00407A.
(24) R. Guimarães, T.; Loong Bong, Y.; W. Thompson, S.; Moad, G.; Perrier, S.; B. Zetterlund, P. Polymerization-Induced Self-Assembly via RAFT in Emulsion: Effect of Z-Group on the Nucleation Step. *Polym. Chem.* **2021**, *12* (1), 122–133. https://doi.org/10.1039/D0PY01311K.
(25) R. Jones, E.; Semsarilar, M.; Wyman, P.; Boerakker, M.; P. Armes, S. Addition of Water to an Alcoholic RAFT PISA Formulation Leads to Faster Kinetics but Limits the Evolution of Copolymer Morphology. *Polym. Chem.* **2016**, *7* (4), 851–859. https://doi.org/10.1039/C5PY01795E.

(26) Dove, A. P. Organic Catalysis for Ring-Opening Polymerization. *ACS Macro Lett.* **2012**, *1* (12), 1409–1412. https://doi.org/10.1021/mz3005956.
(27) Kamber, N. E.; Jeong, W.; Waymouth, R. M.; Pratt, R. C.; Lohmeijer, B. G. G.; Hedrick, J. L. Organocatalytic Ring-Opening Polymerization. *Chem. Rev.* **2007**, *107* (12), 5813–5840. https://doi.org/10.1021/cr068415b.
(28) Pratt, R. C.; Lohmeijer, B. G.; Long, D. A.; Waymouth, R. M.; Hedrick, J. L. Triazabicyclodecene: A Simple Bifunctional Organocatalyst for Acyl Transfer and Ring-Opening Polymerization of Cyclic Esters. *J Am Chem Soc* **2006**, *128* (14), 4556–4557. https://doi.org/10.1021/ja060662+.
(29) Pratt, R. C.; Lohmeijer, B. G. G.; Long, D. A.; Lundberg, P. N. P.; Dove, A. P.; Li, H.; Wade, C. G.; Waymouth, R. M.; Hedrick, J. L. Exploration, Optimization, and Application of Supramolecular Thiourea−Amine Catalysts for the Synthesis of Lactide (Co)Polymers. *Macromolecules* **2006**, *39* (23), 7863–7871. https://doi.org/10.1021/ma061607o.
(30) Lohmeijer, B. G. G.; Pratt, R. C.; Leibfarth, F.; Logan, J. W.; Long, D. A.; Dove, A. P.; Nederberg, F.; Choi, J.; Wade, C.; Waymouth, R. M.; Hedrick, J. L. Guanidine and Amidine Organocatalysts for Ring-Opening Polymerization of Cyclic Esters. *Macromolecules* **2006**, *39* (25), 8574–8583. https://doi.org/10.1021/ma0619381.
(31) Czajka, A.; P. Armes, S. In Situ SAXS Studies of a Prototypical RAFT Aqueous Dispersion Polymerization Formulation: Monitoring the Evolution in Copolymer Morphology during Polymerization-Induced Self-Assembly. *Chem. Sci.* **2020**, *11* (42), 11443–11454. https://doi.org/10.1039/D0SC03411H.
(32) György, C.; J. Hunter, S.; Girou, C.; J. Derry, M.; P. Armes, S. Synthesis of Poly(Stearyl Methacrylate)-Poly(2-Hydroxypropyl Methacrylate) Diblock Copolymer Nanoparticles via RAFT Dispersion Polymerization of 2-Hydroxypropyl Methacrylate in Mineral Oil. *Polym. Chem.* **2020**, *11* (28), 4579–4590. https://doi.org/10.1039/D0PY00562B.
(33) Ilday, S.; Makey, G.; Akguc, G. B.; Yavuz, Ö.; Tokel, O.; Pavlov, I.; Gülseren, O.; Ilday, F. Ö. Rich Complex Behaviour of Self-Assembled Nanoparticles Far from Equilibrium. *Nat. Commun.* **2017**, *8* (1), 14942. https://doi.org/10.1038/ncomms14942.
(34) Szavits-Nossan, J.; Eden, K.; Morris, R. J.; MacPhee, C. E.; Evans, M. R.; Allen, R. J. Inherent Variability in the Kinetics of Autocatalytic Protein Self-Assembly. *Phys. Rev. Lett.* **2014**, *113* (9), 098101. https://doi.org/10.1103/PhysRevLett.113.098101.
(35) Dighe, A. V.; Huelsenbeck, L.; Bhawnani, R. R.; Verma, P.; Stone, K. H.; Singh, M. R.; Giri, G. Autocatalysis and Oriented Attachment Direct the Synthesis of a Metal–Organic Framework. *JACS Au* **2022**, *2* (2), 453–462. https://doi.org/10.1021/jacsau.1c00494.
(36) Shen, L.; Bu, H.; Yang, H.; Liu, W.; Li, G. Investigation on the Behavior of Collagen Self-Assembly in Vitro via Adding Sodium Silicate. *Int. J. Biol. Macromol.* **2018**, *115*, 635–642. https://doi.org/10.1016/j.ijbiomac.2018.04.074.
(37) McQuade, D. T.; McKay, S. L.; Powell, D. R.; Gellman, S. H. Indifference to Hydrogen Bonding in a Family of Secondary Amides. *J. Am. Chem. Soc.* **1997**, *119* (36), 8528–8532. https://doi.org/10.1021/ja9711019.

(38) Rizvi, A.; Mulvey, J. T.; Carpenter, B. P.; Talosig, R.; Patterson, J. P. A Close Look at Molecular Self-Assembly with the Transmission Electron Microscope. *Chem. Rev.* **2021**, *121* (22), 14232–14280. https://doi.org/10.1021/acs.chemrev.1c00189.
(39) Inam, M.; Cambridge, G.; Pitto-Barry, A.; Laker, Z. P. L.; Wilson, N. R.; Mathers, R. T.; Dove, A. P.; O'Reilly, R. K. 1D vs. 2D Shape Selectivity in the Crystallization-Driven Self-Assembly of Polylactide Block Copolymers. *Chem. Sci.* **2017**, *8* (6), 4223–4230. https://doi.org/10.1039/C7SC00641A.
(40) He, X.; He, Y.; Hsiao, M.-S.; Harniman, R. L.; Pearce, S.; Winnik, M. A.; Manners, I. Complex and Hierarchical 2D Assemblies via Crystallization-Driven Self-Assembly of Poly(l-Lactide) Homopolymers with Charged Termini. *J. Am. Chem. Soc.* **2017**, *139* (27), 9221–9228. https://doi.org/10.1021/jacs.7b03172.
(41) Parent, L. R.; Bakalis, E.; Ramírez-Hernández, A.; Kammeyer, J. K.; Park, C.; de Pablo, J.; Zerbetto, F.; Patterson, J. P.; Gianneschi, N. C. Directly Observing Micelle Fusion and Growth in Solution by Liquid-Cell Transmission Electron Microscopy. *J. Am. Chem. Soc.* **2017**, *139* (47), 17140–17151. https://doi.org/10.1021/jacs.7b09060.

Chapter 4: Drug Catalyzed ROPI-CDSA Yields One Pot Nanomedicines

4.0. Abstract

Ring-opening polymerization (ROP) is a powerful method for the synthesis of biocompatible and biodegradable polyester-based amphiphilic block copolymers, which are an excellent nanomaterial class for a wide range of pharamaceutical applications. These block copolymers are synthesized using a catalyst, which is typically purified out. In a separate step, the purified block copolymers are then assembled and drug-loaded for medical use. This multistep process limits the scalability of these nanomaterials restraining their industrial use. Recently, I developed a synchronous polymerization and self-assembly process for polyester-based block copolymer nanomaterials coined Ring-Opening Polymerization-Induced Crystallization-Driven Self Assembly (ROPI-CDSA). In ROPI-CDSA, an organocatalyst facilitates the chain extension of mPEG with L-lactide, yielding semicrystalline self-assemblies. Here, I demonstrate that pharmaceuticals with similar functional groups to ROP organocatalysts can catalyze ROPI-CDSA reactions, resulting in the formation of drug-embedded nanomaterials. The major advantage of this one pot approach is that no additional synthetic steps or purification are required. As a proof-of-principle study, I use two antibiotic drug molecules, chlorhexidine and trimethoprim, as catalysts. The resulting drug-embedded block copolymer nanoparticles retain potent antibacterial activity. I anticipate that this strategy can be extended to other examples of PISA for the scalable production of drug-loaded polymer suspensions.

4.1. Introduction

Nanotechnology is a powerful tool for the development of new medicines. Embedding drugs within nanomaterials is a strategy used to improve drug efficacy and reduce side-effects. In 1995, Doxil became the first ever FDA approved “nanodrug”.[1] Doxil uses lipid vesicles to encapsulate and deliver nanocrystals of the chemotherapy drug doxorubicin. The lipid vesicle delivery system significantly reduces the cardiotoxic side effects of doxorubicin, making it safer than the free drug. More recently, a similar lipid system was used for the mRNA delivery system in the Moderna and Pfizer COVID vaccines.[2] The lipid delivery system protects the mRNA from degradation and ensures its uptake into cells. Lipid delivery systems are versatile as they can be used for multiple therapies, however the technology hasn’t significantly changed since it was developed in the 1960’s.[2] Amphiphilic copolymers (e.g. diblock copolymers), which are polymeric analogues of lipids, have been widely studied in academia as next generation drug delivery systems because they offer highly tunable chemical and physical properties.[3,4] These properties enables them to be robust allowing them to be used in a wider range of therapeutic applications than lipids. However, block copolymer delivery systems have had limited use in industry as their synthesis is typically neither scalable nor reproducible. Recently, the development of polymerization-induced self-assembly (PISA) has emerged as a one pot solution to the scalability and reproducibility of block copolymer nanoparticles.[5–8] In PISA, a soluble homopolymer is chain-extended with a monomer, that when polymerized becomes insoluble, triggering self-assembly. PISA has resulted in solutions with up to 50 % polymer wt. and has been applied to a variety of polymer blocks and polymerization techniques.[5,7,9–13] Furthermore, PISA is promising in the application

of drug delivery, primarily through encapsulation or post polymerization functionalization.[14–18]

Recently, I developed a one pot scalable and reproducible synthesis for polyester-based block copolymer nanostructures coined Ring-Opening Polymerization-Induced Crystallization-Driven Self Assembly (ROPI-CDSA).[13,19] In this approach, polyethylene glycol is chain extended with L-lactide using organocatalysts in toluene, a selective solvent to form poly(L)-lactide-*b*-polyethylene glycol (PLLA-*b*-PEG). The resulting semicrystalline self-assemblies can then be transferred to aqueous solutions via extraction or lyophilization and resuspension. Here, I show that pharmaceuticals with similar functional groups to ring-opening organocatalysts can catalyze ROPI-CDSA reactions, resulting in the formation of drug embedded nanomaterials. The major advantage of this one pot approach is that no additional synthetic steps or purification are required. As a proof-of-principle study, I use two antibiotic drug molecules as catalysts: chlorhexidine and trimethoprim. The resulting drug polymer nanoparticles are then characterized by cryoEM, WAXS, and FTIR. When suspended into water, the drug polymer nanoparticles retain potent activity as demonstrated by minimum inhibitory concentration antibacterial studies.

4.2. Results

4.2.1. Synthesis and characterization

ROP can be performed with a wide range of organocatalytic systems including triazabicyclodecene (TBD), diazabicycloundecene (DBU), and a thiourea-based catalyst paired with (-)-sparteine, a tertiary amine.[13,19–22] The key functional group of TBD, guanidine, is present in a large number of drugs.[23] For this study, I selected the

bisguanidine, chlorhexidine, and the dihydropyrimidine, trimethoprim. Both drugs contain guanidine-like groups, are affordable, can be purchased in their free base form, and don't contain side amine or alcohol groups that would out-initiate the polyethylene glycol macroinitiator (Figure 4.1A-B).

Chlorhexidine was found to efficiently catalyze the polymerization of L-lactide in toluene with the presence of a mono methylated polyethylene glycol (mPEG) macroinitiator. At 5% molar ratio to the monomer, >95% conversion was achieved in 30 minutes (Figure 4.1A, Table 4.1). At 10% solids wt., self-assembly occurred (as determined by visual inspection of turbidity) when using monomer to initiator ratios of 45:1 and 68:1 (**1-C** and **2-C**). At 20% solids wt., self-assembly occurred at monomer to initiator ratios of 23:1, 45:1, and 68:1 (**3-C**, **4-C**, and **5-C** respectively). Gel permeation chromatography (GPC) was used to track chain extension and dispersity (Đ) (Figure 4.1C). The Đ of the resulting polymers were between 1.12 and 1.33, indicating a relatively controlled polymerization. These dispersity values are comparable for those in my previous ROPI-CDSA study where TBD was used as the ROP catalyst.[13] However, in a control sample where all conditions are identical to **1-C** except chlorhexidine is replaced with DBU, **1-C** exhibited a lower molar mass, as indicated by a higher retention time in the GPC data (7.95 min vs. 7.45 min) (Figure 4.1C). Samples at 20 % solids wt. also show better dispersity and lower retention times by GPC than samples at 10 % solids wt., which was different from the previous TBD results.

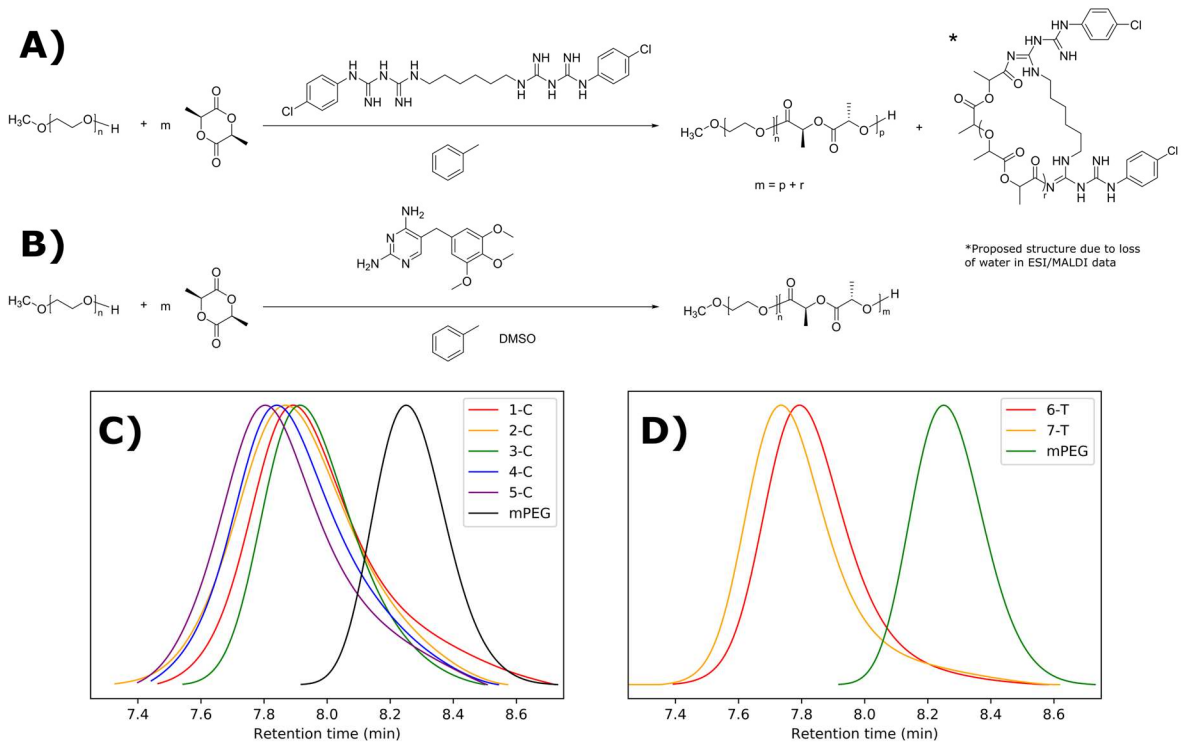

Figure 4.1: Synthetic scheme and GPC results for guanidine-drug catalyzed ROPI-CDSA: A) chlorhexidine catalyzed and initiated synthesis of $PLLA_m$-b-PEG_{45} and $PLLA_r$-chlorhexidine showing a proposed structure for the latter. B) trimethoprim catalyzed synthesis of $PLLA_m$-b-PEG_{45}. C) and D) GPC data for chlorhexidine and trimethoprim $PLLA_m$-b-PEG_{45} series respectively. Note that the retention times of the trimethoprim series is lower than the chlorhexidine series, suggesting the trimethoprim-catalyzed polymer series reaches higher molecular weights than the chlorhexidine-catalyzed series.

One rationalization for the lower molar mass is that chlorhexidine acts as both a catalyst and a co-initiator with mPEG. This would result in a mixture of PLLA-*b*-PEG and chlorhexidine acylated to PLLA at the bisguanidine. Chlorhexidine has C_2 symmetry and 2 pairs of pKa values (10.3 and 2.2)[24] with only one pair (10.3) likely being sufficiently basic for ROP (pKa of TBD ≥ 19.4).[25] Therefore, I predicted that chlorhexidine conjugation would either have 2 or 4 active acylation sites. To test this hypothesis, I mixed chlorhexidine with excess vinyl acetate (1:20) following a modified procedure by Hedrick et. al.[20] Here, the vinyl alkoxide leaving group of the acylation readily rearranges as an aldehyde making the N-acylation irreversible under the experimental conditions. Two

equivalents of vinyl acetate reacted with chlorhexidine confirming the presence of two active acylation sites as shown by ^{1}H NMR (Figure C.2, Table C.1). Following the acylation with vinyl acetate, 2 equivalents of benzyl alcohol were added. Benzyl alcohol can cleave the amide, undoing the N-acylation. With excess vinyl acetate, this led to a total turnover of 2.75 equivalents of vinyl acetate. This shows that although the alcohol was able to cleave the chlorhexidine amide, it was unable to do so to full conversion. To further test the hypothesis that chlorhexidine acts as a catalyst and an initiator, chlorhexidine was reacted with L-lactide in dichloromethane to produce homopolymers with Đ > 1.25 (Figure C.3). Matrix assisted laser desorption/ionization (MALDI) and electron spray ionization (ESI) mass spectra of these homopolymers revealed the presence of a 2 chlorine isotope pattern consistent with the conjugation of chlorhexidine to the poly(L)-lactide chains (Figures C.4-5). MALDI and ESI data also revealed the presence of chlorhexidine initiated homopolymers in samples **1-C** through **5-C** (Figures C.6-7). ESI and MALDI mass spectrometry both revealed a loss of 18 for all polymer peaks, indicating the removal of either H_2O or NH_4. Loss of NH_4 is ruled out due to the odd mass values of the peaks. Loss of H_2O could be the result of an intramolecular cyclization resulting from a substitution reaction. However, I was not able to definitively prove this (see discussion). ^{1}H NMR and Fourier transform infrared (FTIR) spectra each confirmed that chlorhexidine was chemically modified through the shifting of peaks (e.g. aromatic peak shift), likely through the N-acylation of guanidine groups (Figure C.8), and the absence of important chlorhexidine stretches, for example 1660 cm^{-1} in Figure 4.2A. TLC plate chromatography in 100% ethyl acetate was able to separate out the PLLA-*b*-PEG block copolymer from the PLLA-chlorhexidine homopolymer, as verified by NMR

(Figures C.9-11). NMR showed the amount of PLLA per PEG unit to give an average degree of polymerization (DP) of PLLA on the resulting PLLA-*b*-PEG block copolymers (Table 4.1, Figure C.9).

Table 4.1: Synthetic conditions and characterization results for drug catalyzed ROPI-CDSA.

Sample ID	Catalyst (% mol)	Monomer to mPEG Ratio	Solids wt. %	Đ	% Conversion	Average PLLA DP on mPEG
1-C	Chlorhex. (5)	45 (90)	10	1.33	>95	18
2-C	Chlorhex. (5)	68 (135)	10	1.21	>95	20
3-C	Chlorhex. (5)	23 (45)	20	1.12	>95	13
4-C	Chlorhex. (5)	45 (90)	20	1.13	>95	24
5-C	Chlorhex. (5)	68 (135)	20	1.19	>95	30
6-T	Trimethop (2.5)	23 (45)	20	1.12	85	20
7-T	Trimethop (2.5)	45 (90)	20	1.15	54	25

In addition to the study of chlorhexidine, trimethoprim was found to catalyze the polymerization of L-lactide in a solution of toluene ~5% DMSO with the presence of a mono methylated polyethylene glycol macroinitiator. Here, a monomer to initiator ratio of 23:1 gave a conversion of about 85%, and a ratio of 45:1 only reached 54% after reaction mixtures were stirred for 2 weeks. ^{1}H NMR peaks of trimethoprim did not shift following the reaction, signifying that there was not any drug conjugation (Figure C.12). FTIR also indicated the incorporation of many trimethoprim peaks (e.g. around 1700 cm^{-1}), although due to the low relative amounts of trimethoprim, these peaks can be difficult to visualize (Figure 4.2B). **6-T** and **7-T** have similar monomer to mPEG initiator ratios and solids wt% to **3-C** and **4-C** respectively but have lower retention times and thus higher molar masses

despite having lower conversions. This data further suggests that a significant amount of L-lactide polymerizes off the chlorhexidine in the chlorhexidine polymer series.

4.2.2. Structural and Morphological Studies

Both chlorhexidine and trimethoprim samples produced turbid suspensions in toluene. Unlike previous ROPI-CDSA studies,[13,19] none of these samples produced organogels. These mixtures could further be studied through lyophilization and resuspension into water or extraction into water from toluene. Lyophilized powders were studied by FTIR and wide-angle X-ray scattering (WAXS) (Figure 4.2, Figures C.13-16 for full spectra). FTIR shows poly(L)-lactide (PLLA) crystallinity in all samples, as signaled by the dual carbonyl stretch (Figure 4.2A-B).[26] WAXS of samples showed offsets from 16.7, which is the most stable peak position for the PLLA peak (Figure 4.2C-D).[26] These offsets, present in all samples, suggest that the semicrystalline structure is slightly different than standard PLLA as well as PLLA-*b*-PEG in previous ROPI-CDSA studies.[13,19,26] The chlorhexidine samples have an estimated crystallinity ranging from 10% (**3-C**) and 11% (**1-C)** to 15% (**2-C**, **4-C**) and 16% (**5-C**), whereas all trimethoprim samples have much lower crystallinity of around 6% for all samples. The lower crystallinity of the trimethoprim catalyzed samples could be a consequence of the lower conversion and presence of DMSO.

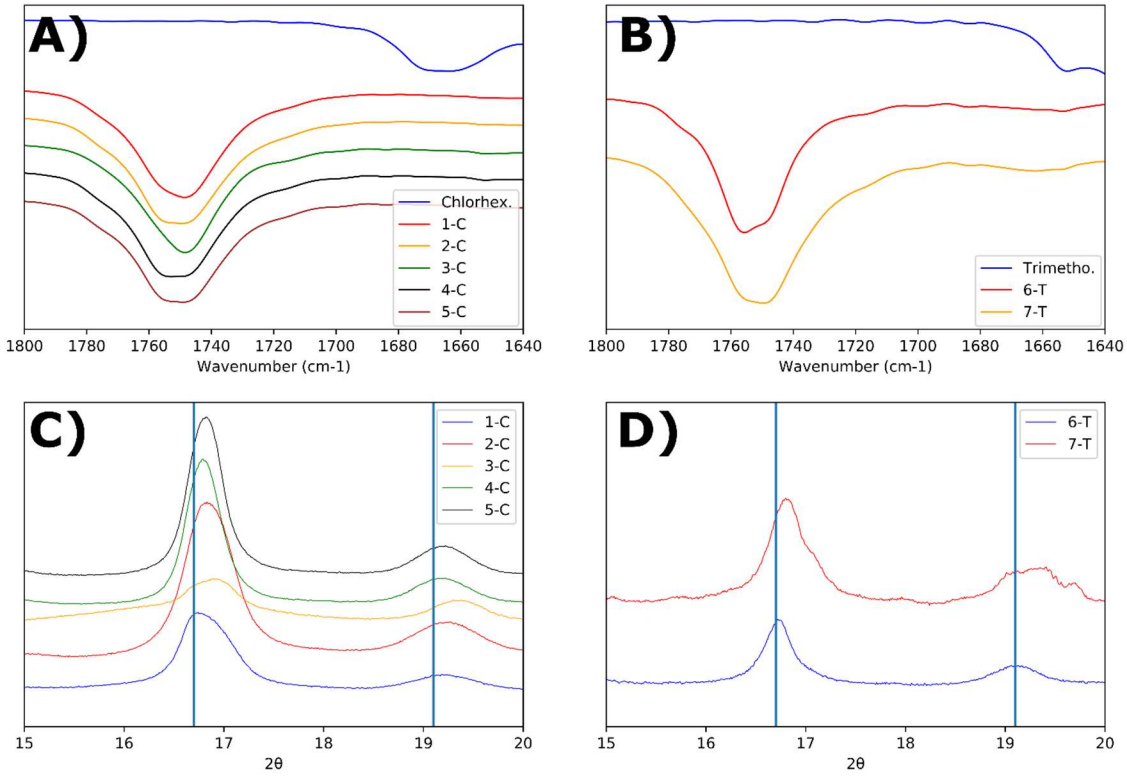

Figure 4.2: Structural characterization of polymers in this study. FTIR carbonyl spectra for (A) chlorhexidine-catalyzed polymers and (B) trimethoprim-catalyzed polymers. WAXS spectra of the two dominant peaks of (C) chlorhexidine-catalyzed polymers and (D) trimethoprim-catalyzed polymers. Lines represent peaks of 16.7 and 19.1 which are the positions of the two largest WAXS peaks in PLLA.

Cryogenic electron microscopy was also performed on all samples to determine the morphologies after transfer to water (Figure 4.3 and Figure C.17). Samples **1-C** through **5-C** contained a mixture of morphologies typically seen in PLLA-*b*-PEG such as lamellae and fibers as well as compound vesicles not typically seen (Figure 4.3A-D). These compound vesicles could be a consequence of the sample containing a mixture of block copolymer and chlorhexidine-conjugated PLLA polymer. Samples **6-T** and **7-T** show lamellae and lamellar vesicles containing less morphological variation than **1-C** through **5-C** (Figure 4.3E-F).

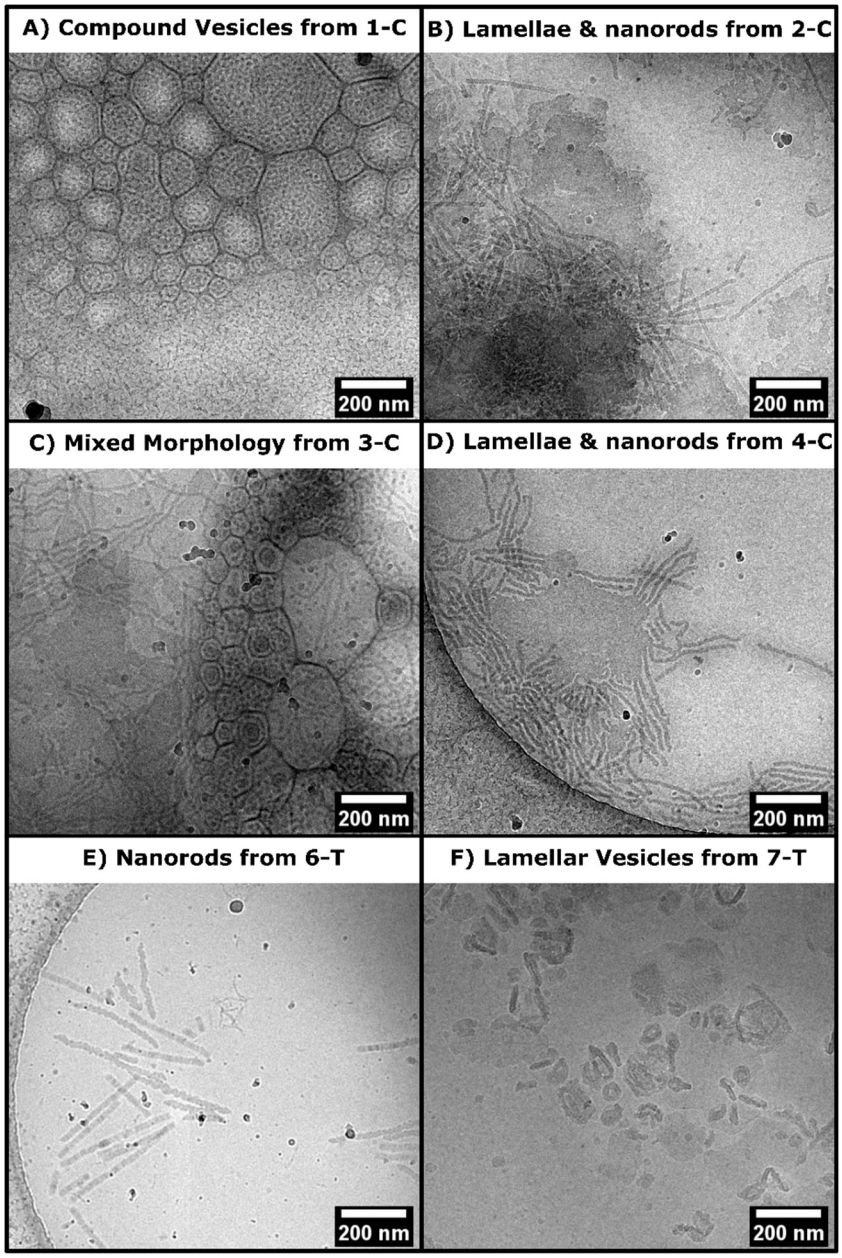

Figure 4.3: CryoEM micrographs from select drug polymer samples (as labelled on image). A-D) Morphologies seen in samples **1-C** to **5-C**. E-F) Morphologies seen in samples **6-T** and **7-T**.

4.2.3. Antibacterial Studies

Antibacterial studies were carried out on aqueous resuspensions of the drug/polymer nanoparticles with help from the Nowick lab. Three types of bacteria, two gram positive, *B. subtilis* and *S. epidermidis*, and one gram negative, *E. coli*, were used

in minimum inhibitory concentration (MIC) studies against four samples, two controls: free-base chlorhexidine, and free-base trimethoprim and two experimental samples: **4-C** and **6-T**. Both experimental samples were prepared from resuspension following lyophilization (Table 2). Additional studies were performed on extracted samples (Table S4). MIC values for free chlorhexidine (0.125 and 0.25 μg/mL) are on the lower end of what is reported in the literature,[27–29] but variations in chlorhexidine MIC are common due to variations on testing of the various salt forms as well as the free base form, as well as expected variations in MIC studies.[30] The MIC values of free trimethoprim are similar to those reported in the literature.[31,32] All polymer samples show antibacterial activity against all three types of bacteria. It should be noted that PLLA-based polymers do not have antibacterial properties.[33,34] The polymer samples had higher MIC values than those of the free drugs, which could be from both slower release kinetics, as polymeric formulations prolong drug release (Table 2).[35,36] In particular, **4-C** has significantly higher MIC values than the free chlorhexidine MIC values, which could be due to the chlorhexidine acylation. The ratio of drug to polymer in all our formulations is commensurate to drug polymer ratios in other antibacterial formulations.[35,36]

Table 4.2: MIC studies of free drugs and polymer drug suspensions. All values are in μg of drug/mL of culture solution.

Bacteria	Free base chlorhexidine	4-C	Free base trimethoprim	6-T
B. subtilis **(ATCC 6051)**	0.25	2	0.25	0.5
S. epidermidis **(ATCC 14990)**	0.125	1	0.5	1
E. coli **(ATCC 10798)**	0.25	2	0.25	1

4.3. Discussion

In developing the drug-catalyzed ROPI-CDSA, we need to understand the nature of the ROP catalysis of chlorhexidine and trimethoprim. Generally, as is the case with TBD, ROP organocatalysis proceeds through two mechanisms: dual hydrogen bonding and through an acylation intermediate, with the latter being less energetically favorable.[37,38] Previous literature shows that an acyclic analogue of TBD could perform ROP through a dual hydrogen bonding mechanism but at a depressed rate when compared to TBD.[37] Our data shows chlorhexidine, which is acyclic, can catalyze ROP of L-lactide; however, some of the resulting PLLA remains tethered to the chlorhexidine. Waymouth et. al.,[39] showed that TBO, a bicyclic guanidine made of two five membered rings (instead of six membered rings in TBD), could undergo acylation but was unable to deacylate. This observation was rationalized by DFT studies that showed that the acyl group in *N*-acyl TBO was stabilized due to the adoption of a planar configuration with respect to the guanidine. In contrast, *N*-acyl TBD adopted a nonplanar configuration, destabilizing the *N*-acyl bond, allowing for efficient turnover in ROP catalysis. Here, chlorhexidine likely adopts an equilibrium concentration of *N*-acylated chlorhexidine and free chlorhexidine, enabling for ROP catalysis but with incomplete turnover, resulting in drug polymer conjugation on some of the growing polymer blocks. Even after the chlorhexidine reacts with L-lactide, it remains active, suggesting that the chlorhexidine facilitates ROP catalysis through a dual hydrogen bonding mechanism and facilitates conjugation through an acylation mechanism.

Regarding the conjugation of PLLA to chlorhexidine, questions remain regarding the nature of the modification. The loss of an equivalent of water (18 mass units) led me

to hypothesize that intramolecular cyclization occurs via substitution of a terminal -OH with another -OH or guanidine =NH, particularly since only a loss of 18 is observed regardless of the degree of polymerization, rather than multiple units of water. The size of the resulting macrocycle would contain 11 + r6 members, where r is the number of L-lactide monomer units in the macrocycle. This large ring size would be free of enthalpic ring strain. However, it remains experimentally difficult to prove cyclization due to the presence of the bisguanidine backbone making a large segment of the cycle. ^{15}N NMR paired with both 1D and 2D proton and carbon studies could deduce if cyclization really occurs, but due to the low abundance of ^{15}N, synthesis of a ^{15}N doped chlorhexidine would be necessary, which is beyond the scope of this study. However, it should be noted that cyclization can occur with PLLA when N-heterocyclic carbene catalysts are used, although in this case, the carbenes merely facilitate cyclization by participating as an intermediate species in cyclization.[40,41]

For the trimethoprim system, the lack of conjugation with PLLA suggests that trimethoprim either operates through a hydrogen bonding mechanism, through acylation with efficient turnover, like TBD, or a combination of the two. Reacting excess vinyl acetate with trimethoprim did not produce any aldehyde like it did with chlorhexidine, suggesting that acylation is not a mechanistic pathway for trimethoprim catalyzed ROP (Figure S18). This lack of acylation may explain why trimethoprim performs ROP at a much slower rate (>10 days) compared to chlorhexidine (30 mins) similar to the comparison between the aforementioned acyclic TBD analog and TBD.[37]

Based on these data I propose that the drug ROPI-CDSA approach produced two different drug delivery systems: a drug-conjugated (prodrug) system with chlorhexidine

and an encapsulated system with trimethoprim. Typically, a block copolymer-based drug delivery system requires a separate polymerization, purification, and drug conjugation,[42,43] or encapsulation step (Figure 4).[44,45] The drug ROPI-CDSA approach is able to produce block copolymer-based drug delivery system in one pot.

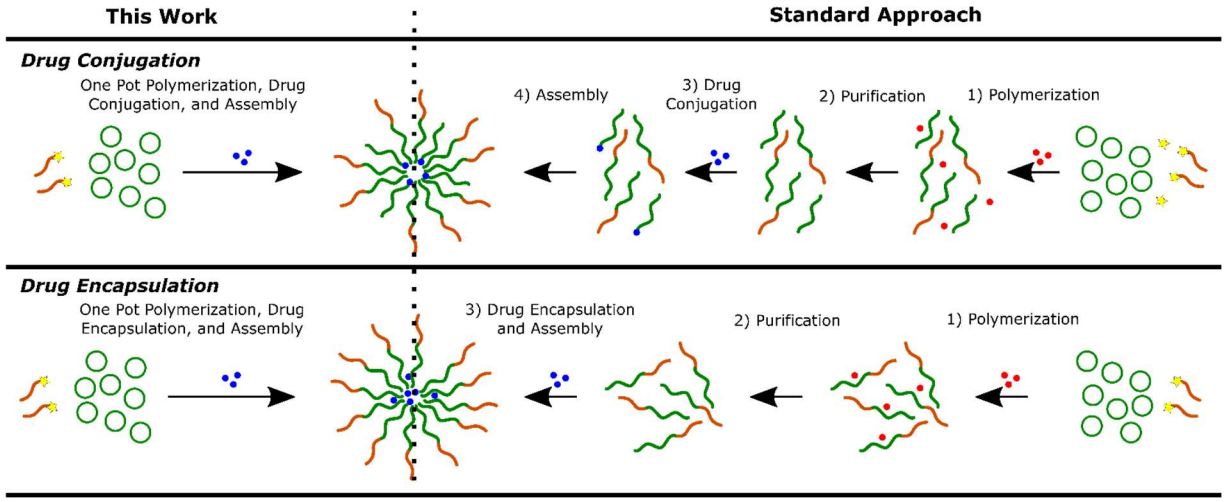

Figure 4.4: The required synthetic steps for block copolymer-based drug conjugation (top) and drug encapsulation (bottom) with the one step approach on the left and the current standard approach on the right. Note that this work combines all previous steps into one step without the need for purification. Additional preparation for both techniques may involve transfer to water or spin-coating which are relatively simple steps compared to the steps listed in this figure.

4.4. Conclusion

In summary, I have devised a new, scalable and reproducible, one pot method for producing nanomedicines coined Drug-catalyzed ROPI-CDSA. I demonstrate that pharmaceuticals can catalyze and create drug carrier systems if they possess the correct functional groups. When paired with a PISA system such as ROPI-CDSA, one pot nanoparticle formulations can be synthesized. With transfer to aqueous suspensions, the resulting polymer drug nanoparticles retained antibacterial activity. In the future, ROPI-CDSA solutions could be spin coated to create antibacterial medical devices such as wound sutures and catheters, applications in which chlorhexidine and trimethoprim are

currently employed. I believe this project will inspire the development of a wide range of drug catalyzed reactions to produce one pot nanomedicines, particularly from PISA-based formulations. Most drugs are highly functionalized organic molecules, and through careful selection they can act as organocatalysts. Organocatalysis has played a major role in the development of new small molecule drugs; it is both exciting and timely that organocatalysis can play a role in the development of the next generation of nanodrugs.

4.5. Experimental Section

Materials: mPEG45 (MW = 2000) (Sigma-Aldrich) was azeotropically distilled ×2 in toluene and high-vacuumed overnight. L-Lactide (TCI) was recrystallized in toluene ×3. Anhydrous toluene (99.8%), and DBU obtained from Sigma-Aldrich and stored under 4 Å molecular sieves. Benzoic acid (Fisher Chemical), chlorhexidine (Sigma-Aldrich), trimethoprim (MP Biomedicals) were used without further purification with trimethoprim being stored in the dark. DMSO was obtained from a dry solvent still. Vinyl acetate and benzyl alcohol were obtained from Sigma-Aldrich and were degassed and stored under molecular sieves. Chemicals were stored in a dry-N_2 atmosphere glovebox. Reactions were performed in a N_2 glovebox. ^{1}H NMR spectra were collected on a 500 MHz Bruker Avance spectrometer in $CDCl_3$. ^{13}C and COSY and HMQC spectra were collected on a 600 MHz Bruker Avance spectrometer in $CDCl_3$.

Chlorhexidine-Catalyzed/Co-initiated ROPI-CDSA: Amounts are for **4-C** (see Table C.2 for all synthetic conditions). mPEG45 (80 mg, 0.04 mmol) was added to a colloidal solution of 5 mol% (relative to L-lactide) of chlorhexidine (45.5 mg, 0.09 mmol) in 1.78 mL of toluene (20% solids w/w). L-lactide (259 mg, 1.8 mmol) was then added to the resulting clear solution and allowing to stir for 30 minutes. The reaction was quenched with 0.05

mL of saturated benzoic acid toluene solution. The reaction mixture was allowed to stir for a day at 400 rpm prior to any structural, morphological, or antibacterial studies. ^{1}H NMR (500 MHz, $CDCl_3$) δ 7-64-7.28 (multiple peaks, chlorhexidine aromatics) 5.16 (q, *J* = 7.0 Hz, CH, PLLA backbone), 3.72–3.59 (m, CH_2 PEG backbone), 3.54 (dd, *J* = 5.6, 3.6 Hz, CH_2, PEG), 3.37 (s, 3H, terminal CH_3 PEG), 1.58 (d, *J* = 6.7 Hz, CH_3 PLLA backbone), 1.50 (dd, *J* = 14.7, 7.0 Hz, terminal CH_3 PLLA). Note: other chlorhexidine-based peaks overlap with other polymer peaks.

Trimethoprim-Catalyzed ROPI-CDSA: Amounts are for **6-T** (see Table C.3 for all synthetic conditions). 2.5 mol% (relative to L-lactide) of trimethoprim (13.2 mg, 0.045 mmol) was dissolved in 0.1 mL DMSO. mPEG45 (160 mg, 0.08 mmol) was dissolved in toluene. Both solutions were mixed and L-lactide (259 mg, 1.8 mmol) was added. The solution was stirred for 2 weeks. Stirring was kept at 400 rpm for reproducibility. ^{1}H NMR (500 MHz, $CDCl_3$) δ 5.16 (q, *J* = 7.0 Hz, CH, PLLA backbone), 3.72–3.59 (m, CH_2 PEG backbone), 3.54 (dd, *J* = 5.6, 3.6 Hz, CH_2, PEG), 3.37 (s, 3H, terminal CH_3 PEG), 1.58 (d, *J* = 6.7 Hz, CH_3 PLLA backbone), 1.50 (dd, *J* = 14.7, 7.0 Hz, terminal CH_3 PLLA).

Chlorhexidine-Catalyzed ROP of PLLA homopolymer: L-lactide (259 mg, 1.8 mmol) was added to a solution of chlorhexidine (75.8 mg, 0.15 mmol) in 2.96 mL of dichloromethane and allowed to stir for 30 minutes. The reaction was quenched with 0.05 mL of saturated benzoic acid in toluene. Different ratios of L-lactide to chlorhexidine were tested keeping all synthetic conditions identical except for altering the amount of L-lactide. ^{1}H NMR (500 MHz, $CDCl_3$) δ 7-64-7.28 (multiple peaks, chlorhexidine aromatics) 5.16 (q, *J* = 7.0 Hz, CH, PLLA backbone), 1.58 (d, *J* = 6.7 Hz, CH_3 PLLA backbone), 1.50 (dd, *J* = 14.7, 7.0

Hz, terminal CH_3 PLLA). Note: other chlorhexidine-based peaks overlap with other polymer peaks.

Acylation control: Following a modified procedure by Hedrick et. al.[20] 20 equivalents of vinyl acetate (344 mg, 4 mmol) was added to a suspension of chlorhexidine (101 mg, 0.2 mmol) in a mixture of dichloromethane (2.0 mL) and DMSO (0.3 mL). Conditions were also varied (see Table C.1). Ratios of the ^{1}H NMR peaks of the aldehyde to the vinyl acetate were compared to measure conversion. Following this acylation, a de-acylation was carried out to the existing solution by adding 2 equivalents of benzyl alcohol (43.3 mg, 0.4 mmol) and then measuring the aldehyde to vinyl acetate ratio again using ^{1}H NMR.

Mass spectrometry (MALDI and ESI): Matrix assisted laser desorption/ionization (MALDI) mass spectrometry was performed using an AB sciex TOF/TOF 5800 system. A linear low mass positive mode was used to obtain mass spectra. MALDI samples were prepared following a modified procedure by Ji et. al.[44] Matrix solutions were prepared by dissolving DCIB (3,5-Dichloro-2-hydroxy-N-isobutylbenzamide) in THF at 10 mg/mL. Sample solutions were prepared by dissolving samples in THF at 10 mg/mL. NaI was dissolved in MeOH at 10 mg/mL to form cationization solutions. These three solutions were combined to form a ratio 10:1:1 of matrix, sample, and cationization agent, respectively. A 1-μL volume of each combined solution was pipetted on the target slide.

Electrospray ionization (ESI) mass spectrometry was performed on a Waters LCT Premier operating in ESI+ mode. A stock solution of 1 mg/mL was diluted in MS grade MeOH to 5 μg/mL, and 10 μL were injected through a capillary with a voltage of 3.0 kV, with the desolvation gas at 300 °C and the source at 100 °C.

Structural/crystallinity studies: Wide-angle X-ray scattering (WAXS) patterns were measured on a Rigaku Smart lab X-ray diffractometer in Bragg–Brentano diffraction mode utilizing X-rays generated at 40 kV and 44 mA with Cu Kα irradiation (step size 0.02°, speed 1.0, IS 0.5°, RS1 4.0°, RS2 13 mm). Approximately 20 mg of a lyophilized sample was used in measurements. Crystallinity was estimated using the Smart lab software after peaks were assigned to PLLA-*b*-PEG. Fourier transform infrared (FTIR) absorbance spectra were collected on a Jasco 4700 FTIR from lyophilized samples. Prior to WAXS and FTIR samples were lyophilized by freezing the toluene solutions (0.5 mL volume) in a round-bottom flask with liquid nitrogen followed by sublimation using a vacuum pump.

CryoEM studies:CryoEM samples were prepared from solutions previously prepared onto Quantifoil R2/2 (Electron Microscopy Sciences) grids. Grids were glow discharged for 70 s to increase hydrophilicity prior to sample loading. Vitrification was carried out by an Automatic Plunge Freeze ME GP2 (Leica Microsystems) with 3 μL of sample. Grid preparation was performed at 95-99% humidity and the grids were blotted for 3 s prior to plunging into liquid propane. Samples were then placed on a Gatan CryoEM holder and imaged on a JEOL 2100 TEM using a Schottky type field emission gun operating at 200 keV. Images were recorded using Serial EM software with a Gatan OneView CMOS camera at 4k x 4k resolution. Prior to cryoEM samples prep, reaction mixtures in toluene were extracted and diluted in water to give samples with concentrations ranging from 16-64 μg drug/mL.

MIC assays: *Bacillus subtilis* (ATCC 6051), *Staphylococcus epidermidis* (ATCC 14990), and *Escherichia coli* (ATCC 10798) were cultured from glycerol stocks in Mueller-Hinton broth overnight in a shaking incubator at 37 °C. An aliquot of the antibiotic/polymer stock

solution (stock solution: 5% DMSO for trimethoprim samples, 100% water for chlorhexidine samples) was diluted with Mueller-Hinton broth to make a 64 μg antibiotic/mL. A 200-μL aliquot of the solution was transferred to a sterile, untreated 96-well plate. Two-fold serial dilutions were made with media across a 96-well plate to achieve a final volume of 100 μL in each well. These solutions had the following concentrations: 64, 32, 16, 8, 4, 2, 1, 0.5, 0.25, 0.125, and 0.0625 μg/mL. The overnight cultures of each bacterium were diluted with Mueller-Hinton broth to an OD_{600} of 0.075 as measured for 200 μL in a 96-well plate. The diluted mixture was further diluted to a 1×10^6 CFU/mL with Mueller-Hinton media. A 100-μL aliquot of the 1×10^6 CFU/mL bacterial solution was added to each well in the 96-well plates, resulting in final bacteria concentrations of 5×10^5 CFU/mL in each well. As 100-μL of bacteria were added to each well, the compounds were also diluted to the following concentrations: 32, 16, 8, 4, 2, 1, 0.5, 0.25, 0.125, 0.0625, and 0.03125 μg/mL. The plate was covered with a lid and incubated at 37 °C for 16 h. The OD_{600} were measured using a 96-well UV/vis plate reader (MultiSkan GO, Thermo Scientific). The MIC values were taken as the lowest concentration that had no bacteria growth. Each MIC assay was run in triplicate (technical replicates). A single row with just the serial diluted antibiotic and no bacteria was used as a control for opacity. For MIC assays of trimethoprim, the antibiotic stock solution was diluted with Mueller-Hinton broth to make a 16 μg/mL solution.

4.6. References

(1) Barenholz, Y. (Chezy). Doxil® — The First FDA-Approved Nano-Drug: Lessons Learned. *J. Controlled Release* **2012**, *160* (2), 117–134. https://doi.org/10.1016/j.jconrel.2012.03.020.

(2) Hou, X.; Zaks, T.; Langer, R.; Dong, Y. Lipid Nanoparticles for MRNA Delivery. *Nat. Rev. Mater.* **2021**, *6* (12), 1078–1094. https://doi.org/10.1038/s41578-021-00358-0.

(3) Mai, Y.; Eisenberg, A. Self-Assembly of Block Copolymers. *Chem. Soc. Rev.* **2012**, *41* (18), 5969–5985. https://doi.org/10.1039/C2CS35115C.

(4) Elsabahy, M.; L. Wooley, K. Design of Polymeric Nanoparticles for Biomedical Delivery Applications. *Chem. Soc. Rev.* **2012**, *41* (7), 2545–2561. https://doi.org/10.1039/C2CS15327K.

(5) Canning, S. L.; Smith, G. N.; Armes, S. P. A Critical Appraisal of RAFT-Mediated Polymerization-Induced Self-Assembly. *Macromolecules* **2016**, *49* (6), 1985–2001. https://doi.org/10.1021/acs.macromol.5b02602.

(6) Charleux, B.; Delaittre, G.; Rieger, J.; D'Agosto, F. Polymerization-Induced Self-Assembly: From Soluble Macromolecules to Block Copolymer Nano-Objects in One Step. *Macromolecules* **2012**, *45* (17), 6753–6765. https://doi.org/10.1021/ma300713f.

(7) D'Agosto, F.; Rieger, J.; Lansalot, M. RAFT-Mediated Polymerization-Induced Self-Assembly. *Angew. Chem. Int. Ed.* **2020**, *59* (22), 8368–8392. https://doi.org/10.1002/anie.201911758.

(8) Liu, C.; Hong, C.-Y.; Pan, C.-Y. Polymerization Techniques in Polymerization-Induced Self-Assembly (PISA). *Polym. Chem.* **2020**, *11* (22), 3673–3689. https://doi.org/10.1039/D0PY00455C.

(9) Wright, D. B.; Touve, M. A.; Adamiak, L.; Gianneschi, N. C. ROMPISA: Ring-Opening Metathesis Polymerization-Induced Self-Assembly. *ACS Macro Lett.* **2017**, *6* (9), 925–929. https://doi.org/10.1021/acsmacrolett.7b00408.

(10) Boott, C. E.; Gwyther, J.; Harniman, R. L.; Hayward, D. W.; Manners, I. Scalable and Uniform 1D Nanoparticles by Synchronous Polymerization, Crystallization and Self-Assembly. *Nat. Chem.* **2017**, *9*, 785. https://doi.org/10.1038/nchem.2721.

(11) Grazon, C.; Salas-Ambrosio, P.; Ibarboure, E.; Buol, A.; Garanger, E.; Grinstaff, M. W.; Lecommandoux, S.; Bonduelle, C. Aqueous Ring-Opening Polymerization-Induced Self-Assembly (ROPISA) of N-Carboxyanhydrides. *Angew. Chem. Int. Ed.* **2020**, *59* (2), 622–626. https://doi.org/10.1002/anie.201912028.

(12) Guégain, E.; Zhu, C.; Giovanardi, E.; Nicolas, J. Radical Ring-Opening Copolymerization-Induced Self-Assembly (RROPISA). *Macromolecules* **2019**, *52* (10), 3612–3624. https://doi.org/10.1021/acs.macromol.9b00161.

(13) Hurst, P. J.; Rakowski, A. M.; Patterson, J. P. Ring-Opening Polymerization-Induced Crystallization-Driven Self-Assembly of Poly-L-Lactide-Block-Polyethylene Glycol Block Copolymers (ROPI-CDSA). *Nat. Commun.* **2020**, *11* (1), 4690. https://doi.org/10.1038/s41467-020-18460-2.

(14) Zhu, C.; Nicolas, J. (Bio)Degradable and Biocompatible Nano-Objects from Polymerization-Induced and Crystallization-Driven Self-Assembly. *Biomacromolecules* **2022**, *23* (8), 3043–3080. https://doi.org/10.1021/acs.biomac.2c00230.

(15) Phan, H.; Cossutta, M.; Houppe, C.; Le Cœur, C.; Prevost, S.; Cascone, I.; Courty, J.; Penelle, J.; Couturaud, B. Polymerization-Induced Self-Assembly (PISA) for in Situ Drug Encapsulation or Drug Conjugation in Cancer Application. *J. Colloid Interface Sci.* **2022**, *618*, 173–184. https://doi.org/10.1016/j.jcis.2022.03.044.
(16) Cao, J.; Tan, Y.; Chen, Y.; Zhang, L.; Tan, J. Expanding the Scope of Polymerization-Induced Self-Assembly: Recent Advances and New Horizons. *Macromol. Rapid Commun.* **2021**, *42* (23), 2100498. https://doi.org/10.1002/marc.202100498.
(17) Khor, S. Y.; Quinn, J. F.; Whittaker, M. R.; Truong, N. P.; Davis, T. P. Controlling Nanomaterial Size and Shape for Biomedical Applications via Polymerization-Induced Self-Assembly. *Macromol Rapid Commun* **2019**, *40* (2), e1800438. https://doi.org/10.1002/marc.201800438.
(18) Zhang, W.-J.; Hong, C.-Y.; Pan, C.-Y. Polymerization-Induced Self-Assembly of Functionalized Block Copolymer Nanoparticles and Their Application in Drug Delivery. *Macromol. Rapid Commun.* **2019**, *40* (2), 1800279. https://doi.org/10.1002/marc.201800279.
(19) Hurst, P. J.; Graham, A. A.; Patterson, J. P. Gaining Structural Control by Modification of Polymerization Rate in Ring-Opening Polymerization-Induced Crystallization-Driven Self-Assembly. *ACS Polym. Au* **2022**, *2* (6), 501–509. https://doi.org/10.1021/acspolymersau.2c00027.
(20) Pratt, R. C.; Lohmeijer, B. G.; Long, D. A.; Waymouth, R. M.; Hedrick, J. L. Triazabicyclodecene: A Simple Bifunctional Organocatalyst for Acyl Transfer and Ring-Opening Polymerization of Cyclic Esters. *J Am Chem Soc* **2006**, *128* (14), 4556–4557. https://doi.org/10.1021/ja060662+.
(21) Lohmeijer, B. G. G.; Pratt, R. C.; Leibfarth, F.; Logan, J. W.; Long, D. A.; Dove, A. P.; Nederberg, F.; Choi, J.; Wade, C.; Waymouth, R. M.; Hedrick, J. L. Guanidine and Amidine Organocatalysts for Ring-Opening Polymerization of Cyclic Esters. *Macromolecules* **2006**, *39* (25), 8574–8583. https://doi.org/10.1021/ma0619381.
(22) Pratt, R. C.; Lohmeijer, B. G. G.; Long, D. A.; Lundberg, P. N. P.; Dove, A. P.; Li, H.; Wade, C. G.; Waymouth, R. M.; Hedrick, J. L. Exploration, Optimization, and Application of Supramolecular Thiourea−Amine Catalysts for the Synthesis of Lactide (Co)Polymers. *Macromolecules* **2006**, *39* (23), 7863–7871. https://doi.org/10.1021/ma061607o.
(23) Kim, S.-H.; Semenya, D.; Castagnolo, D. Antimicrobial Drugs Bearing Guanidine Moieties: A Review. *Eur. J. Med. Chem.* **2021**, *216*, 113293. https://doi.org/10.1016/j.ejmech.2021.113293.
(24) Gadde, R. R.; McNiff, E. F.; Peer, M. M. High-Performance Liquid Chromatographic Analysis of Chlorhexidine Phosphanilate, a New Antimicrobial Agent. *J. Pharm. Biomed. Anal.* **1991**, *9* (10), 1031–1036. https://doi.org/10.1016/0731-7085(91)80040-G.
(25) Kaljurand, I.; Rodima, T.; Pihl, A.; Mäemets, V.; Leito, I.; Koppel, I. A.; Mishima, M. Acid−Base Equilibria in Nonpolar Media. 4. Extension of the Self-Consistent Basicity Scale in THF Medium. Gas-Phase Basicities of Phosphazenes. *J. Org. Chem.* **2003**, *68* (26), 9988–9993. https://doi.org/10.1021/jo034537h.
(26) Pan, P.; Inoue, Y. Polymorphism and Isomorphism in Biodegradable Polyesters. *Prog. Polym. Sci.* **2009**, *34* (7), 605–640. https://doi.org/10.1016/j.progpolymsci.2009.01.003.

(27) El-Falaha, B. M. a.; Russell, A. D.; Furr, J. R. Effect of Chlorhexidine Diacetate and Benzalkonium Chloride on the Viability of Wild Type and Envelope Mutants of Escherichia Coli and Pseudomonas Aeruginosa. *Lett. Appl. Microbiol.* **1985**, *1* (1), 21–24. https://doi.org/10.1111/j.1472-765X.1985.tb01480.x.
(28) Hennessey, T. D. Some Antibacterial Properties of Chlorhexidine. *J. Periodontal Res.* **1973**, *8* (s12), 61–67. https://doi.org/10.1111/j.1600-0765.1973.tb02166.x.
(29) Horstmann Risso, N.; Ottonelli Stopiglia, C. D.; Oliveira, M. T.; Haas, S. E.; Ramos Maciel, T.; Reginatto Lazzari, N.; Kelmer, E. L.; Pinto Vilela, J. A.; Beckmann, D. V. Chlorhexidine Nanoemulsion: A New Antiseptic Formulation. *Int. J. Nanomedicine* **2020**, *15*, 6935–6944. https://doi.org/10.2147/IJN.S228280.
(30) Schuurmans, J. M.; Nuri Hayali, A. S.; Koenders, B. B.; ter Kuile, B. H. Variations in MIC Value Caused by Differences in Experimental Protocol. *J. Microbiol. Methods* **2009**, *79* (1), 44–47. https://doi.org/10.1016/j.mimet.2009.07.017.
(31) Amyes, S. G. B. Comparative Antibacterial Spectrum of Trimethoprim and Brodimoprim. *J. Chemother.* **1993**, *5* (6), 417–421. https://doi.org/10.1080/1120009X.1993.11741089.
(32) Richards, R. M. E.; Taylor, R. B.; Zhu, Z. Y. Mechanism for Synergism between Sulphonamides and Trimethoprim Clarified. *J. Pharm. Pharmacol.* **1996**, *48* (9), 981–984. https://doi.org/10.1111/j.2042-7158.1996.tb06017.x.
(33) Chung, Y.-Y. H., T. W. Microencapsulation of Gentamicin in Biodegradable PLA and/or PLA/PEG Copolymer. *J. Microencapsul.* **2001**, *18* (4), 457–465. https://doi.org/10.1080/02652040010019479.
(34) Shameli, K.; Ahmad, M. B.; Yunus, W. M. Z. W.; Ibrahim, N. A.; Rahman, R. A.; Jokar, M.; Darroudi, M. Silver/Poly (Lactic Acid) Nanocomposites: Preparation, Characterization, and Antibacterial Activity. *Int. J. Nanomedicine* **2010**, *5*, 573–579. https://doi.org/10.2147/IJN.S12007.
(35) Moraes Moreira Carraro, T. C.; Altmeyer, C.; Maissar Khalil, N.; Mara Mainardes, R. Assessment of in Vitro Antifungal Efficacy and in Vivo Toxicity of Amphotericin B-Loaded PLGA and PLGA-PEG Blend Nanoparticles. *J. Mycol. Médicale* **2017**, *27* (4), 519–529. https://doi.org/10.1016/j.mycmed.2017.07.004.
(36) Radovic-Moreno, A. F.; Lu, T. K.; Puscasu, V. A.; Yoon, C. J.; Langer, R.; Farokhzad, O. C. Surface Charge-Switching Polymeric Nanoparticles for Bacterial Cell Wall-Targeted Delivery of Antibiotics. *ACS Nano* **2012**, *6* (5), 4279–4287. https://doi.org/10.1021/nn3008383.
(37) Zhang, L.; Pratt, R. C.; Nederberg, F.; Horn, H. W.; Rice, J. E.; Waymouth, R. M.; Wade, C. G.; Hedrick, J. L. Acyclic Guanidines as Organic Catalysts for Living Polymerization of Lactide. *Macromolecules* **2010**, *43* (3), 1660–1664. https://doi.org/10.1021/ma901776x.
(38) Simon, L.; Goodman, J. M. The Mechanism of TBD-Catalyzed Ring-Opening Polymerization of Cyclic Esters. *J. Org. Chem.* **2007**, *72* (25), 9656–9662. https://doi.org/10.1021/jo702088c.
(39) Kiesewetter, M. K.; Scholten, M. D.; Kirn, N.; Weber, R. L.; Hedrick, J. L.; Waymouth, R. M. Cyclic Guanidine Organic Catalysts: What Is Magic About Triazabicyclodecene? *J. Org. Chem.* **2009**, *74* (24), 9490–9496. https://doi.org/10.1021/jo902369g.

(40) Culkin, D. A.; Jeong, W.; Csihony, S.; Gomez, E. D.; Balsara, N. P.; Hedrick, J. L.; Waymouth, R. M. Zwitterionic Polymerization of Lactide to Cyclic Poly(Lactide) by Using N-Heterocyclic Carbene Organocatalysts. *Angew. Chem.* **2007**, *119* (15), 2681–2684. https://doi.org/10.1002/ange.200604740.
(41) Brown, H. A.; Waymouth, R. M. Zwitterionic Ring-Opening Polymerization for the Synthesis of High Molecular Weight Cyclic Polymers. *Acc. Chem. Res.* **2013**, *46* (11), 2585–2596. https://doi.org/10.1021/ar400072z.
(42) Taresco, V.; Abelha, T. F.; Cavanagh, R. J.; Vasey, C. E.; Anane-Adjei, A. B.; Pearce, A. K.; Monteiro, P. F.; Spriggs, K. A.; Clarke, P.; Ritchie, A.; Martin, S.; Rahman, R.; Grabowska, A. M.; Ashford, M. B.; Alexander, C. Functionalized Block Co-Polymer Pro-Drug Nanoparticles with Anti-Cancer Efficacy in 3D Spheroids and in an Orthotopic Triple Negative Breast Cancer Model. *Adv. Ther.* **2021**, *4* (1), 2000103. https://doi.org/10.1002/adtp.202000103.
(43) Salmanpour, M.; Yousefi, G.; Mohammadi-Samani, S.; Abedanzadeh, M.; Tamaddon, A. M. Hydrolytic Stabilization of Irinotecan Active Metabolite (SN38) against Physiologic PH through Self-Assembly of Conjugated Poly (2-Oxazoline) - Poly (l-Amino Acid) Block Copolymer: A-Synthesis and Physicochemical Characterization. *J. Drug Deliv. Sci. Technol.* **2020**, *60*, 101933. https://doi.org/10.1016/j.jddst.2020.101933.
(44) Azhari, Z.; Smith, P.; McMahon, S.; Wang, W.; Cameron, R. E. Modulating Drug Release from Short Poly(Ethylene Glycol) Block Initiated Poly(L-Lactide) Di-Block Copolymers. *Pharm. Res.* **2022**. https://doi.org/10.1007/s11095-022-03228-8.
(45) Lu, A.; Petit, E.; Jelonek, K.; Orchel, A.; Kasperczyk, J.; Wang, Y.; Su, F.; Li, S. Self-Assembled Micelles Prepared from Bio-Based Hydroxypropyl Methyl Cellulose and Polylactide Amphiphilic Block Copolymers for Anti-Tumor Drug Release. *Int. J. Biol. Macromol.* **2020**, *154*, 39–47. https://doi.org/10.1016/j.ijbiomac.2020.03.094.
(46) Ji, E.; Cummins, C.; Fleury, G. Precise Synthesis and Thin Film Self-Assembly of PLLA-b-PS Bottlebrush Block Copolymers. *Molecules* **2021**, *26* (5), 1412. https://doi.org/10.3390/molecules26051412.

Chapter 5: Hybrid photoiniferter and ROPI-CDSA of polyacrylamido-*b*-polyester block copolymers

5.0. Abstract

Recently, we developed a one pot synthesis of polyethylene glycol-*b*-poly(L)-lactide block copolymer nanoparticles from building blocks coined ring-opening polymerization-induced crystallization-driven self-assembly (ROPI-CDSA). ROPI-CDSA is one of the most scalable techniques to form biocompatible polyester-based nanoparticles. Here, to diversify ROPI-CDSA to a wider range of polymers, I utilize a dual functionalized photoiniferter for the one pot two step synthesis of polyacrylamido-*b*-polyester nanoparticles. CryoEM analysis reveals the presence of anisotropic rods and lamellae. This development will enable further mechanistic studies of ROPI-CDSA.

5.1. Introduction

Polymerization-induced self-assembly (PISA) has revolutionized the field of block copolymer self-assembly as it enables the reproducible scaled-up production of nanoparticles.[1–3] In PISA, a macromolecular stabilizing block is chain extended with monomer which will form the solvophobic block. PISA can garner solutions ranging from 10 to 50% solids w/w in contrast to traditional methods which typically yield solutions around 1% solids w/w.[1,3,4] PISA has been developed for a wide range of polymerization techniques.[2,4] In addition, PISA for crystalline and semicrystalline polymers, termed polymerization-induced crystallization-driven self-assembly (PI-CDSA), has been developed allowing for the scaled-up production of anisotropic nanostructures such as rods and lamellae.[5–9]

Recently, I developed PISA for the ring-opening polymerization (ROP) of semicrystalline polyesters, termed ring-opening polymerization-induced crystallization-driven self-assembly (ROPI-CDSA).[8,9] This process occurred by chain extending polyethylene glycol (PEG) with L-lactide in toluene using various organocatalytic systems. The resulting poly(L)-lactide-block-polyethylene glycol (PLLA-*b*-PEG) particle morphology varied from 1-D nanorods to 2-D lamellae, including 3-D stacked lamellae. With a desire to expand the scope of ROPI-CDSA, I wanted to change the solvophilic corona block from PEG to polyacrylamides such as poly(*N,N*-dimethyl acrylamide (PDMA) as poly(*N,N*-dimethyl acrylamide-*block*-poly(L)-lactide (PDMA-*b*-PLLA) is a great block copolymer for controlled crystallization-driven self-assembly of anisotropic nanorods and lamellae (CDSA).[10,11] In those examples, the PLLA block was synthesized first. Developing a PISA process for PDMA-*b*-PLLA would require performing a controlled radical polymerization technique, followed by ROP. However, to the best of my

knowledge, there are not any literature examples of controlled radical polymerization of dimethyl acrylamide (DMA) being performed before the ROP of L-lactide.[12]

Recently, Xia et. al.[13] showed that photoiniferter polymerization and organocatalytic ROP could be performed stepwise or synchronously using a hydroxy-functionalized trithiocarbonate (TTC) dual-initiator for the one pot production of polyacrylamido-*b*-polyether block copolymers. Photoiniferters enable the polymerization of vinyl monomers with predictable molecular weights, low dispersity (Đ) and high end-group fidelity with the added bonus of being performed at ambient conditions.[14] Organocatalytic ROP of lactides and lactones is a developed field, with a variety of catalytic systems to choose from.[15,16] However, these ROP are performed in solvents with concentrations around 1.0 M,[17,18] whereas the photoiniferter polymerization of polyacrylamides is done in near-neat conditions.[13]

Here, I describe a two-step one pot process to produce polyacrylamide-*b*-polyester based self-assemblies. A TTC dual-initiator photoiniferter first polymerizes acrylamide-based monomers and then is used to initiate the organocatalytic ROP of L-lactide in toluene to generate block copolymer self-assemblies. Block lengths of the corona and core were modified and studied by cryogenic transmission electron microscopy (cryoEM), showing how block length impacts the resulting morphology.

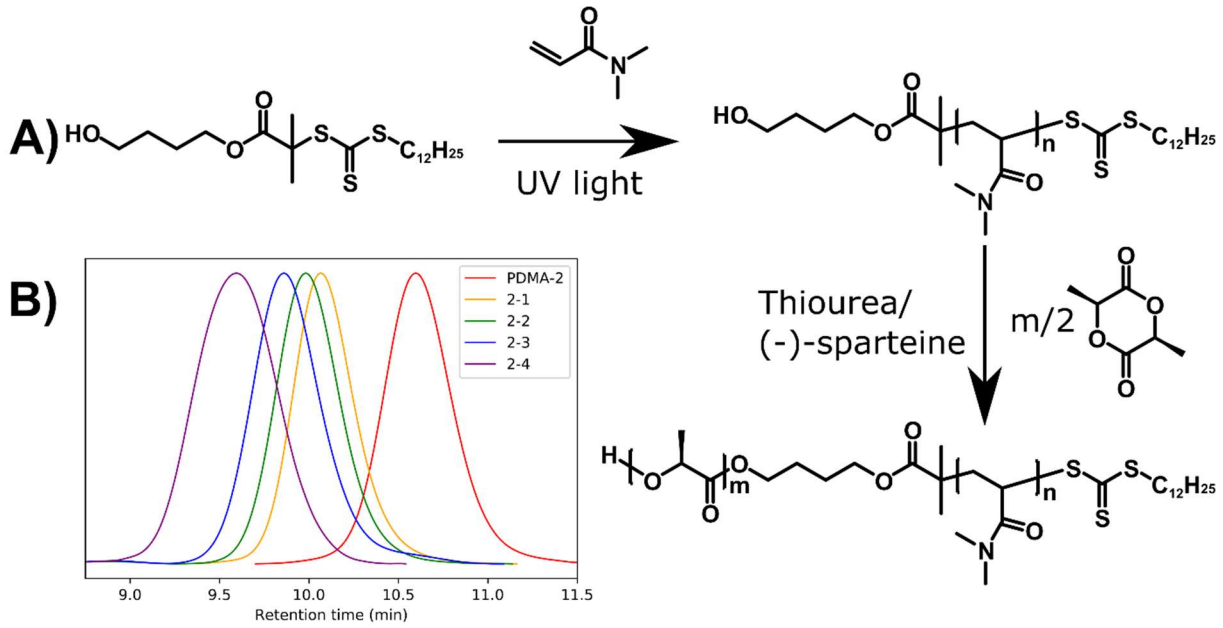

Figure 5.1: Synthesis of PDMA-b-PLLA. A) Scheme, showing the photoiniferter polymerization of DMA (Step 1) followed by the polymerization of L-lactide to make PDMA-b-PLLA (Step 2). The second step is carried out in toluene, which leads to self-assembly. B) Gel permeation chromatography showing the chain extension of PDMA by PLLA at varying degrees of polymerization at a flow rate of 0.75 mL/min.

5.2. Results

As previously mentioned, photoiniferter polymerization of acrylamides and ROP of lactides and lactones are done at different concentrations which necessitates a two-step one-pot approach. For the photoiniferter polymerization I first synthesized PDMA which the synthetic conditions were previously well understood.[13] Next, I developed and optimized the synthetic conditions for the second-step, the organocatalytic ROP. First, I used diazabicyclodecene (DBU), an excellent catalyst for the ROP of L-lactide, but the resulting PDMA-*b*-PLLA block copolymers did not achieve low dispersity (Figure D.1: GPC of DBU). Additionally, I reasoned that a slower reaction rate would give more control over self-assembly.[9] Therefore, I switched to a milder and slower catalytic system, utilizing thiourea (TU) and (-)-sparteine (Figure 5.1, Table 5.1).[17] By varying the conditions, I learned that keeping the L-lactide weight at 10% w/w for all tested reactions

gave the lowest dispersity while maintaining decently high conversions after four days of stirring at room temperature. The target degree of polymerization (DP) of both PDMA and PLLA was varied from 50-200 to produce a library of block copolymers. All polymers obtained excellent dispersity with shorter PDMA blocks giving better conversion. Most of the resulting polymers also became turbid, indicating assembly.

Table 5.1: Synthetic parameters and results for one pot two step PDMA-*b*-PLLA synthesis.

Sample ID	Target PDMA DP	PDMA Conversion	Target PLLA DP	PLLA Conversion	Đ	M_n	Polymer Structure	Turbid
1-PDMA	50	84%	N/A		1.08	4200	$PDMA_{42}$	N/A
1-1	50		50	95%	1.03	7900	$PDMA_{45}$-*b*-$PLLA_{48}$	No
1-2	50		100	92%	1.09	11200	$PDMA_{46}$-*b*-$PLLA_{92}$	No
1-3	50		150	95%	1.06	14800	$PDMA_{45}$-*b*-$PLLA_{143}$	Yes
1-4	50		200	95%	1.08	18200	$PDMA_{45}$-*b*-$PLLA_{190}$	Yes
2-PDMA	100	93%	N/A		1.06	9200	$PDMA_{93}$	N/A
2-1	100		50	89%	1.06	12100	$PDMA_{89}$-*b*-$PLLA_{45}$	No
2-2	100		100	85%	1.04	14800	$PDMA_{88}$-*b*-$PLLA_{85}$	Yes
2-3	100		150	85%	1.06	18300	$PDMA_{92}$-*b*-$PLLA_{128}$	Yes
2-4	100		200	89%	1.08	22000	$PDMA_{93}$-*b*-$PLLA_{178}$	Yes
3-PDMA	150	88%	N/A		1.07	13100	$PDMA_{132}$	N/A
3-1	150		50	91%	1.06	16900	$PDMA_{137}$-*b*-$PLLA_{46}$	Yes
3-2	150		100	73%	1.06	18600	$PDMA_{135}$-*b*-$PLLA_{73}$	Yes

3-3	150		150	71%	1.07	21800	$PDMA_{142}$-*b*-$PLLA_{107}$	Yes
3-4	150		200	70%	1.07	23900	$PDMA_{139}$-*b*-$PLLA_{140}$	Yes
4-PDMA	200	90%	N/A		1.07	17800	$PDMA_{180}$	N/A
4-1	200		100	74%	1.07	23100	$PDMA_{179}$-*b*-$PLLA_{74}$	Yes
4-2	200		150	69%	1.06	25600	$PDMA_{183}$-*b*-$PLLA_{104}$	Yes
4-3	200		200	66%	1.07	27300	$PDMA_{179}$-*b*-$PLLA_{132}$	Yes

Next, cryoEM was used to determine the morphology of the PDMA-*b*-PLLA suspensions (Figure 5.2). As done in previous ROPI-CDSA works, some of the toluene solution was extracted into excess water to yield concentrations around 0.25-5 mg/mL. Solutions with both short PDMA blocks and long PLLA blocks were unable to be resuspended due to high hydrophobicity. All samples consisted primarily of nanorods with little to no lamellae. Some of the nanorods were anisotropic while others appeared a bit jagged. Anisotropic nanorods from all imaged samples were able to be measured with discernable core and corona blocks (Table D.1). Samples **3-2**, **3-3**, and **3-4**, representing $PDMA_{135}$-*b*-$PLLA_n$ polymers with n = 73, 107, and 140 respectively showed a clear trend in core thickness increasing with PLLA block length from 12.9 ± 1.0 nm core thickness in **3-2**, 13.8 ± 1.0 nm in **3-3**, and 14.3 ± 0.9 nm. Samples **3-2** and **4-1** varied corona block length with PDMA DPs of 135 and 179 respectively with PLLA DPs of 73 and 74 respectively. Corona thickness measured as the total thickness of the nanorods minus the core was 27.1 ± 2.8 nm for **3-2** and 35.6 ± 2.6 nm for **4-1**. These results are expected

as core and corona thickness should increase with increasing DP. In future studies, the growth can likely be controlled through the addition of seeds as it has in other PI-CDSA processes.[6,19,20]

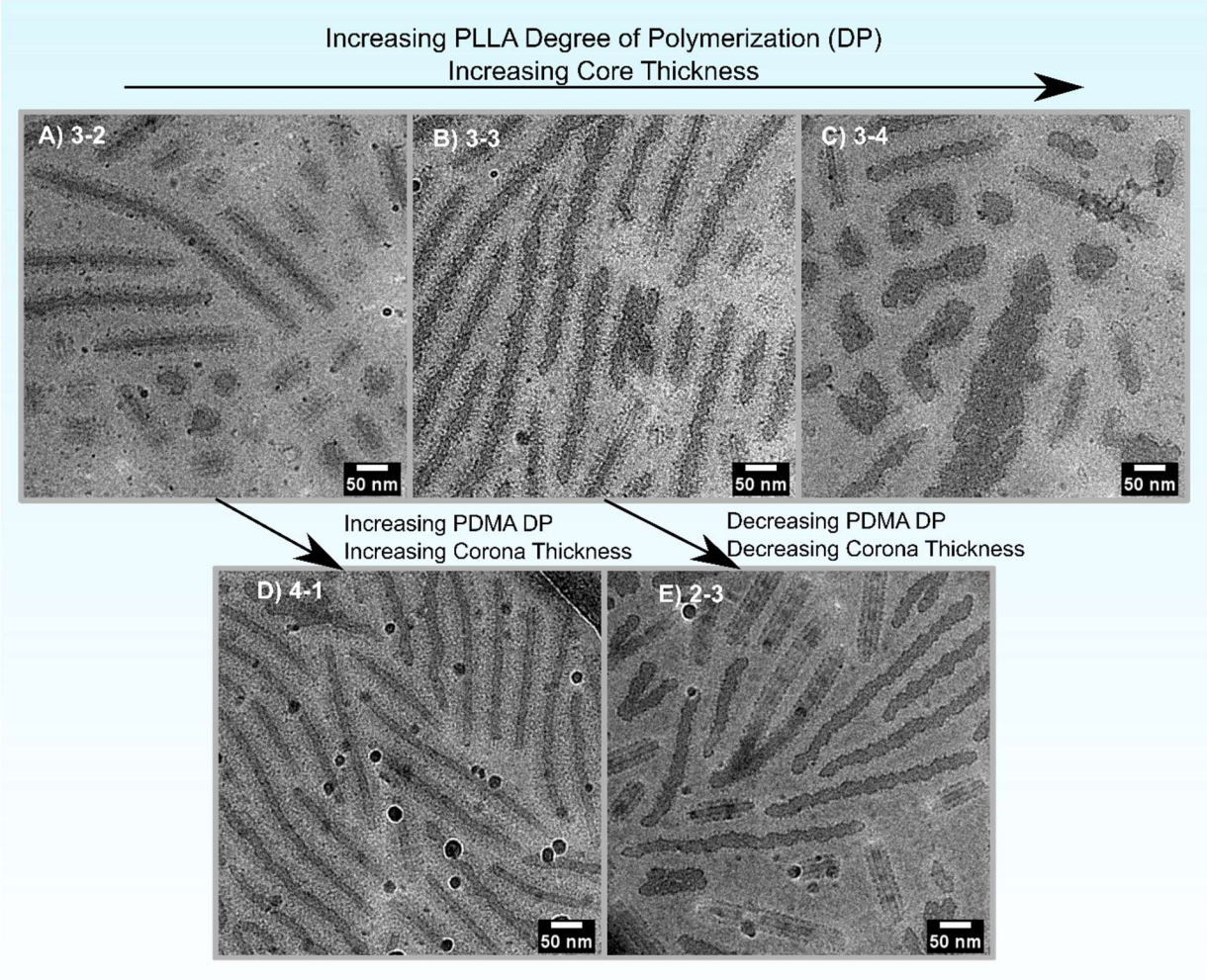

Figure 5.2: CryoEM images of select PDMA-b-PLLA block copolymers. Images are labelled with the representative sample number. Samples A-C show the effect on core thickness with increasing PLLA chain length. Samples D-E show the effect on corona thickness with changes in the PDMA chain length with D having a longer PDMA chain than A with similar PLLA lengths and E having a shorter PDMA chain than B with similar PLLA lengths.

Next, I showed the synthetic versatility of this hybrid polymerization approach by alternative monomers (Figure 5.3). PDMA was swapped out for both poly(*N,N*-diethyl acrylamide) (PDEA) to produce turbid PDEA-*b*-PLLA suspensions with excellent yield and

dispersity mirroring the PDMA-*b*-PLLA system (Figure 5.3A, Table 5.2). PLLA was swapped out for poly(δ)valerolactone (PVL) to produce turbid PDMA-*b*-PVL suspensions (Figure 5.3B, Table 5.3). As δ-valerolactone has reduced reactivity than L-lactide, a DBU/TU co-catalytic system was utilized rather than the gentler TU/(-)-sparteine system which led to higher dispersity values than PDMA-*b*-PLLA polymers in this study.[18] PVL also does not show selectivity in toluene, so the solvent was switched to methyl isobutyl ketone, a solvent that poly(ε)caprolactone, a similar polymer to PVL, is sparingly soluble in.[21] CryoEM studies for these systems are ongoing but I expect these systems to possess similar morphologies to PDMA-*b*-PLLA.

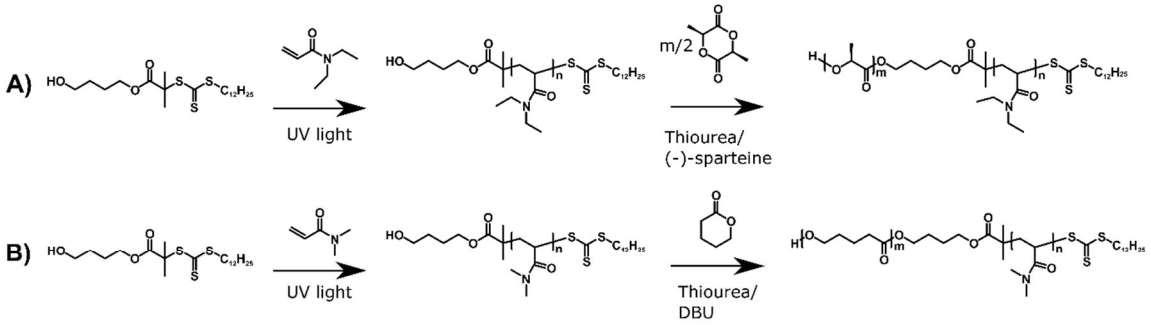

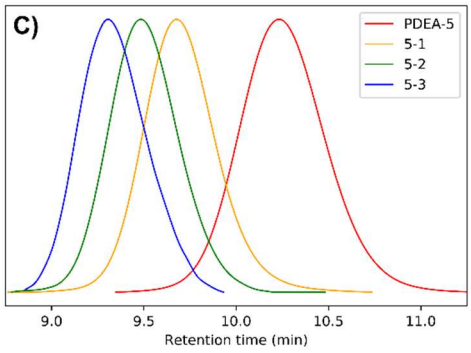

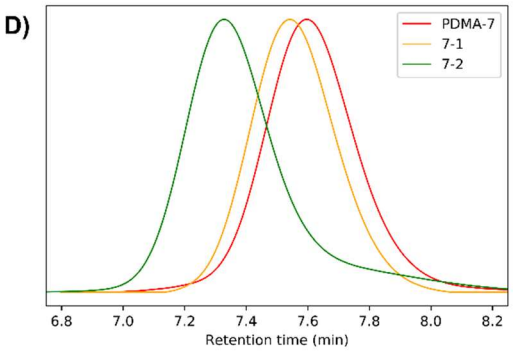

Figure 5.3: Synthesis of alternative polyacrylamide-block-polyesters . A) Scheme showing the photoiniferter polymerization of DEA (Step 1) followed by the polymerization of L-lactide in toluene to make PDEA-b-PLLA (Step 2). B) Scheme showing the photoiniferter polymerization of DMA (Step 1) followed by the polymerization of δ-valerolactone in toluene to make PDMA-b-PVL. C-D) Gel permeation chromatographs showing the successful block copolymerization of the polymers in scheme A (C) and scheme B (D). With flow rates of 0.75 mL/min and 1.0 mL/min respectively.

Table 5.2: Synthetic parameters and results for one pot two step PDEA-*b*-PLLA synthesis.

Sample ID	Target PDEA DP	PDEA Conversion	Target PLLA DP	PLLA Conversion	Đ	M_n	Polymer Structure	Turbid
PDEA-5	150	95%	N/A	N/A	1.07	18200	$PDEA_{143}$	
5-1	150	96%	100	84%	1.07	24400	$PDEA_{144}$-*b*-$PLLA_{84}$	Yes
5-2	150	94%	150	84%	1.07	27000	$PDEA_{141}$-*b*-$PLLA_{126}$	Yes
5-3	150	96%	200	92%	1.07	31600	$PDEA_{144}$-*b*-$PLLA_{184}$	Yes
PDEA-6	200	98%	N/A	N/A	1.08	24900	$PDEA_{196}$	N/A
6-1	200	97%	100	77%	1.10	30200	$PDEA_{194}$-*b*-$PLLA_{77}$	Yes
6-2	200	99%	150	81%	1.08	34000	$PDEA_{198}$-*b*-$PLLA_{122}$	Yes
6-3	200	99%	200	83%	1.08	37100	$PDEA_{198}$-*b*-$PLLA_{166}$	Yes

Table 5.3: Synthetic parameters and results for one pot two step PDMA-*b*-PVL synthesis.

Sample ID	Target PDMA DP	PDMA Conv.	Target PVL DP	PVL Conv.	Đ	M_n	Polymer Structure	Turbid
PDMA-7	150	93%	N/A	N/A	1.09	13900	$PDMA_{140}$	N/A
7-1	150	87%	25	61%	1.08	14100	$PDMA_{130}$-*b*-PVL_{12}	No

7-2	150	93%	75	88%	1.15	20500	$PDMA_{140}$-*b*-PVL_{66}	Yes

5.3. Conclusion

In conclusion, I demonstrate a new synthetic approach to well-defined polyacrylamide-*block*-polyesters nanoparticles produced using a dual photoiniferter, ROPI-CDSA approach. To the best of my knowledge, this report contains the first examples of controlled radical polymerization of DMA or DEA followed by ROP of L-lactide or δ-valerolactone.

5.4. Experimental Section

Materials: *N,N*-Dimethylacrylamide (DMA, Sigma Aldrich) *N,N*-diethylacrylamide (DEA, Sigma Aldrich), and δ-valerolactone (Thermo Fisher) were dried using calcium hydride and vacuum distilled and stored under 4 Å molecular sieves. 4-Hydroxybutyl 2-((dodecylthiocarbonothioyl)thio)-2-methylpropanoate was synthesized according to previous literature procedures.[1] L-Lactide (TCI) was recrystallized in toluene ×3. Anhydrous toluene (99.8%), DBU, and (−)-sparteine were obtained from Sigma-Aldrich and stored under 4 Å molecular sieves. Benzoic acid (Fisher Chemical) was used without further purification. Thiourea (TU) derived from cyclohexylamine (Sigma-Aldrich) and 3,5-bis(trifluoromethyl)phenyl isothiocyanate (TCI) was synthesized following established literature procedures.[2] (29) Chemicals were stored in a dry-N_2 atmosphere glovebox. Reactions were performed in a N_2 glovebox.

Structural characterization: Proton nuclear magnetic resonance (^{1}H NMR) spectra were collected on a 500 MHz Bruker Avance spectrometer in $CDCl_3$. Chemical shifts are given in ppm, calibrated from residual $CHCl_3$. Conversion was calculated for DMA and DEA

polymerization by comparing the monomer peaks (5.7, 6.3, 6.6) ppm to the end group 0.95 ppm. Conversion was calculated for L-lactide polymerization by comparing the peak area of the PLLA peak at 5.16 ppm to the l-lactide monomer peak at 5.03 ppm. Conversion was calculated for δ-valerolactone by comparing the δ-valerolactone monomer peak at 4.35 ppm, to the polymer peak at 4.07 ppm. Size exclusion chromatography (SEC) was performed in DMF using an Agilent 1100 chromatograph equipped with RID detector and a PL gel 5 μm 300 × 7.5 mm mixed column. Samples were calibrated against polystyrene standards.

Main Synthetic Procedures:

Photoiniferter polymerization of DMA (Step 1): DMA (208 mg, 2.1 mmol, target DP = 150) and 0.1 mL stock solution of 4-Hydroxybutyl 2-((dodecylthiocarbonothioyl)thio)-2-methylpropanoate in toluene (6.0 mg, 1.4 × 10-2 mmol) were charged to a 8-mL vial. The vial and sealed with a chemically-inert screw cap and irradiated with UV light (365 nm, 3.5 mW cm^{-2}) for 8 h under stirring.

Ring-opening polymerization of L-lactide (Step 2): L-Lactide (151 mg, 1.1 mmol, target DP = 150) was added to a solution of hydroxy functionalized PDMA from Step 1 (214 mg, 1.4 × 10-2 mmol mmol) and 10% mol TU (35 mg, 103 μmol) in 1.16 mL of toluene (10% L-lactide w/w). Next, 10% mol (−)-sparteine (24 μL, 103 μmol) was added. The solution was stirred for 4 days at 400 rpm and subsequently quenched with 0.05 mL of saturated benzoic acid toluene solution.

Alternative Synthetic Procedures:

Photoiniferter polymerization of DEA: DEA (267 mg, 2.1 mmol) and 0.1 mL stock solution of 4-Hydroxybutyl 2-((dodecylthiocarbonothioyl)thio)-2-methylpropanoate in toluene (6.0

mg, 1.4 × 10-2 mmol) were charged to a 8-mL vial. The vial and sealed with a inert screw cap and irradiated with UV light (365 nm, 3.5 mW cm-2) for 8 h under stirring.

Ring-opening polymerization of δ-valerolactone:): δ-valerolactone (105 mg, 1.1 mmol, target DP = 75) was added to a solution of hydroxy functionalized PDMA from Step 1 (214 mg, 1.4 × 10-2 mmol mmol) and 5% mol TU (17.7 mg, 52 μmol) in 0.73 mL of methyl isobutyl ketone. Next, 5% mol DBU (8 μL, 52 μmol) was added. The solution was stirred for 24 hours at 400 rpm and subsequently quenched with 0.05 mL of saturated benzoic acid toluene solution.

Cryogenic-transmission electron microscopy (cryo-TEM) samples were prepared on Quantifoil grids (R 2/2 40 Mesh, Electron Microscopy Sciences) from original samples that were extracted into excess water giving final concentrations of ≈ 0.1 μg/mL Vitrification was carried out by an Automatic Plunge Freezer ME GP2 (Leica Microsystems) with 3 μL of sample. Grid preparation was performed at >95% humidity and the grids were blotted for 3 s prior to plunging into liquid nitrogen. Cryo-TEM samples were then placed on a Gatan cryo-TEM holder and imaged on a JEOL 2100F transmission electron microscope using a Schottky type field emission gun operating at 200 keV. Images were recorded using SerialEM software in low dose imaging mode with a Gatan OneView CMOS camera at 4k × 4k resolution.

5.5. References

(1) Canning, S. L.; Smith, G. N.; Armes, S. P. A Critical Appraisal of RAFT-Mediated Polymerization-Induced Self-Assembly. *Macromolecules* **2016**, *49* (6), 1985–2001. https://doi.org/10.1021/acs.macromol.5b02602.

(2) Cao, J.; Tan, Y.; Chen, Y.; Zhang, L.; Tan, J. Expanding the Scope of Polymerization-Induced Self-Assembly: Recent Advances and New Horizons. *Macromol. Rapid Commun.* **2021**, *42* (23), 2100498. https://doi.org/10.1002/marc.202100498.

(3) Phan, H.; Cossutta, M.; Houppe, C.; Le Cœur, C.; Prevost, S.; Cascone, I.; Courty, J.; Penelle, J.; Couturaud, B. Polymerization-Induced Self-Assembly (PISA) for in Situ Drug Encapsulation or Drug Conjugation in Cancer Application. *J. Colloid Interface Sci.* **2022**, *618*, 173–184. https://doi.org/10.1016/j.jcis.2022.03.044.

(4) Liu, C.; Hong, C.-Y.; Pan, C.-Y. Polymerization Techniques in Polymerization-Induced Self-Assembly (PISA). *Polym. Chem.* **2020**, *11* (22), 3673–3689. https://doi.org/10.1039/D0PY00455C.

(5) Sha, Y.; Rahman, M. A.; Zhu, T.; Cha, Y.; McAlister, C. W.; Tang, C. ROMPI-CDSA: Ring-Opening Metathesis Polymerization-Induced Crystallization-Driven Self-Assembly of Metallo-Block Copolymers. *Chem. Sci.* **2019**, *10* (42), 9782–9787. https://doi.org/10.1039/C9SC03056E.

(6) Boott, C. E.; Gwyther, J.; Harniman, R. L.; Hayward, D. W.; Manners, I. Scalable and Uniform 1D Nanoparticles by Synchronous Polymerization, Crystallization and Self-Assembly. *Nat. Chem.* **2017**, *9*, 785. https://doi.org/10.1038/nchem.2721.

(7) Hwang, S.-H.; Kang, S.-Y.; Yang, S.; Lee, J.; Choi, T.-L. Synchronous Preparation of Length-Controllable 1D Nanoparticles via Crystallization-Driven In Situ Nanoparticlization of Conjugated Polymers. *J. Am. Chem. Soc.* **2022**, *144* (13), 5921–5929. https://doi.org/10.1021/jacs.1c13385.

(8) Hurst, P. J.; Rakowski, A. M.; Patterson, J. P. Ring-Opening Polymerization-Induced Crystallization-Driven Self-Assembly of Poly-L-Lactide-Block-Polyethylene Glycol Block Copolymers (ROPI-CDSA). *Nat. Commun.* **2020**, *11* (1), 4690. https://doi.org/10.1038/s41467-020-18460-2.

(9) Hurst, P. J.; Graham, A. A.; Patterson, J. P. Gaining Structural Control by Modification of Polymerization Rate in Ring-Opening Polymerization-Induced Crystallization-Driven Self-Assembly. *ACS Polym. Au* **2022**, *2* (6), 501–509. https://doi.org/10.1021/acspolymersau.2c00027.

(10) Inam, M.; Cambridge, G.; Pitto-Barry, A.; Laker, Z. P. L.; Wilson, N. R.; Mathers, R. T.; Dove, A. P.; O'Reilly, R. K. 1D vs. 2D Shape Selectivity in the Crystallization-Driven Self-Assembly of Polylactide Block Copolymers. *Chem. Sci.* **2017**, *8* (6), 4223–4230. https://doi.org/10.1039/C7SC00641A.

(11) Yu, W.; Inam, M.; Jones, J. R.; Dove, A. P.; O'Reilly, R. K. Understanding the CDSA of Poly(Lactide) Containing Triblock Copolymers. *Polym. Chem.* **2017**, *8* (36), 5504–5512. https://doi.org/10.1039/C7PY01056G.

(12) Yildirim, I.; Weber, C.; Schubert, U. S. Old Meets New: Combination of PLA and RDRP to Obtain Sophisticated Macromolecular Architectures. *Prog. Polym. Sci.* **2018**, *76*, 111–150. https://doi.org/10.1016/j.progpolymsci.2017.07.010.

(13) Xia, Y.; Scheutz, G. M.; Easterling, C. P.; Zhao, J.; Sumerlin, B. S. Hybrid Block Copolymer Synthesis by Merging Photoiniferter and Organocatalytic Ring-Opening

Polymerizations. *Angew. Chem.* **2021**, *133* (34), 18685–18689. https://doi.org/10.1002/ange.202106418.
(14) Hartlieb, M. Photo-Iniferter RAFT Polymerization. *Macromol. Rapid Commun.* **2022**, *43* (1), 2100514. https://doi.org/10.1002/marc.202100514.
(15) Kamber, N. E.; Jeong, W.; Waymouth, R. M.; Pratt, R. C.; Lohmeijer, B. G. G.; Hedrick, J. L. Organocatalytic Ring-Opening Polymerization. *Chem. Rev.* **2007**, *107* (12), 5813–5840. https://doi.org/10.1021/cr068415b.
(16) Thomas, C.; Bibal, B. Hydrogen-Bonding Organocatalysts for Ring-Opening Polymerization. *Green Chem.* **2014**, *16* (4), 1687–1699. https://doi.org/10.1039/C3GC41806E.
(17) Pratt, R. C.; Lohmeijer, B. G. G.; Long, D. A.; Lundberg, P. N. P.; Dove, A. P.; Li, H.; Wade, C. G.; Waymouth, R. M.; Hedrick, J. L. Exploration, Optimization, and Application of Supramolecular Thiourea−Amine Catalysts for the Synthesis of Lactide (Co)Polymers. *Macromolecules* **2006**, *39* (23), 7863–7871. https://doi.org/10.1021/ma061607o.
(18) Lohmeijer, B. G. G.; Pratt, R. C.; Leibfarth, F.; Logan, J. W.; Long, D. A.; Dove, A. P.; Nederberg, F.; Choi, J.; Wade, C.; Waymouth, R. M.; Hedrick, J. L. Guanidine and Amidine Organocatalysts for Ring-Opening Polymerization of Cyclic Esters. *Macromolecules* **2006**, *39* (25), 8574–8583. https://doi.org/10.1021/ma0619381.
(19) Ellis, C. E.; Garcia-Hernandez, J. D.; Manners, I. Scalable and Uniform Length-Tunable Biodegradable Block Copolymer Nanofibers with a Polycarbonate Core via Living Polymerization-Induced Crystallization-Driven Self-Assembly. *J. Am. Chem. Soc.* **2022**, *144* (44), 20525–20538. https://doi.org/10.1021/jacs.2c09715.
(20) Scanga, R. A.; Shahrokhinia, A.; Borges, J.; Sarault, S. H.; Ross, M. B.; Reuther, J. F. Asymmetric Polymerization-Induced Crystallization-Driven Self-Assembly of Helical, Rod-Coil Poly(Aryl Isocyanide) Block Copolymers. *J. Am. Chem. Soc.* **2023**, *145* (11), 6319–6329. https://doi.org/10.1021/jacs.2c13354.
(21) Bordes, C.; Fréville, V.; Ruffin, E.; Marote, P.; Gauvrit, J. Y.; Briançon, S.; Lantéri, P. Determination of Poly(ε-Caprolactone) Solubility Parameters: Application to Solvent Substitution in a Microencapsulation Process. *Int. J. Pharm.* **2010**, *383* (1), 236–243. https://doi.org/10.1016/j.ijpharm.2009.09.023.

Chapter 6: CryoEM Reveals the Complex Evolution of a Thermodynamically Unstable Phase in the Chemically Fueled Dissipative Assembly of a Disulfide Building Block

6.0. Abstract

Inspired by the adaptability of biological materials, a variety of synthetic fuel-driven dissipative processes have recently been developed. A general hypothesis in the field is that dissipative systems form unique structures compared to conventional self-assembly processes due to the non-equilibrium nature of dissipative chemistry. However, comparing dissipative and non-dissipative processes in chemically-fueled systems is challenging, which has limited our understanding of how these processes differ. Here, I use a chemically-fueled redox system where the forward activation and backward deactivation reactions can be fully separated. I study the forward and backward reactions sequentially and synchronously (dissipative) using time-resolved cryoEM. The data shows that the dissipative process is more complex and heterogenous than the sequential process. My key finding is that a thermodynamically unstable stacked nanorod phase observed in the backward reaction is sustained for ~ 6 hours in the dissipative process. With the help of collaborators, quantitative analysis of cryoEM data and kinetic Monte Carlo modelling show that the dissipative process is driven by multiple cycles of activation, deactivation, assembly, and disassembly, and diffusive kinetics and concentration gradients. The data shed light on how dissipative systems create unique structures and provide plausible design principles to develop and optimize dissipative materials with unique functions.

6.1. Introduction

Living organisms rely on the thermodynamically unstable states of dynamic materials.[1–5] These materials often assemble from molecular building blocks, with higher-order structures that exist only when there is a flux of energy.[5–8] At least two competing reactions are necessary to drive the formation of structure: a forward reaction assembling the material and a backward reaction dismantling it.[5] For example, GTP promotes the polymerization of microtubules, part of the cytoskeleton of eukaryotic cells, while the hydrolysis of GTP to GDP induces their depolymerization.[2,5,9,10] The kinetics of chemical reactions can make biological materials adaptable and agile in responding to their environment. This feature of biological systems has inspired synthetic systems stimulated by chemical fuel, light or electricity as an energy source.[6,11–26] It is possible to fuel the transient self-assembly of molecular building blocks through environmental changes, such as an increase of pH, or through chemical modification of an assembling precursor. An important feature of these dynamic materials is the asymmetry of the chemical kinetics: the forward reaction preferentially activates the precursor molecules while the backward reaction preferentially deactivates the assembled state.[5] Initially, the forward reaction occurs faster than the backward reaction to build up a critical concentration of assembling species,[5] but the kinetics of the backward reaction dominates as the fuel depletes and returns the system to a state of equilibrium.

A central tenet of dissipative self-assembly is that fluxes of energy and material can form unique structures, with dynamic behaviors capable of useful functions.[8,23,27–30] The chemically-fueled assembly of supramolecular structures dissipates both energy and matter by repeatedly executing the assembly and disassembly reactions. However, few examples have been able to directly compare dissipative and non-dissipative processes

in chemically-fueled materials and isolate each reaction in the dissipative cycle. The lack of comparison is likely due to the difficulty in decoupling the forward and backward reaction, as one or more of the steps is often dependent on the solvent, or the fuel source participates in the forward and backward reaction.[11,12] For example, Rizzuto et. al.[31] developed a supramolecular DNA fiber system where annealing by slow proton dissipation selects for morphologies otherwise inaccessible by conventional self-assembly. Comparison of the forward reaction to the coupled dissipative reaction was key to showing that a coupled process can lead to the formation of higher order structures, suggesting a coupled reaction is more dissipative than a sequential reaction. However, with this system, it was not possible to isolate the backward reaction from the dissipative process as the forward assembly reaction cannot be “turned off”.

Recently, Ogden and Guan developed a chemically-fueled redox system that can fully separate out both the forward and backward reactions in the dissipative assembly of supramolecular materials.[24] The redox process uses separate small molecule fuels for the forward and backward reactions, making it possible to isolate them and the effect of their dissipative coupling. In the forward reaction, an aryl-containing cysteine-based thiol (CSH) is oxidized by H_2O_2 into its disulfide species (CSSC) which spontaneously self-assembles into fibers forming a hydrogel. Simultaneously, at an initially slower rate, excess dithiothreitol (DTT) reduces the CSSC back to CSH disassembling the fibers. As the H_2O_2 depletes, the system returns to CSH. Here, I directly observe this disulfide-based hydrogelator system with time-resolved CryoEM,[32] which reveals the mechanism of fiber formation in both a sequential (forward followed by backward) and dissipative system. I observe a transient, yet highly ordered phase in the backward reaction which is

sustained over long time periods in the dissipative system. To analyze this behavior, my colleague, Justin Mulvey, developed image analysis algorithm to quantify the evolution of the highly ordered phase. Through collaboration with the Green group (UMass), we also implemented and optimized a kinetic model for stochastic simulations of the dissipative assembly to establish the importance of physical kinetics and dissipative cycles in creating and maintaining the unstable phase.

6.2. Results

6.2.1. Experimental Parameters

The dissipative CSH/CSSC-based process is maintained by the presence of both H_2O_2 (oxidizing fuel) and DTT (reductant). Thus, through the inclusion or exclusion of H_2O_2 and DTT, we can isolate and study the forward (**F**) oxidation of CSH, the backward (**B**) reduction of CSSC, and the chemically fueled dissipative (**D**) system separately (Table 6.1) with the goal of comparing the sequential (**F** followed by **B**) and dissipative processes. All experiments were performed with a pH of 6.0 in a buffer solution. For each set of conditions, multiple time points were sampled for CryoEM (See Table 6.1 and experimental information for more details). Time-resolved ultra-performance liquid chromatography (UPLC) and rheology experiments were performed to determine the conversion times and obtain bulk data on gel formation and strength (Figures E.1-5).

Table 6.1: Experimental parameters for forward (assembly) and backward (disassembly) as well as dissipative self-assembly for CSH/CSSC system. All experiments were conducted at a pH of 6.0. **B** is performed from a completed sample of **F** and the collection time builds off **F**.

Run*	Initial Materials	#CryoEM time points	Collection time range
F	10 mM CSH, 10 mM H_2O_2	4	8 s-1500 s
B	5 mM CSSC (**F** after 1500 s), 200 mM DTT	4	1575 s-3375s (& 21 days)

D	10 mM CSH, 150 mM H_2O_2, 200 mM DTT	22	8 s-24000 s, (& 19 days)

*__F__=forward, __B__=backward __D__=dissipative

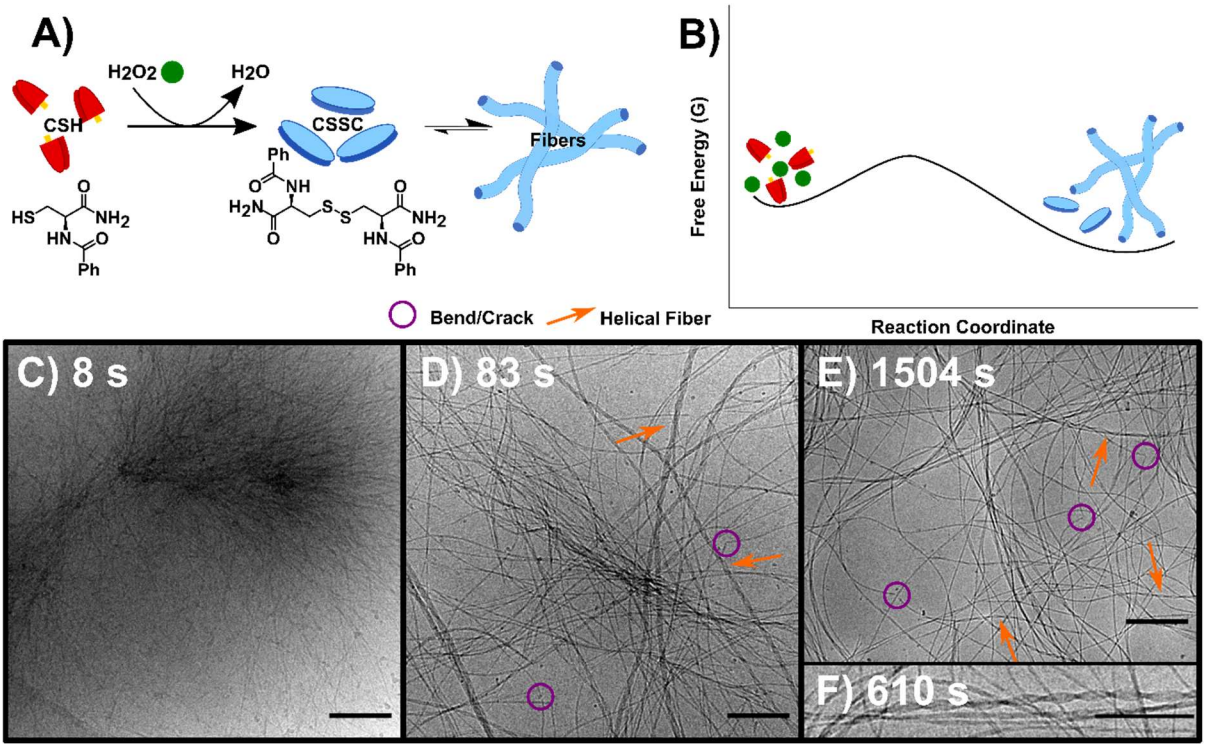

Figure 6.1: The forward reaction converting CSH to assembling CSSC A) Reaction scheme, using H_2O_2 to oxidize the thiol CSH (red) to the disulfide CSSC (blue) leading to fiber formation. B) Schematic free energy diagram of F. C) 8 s into the assembly of CSSC shows the presence of centrosome-like structures. D) CryoEM image at 83 s showing fibers become more well defined with a variety of diameters and twists and helical structures. E) At 1504 s, fibers are more evenly spaced and remain as hydrogels in thermodynamic equilibrium. Legend provided with purple circles showing examples of bends and cracks in fibers and orange arrows to highlight helical fibers. F) Inset of CryoEM images at 610 s of a helical fiber, a structure that is present after the initial time point. Scale bars are 200 nm except for F, which is 10 nm.

6.2.2. CryoEM Studies

In the sequential process, the forward reaction rapidly forms fibers. This reaction, **F**, (Figure 6.1A-B) was studied by the oxidation of CSH (10 mM) using H_2O_2 (10 mM). The gel storage modulus quickly increases until remaining constant after 1500 s indicating maximum conversion (Figure E.1). CryoEM images of **F** and control experiments reveal the presence of long flexible nanofibers (See experimental controls in SI). The images

show that the nanofibers (diameter ≈ 5 nm) can coil to form thicker hierarchical fibers (Figure 6.1C-F, Figures E.6-7). As the average molecular length of CSSC is approximately 14 Å (Figure E.8), the base fiber diameter is about three to four times thicker than the length of a CSSC molecule. This indicates that the fibers are formed from multiple layers of CSSC molecules. Time-resolved CryoEM of **F** reveals that the fibers initially form from high density regions (t = 8 s, Figure 6.1C, Figure E.9). From 83 s to 1504 s the fibers become more uniformly distributed, likely driven by translational entropy (Figure 6.1D-E). A few of these fibers have a helical structure with a pitch of 5.7 ± 0.7 nm (n = 218, see Figure 6.1F). Some fibers display bends and cracks which may indicate rearrangement occurs even after the global structure is stable (Figure 6.1D-E).

Initiating the backward reaction causes the quick disassembly of any fibers formed, and transiently creates a thermodynamically unstable phase. The backward reaction (**B**) was studied by taking a stable sample of the sample **F** (10 mM CSH, 10 mM H_2O_2) at 1500 s, consisting of CSSC, and treating it with 200 mM DTT (Figure 6.2A-B). UPLC shows >99% conversion from CSSC to CSH was reached in 1200 s and rheological data shows a plateau in the storage modulus around 1200 – 1800 s (Figure E.2). Time resolved cryoEM shows the breakdown of fibers (aspect ratio >> 25) into nanorods (aspect ratio 3-25), Figure 6.2C-E.[33] At 1575 s (75 s after addition of DTT), the presence of a stacked nanorod phase is also observed (Figure 6.2D). The stacks are also observed in a control where 5 mM of H_2O_2 was used to ensure full depletion of fuel before DTT addition (Figure E.10). Importantly, these stacks are not observed in any subsequent time points, indicating this phase is transient and thermodynamically unstable. After the stacked nanorod phase breaks down (t > 75 s after addition of DTT) only minor clustering of 2-3

nanorods/fibers is seen and the majority of the cryoEM grid area is void of fibers (Figure 6.2E). CryoEM data show that trace fibers persist 21 days after initiation indicating that either a small number of fibers are kinetically trapped, an observation which has been made previously in other systems,[34] or that there is a small amount of air oxidation. With the observation of a short-lived unstable phase, a logical question arises: Can the lifetime of this phase be prolonged by the forward and reverse reactions occurring simultaneously?

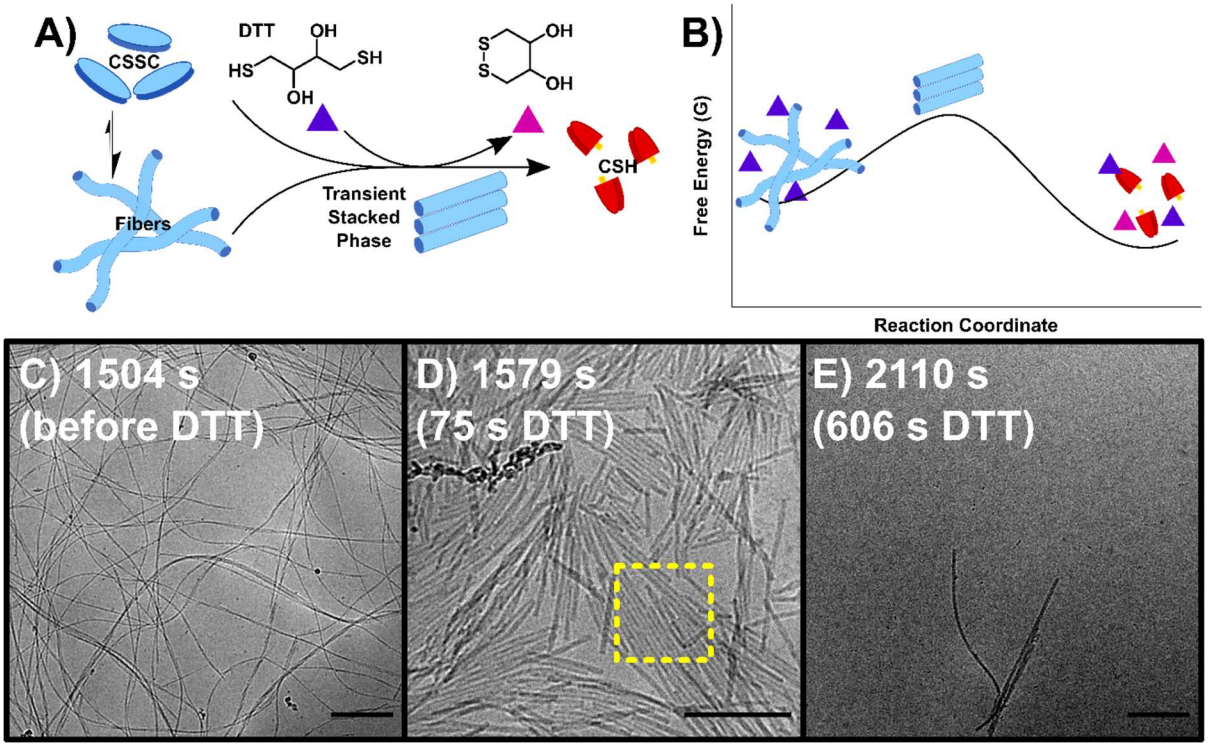

Figure 6.2: The backward reaction of CSSC back to the CSH precursor. A) The addition of DTT causes the breakdown of CSSC fibers back into CSH with the appearance of transient stacked nanorods. B) Free energy diagram of **B**. C) Fibers before the addition of DTT. D) At 1579 s, 75 s after the addition of DTT, fibers break up into nanorods with some of these rods showing 2-D stacking E) At 2110 s, most fibers have disassembled as the solutions return to a sol state, however a few fibers/nanorods can be seen in samples by cryoEM indicating that a small number of fibers could be kinetically trapped.

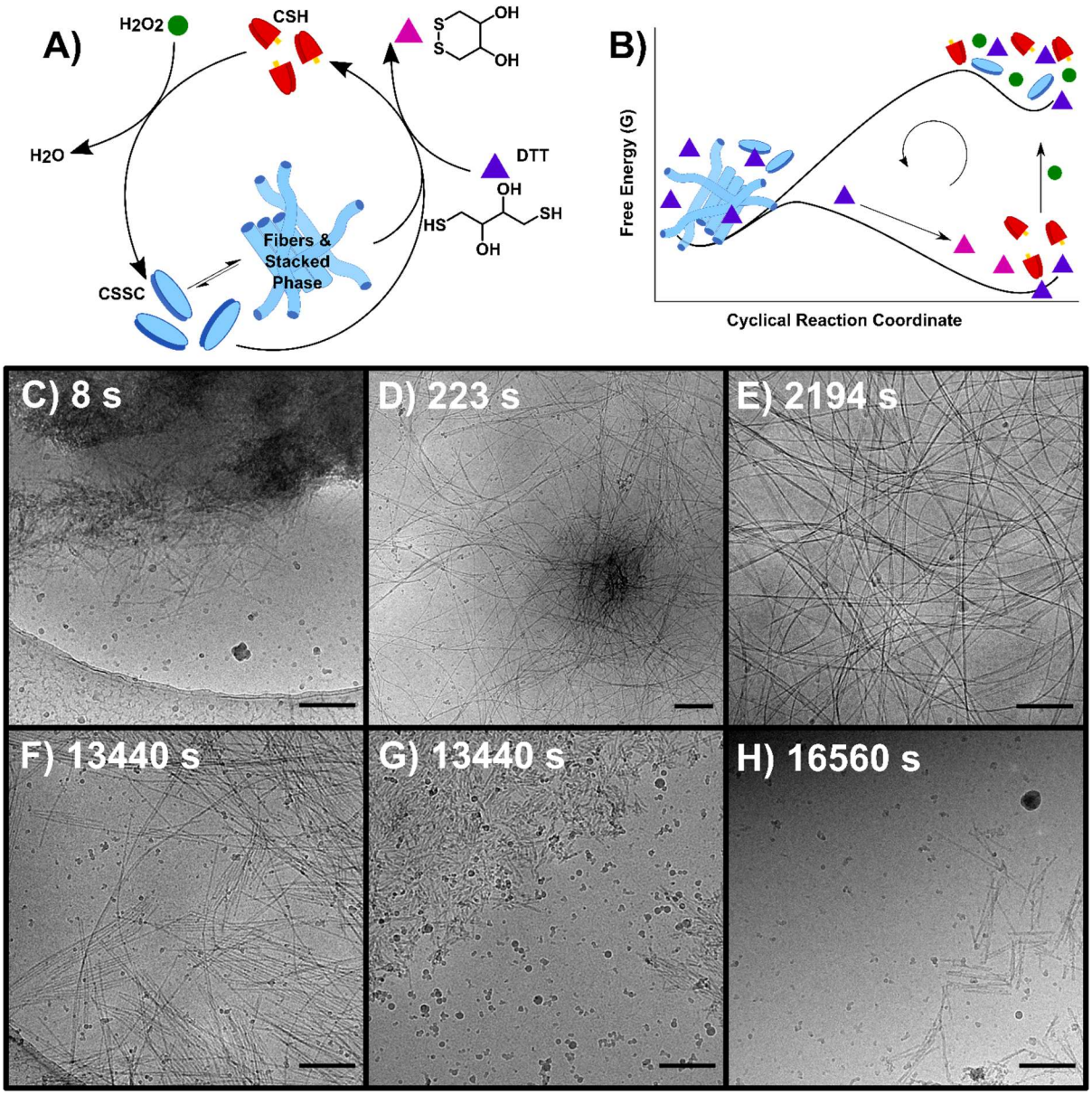

Figure 6.3: The dissipative system allowing for the oscillation of CSH and CSSC. A) The dissipation is sustained by the oxidation of CSH to CSSC by H_2O_2 and the simultaneous reduction of CSSC to CSH by DTT. B) Free energy diagram of **D** highlighting the directionality of the process. Upon the addition of H_2O_2, the system increases in free energy and slowly relaxes through the formation of fibers and depletion of H_2O_2. C-H) CryoEM images of representative structures of **D** C) 8 s D) 223 s E) 2194 s F-G) 13440 s H) 16560 s.

Performing the forward and backward reactions in concert leads to a dissipative process (**D**) that can stabilize the thermodynamically unstable phase. Coupling of these antagonistic reactions also creates a “dissipative cycle” in which molecular building blocks

are repeatedly activated and deactivated. **D** was initiated by adding the fuel of both reactions: 150 mM H_2O_2 to a solution of 10 mM CSH and 200 mM DTT (Figure 6.3). **D** was studied over a greater than six hour period based on previous kinetic data.[24] A t = 0 sample was taken prior to the addition of H_2O_2 and showed that no precursor structures were present (Figure E.11). At 8 s, cryoEM shows the formation of unstructured aggregates with nanorod-like structures at the surface (Figure 6.3C, Figure E.12), similar to observations in the early stages of **F** (Figure E.8). Although most fibers appear to form from these nucleation hot spots, individual isolated fibers were also observed (Figure E.12) indicating that some fibers may form from a unimer growth mechanism. At 44 s, high density fiber regions were observed, which I interpret to have emerged from the unstructured aggregates (Figure 6.3D). As time progresses (t > 225 s), these high-density fiber regions become less common as the fibers spread out (Figure 6.3E). This observation is supported by the increase in gel strength as the reaction proceeds, indicating the development of a hydrogel network (Figure E.3). The dissipative system forms long nanofibers that coil, comparable to **F,** including the presence of helical fibers (pitch = 5.1 ± 0.7 nm, n = 231). At t > 460 s, samples contain a stacked fibers/rod phase comparable to the stacked phase observed in **B**. The stacked phase is observed from 460 s to 23400 s (6.5 h) (Figure E.13), which shows that the dissipative chemistry can stabilize a thermodynamically unstable phase for ~ 6 hours. Therefore, while this phase is thermodynamically unstable in that it only appears transiently in the backward process, it can be stabilized away from equilibrium through the dissipative cycles present in the dissipative chemistry.

Compared to the sequential process, **F** and **B**, the dissipative process, **D**, produces a system that appears more heterogenous. For instance, following the emergence of the stacked phase (t > 460 s), many examples of long flexible dispersed nanofibers can be found that are morphologically similar to those found in **F**. As disassembly dominates, (t > 4300 s) the stacked phase becomes more prevalent (Figure 6.3F) as well as a phase of disordered nanorod-aggregates (Figure 6.3G). At later times, the prevalence of fibers and rods becomes sparse (Figure 6.3H); although, the imaging of a 19-day sample shows traces of assembled structures comparable to those found at 21-day sample of **B**. Figure 6.4 shows a summary of the different structures and general mechanistic trend in **D**. This mechanism is suggested based on the emergence and prevalence of different structural features from time-resolved cryoEM data (Figure 6.3C-H), but I stress that each time point sampled contains mixed morphologies, notably those found in Figure 6.3 D-G. To illustrate this assertion, Figure 6.4 also shows a low magnification representation of an early time point where assembly is largely dominant (under 600 s), a middle time point, where both assembly and disassembly are prevalent (600 – 4300 s), and a late time point where disassembly is dominant (4300 – 23400 s). The early time point representation shows a mix of the centrosome-like structures and dispersed fibers. The intermediate time point representation contains multidirectional flexible fibers as well as fibers and rods displaying stacking behavior. The late time points contain more stacked and disordered rods but still includes nanorods that display some stacking.

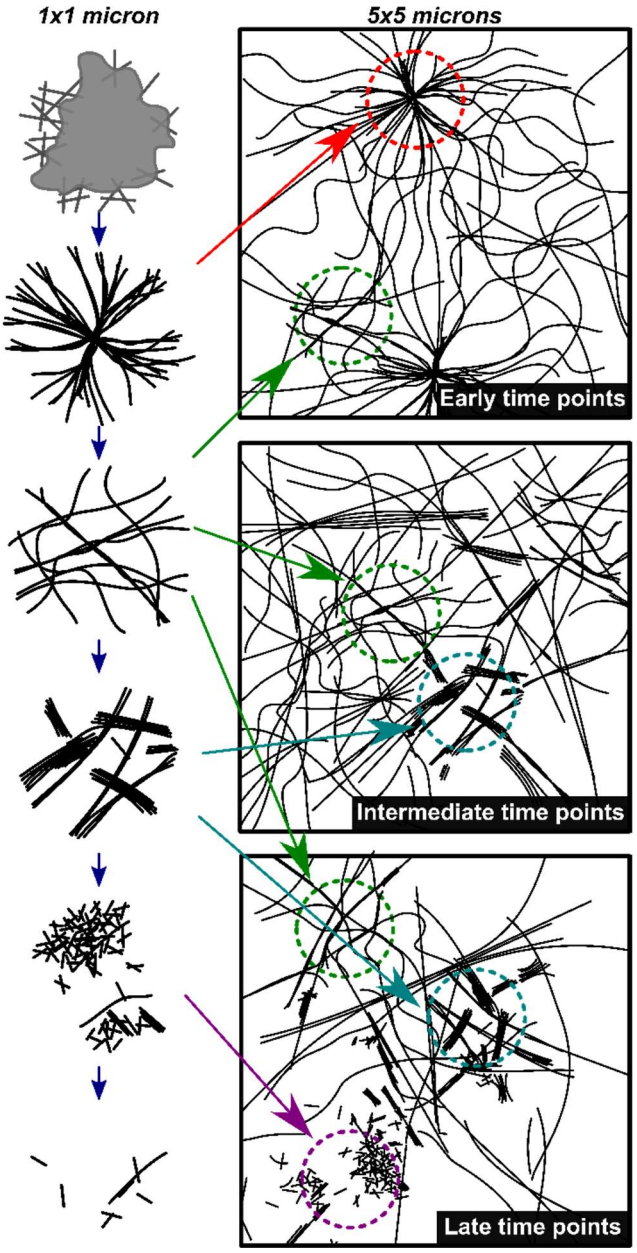

Figure 6.4: Mechanistic depiction of the dissipative process over time. The left column represents structures observed on a 1x1 micron scale (high magnification) and the right column is a representation of an overall sample (5x5 micron scale) highlighting the heterogeneity of fiber states observed. The depictions in the left column are representative of the cryoEM images in Figure 6.3C-H in chronological order.

6.2.3. Image Analysis

To quantify and track the fiber stacking, my colleague, Justin Mulvey, developed an in-house MATLAB script to segment and analyze the stacked fiber phase (Figure 6.5, Appendix E). Stacked fiber domains were identified by first producing normalized cross-correlation maps using 108 generated templates to select for the stacked phase at different fiber spacings and angles in the images (Figure E.15). It was found that the variation in TEM defocus impacted the normalized cross-correlation, so correlation map thresholding was adjusted depending on the defocus of each image, which was estimated via radial integration of the fast-Fourier transform (Figure E.17). Finally, fibers within the segmented domains were identified and labeled with the number of adjacent fibers, defined here as the degree of stacking (DoS) (Figure

6.5 A-D, Figure E.18). The script was used to analyze 770 CryoEM images across 24 experimental conditions generating 398 million datapoints. All CryoEM images were captured at the same nominal magnification (30k). The data is summarized in Figure 6.5E-F, presented as a % coverage distribution (Figure 6.5E), which shows how the density of the stacked fibers changes over time, and a normalized distribution (Figure 6.5F) which compares relative distributions between experimental conditions.

Both the sequential and dissipative process show a general increase in stacking followed by a decrease in stacking (Figure 6.5E). The forward process shows distributions dominated by low DoS (< 5), which come from the random distribution of fiber locations and relatively weak inter-fiber interactions (Figure 6.5A). In contrast, the first timepoint in the backward reaction shows a sharp increase in high DoS (≥ 5), indicating a substantial increase in the inter-fiber interactions (Figure 6.5B). The next timepoint shows the system returning to a low DoS distribution, supportive of my previous qualitative observations that the highly ordered stacked phase is transient (Figure 6.5F).

In the dissipative process, the normalized distributions show a gradual shift towards higher DoS during the first hour. At the 6066 s and 13440 s timepoint, there is a sharp increase in the stacked phase density and normalized distributions are dominated by high DoS (Figure 6.5E-F). This observation suggests that conditions can be exploited to control the DoS and amount of the stacked fiber phase present in the system. Later timepoints reveal a drop in stacked phase density, while some high DoS domains persist. The data shows that the higher DoS is present for a period of > 6 hours, supporting my qualitative assessment. The data also suggests that evolution of the stacked phase is a complex process. In 13 of the 24 timepoints, the standard deviation is greater than the

mean, signifying a large variation in local stacking density. I attribute this variance to inhomogeneity in local chemical concentrations.

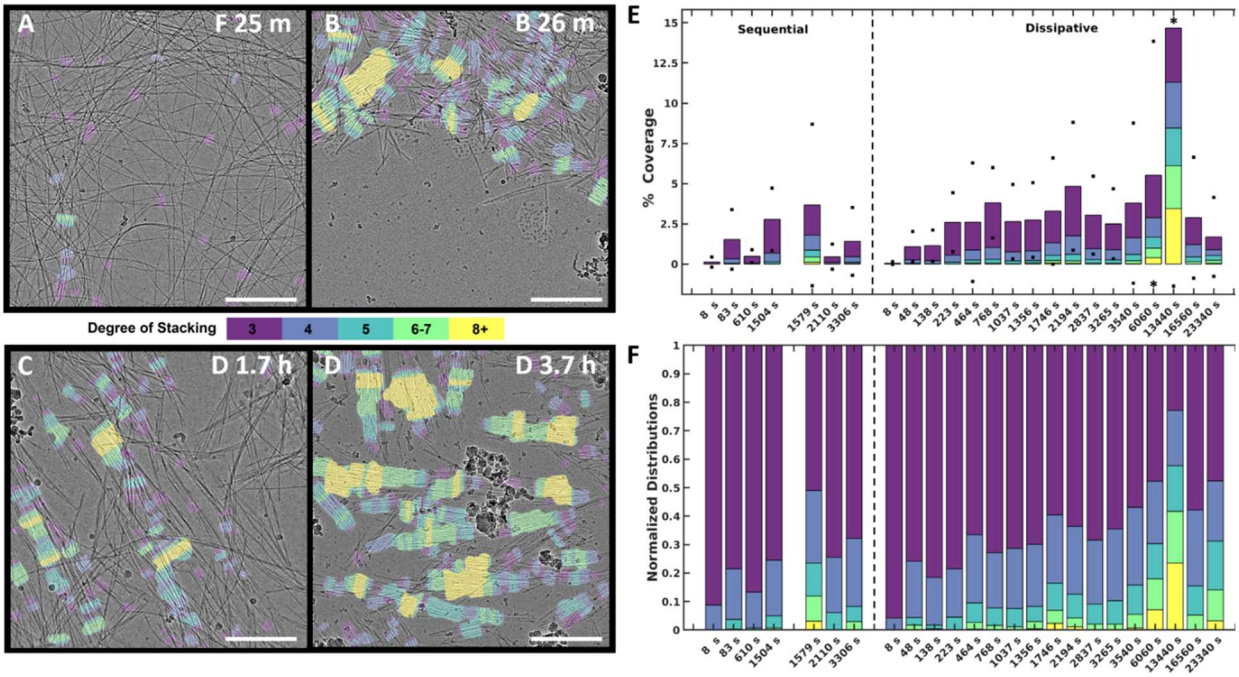

Figure 6.5: Quantitative image analysis of stacked fiber phase. **A-D)** Selection of labeled frames from key timepoints. Colored tinting corresponds to the degree of stacking. F=forward, B=backward, D=dissipative. **E)** Density distribution of each timepoint, defined as the total number of labeled pixels divided by the total number of pixels in each timepoint. Black dots represent standard deviation of image densities within each timepoint. (*) represents standard deviation points omitted for visibility. **F)** Density distribution normalized for distribution comparison. Scale bars 300 nm. Credit: Justin Mulvey.

6.2.4. Simulations

To understand the chemical and physical origins of the stacked phase as well as the differences between a sequential and dissipative process, my collaborators, Rebecca Bone and Jason Green (UMass) used simulations of the stochastic kinetics for both the chemistry and (dis)assembly in small, well-mixed volume elements (See Appendix E for more details on simulation: setup, rate constant determination, full results).[35] A kinetic model of eleven reactions was devised, including the redox reactions and fiber assembly and disassembly (Table 6.2).[24] For each reaction, counts of chemical species, and fibers

were simulated in time with kinetic Monte Carlo in order to account for the stochastic nature of the fiber growth and decay. These counts were recorded every 0.1 s for the forward, backward, and dissipative processes with the initial conditions matching the experiments. Rate constants of diffusion-limited reactions were taken to be the diffusion coefficient of the relevant species.[36] Once there is at least one fiber formed via reaction 4, the addition and removal of subunits to/from fibers has finite probability. Each time this reaction is selected to occur, a fiber is chosen at random to gain or lose one subunit. These simulations gave statistics for the number of fibers and their length.

Most rate constants in the chemical mechanism were measured experimentally (Appendix F). Unknown rate constants were optimized to match experimental timescales. Using **F** as a starting point, a range of rate constants for (k_{sp}, k_3, and k_6) that gave agreement were further narrowed down to ensure agreement with the observed timescale of **B**. For these steps, k_{sp} and k_6 were varied because they had not been previously experimentally determined, and k_3 was varied because the experimental value did not result in fiber growth in the simulations (see Appendix E for detailed explanation of rate constant determination). Here, the forward process involves reactions 1-4 and 11 and the backward involves 4-8 and, to a lesser extent, 9-10 with any remaining H_2O_2. In the dissipative process, all reactions in the chemical mechanism in Table 6.2 can occur. Using the parameters and ranges from the sequential process, the timescale of the simulated dissipative process was then optimized to be as close to the experimental timescale as possible by varying the rate constants unimportant to **F** and **B** or still having a range of possible values. This procedure gave simulation timescales that agreed with

those observed for **F** and **B** within an acceptable error and a timescale of ~22535 s in agreement with the timescale for **D**.

Table 6.2: Chemical reactions of CSH/CSSC systems used to simulate the stochastic kinetics.

Number	Reaction	Forward rate constant	Reverse rate constant
1	$CSH + OH^- \rightleftarrows CS^- + H_2O$	$k_f^{CSH} = 10^{pH-pK_a} k_r^{CSH}$	$k_r^{CSH} = rD(CSH)/V$
2	$CS^- + H_2O_2 \rightarrow CSOH + OH^-$	$k_3 = 25\ M^{-1}s^{-1}$	
3	$CS^- + CSOH \rightarrow CSSC_{sol} + OH^-$	$k_4 = 720\ M^{-1}s^{-1}$ [4]	
4	$CSSC_{sol} \rightleftarrows CSSC_{fib}$	$k_7 = 1.46 * 10^{-17}\ M^{-1}s^{-1}$	$k_{sp} = 1000\ M^{-1}s^{-1}$
5	$DTT + OH^- \rightleftarrows DTT^- + H_2O$	$k_f^{DTT} = 10^{pH-pK_a} k_r^{DTT}$	$k_r^{DTT} = rD(DTT)/V$
6	$DTT^- + CSSC_{sol} \rightarrow DTTSC + CS^-$	$k_6 = 5\ M^{-1}s^{-1}$	
7	$DTT^- + CSOH \rightarrow DTTSC + OH^-$	$k_5 = 10\ M^{-1}s^{-1}$	
8	$DTTSC \rightarrow DTT_{cyc} + CSH$	$k_d = 2.83 * 10^{-17}\ M^{-1}s^{-1}$	
9	$DTT^- + H_2O_2 \rightarrow DTTOH + OH^-$	$k_1 = 0.0046\ M^{-1}s^{-1}$	
10	$DTTOH \rightarrow DTT_{cyc} + OH^-$	$k_d = 2.83 * 10^{-17}\ M^{-1}s^{-1}$	
11	$2CSSC_{sol} \rightarrow 2CSSC_{fib}$	$k_7 = 1.46 * 10^{-17}\ M^{-1}s^{-1}$	

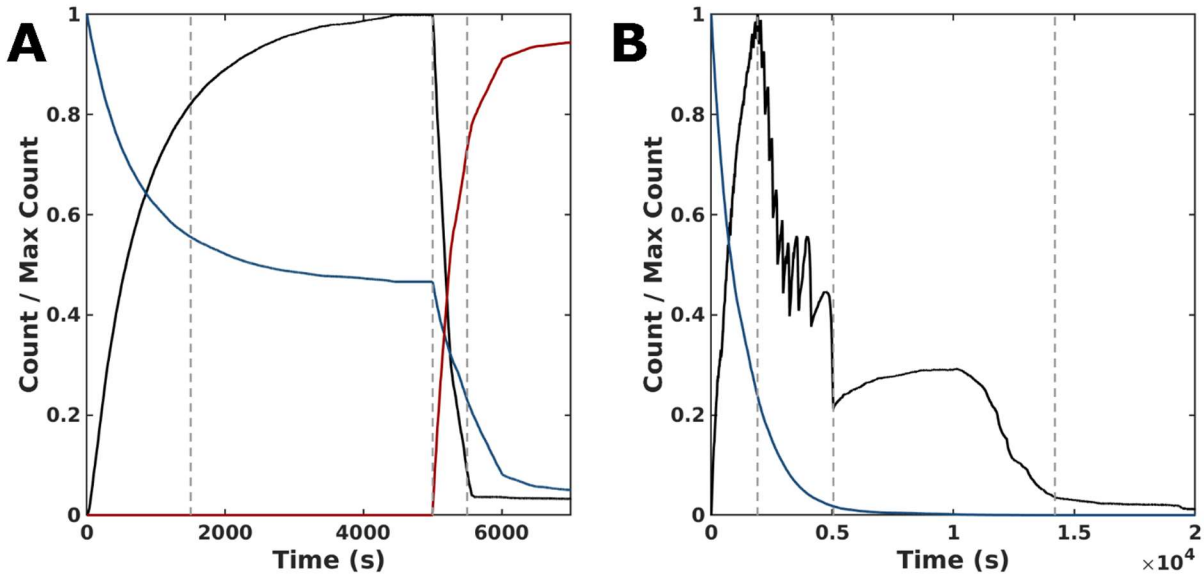

Figure 6.6: Simulation data for the sequential and the dissipative processes. A) Normalized time series of count of species for the forward ($0\ s \leq t \leq 5000$ s) and backward ($t > 5000\ s$) processes reported in $\Delta t = 0.1\ s$ time intervals: CSSC in fibers (black), H_2O_2 (blue), and DTT_{cyc} (red). 1st dashed line indicates a >75% completion of the forward reaction. 2nd dashed line indicates the addition of DTT which is then converted to DTT_{cyc}. 3rd dashed line represents >75% completion of the backward reaction. B) Normalized count of assembled subunits $CSSC_{fib}$ (black) and fuel H_2O_2 (blue) in time reported in $\Delta t = 0.1\ s$ time intervals. 1st Dashed vertical line indicates time of peak amount of CSSC incorporated into fibers. 2nd dashed line marks the end of the rigorous oscillatory stage. 3rd dashed line marks the near depletion of CSSC fibers. Credit: Rebecca Bone and Jason Green

In the sequential process, the simulations show a rapid conversion of CSH to an intermediate CSOH, which resolved to CSSC and constitutes **F**. During the forward process, rapid fiber growth leads to steady values of both fiber count and length (average 35 units) by 4000 s. To start the backward process, DTT is injected at 5000 s. The presence of this fuel causes the CSSC count to quickly fall through the conversion of DTT to the cyclic form of DTT (DTT_{cyc}) (Figure 6.6A) leading to the fast degradation of fibers. The timescale of these simulations matches the magnitude of the experimental timescale. Simulations of the dissipative process also show an initial rapid buildup of CSSC and fibers within the first several minutes (2500 s). Following this initial buildup of CSSC, fibers

then oscillate in count while steadily dropping in count. Around 5000 s, when the fuel is roughly depleted, the value of CSSC plateaus until a final decrease to trace counts of CSSC around (15,000 s) (Figure 6.6B). The dissipative fibers are shorter (30 units) than the forward process (35 units). Even accounting for the concentration dependence of rate constants, the timescale of the simulations is about 20,000 s (~5.6 h) which is shorter than the experimental results (~8 h), suggesting the importance of the kinetics of diffusion and fiber growth. These simulations led to the identification of a dissipative cycle (fiber growth through reactions 2, 3 and fiber decay through reactions 6 and 8), a sequence of chemical reactions that occurs approximately 10 times more often in the dissipative process than in the sequential process (Appendix E).

6.3. Discussion

Collectively, the experimental and computational data shows that the dissipative system executes multiple cycles of activation, deactivation, assembly, and disassembly of the material building blocks. The operation of a dissipative cycle means this process is not simply a combination of a stepwise assembly and disassembly process. For example, the time scale of the dissipative process (~ 8 h) is longer than the sequential forward and backward processes (< 1 h). One reason is that a dissipative process can locally cycle between assembly and disassembly until the excess fuel (150 mM H_2O_2) is depleted. This cycling increases the total number of reactions that occur in the dissipative process than the sequential process. The sequential process cannot execute this cycle and the amount of H_2O_2 and DTT used is limited by the initial concentration of CSH (10 mM). However, the cycle alone is likely not sufficient to explain the disparity in the time scale of the dissipative and sequential process. The simulations, which account for the cycling and

stochasticity of the reaction and fiber growth kinetics, predict the dissipative process to be ~20000 s (5.6 h) and the sequential process to be ~ 5000 s (1.4 h). They also suggest that accurately modeling the high energy structures formed by dissipative chemistry requires not only detailed modeling of chemical kinetics but also the diffusive kinetics and concentration gradients across longer length scales. This is consistent with previous work showing a time delay results between the activation process and the self-assembly.[37] This discrepancy could account for the difference between the experimental and simulation timescales of the dissipative process. Additionally, local diffusion gradients are likely one reason why the dissipative system is more complex and heterogenous compared to the sequential process. The presence of gradients may arise from the asymmetric evolution of fibers (and CSSC) in the dissipative process, which exhibits complex fluctuations followed by a maximum value and a quick collapse. Similarly, the quantified stacked phase data also shows oscillations in the normalized density distribution of the stacked phase.

Several dissipative systems have been shown to display oscillatory behavior,[38,39] indicating this could be a common feature of dissipative chemistry. Such oscillatory behavior could explain the high stochasticity associated with dissipative systems.[40] In contrast, conventional sequential processes shows a logarithmic growth and decay of fibers. Dissipative systems, being out-of-equilibrium must exist in a state of high energy flux and must produce entropy upon activation by a chemical fuel.[30] In another dissipative assembly process, Nicholson et. al.[40] found the diversity in length and number of fibers correlated with the entropy in the system. As entropy is a measure of the number of microstates, I postulate that greater diversity in fiber features and mixed morphologies

observed in the dissipative system indicates it produces more entropy than the sequential process.

The sequential and dissipative processes are most similar in the early and late time points, when the assembly and disassembly reactions respectively dominate. For example, both the dissipative and sequential processes begin with the formation of large (>1 micron diameter) unstructured aggregates. Such aggregates, which are known as liquid or solid phase precursors, are very common in fiber formation and crystallization processes.[41–43] These precursors phases contain high local concentration of building blocks and can result in rapid fiber nucleation.[42–44] For example, microtubules, which grow as supramolecular fibers, have been shown to form via a liquid droplet precursor mechanism.[45,46] These liquid precursors convert into centrosomes, which are the organization centers for microtubule growth.[46,47] I postulate that the high-density fiber regions observed are analogous to these organization centers and therefore I will refer to them as centrosome-like structures (Figure 6.1C, Figure 6.3C-D). Interestingly these centrosome-like structures appear in both the sequential and dissipative processes indicating they are part of a general feature of fiber formation rather than a specific feature of dissipative chemistry. At the late time points both processes show trace amounts of assembled structures either due to kinetic trapping or residual oxidation of CSH.

The most distinctive difference between the sequential and dissipative processes are seen in the intermediate time points when the kinetics of both the forward and backward processes are sufficiently high to influence the morphology of the assemblies. During the forward reaction, the sequential process rapidly forms a thermodynamically stable product (Figure 6.1B, D-E). In the backward disassembly step, as DTT is added,

the fibers become unstable, form a transient intermediate stacked phase which rapidly disassembles (Figure 6.2B, D). During the dissipative process the constant cycling enables the stacked phase to be sustained for ~ 6 hours and is present in combination with disperse fibers (Figure 6.3B, F, Figure E.13). In the sequential process, fibers have time to grow to greater lengths and diffuse away from each other without also being simultaneously decayed. The diffusion of fibers away from each other prevents there from being dense pockets of decaying fibers. The diffusion and the longer fiber length result in less entropic driving force toward creating the stacked conformation in the sequential process. This can happen because fibers are not being decayed while they are simultaneously being built in the forward process. Conversely, the decay in the dissipative process is also happening when fibers would otherwise be diffusing away from each other with very little decomposition in the sequential process. The occurrence of this stacked phase in the backward process is also likely prolonged in the dissipative process due to the general lengthening of the timescale on which the dissipative process occurs.

Importantly, the stacked phase in the backward reaction is limited to short rods whereas in the dissipative process, both fibers and rods can show ordered stacking. This indicates that although the dissipative process is stabilizing a transient intermediate in the sequential process, it is also capable of providing structures with order over larger distances e.g., stacked fibers. The degree of stacking reaches a maximum in later time points (Figure 6.5) which coincides with a period of sustained fiber count in the simulations when the fuel is almost depleted. From this data, a plausible design principle emerges because of the nonlinear nature of the kinetics: smaller amounts of fuel might be necessary to sustain the fibers compared to the amount of fuel needed to create them

initially. To test this hypothesis, my collaborators simulated the addition of small doses of fuel at regular intervals in the dissipative process to sustain the fiber population (Appendix E simulation section). The simulations show that fibers can indeed be sustained with a small amount of fuel when there is feedback between fiber structures and fuel added. Future work is needed to fully exploit this principle; however, we believe that minimal fuel doping could be a promising method to maintain highly ordered thermodynamically unstable structures.

6.4. Conclusion

In summary, I have compared the self-assembly mechanisms for a conventional sequential assembly-disassembly process and dissipative process using time-resolved CryoEM, quantitative image analysis, and kinetic Monte Carlo simulations. A central tenet of dissipative self-assembly is that thermodynamically unstable structures can be sustained by the continuous input of fuel.[17] Here, by isolating and studying the sequential process, I am able to identify which morphologies are thermodynamically stable and which are thermodynamically unstable. In the dissipative process, I show early and late timepoints of the system resembles that of a conventional assembly process. During the middle stages of the dissipative reaction the samples display structural features which can be found in the sequential process. However, each time point in the dissipative process is more heterogenous and the evolution of structures is more complex. Importantly, I show that transient yet highly ordered intermediates in the sequential self-assembly process can be stabilized using dissipative chemistry. Simulations were used to rationalize these differences, suggesting they may arise from less diffusion and shorter fiber lengths in the dissipative process compared to the sequential process. They also

reveal the chemical kinetics of the dissipative process display oscillatory behavior which is in line with a highly stochastic process. From a design point of view, these findings are extremely important as I can now tune the reaction kinetics to select for and enhance the yield of this unstable phase. I anticipate that these findings will also be useful for understanding how higher-ordered systems are maintained using dissipative chemistry. These mechanistic distinctions will be key in streamlining the development of dissipative materials with unique structures, dynamics, and functions that are unattainable by conventional processes.

6.5. Experimental Section

Chemicals and Reagents: CSH was synthesized according to previously described procedures and was stored in an N_2 glove box.[24] (Need to list where synthetic reagents came from for this). Hydrogen Peroxide was purchased from Fisher Chemical, DL-Dithiothreitol (DTT) was purchased from Sigma Aldrich. Dithiobutylamine (DTBA) was purchased from Sigma Aldrich.

Buffer Preparation: Buffers were prepared by combining 0.1 M citric acid solution and 0.2 M Na_2HPO_4 solution in amounts adapted from the Sigma-Aldrich buffer center guide. The pH of the buffer solutions was then measured with a pH meter and adjusted with dropwise amounts of 1 M citric acid or 10 M sodium hydroxide solutions to reach the desired pH (pH = 6.0).

Representative Procedure for Dissipative Material Preparation: To a solution of CSH in methanol (200 mM, 50 µL) was added a buffer solution contained DTT (250 mM, 800 µL). An additional 100µL of buffer solution was added. Individual solutions were briefly heated (40° C) or sonicated before mixing to dissolve components. To start the dissipative

process, a solution of H_2O_2 was added (3M, 50μL) via syringe and vortexted for 10 s to initiate the reaction. The final solution had a concentration of 200 mM DTT, 150 mM H_2O_2 and 10 mM CSH. In one control, DTBA was substituted for DTT.

Representative Procedure for Sequential Assembly, Disassembly Material Preparation: The assembly of CSH to CSSC was carried out by following the above procedure but omitting the DTT from the process. The amounts of H_2O_2 and CSH were varied keeping the overall volume the same. The disassembly process was then initiated from an assembly reaction that sat for at least several hours by adding DTT dissolved in a minimal amount of buffer. The vial was then vortexed for 10 s to mix the DTT into the hydrogel.

Ultra-High-Performance Liquid Chromatography (UPLC) analysis was conducted on an ACQUITY H Class Plus equipped with an ACQUITY UPLC BEH C18 (2.1 x 50 mm, 1.7 μm) reverse-phase column. The absorbance data was captured with a poly diode array at 225 nm and compared to the absorbance of a standard curve of known concentrations. The analysis was carried out with N-acetylcysteine amide (NACA) as a non-gelating analogue for CSH.

Rheology: Oscillatory rheology was collected from CSH/CSSC samples on a TA DHR 2 rheometer. Gels were loaded using a 20 mm steel Peltier plate. Samples for rheology experiments were prepared as above and were immediately placed on the rheometer plate. Loading took about 100 s. Time sweeps were measured by subjecting the materials to an oscillatory strain of 0.5% at 1 Hz and the plate was kept at 25° C. The storage modulus was measured at 6 s intervals until the storage modulus reached a stable value.

Cryogenic-Transmission electron microscopy (Cryo-TEM): Cryo-TEM samples were prepared from solutions previously prepared onto Quantifoil R3.5/1 (Electron Microscopy

Sciences) grids. Grids were glow discharged for 70 s to increase hydrophilicity prior to sample loading. Vitrification was carried out by an Automatic Plunge Freeze ME GP2 (Leica Microsystems) with 3 µL of sample. Grid preparation was performed at 95-99% humidity and the grids were blotted for 3 s prior to plunging into liquid propane. Time points were noted as the grids were plunged. For the 8 s time points, the reactions were mixed on the grids and immediately blotted, the whole process taking 8 s. Select CryoEM samples were then placed on a Gatan CryoEM holder and imaged on a JEOL 2100 TEM using a Schottky type field emission gun operating at 200 keV. Images were recorded using Serial EM software with a Gatan OneView CMOS camera at 4kx4k resolution.

For detailed information of image processing and simulations see Appendix E.

6.5. References

(1) Weißenfels, M.; Gemen, J.; Klajn, R. Dissipative Self-Assembly: Fueling with Chemicals versus Light. *Chem* **2021**, *7* (1), 23–37. https://doi.org/10.1016/j.chempr.2020.11.025.

(2) Walther, A. Viewpoint: From Responsive to Adaptive and Interactive Materials and Materials Systems: A Roadmap. *Adv. Mater.* **2020**, *32* (20), 1905111. https://doi.org/10.1002/adma.201905111.

(3) Deng, J.; Walther, A. ATP-Responsive and ATP-Fueled Self-Assembling Systems and Materials. *Adv. Mater.* **2020**, *32* (42), 2002629. https://doi.org/10.1002/adma.202002629.

(4) Merindol, R.; Walther, A. Materials Learning from Life: Concepts for Active, Adaptive and Autonomous Molecular Systems. *Chem. Soc. Rev.* **2017**, *46* (18), 5588–5619. https://doi.org/10.1039/C6CS00738D.

(5) Ragazzon, G.; Prins, L. J. Energy Consumption in Chemical Fuel-Driven Self-Assembly. *Nat. Nanotechnol.* **2018**, *13* (10), 882–889. https://doi.org/10.1038/s41565-018-0250-8.

(6) te Brinke, E.; Groen, J.; Herrmann, A.; Heus, H. A.; Rivas, G.; Spruijt, E.; Huck, W. T. S. Dissipative Adaptation in Driven Self-Assembly Leading to Self-Dividing Fibrils. *Nat. Nanotechnol.* **2018**, *13* (9), 849–855. https://doi.org/10.1038/s41565-018-0192-1.

(7) England, J. L. Dissipative Adaptation in Driven Self-Assembly. *Nat. Nanotechnol.* **2015**, *10* (11), 919–923. https://doi.org/10.1038/nnano.2015.250.

(8) Rossum, S. A. P. van; Tena-Solsona, M.; Esch, J. H. van; Eelkema, R.; Boekhoven, J. Dissipative Out-of-Equilibrium Assembly of Man-Made Supramolecular Materials. *Chem. Soc. Rev.* **2017**, *46* (18), 5519–5535. https://doi.org/10.1039/C7CS00246G.

(9) Desai, A.; Mitchison, T. J. MICROTUBULE POLYMERIZATION DYNAMICS. *Annu. Rev. Cell Dev. Biol.* **1997**, *13* (1), 83–117. https://doi.org/10.1146/annurev.cellbio.13.1.83.

(10) Tena-Solsona, M.; Boekhoven, J. Dissipative Self-Assembly of Peptides. *Isr. J. Chem.* **2019**, *59* (10), 898–905. https://doi.org/10.1002/ijch.201900018.

(11) Boekhoven, J.; Brizard, A. M.; Kowlgi, K. N. K.; Koper, G. J. M.; Eelkema, R.; van Esch, J. H. Dissipative Self-Assembly of a Molecular Gelator by Using a Chemical Fuel. *Angew. Chem. Int. Ed.* **2010**, *49* (28), 4825–4828. https://doi.org/10.1002/anie.201001511.

(12) Boekhoven, J.; Hendriksen, W. E.; Koper, G. J. M.; Eelkema, R.; van Esch, J. H. Transient Assembly of Active Materials Fueled by a Chemical Reaction. *Science* **2015**, *349* (6252), 1075. https://doi.org/10.1126/science.aac6103.

(13) Maiti, S.; Fortunati, I.; Ferrante, C.; Scrimin, P.; Prins, L. J. Dissipative Self-Assembly of Vesicular Nanoreactors. *Nat. Chem.* **2016**, *8* (7), 725–731. https://doi.org/10.1038/nchem.2511.

(14) Pezzato, C.; Prins, L. J. Transient Signal Generation in a Self-Assembled Nanosystem Fueled by ATP. *Nat. Commun.* **2015**, *6* (1), 7790. https://doi.org/10.1038/ncomms8790.

(15) Dhiman, S.; Jain, A.; George, S. J. Transient Helicity: Fuel-Driven Temporal Control over Conformational Switching in a Supramolecular Polymer. *Angew. Chem. Int. Ed.* **2017**, *56* (5), 1329–1333. https://doi.org/10.1002/anie.201610946.

(16) Dhiman, S.; Jain, A.; Kumar, M.; George, S. J. Adenosine-Phosphate-Fueled, Temporally Programmed Supramolecular Polymers with Multiple Transient States. *J. Am. Chem. Soc.* **2017**, *139* (46), 16568–16575. https://doi.org/10.1021/jacs.7b07469.
(17) Tena-Solsona, M.; Rieß, B.; Grötsch, R. K.; Löhrer, F. C.; Wanzke, C.; Käsdorf, B.; Bausch, A. R.; Müller-Buschbaum, P.; Lieleg, O.; Boekhoven, J. Non-Equilibrium Dissipative Supramolecular Materials with a Tunable Lifetime. *Nat. Commun.* **2017**, *8* (1), 15895. https://doi.org/10.1038/ncomms15895.
(18) Sorrenti, A.; Leira-Iglesias, J.; Sato, A.; Hermans, T. M. Non-Equilibrium Steady States in Supramolecular Polymerization. *Nat. Commun.* **2017**, *8* (1), 15899. https://doi.org/10.1038/ncomms15899.
(19) van Ravensteijn, B. G. P.; Hendriksen, W. E.; Eelkema, R.; van Esch, J. H.; Kegel, W. K. Fuel-Mediated Transient Clustering of Colloidal Building Blocks. *J. Am. Chem. Soc.* **2017**, *139* (29), 9763–9766. https://doi.org/10.1021/jacs.7b03263.
(20) della Sala, F.; Maiti, S.; Bonanni, A.; Scrimin, P.; Prins, L. J. Fuel-Selective Transient Activation of Nanosystems for Signal Generation. *Angew. Chem. Int. Ed.* **2018**, *57* (6), 1611–1615. https://doi.org/10.1002/anie.201711964.
(21) Mishra, A.; Korlepara, D. B.; Kumar, M.; Jain, A.; Jonnalagadda, N.; Bejagam, K. K.; Balasubramanian, S.; George, S. J. Biomimetic Temporal Self-Assembly via Fuel-Driven Controlled Supramolecular Polymerization. *Nat. Commun.* **2018**, *9* (1), 1295. https://doi.org/10.1038/s41467-018-03542-z.
(22) Pappas, C. G.; Sasselli, I. R.; Ulijn, R. V. Biocatalytic Pathway Selection in Transient Tripeptide Nanostructures. *Angew. Chem. Int. Ed.* **2015**, *54* (28), 8119–8123. https://doi.org/10.1002/anie.201500867.
(23) De, S.; Klajn, R. Dissipative Self-Assembly Driven by the Consumption of Chemical Fuels. *Adv. Mater.* **2018**, *30* (41), 1706750. https://doi.org/10.1002/adma.201706750.
(24) Ogden, W. A.; Guan, Z. Redox Chemical-Fueled Dissipative Self-Assembly of Active Materials. *ChemSystemsChem* **2020**, *2* (4), e1900030. https://doi.org/10.1002/syst.201900030.
(25) Selmani, S.; Schwartz, E.; Mulvey, J. T.; Wei, H.; Grosvirt-Dramen, A.; Gibson, W.; Hochbaum, A. I.; Patterson, J. P.; Ragan, R.; Guan, Z. Electrically Fueled Active Supramolecular Materials. *J. Am. Chem. Soc.* **2022**, *144* (17), 7844–7851. https://doi.org/10.1021/jacs.2c01884.
(26) Barpuzary, D.; Hurst, P. J.; Patterson, J. P.; Guan, Z. Waste Free Fully Electrically Fueled Dissipative Self-Assembly System. *JACS* **2023**, *ASAP*.
(27) Kondepudi, D. K.; De Bari, B.; Dixon, J. A. Dissipative Structures, Organisms and Evolution. *Entropy* **2020**, *22* (11), 1305. https://doi.org/10.3390/e22111305.
(28) Qin, B.; Yin, Z.; Tang, X.; Zhang, S.; Wu, Y.; Xu, J.-F.; Zhang, X. Supramolecular Polymer Chemistry: From Structural Control to Functional Assembly. *Prog. Polym. Sci.* **2020**, *100*, 101167. https://doi.org/10.1016/j.progpolymsci.2019.101167.
(29) Tagliazucchi, M.; Weiss, E. A.; Szleifer, I. Dissipative Self-Assembly of Particles Interacting through Time-Oscillatory Potentials. *Proc. Natl. Acad. Sci.* **2014**, *111* (27), 9751–9756. https://doi.org/10.1073/pnas.1406122111.

(30) Arango-Restrepo, A.; Rubi, J. M.; Barragán, D. The Role of Energy and Matter Dissipation in Determining the Architecture of Self-Assembled Structures. *J. Phys. Chem. B* **2019**, *123* (27), 5902–5908. https://doi.org/10.1021/acs.jpcb.9b02928.
(31) Rizzuto, F. J.; Platnich, C. M.; Luo, X.; Shen, Y.; Dore, M. D.; Lachance-Brais, C.; Guarné, A.; Cosa, G.; Sleiman, H. F. A Dissipative Pathway for the Structural Evolution of DNA Fibres. *Nat. Chem.* **2021**. https://doi.org/10.1038/s41557-021-00751-w.
(32) Rizvi, A.; Mulvey, J. T.; Carpenter, B. P.; Talosig, R.; Patterson, J. P. A Close Look at Molecular Self-Assembly with the Transmission Electron Microscope. *Chem. Rev.* **2021**, *121* (22), 14232–14280. https://doi.org/10.1021/acs.chemrev.1c00189.
(33) Hurst, P. J.; Rakowski, A. M.; Patterson, J. P. Ring-Opening Polymerization-Induced Crystallization-Driven Self-Assembly of Poly-L-Lactide-Block-Polyethylene Glycol Block Copolymers (ROPI-CDSA). *Nat. Commun.* **2020**, *11* (1), 4690. https://doi.org/10.1038/s41467-020-18460-2.
(34) Wojciechowski, J. P.; Martin, A. D.; Thordarson, P. Kinetically Controlled Lifetimes in Redox-Responsive Transient Supramolecular Hydrogels. *J. Am. Chem. Soc.* **2018**, *140* (8), 2869–2874. https://doi.org/10.1021/jacs.7b12198.
(35) Gillespie, D. T. Exact Stochastic Simulation of Coupled Chemical Reactions. *J. Phys. Chem.* **1977**, *81* (25), 2340–2361. https://doi.org/10.1021/j100540a008.
(36) Zwanzig, R. *Nonequilibrium Statistical Mechanics*; Oxford University Press, 2001.
(37) Chen, X.-M.; Feng, W.-J.; Bisoyi, H. K.; Zhang, S.; Chen, X.; Yang, H.; Li, Q. Light-Activated Photodeformable Supramolecular Dissipative Self-Assemblies. *Nat. Commun.* **2022**, *13* (1), 3216. https://doi.org/10.1038/s41467-022-30969-2.
(38) Goldbeter, A. Dissipative Structures in Biological Systems: Bistability, Oscillations, Spatial Patterns and Waves. *Philos. Trans. R. Soc. Math. Phys. Eng. Sci.* **2018**, *376* (2124), 20170376. https://doi.org/10.1098/rsta.2017.0376.
(39) Sharko, A.; Livitz, D.; De Piccoli, S.; Bishop, K. J. M.; Hermans, T. M. Insights into Chemically Fueled Supramolecular Polymers. *Chem. Rev.* **2022**, *122* (13), 11759–11777. https://doi.org/10.1021/acs.chemrev.1c00958.
(40) Nicholson, S. B.; Bone, R. A.; Green, J. R. Typical Stochastic Paths in the Transient Assembly of Fibrous Materials. *J. Phys. Chem. B* **2019**, *123* (22), 4792–4802. https://doi.org/10.1021/acs.jpcb.9b02811.
(41) De Yoreo, J. J.; Gilbert, P. U. P. A.; Sommerdijk, N. A. J. M.; Penn, R. L.; Whitelam, S.; Joester, D.; Zhang, H.; Rimer, J. D.; Navrotsky, A.; Banfield, J. F.; Wallace, A. F.; Michel, F. M.; Meldrum, F. C.; Cölfen, H.; Dove, P. M. Crystallization by Particle Attachment in Synthetic, Biogenic, and Geologic Environments. *Science* **2015**, *349* (6247), aaa6760. https://doi.org/10.1126/science.aaa6760.
(42) Homeijer, S. J.; Barrett, R. A.; Gower, L. B. Polymer-Induced Liquid-Precursor (PILP) Process in the Non-Calcium Based Systems of Barium and Strontium Carbonate. *Cryst. Growth Des.* **2010**, *10* (3), 1040–1052. https://doi.org/10.1021/cg800918g.
(43) Padrick, S. B.; Miranker, A. D. Islet Amyloid: Phase Partitioning and Secondary Nucleation Are Central to the Mechanism of Fibrillogenesis. *Biochemistry* **2002**, *41* (14), 4694–4703. https://doi.org/10.1021/bi0160462.
(44) Bleem, A.; Daggett, V. Structural and Functional Diversity among Amyloid Proteins: Agents of Disease, Building Blocks of Biology, and Implications for Molecular

Engineering. *Biotechnol. Bioeng.* **2017**, *114* (1), 7–20. https://doi.org/10.1002/bit.26059.
(45) Zhang, H.; Ji, X.; Li, P.; Liu, C.; Lou, J.; Wang, Z.; Wen, W.; Xiao, Y.; Zhang, M.; Zhu, X. Liquid-Liquid Phase Separation in Biology: Mechanisms, Physiological Functions and Human Diseases. *Sci. China Life Sci.* **2020**, *63* (7), 953–985. https://doi.org/10.1007/s11427-020-1702-x.
(46) Ahn, J. I.; Park, J.-E.; Meng, L.; Zhang, L.; Kim, T.-S.; Kruhlak, M. J.; Kim, B. Y.; Lee, K. S. Phase Separation of the Cep63•Cep152 Complex Underlies the Formation of Dynamic Supramolecular Self-Assemblies at Human Centrosomes. *Cell Cycle* **2020**, *19* (24), 3437–3457. https://doi.org/10.1080/15384101.2020.1843777.
(47) Ambadipudi, S.; Biernat, J.; Riedel, D.; Mandelkow, E.; Zweckstetter, M. Liquid–Liquid Phase Separation of the Microtubule-Binding Repeats of the Alzheimer-Related Protein Tau. *Nat. Commun.* **2017**, *8* (1), 275. https://doi.org/10.1038/s41467-017-00480-0.

Chapter 7: Visualizing teixobactin supramolecular assemblies and cell wall damage in B. subtilis using CryoEM

This chapter is adapted from a research article: “Visualizing teixobactin supramolecular assemblies and cell wall damage in B. subtilis using CryoEM. Paul Joshua Hurst, Michael A Morris, Annissa A Graham, James S Nowick, Joseph P Patterson, ACS Omega, 2021, 6 [41] 27412-27417.”

7.0. Abstract

The antibiotic teixobactin targets bacterial cell walls. Previous research has proposed that the active form a teixobactin is a nano/micron sized supramolecular assembly. Here I use cryo-EM to show that at 1 mg/mL teixobactin forms sheet-like assemblies that selectively act upon the cell wall. At 4 μg/mL, teixobactin is active and aggregates form either transiently or sparingly at the cell surface.

7.1. Introduction

The peptide antibiotic teixobactin was reported in 2015,[81] and shows promise for addressing antibiotic resistance in Gram-positive bacteria.[81-87] The proposed mechanism of action is inhibition of cell wall biosynthesis and peptidoglycan precursor recycling, leading to cellular lysis of bacteria.[81, 82] Teixobactin targets the pyrophosphates of lipid II (peptidoglycan), and lipid III (teichoic acid) cell wall building blocks.[81, 88] As these targets are extracellular and nearly immutable, it makes it difficult for bacteria to become resistant to teixobactin.[89]

To enable the design of antibiotics with improved pharmacological properties, several studies have tried to obtain a more detailed understanding of teixobactin's mechanism of action. Teixobactin has been shown to dimerize as a consequence of its stereochemical configuration and amphiphilicity.[81, 90, 91] The dimerization of teixobactin results in the formation of antiparallel β-sheets and higher order fibrils.[91] Solid-state NMR studies of a teixobactin analogue in the presence of lipid II indicate the N-terminal tail of teixobactin forms a β-sheet conformation that aggregates beyond the dimer state.[88] NMR spectroscopy and fluorescence microscopy studies of a teixobactin analogue in the presence of lipid II giant unilamellar vesicles (GUVs) showed the formation of micron sized teixobactin-lipid II aggregates at the surface of the GUVs.[88, 90] Fluorescence microscopy studies of a fluorescent teixobactin analogue in the presence several Gram-positive bacteria, including *B. subtilis*, corroborated that teixobactin binds to the cell walls of bacteria.[92] Collectively, these studies provide evidence that the active form of teixobactin, and its analogues, are nano/micron sized aggregates that form at the cell wall of bacteria.

To test this hypothesis, I performed cryo-transmission electron microscopy (cryoEM) experiments on *B. subtilis* in the presence and absence of teixobactin. The advantage of cryoEM is that it can provide high resolution images of the bacteria in a near-native state. This allows us to distinguish and inspect features of bacteria, such as the cell wall, and how they respond to treatment with teixobactin. CryoEM also enables visualization of the aggregation behavior of teixobactin at nanoscale resolution. While most CryoEM antibiotic research focuses structural deduction of antibiotic interaction,[93-95] this study focuses on observing the presence of teixobactin aggregates and the effect teixobactin has on cellular features of *B. subtilis*.

7.2. Results and Discussion

As a control, CryoEM experiments were performed on untreated *B. subtilis* (in PBS containing 5% DMSO) to identify structural features of the cells in their native state (Figure 7.1).[96] *B. subtilis* was selected for this study due to its large size and its structural rigidity.[97] Suspensions of live *B. subtilis* were added to cryoEM grids, plunge frozen, and imaged directly. In contrast to previous cryoEM studies on *B. subtilis*, I did not microtome or mill the cells with a focus-ion beam.[98-100] Consistent with previous transmission electron microscopy studies on untreated *B. subtilis*, I was able to identify detailed intra- and extracellular features of *B. subtilis*, including vesicles, the cell membrane, cell wall, bacterial fibrils and the periplasmic space (Figure 7.1, Figures F.1-2).[98-104] Bacterial cell walls were classified as being “intact” or “degraded”. Degraded cell walls were then sub-classified as containing a “low density region”, a “hole” or being “fully degraded”. Details and examples of these classifications are given in Figures F.3-6, Table F.1. In the *B. subtilis* control sample, 19% of cells displayed cell wall degradation with 12% being low

density regions, 7% from the presence of a hole and no cells were observed to be fully degraded (n=85). I believe that some of the observed cell wall degradation is related to natural processes that are a part of the bacterial life cycle. For example, sporulation is a process that results in the cell wall degradation due to release of a bacterial spore (see Figure 7.1B).[100, 105] Cell wall or bacterial damage could also be the result of the shear forces exerted on the cells during the blotting stage of the cryoEM prepration.[106, 107] Although I cannot identify the exact nature of each degraded cell wall, classification is important for comparison with *B. subtilis* treated with teixobactin. The *B. subtilis* control sample shows that bacterial fibrils were present in 86% of the micrographs. These fibrils are long and flexible with a diameter of 10.9 ± 0.8 nm (n=55, Figure 7.1E, Table F.2) and could be bacterial flagella, or TasA protein fibrils. TasA protein fibrils are thought to be responsible for forming biofilms.[104, 108, 109] Treatment with formic acid indicates the fibrils are TasA (Figure F.7).

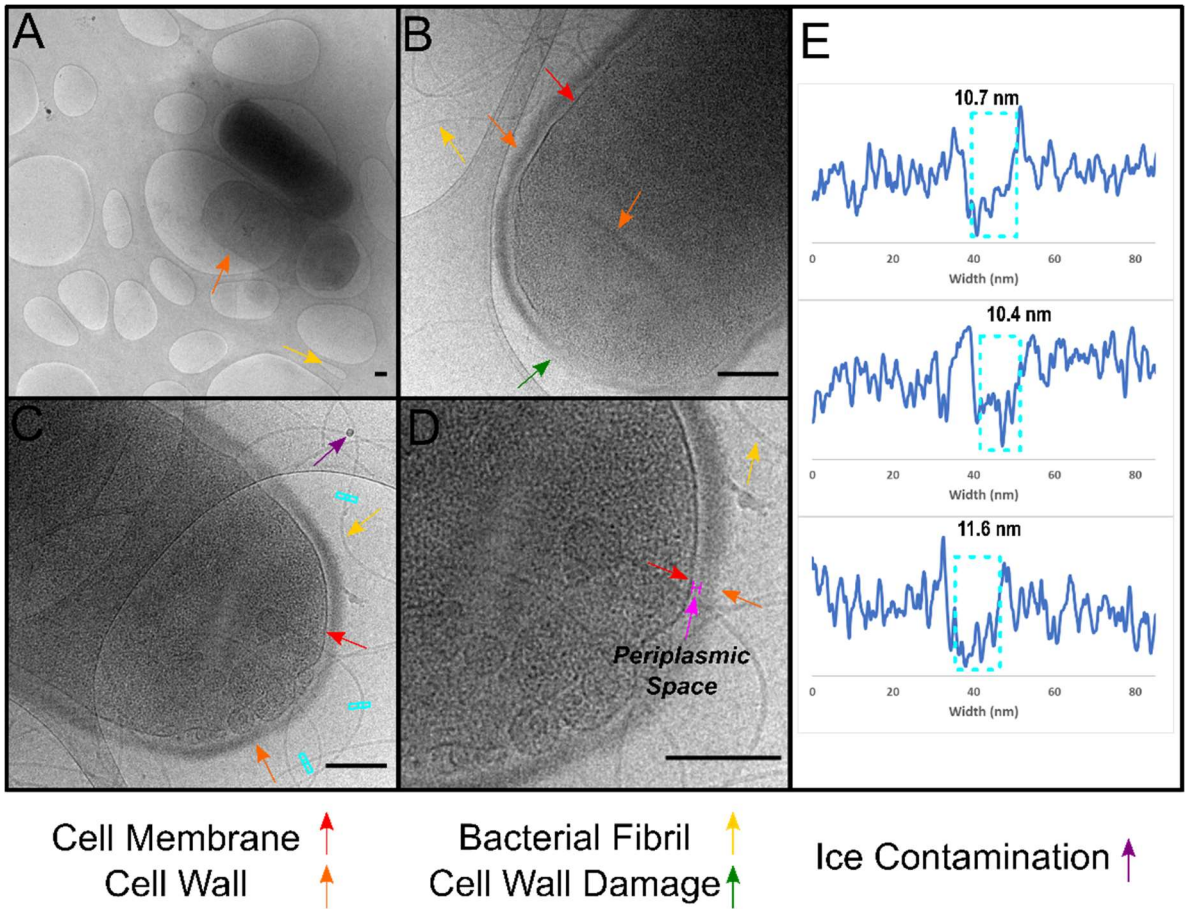

Figure 7.1: CryoEM images of *B. subtilis* in PBS buffer and 5% DMSO. Scale bar is 200 nm. A) Overview of bacteria. B-C) Images showing intra and extracellular features such as the cell wall and bacterial fibrils. D) Cropped region of image C highlighting the periplasmic space between the cell wall and cell membrane. E) Line profiles from bacterial fibrils from image C (order from top to bottom), insets boxed in light blue.

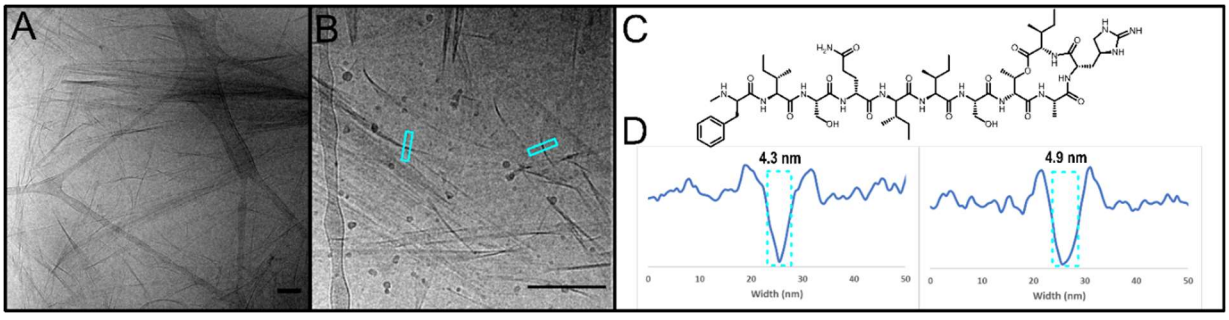

Figure 7.2: CryoEM images of 1 mg/mL teixobactin in PBS buffer and 5% DMSO. Scale bar is 200 nm. A) Overview of teixobactin aggregates. B) Teixobactin aggregates show the presence of sheet-like structures. C) Molecular structure of teixobactin. D) Line

profiles measuring the thickness of sheets from B that are perpendicular to the imaging plane.

As a second control, the aggregation behavior of teixobactin in solution, without *B. subtilis*, was studied by light scattering and cryoEM. Light scattering experiments were performed on a series of teixobactin solutions from 4 µg/mL to 1 mg/mL. The lower concentration is in-line with the previous fluorescence microscopy studies of a fluorescent teixobactin analogue,[92] and the higher concentrations are in line with previous structural studies by solid-state NMR.[90] The light scattering results indicate a critical aggregation concentration of ~0.2 mg/mL (Figure F.8). CryoEM experiments on a 4 µg/mL teixobactin solution did not reveal any nano/micron sized aggregates (Figure F.9). However, it should be noted that at such low concentrations it would be difficult to find aggregates by cryoEM even if they were present. CryoEM experiments on the 1 mg/mL solution revealed that teixobactin forms nano/micron sized sheet-like structures, (Figure 7.2, Figure F.10) When the sheets are perpendicular to the imaging plane, they present as high contrast “rod-like” structures, which enables measurement of the sheet thickness, 4.6 ± 0.9 nm (n=216) (Table F.3, Figure F.11). This thickness is similar to the diameter of the double helix of β-sheets formed by a Lys_{10}-teixobactin analogue.[91] The thickness and morphology of the teixobactin sheets is significantly different from the bacterial fibrils, making it easy to distinguish between them. It is important to note that the minimum inhibitory concentration (MIC) of teixobactin against *B. subtilis* is 0.06 µg/mL. Although these results show that there is no significant aggregation of teixobactin at low concentrations, aggregation in the presence of a bacteria could occur due to binding with cell wall building blocks or a high local concentration at the bacteria surface.

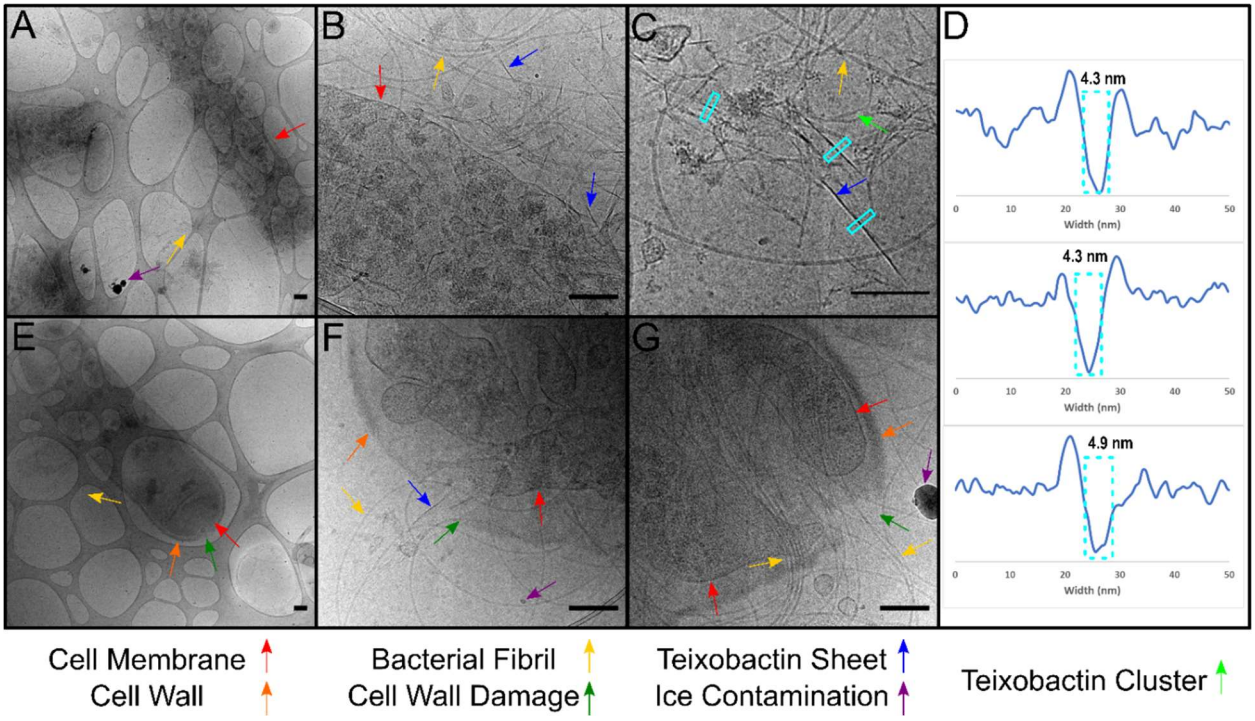

Figure 7.3: CryoEM images of *B. subtilis* treated with 1 mg/mL (A-D) and 4 µg/mL (E-G) teixobactin in PBS buffer and 5% DMSO. Scale bar is 200 nm. A) Overview of bacteria in sample. Teixobactin aggregates are low contrast and difficult to see at this magnification B-C) Images showing low-contrast teixobactin clusters, higher-contrast teixobactin sheets and bacterial remnants. D) Line profile of teixobactin sheets measured in image C (order is left to right). E) Overview of bacterium with cell wall damage. F-G) Images showing cell wall damage in bacteria. Image F shows a possible teixobactin sheet.

To visualize interactions between *B. subtilis* and teixobactin using CryoEM, *B. subtilis* was treated with teixobactin at 1 mg/mL and 4 µg/mL.To optimize the imaging conditions for cryoEM, the concentration of bacteria used in our cultures was significantly increased compared to the MIC assay ($2.4x10^8$ CFU/mL compared to $5x10^5$ CFU/mL),[1] and the bacteria were treated for 4 h, compared to 16 h for the MIC assay. The purpose of the high concentration experiments is to determine if teixobactin aggregates can be identified at the surface of B. subtilis, if the structure of the teixobactin aggregates changes due to the presence of B. subtilis, and what structural effects the teixobactin aggregates have on the cell wall. CryoEM experiments at 1 mg/mL (Figure 7.3A-D, Figure

F.12) showed that 100% of the cells had cell wall damage. 96% of cells displayed complete degradation and 4% displayed a hole (n = 146). Interestingly, many bacteria display an intact cell membrane, even though the cell wall has been completely degraded, indicating the formation of a protoplast.[110] This indicates that teixobactin has a specificity towards the cell wall and supports the hypothesis that teixobactin aggregates play a role in the destruction of the cell walls of Gram-positive bacteria. The cryoEM images show the presence of teixobactin sheets, which are most easily identified when oriented perpendicular to the imaging plane (Figure 7.3C-D). The sheet structures have a thickness of 4.5 ± 0.7 nm (n = 128) consistent with the measurements in teixobactin samples prepared in the absence of bacteria. The cryoEM images also show the presence of clusters composed of rod/fiber-like structures which are structurally distinct from both the teixobactin and the bacterial fibrils with a diameter of 7.2 ± 0.7 nm (n=67) (Figure 7.3C, Figure F.13 for histogram). Considering these clusters are not observed in either control sample, I believe they are the result of teixobactin binding to cell wall precursors, consistent with previous reports.[88, 90]

CryoEM images of the 4 μg/mL (Figure 7.3E-G, Figure F.14) sample showed that 69% of cells had cell wall degradation. 6% contained low density regions, 53% contained holes, and 10% displayed complete degradation (n=169). This shows that teixobactin is active in this sample, as evidenced by the increase in cell wall degradation compared to the control, and that I can image both pre-degradation and post-degradation cells. Despite imaging 169 cells, only 6 sheet-like structures were found (6%, n = 104), and I found no evidence of the cluster structures (Figure F.15). Additional experiments at 4 μg/mL using 0.2% DMSO showed little to no sheet-like structures (3% of 75 images and 0% of 58

images) and no cluster structures were found. The sheets had an average thickness of 4.8 ± 0.6 nm which is consistent with the teixobactin control. In only one case, a sheet is spatially correlated with a cell wall hole (Figure 7.3F). This could be seen as evidence to support the hypothesis that the active form of teixobactin is an aggregated state. However, I believe the observation is inconsistent with frequency of cell wall degradation. Furthermore, based on the previous fluorescence microscopy studies I would expect to see aggregates present around all of the bacterial cells.[92] There are two possible interpretations of this data. 1) The majority of the teixobactin molecules do not form nano/micron aggregates at the surface of the bacteria and are in a non-aggregated state. 2) Most teixobactin molecules form nano/micron sized aggregates at the bacteria surface, but they form transiently and disassemble after acting upon the cell wall. It is important to note that the “non-aggregated states” I am referring to here could include teixobactin dimers or higher order oligomers which would be too small to be observed under these imaging conditions. In both interpretations, teixobactin is present at the surface of the bacteria in both a nano/micron sized aggregated state and non-aggregated state. This mixture of species makes it difficult to conclude if one or both species are active upon the cell wall. Another interesting observation is that the bacterial fibrils seem unaffected by teixobactin. The average diameters and abundance were consistent across all samples (Table F.3). Although bacterial fibrils have been hypothesized to provide some antibacterial resistance, our data indicates that teixobactin does not degrade or interact the fibrils.

7.3. Conclusion

In summary, cryoEM data shows that at concentrations of ~ 1 mg/mL teixobactin forms sheets and clusters in the presence of *B. subtilis,* which correlates with cell wall degradation. At 4 µg/mL, teixobactin is still active upon the cell wall, but teixobactin aggregates are only found in 6% of micrographs. One possible interpretation of the data is that at low concentrations, the aggregates form transiently, making their observation by cryoEM challenging. Collectively, the data support the hypothesis that teixobactin acts upon the cell wall, [88, 90, 92] and provides evidence that teixobactin is present in both an aggregated and non-aggregated state. Further studies are required to determine if aggregation is a prerequisite for activity. This study also shows that cryoEM can provide important information regarding the aggregation behavior of antibiotics in the presence of cells.

7.4. Experimental section

Culturing Bacteria for Imaging: *Bacillus subtilis* (ATCC 6051) was cultured overnight (ca. 16 h) in Mueller-Hinton broth in a shaking incubator at 37 °C. The following morning, the cultures were diluted 1:100 in Mueller-Hinton broth and were allowed to grow exponentially in a shaking incubator (225 rpm) at 37 °C. Once an OD_{600} of ca. 0.3 was achieved, 500 µL of bacteria was transferred to a sterile Eppendorf tube, and the bacteria were centrifuged at 4000 rpm (1300 *g*) for 5 min.

Treatment with teixobactin: While the bacteria were being centrifuged, 1 mg/mL and 4 µg/mL solutions of teixobactin (HCl salt, NovoBiotic Pharmaceuticals, characterized by HPLC and MALDI Figures F.16-18) were freshly prepared. The 1 mg/mL teixobactin solution was prepared by diluting 50 µL of the 20 mg/mL DMSO stock solution of

teixobactin in 950 µL of sterile PBS. The 4 µg/mL teixobactin solution was prepared by combing 4 µL of the 1 mg/mL DMSO stock solution of teixobactin and 46 µL of sterile DMSO so that the final concentration of DMSO in the solution was 5%. To this solution, 950 µL of sterile PBS was then added to create a 4 µg/mL teixobactin solution. After centrifuging the bacteria (see above), the supernatant was removed, the pellet was resuspended in 500 µL of either 1 mg/mL or 4 µg/mL of the teixobactin solution, or 5% v/v DMSO in sterile DMSO as a control, and the bacteria were incubated in a shaking incubator (225 rpm) at 37 °C for 4 h. The samples were then prepared for CryoEM analysis.

Light scattering: Measurements were taken with a Malvern Zetasizer ZS Nano dynamic light scattering instrument. For each sample, the instrument was set to automatic runs (ranging from 10 to 20) to ensure the instrument achieved sufficient signal and averages of three measurements were taken. The data displayed poor fit to the autocorrelation function which is typical for highly anisotropic samples with broad size distributions (lengths and widths of the sheets). Consequently, derived count rate was plotted to look for changes in the total scattering.

Cryogenic-Transmission electron microscopy (CryoEM): CryoEM samples were prepared from bacterial solutions within less than hour after sample preparation onto Lacey Carbon or Quantifoil R2/2 (Electron Microscopy Sciences) grids. Grids were glow discharged for 70 s to increase hydrophilicity prior to sample loading. Vitrification was carried out by an Automatic Plunge Freeze ME GP2 (Leica Microsystems) with 3 µL of sample. Grid preparation was performed at 95-99% humidity and the grids were blotted for 3 s prior to plunging into liquid propane. CryoEM samples were then placed on a Gatan CryoEM

holder and imaged on a JEOL 2100 TEM using a Schottky type field emission gun operating at 200 keV. Images were recorded using Serial EM software with a Gatan OneView CMOS camera at 4kx4k resolution. Additional CryoEM samples of this study are provided in Figures F.19-20. Image measurements were performed on Digital Micrograph (Gatan) by creating line profiles and measured the half width minimum of intensity peaks.

7.5. References

1. Ling, L. L.; Schneider, T.; Peoples, A. J.; Spoering, A. L.; Engels, I.; Conlon, B. P.; Mueller, A.; Schäberle, T. F.; Hughes, D. E.; Epstein, S.; Jones, M.; Lazarides, L.; Steadman, V. A.; Cohen, D. R.; Felix, C. R.; Fetterman, K. A.; Millett, W. P.; Nitti, A. G.; Zullo, A. M.; Chen, C.; Lewis, K. A new antibiotic kills pathogens without detectable resistance. *Nature* **2015,** *517*, 455-459.
2. Homma, T.; Nuxoll, A.; Gandt, A. B.; Ebner, P.; Engels, I.; Schneider, T.; Götz, F.; Lewis, K.; Conlon, B. P. Dual Targeting of Cell Wall Precursors by Teixobactin Leads to Cell Lysis. *Antimicrob. Agents Chemother.* **2016,** *60*, 6510-6517.
3. Abdel Monaim, S. A. H.; Jad, Y. E.; El-Faham, A.; de la Torre, B. G.; Albericio, F. Teixobactin as a scaffold for unlimited new antimicrobial peptides: SAR study. *Bioorg. Med. Chem.* **2018,** *26*, 2788-2796.
4. Yang, H.; Chen, K. H.; Nowick, J. S. Elucidation of the Teixobactin Pharmacophore. *ACS Chem. Biol.* **2016,** *11*, 1823-1826.
5. Wen, P.-C.; Vanegas, J. M.; Rempe, S. B.; Tajkhorshid, E. Probing key elements of teixobactin–lipid II interactions in membranes. *Chem. Sci.* **2018,** *9*, 6997-7008.
6. Karas, J. A.; Chen, F.; Schneider-Futschik, E. K.; Kang, Z.; Hussein, M.; Swarbrick, J.; Hoyer, D.; Giltrap, A. M.; Payne, R. J.; Li, J.; Velkov, T. Synthesis and structure−activity relationships of teixobactin. *Ann. N. Y. Acad. Sci.* **2020,** *1459*, 86-105.
7. Gunjal, V. B.; Thakare, R.; Chopra, S.; Reddy, D. S. Teixobactin: A Paving Stone toward a New Class of Antibiotics? *J. Med. Chem.* **2020,** *63*, 12171-12195.
8. Shukla, R.; Medeiros-Silva, J.; Parmar, A.; Vermeulen, B. J. A.; Das, S.; Paioni, A. L.; Jekhmane, S.; Lorent, J.; Bonvin, A. M. J. J.; Baldus, M.; Lelli, M.; Veldhuizen, E. J. A.; Breukink, E.; Singh, I.; Weingarth, M. Mode of action of teixobactins in cellular membranes. *Nat. Commun.* **2020,** *11*, 2848.
9. Lloyd, D. G.; Schofield, B. J.; Goddard, M. R.; Taylor, E. J. De Novo Resistance to Arg_{10}-Teixobactin Occurs Slowly and Is Costly. *Antimicrob. Agents Chemother.* **2020,** *65*, e01152-20.
10. Öster, C.; Walkowiak, G. P.; Hughes, D. E.; Spoering, A. L.; Peoples, A. J.; Catherwood, A. C.; Tod, J. A.; Lloyd, A. J.; Herrmann, T.; Lewis, K.; Dowson, C. G.; Lewandowski, J. R. Structural studies suggest aggregation as one of the modes of action for teixobactin. *Chem. Sci.* **2018,** *9*, 8850-8859.
11. Yang, H.; Du Bois, D. R.; Ziller, J. W.; Nowick, J. S. X-ray crystallographic structure of a teixobactin analogue reveals key interactions of the teixobactin pharmacophore. *Chem. Commun.* **2017,** *53*, 2772-2775.
12. Morris, M. A.; Malek, M.; Hashemian, M. H.; Nguyen, B. T.; Manuse, S.; Lewis, K.; Nowick, J. S. A Fluorescent Teixobactin Analogue. *ACS Chem. Biol.* **2020,** *15*, 1222-1231.
13. Tegunov, D.; Xue, L.; Dienemann, C.; Cramer, P.; Mahamid, J. Multi-particle cryo-EM refinement with M visualizes ribosome-antibiotic complex at 3.5 Å in cells. *Nat. Methods* **2021,** *18*, 186-193.
14. Su, W.; Kumar, V.; Ding, Y.; Ero, R.; Serra, A.; Lee, B. S. T.; Wong, A. S. W.; Shi, J.; Sze, S. K.; Yang, L.; Gao, Y.-G. Ribosome protection by antibiotic resistance ATP-binding cassette protein. *Proc. Natl. Acad. Sci. U. S. A.* **2018,** *115*, 5157-5162.
15. Crowe-McAuliffe, C.; Graf, M.; Huter, P.; Takada, H.; Abdelshahid, M.; Nováček, J.; Murina, V.; Atkinson, G. C.; Hauryliuk, V.; Wilson, D. N. Structural basis for antibiotic

resistance mediated by the Bacillus subtilis ABCF ATPase VmlR. *Proc. Natl. Acad. Sci. U. S. A.* **2018,** *115*, 8978-8983.
16. Because the teixobactin stock solution is 20 mg/mL in DMSO, a dilution to 1 mg/mL which is used in this study is 5% DMSO. Therefore, to ensure the sample matrix was identical in all samples, all samples in the paper were run with 5% DMSO in a PBS buffer.
17. Pasquina-Lemonche, L.; Burns, J.; Turner, R. D.; Kumar, S.; Tank, R.; Mullin, N.; Wilson, J. S.; Chakrabarti, B.; Bullough, P. A.; Foster, S. J.; Hobbs, J. K. The architecture of the Gram-positive bacterial cell wall. *Nature* **2020,** *582*, 294-297.
18. Matias, V. R. F.; Beveridge, T. J. Cryo-electron microscopy reveals native polymeric cell wall structure in Bacillus subtilis 168 and the existence of a periplasmic space. *Mol. Microbiol.* **2005,** *56*, 240-251.
19. Matias, V. R. F.; Beveridge, T. J. Lipoteichoic Acid Is a Major Component of the Bacillus subtilis Periplasm. *J. Bacteriol.* **2008,** *190*, 7414.
20. Khanna, K.; Lopez-Garrido, J.; Zhao, Z.; Watanabe, R.; Yuan, Y.; Sugie, J.; Pogliano, K.; Villa, E. The molecular architecture of engulfment during Bacillus subtilis sporulation. *eLife* **2019,** *8*, e45257.
21. Brown, L.; Kessler, A.; Cabezas-Sanchez, P.; Luque-Garcia, J. L.; Casadevall, A. Extracellular vesicles produced by the Gram-positive bacterium Bacillus subtilis are disrupted by the lipopeptide surfactin. *Mol. Microbiol.* **2014,** *93*, 183-198.
22. Liu, B.; Qiao, H.; Huang, L.; Buchenauer, H.; Han, Q.; Kang, Z.; Gong, Y. Biological control of take-all in wheat by endophytic Bacillus subtilis E1R-j and potential mode of action. *Biol. Control* **2009,** *49*, 277-285.
23. Liu, H.; Pei, H.; Han, Z.; Feng, G.; Li, D. The antimicrobial effects and synergistic antibacterial mechanism of the combination of ε-Polylysine and nisin against Bacillus subtilis. *Food Control* **2015,** *47*, 444-450.
24. Romero, D.; Aguilar, C.; Losick, R.; Kolter, R. Amyloid fibers provide structural integrity to Bacillus subtilis biofilms. *Proc. Natl. Acad. Sci. U. S. A.* **2010,** *107*, 2230-2234.
25. Stephens, C. Bacterial sporulation: A question of commitment? *Curr. Biol.* **1998,** *8*, R45-R48.
26. Zheng, Y.; Lin, Z.; Zakin, J. L.; Talmon, Y.; Davis, H. T.; Scriven, L. E. Cryo-TEM Imaging the Flow-Induced Transition from Vesicles to Threadlike Micelles. *J. Phys. Chem. B* **2000,** *104*, 5263-5271.
27. Glaeser, R. M. Preparing Better Samples for Cryo–Electron Microscopy: Biochemical Challenges Do not End with Isolation and Purification. *Annu. Rev. Biochem.* **2021**.
28. Huang, J.; Liu, S.; Zhang, C.; Wang, X.; Pu, J.; Ba, F.; Xue, S.; Ye, H.; Zhao, T.; Li, K.; Wang, Y.; Zhang, J.; Wang, L.; Fan, C.; Lu, T. K.; Zhong, C. Programmable and printable Bacillus subtilis biofilms as engineered living materials. *Nat. Chem. Biol.* **2019,** *15*, 34-41.
29. Branda, S. S.; Chu, F.; Kearns, D. B.; Losick, R.; Kolter, R. A major protein component of the Bacillus subtilis biofilm matrix. *Mol. Microbiol.* **2006,** *59*, 1229-1238.
30. Cushnie, T. P. T.; O'Driscoll, N. H.; Lamb, A. J. Morphological and ultrastructural changes in bacterial cells as an indicator of antibacterial mechanism of action. *Cell. Mol. Life Sci.* **2016,** *73*, 4471-4492.

Author's Concluding Remarks

The second law of thermodynamics is that the entropy of the universe is always increasing. Entropy can be defined as the possible number of microstates or configurations a system has. However, it is often more simply referred to as the maximization of disorder or chaos. The universe is inherently stochastic. The fact that life exists on Earth is less than a one in a million chance. Yet, against all odds, we exist as highly intelligent beings. Life would be impossible without the organization of complex molecules into higher-ordered structures. These structures form as a result of the constant flux of energy and matter, driving these systems out of equilibrium. In contrast, the materials that made our modern world are lifeless, unable to respond to environmental changes and doomed to the impending degradation of nature. In our quest to conquer the mysteries of the origin of life, we need to understand the mechanisms of self-assembly, particularly how ordered structures exist and are maintained despite the chaos that defines the universe. The work in this dissertation represents a very small piece of that puzzle. I hope to expand my expertise of molecular self-assembly to tackle problems of the modern era such as environmental threats and improving healthcare and human well-being. With increasing research and development, synthetic non-equilibrium molecular self-assemblies can perhaps be endowed with adaptability and functionality rivaling that of biological systems.

Appendix A: Supplementary Information for Chapter 2

A.1. Supplementary Discussion

% Crystallinity Calculations: Crystallinity is tracked over time by comparing the area of the crystalline peaks to the total area in WAXS patterns. The data shows that the crystallinity is predominantly from the PLLA block, however we noted additional peaks in diffraction pattern of samples with PLLA DP 25 and 45 which corresponds to PEG crystallinity. An analysis of WAXS patterns of PLLA-*b*-PEG with increasing DP of PLLA at 20% solids w/w also show PEG crystallinity present for $PLLA_{25}$-*b*-PEG_{45} **6** and $PLLA_{45}$-*b*-PEG_{45} **10** but absent for $PLLA_{90}$-*b*-PEG_{45} **16** and $PLLA_{135}$-*b*-PEG_{45} (Figure A.5). It is known that in bulk BCP crystallization of PLLA-*b*-PEG, lower DP PLLA BCPs exhibit marked PEG crystallinity.[111] Thus, we split the PLLA peaks from PEG peaks using previous polymer crystallization data (Figure A.4, Tables A.6-7, Supplementary Methods)[45, 46] For the PLLA 90 samples the kinetic study shows that the PEG crystallinity is relatively constant over time (unlike the PLLA crystallinity which increases overtime) and therefore we do not believe the PEG crystallinity is a significant driving force of the self-assembly. We also note that both models (convoluted and unconvoluted peaks) discussed in the methods section show the same general trend with respect to the differences between the PLLA DP 45 and 90 samples (Tables A.4-7, Supplementary Methods).

Controls: A control experiment was performed by re-dispersing poly-L-lactide-*block*-polyethylene glycol (PLLA-*b*-PEG) block copolymer (BCP) into water that has been synthesized in dichloromethane, where no self-assembly take place (Figure A.6). The control BCP failed to disperse in water whereas the ROPI-CDSA polymers readily formed

turbid solutions. A second control was performed by preparing PLLA-*b*-PEG through a solvent switch process (tetrahydrofuran to water) and a CDSA process (heating to 65 °C and cooling), in both cases the structure formed are significantly different to those generated by ROPI-CDSA (Figure A.7-10). This shows that the structures formed during the ROPI-CDSA processes are essential for creating the assemblies in water. Preparation of the cryogenic-transmission electron microscopy (cryo-TEM) samples directly in toluene was challenging due to partial/full evaporation of the toluene during the blotting stages, however comparison of the same samples prepared directly in toluene and by freeze drying showed similar structures (Figure A.11).

Dispersion vs. emulsion PISA: PISA processes can be categorized as dispersion PISA, where both the monomer and stabilizer block are soluble in the reaction solvent or emulsion PISA, where the monomer is stabilized by an emulsifier.[14] Here, L-lactide monomer has a limited solubility in toluene of about 60 mg/mL. Consequently, in solutions with lower target DP or lower solids content, ROPI-CDSA is a dispersion PISA process, However, in solutions with higher target DP and/or high % solids w/w, not all L-lactide dissolves in toluene (even with long stir times). Upon the beginning of the polymerization, the excess L-lactide dissolves in solution because of decreasing L-lactide concentration. Following polymerization, the solutions remain clear until the onset of turbidity. In these experiments ROPI-CDSA has features of both dispersion and emulsion PISA. In addition, from low conversion of homopolymerization in toluene, we know the PEG stabilizer block is necessary to enable the polymerization in toluene. This observation is analogous with the ability of the macroinitiator increasing the polymerization rate constant (k_p) as the growing block becomes more insoluble.

Non-equilibrium PISA: The term “non-equilibrium” is often used interchangeably with “far-from-equilibrium” assemblies.[55, 70] Mattia and Otto,[55] have provided clear descriptions of the following important terms which we quote from their paper:

“Equilibrium assemblies. Systems that are likely to persist for a long time due to their thermodynamic stability.

Kinetically trapped assemblies. Systems that are transiently durable, trapped in a local minimum of the energy landscape. It would take time, or activation energy, for them to be converted to more stable structures.

Far-from-equilibrium assemblies. Systems that require a continuous supply of energy to persist. If the energy supply stops, the system would fall apart and end up in a thermodynamic minimum state (or in a kinetic trap en route). The continuous energy-driven transformation that these structures undergo makes it possible for them to have interesting, and sometimes unpredictable, emergent functions.”

Here, we refer to “equilibrium assemblies” as being “thermodynamically controlled” processes because for polymeric assemblies it is almost impossible to determine if they are really in-equilibrium. But it is possible to provide evidence they are thermodynamically controlled, for example, by assembling them under different conditions to see if they form the same structures.[8]

It is clear that in any PISA process there is some non-equilibrium behavior as PISA inherently creates an unstable building block (the growing amphiphile) from a stable building block (the soluble homopolymer). However, we believe it is only useful to apply the term non-equilibrium if there is some practical advantage to the creation of this non-equilibrium state. In situations where the structural evolution of the assemblies is much

faster than the polymerization time,[28, 68, 69, 112] the non-equilibrium state that occurs after the monomer is added (but before the system reorganizes to a new structure) is so transient that it is not practically useful, or at least, there have been no demonstrations that it is practically useful. Consequently, we refer to these situations as being thermodynamically controlled because the structures at each stage can be predicted based on the thermodynamics of the polymer structures and its environment. In this regime, changing the polymerization kinetics will only change the rate at which the structures evolve but it will not provide access to different structures. For PISA processes that result in kinetic trapping it is important to note that if the evolution of the assemblies is much faster than the polymerization time then the formed structures are still based on thermodynamics, because the result is a trapped structure that was formed by an 'in-equilibrium' assembly process. In this paper, the practical advantage comes from the ability to trap multiple different structures as they evolve in solution after the polymerization has finished.

A.2. Supplementary Methods

Homopolymer Synthesis: Homopolymer synthesis was carried out following the procedure in the text apart from exchanging mPEG for ethanol. Samples were synthesized in both toluene and dichloromethane.

% PLLA Crystallinity Calculations

To calculate %PLLA crystallinity values the area of the discernable crystalline peaks was divided by the total area subtracted from the background as in Equation A.1:

$$\%\ Crystallinity = \frac{Area\ Under\ Crystalline\ Peaks}{Total\ Area\ under\ Peaks - Backg} * 100\% \quad \text{(A.1)}$$

As preparing WAXS samples was time-intensive, several triplicate of one sample **15** ($PLLA_{90}$-*b*-PEG_{45} 10% solids w/w 24 hours) were used establish a baseline error of ± 5.0%. FTIR peak ratio error was also established by the same method giving a baseline error of ± 0.045.

PLLA Crystallinity was calculated by dividing crystallinity by the % wt. PLLA of PLLA-*b*-PEG block copolymers as in Equation A.2:

$$\%\ PLLA\ Crystallinity = \frac{\%\ Crystallinity}{\%\ wt\ PLLA} * 100\% \quad (2)$$

% wt. PLLA for $PLLA_{45}$-*b*-PEG_{45} (10% solids w/w **9**) and $PLLA_{90}$-*b*-PEG_{45} (10% solids w/w **15**) is 62% and 76% respectively.

Control Self-Assembly Experiments: All controls were synthesized using TBD in dichloromethane (rather than toluene) where no self-assembly or crystallization should take place. Controls were also purified by precipitation in diethyl ether.

Resuspension in water: Amorphous PLLA-*b*-PEG and Milli-Q water (ρ> 18 MΩ cm) were mixed to give a concentration of 0.5 mg/mL. The resulting suspension was sonicated for 30 minutes. The suspension did not dissolve as indicated visually in Figure A.6.

Self-assembly by solvent switch: PLLA-*b*-PEG was dissolved in THF to give a concentration of 10mg/mL. Milli-Q water was added in fractions a tenth of the THF added. Fractions were spaced twenty minutes apart while the sample stirred. Once samples had reached turbidity, no more additional water was added, and samples were dialyzed three times overnight to remove residual THF.

CDSA in water: PLLA-*b*-PEG and Milli-Q water were mixed and heated to 65 °C. Water was added until the polymer fully dissolved. The solution was heated at 65 °C while stirring and was rapidly cooled to room temperature.

CDSA in toluene: PLLA-*b*-PEG was mixed with toluene to give similar concentrations as in ROPI-CDSA. Solutions were stirred for one day and inspected visually for signs of gelation (e.g. how viscous the solution was on upon inverting the vial).

Organic cryo-TEM grid preparation: Cryo-TEM samples from toluene were prepared from Quantifoil grids or graphene oxide coated lacey carbon grids (Electron Microscopy Sciences). Samples were diluted with toluene to give a concentration of 0.5 mg/mL right before sample preparation. Vitrification was attempted by an Automatic Plunge Freezer ME GP2 (Leica Microsystems) with 3 µL of sample. Sample preparation was carried without utilization of a humidity chamber and blotted for 1 s before auto-plunging into liquid nitrogen. Blot times longer than 1 s resulted in grids too thick to image caused by toluene evaporation.

Measurements of Cryo-TEM images: Cryo-TEM images were measured using DigitalMicrograph (Gatan) software. Line profiles with integrations of 50 pixels were made to measure width accurately. Length was measured from structure end to end. Lamella width and length were measured from the widest and longest points respectively. Lamella thickness was determined by measuring lamellae perpendicular to the image plane (For an example of this, see Figure 2.4i). About 10-50 measurements were made on each sample.

Rheology: Oscillatory rheology was collected from organogels on a TA DHR 2 rheometer. Gels were loaded using a 20 mm steel Peltier plate. Measurements were taken from $1.0e^{-3}$ to 100.0 strain % at 25 °C.

PLLA Length Calculation: Using CrystalMaker®, a short PLLA chain was simulated and allowed to relax to a minimum energy configuration. After which the distance was measured between one PLLA unit as shown in Figure A.24.

A.3. Supplementary Tables

Table A.1: Synthesis and Structural Characterization of PLLA-*b*-PEG in ROPI-CDSA for experimental information see the methods section and Table A.2.

Reference	[M]/[I]	DP	% Conv.	% solids w/w	NMR M_n	GPC M_n	M_w	Đ	Structure*
1	5	10	90.1	5.0	2700	10820	11540	1.066	N
2	5	10	91.3	7.5	2700	10600	11340	1.070	N
3	5	10	92.6	10.0	2700	10960	11810	1.078	N
4	5	10	97.0	20.0	2700	10103	11990	1.089	N
5	12.5	25	97.1	10.0	3700	13990	15460	1.105	S/R
6	12.5	25	97.1	20.0	3700	13320	15260	1.145	L/R
7	22.5	45	93.8	5.0	5200	17230	19360	1.124	S/R
8	22.5	45	94.3	7.5	5400	19620	21930	1.118	S/R
9	22.5	45	96.7	10.0	5300	17810	20570	1.155	L/R
10	22.5	45	94.0	20.0	5200	18840	23480	1.246	L/R
11	30	60	93.3	10.0	6000	18830	21740	1.154	L/R
12	37.5	75	92.1	10.0	6900	22020	25130	1.141	L/R
13	45	90	94.5	5.0	8000	26010	28660	1.102	L
14	45	90	96.2	7.5	8100	26970	31140	1.155	L
15	45	90	96.2	10.0	8400	25770	30900	1.199	SL/L

16	45	90	99.0	20.0	8400	23370	31670	1.355	SL/L
17	60	120	96.8	7.5	10400	30150	35140	1.165	SL/L
18	67.5	135	93.5	10.0	11100	31980	35160	1.099	SL/L
19	67.5	135	99.0	20.0	11600	27030	37130	1.374	SL/L

* Structure legend: SL=stacked lamella L=lamella, R=rods, S=spheres, N=no self-assembly

Note that GPC results are calibrated to PS standards and don't accurately reflect the molar mass of PLLA-*b*-PEG.

Table A.2: Experimental Setup for synthesis of PLLA-*b*-PEG in ROPI-CDSA. For experimental information see the methods section. For the structural outcome of the synthesis of PLLA-*b*-PEG see Table A.1.

Reference	[M]/[I]	Target DP	L-lactide (mg)	L-lactice (mmol)	% solids w/w	Toluene (mL)	TBD stock (µL)	% Conv.
1	5	10	14.4	0.10	5.0	1.19	4	90.1
2	5	10	14.4	0.10	7.5	0.77	4	91.3
3	5	10	14.4	0.10	10.0	0.56	4	92.6
4	5	10	14.4	0.10	20.0	0.25	4	97.0
5	12.5	25	36.0	0.25	10.0	0.79	8	97.1
6	12.5	25	36.0	0.25	20.0	0.35	8	97.1
7	22.5	45	64.9	0.45	5.0	2.29	15	93.8
8	22.5	45	64.9	0.45	7.5	1.49	15	94.3
9	22.5	45	64.9	0.45	10.0	1.08	15	96.7
10	22.5	45	64.9	0.45	20.0	0.49	15	94.0
11	30	60	86.5	0.60	10.0	1.31	20	93.3
12	37.5	75	108.1	0.75	10.0	1.53	25	92.1
13	45	90	129.7	0.90	5.0	3.71	30	94.5
14	45	90	129.7	0.90	7.5	2.42	30	96.2
15	45	90	129.7	0.90	10.0	1.75	30	96.2
16	45	90	129.7	0.90	20.0	0.78	30	99.0
17	60	120	173.0	1.20	7.5	3.03	39	96.8
18	67.5	135	194.6	1.35	10.0	2.43	44	93.5
19	67.5	135	194.6	1.35	20.0	1.08	44	99.0

Note that all polymerizations use 40 mg (20 µmmol) of $mPEG_{45}$ and 0.1% molar to L-lactide of TBD. The TBD stock solution has a concentration of 4.3 mg/mL

Supplementary Table 3: Homopolymer Synthesis Results

Target DP	Solvent	% Conversion	NMR M_n
45	Toluene	22.5	780
90	Toluene	28.6	1900
45	Dichloromethane	96.9	3200
90	Dichloromethane	97.9	6400

Table A.4: Unconvoluted WAXS Data for **9**: $PLLA_{45}$-*b*-PEG_{45} 10% solids w/w. Units are degrees unless otherwise stated. Note that the WAXS experimental parameters are given in the main text whereas the crystallinity calculations are given in the supplementary information.

Time point	103	010	110 / 201	203	Amorphous	210	216	PEG	Crystallinity (%)	PLLA Cryst. (%)
5min	-	-	16.37	-	21.92	-	-	-	10.3	16.7
1hr	-	16.15	16.911	19.283	21.4	-	-	23.46	21.4	34.6
2hr	12.03	15.28	16.815	19.272	22.46	22.51	-	23.42	28.8	46.6
3hr	12.61	15.04	16.821	19.255	20.84	22.84	29.06	23.43	36.3	58.7
6hr	12.49	16.22	16.808	19.242	21.03	22.48	29.33	23.44	40.30	65.2
12hr	13.8	15.92	16.774	19.248	21.33	22.59	29.27	23.34	43.8	70.8
24hr	12.73	14.88	16.75	19.180	20.43	22.46	29.19	23.43	54.26	87.3

Table A.5: Unconvoluted WAXS Data for **15**: $PLLA_{90}$-*b*-PEG_{45} 10% solids w/w. Units are degrees unless otherwise stated. Note that the WAXS experimental parameters are given in the main text whereas the crystallinity calculations are given in the supplementary information.

Time point	103	010	110 / 201	203	Amorphous	210	216	Crystallinity (%)	PLLA Cryst. (%)
5min	-	-	16.504	-	25.23	-	-	15.11	19.8

1hr	12.86	14.90	16.877	19.31	20.85	22.57	29.22	50.10	65.6
3hr	12.81	15.04	16.847	19.24	19.55	22.56	29.20	54.9	71.9
6hr	12.73	15.17	16.946	19.30	19.07	22.82	29.46	57.14	74.7
24hr	12.91	15.05	16.905	19.29	21.9	22.61	29.26	59.10	77.4

Table A.6: Convoluted WAXS data with Voigt/Gaussian model for **9**: PLLA$_{45}$-*b*-PEG$_{45}$ 10% solids w/w. Units are degrees unless otherwise stated. Peaks are color coded with the following: PLLA-green, PEG-yellow, amorphous-blue. Amorphous peaks used are listed in numerical order (Amorp.). Note that the WAXS experimental parameters are given in the main text whereas the crystallinity calculations are given in the supplementary methods.

Time point	**1 0 3**	**0 1 0**	**1 1 0 / 2 0 1**	**2 0 3**	**2 1 0**	**2 1 6**	**0 2 1**	**1 2 0**	**-2 1 2**	**-1 3 1**	**-2 2 4**
5 min	-	-	16.41	-	-	-	-	18.39	-	-	-
1 hr	-	-	16.47	19.29	-	29.47	-	18.55	23.23	23.58	-
2 hr	-	-	16.79	19.25	22.46	29.76	12.71	-	23.47	-	-
3 hr	-	-	16.82	19.26	22.50	29.44	-	18.39	23.47	-	-
6 hr	-	14.78	16.82	19.24	22.52	29.26	-	18.39	23.45	-	-
12 hr	-	-	16.84	19.28	22.59	29.45	-	18.39	23.48	-	-
24 hr	12.52	14.98	16.76	19.15	20.89	29.28	-	-	23.08	23.42	-
7 days	12.38	-	16.81	19.21	22.52	29.32	-	18.39	23.07	23.45	27.10

Time point	**Amorp. 1**	**Amorp. 2**	**Amorp. 3**	**Amorp. 4**	**Amorp. 5**	**Amorp. 6**	**% Area PEG Cryst.**	**% Area PLLA Cryst.**	**PLLA Cryst. (%)**
5 min	17.90	21.64	30.00	-	-	-	1.9	19.4	31.4
1 hr	12.92	15.30	16.72	20.45	22.93	26.18	7.0	15.5	25.1
2 hr	10.93	15.30	18.39	20.65	23.01	26.18	7.1	26.9	43.5

3 hr	12.90	15.30	20.96	21.37	26.18	-	16.0	31.8	51.3
6 hr	12.20	15.30	20.47	21.93	23.07	27.18	13.6	40.6	65.7
12 hr	12.64	15.30	20.47	25.66	-	-	17.9	45.6	73.6
24 hr	12.73	19.39	21.93	26.52	-	-	23.8	50.3	81.4
7 days	14.25	15.14	20.44	23.08	-	-	18.7	52.0	84.0

Table A.7: Convoluted WAXS data with Voigt/Gaussian model for **15**: $PLLA_{90}$-*b*-PEG_{45} 10% solids w/w. Units are degrees unless otherwise stated. Peaks are color coded with the following: PLLA-green, PEG-yellow, amorphous-blue. Amorphous peaks used are listed in numerical order (Amorp.) Note that the WAXS experimental parameters are given in the main text whereas the crystallinity calculations are given in the supplementary methods.

Time point	**1 0 3**	**0 1 0**	**1 1 0 / 2 0 1**	**2 0 3**	**2 1 0**	**2 1 6**	**0 2 1**	**1 2 0**	**-2 1 2**	**-1 3 1**	**-2 2 4**
5 min	-	-	16.36	-	-	-	-	18.39	-	-	-
1 hr	-	-	16.91	19.31	22.59	29.48	12.82	18.39	-	-	-
3 hr	-	-	16.90	19.27	22.58	29.36	-	18.39	23.51	-	-
6 hr	-	-	16.91	19.29	22.74	29.43	-	-	23.49	-	-
24 hr	-	-	16.93	19.31	22.56	29.41	-	18.39	22.93	-	-

Time point	**Amorp. 1**	**Amorp. 2**	**Amorp. 3**	**Amorp. 4**	**Amorp. 5**	**Amorp. 6**	**Amorp. 7**	**% Area PEG Cryst.**	**% Area PLLA Cryst.**	**PLLA Cryst. (%)**
5 min	14.01	20.91	22.50	-	-	-	-	2.0	18.9	24.7
1 hr	11.90	14.45	15.25	20.55	21.93	23.60	26.52	5.5	47.7	62.4
3 hr	12.03	14.31	15.25	20.57	23.13	27.18	-	3.4	52.3	68.4
6 hr	11.92	15.12	15.30	21.93	26.18	-	-	2.6	44.6	58.4
24 hr	10.69	12.71	14,25	15.19	23.74	27.18	-	5.6	63.2	82.7

A.4. Supplementary Figures

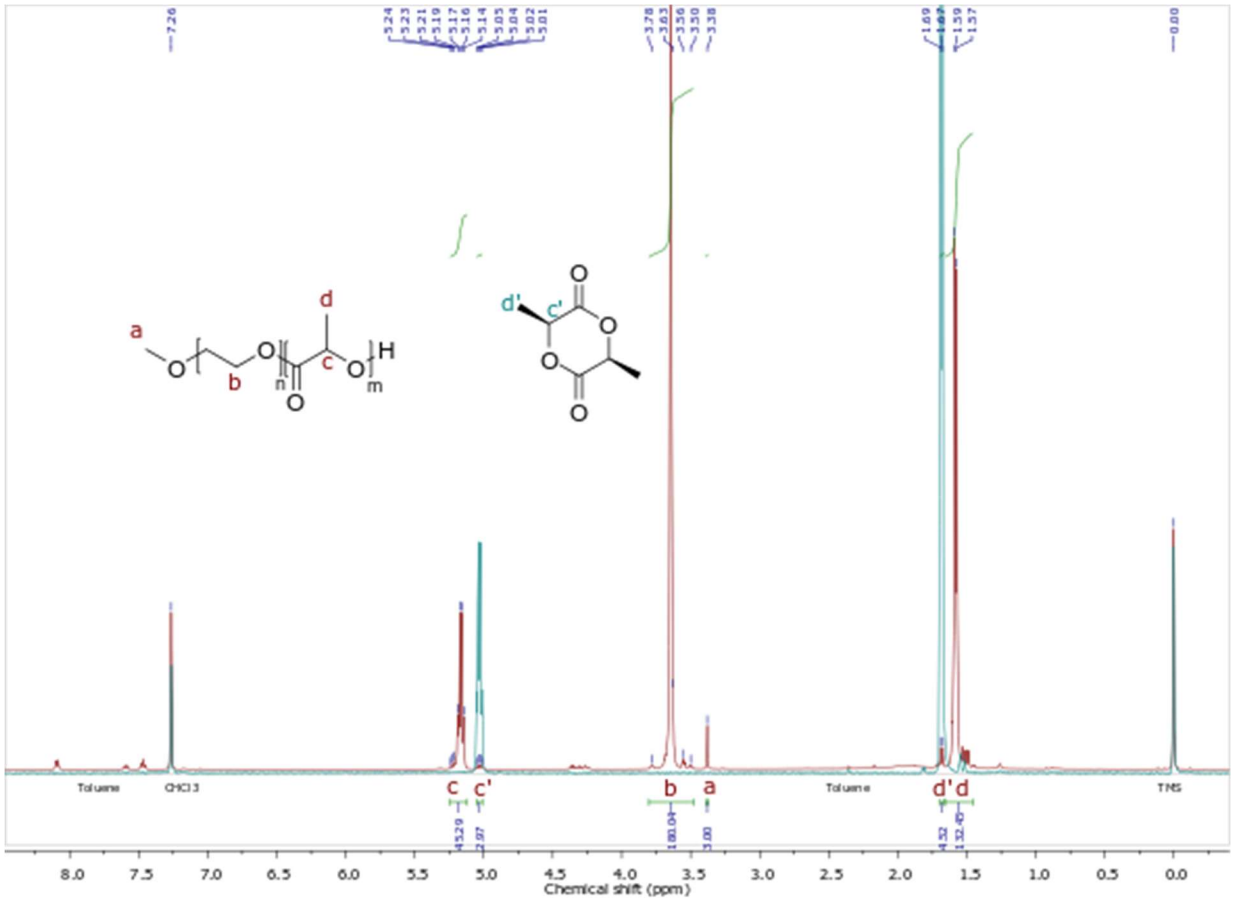

Figure A.1: Representative ^{1}H NMR spectrum for **7** (red,PLLA$_{45}$-*b*-PEG$_{45}$ 5% solids w/w) overlaid with L-lactide (blue). Due to broad peak around 1.6, conversion was calculated from peaks around 5ppm. Conversion was then calculated from ^{1}H NMR data as shown in Equation A.3:

$$\%Conversion = \frac{Area\ of\ PLLA\ peak\ at\ 5.2}{Area\ of\ LL\ peak\ at\ 5.0 + Area\ of\ PLLA\ peak\ at\ 5.2} * 100\% \qquad (A.3)$$

For calculated ^{1}H NMR results see Table A.1 and for a list of peak assignments see the methods section.

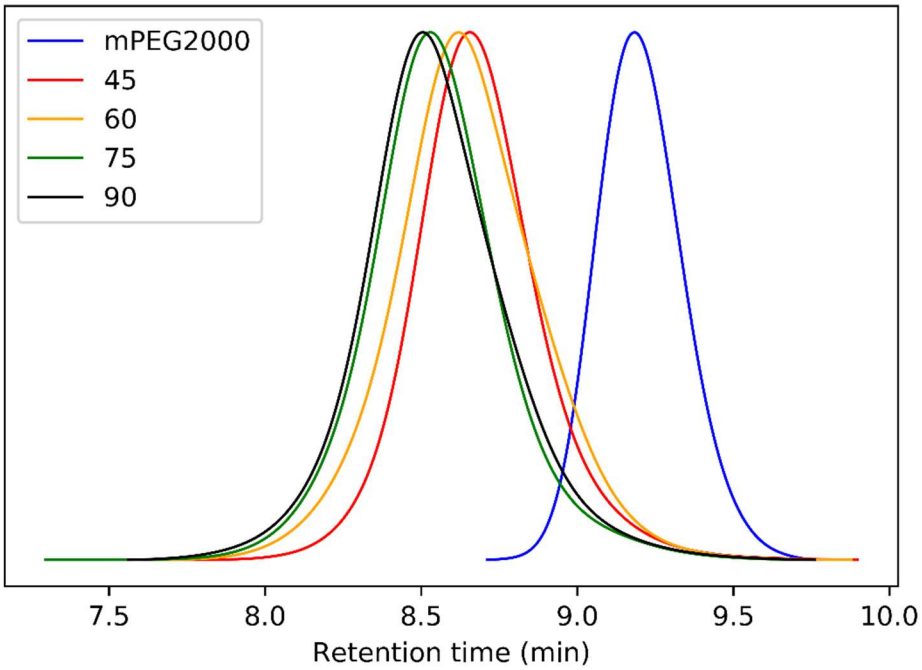

Figure A.2: Representative GPC traces for PLLA$_n$-*b*-PEG$_{45}$ for samples **9** (n=45), **11** (n=60), **12** (n=75), and **15** (n=90) all at 10% solids w/w. mPEG$_{45}$ (MW = 2000) is shown to prove chain extension from the macroinitiator. For the GPC results see Table A.1 and for the set-up see the methods section.

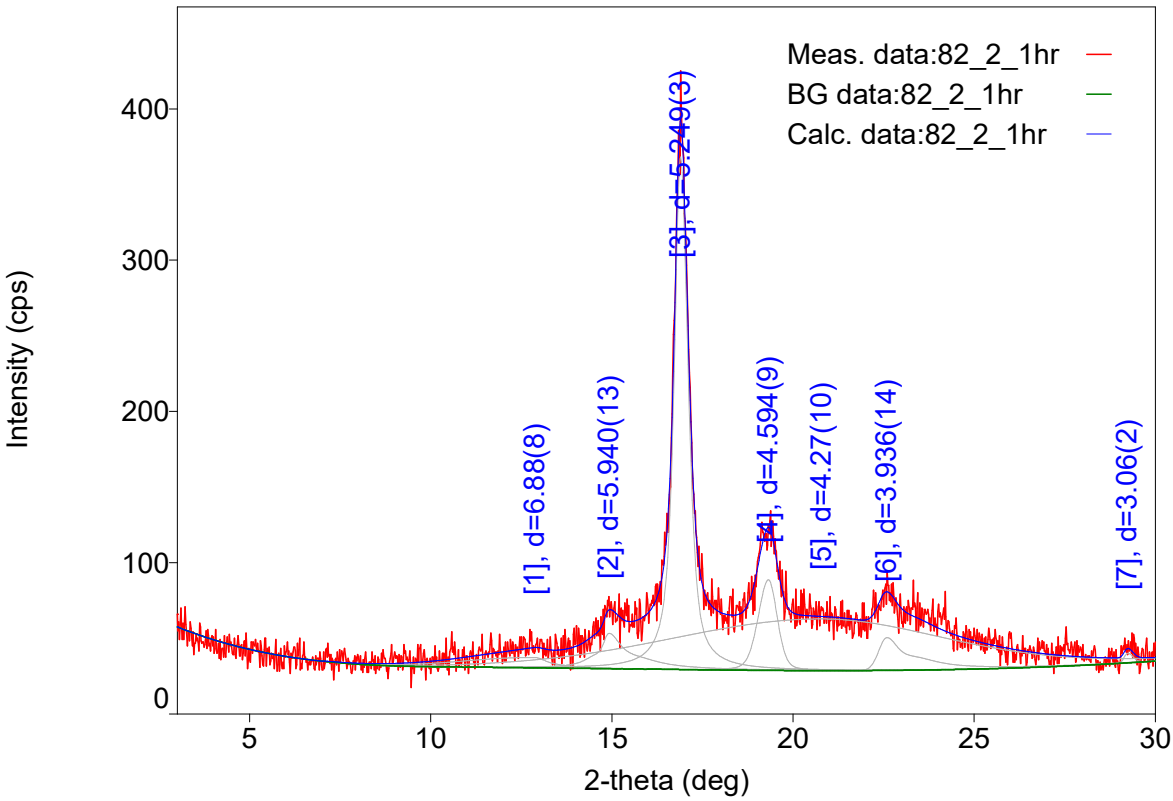

Figure A.3: Example of WAXS pattern peak selection for determination of % crystallinity. The green baseline represents the background. Peaks 1-4, 6-7 are crystalline peaks whereas peak 5 is the broad amorphous peak. The sample is **15** ($PLLA_{90}$-*b*-PEG_{45} 10% solids w/w) at 1-hour post polymerization. See Tables A.4-5 for peak assignments and crystallinity. See also methods section, results (section b) and Figure 2.2a-b in the main text for additional WAXS information and results.

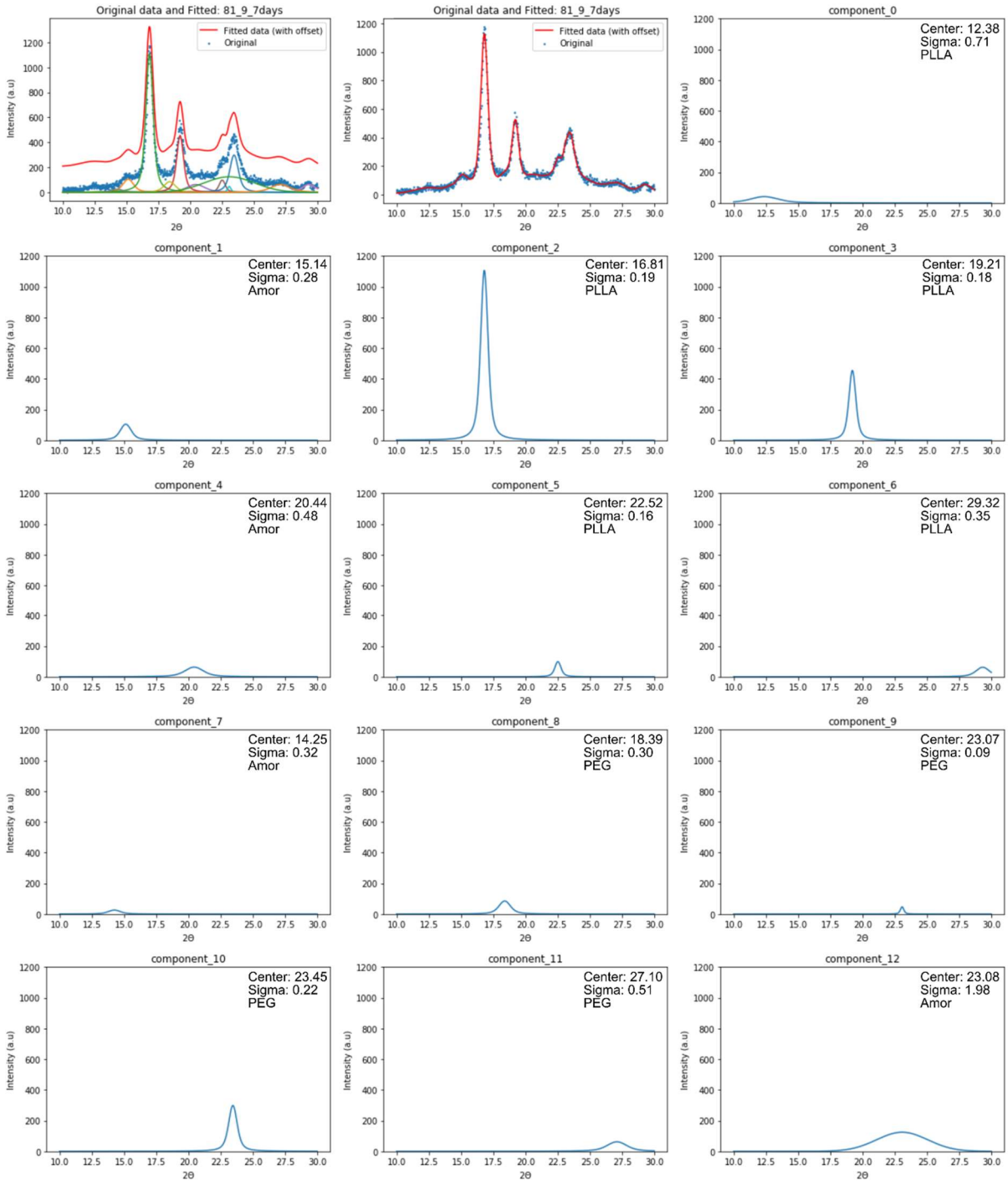

Figure A.4: Representative peak deconvolution which separates PLLA, PEG, and amorphous peaks enabling the tracking of PLLA and PEG crystallinity. The sample $PLLA_{45}$-*b*-PEG_{45} (10% solids w/w **9**) was taken seven days post polymerization. See Tables A.6-7 for peak assignments, integration, and crystallinity. See also methods section, results (section b) and Figure 2.2a-b in the main text for additional WAXS information and results.

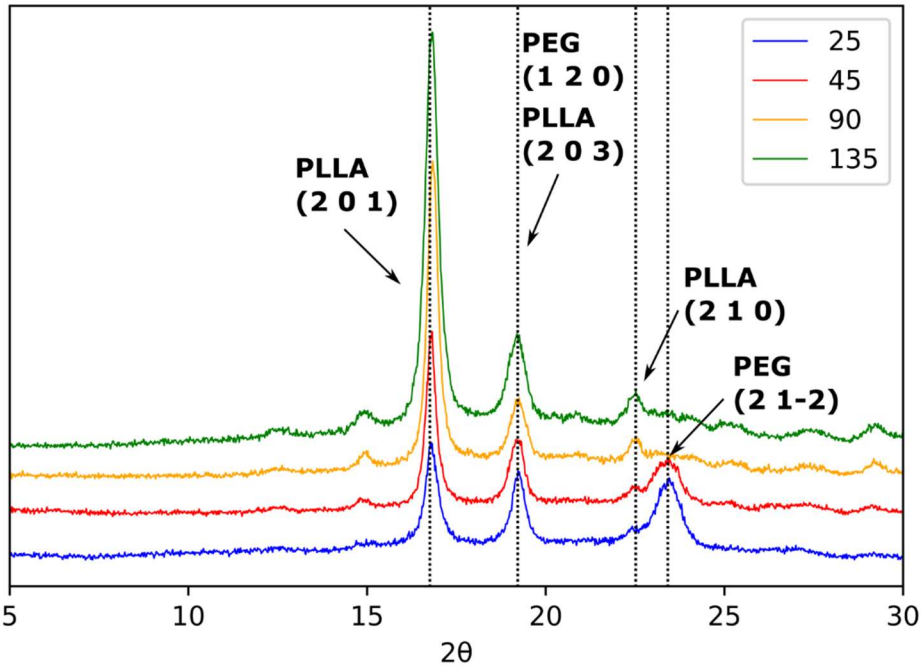

Figure A.5: WAXS diffraction patterns for $PLLA_{25}$-b-PEG_{45} (**6**), $PLLA_{45}$-b-PEG_{45} (**10**), $PLLA_{90}$-b-PEG_{45} (**16**), $PLLA_{135}$-b-PEG_{45} (**19**). All polymer samples were prepared from 20% solids w/w toluene solutions before freeze-drying. Dominant WAXS peaks for PLLA and PEG are labeled above showing that PEG peaks are much more prevalent at lower PLLA DPs. See also results (self-assembly and crystallization kinetics) in the main text.

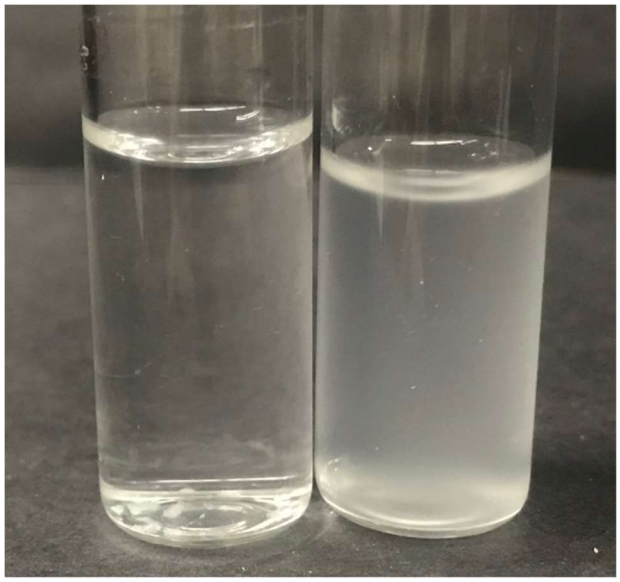

Figure A.6: Sample on the left is a control $PLLA_{90}$-*b*-PEG_{45} (synthesized in dichloromethane) that was sonicated in water for 30 mins. Notice the polymer precipitate at the bottom of the vial. Sample on the right is a ROPI-CDSA sample of $PLLA_{90}$-*b*-PEG_{45} that was lyophilized and then sonicated in water for 30 mins. Both samples have a PLLA DP=90 and the concentration of these samples is 0.5mg/mL or 0.5% solids w/w. This demonstrates that aqueous solutions are kinetically-trapped and that some microphase separation of PLLA and PEG (from self-assembly) is necessary to form stable nanoparticle based solutions.

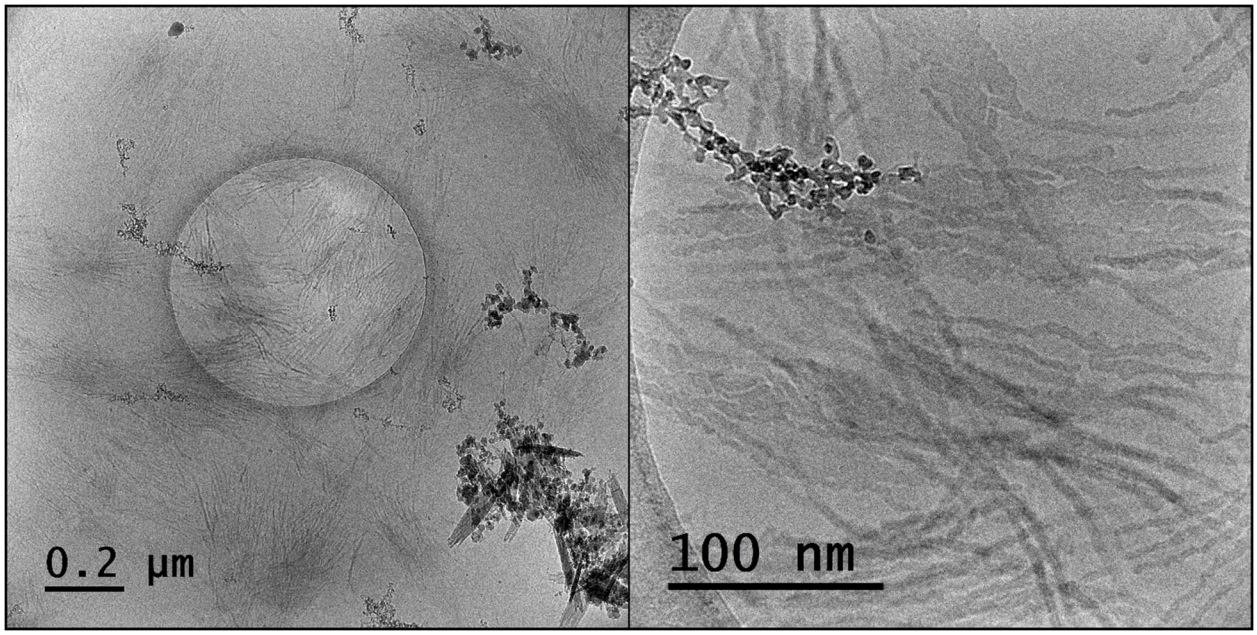

Figure A.7: Cryo-TEM images of PLLA$_{45}$-*b*-PEG$_{45}$ worms resulting from solvent switch (5mg/mL) in water. The dark contrast in the bottom right of the left image and the top left of the right image corresponds to ice contamination. These structures are markedly different from structures obtained from ROPI-CDSA that have been transferred to water demonstrating that PLLA-*b*-PEG assemblies in pure water are likely kinetically-trapped.

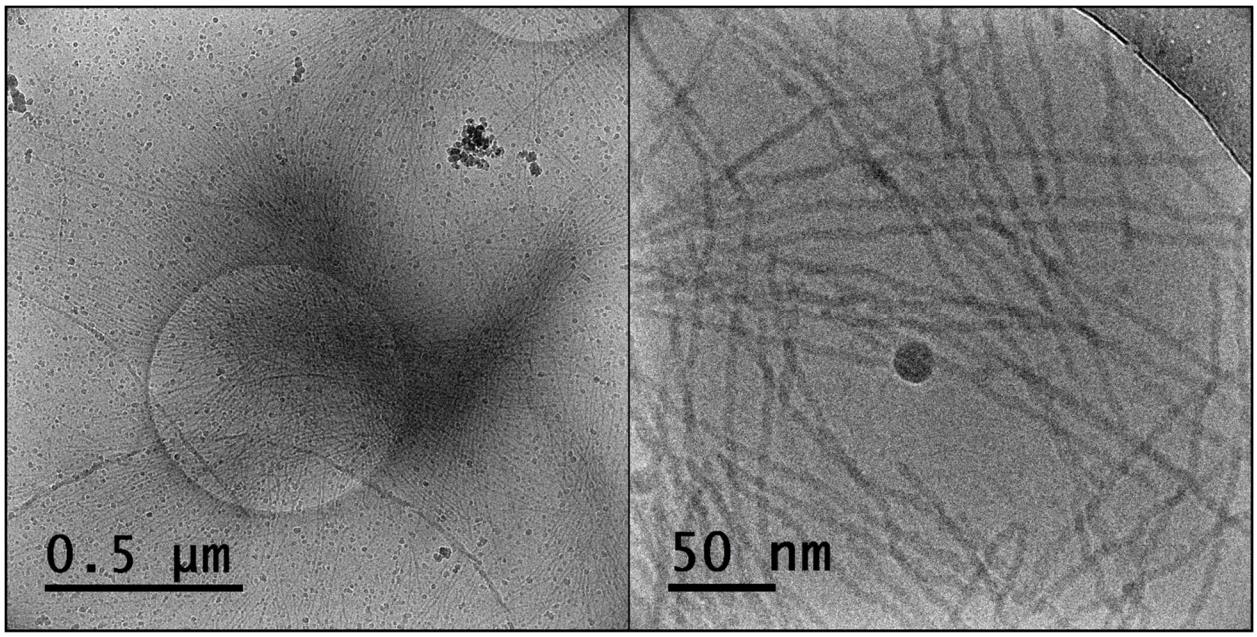

Figure A.8: Cryo-TEM images of PLLA$_{90}$-*b*-PEG$_{45}$ worms/rods resulting from solvent switch (5mg/mL) in water. The dark contrast in the top right of the left image corresponds to ice contamination. These structures are markedly different from structures obtained from ROPI-CDSA that have been transferred to water demonstrating that PLLA-*b*-PEG assemblies in pure water are likely kinetically-trapped.

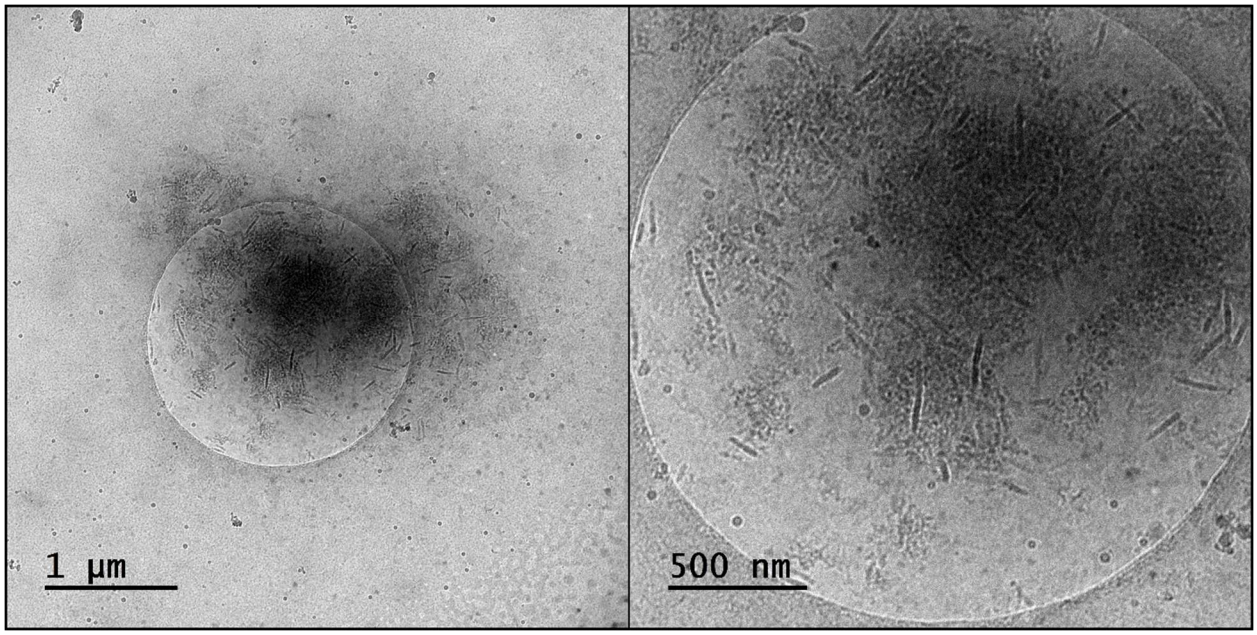

Figure A.9: Cryo-TEM images of $PLLA_{45}$-*b*-PEG_{45} particles resulting from CDSA in water showing short lamellar aggregations. These structures are markedly different from structures obtained from ROPI-CDSA that have been transferred to water. Additionally, CDSA only occurs in water upon heating of the sample to 65° C and letting it cool. This demonstrates that aqueous solutions of PLLA-*b*-PEG are kinetically trapped when left at room temperature.

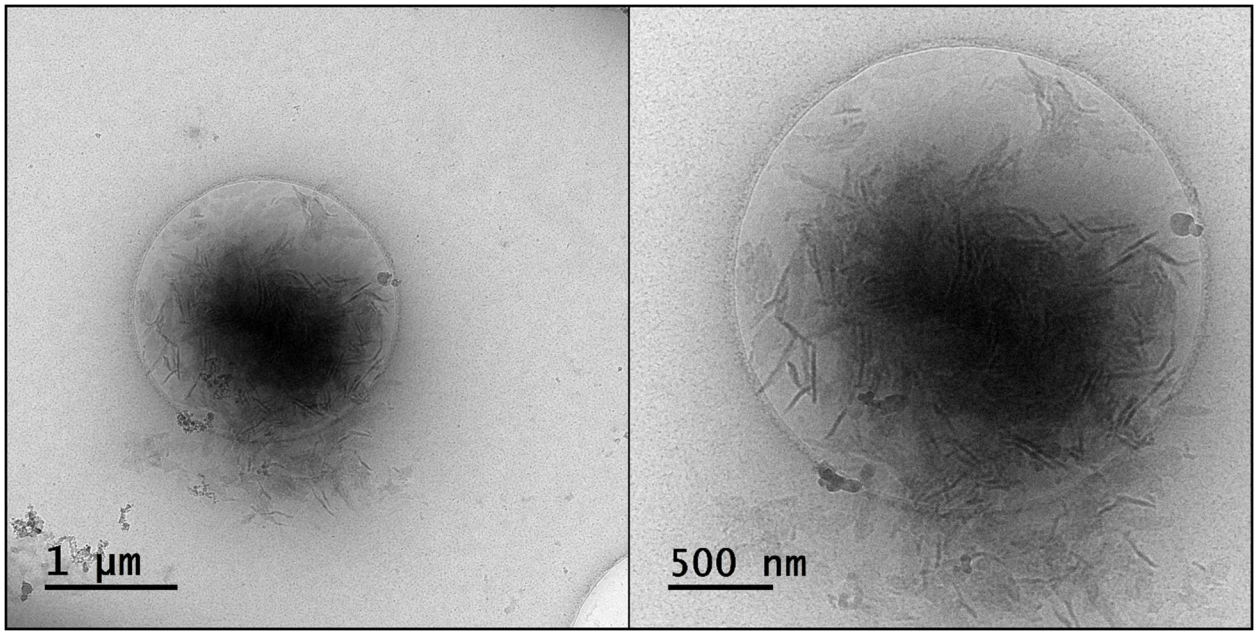

Figure A.10: Cryo-TEM images of $PLLA_{90}$-*b*-PEG_{45} particles resulting from CDSA in water showing short lamellae. These structures are markedly different from structures obtained from ROPI-CDSA that have been transferred to water. Additionally, CDSA only occurs in water upon heating of the sample to 65° C and letting it cool. This demonstrates that aqueous solutions of PLLA-*b*-PEG are kinetically trapped when left at room temperature.

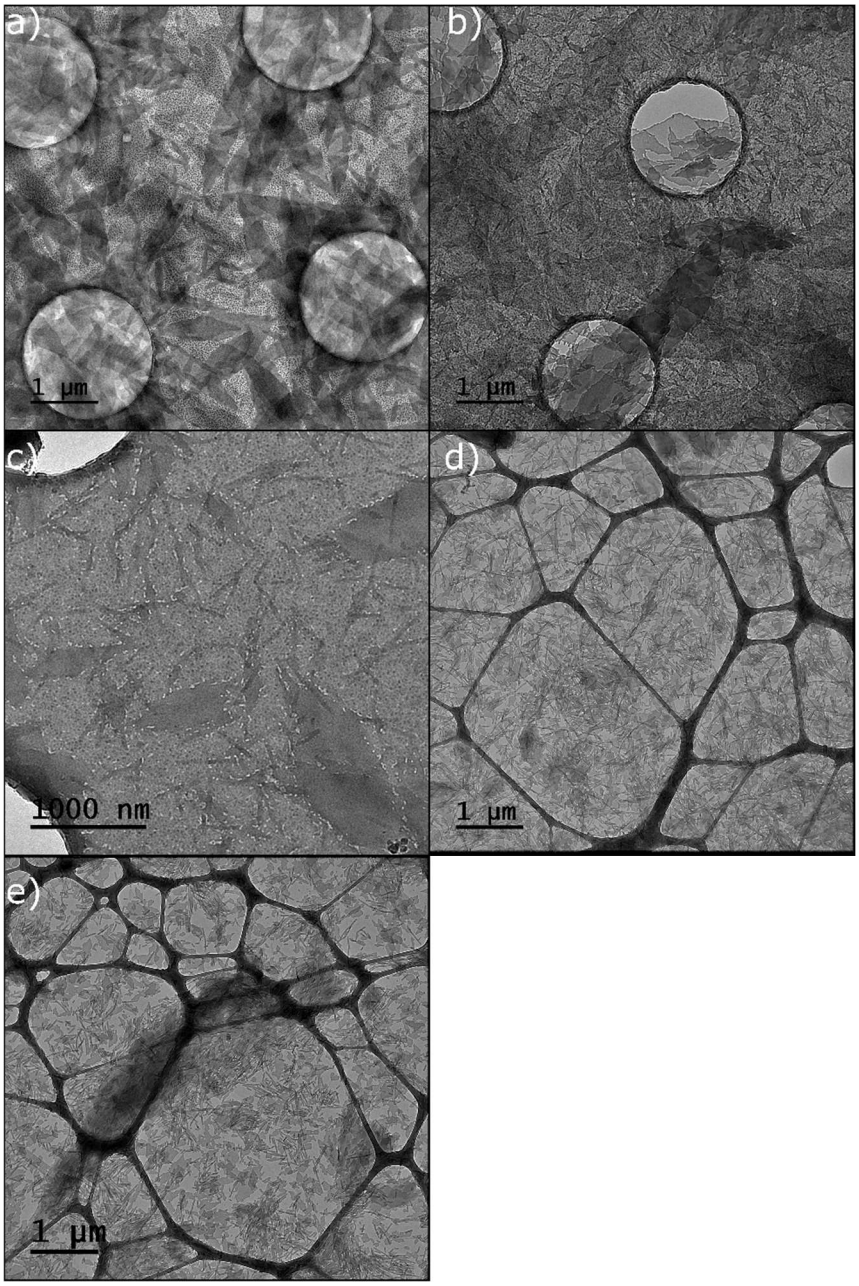

Figure A.11: Toluene cryo-TEM images. a) **9** ($PLLA_{45}$-*b*-PEG_{45} 10% solids w/w) b) **13** ($PLLA_{90}$-*b*-PEG_{45} 5% solids w/w) c) **9** d-e) graphene oxide coated grid with **9**. While images indicate the presence of lamellae and rods of various sizes, the ice layer is absent in (a-c) from the holes visible. Evaporation of toluene during grid preparation concentrated and dehydrated the sample. Dry-state TEM gives a similar result. Performing cryo-TEM on a graphene-oxide coated lacey carbon grid gave a better, albeit poor, ice layer. However, the solutions are still too concentrated to resolve structural features. Thus, toluene-based cryo-TEM prep would be replaced by water-based cryo-TEM. For information on water-based cryo-TEM sample preparation, see the methods section.

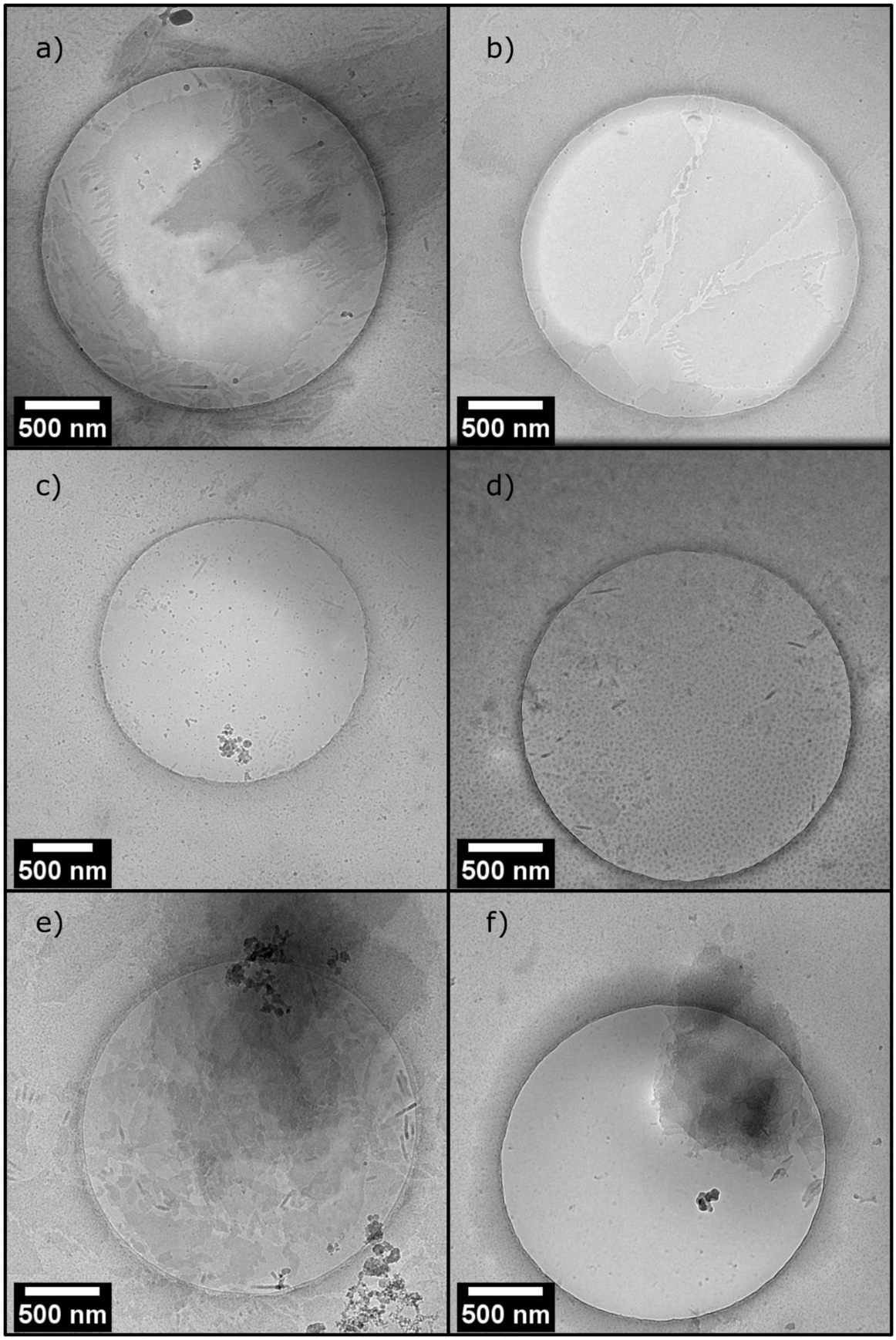
a)
500 nm
b)
500 nm
c)
500 nm
d)
500 nm
e)
500 nm
f)
500 nm

Figure A.12: Cryo-TEM images of aqueous resuspensions that were taken shortly after resuspensions (a,c,e), months after resuspension (b), and from resuspensions made from aged freeze-dried samples over six months aged (d, f). Images (a) and (b) are lamellae from $PLLA_{75}$-*b*-PEG_{45} (10% solids w/w **12**) resuspensions relaxed several days in toluene prior to resuspension. Images (c) and (d) are nanorods and spheres from $PLLA_{45}$-*b*-PEG_{45} (10% solids w.w **9**) resuspensions relaxed six hours in toluene prior to freeze-drying. Images (e) and (f) are lamellae aggregates from $PLLA_{90}$-*b*-PEG_{45} relaxed one day in toluene prior to freeze-drying. In each case, the morphologies are maintained showing that PLLA-*b*-PEG morphologies are stable and kinetically-trapped once freeze-dried and transferred to water. For more information see section **c**, self-assembly mechanism, in the results.

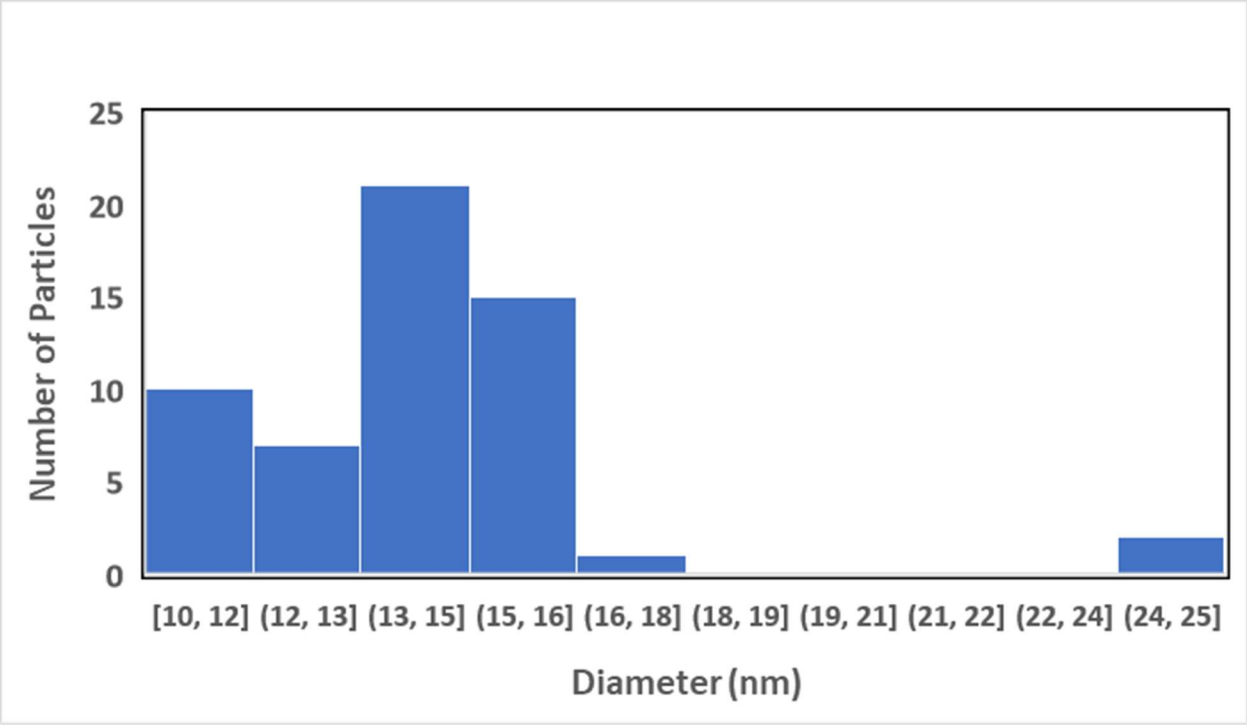

Figure A.13: Histogram for the sphere diameter (14.4±2.6 nm) of $PLLA_{45}$-b-PEG_{45} measured t = 1 hour of self-assembly from cryo-TEM. See also the results section (self-assembly mechanism) in the main text.

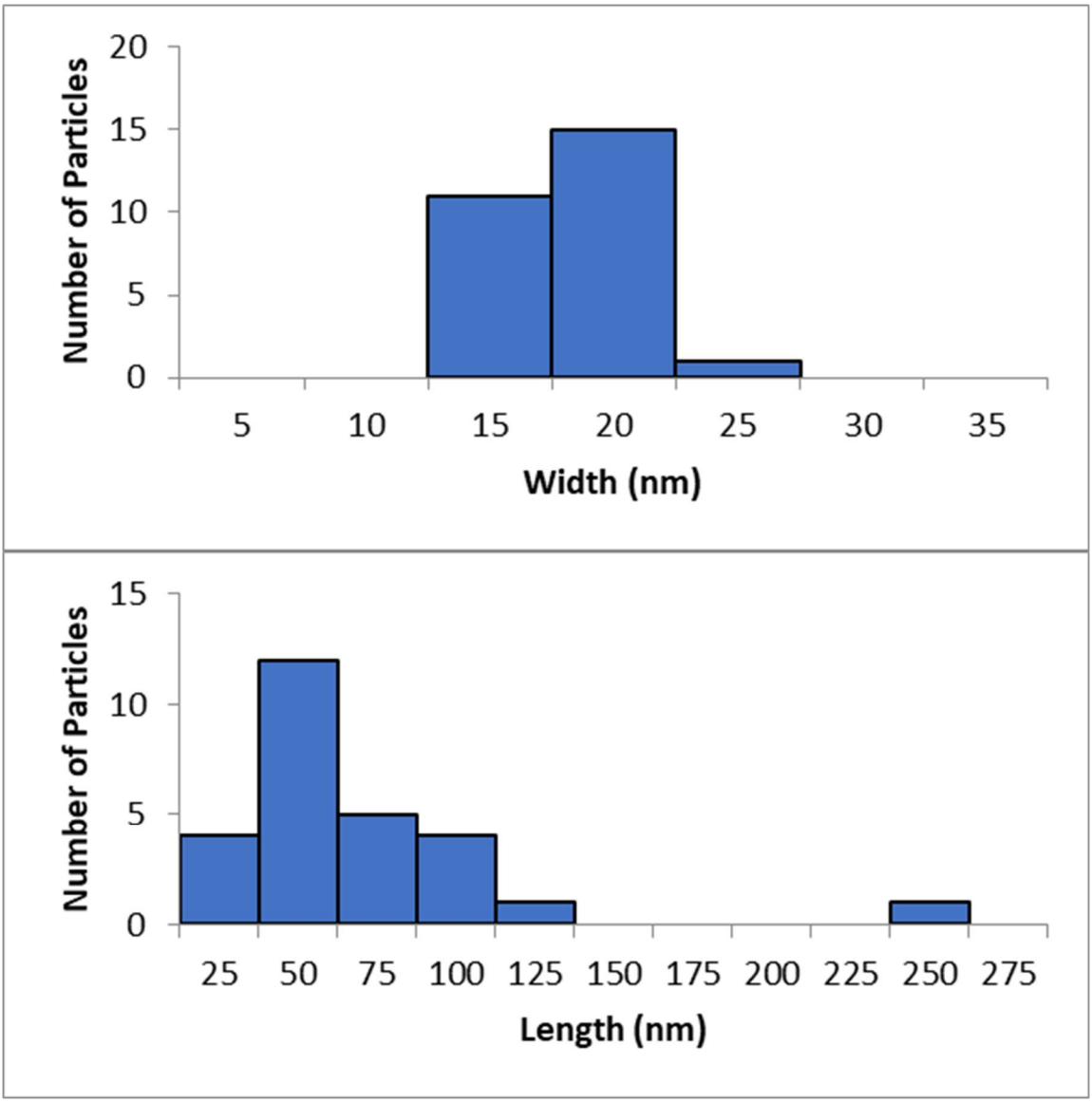

Figure A.14: Histograms for the rod width/diameter (15.8±2.3) (top) and length (56.1±42.4 nm) (bottom) of $PLLA_{45}$-b-PEG_{45} measured t = 3 hours of self-assembly from cryo-TEM. See also the results section (self-assembly mechanism) in the main text.

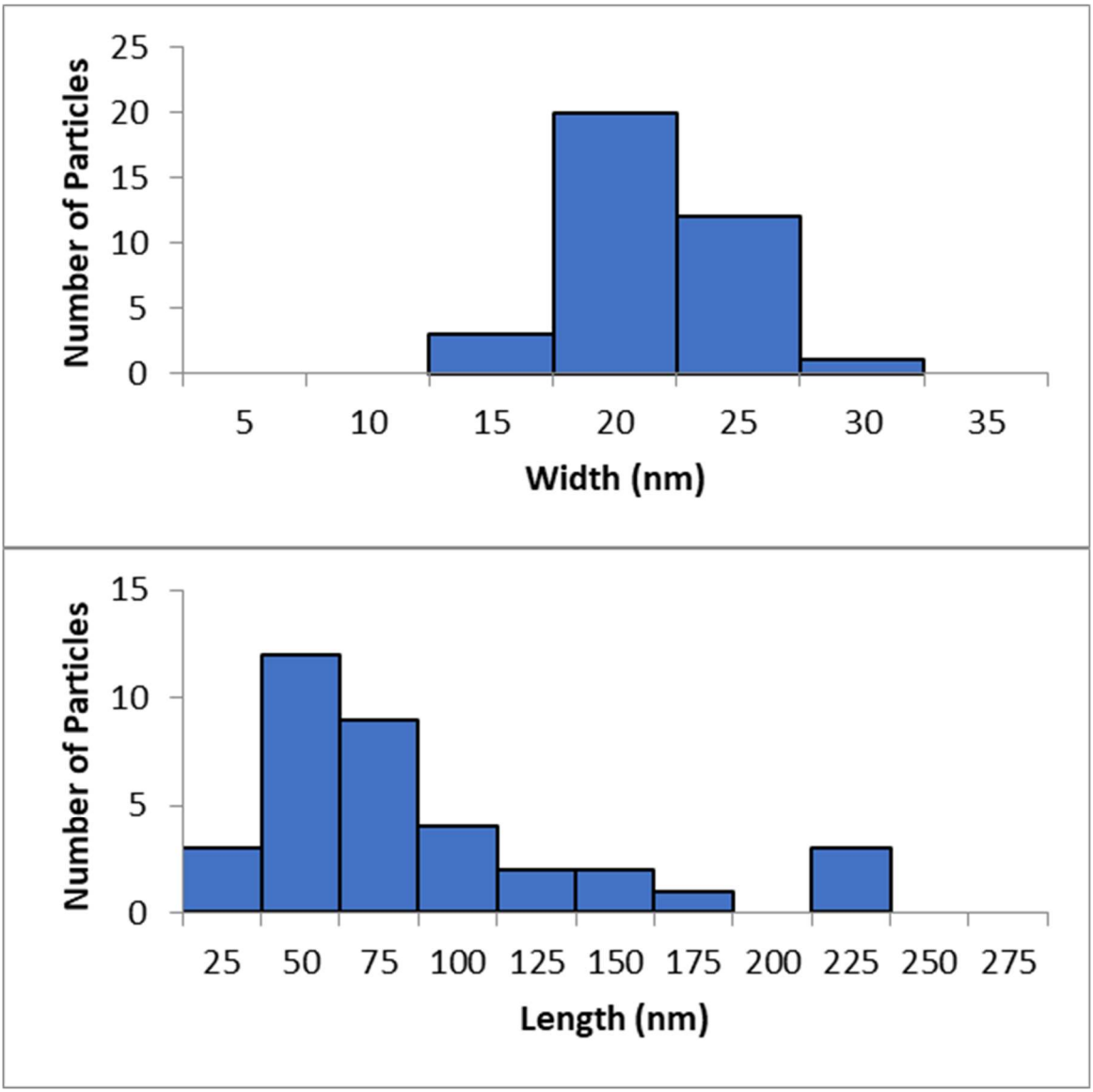

Figure A.15: Histograms for the rod width/diameter (19.1±3.1 nm) (top) and length (75.2±53.6 nm) (bottom) of $PLLA_{45}$-b-PEG_{45} measured t = 6 hours of self-assembly from cryo-TEM. See also the results section (self-assembly mechanism) in the main text.

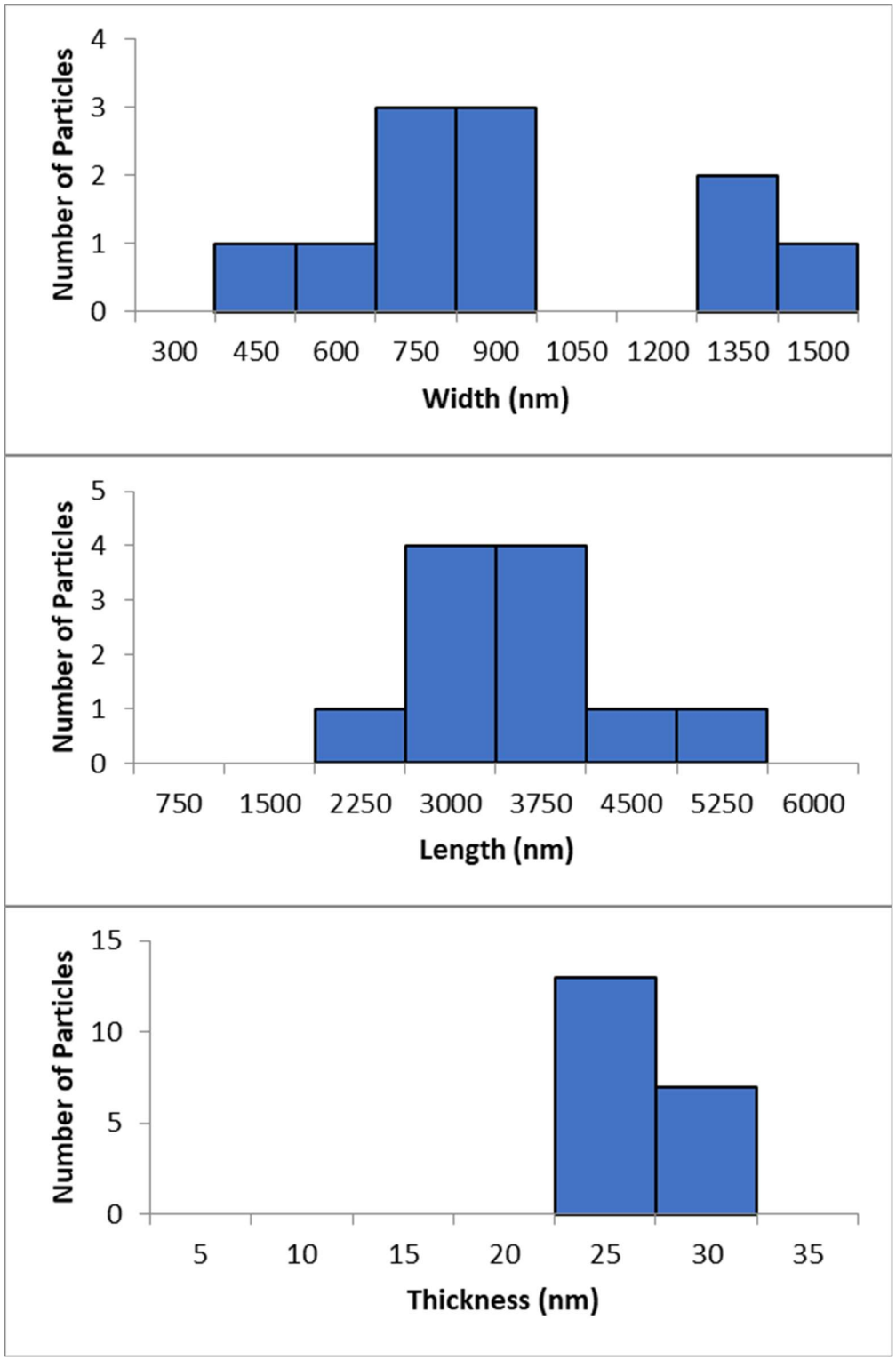

Figure A.16: Histograms for the lamellae width (859±308 nm) (top), length (3212±927 nm) (middle) and thickness (24.7±2.2 nm) (bottom) of $PLLA_{45}$-b-PEG_{45} measured t = 24 hours of self-assembly from cryo-TEM. See also the results section (self-assembly mechanism) in the main text.

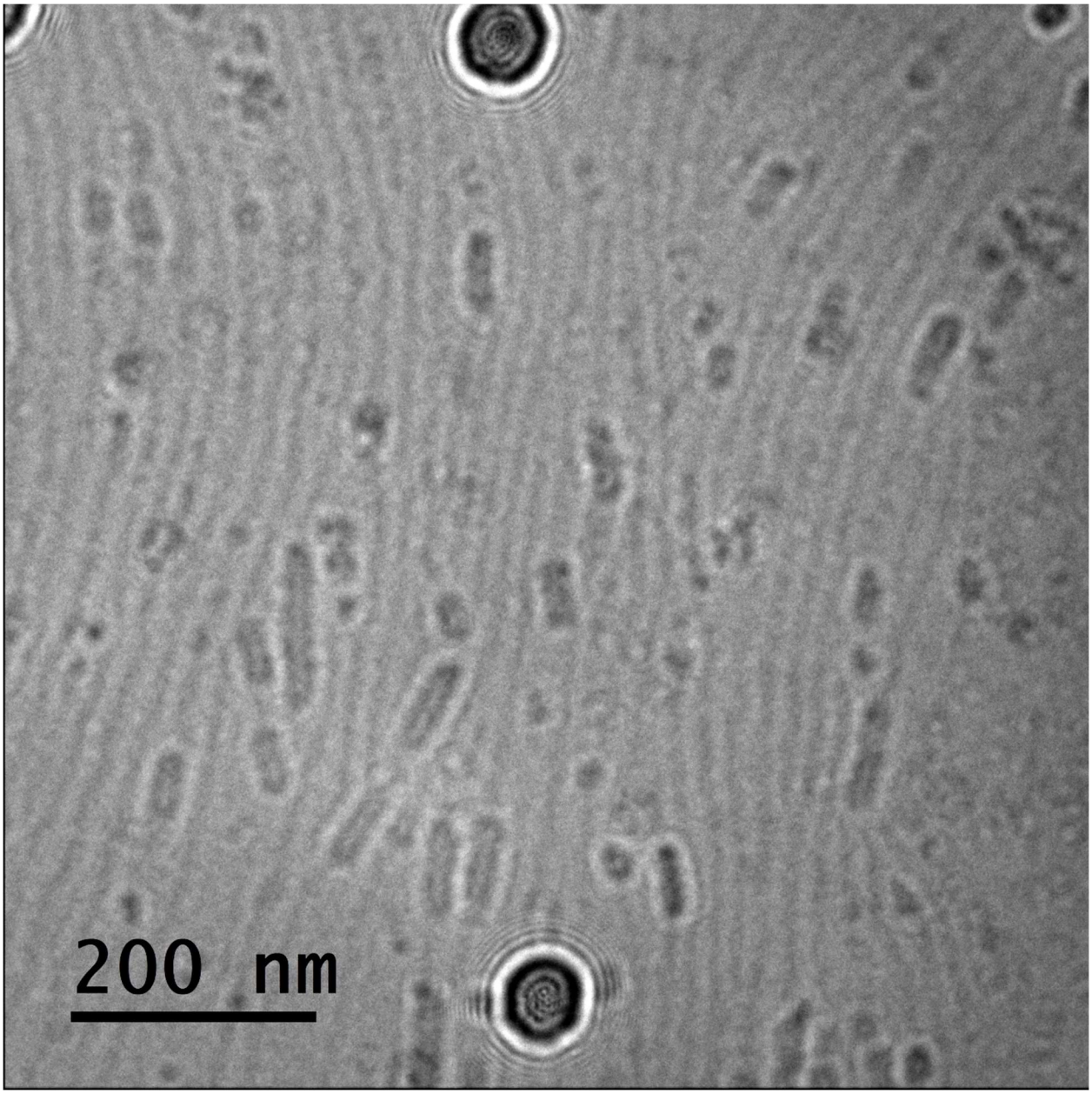

Figure A.17: Cryo-TEM image of fibers observed in a sample of $PLLA_{45}$-*b*-PEG_{45} (10% solids w/w **9**) that is primarily rods. Rods appear to be growing from fibers of a diameter of approximately 10 nm. The spheres which are highly defocused are ice contamination. Here fibers are defined as long thin nanostructures whereas rods are short and more defined.

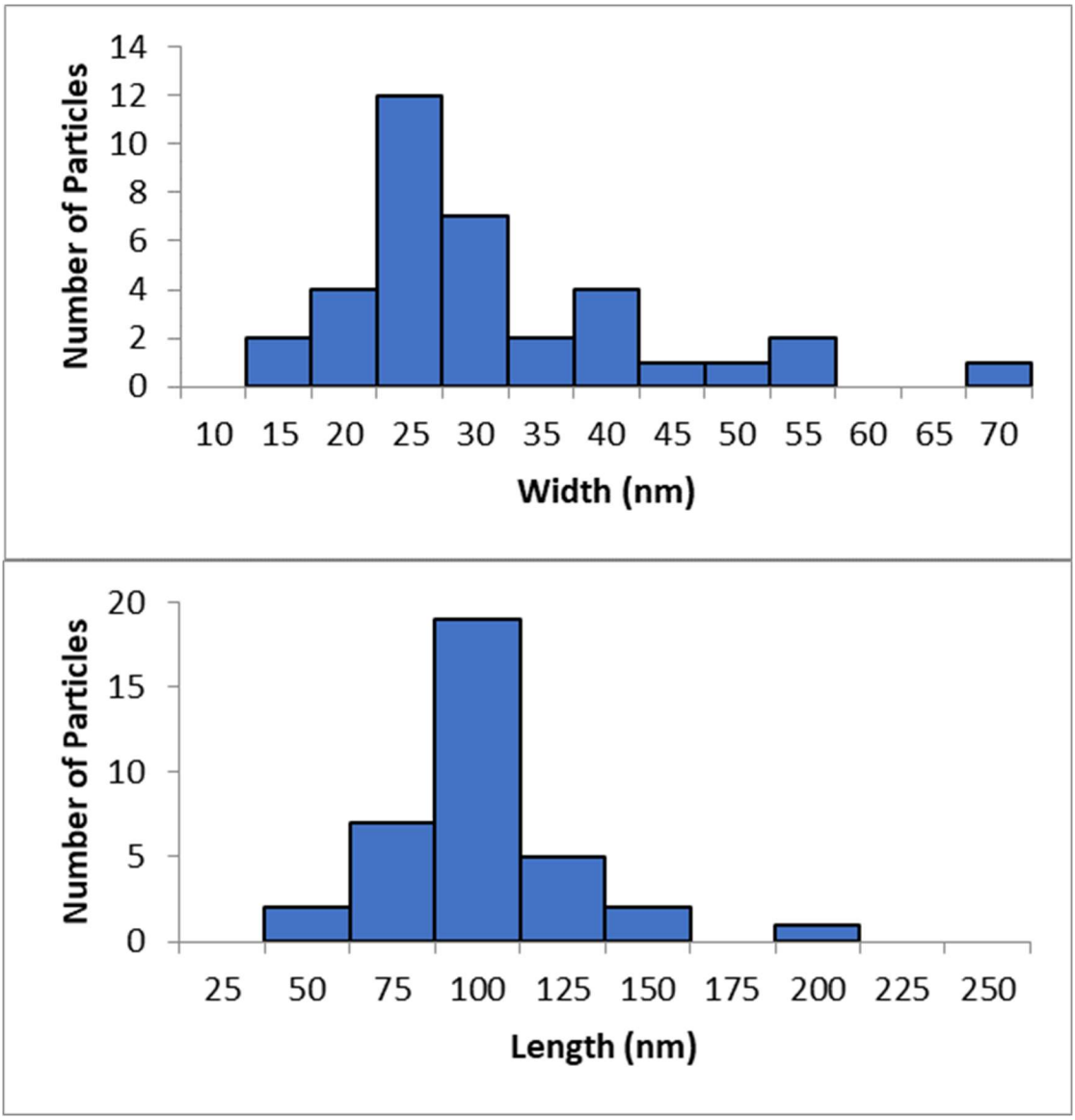

Figure A.18: Histograms for the rod-like precursor width/diameter (29±12 nm) (top) and length (90±27 nm) (bottom) of $PLLA_{90}$-b-PEG_{45} measured t = 5 min of self-assembly from cryo-TEM. See also the results section (self-assembly mechanism) in the main text.

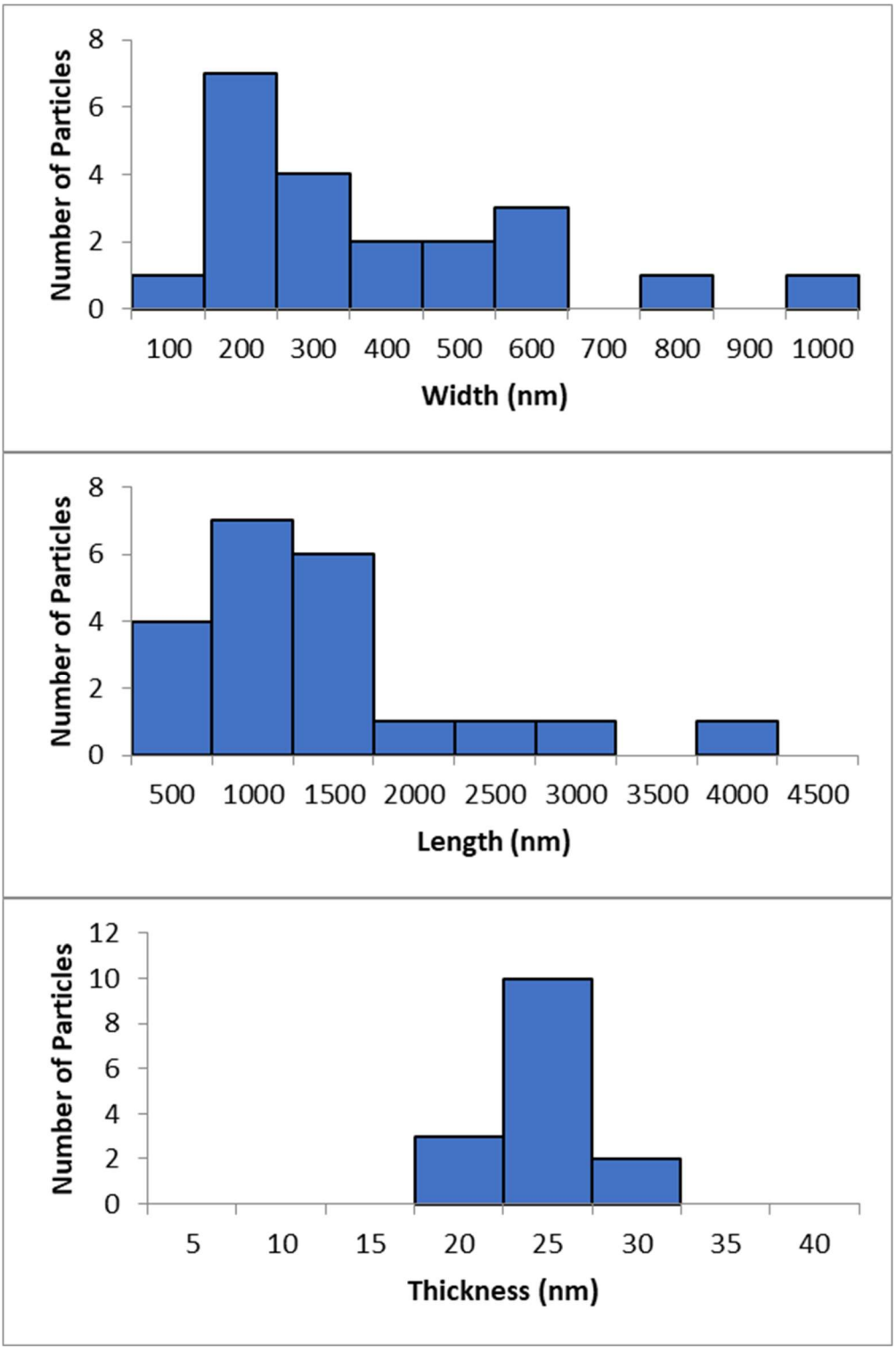

Figure A.19: Histograms for the lamellae width (360±250 nm) (top), length (1270±910 nm) (middle) and thickness (22±2 nm) (bottom) of $PLLA_{90}$-b-PEG_{45} measured t = 3 hours of self-assembly from cryo-TEM. See also the results section (self-assembly mechanism) in the main text.

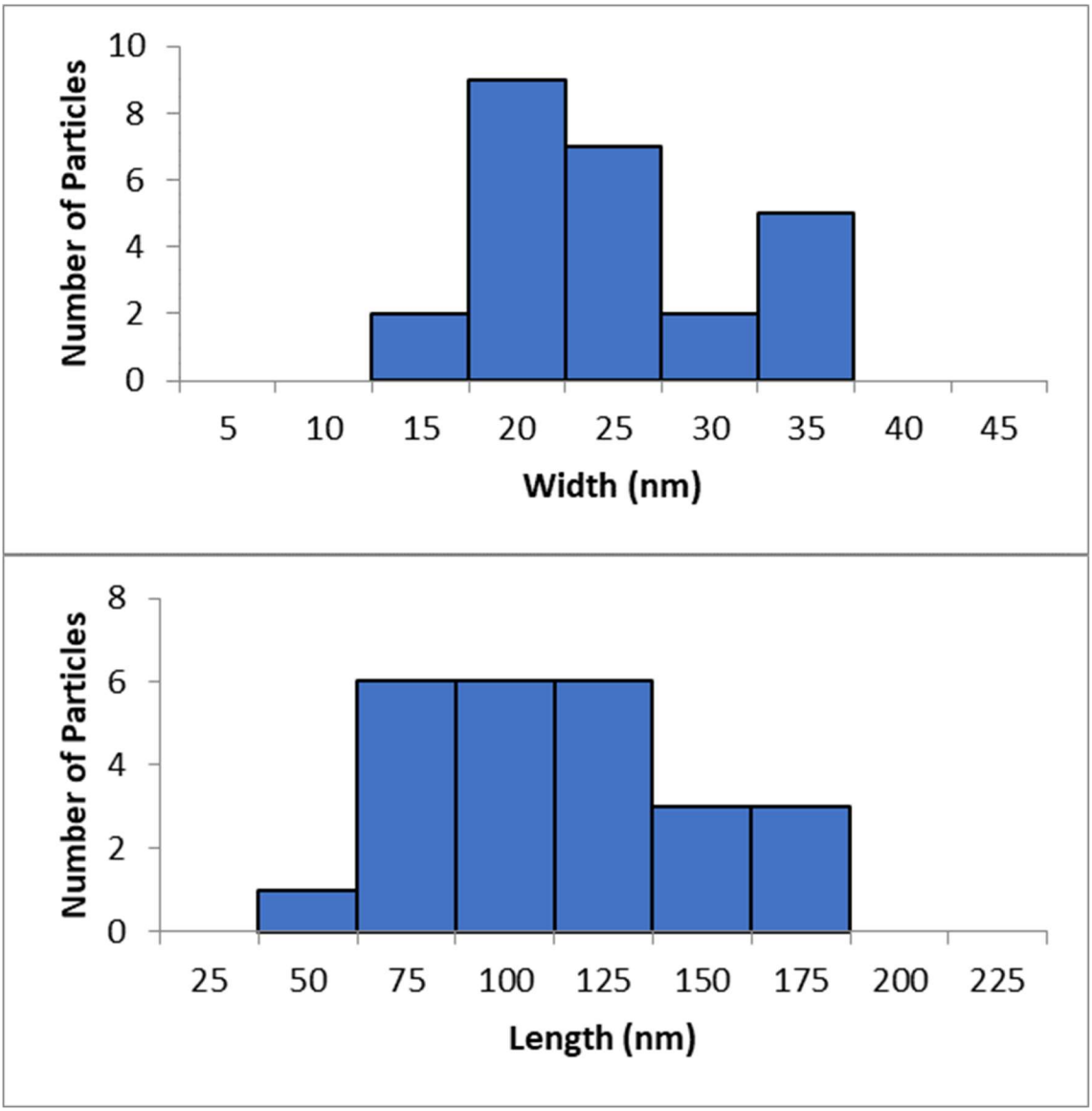

Figure A.20: Histograms for the rod width/diameter (22±6 nm) (top) and length (101±35 nm) (bottom) of $PLLA_{90}$-b-PEG_{45} measured t = 3 hours of self-assembly from cryo-TEM. Also see the results section (self-assembly mechanism) in the main text.

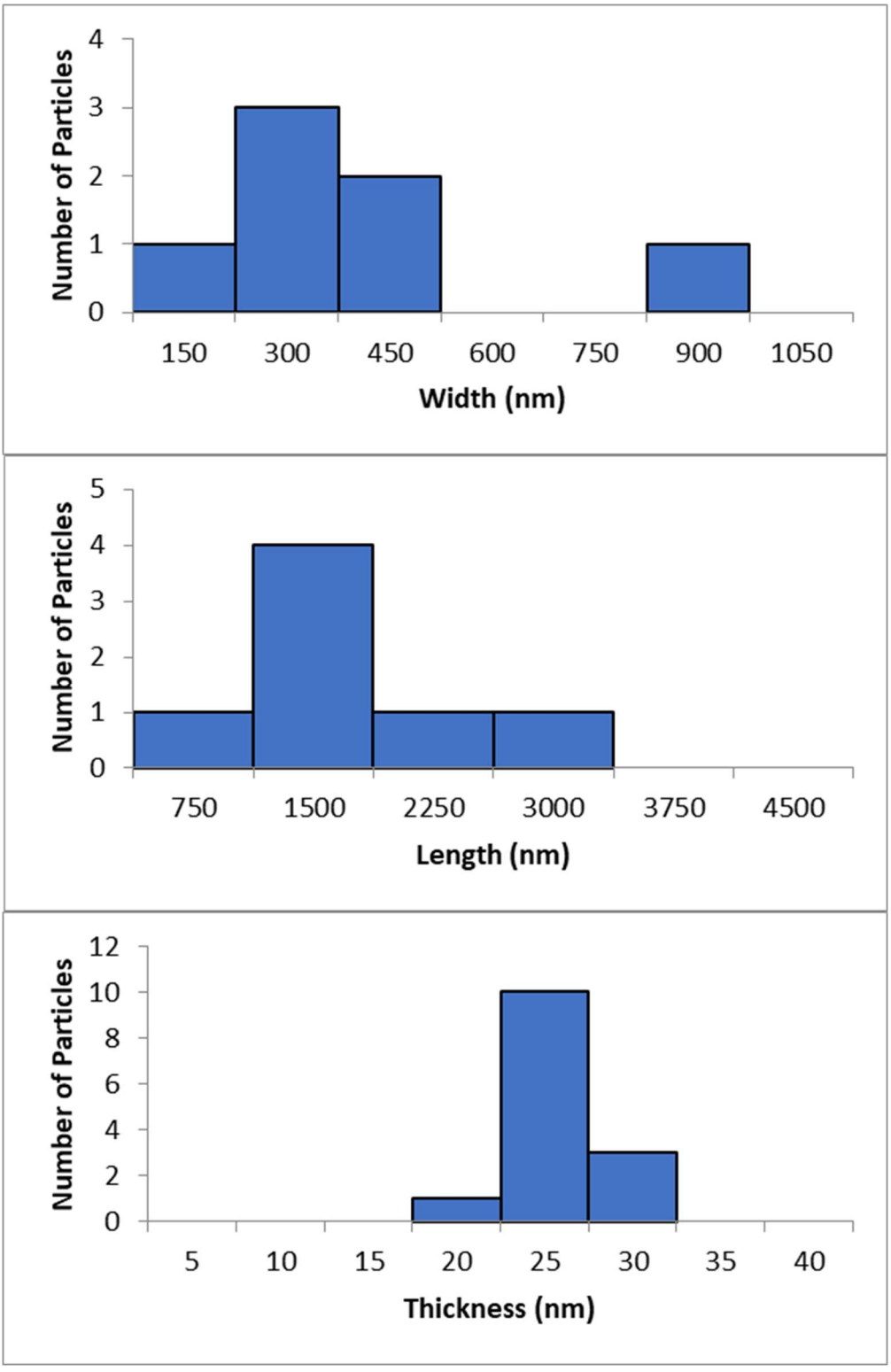

Figure A.21: Histograms for the lamellae width (360±230 nm) (top), length (1300±700 nm) (middle) and thickness (23±2 nm) (bottom) of $PLLA_{90}$-b-PEG_{45} measured t = 6 hours of self-assembly from cryo-TEM. Also see the results section (self-assembly mechanism) in the main text

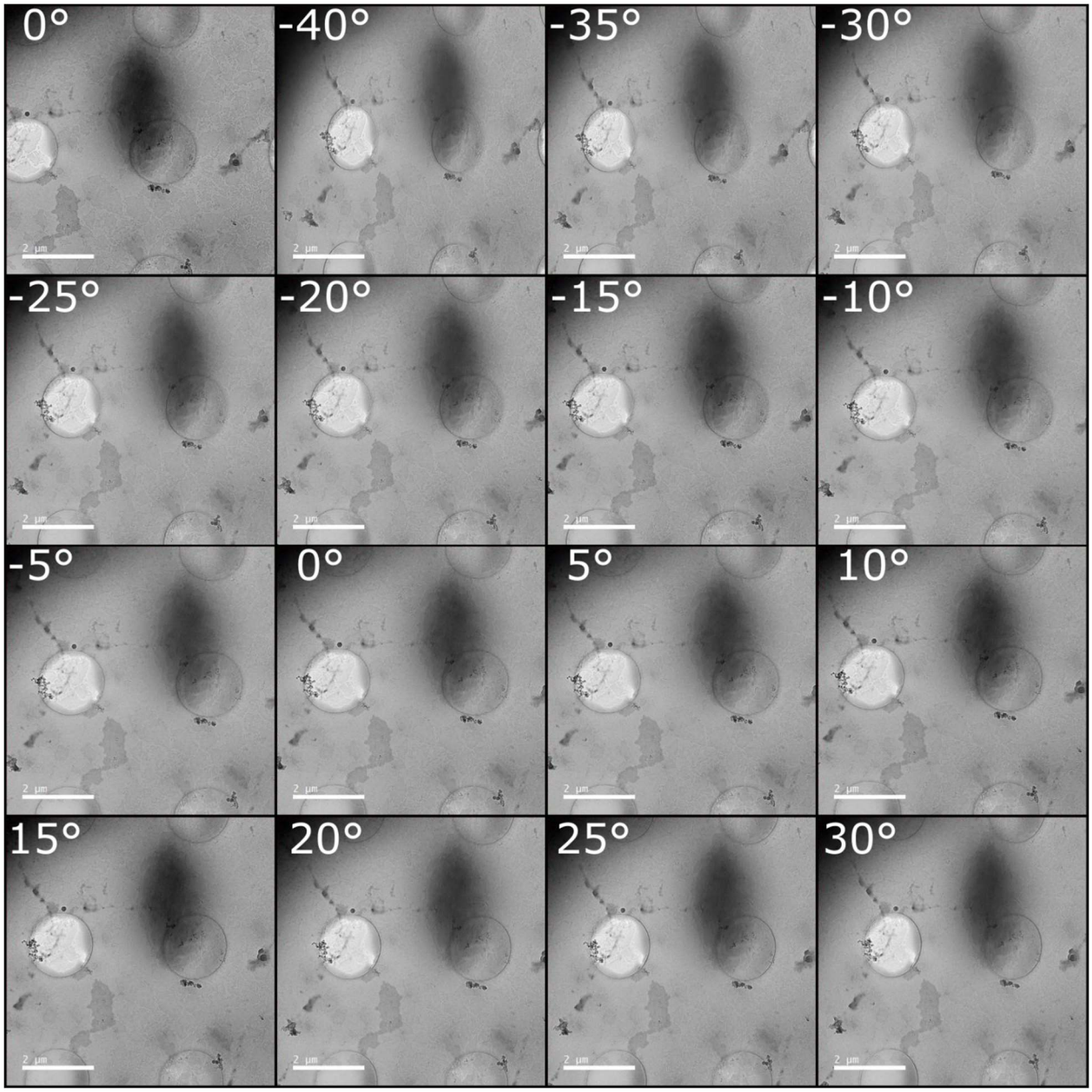
0°
-40°
-35°
-30°
-25°
-20°
-15°
-10°
-5°
0°
5°
10°
15°
20°
25°
30°

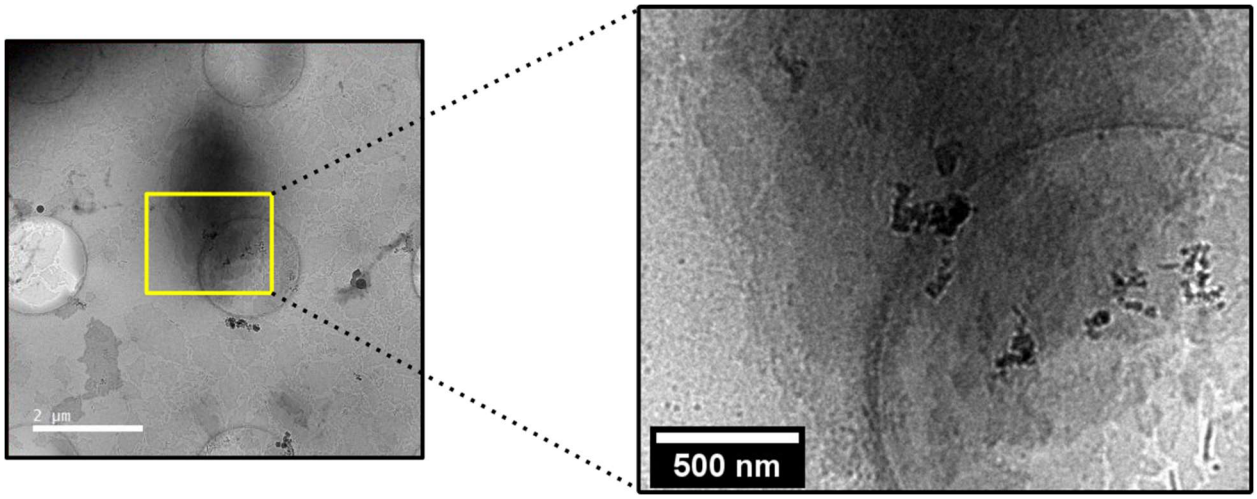

Figure A.22: (top) Cryo-TEM images of a tilt Angle series of a lamellar stack **15** ($PLLA_{90}$-*b*-PEG_{45} 10% solids w/w). Scale bar is 2 µm. (bottom) Zoomed in cryo-TEM image of lamellae in tilt angle series at 0°. For more information on lamellae stacking see section c, self-assembly mechanism and section d, phase diagram, in the results section.

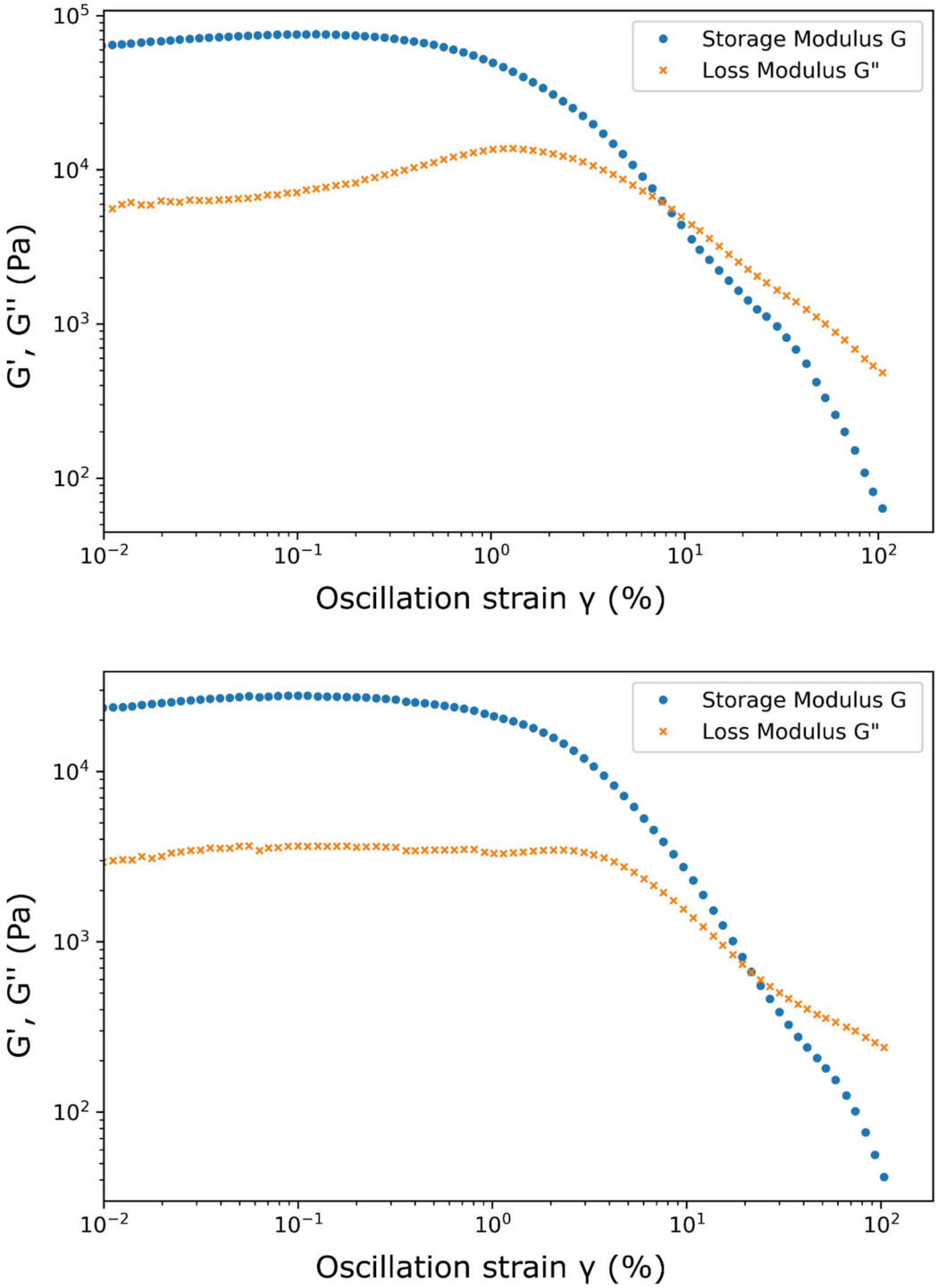

Figure A.23: Oscillatory rheology for organogels from triplicate runs of $PLLA_{90}$-*b*-PEG_{45} (20% solids w/w **16**, top) and $PLLA_{135}$-*b*-PEG_{45} (20% solids w/w **19**, bottom). The crossover of the loss modulus and the storage modulus indicate the point of gelation. The point of gelation of **16** and **19** are about 8 and 10 γ(%) respectively. Polymers at higher PLLA DP (90 and above) and/or higher % solids w/w (10-20) form into organogels including **15**-**19**.

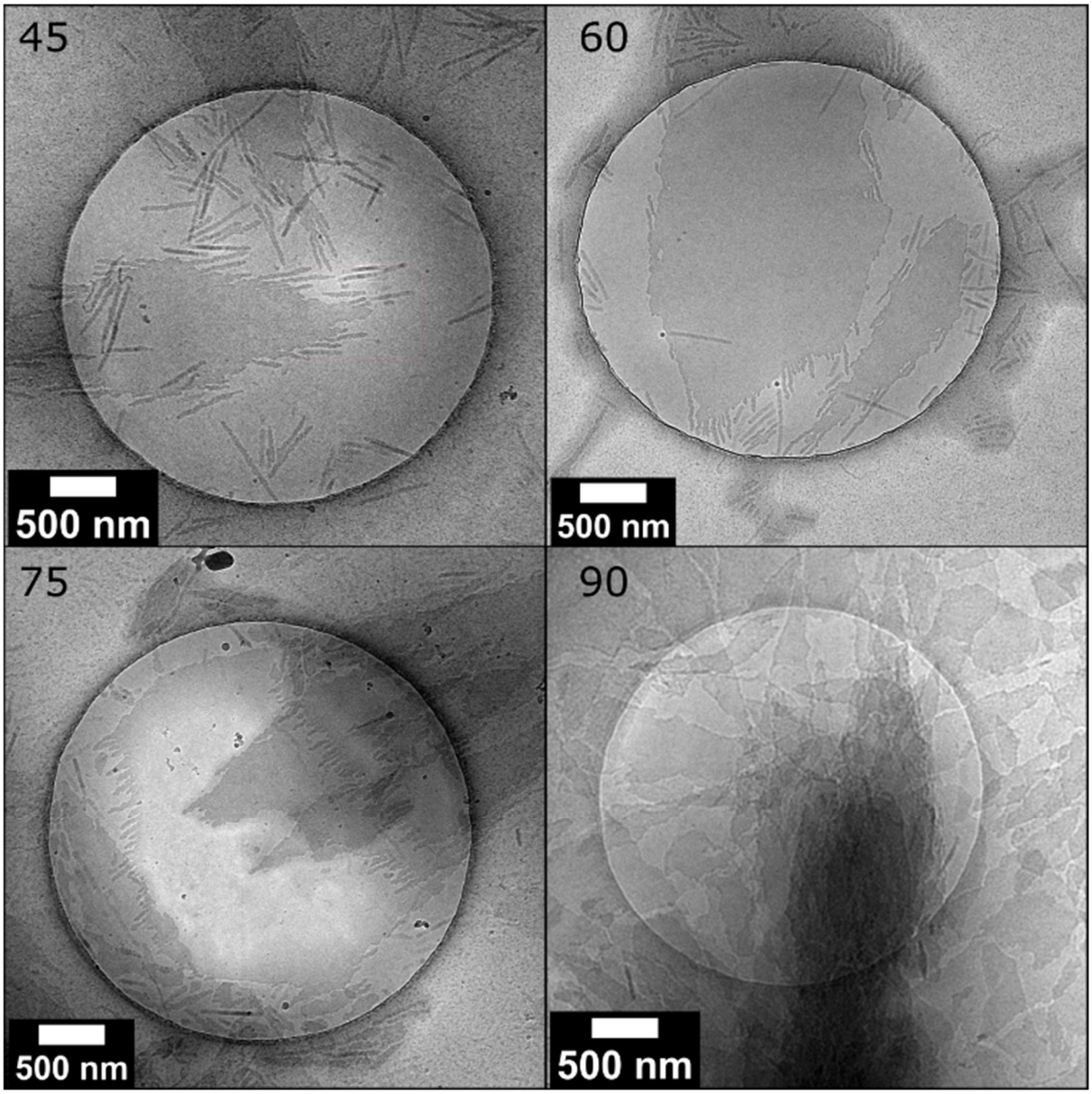

Figure A.24: Cryo-TEM images of relaxed $PLLA_n$-*b*-PEG_{45} samples: **9** (n=45), **11** (n=60), **12** (n=75), and **15** (n=90) all at 10% solids w/w**11** and **12** lamellae exhibit similarities to **11** in that they form from rods, but they appear less ordered such as the lamellae in **15**. For further information see the turbidity data in Figure 2.1 and the discussion (section a) in the main text.

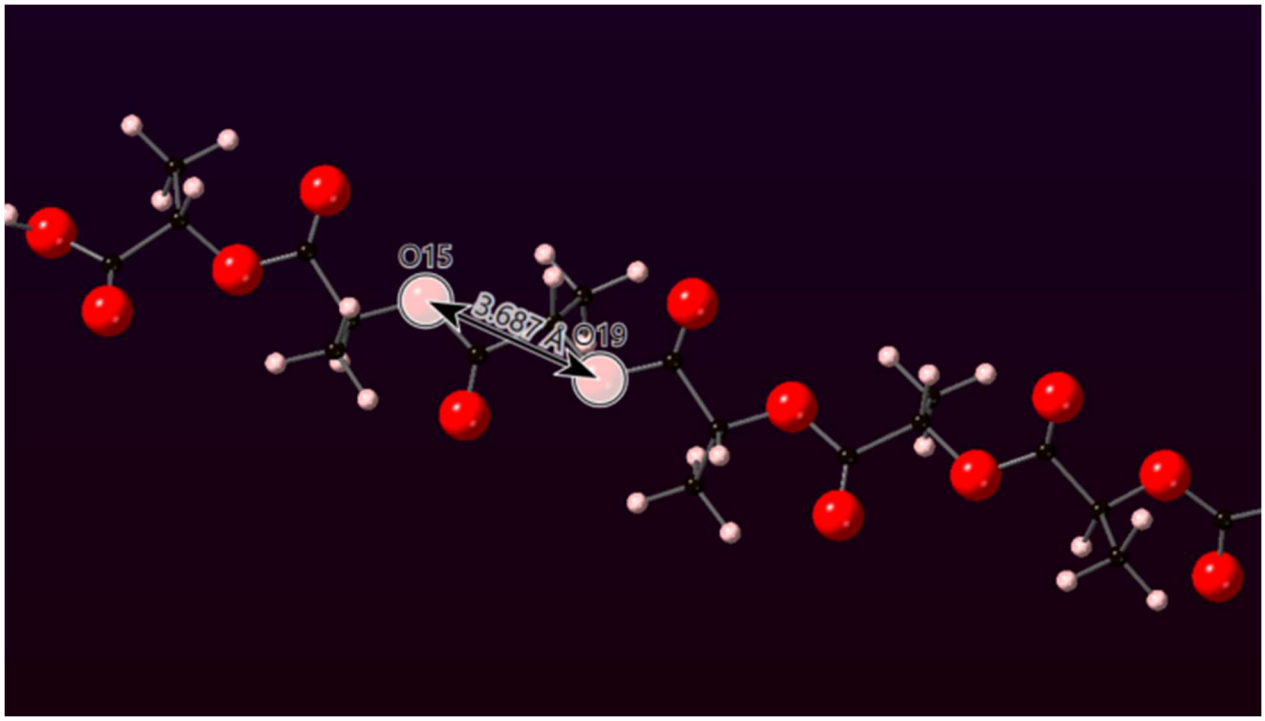

Figure A.25: Measurement of a PLLA polymeric unit from CrystalMaker® software. This measurement is used to calculate L_{max} as shown in the discussion (section a) in the main text.

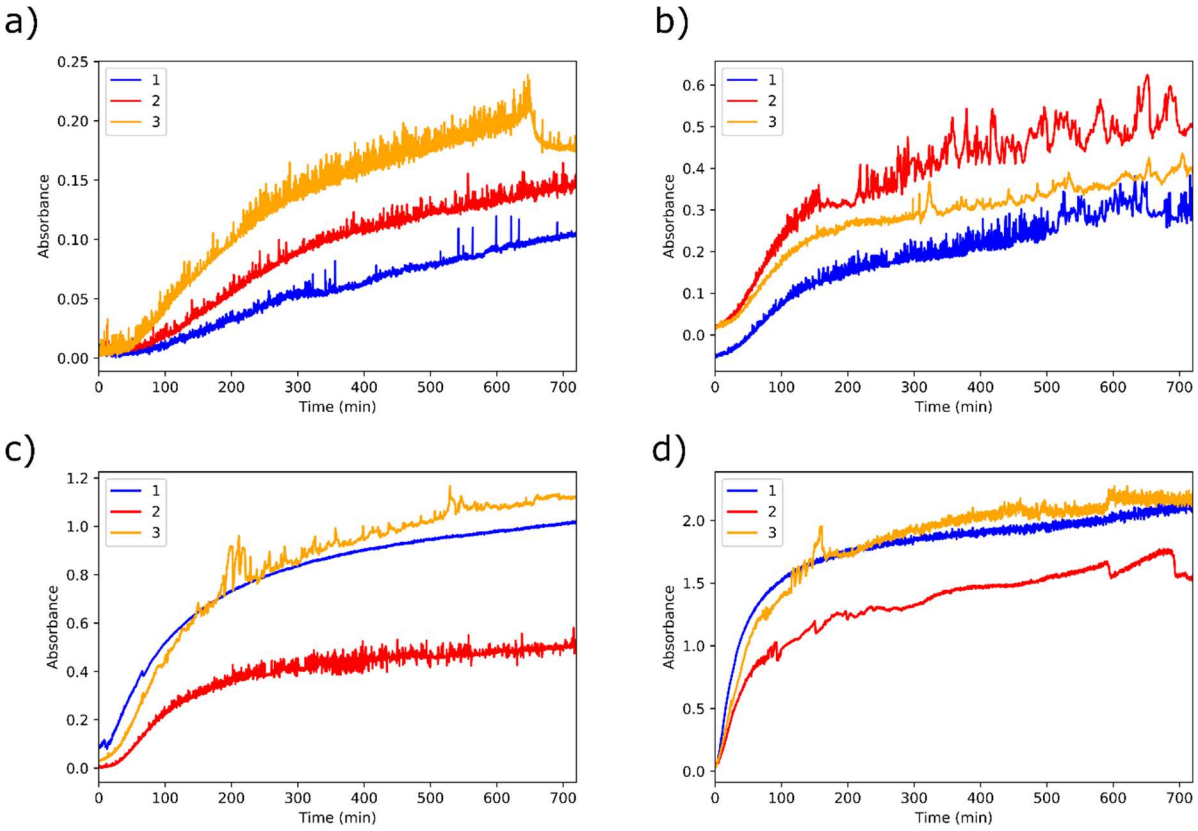

Figure A.26: Triplicate data from turbidity studies (600nm) for $PLLA_n$-*b*-PEG_{45} for (a) **9** (n=45), (b) **11** (n=60), (c) **12** (n=75), and (d) **15** (n=90) all at 10% solids w/w. Data presented in the main text is binned by a factor of 20 to reduce the noise. For the averaged data with error bars from the turbidity studies see Figure 2.1b in the main text. For the setup see the methods section.

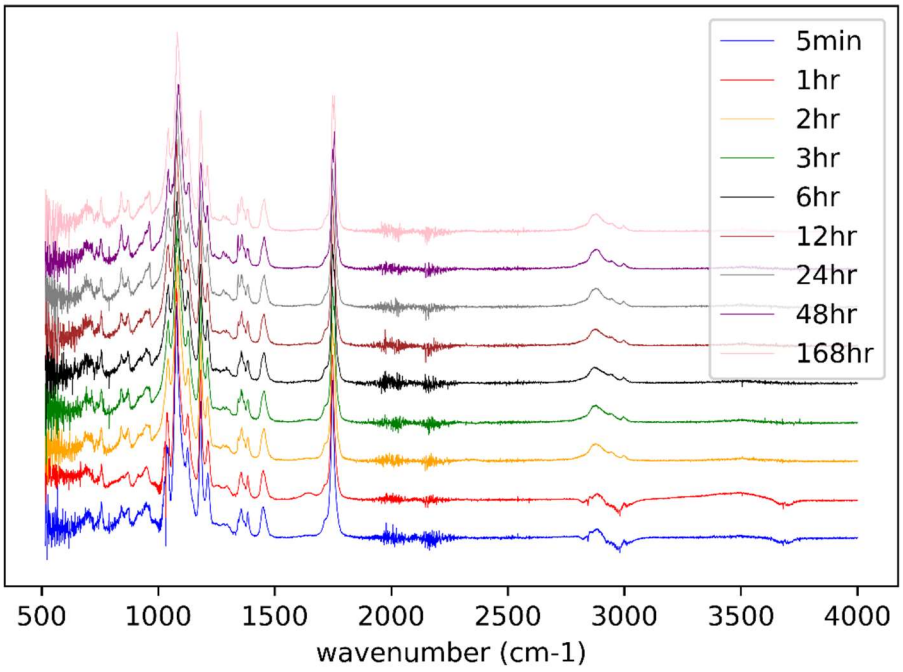

Figure A.27: Full FTIR spectra for time studies of $PLLA_{45}$-*b*-PEG_{45} (10% solids w/w **9**).

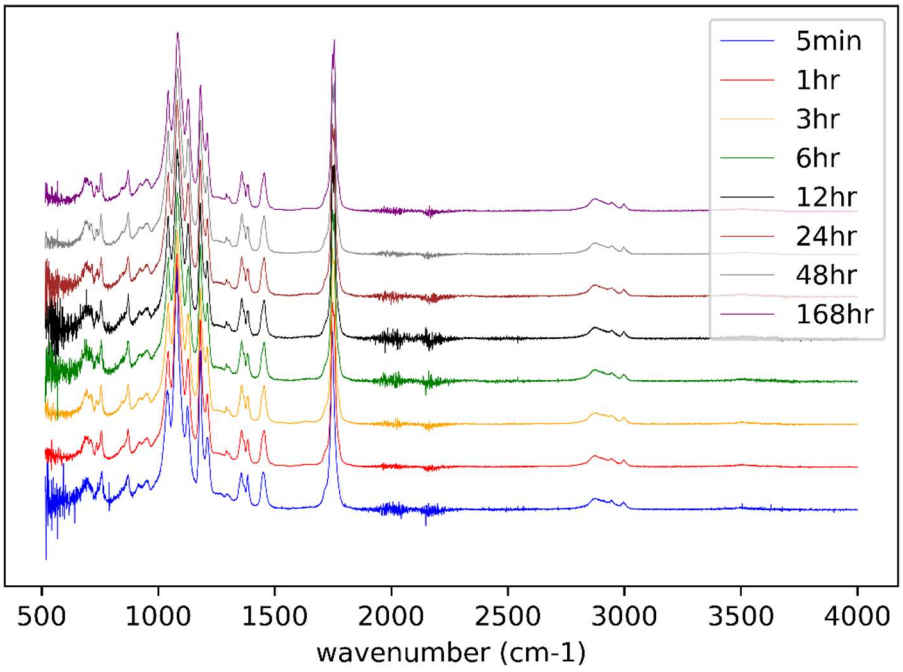

Figure A.28: Full FTIR spectra for time studies of $PLLA_{90}$-*b*-PEG_{45} (10% solids w/w **15**).

A.5. References

1. Yang, J.; Zhao, T.; Cui, J.; Liu, L.; Zhou, Y.; Li, G.; Zhou, E.; Chen, X., Nonisothermal crystallization behavior of the poly(ethylene glycol) block in poly(L-lactide)–poly(ethylene glycol) diblock copolymers: Effect of the poly(L-lactide) block length. *Journal of Polymer Science Part B: Polymer Physics* **2006,** *44* (22), 3215-3226.
2. Kricheldorf, H. R.; Meier-Haack, J., Polylactones, 22 ABA triblock copolymers of L-lactide and poly(ethylene glycol). *Die Makromolekulare Chemie* **1993,** *194* (2), 715-725.
3. Aldén, M.; Lydén, M.; Tegenfeldt, J., Effect of counterions on the interactions in solid dispersions between polyethylene glycol, griseofulvin and alkali dodecyl sulphates. *International Journal of Pharmaceutics* **1994,** *110* (3), 267-276.
4. Canning, S. L.; Smith, G. N.; Armes, S. P., A Critical Appraisal of RAFT-Mediated Polymerization-Induced Self-Assembly. *Macromolecules* **2016,** *49* (6), 1985-2001.
5. Mattia, E.; Otto, S., Supramolecular systems chemistry. *Nat. Nanotechnol.* **2015,** *10* (2), 111-119.
6. Marolf, D. M.; Jones, M. R., Measurement Challenges in Dynamic and Nonequilibrium Nanoscale Systems. *Analytical Chemistry* **2019**.
7. Nicolai, T.; Colombani, O.; Chassenieux, C., Dynamic polymeric micelles versus frozen nanoparticles formed by block copolymers. *Soft Matter* **2010,** *6* (14), 3111-3118.
8. Takahashi, R.; Miwa, S.; Sobotta, F. H.; Lee, J. H.; Fujii, S.; Ohta, N.; Brendel, J. C.; Sakurai, K., Unraveling the kinetics of the structural development during polymerization-induced self-assembly: decoupling the polymerization and the micelle structure. *Polym. Chem.* **2020,** *11* (8), 1514-1524.
9. Cheng, G.; Perez-Mercader, J., Polymerization-Induced Self-Assembly for Artificial Biology: Opportunities and Challenges. *Macromol. Rapid Commun.* **2019,** *40* (2), e1800513.
10. Varlas, S.; Foster, J. C.; O'Reilly, R. K., Ring-opening metathesis polymerization-induced self-assembly (ROMPISA). *Chem Commun (Camb)* **2019,** *55* (62), 9066-9071.
11. Penfold, N. J. W.; Yeow, J.; Boyer, C.; Armes, S. P., Emerging Trends in Polymerization-Induced Self-Assembly. *Acs Macro Letters* **2019,** *8* (8), 1029-1054.

Appendix B: Supplementary Information for Chapter 3

B.1. Supplementary Tables

Table B.1: Detailed table of polymers synthesized.

ID	Co-catalyst	PLLA DP	Solids w/w %	NMR M_n	SEC M_n	SEC M_w	Đ	Gel (Y/N)
1	DBU	200	10	16600	42500	45200	1.06	N
2	DBU	200	10	17400	41800	48700	1.17	N
3	DBU	200	10	16100	39500	44200	1.12	N
4	DBU	200	15	16600	42500	48600	1.14	N
5	DBU	200	20	16900	40400	47200	1.17	Y
6	DBU	400	10	29500	71900	82100	1.14	N
7	(-)-sparteine	200	10	16500	38900	45100	1.16	Y
8	(-)-sparteine	200	10	17100	43300	47500	1.10	Y
9	(-)-sparteine	200	10	15800	38100	44500	1.17	Y
10	(-)-sparteine	200	15	16300	41600	48200	1.16	Y
11	(-)-sparteine	200	20	18300	48200	54600	1.13	Y
12	(-)-sparteine	400	10	28800	66700	77000	1.15	Y
13	DMAP	200	10	17000	36800	47000	1.28	Y

Note: 1% DBU co-catalyst was used. 7.5% of (-)-sparteine and DMAP co-catalyst were used. The thiourea(TU) was 7.5%. Catalyst % is relative to the number of moles of the monomer. All reactions ran > 95% conversion. Gel was determined by the inversion test and further verified with oscillatory rheology. Target molecular weight for DP = 200 is 16400 and for DP = 400 is 30800

Table B.2: Crystallinity calculated using the SmartLab software

ID	Co-catalyst	PLLA DP	Solids w/w %	% Crystallinity
1	DBU	200	10	21.9
4	DBU	200	15	27.6
5	DBU	200	20	23.9
6	DBU	400	10	26.2
7	(-)-sparteine	200	10	22.2
10	(-)-sparteine	200	15	26.3
11	(-)-sparteine	200	20	23.0
12	(-)-sparteine	400	10	24.8

B.2. Supplementary Discussion

Additional slow polymerization: One additional slow polymerization was developed and but not extensively studied. Using 7.5% DMAP co-catalyst with 7.5% TU polymerized L-lactide in 48 hours to >95% conversion. The resulting PLLA$_{200}$-*b*-PEG$_{45}$ solution gelled (**13**), which is consistent with data in the main text.This polymerization was not as controlled having a Đ = 1.28 (Figure B.16), however this polymerization is another example of a slow polymerization leading to an organogel.

B.3. Supplementary Figures

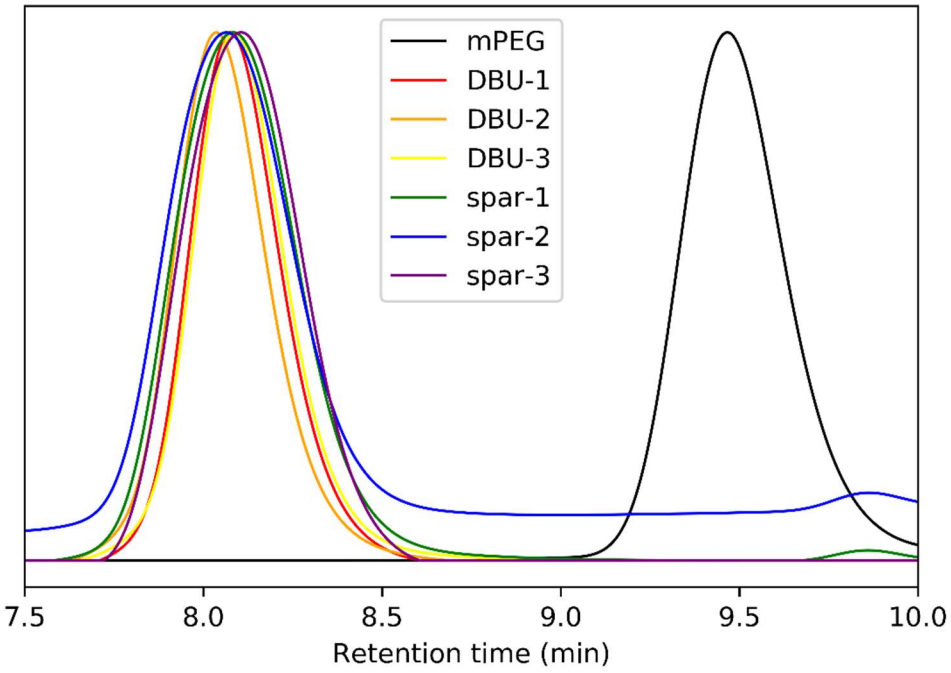

Figure B.1: SEC traces of triplicates of PLLA$_{200}$-*b*-PEG$_{45}$ synthesized at 10% solids w/w with the mPEG homopolymer trace (black) to show chain extension.

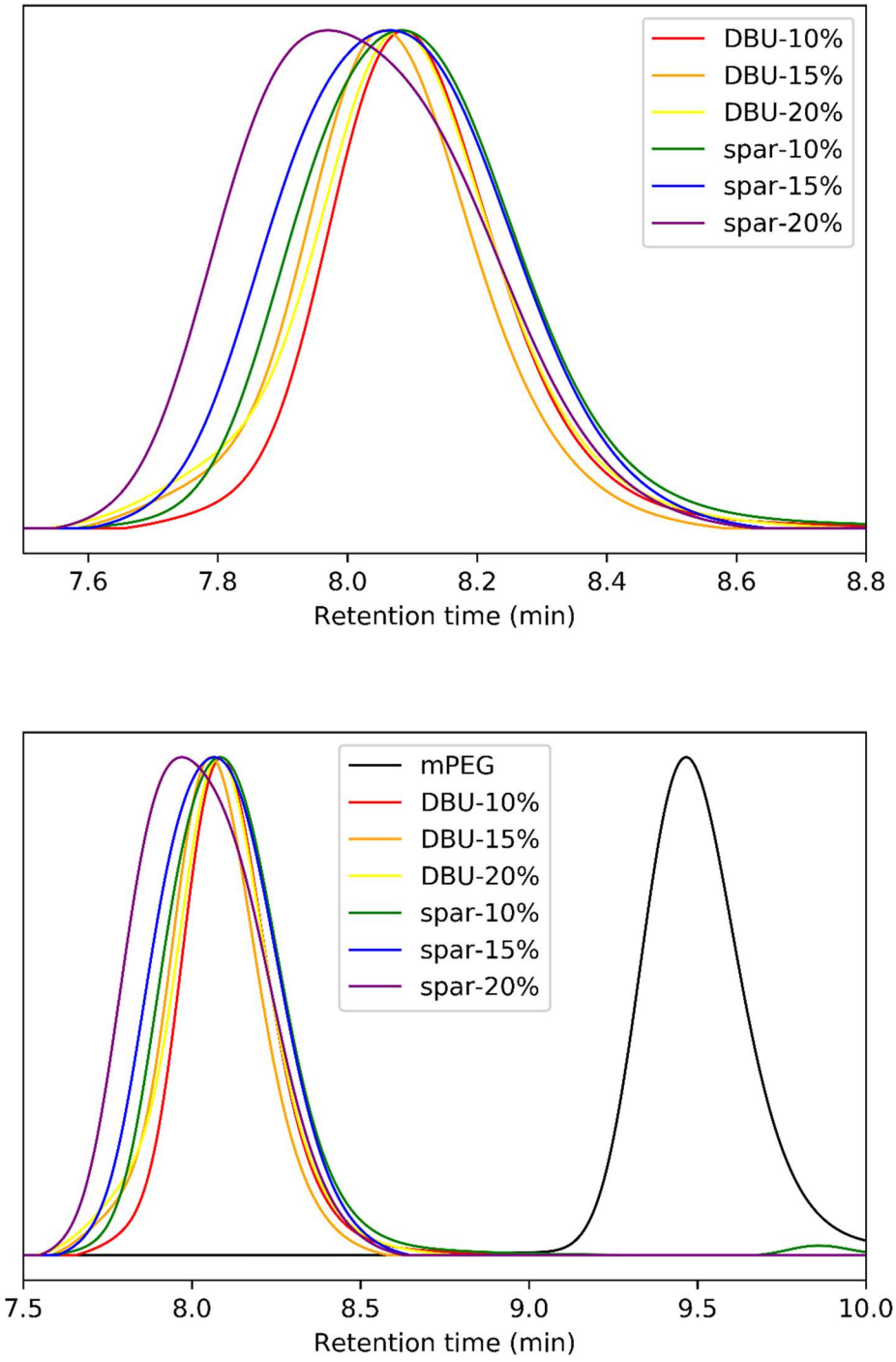

Figure B.2: SEC traces of $PLLA_{200}$-*b*-PEG_{45} synthesized at various solids w/w% with both DBU and (-)-sparteine as co-catalysts. Without (top) and with (bottom) mPEG homopolymer trace to show chain extension. Here the target molecular weight is 16400 but 20% (-)-sparteine ended up having a higher actual molecular weight (18300) which explains the shifted value.

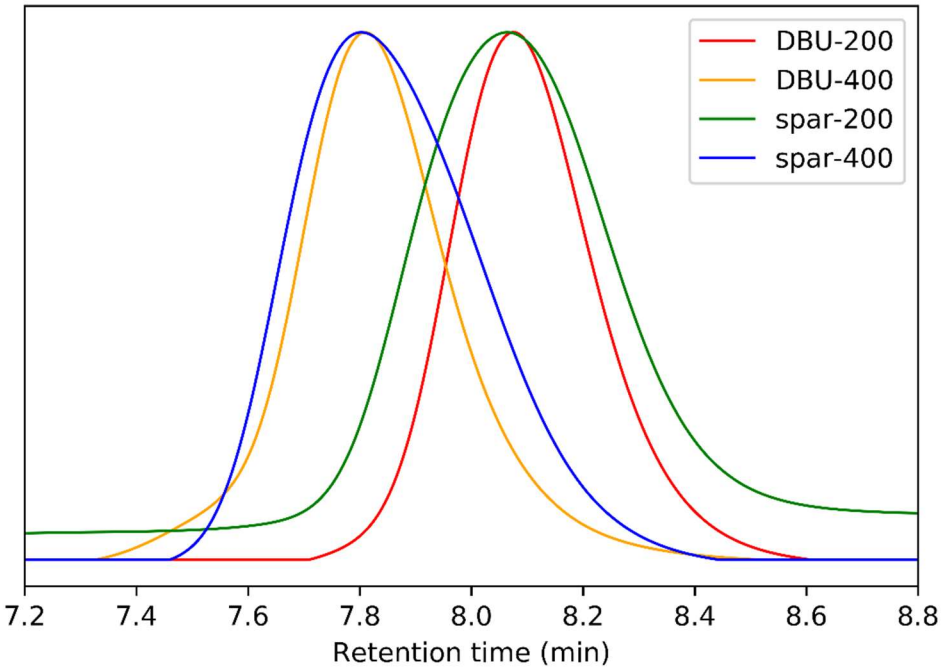

Figure B.3: SEC traces of $PLLA_{200}$-*b*-PEG_{45} and $PLLA_{400}$-*b*-PEG_{45} synthesized at 10% solids w/w% with both DBU and (-)-sparteine as co-catalysts. Đ for all these polymers are similar being between 1.1 and 1.2.

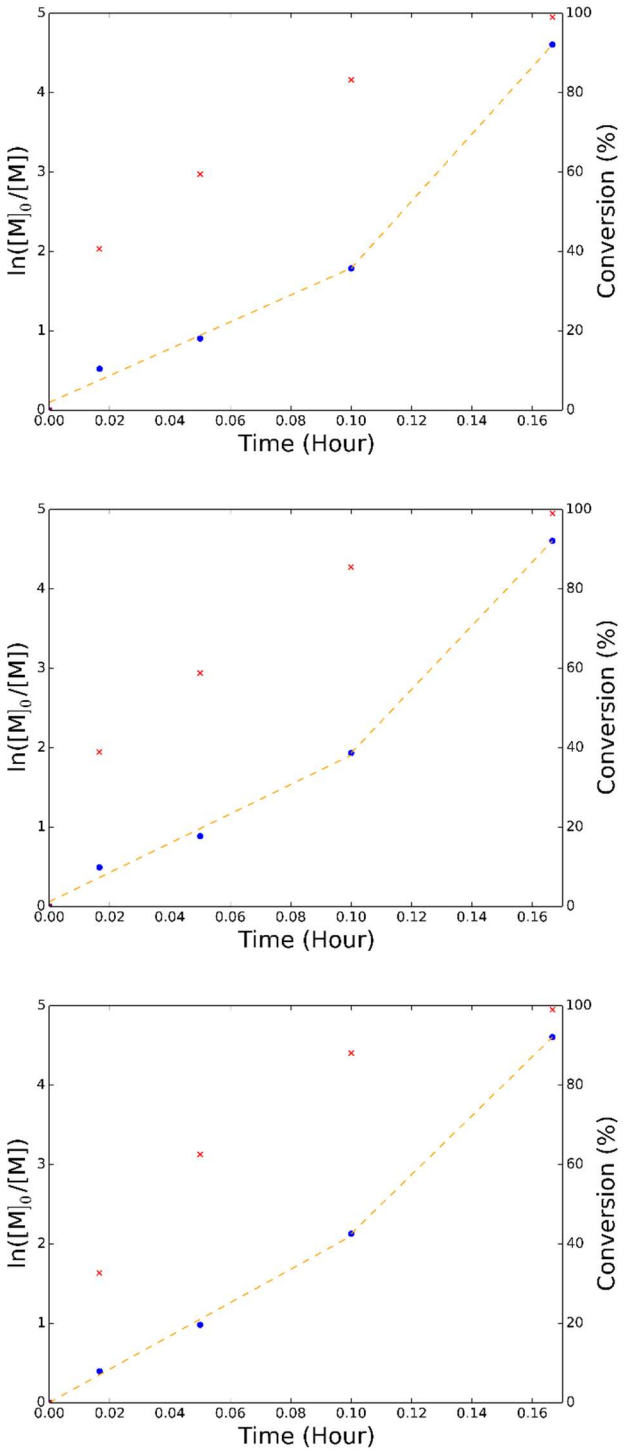

Figure B.4: Polymerization kinetics triplicates for the fast polymerization of L-lactide to form PLLA$_{200}$-*b*-PEG$_{45}$ co-catalyzed by DBU (1% mol). The slope measures k_{app}, the apparent polymerization propagation rate constant. k_{app} shows an uptick near the end of the polymerization when turbidity is noted visually or by UV/Vis. The red ticks represent the conversion % of L-lactide into poly(L)-lactide.

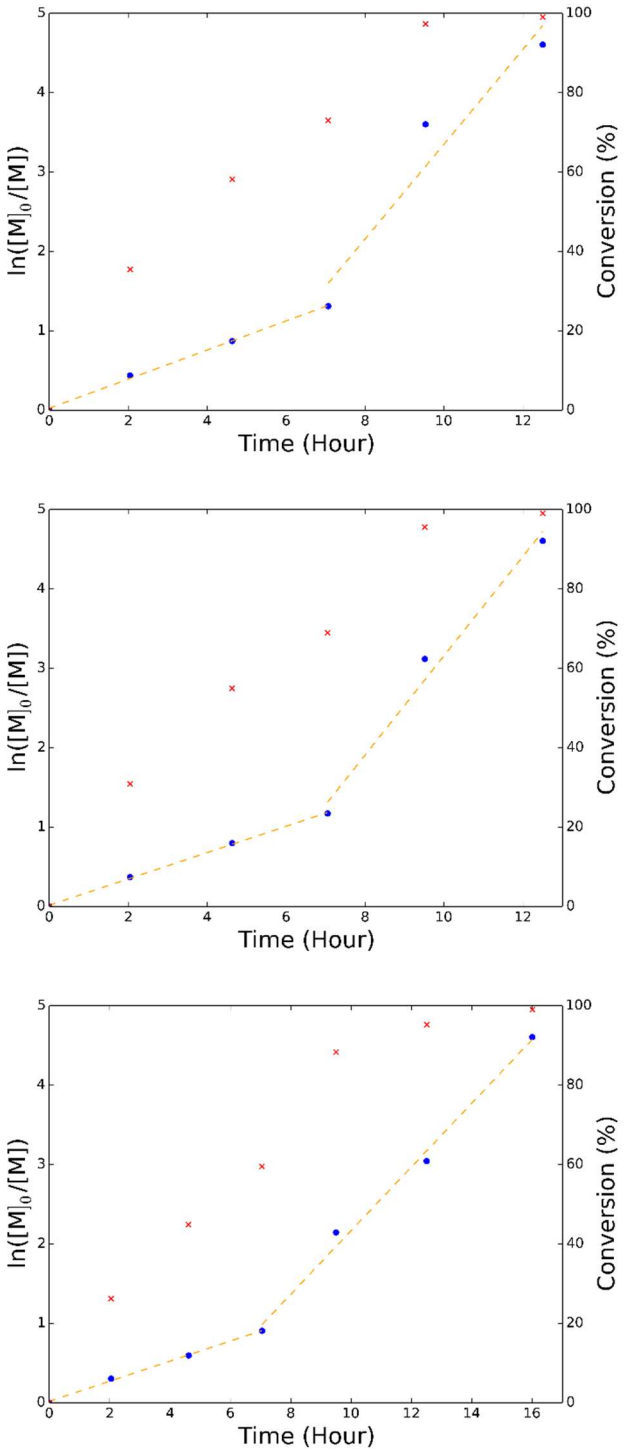

Figure B.5: Polymerization kinetics triplicates for the slow polymerization of L-lactide to form PLLA$_{200}$-*b*-PEG$_{45}$ co-catalyzed by (-)-sparteine (7.5% mol). All samples show an uptick in k_{app} slightly midway through the polymerization when turbidity is noted visually or by UV/Vis. The red ticks represent the conversion % of L-lactide into poly(L)-lactide.

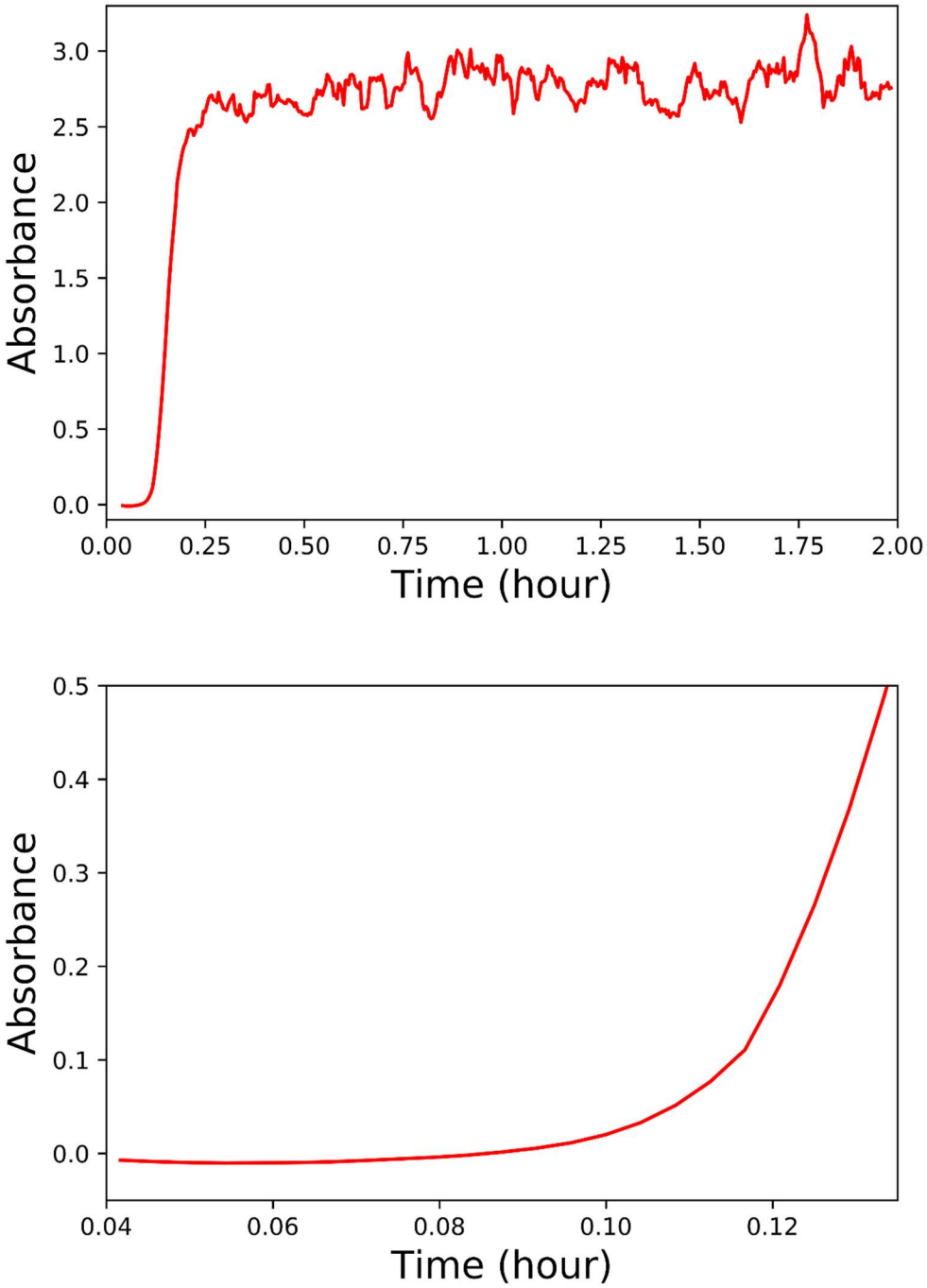

Figure B.6: Turbidity kinetics of the fast DBU co-catalyzed ROPI-CDSA process during both the polymerization of $PLLA_{200}$-*b*-PEG_{45} and time post polymerization. The polymerization was quenched at 0.28 hours into the measurement. The measurement above was taken at 600 nm, a wavelength in which no molecular species present absorb light.

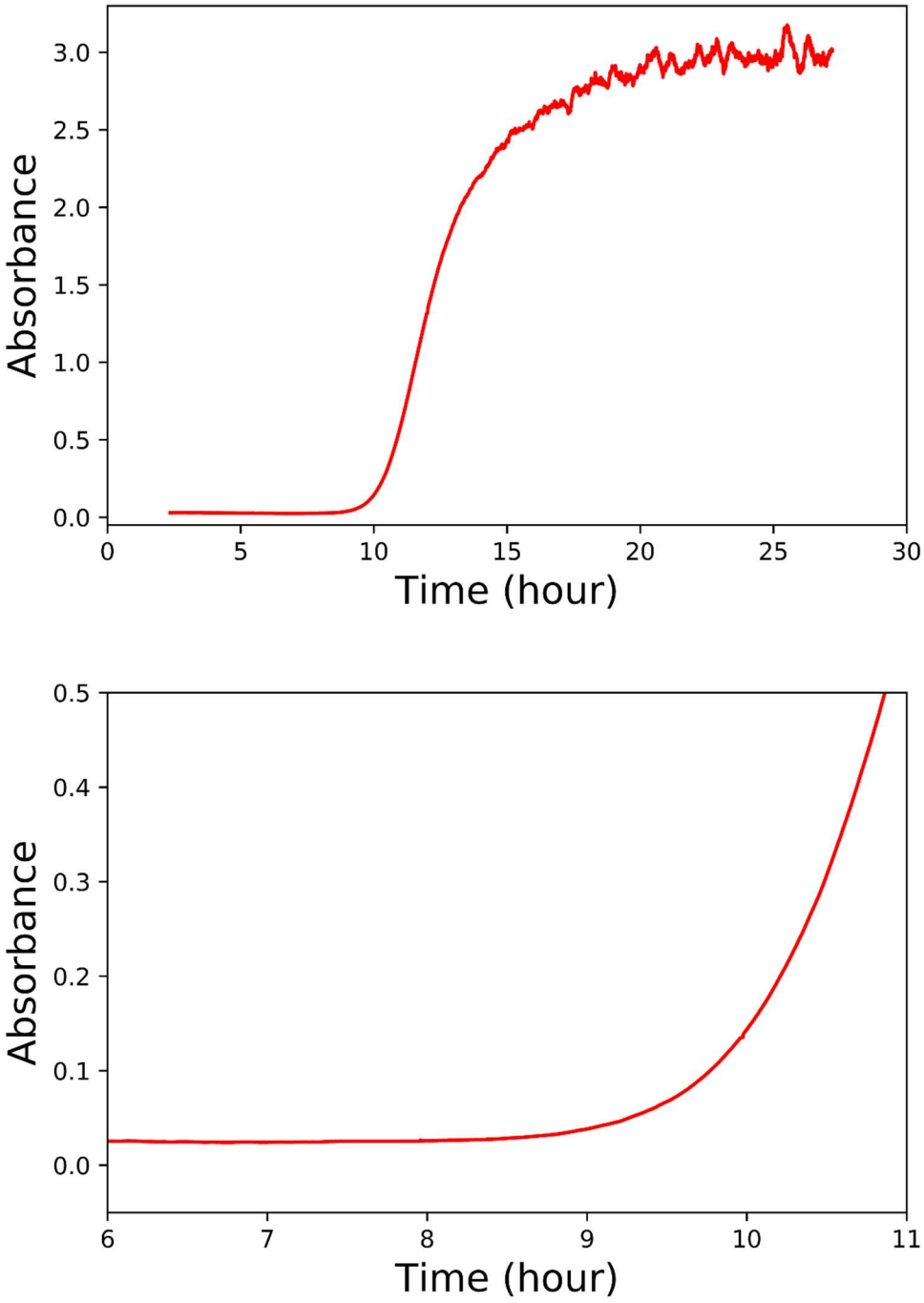

Figure B.7: Turbidity kinetics of the slow (-)-sparteine co-catalyzed ROPI-CDSA process during both the polymerization of $PLLA_{200}$-*b*-PEG_{45} and time post polymerization. The measurement above was taken at 600 nm, a wavelength in which no molecular species present absorb light.

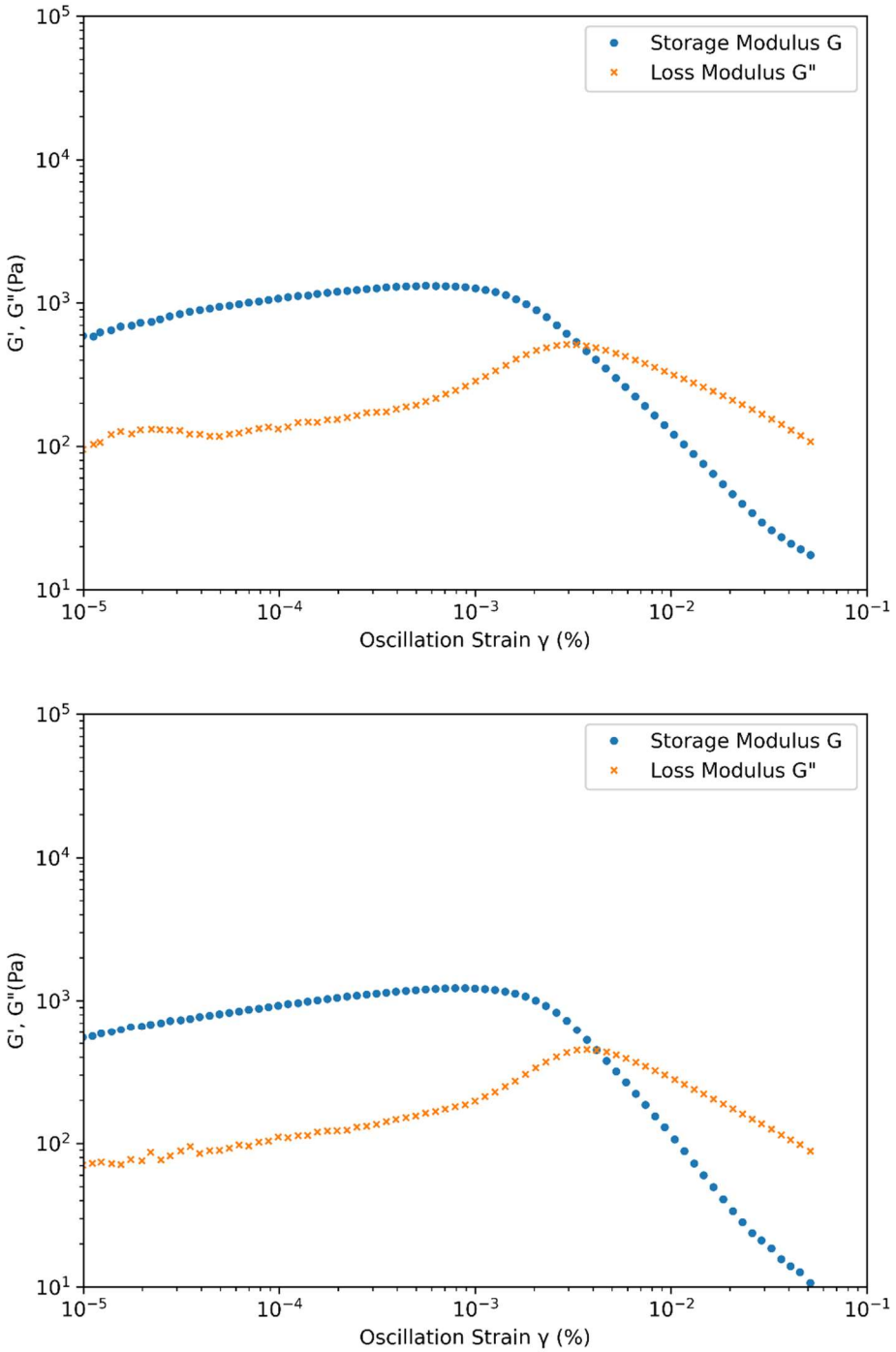

Figure B.8: Oscillatory rheology for organogel **7** ($PLLA_{200}$-*b*-PEG_{45}, 10% w/w solids, (-)-sparteine co-catalyst) top and a sample of **7** that had 1% mol DBU immediately after quenching the polymerization through the addition of benzoic acid. No significant difference in the storage or loss moduli was detected between the samples indicating that catalyst differences likely don't play a role in morphological differences.

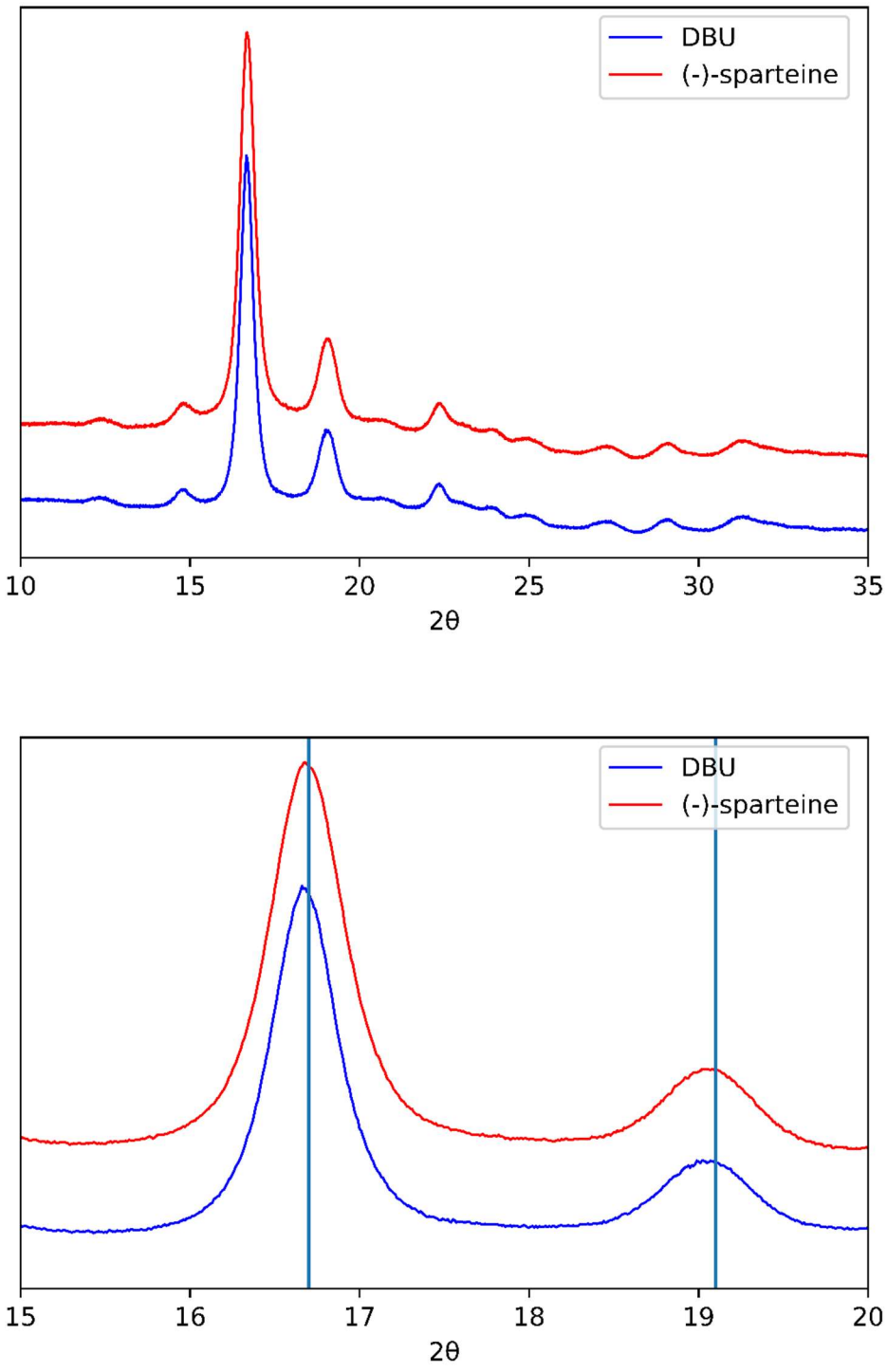

Figure B.9: WAXS patterns of samples **6** and **12**, $PLLA_{400}$-*b*-PEG_{45}.

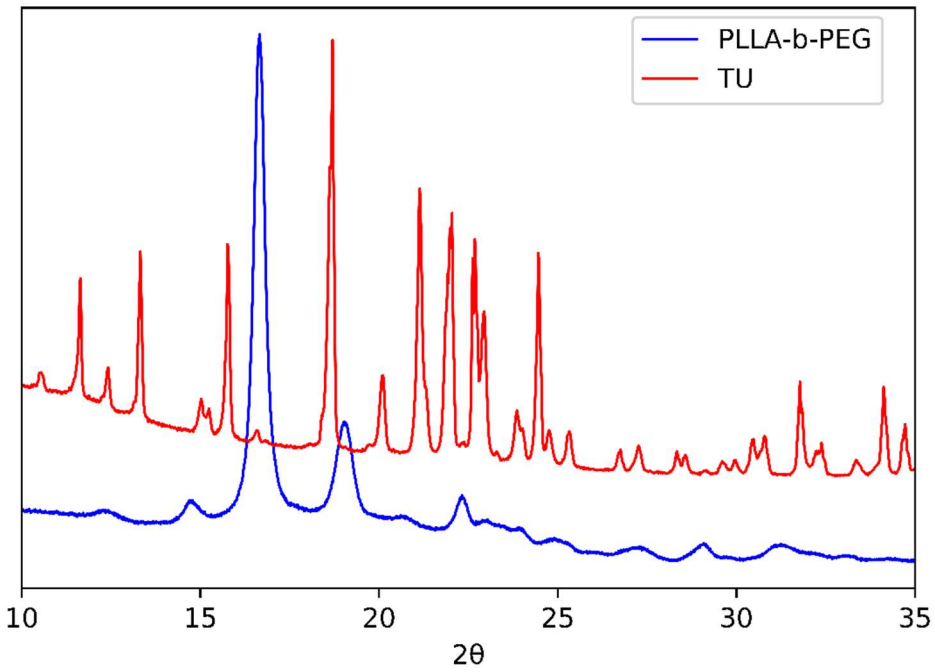

Figure B.10: WAXS pattern of PLLA-*b*-PEG (sample **7**) and TU. The lack of overlap indicates a lack of TU crystallization despite a loading of 7.5% mol TU relative to the monomer in each sample.

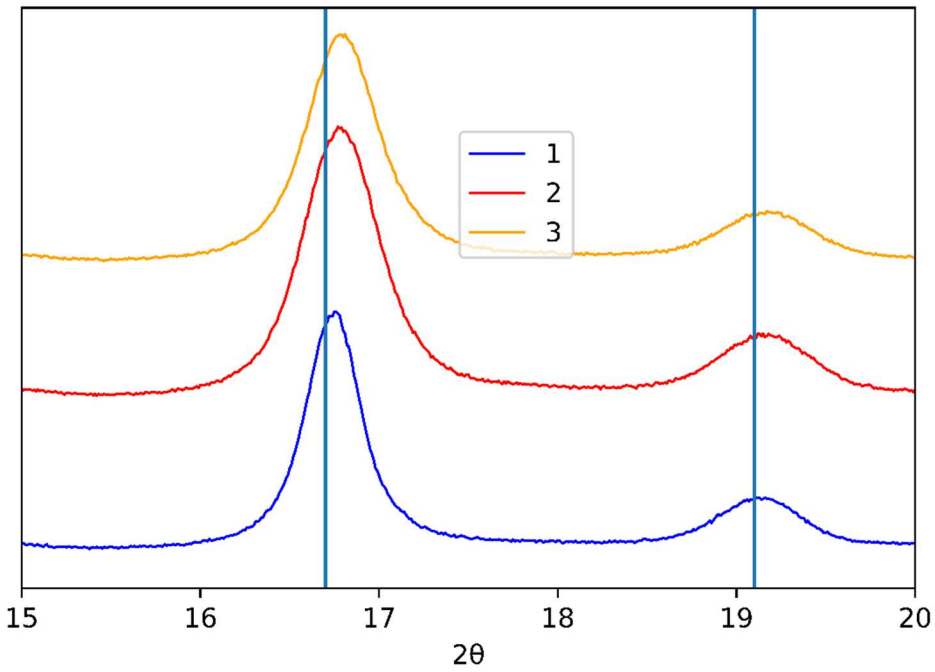

Figure B.11: Triplicate runs of WAXS from triplicates samples (**7**-**9**) of (-)-sparteine co-catalyzed $PLLA_{200}$-*b*-PEG_{45} showing that there are slight peak shifts from sample to sample. The average peak values here are 16.78 ± 0.03 and 19.14 ± 0.03.

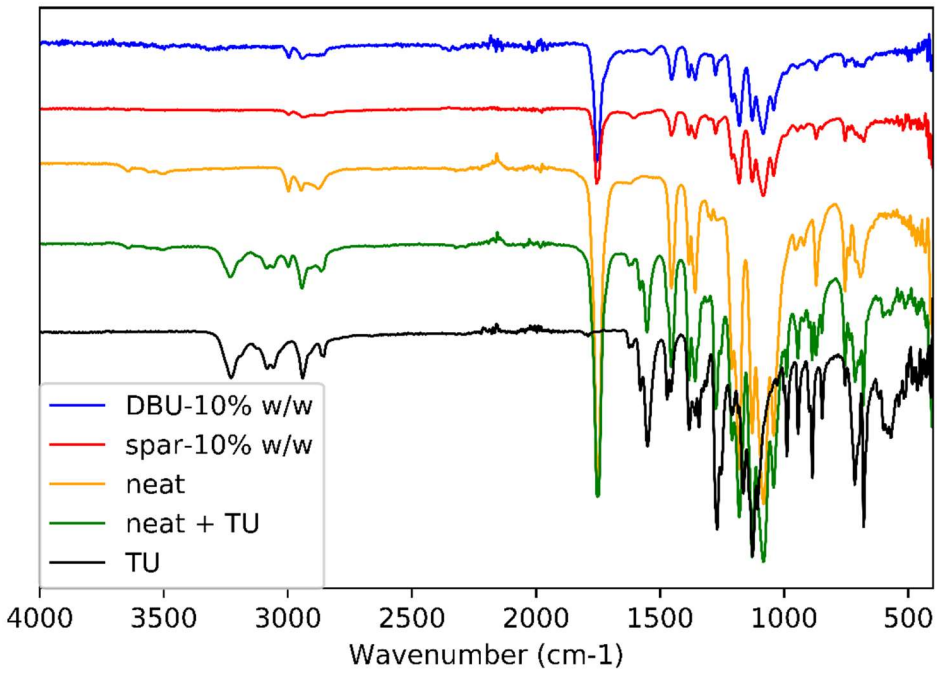

Figure B.12: Full FTIR spectra for PLLA$_{200}$-*b*-PEG$_{45}$ freeze-dried samples at 10% w/w, neat PLLA$_{200}$-*b*-PEG$_{45}$, neat PLLA$_{200}$-*b*-PEG$_{45}$ spiked with 7.5% mol thiourea (TU) and TU. Notable is a lack of N-H stretches in the experimental samples which is an indicator that the N-H groups in the TU are hydrogen bonding with C=O. Purified (neat) polymer mixed with TU shows the same peaks as a TU sample, indicating a lack of supramolecular interactions between neat polymer and TU.

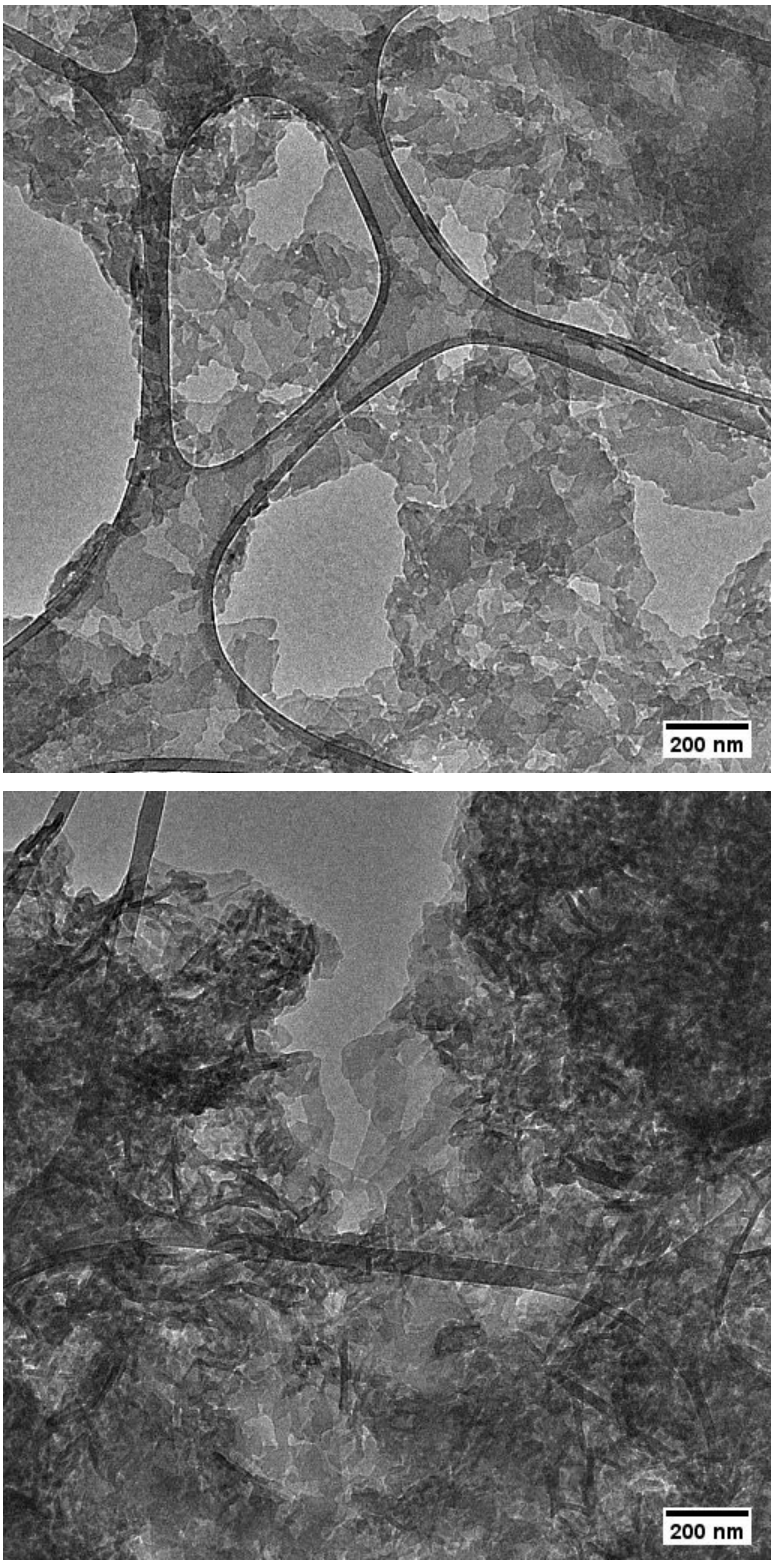

Figure B.13: Additional dry cryoTEM images. Structures from fast polymerization (top) and slow polymerization (bottom).

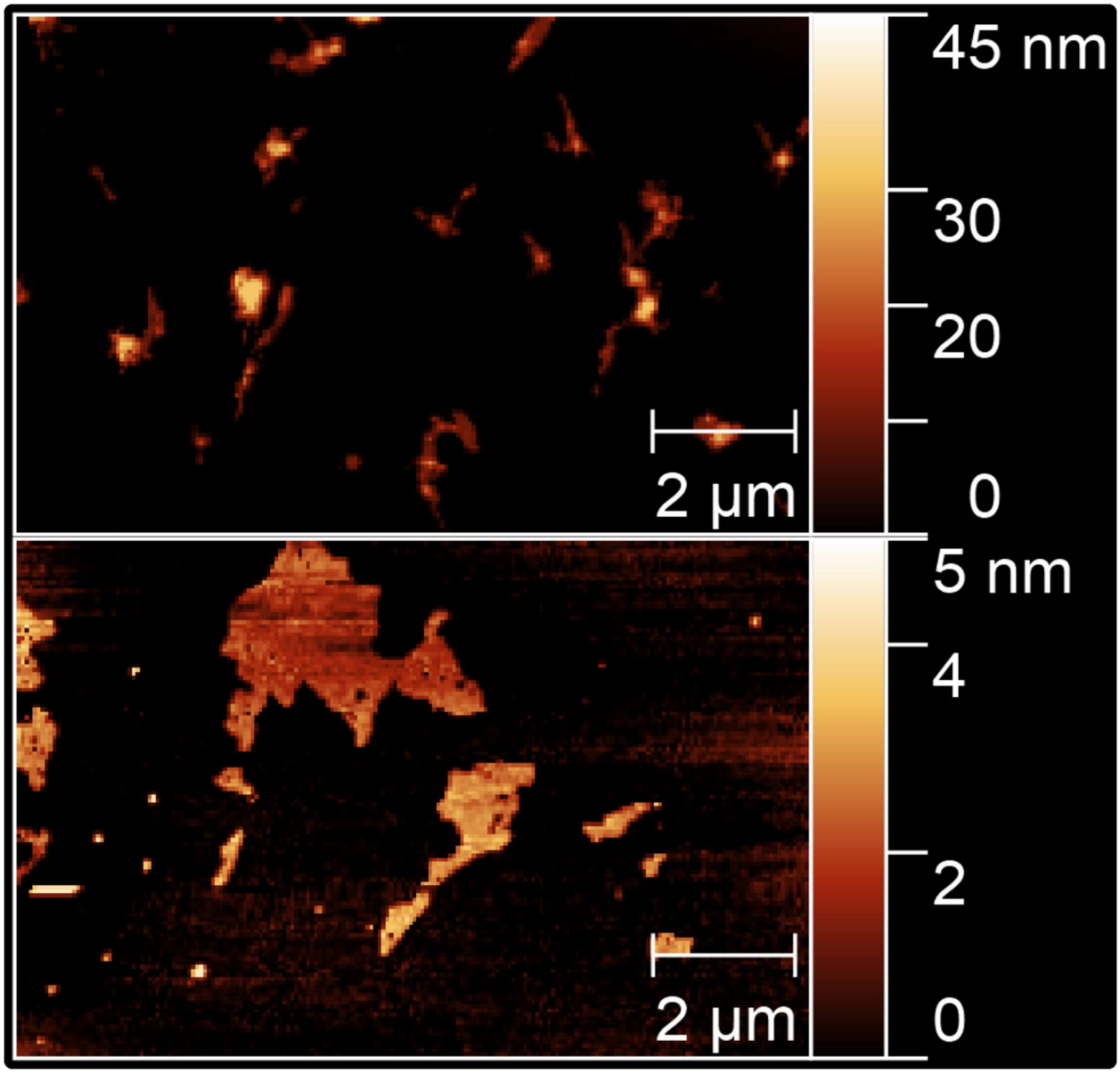

Figure B.14: AFM image in main paper with appropriate scale bars for individual images. Structures from fast polymerization (top) and slow polymerization (bottom).

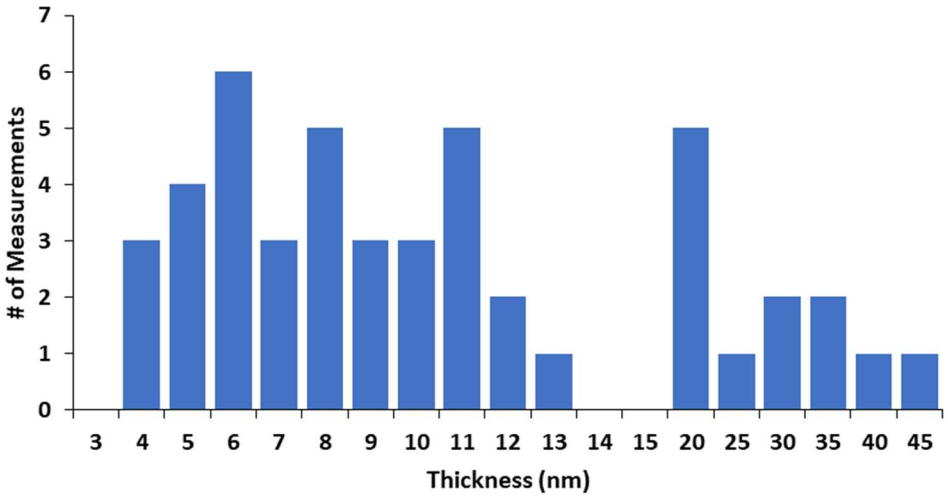

Figure B.15: Histogram of AFM measurements for PLLA$_{200}$-*b*-PEG$_{45}$ co-catalyzed by DBU. This histogram includes the thicker measurements above 15 nm which were excluded from the main text.

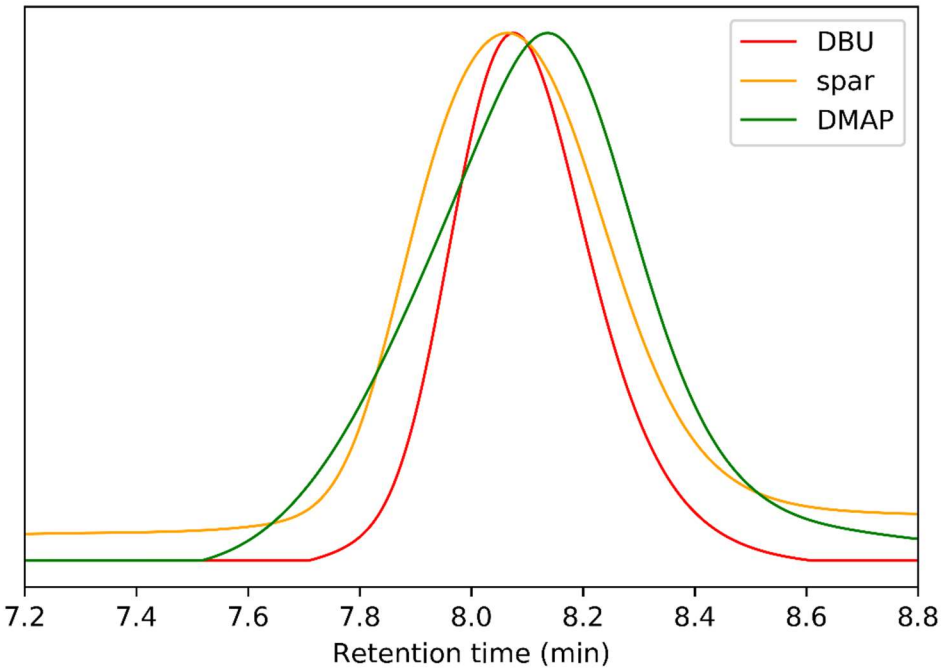

Figure B.16: SEC of PLLA$_{200}$-*b*-PEG$_{45}$ synthesized using DBU, (-)-sparteine, and DMAP as cocatalysts. The Đ of DMAP is significantly higher than DBU and (-)-sparteine.

Appendix C: Supplementary Information for Chapter 4

C.1. Supplementary Tables

Table C.1: Acylation control experiments: Run 1 is the condition discussed in the main text.

Run	Vinyl acetate to CHX Ratio	Conditions	Conversion
1	20:1	2.4 mL DCM 0.3 mL DMSO	10%
2	20:1	2.7 mL DCM 0.05 m2PEG	8.3%
3	10:1	2.7 mL DCM 0.05 m2PEG + 35 °C	20%
4	10:1	2.7 mL DCM	<1%

Table C.2: Synthetic conditions for chlorhexidine based ROPI-CDSA

Sample ID	Solids w/w %	L-lactide (mg)	mPEG (mg)	Chlorhex. (mg)	Toluene (mL)
1-C	10	259	80	45.5	4.00
2-C	10	389	80	68.2	5.58
3-C	20	195	80	34.1	1.61
4-C	20	259	80	45.5	1.78
5-C	20	389	80	68.2	2.48

Table C.3: Synthetic conditions for chlorhexidine based ROPI-CDSA

Sample ID	Solids w/w %	L-lactide (mg)	mPEG (mg)	Trimethop. (mg)	Toluene (mL)	DMSO (mL)
6-T	20	259	160	13.2	2	0.1
7-T	20	389	120	19.5	2.43	0.15

Table C.4: All MIC studies including an extracted sample.

Bacteria	Free[1] CHX	Free CHX t[2]	4-C **RL**	4-C **EX**	Free TMP	6-T **RL**
B. subtilis	0.25	0.25	2	2	0.25	0.5
S. epi.	0.125	0.25	1	2	0.5	1
E. coli	0.25	0.25	2	2	0.25	1

1. Free Drug is the drug in its freebase form
2. Sample contains trace toluene identical to 4-D EX
3. RL= resuspension following lyophilization, EX=extracted and diluted from toluene into water

C.2. Supplementary Figures

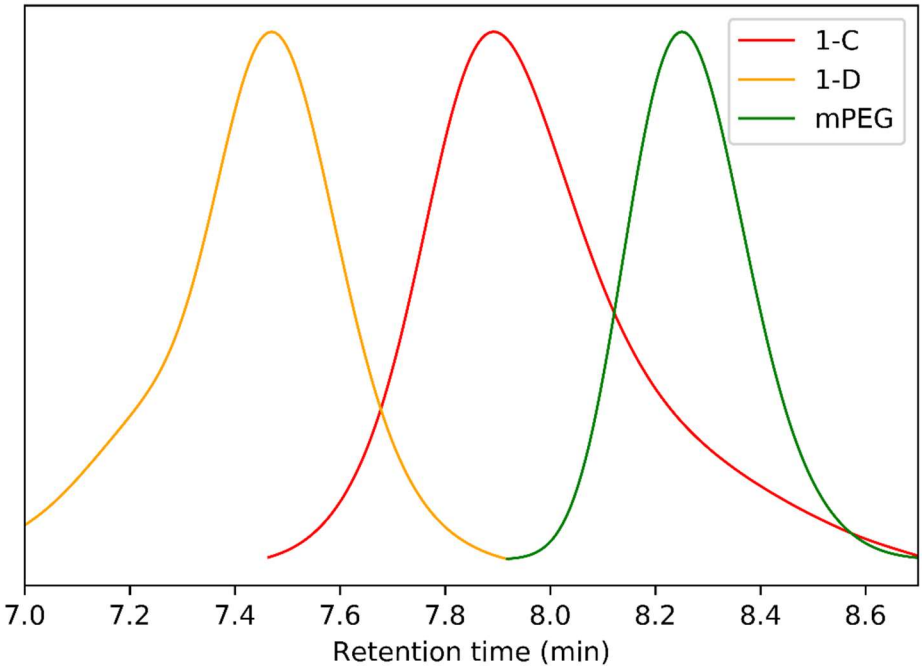

Figure C.1: GPC trace showing that **1-C** has a longer retention time than that of **1-D**, a sample identical to **1-C** in setup except that chlorhexidine is swapped for DBU.

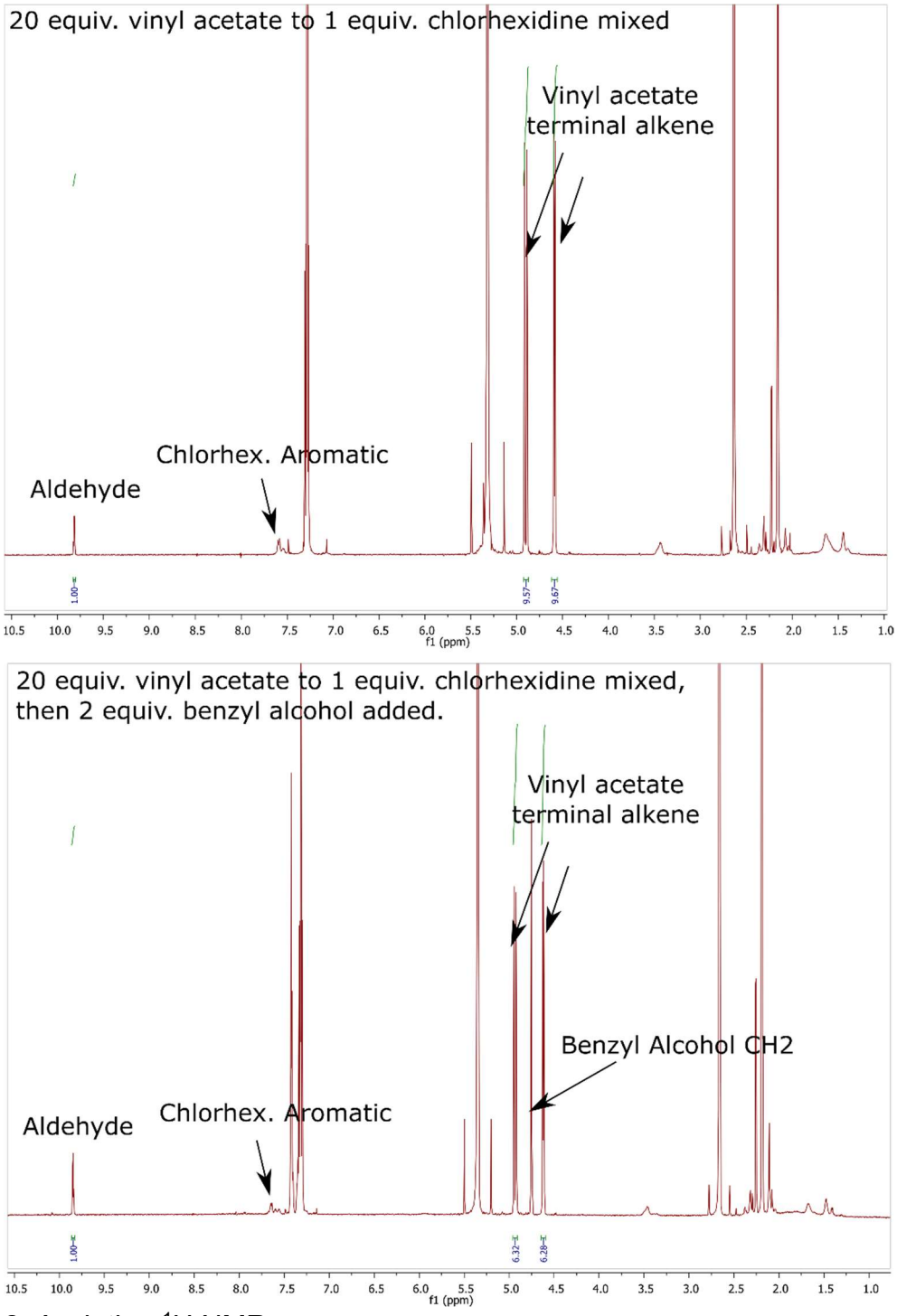

Figure C.2: Acylation ^{1}H NMR

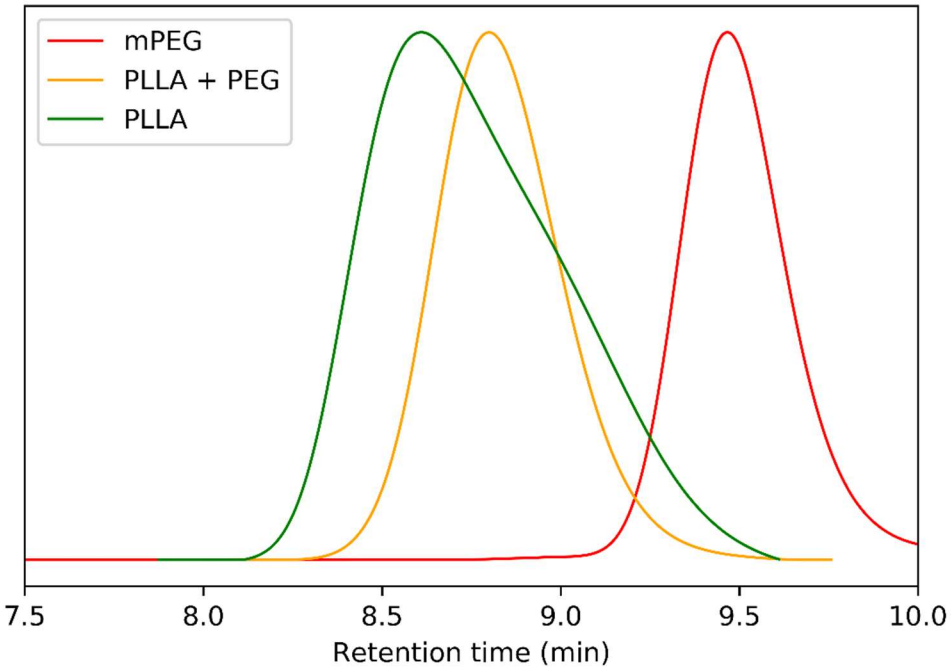

Figure C.3: Homopolymer GPC results

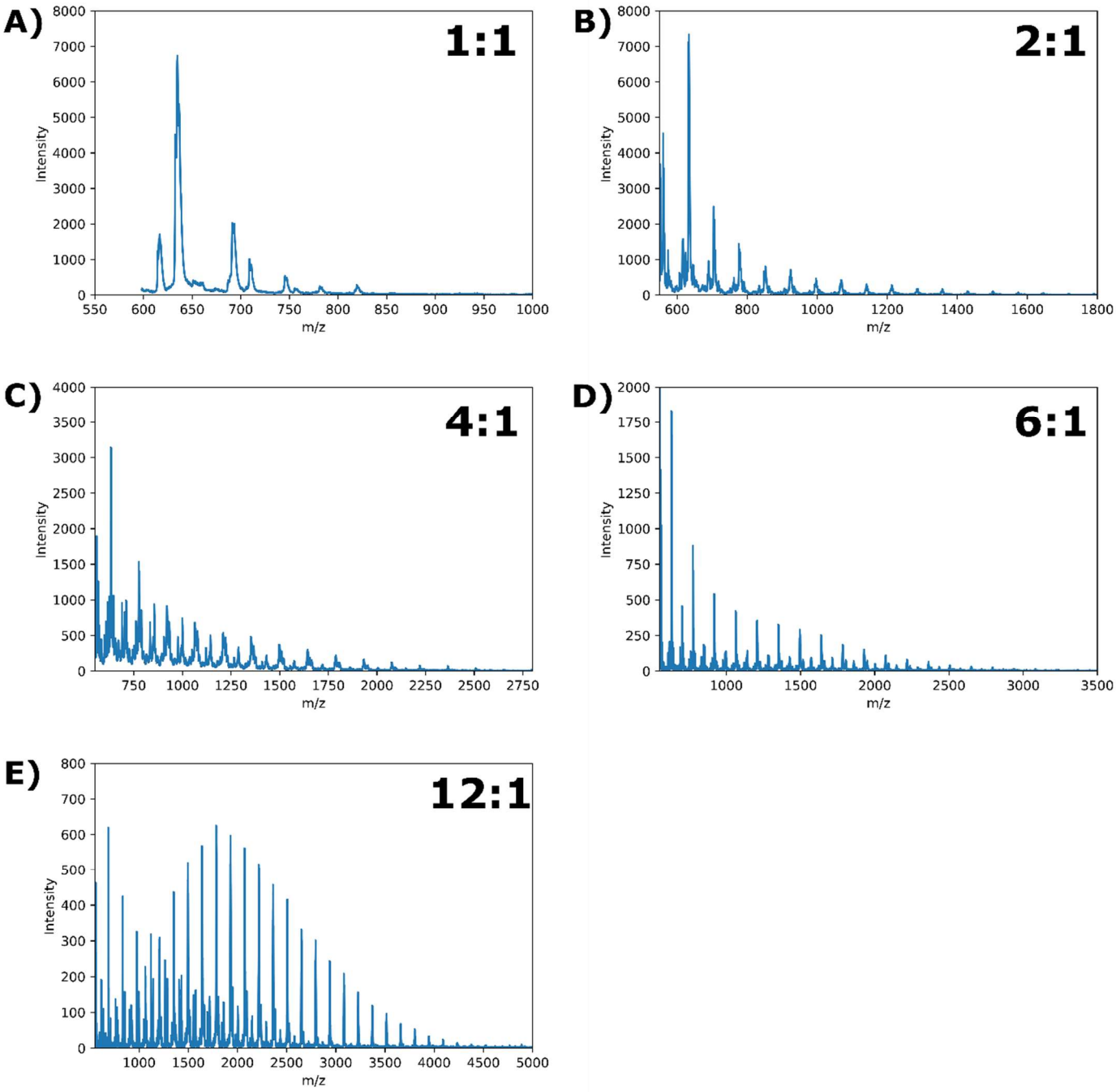

Figure C.4: MALDI spectra of chlorhexidine initiated PLLA homopolymers. The ratio at the top right of each spectrum represents the ratio of L-lactide to chlorhexidine in each reaction. Peaks in the spectra are approximately 144 or 72 Da (mass unit) apart. The 72 Da is from transesterification. The lowest mass polymer peaks appear at 631 or 559 m/z corresponding to a loss of water (approximately 18 mass units) as chlorhexidine is approximately 505 Da apart.

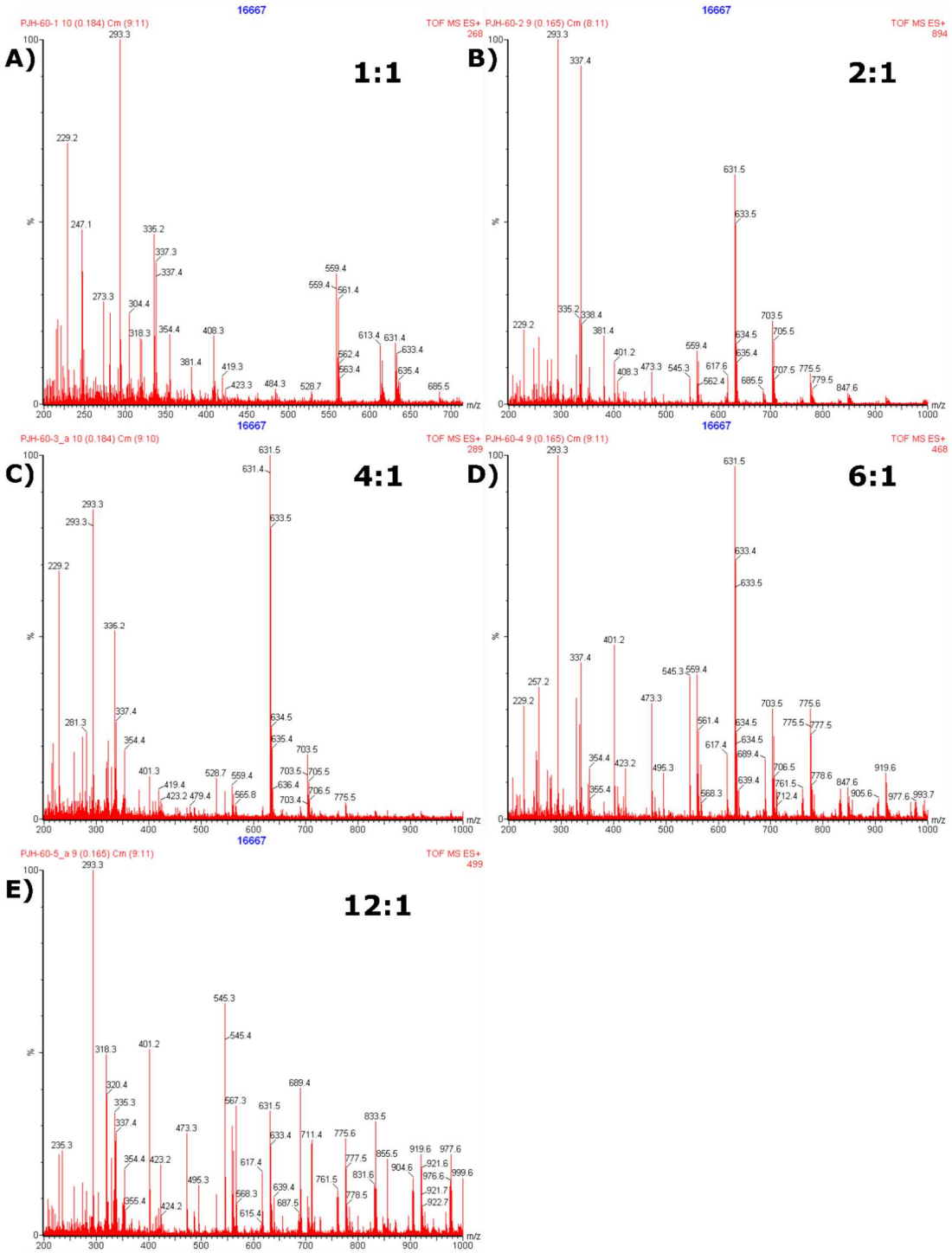

Figure C.5: ESI spectra of chlorhexidine initiated PLLA homopolymers. The ratio at the top right of each spectrum represents the ratio of L-lactide to chlorhexidine in each reaction. Peaks in the spectra are approximately 144 or 72 Da. The 72 Da is from transesterification. The lowest mass polymer peaks are 631 or 559 m/z corresponding to a loss of water (approx.. 18 mass units) as chlorhexidine is approximately 505 Da.

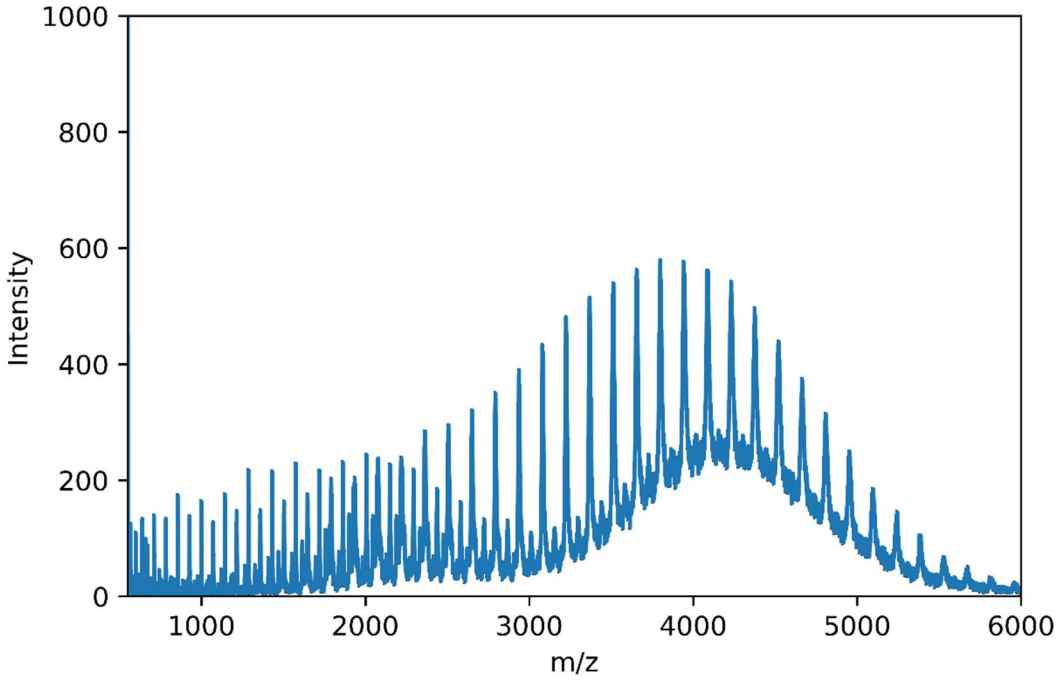

Figure C.6: Representative MALDI spectrum for drug catalyzed ROPI-CDSA (**4-C**). This MALDI spectrum shows the chlorhexidine initiated PLLA homopolymer. PLLA-b-PEG was not detectable with our protocol as a MALDI run of a pure block copolymer yielded a blank signal.

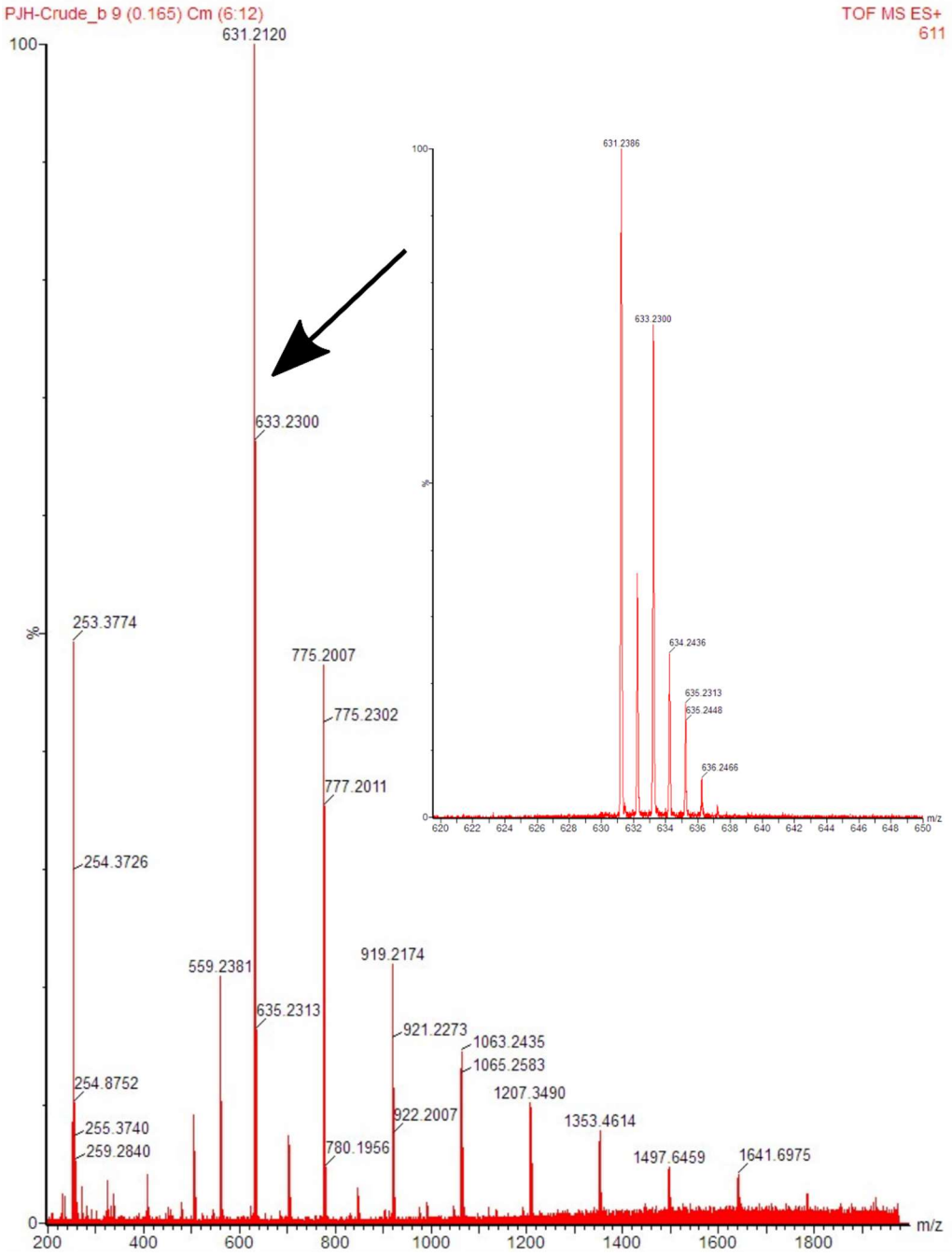

Figure C.7: Representative ESI spectrum for drug catalyzed ROPI-CDSA (**4-C**). This ESI spectrum shows the chlorhexidine initiated PLLA homopolymer. PLLA-b-PEG was not detectable with our protocol as an ESI run of a pure block copolymer yielded a blank signal. An inset in the top right corner shows zoomed in section of 631 Da. The splitting pattern is consistent with an organic molecule that has 2 chlorine atoms.

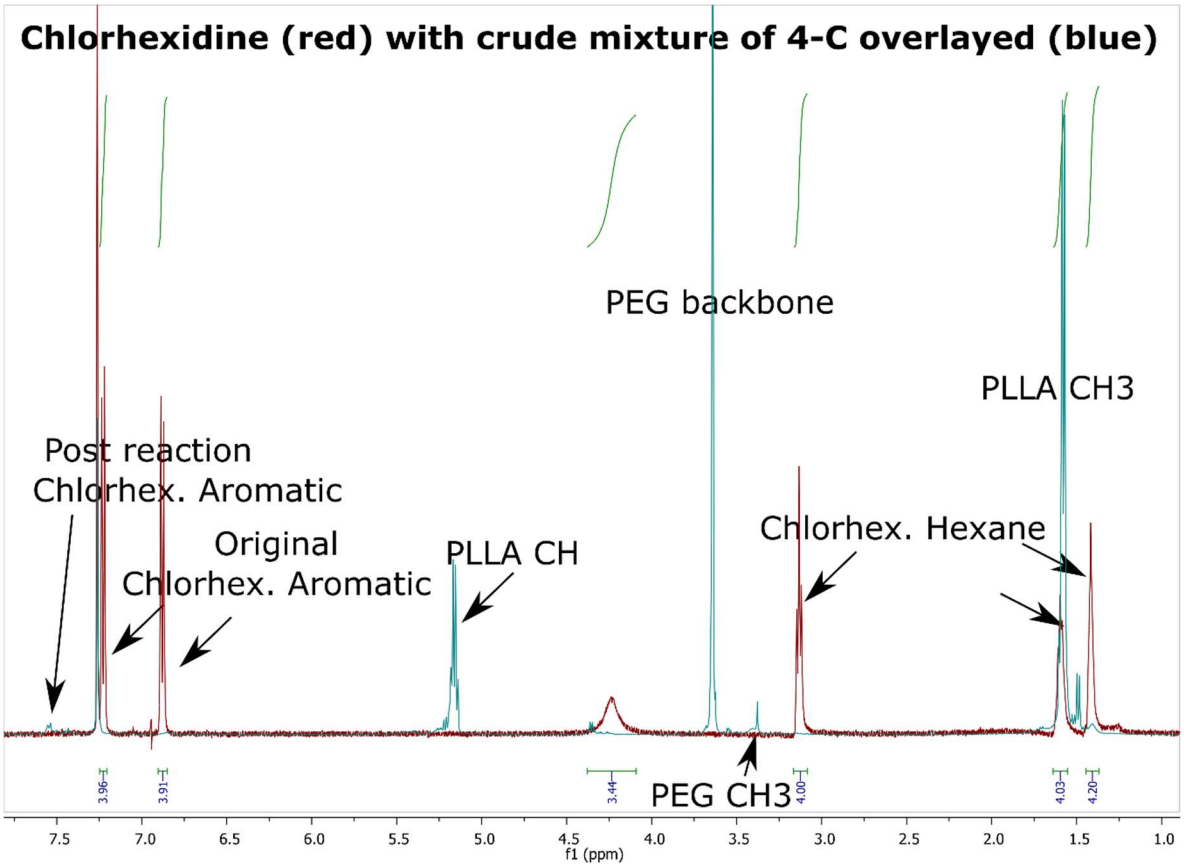

Figure C.8: Chlorhexidine overlayed ^{1}H NMR for a crude mixture of **4-C**. Note that all chlorhexidine peaks disappear from the crude mixture indicating chemical modification of chlorhexidine.

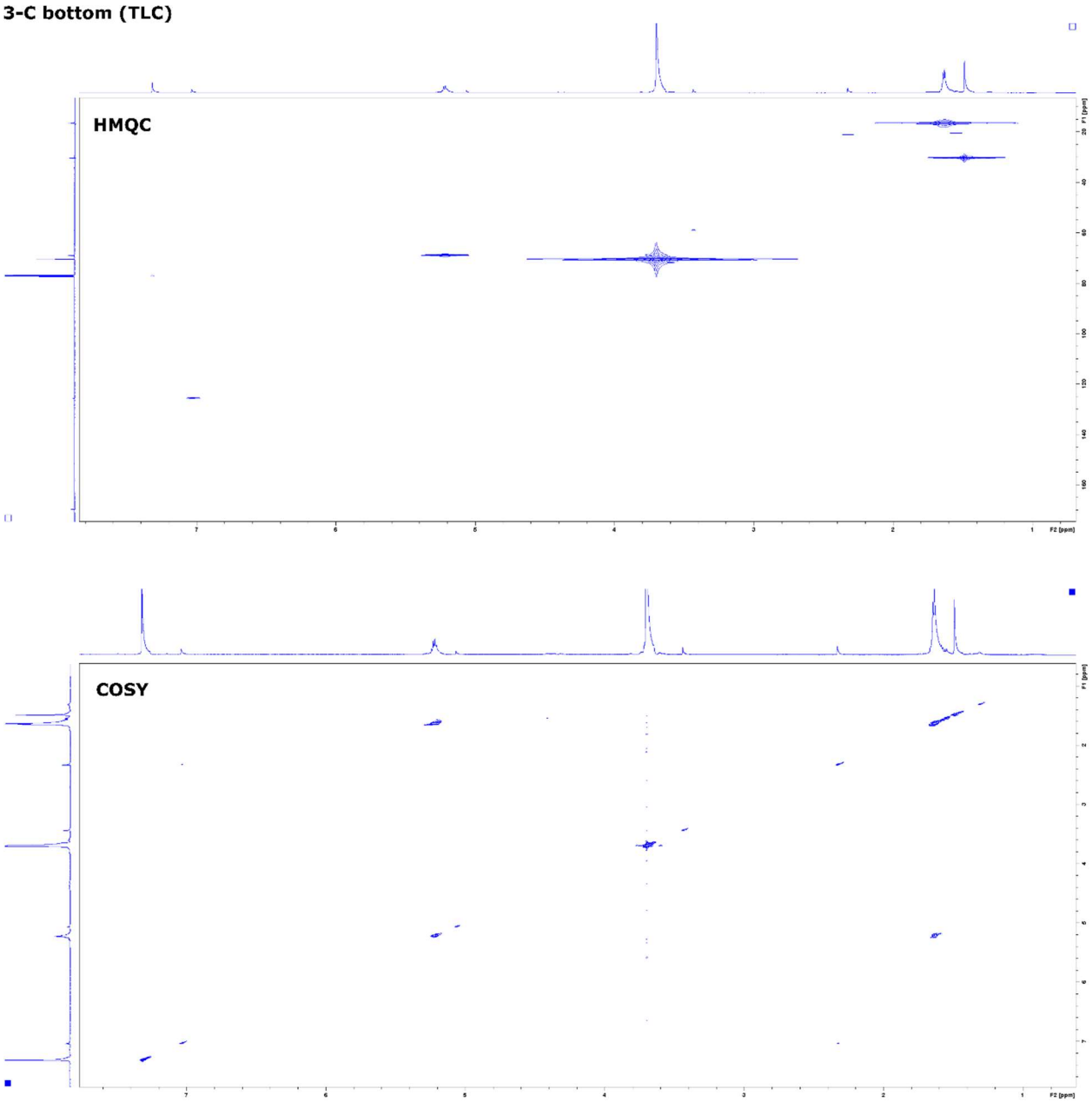

Figure C.9: 2-D NMR of **3-C** bottom TLC spot. The top shows HMQC and the bottom shows COSY. Note the mPEG backbone peak around 3.5 ppm. Note the absence of aromatic peaks around 7.5 ppm.

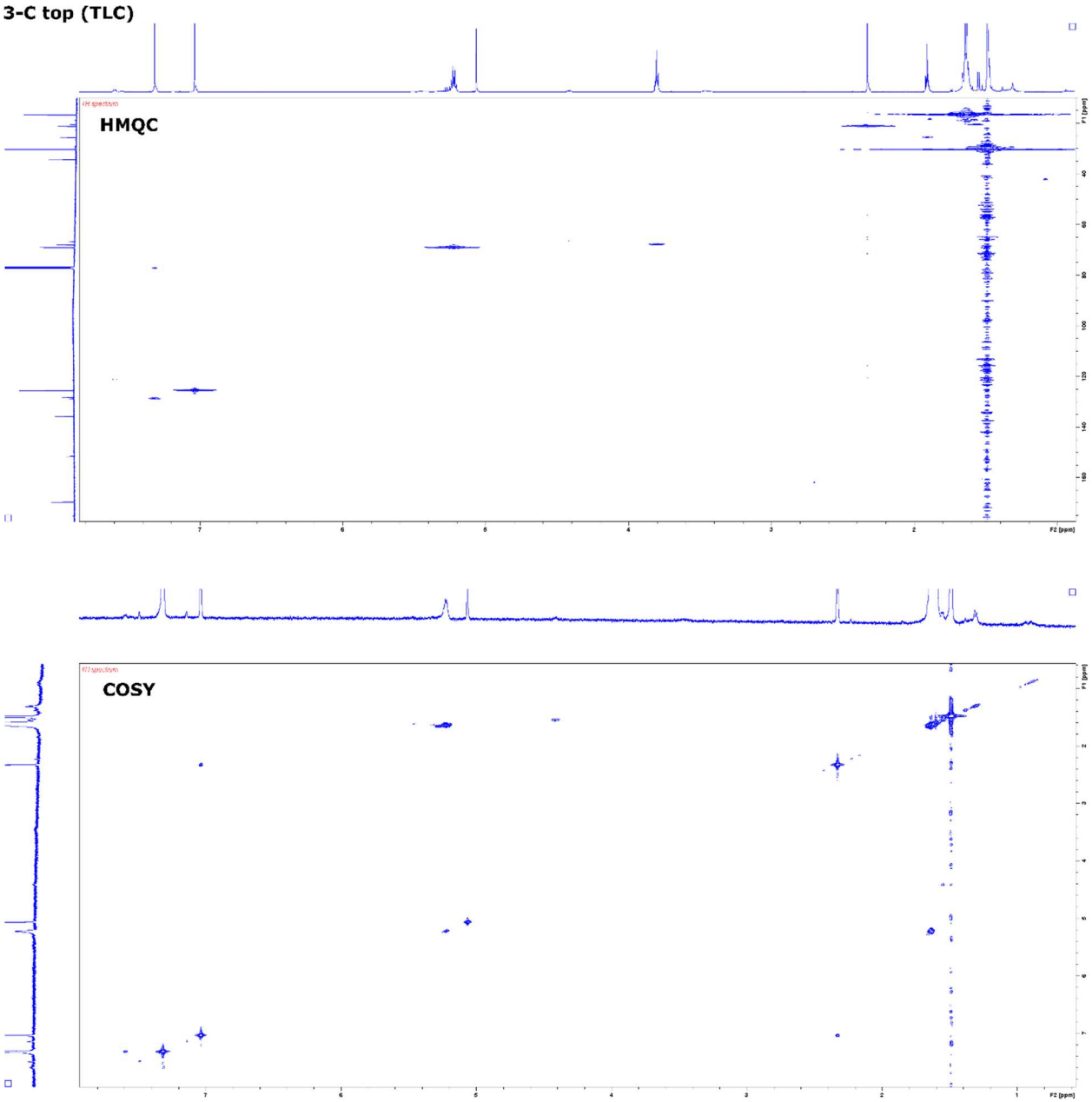

Figure C.10: 2-D NMR 3-C top TLC spot. The top shows HMQC and the bottom show COSY. Note the aromatic peaks around 7.5 ppm signifying chlorhexidine. Note the absence of a mPEG backbone peak around 3.5 ppm.

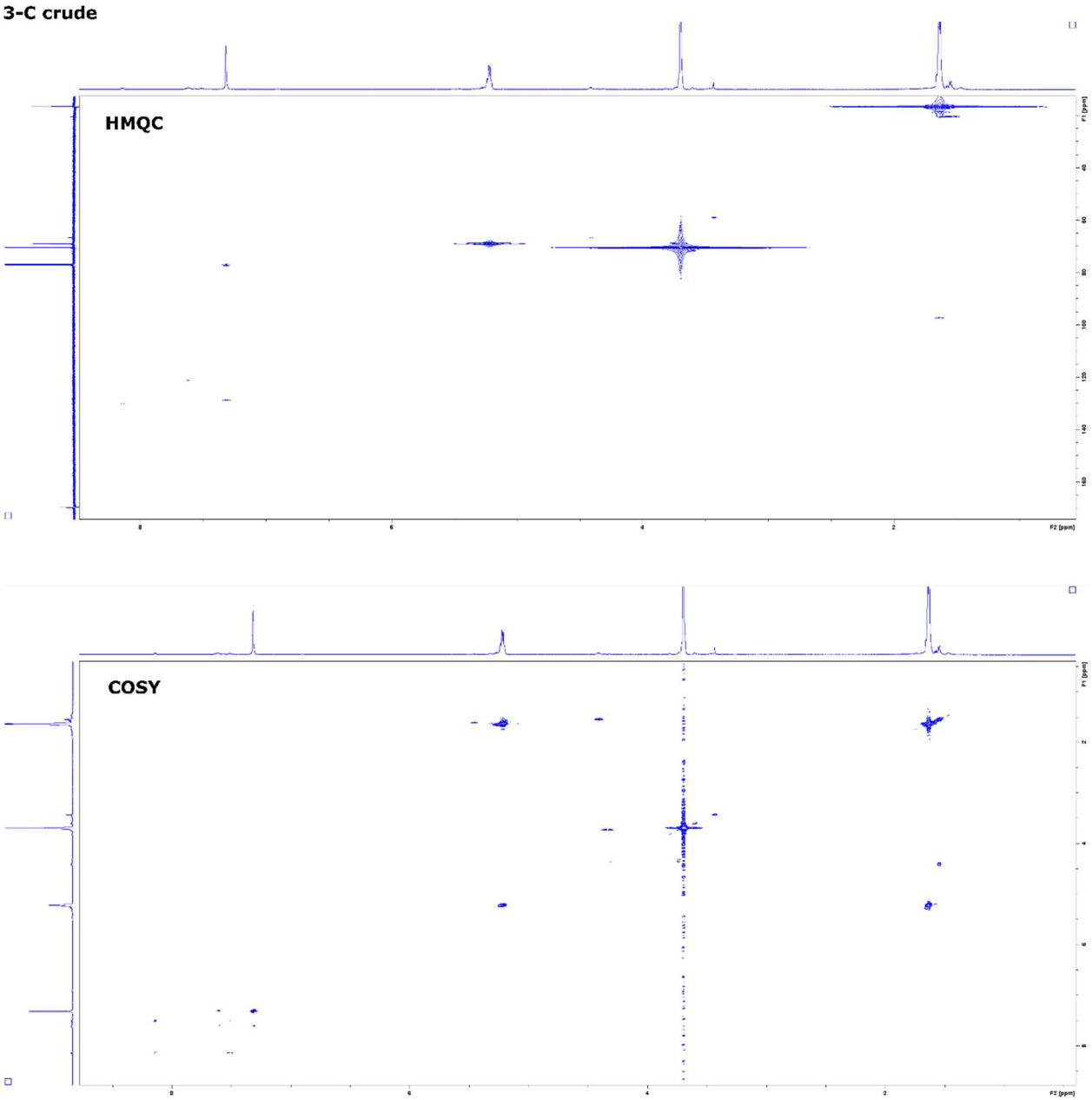

Figure C.11: 2-D NMR 3-C crude. The top shows HMQC and the bottom shows COSY.

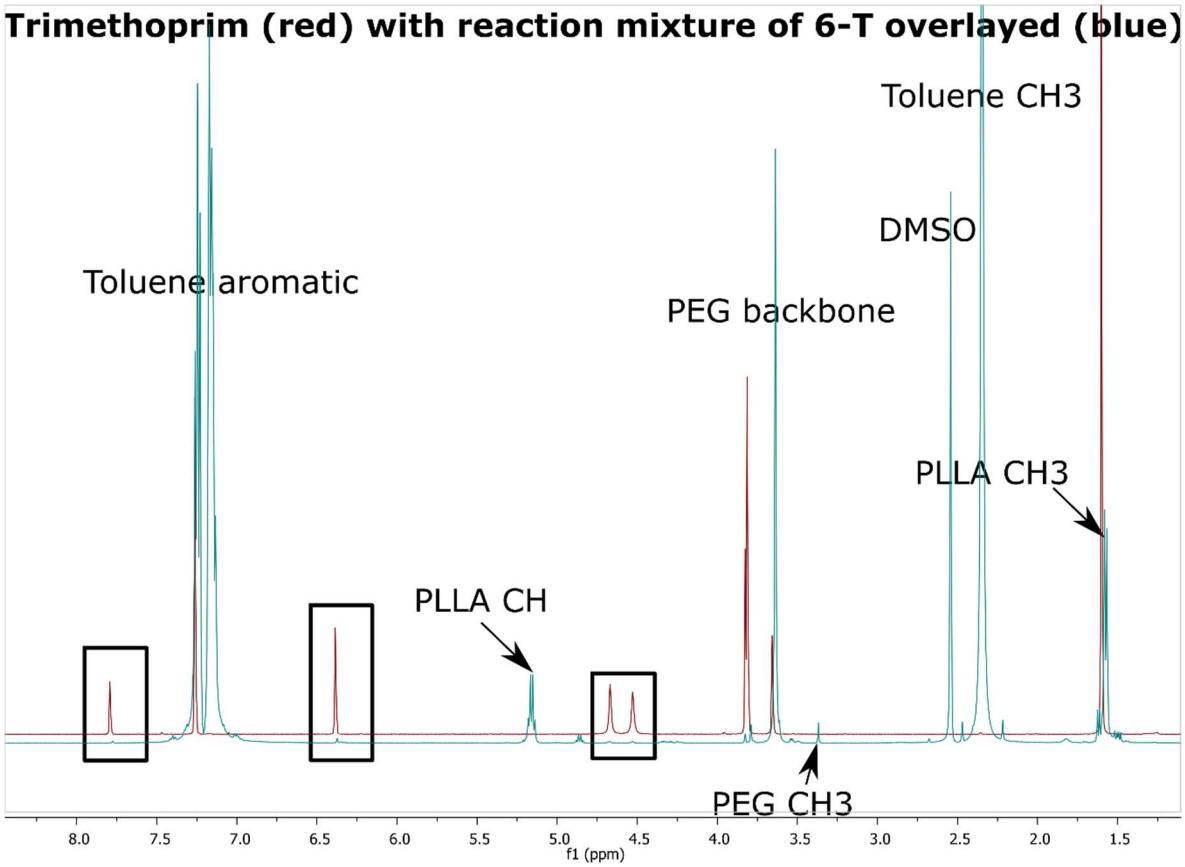

Figure C.12: Trimethoprim ^{1}H NMR. Boxes show non-overlapping trimethoprim peaks suggesting that there is no shift in trimethoprim peaks in a trimethoprim sample (red) with a reaction mixture (**6-T**) using 2.5 mol% trimethoprim.

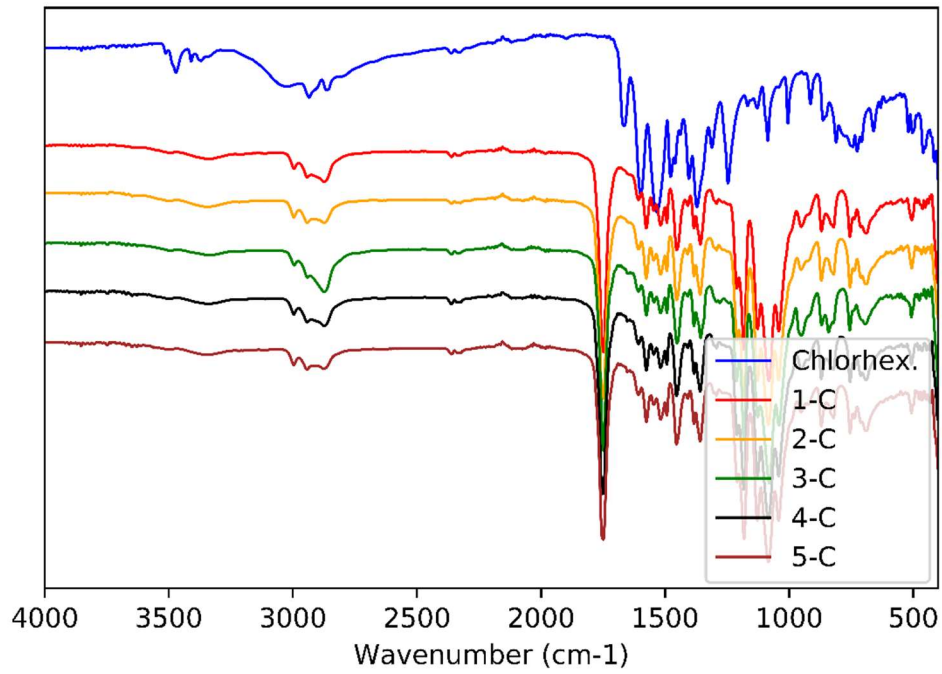

Figure C.13: FTIR spectra of chlorhexidine and chlorhexidine catalyzed ROPI-CDSA polymers.

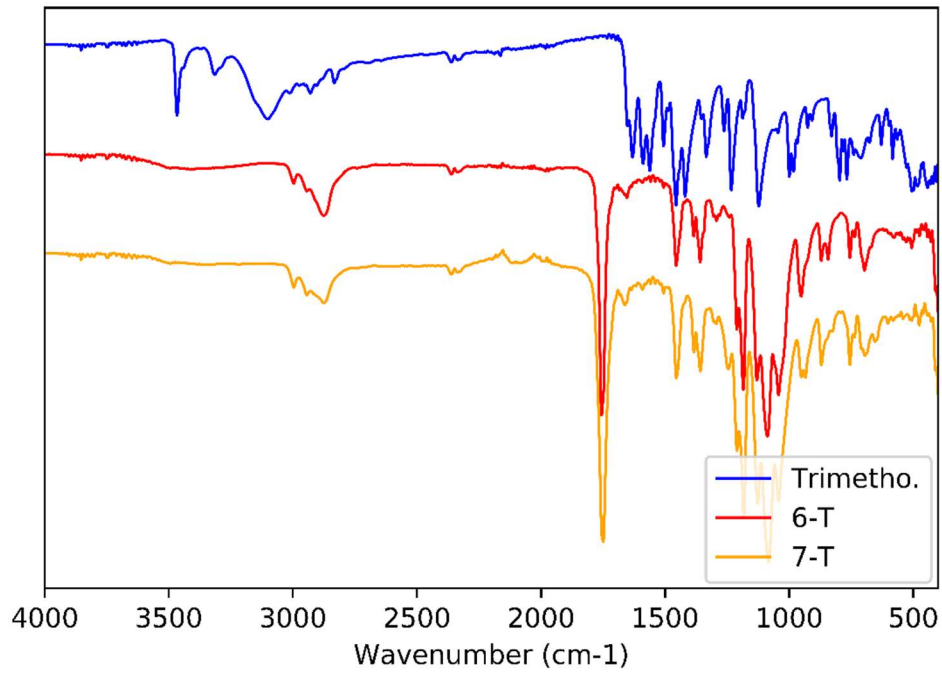

Figure C.14: FTIR spectra of trimethoprim and trimethoprim catalyzed ROPI-CDSA polymers.

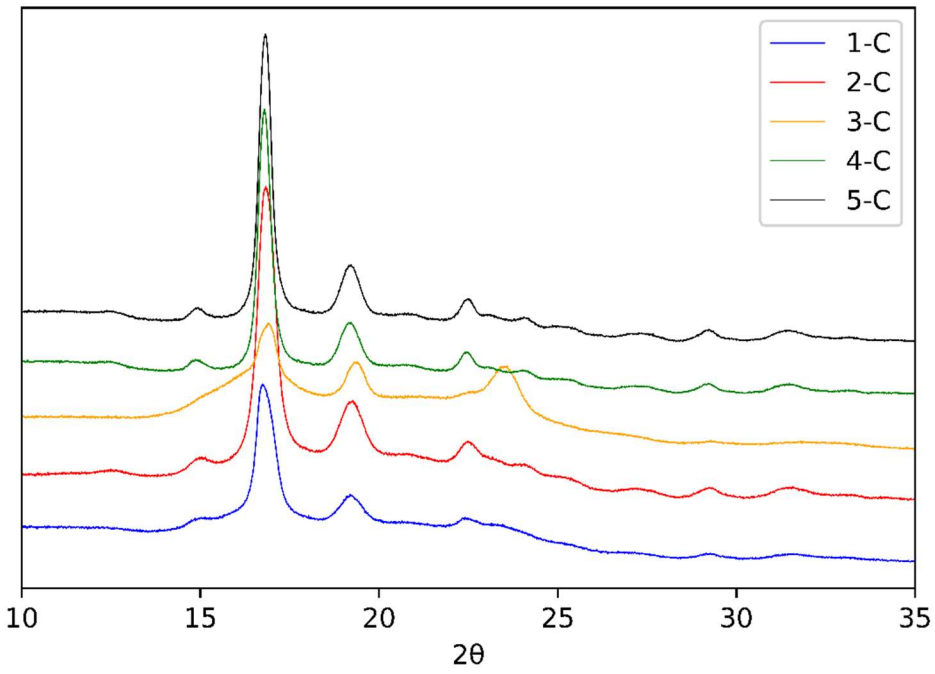

Figure C.15: WAXS patterns of chlorhexidine catalyzed ROPI-CDSA polymers.

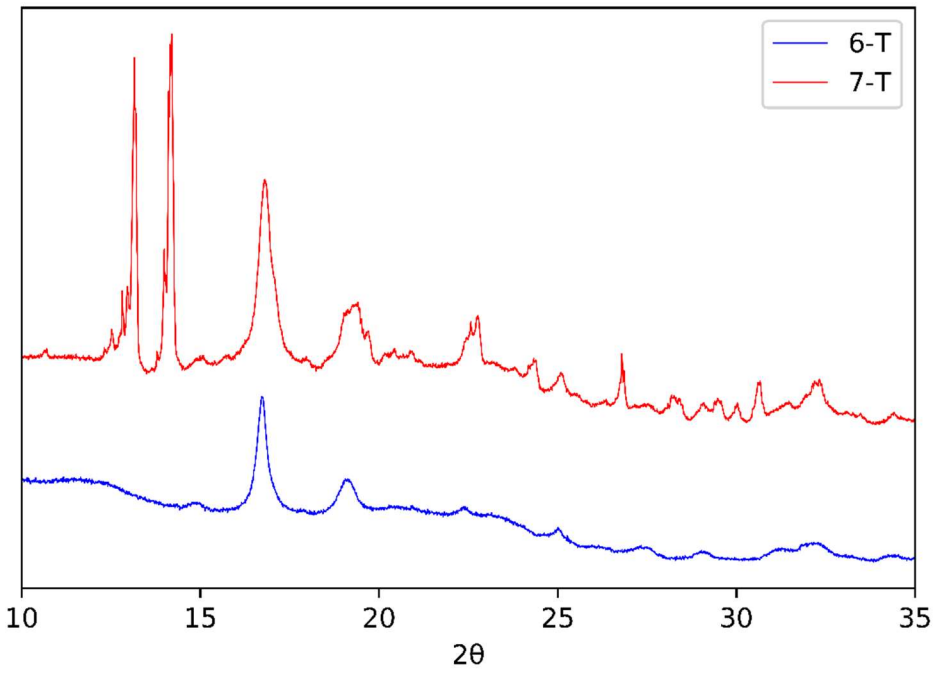

Figure C.16: WAXS patterns of trimethoprim catalyzed ROPI-CDSA polymers. Note in **7-T** that there are some sharper peaks, likely L-lactide due to the relatively low conversion of **7-T** compared to **6-T**.

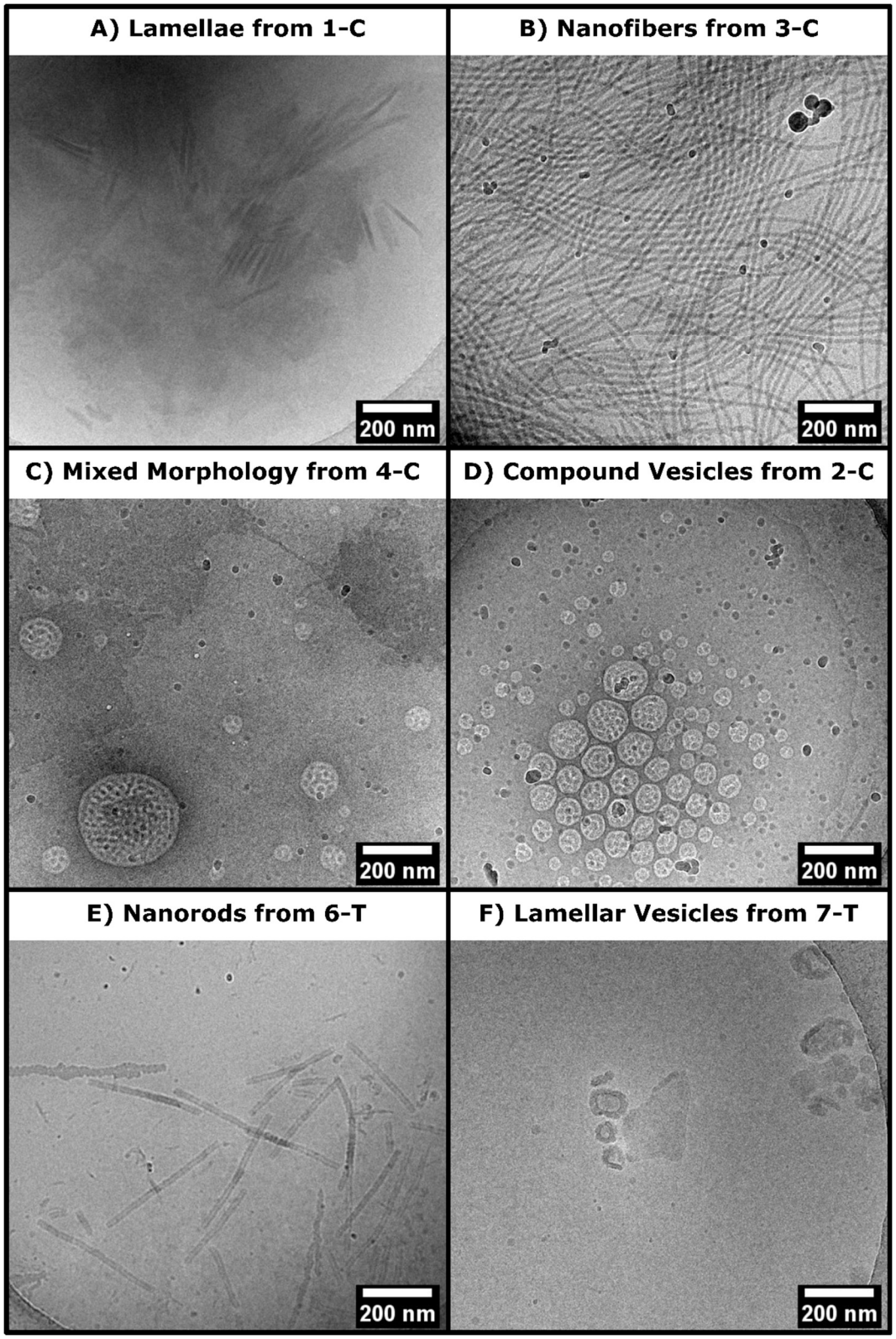

Figure C.17: Additional cryoEM images of drug catalyzed ROPI-CDSA samples. Each image is labelled with its corresponding polymer sample.

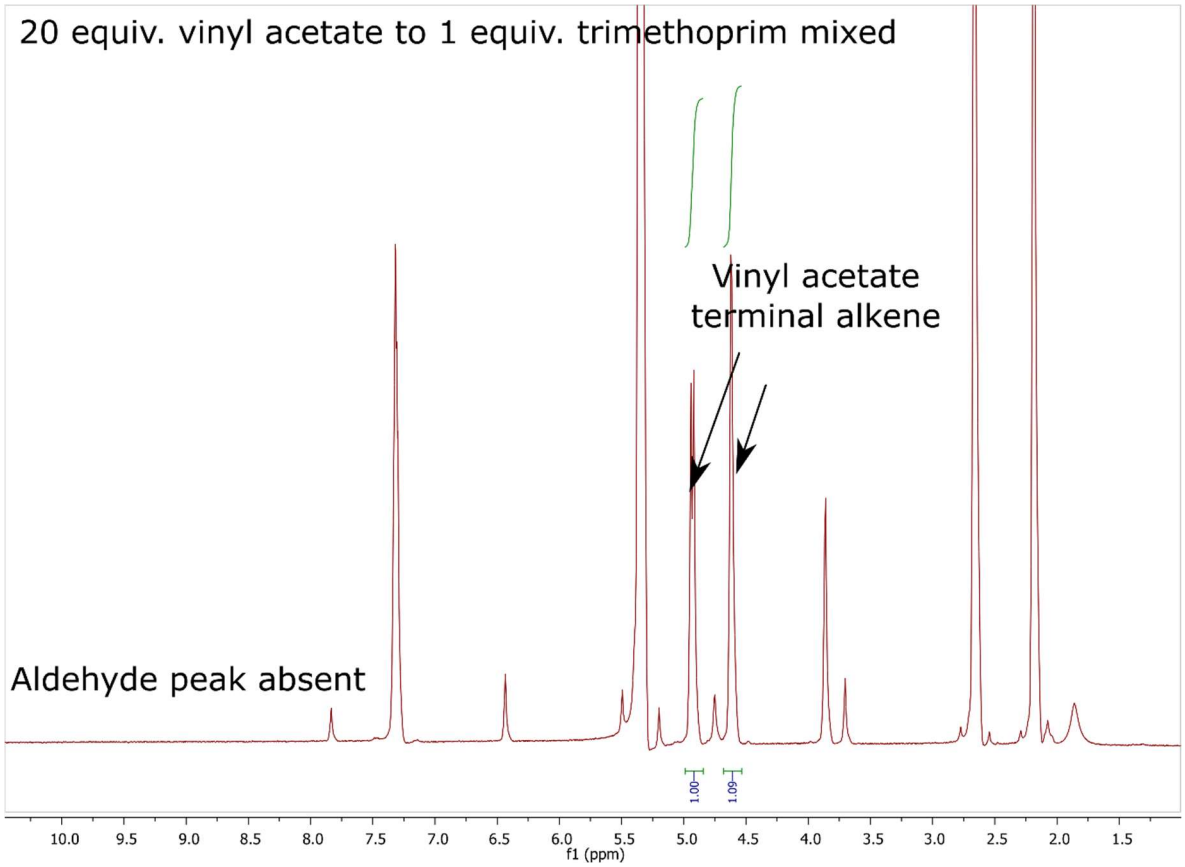

Figure C.18: Attempted trimethoprim acylation ^{1}H NMR data.

Appendix D: Supplementary Information for Chapter 5

D.1. Supplementary Tables

Table D.1: CryoEM measurements

Sample ID	Total thickness (nm)	Core thickness (nm)	Corona thickness (nm)
3-2	40.0 ± 2.6	12.9 ± 1.0	27.1 ± 2.8
3-3	43.3 ± 2.4	13.8 ± 1.1	29.5 ± 2.6
3-4	44.5 ± 2.2	14.3 ± 0.9	30.2 ± 2.1
2-3	33.5 ± 1.5	13.6 ± 0.8	19.9 ± 1.7
4-1	48.8 ± 2.5	13.2 ± 0.8	35.6 ± 2.6

Table D.2: Reaction Set-up for PDMA-*b*-PLLA block copolymers

Sample ID	PDMA Target DP	DMA (mg)	PLLA Target DP	L-lactide (mg)	Toluene (mL)	TU (mg)	(-)-sparteine (µL)
1-1	50	69	50	50	0.32	12	8
1-2	50	69	100	101	0.82	24	16
1-3	50	69	150	151	1.32	35	24
1-4	50	69	200	202	1.82	47	32
2-1	100	139	50	50	0.24	12	8
2-2	100	139	100	101	0.74	24	16
2-3	100	139	150	151	1.24	35	24
2-4	100	139	200	202	1.74	47	32
3-1	150	208	50	50	0.16	12	8
3-2	150	208	100	101	0.66	24	16
3-3	150	208	150	151	1.16	35	24
3-4	150	208	200	202	1.66	47	32
4-1	200	278	100	101	0.58	24	16
4-2	200	278	150	151	1.08	35	24
4-3	200	278	200	202	1.58	47	32

Table D.3: Reaction Setup for PDEA-*b*-PLLA block copolymers

Sample ID	PDEA Target DP	DEA (mg)	PLLA Target DP	L-lactide (mg)	Toluene (mL)	TU (mg)	(-)-sparteine (µL)
5-1	150	267	50	50	0.19	12	8
5-2	150	267	100	101	0.69	24	16
5-3	150	267	150	151	1.19	35	24
5-4	150	267	200	202	1.69	47	32
6-1	200	356	100	101	0.59	24	16
6-2	200	356	150	151	1.09	35	24
6-3	200	356	200	202	1.59	47	32

Table D.4: Reaction Setup for PDMA-*b*-PVL block copolymers

Sample ID	PDMA Target DP	DMA (mg)	PVL Target DP	Valero-lactone (mg)	MIK (mL)	TU (mg)	DBU (µL)
7-1	150	208	25	35	0.66	12	8
7-2	150	208	75	105	1.32	35	24

D.2. Supplementary Figure

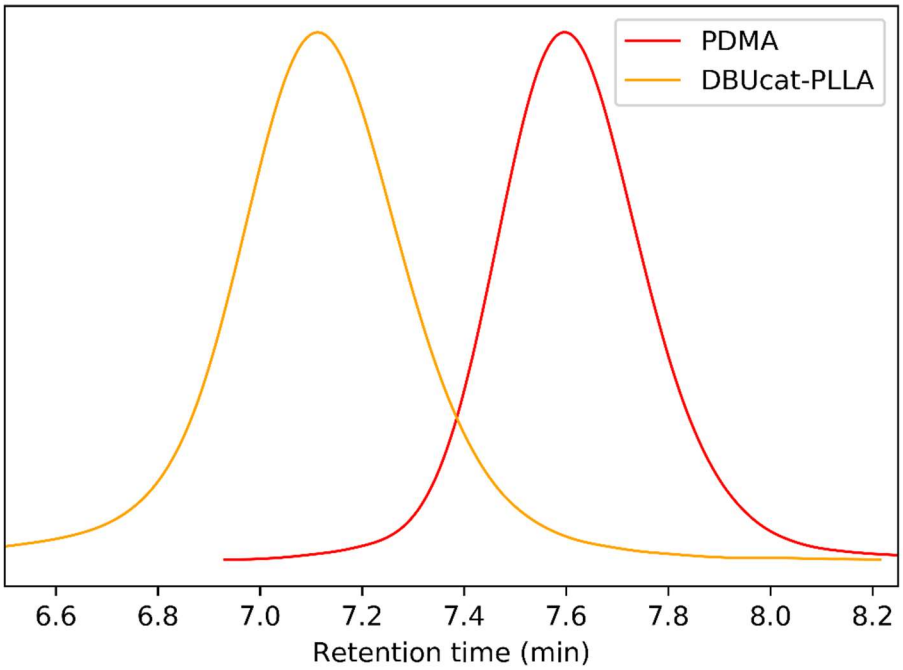

Figure D.1: GPC of PDMA-*b*-PLLA where the PLLA block was synthesized using DBU (4% mol) as the ROP catalyst. A higher than normal amount of DBU had to be used due to potential lower reactivity in the presence of PDMA and/or the photoiniferter. Typically only 1% mol is used.[3] The homopolymer PDMA is also shown. Đ of the block copolymer is 1.16 whereas it is 1.09 for the PDMA homopolymer. Đ is higher than for PDMA-*b*-PLLA polymers synthesized using the TU/(-)-sparteine system indicating less control when DBU is used.

Appendix E: Supplementary Information for Chapter 6

E.1. Experimental/Cryogenic transmission electron microscopy

Table E.1: Experimental conditions for the sequential process as well as controls.

Run*	[CSH/CSSC] mM	[H_2O_2] mM	[DTT] mM	# Time Points
F	10	10	n/a	4
F-1C	10	150	n/a	3
F-2C	4	150	n/a	1
B	10	10	200	4
B-1C	10	5	200	1

Experimental Controls:

According to the kinetic data from the previous CSSC study, CSSC reaches a maximum conversion of 40%. The reaction cannot reach 100% because of the presence of DTT. Therefore, to understand the nature of CSSC at lower conversions and indicate if CSH (the inactive building block) participates in the assembled structures, we focus our study on **F** with one equivalent of H_2O_2 and CSH. Control experiments were performed by running the forward reaction rapidly to 100% conversion with excess H_2O_2 as outlined in conditions **F-1C** and **F-2C** (Table E.1, Figures E.4-5). In **F-1C**, the amount of H_2O_2 and CSH is kept identical to the dissipative conditions which leads to rapid conversion. In **F-2C**, the amount of H_2O_2 is kept identical to the dissipative conditions but the amount of CSH is reduced to 4mM, thus achieving the same maximum concentration of CSSC as the dissipative conditions. These controls yield nanofibers similar to **F** (Figures E.6-7)

The backward reaction was selected by taking **F** and treating it with 200 mM DTT, the same concentration of DTT in the dissipative process. This led to rapid degradation of CSSC back to CSH. However, due to trace amounts of H_2O_2 left in **F**, another forward

reaction with 5 mM H_2O_2 was run to completion and DTT was subsequently added (**B-1C**). In this sample, the stacked phase was still visible at an early time point indicating that the trace H_2O_2 does not affect the morphology (Figure E.10).

Lastly, we wanted to see if DTT impacted the morphologies we obtained due to the potential for dual hydrogen bonding so we used an alternative reducing agent, dithiobutyl amine (DTBA), which is not capable of dual hydrogen bonding. We obtained similar types of fibers with DTBA (Figure E.14). It should be noted that DTBA has differing kinetics to DTT.

Selection of CryoEM Parameters:

Preliminary studies were carried out to optimize all cryoEM parameters. During these optimization experiments we observed results consistent with the main data presented in this manuscript. A blot time of 3s gave a good ice layer. We did not use a post blot time. Post blot times are typically used to relax structures back to equilibrium following an application of shear force from blotting.[1,2] However, our system is out-of-equilibrium and is in constant flux and will not return to equilibrium during a post blot relaxation. For this reason, we believe that a post blot relaxation time would just result in the reorganization of structures within the confined environment of the thin water layers on the cryoEM grid which would not be representative of the bulk structure. Consequently, we believe that trapping the structures though vitrification as quickly as possible is the best preparation method for these samples. As this study is comparative, cryoEM parameters were kept the same for every sample and timepoint. It is also important to highlight that ,any well-known time-resolved cryoEM studies have also foregone post blot times.[3,4]

30k was selected for magnification as it is the highest magnification that does not cause visible beam damage of the sample using low dose imaging. This allows a large area of the sample to be inspected in a single image. On average, each timepoint had approximately 30 images collected. We opted to capture additional timepoints rather than repeating the sample multiple times with a smaller number of time points. We were also sensitive to the image processing time and therefore had to find a balance between the number of images collected and time required for image processing. Our study alone, encompassing 770 images which were processed in parallel using the UCI HP3. Each image was allocated 30 cores, 100GB of RAM, and 1 hour of processing time. It took approximately 23,000 core-hours in total. Because of efficient parallelization, the time to complete the entire analysis was 5 hours for a given set of parameters. This processing collected 398 million data points with an average of over 500,000 per image with a very large standard deviation as images contain little to no stacking.

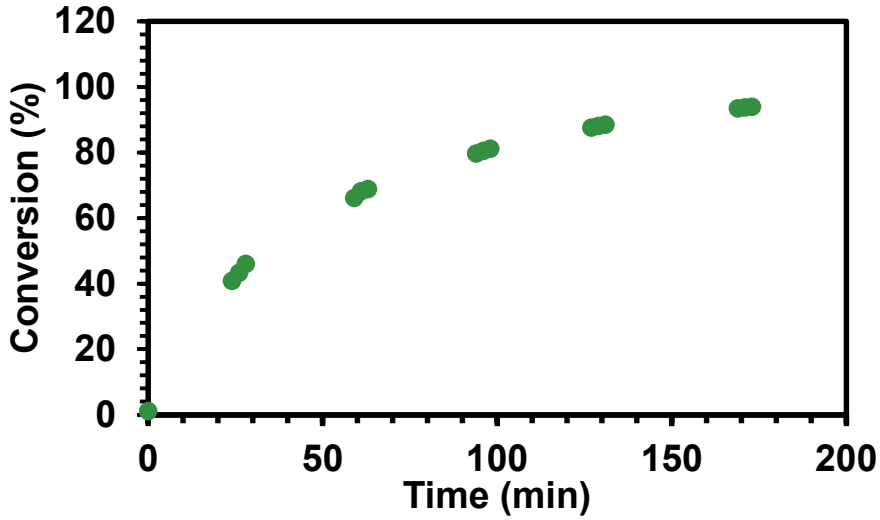

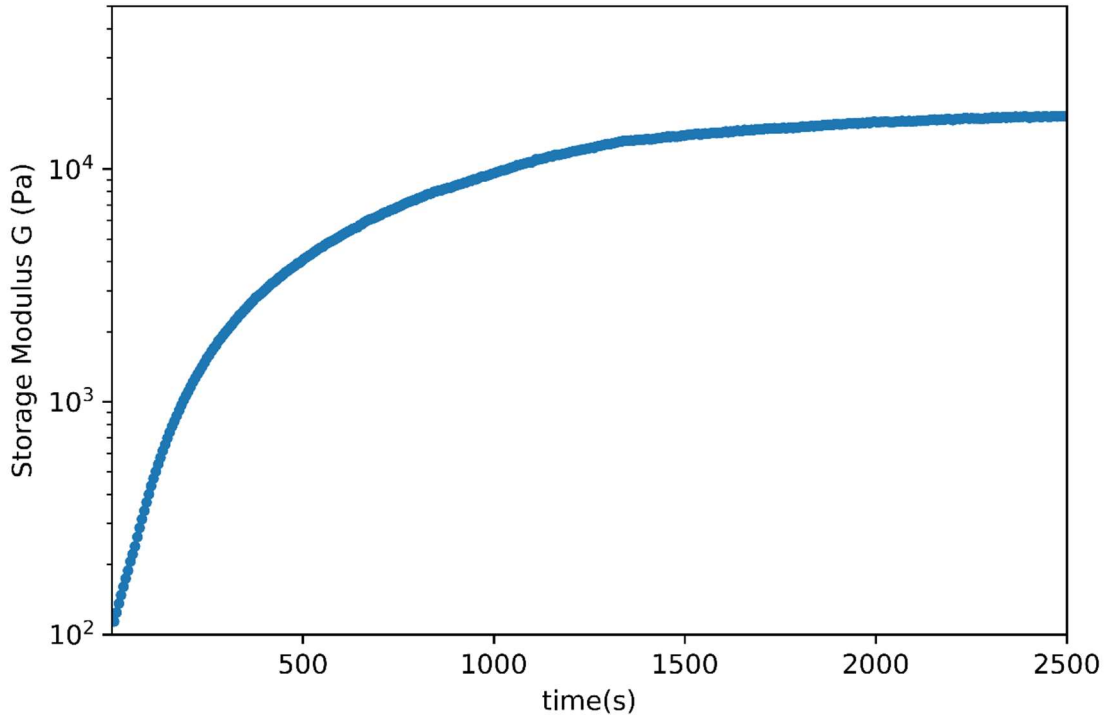

Figure E.1: UPLC and rheology data for forward reaction. The rheology is of sample **F**. After about 30 minutes, the rheology data plateaus indicating a maximum development in gel strength. The HPLC data is of an analog of CSH that does not contain an aryl group which can explain the discrepancy between the rheology and UPLC data.

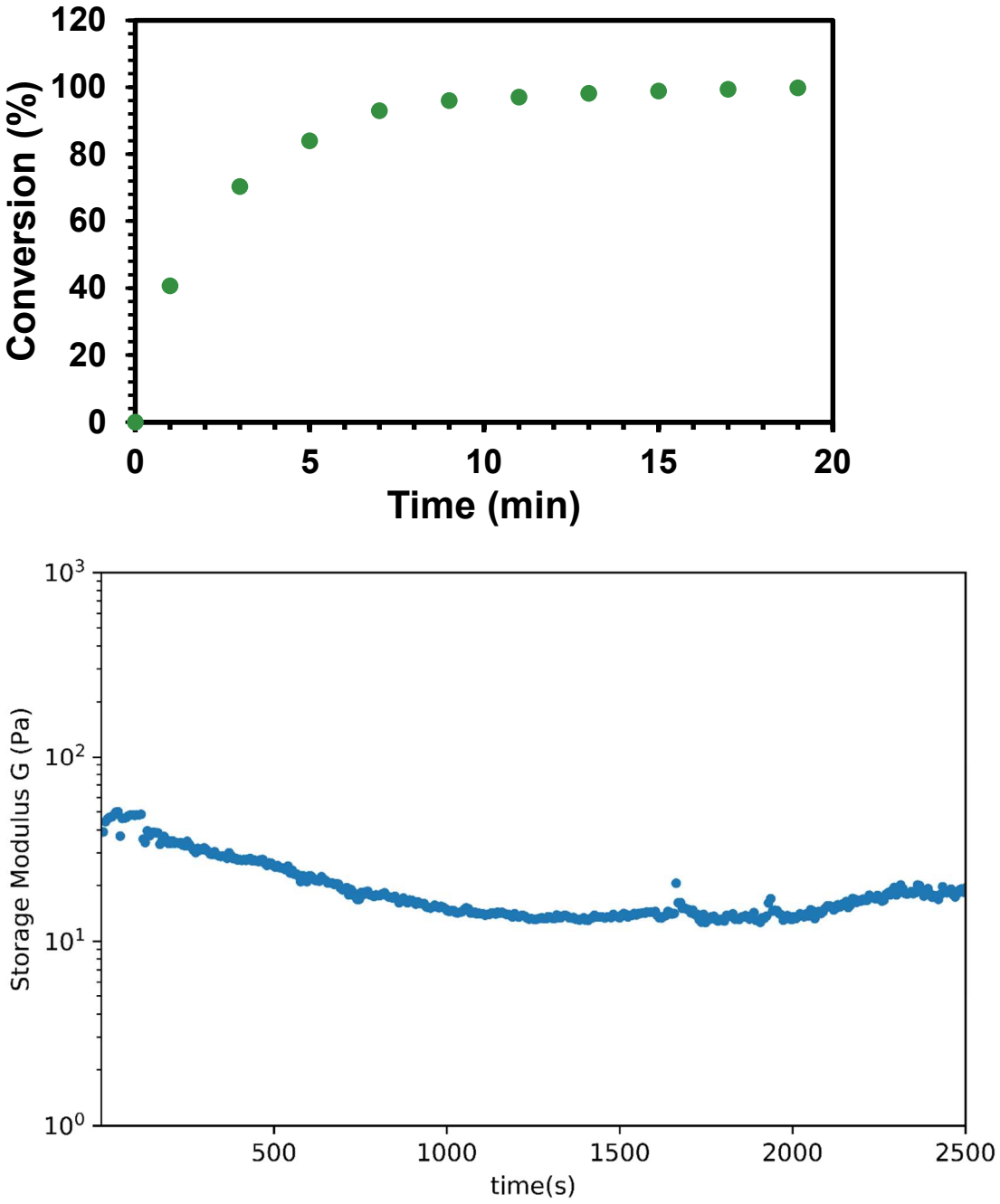

Figure E.2: HPLC and rheology data for backward reaction. The HPLC data is of an analog of CSH that does not contain an aryl group. The rheology is of sample **B** and instantly de-gels following the addition of DTT.

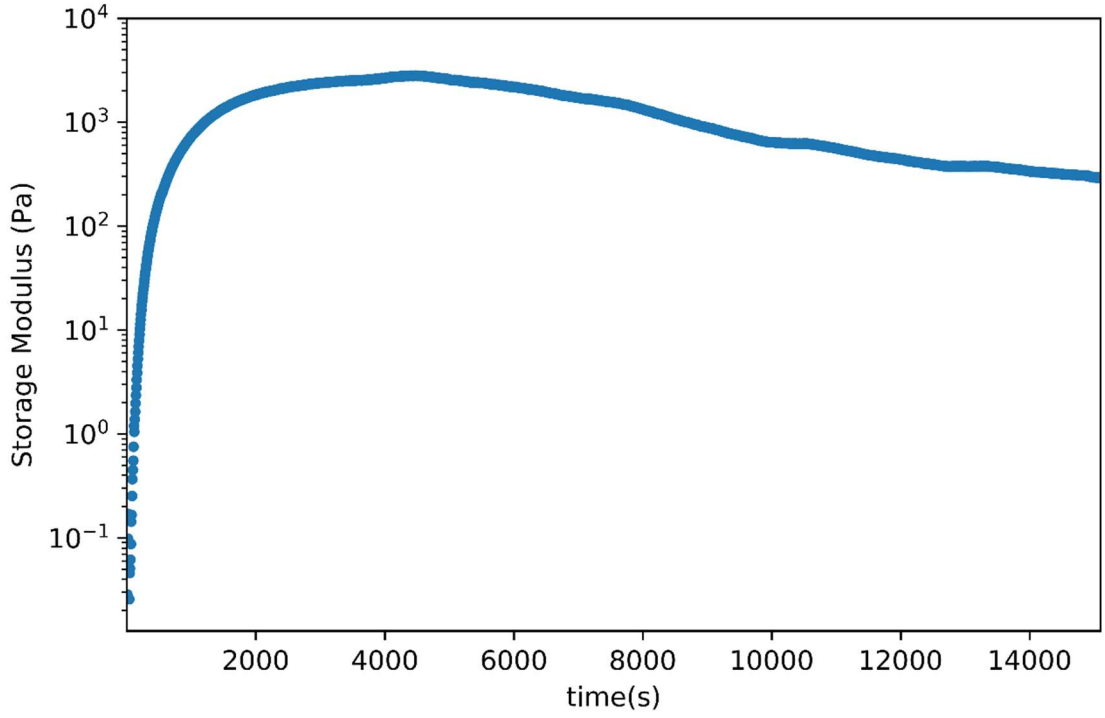

Figure E.3: Rheology data for dissipative process **D**.

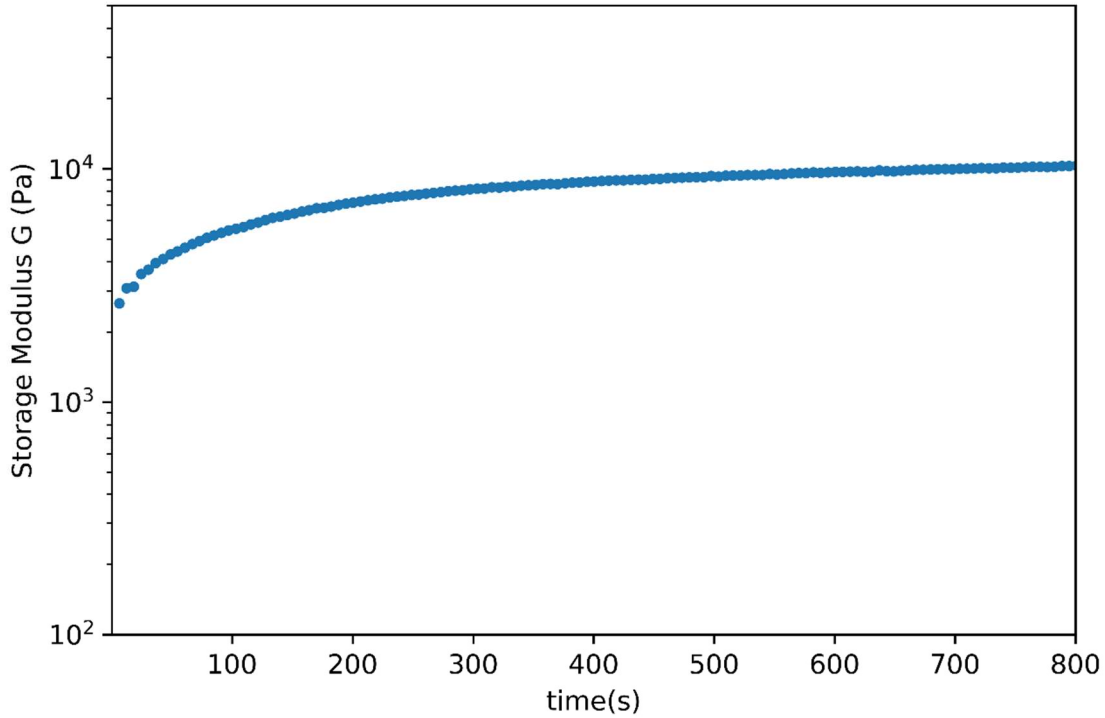

Figure E.4: Rheology data for forward reaction **F-1C** with excess H_2O_2 at 10 mM CSH.

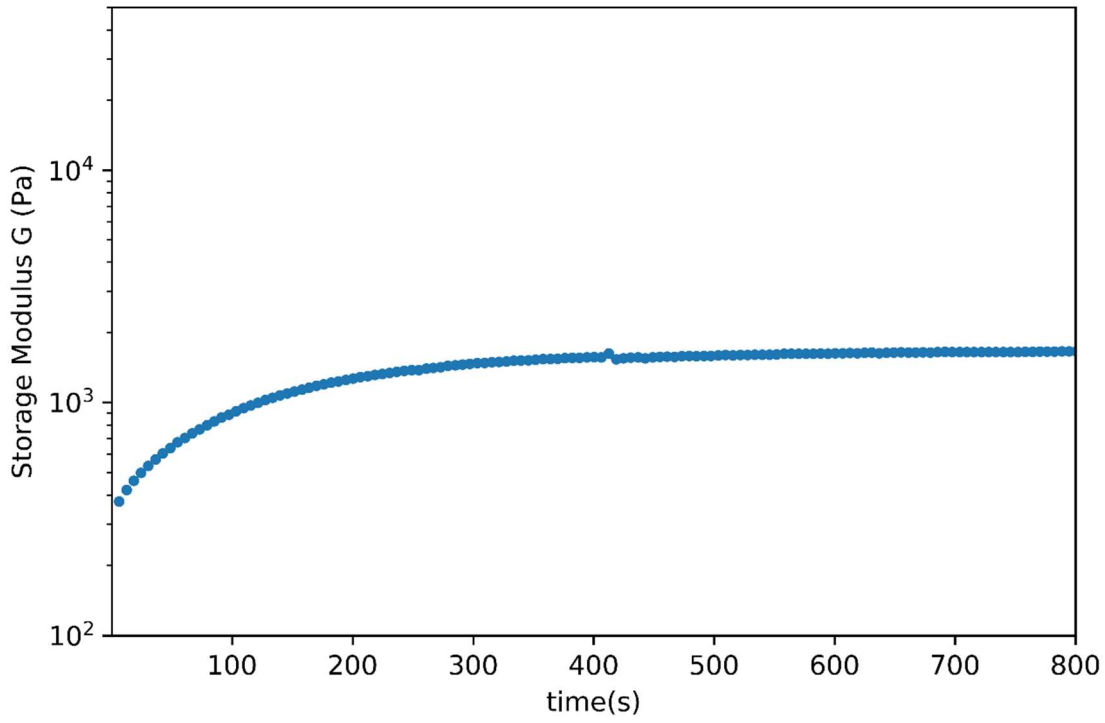

Figure E.5: Rheology data for forward reaction **F-2C** with excess H_2O_2 at 4 mM CSH.

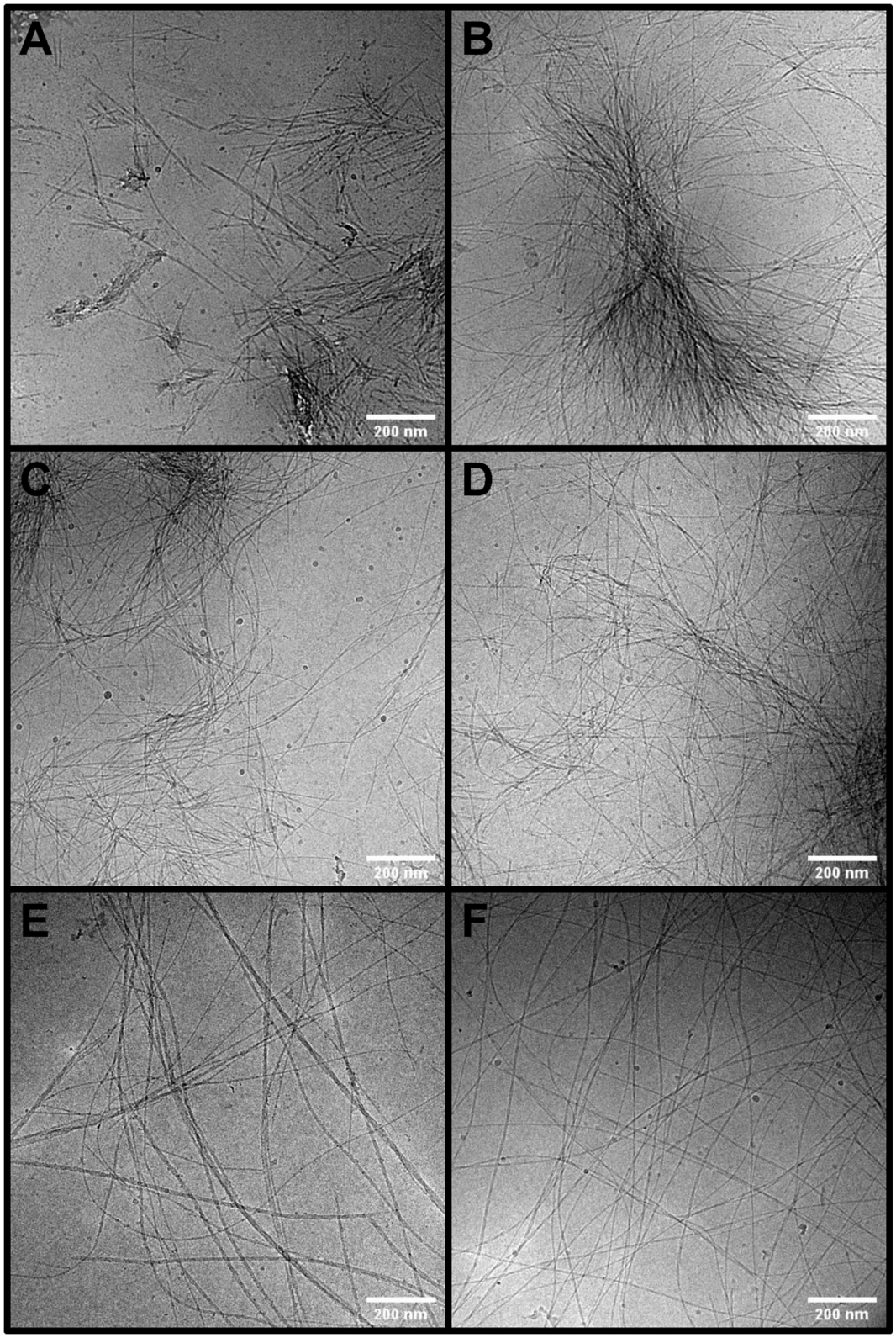

Figure E.6: Time-resolved CryoEM images of **F-1C**. A-B) 8 s C-D) 55 s E-F) 10 min 3 s

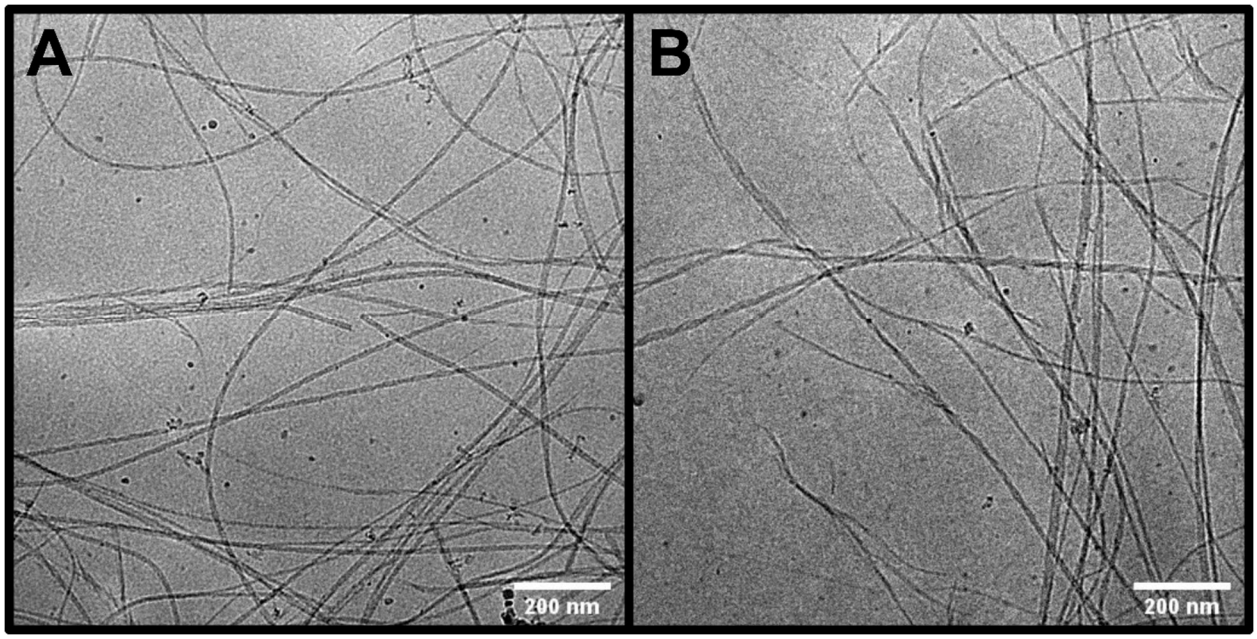

Figure E.7: CryoEM images of **F-2C** taken at 2 min 15 s

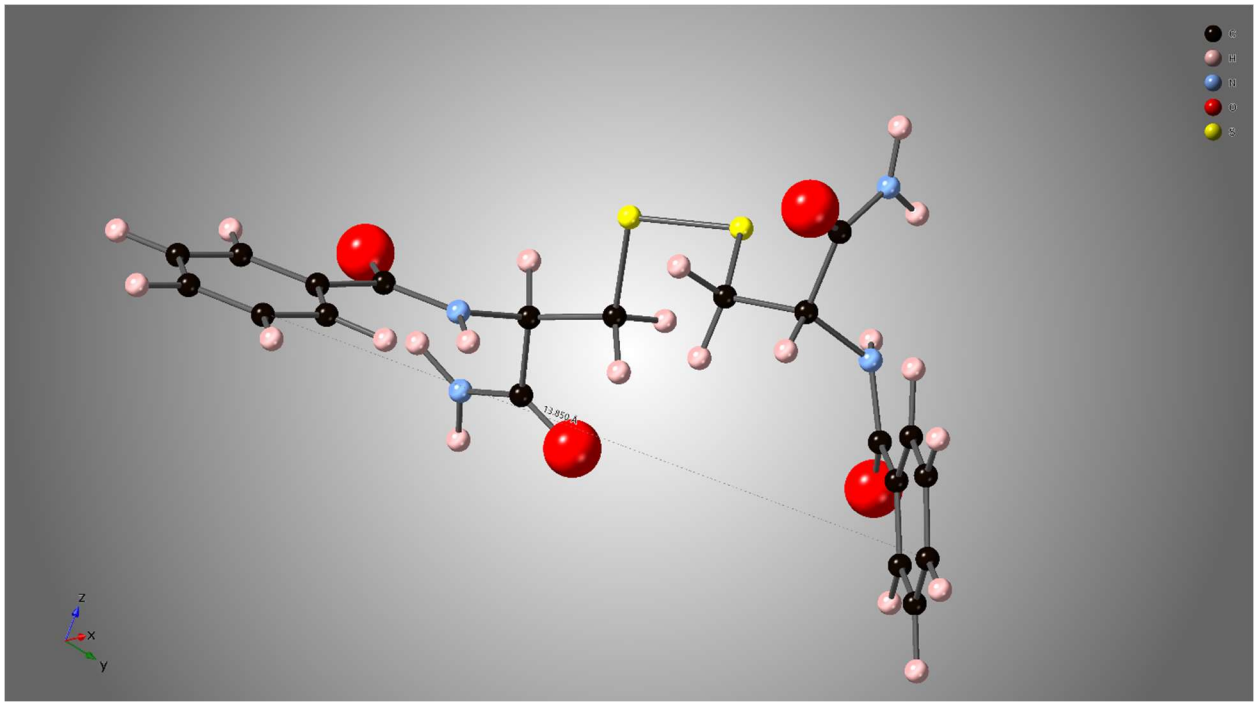
Figure E.8: Representative CSSC molecule made in Crystal Maker. The distance between carbon 4 in the aryl rings is about 13.8 Å. The distance between the sulfur and the aryl groups is approximately 12 Å. This structure does not represent a solved crystal structure and is used to get an idea of molecular length only.

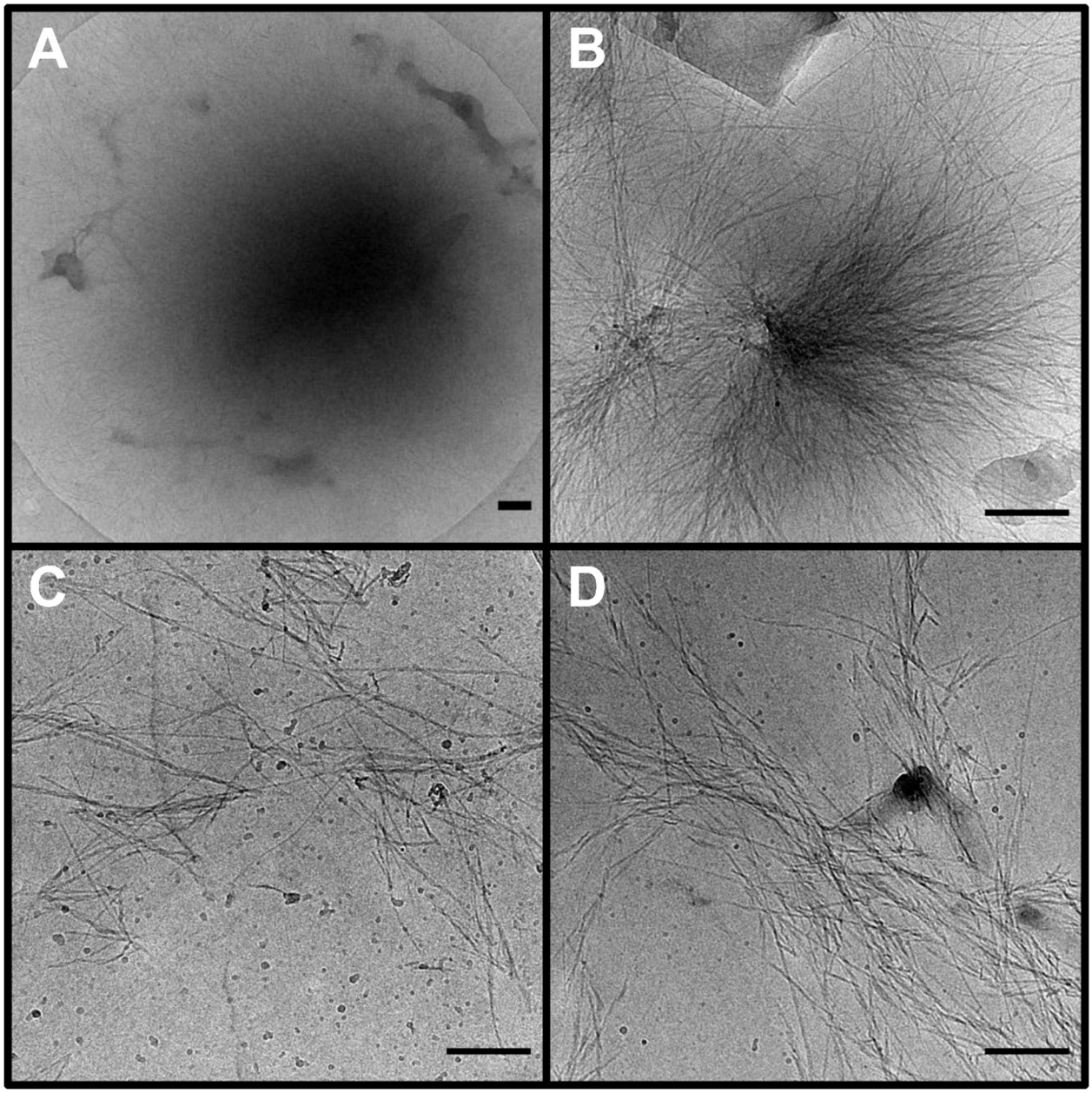

Figure E.9: CryoEM images of **F** from 8 s. A shows what appears to be a liquid droplet precursor to fibers. B shows a centrosome-like structure whereas C and D show some fibers that do not appear to originate from a larger (micron-scaled) cluster. Scale bars are 200 nm.

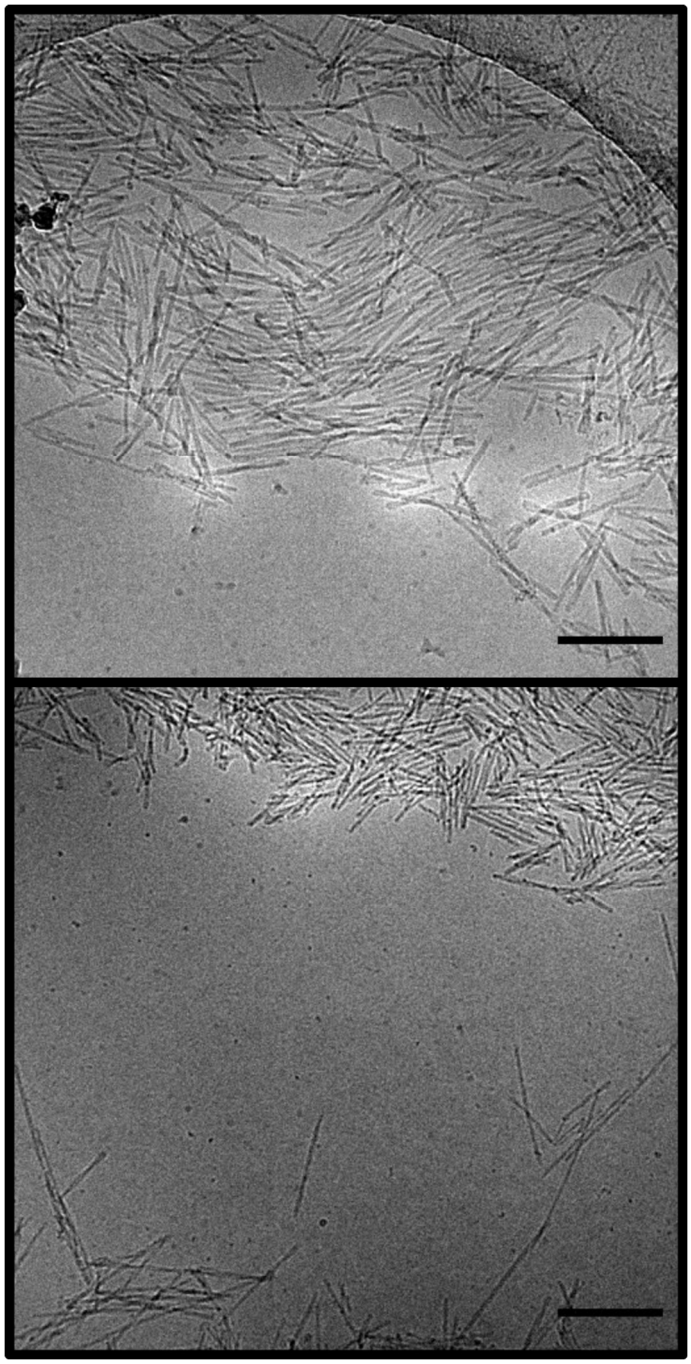

Figure E.10: CryoEM images of **B-1C** at 44 s after adding DTT. The stacked phase is still present even though there is no residual fuel remaining (5 mM of H_2O_2 used to assemble 10 mM of CSH before the addition of 200 mM DTT).

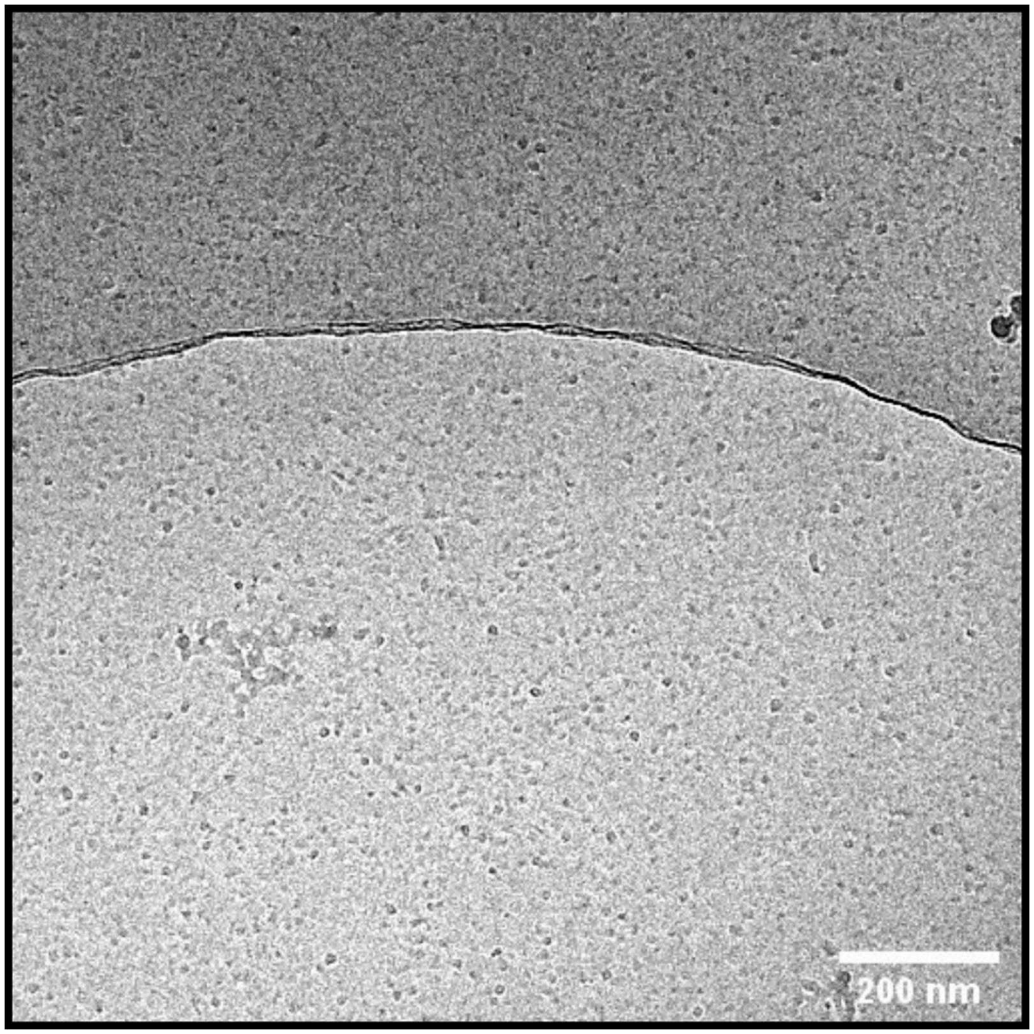

Figure E.11: Representative cryoEM image for the t=0 timepoint for **D**. This timepoint is before the addition of H_2O_2. The black spheres represent ice contamination.

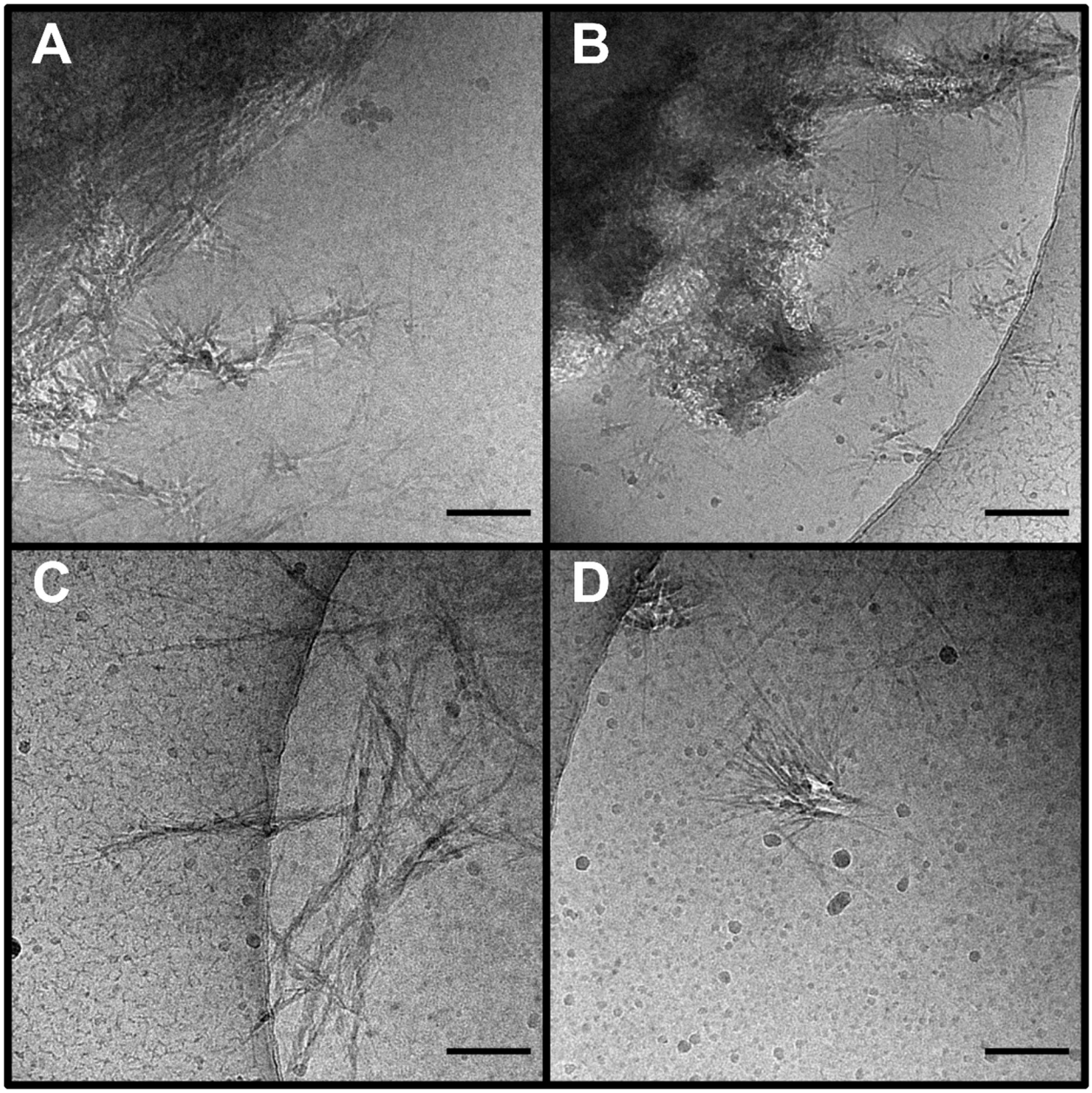

Figure E.12: CryoEM images of **D** at t = 8s. A and B show liquid droplet precursors whereas C and D show more isolated structures that could have nucleated from unimer growth.

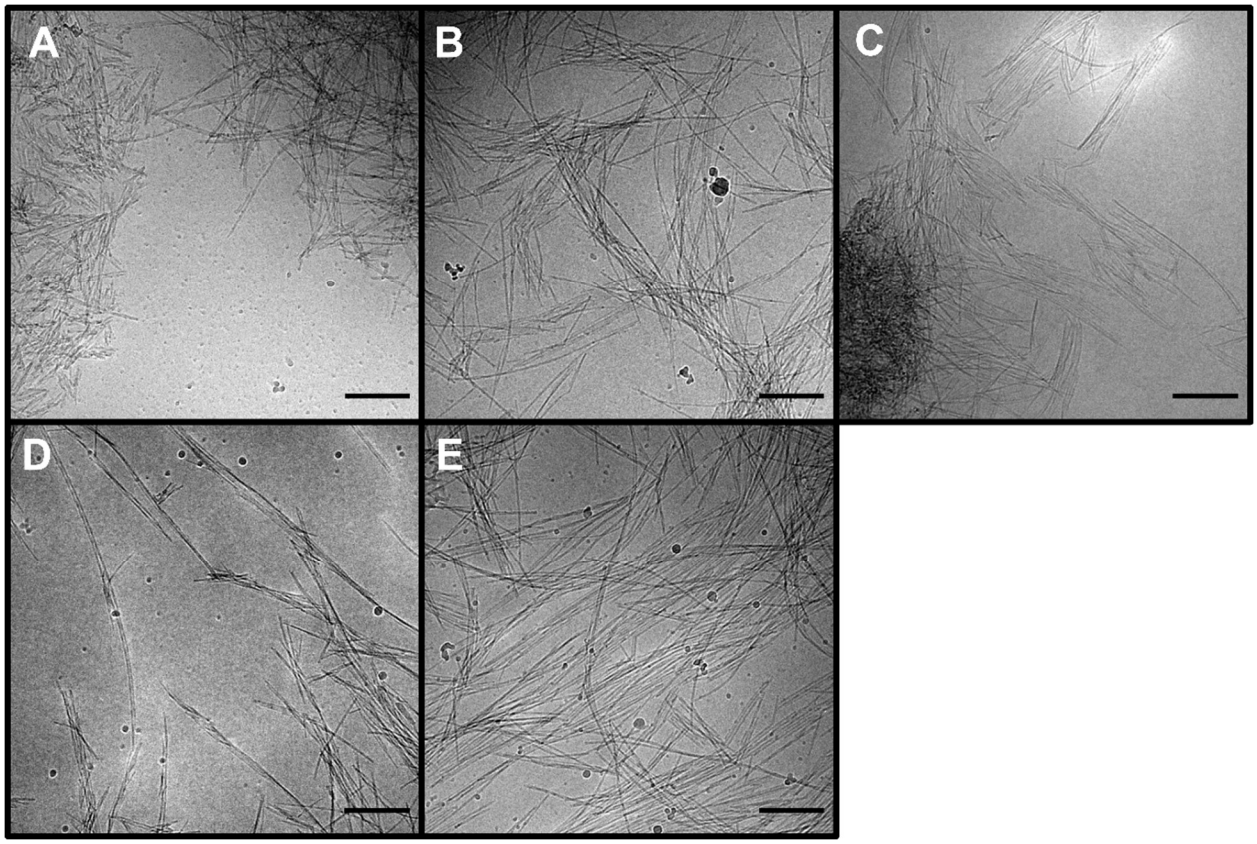

Figure E.13: CryoEM images of **D** from multiple time points showing stacked phase. A) The first stacked phase was seen at 7 min 44 s B) 22 min 36 s C) 29 min 6 s D) 36 min 34 s E) 1 h 41 min

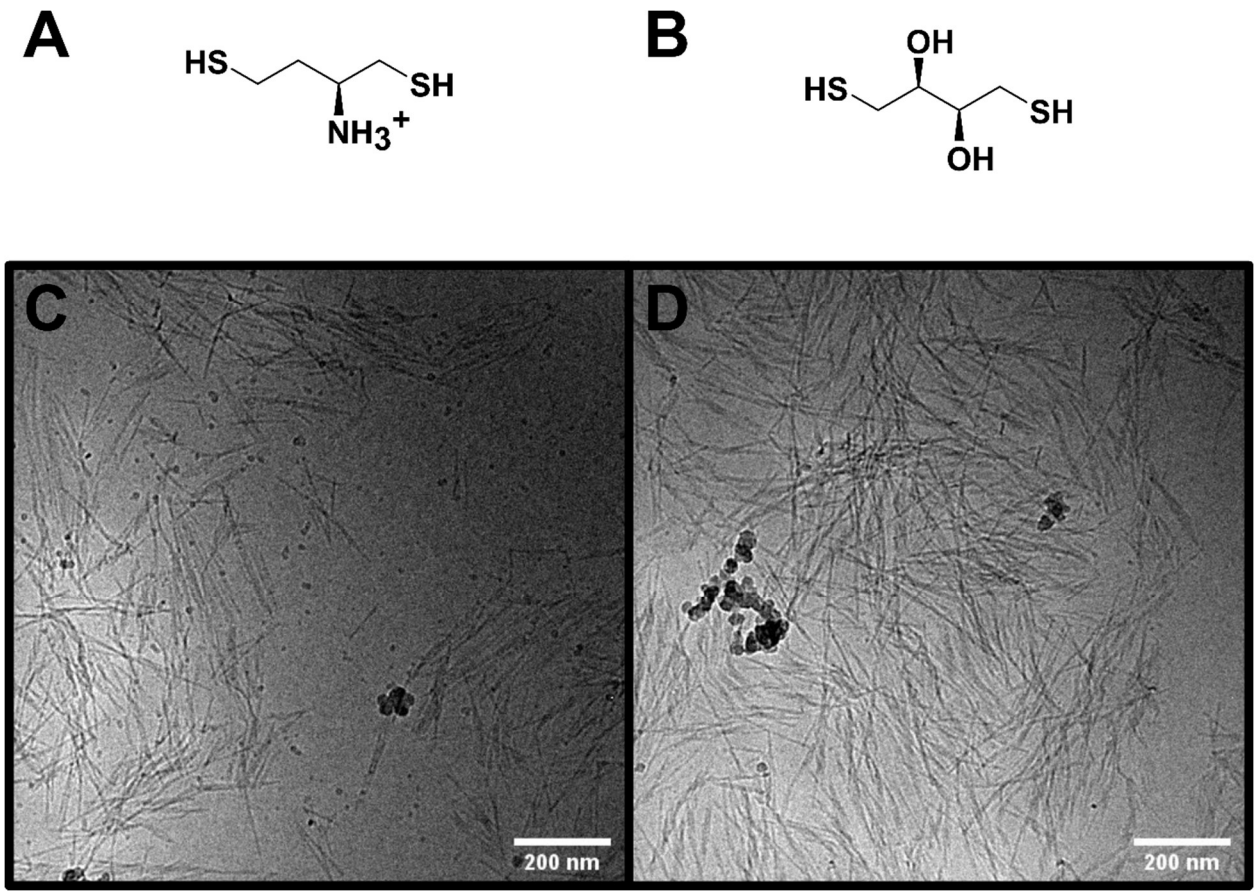

Figure E.14: Dithiobutyl amine (DTBA) used in the dissipative process instead of DTT. A) Chemical structure of DTBA. B) Chemical structure of DTT for comparison C-D) CryoEM images of nanorods from a dissipative process using DTBA instead of DTT. These morphologies suggest some 2D stacking although it is not as prominent as some examples of the dissipative process with DTT (**D**).

E.2. Image Processing (Credit Justin T. Mulvey, UCI)

The stacked fiber phase observed in CryoEM was analyzed with a custom cross-correlation based template matching algorithm (Figure E.15). The stacked fiber phase has a periodic pattern of alternative dark fiber cores and bright Fresnel fringes. These periodic features are used to segment, or identify, the stacked fiber phase in each CryoEM image collected in this study. Once the stacked fiber phase was segmented, the number of locally aligned fibers was labeled. The resulting data were analyzed to track the structure of the stacked fiber phase across all experimental conditions in this study.

Stacked Fiber Phase Segmentation

Template Generation

Several symmetric templates of alternating black and white stripes were systematically generated to act as templates of the stacked fiber phase. Fibers of different thicknesses were accounted for by generating template sets with three different pixel spacings: 15, 20, and 25 pixels (Figure E.16). Furthermore, templates were rotated 175 degrees at 5-degree intervals, resulting in 36 templates for each pixel spacing, and 108 templates in total. Finally, the templates were masked to be circular which makes them symmetric to all fiber directions, such that diagonal fibers do not have higher cross-correlations compared to vertical fibers.

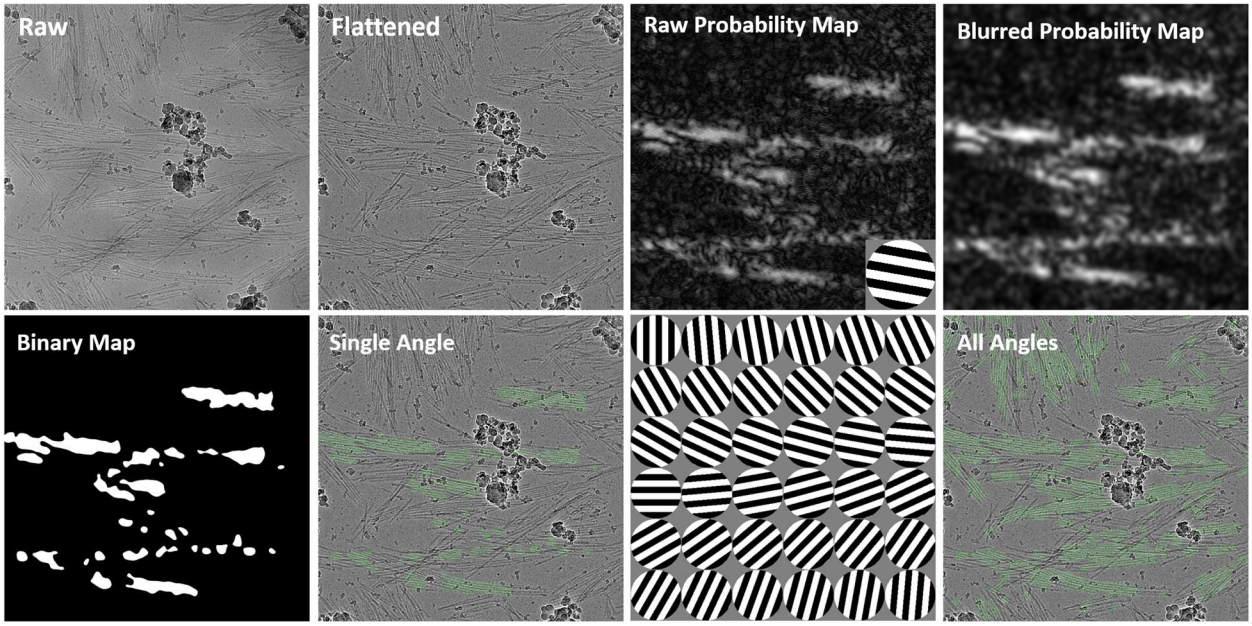

Figure E.15: Image processing pipeline for stacked fiber phase segmentation. The image processing steps are outlined for a representative image. A more detailed description of each step can be found in the text below. The templates have been increased in size for display purposes.

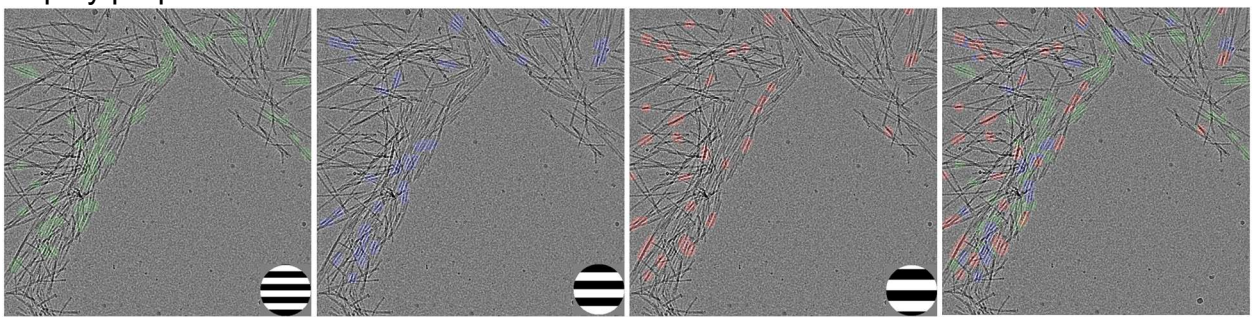
Figure E.16. Individual segmentation maps for template pixel spacings of 15, 20, and 25 pixels. The templates have been increased in size by 4x for display purposes. The right figure shows an overlay of the 3 individual maps and demonstrates how different template spacings are used to identify different fiber stack spacings in the image. Note some highlighted regions are single fibers and not fiber stacks, these will be removed from the dataset during fiber stack labeling.

Stacked Fiber Phase Segmentation

Figure E.15 shows the image processing pipeline applied to each CryoEM image. First, a high pass filter was applied to remove background features and create a flat image. Next, the normalized cross-correlation is computed between each template and the flattened image which results in a correlation probability map. The absolute value of this

map is taken, which results in equal positive weight to correlation and anticorrelation. This is helpful because a high probability is returned both when the black pixels line up with the fibers and white pixels line up with the fringes (correlation), and also when white pixels line up with the fibers and black pixels line up with the fringes (anticorrelation). Next, the correlation probability map is smoothed with a Gaussian blur to smooth out the high correlation regions. Then, a probability threshold was used to convert the probability map into a binary segmentation map. Different probability thresholds were used for each image and were based on the estimated defocus of the image (Figure E.17, details in 'Defocus Threshold Correction'). Binary maps for the 36 angles are calculated individually for each of the 3 templated spacings, resulting in 108 total binary maps. Finally, angles are combined across the 3 template spacings by adding the binary maps together for each angle, producing 36 binary maps which contain information about both the fiber stack location and fiber stack angle. Note the angular information is used to label the degree of stacking, as discussed in 'Labeling Degree of Stacking'.

Defocus Threshold Correction

It is well known that the brightness of the Fresnel fringes around an object will depend on the defocus of the microscope; larger microscope defocus values lead to higher intensity of the Fresnel fringes. We found that TEM images taken at higher defocus values were more sensitive to the segmentation algorithm and had higher normalized cross-correlations values. This makes physical sense, because the algorithm relies on the pattern of alternating dark fibers and bright fringes. If the fringes are brighter in some images due to differences in focus, it will increase the values of the normalized cross-correlations. To minimize this effect, all images were taken around 11 μm of defocus using

the autofocus feature in SerialEM. However, there was still significant variation in defocus between images. To account for this variation in the segmentation algorithm, we estimated the defocus of every image and adjusted the probability threshold for segmentation on a per-image basis.

We estimated the defocus of every image by first calculating the Fast Fourier transform (FFT) image and then taking a radial integration (Figure E.17A-B). Then, we used a peak-finding algorithm to find the distance to the second peak in the radial integration, which is characteristic of the defocus value (Figure E.17C). The second peak was chosen because the first peak appeared distorted in many images, likely from high-frequency components generated by small features in the images such as fibers. We then took CryoEM images of amorphous ice with no sample at known defocus values to use as a calibration curve to convert the second-peak distances to the defocus of the images (Figure E.17D). Note that our algorithm was unable to detect peaks below 7 μm of defocus, but this was below the range of defocus values found in the experimental datasets. Once all images were labeled with the defocus value, the probability threshold for segmentation was adjusted with an empirically determined function (Figure E.17E).

Originally, a static threshold of .145 was used to segment all images, which appeared to work well for most images. However, we observed that images taken at high defocus had inaccurate segmentation and were over segmented. We quantified this observation by examining the correlation between image defocus and the number of segmented pixels in an image, which should be random and uncorrelated features. To examine these features, we plotted the mean segmented pixels across images in different 1 μm defocus ranges, from 7-8 μm, 8-9 μm, 9-10 μm etc. (Figure E.17F). Defocus and mean segmented

pixels should be uncorrelated features and yet there is clearly a trend when a static threshold of .145 was used; high defocus images had a greater number of segmented pixels. After the defocus threshold correction was applied, the trend was reduced and a more random correlation between defocus and the number of segmented pixels was observed (Figure E.17F). Figure E.17G shows an uncorrected image which was over segmented while Figure E.17H shows more accurate segmentation after the defocus threshold correction.

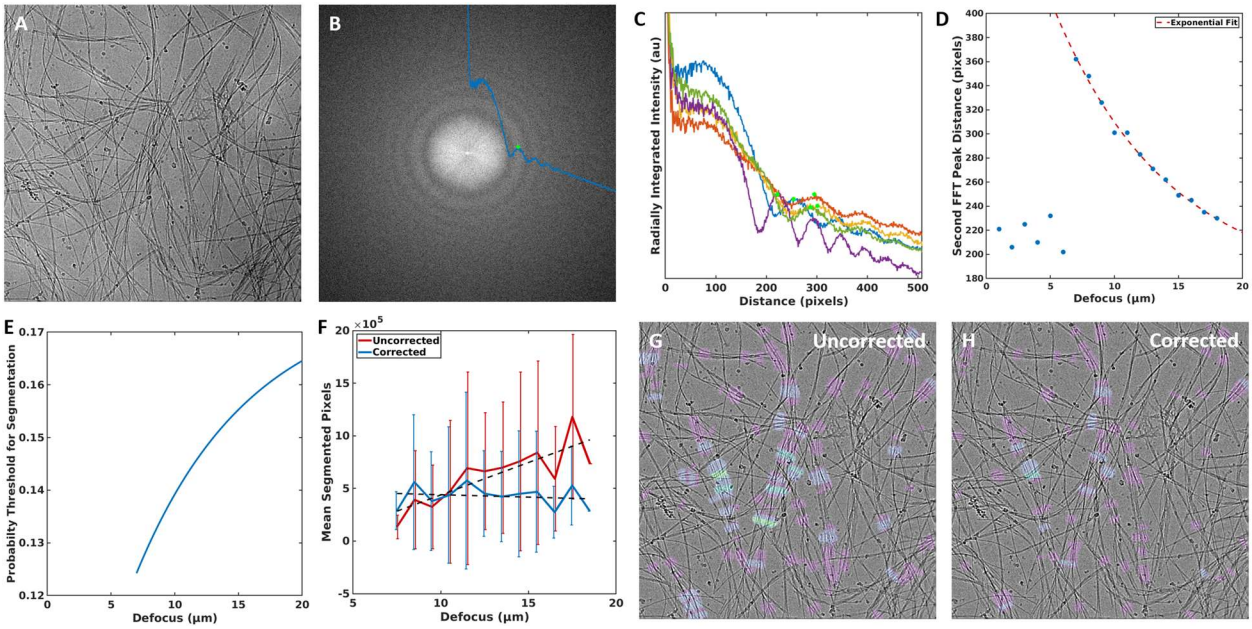

Figure E.17. A) Typical TEM image with B) corresponding FFT image. Blue line represents radial integration of the FFT, with the green dot labeling the calculated second-peak distance. C) Examples of several radially integrated FFTs from images at different defocuses with the calculated second-peak distance. D) Calibration curve which relates defocus value to the calculated second-peak distance. Points below 7 μm were omitted from the fit. E) Empirically determined curve which adjusts probability threshold for segmentation as a function of image defocus. F) Mean segmented pixels across different defocus ranges. There was a clear correlation in the uncorrected curve which does not appear in the corrected curve. Dashed line represents linear fit. Error bars represent standard deviation. G) Uncorrected image with threshold of .145 showing over segmentation compared to H) segmentation after defocus threshold correction.

Labeling Degree of Stacking

After the stacked fiber phase was segmented, the goal was to track how well-ordered the stacked phase was by quantifying the degree of stacking (DoS) within each stack. The DoS is the number of fibers present in the local region of the stacked fiber phase. Higher degrees of stacking are more ordered and entropically less favorable than lower degrees of stacking. To understand how the structures were evolving during the sequential and dissipative processes, it was important to accurately quantify the amount and distribution of stacking present at each experimental condition.

The output of the fiber stack phase segmentation algorithm is 36 binary maps of the stacked phase at each angle. Each angle was analyzed individually. For each binary object in the segmentation map, the stacked phase was cropped, then rotated to be oriented vertically. The rotation angle is equal to the rotation angle of the template. Once oriented vertically, a sliding window vertical integration was performed across 100 pixels (Figure E.18A) to produce a high signal-to-noise 1D intensity profile (Figure E.18B). A peak-finding algorithm was applied to find the intensity valleys created by the fibers, which were then labeled (Figure E.18D). This resulted in a local label for the number of fibers at every location in the stacked phase. Small gaps in the labeling resulting from noise and non-fiber objects were smoothed over.

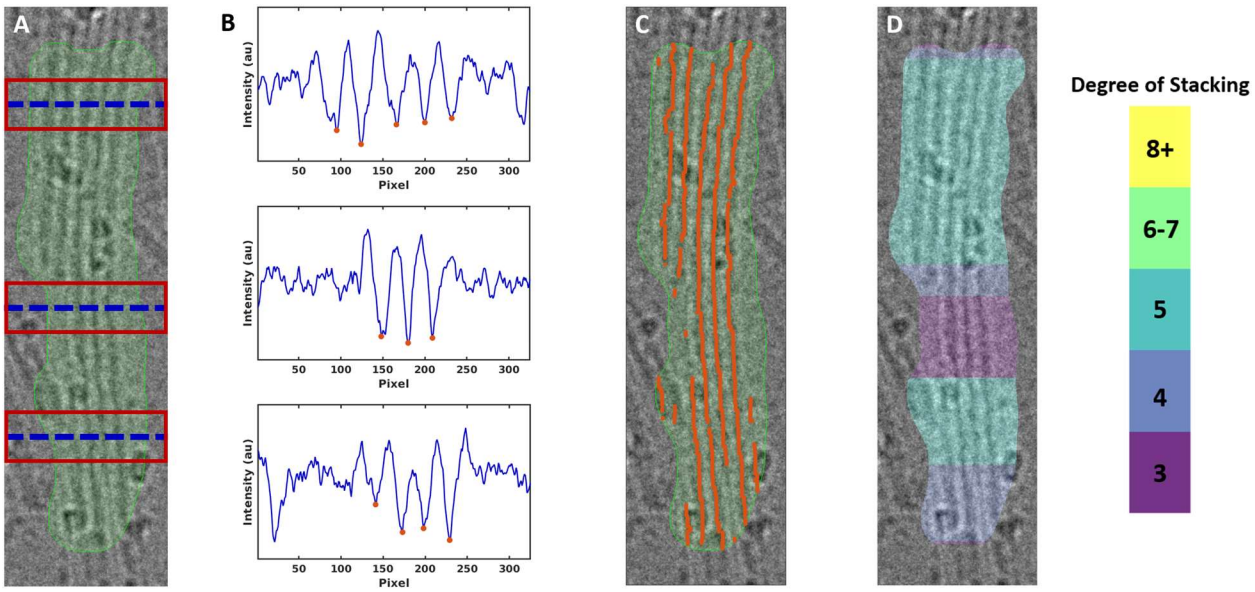

Figure E.18. Labeling degree of stacking. A,B) snapshots of integrated profiles at different locations in the fiber stack. Fibers are labeled with orange dots. C,D) The number of fibers at each location is then counted and labeled.

Once each of the 36 angles were analyzed, they were combined into a single DoS map. Because of the large number of angles used, the same fiber stack was often segmented and labeled by 2 or more different angles of the templates. To resolve this conflict between angles and prevent multiple counting, the maximum DoS was taken for each labeled pixel. This was done because the most fibers were counted when the angle of the template best matched the angle of the stacked phase, and the highest DoS was recorded.

Fiber Stack Analysis

Stack fiber phase segmentation and labeling was completed on 770 CryoEM images across 24 experimental conditions generating 398 million datapoints. A subset of labeled images is seen in Figure E.19. The data generated from segmentation and labeling was used to track the structure of the stacked fiber phase across all experimental conditions in this study. For each experimental condition, the labeled pixels in each image were combined and then divided by the total pixels (resolution multiplied by number of images

in the experimental condition). In addition, the percent coverage was calculated individually for each image within an experimental condition and used to calculate the standard deviation of coverage. Note the standard deviation is of labeled pixels and treats all DoS values equally. This resulted in the ‘percent coverage’ plot (Figure 6.5E). Finally, the distributions in Figure 6.5E were all normalized to 1, resulting in Figure 6.5F.

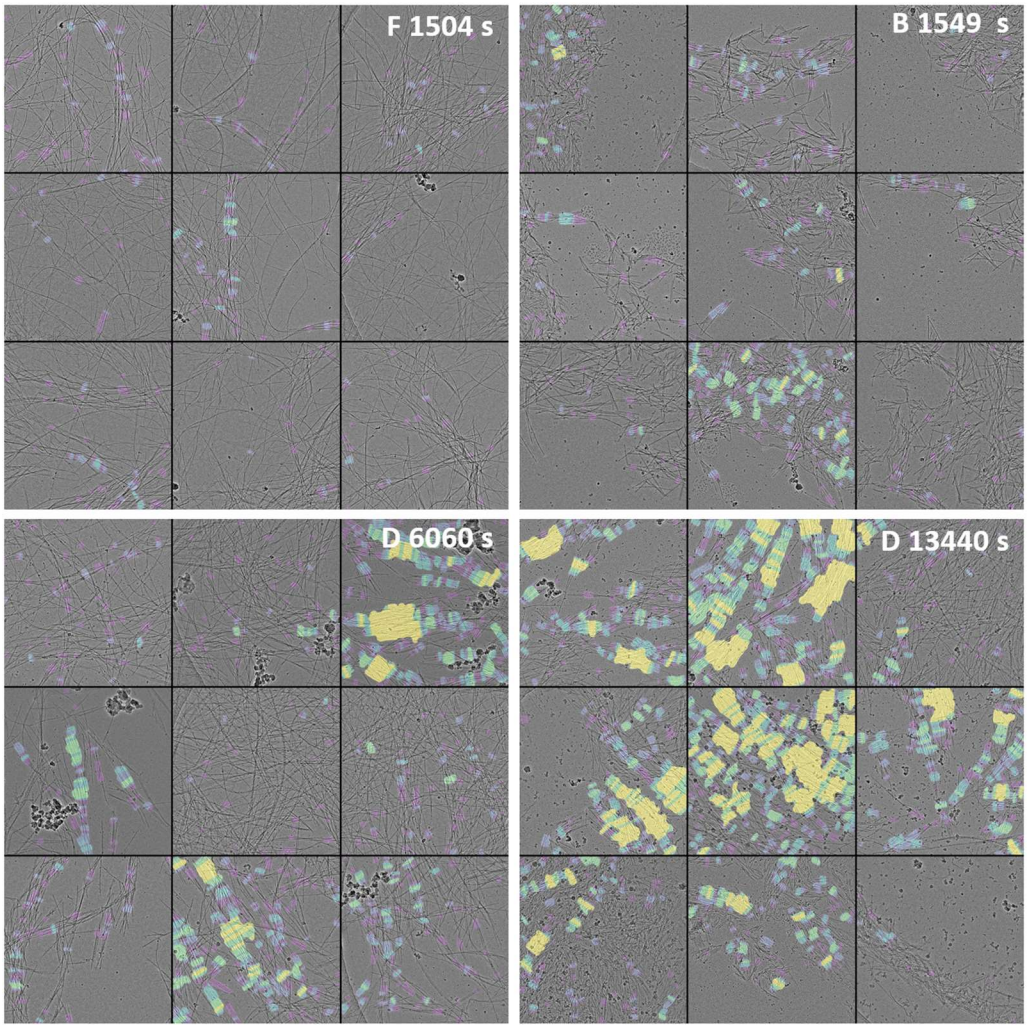

Figure E.19. Examples of labeled images

E.3. Simulations (Credit Rebecca Bone and Jason Green, UMass)

Gillespie Simulations of Separable Self-assembly process

Chemical mechanism

There are ten reactions in the experimental chemical mechanism we consider here (Table E.2). A distinguishing feature of the dissipative process is the abundance of fibers. To model this feature of the experiments, we add a reaction constituting fiber birth:

$$2CSSC_{sol} \rightarrow 2CSSC_{fib}$$

This reaction is necessary to generate information regarding the fibers formed and to ensure that the counting of CSSC species in solution and in fibers is correct. Inclusion of a fiber birth reaction has been used previously to model the self-assembly of microtubules.[5]

Table E.2. Chemical mechanism of assembly process.

Number	Reaction	Forward rate constant	Reverse rate constant
1	$CSH + OH^- \rightleftarrows CS^- + H_2O$	$k_f^{CSH} = 10^{pH-pK_a} k_r^{CSH}$	$k_r^{CSH} = rD(CSH)/V$
2	$CS^- + H_2O_2 \rightarrow CSOH + OH^-$	$k_3 = 25\ M^{-1}s^{-1}$	
3	$CS^- + CSOH \rightarrow CSSC_{sol} + OH^-$	$k_4 = 720\ M^{-1}s^{-1}$ source[6]	
4	$CSSC_{sol} \rightleftarrows CSSC_{fib}$	$k_7 = 1.46 * 10^{-17}\ M^{-1}s^{-1}$	$k_{sp} = 1000\ M^{-1}s^{-1}$
5	$DTT + OH^- \rightleftarrows DTT^- + H_2O$	$k_f^{DTT} = 10^{pH-pK_a} k_r^{DTT}$	$k_r^{DTT} = rD(DTT)/V$
6	$DTT^- + CSSC_{sol} \rightarrow DTTSC + CS^-$	$k_6 = 5\ M^{-1}s^{-1}$	
7	$DTT^- + CSOH \rightarrow DTTSC + OH^-$	$k_5 = 10\ M^{-1}s^{-1}$	
8	$DTTSC \rightarrow DTT_{cyc} + CSH$	$k_d = 2.83 * 10^{-17}\ M^{-1}s^{-1}$	
9	$DTT^- + H_2O_2 \rightarrow DTTOH + OH^-$	$k_1 = 0.0046\ M^{-1}s^{-1}$	
10	$DTTOH \rightarrow DTT_{cyc} + OH^-$	$k_d = 2.83 * 10^{-17}\ M^{-1}s^{-1}$	

11	$2CSSC_{sol} \rightarrow 2CSSC_{fib}$	$k_7 = 1.46 * 10^{-17}\ M^{-1}s^{-1}$

Simulation Details

We simulate these chemical kinetics with the Gillespie Stochastic Simulation Algorithm (SSA)[7] with home-built code. The Gillespie SSA stochastically solves single realizations of the master equation, $\dot{p}(t) = Wp(t)$.[8] We simulate trajectories representing single evolutions of the species counts and fibers in time. The count of each species, fiber statistics, and reaction occurrence counts are recorded every $\Delta t = 0.1\ s$ for the forward, reverse, and dissipative processes. The initial conditions for each simulations use the same concentrations of species and conditions as in the experiments within a simulation volume of $V = 5 * 10^{-18}\ L$. We take the rate constants of diffusion-limited reactions as the diffusion coefficient of the relevant species.[8]

We also generate statistics of fibers in these simulations. Each time the fiber birth reaction (Rxn. 11) is chosen, a new fiber is created that is two subunits in length. Once there is at least one fiber formed, reaction 4, the addition and removal of subunits to/from fibers via Rxn. 4 has a finite probability. Each time this reaction is selected to occur, a fiber is chosen at random to gain or lose one subunit. If a fiber chosen to lose a subunit has a length of 2, that fiber is destroyed, and two subunits are released to the solution rather than one. At each interval on which the species counts are recorded ($\Delta t = 0.1\ s$), the number of fibers, mean length of fibers, and standard deviation of the length of fibers are also recorded.

The simulation code was written in C, and simulation output was analyzed in MatLab.

Rate constant determinations

In order to benchmark our simulations, we compare the profiles of various species counts and fiber statistics in time to experimental observations. The total time for each process to complete was the initial point of comparison. To match the timescales of simulations to experiments, we varied the rate constant values in the chemical mechanism. The goal of this was to find a single set of rate constant values that could be used in the forward, reverse, and dissipative processes that would match the timescale of experiments of the same processes. The forward process has the fewest unknown rate constants and was therefore considered first. The reverse process was subsequently analyzed while using the ranges of rate constant values determined in the exploration of the forward process. Following this, ranges of rate constant values were used from a combined understanding of the analysis of the forward and reverse processes to consider the dissipative process. The dissipative process was then optimized to be as close to the experimental timescale as possible by varying the remaining rate constants that were not important in the forward or reverse process or which had a range of possible values in the forward and reverse process.

In the forward process, only reactions 1-4 and reaction 11 occur. Of these reactions, only the rate constant for the dissociation of CSSC monomers from fibers (k_{sp}, reaction 4) is experimentally unknown. We varied the values of these rate constants in our simulations to match the simulation timescale of the three processes with the timescale of experiments. In addition to these, we varied the rate constant for reaction 2 (k_3) because we found in our simulations of the forward process that the experimentally determined value ($k_3 = 0.288\ M^{-1}s^{-1}$) did not result in any fiber growth. A series of pairs of values of k_3 and k_{sp} were identified for which the timescale of simulations closely

matched the timescale of experiments. The timescale comparison was made by observing the profile of the count of subunits incorporated into fibers and the number of fibers in the simulations. These values plateaued around 1500 s, which matches the experiments whose fiber growth periods are largely, though not entirely, complete by 1500 s. We then used these pairs of values for the reverse process to narrow down the values of these rate constants to a single value each that can be held consistent over simulations of all three processes.

We then considered matching the timescale of the reverse process to experiments by using the narrowed scope of values for rate constants determined by optimization of the forward process. The reactions that occur in the reverse process are reactions 4-8. Of the rate constants corresponding to these reactions, the rate constants that do not appear to have been previously measured experimentally are k_{sp} and k_6. We determined a series of possible values of k_{sp} for the forward process. We therefore considered values of k_6 for each previously determined value of k_{sp}. In this optimization of the reverse process, we noted that an excess amount of H_2O_2 was used. Therefore, after the completion of the forward process, there is remaining H_2O_2 and CSOH in the solution. Reactions 9 and 10 then still need to be considered in the reverse process, though to a lesser extent than in the dissipative process. The profiles of the count of subunits incorporated into fibers and the count of fibers in time were again compared to experiments to determine the time at which the reverse process could be considered complete in our simulations. This time was then matched to experiments by varying the specified rate constant values.

In the dissipative process, all reactions in the chemical mechanism can occur. Of these reactions, we have a set of values of k_{sp}, k_3, and k_6 that, when used in our simulations, result in correct timescales of the forward and reverse processes from our previous analysis of these processes. The only remaining rate constant to determine is k_5, which corresponds to the deactivation of CSSC monomers in solution by DTT. We varied this rate constant for each set of values of the rate constants k_{sp}, k_3, and k_6, looking to match the timescale of simulations to the timescale of experiments. The best timing found through this method is one order of magnitude smaller than the timescale of experiments for the dissipative process but matches the timescale of experimental observations for the forward and reverse processes. The rate constant values determined from this analysis are provided in the table above.

Forward process

The forward process begins with equal concentrations of CSH and H_2O_2. The CSH species are quickly deprotonated to CS^-, Figure E.20(a, gold). These resulting CS^- species then react with H_2O_2 to produce the alcohol CSOH, Figure E.20(a, gray). The CSOH can then react with other CS^- to produce the subunit for assembly $CSSC_{sol}$ in solution. Subunits in solution assemble almost as quickly as they are formed, so only nominal amounts of free CSSC in solution are present in solution at any given time. Meanwhile, the length and number of fibers in solution grows quickly until there are no more available subunits to incorporate, Figure E.20(b-c). The CS^- required for these reactions continue to be produced by deprotonation of CSH because the conjugate base CS^- is quickly consumed in subsequent reactions. Following full consumption of all CSH

in solution, reactions adding and removing a subunit from the assembly dominates. Non-zero amounts of CSOH and H_2O_2 remain in solution at this point in time, Figure E.20a.

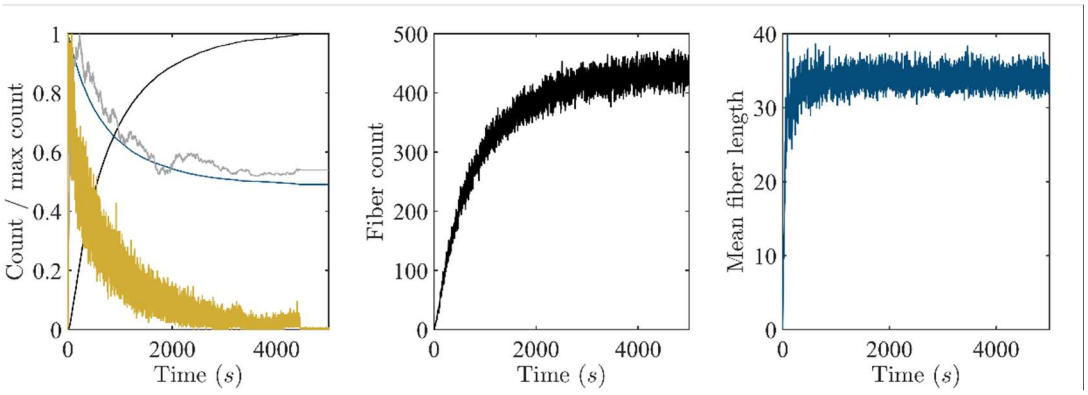

Figure E.20. (a) Normalized count of assembled subunits $CSSC_{fib}$ (black), fuel H_2O_2 (blue), intermediate formative species CSOH (gray), and deprotonated CS^- (gold) in time reported in $\Delta t = 0.1\,s$ time intervals. **(b)** Count of fibers in time reported in $\Delta t = 0.1\,s$ time intervals. **(c)** Mean length of fibers in time reported in $\Delta t = 0.1\,s$ time

We can track the forward process not only with species counts (Figure E.20(a)) and fiber statistics (Figure E.20(b-c)) but also through the count of occurrences of each possible reaction in the chemical mechanism. Initially, CSH is deprotonated (Figure E.21(a, black)) in an effort to move toward an equilibrium concentration of CSH and its conjugate base CS^- as defined in the Henderson-Hasselbalch equation. However, the produced CS^- is quickly consumed by reaction with hydrogen peroxide in solution to produce CSOH and subsequent reaction of CSOH and CS^- to form subunits for assembly, Figure E.21(b). Re-protonation of CS^- to CSH does occur (Figure E.21(a, blue)), but the count of occurrences of this reaction are less than the count of occurrences of the deprotonation reaction because the product of deprotonation is used to make subunits in addition to being a reactant in the re-protonation reaction. Both of these reactions have a plateau in counts (Figure E.21(a)) when all CSH is turned to CS^- and

subsequently used for subunit production. The subunits cannot be decomposed back to CS^- in the forward process due to the lack of DTT in solution. Therefore, with excess hydrogen peroxide in solution, all of the CSH initially in solution becomes either subunits CSSC or CSOH by the end of the forward process. This consumption of available CSH/CS^- is also the reason for the plateau in the count of occurrence of subunit-generating reactions.

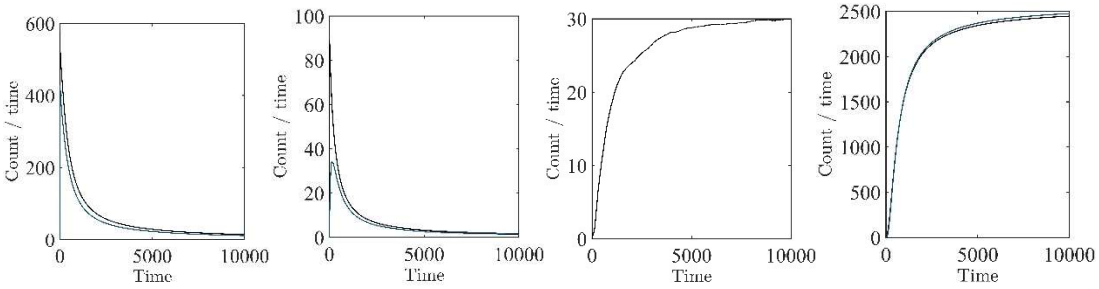

Figure E.21. (a) Time profile of count of occurrences of reaction 1 per unit time, both forward (black) and reverse (blue) (the deprotonation of CSH and protonation of CS^-), reported in $\Delta t = 0.1\ s$ increments. **(b)** Time profile of count of occurrences of reactions 2 (black) and 3 (blue), formation of CSSC in solution, per unit time reported in $\Delta t = 0.1\ s$ increments. **(c)** Time profile of fiber births per unit time, reported in $\Delta t = 0.1\ s$ increments. **(d)** Time profile of count of occurrences of reaction 4, forward (black) and reverse (blue) (the addition and removal of subunits from fibers) per unit time, reported in $\Delta t = 0.1\ s$ increments.

The other three reactions (fiber birth, addition of CSSC to fiber, and removal of CSSC from fiber) that occur in the forward process do not exhibit plateaus in their count of occurrences when the forward process is complete at late times in simulations, Figure E.21(c-d). This is because the addition and removal of CSSC to/from fibers continues after the depletion of CSH/CS^- in solution, Figure E.21(d). Because these fluctuations between fibers and solution continue, enough CSSC (2 species in a simulation as the simulation is assumed to be well-mixed) can be present in solution at late times to continue to make new fibers and grow existing fibers.

Reverse process

Following completion of the forward assembly process, DTT can be added to solution to start the reverse (disassembly) process. DTT immediately begins to be deprotonated to DTT^-, Figure E.24a, black). This deprotonated DTT can then scavenge any subunits in solution as well as any CSOH and H_2O_2 remaining in solution via reactions 6, 7, and 9. This scavenging process forms DTTSC and DTTOH. These species can then decompose via reactions 8 and 10, deactivating the contained DTT to DTT_{cyc} and preventing that resulting molecule of DTT_{cyc} from having subsequent reactions. DTT_{cyc} in solution increases over time as a result, Figure E.22(a, blue). Through this process, the DTT in solution decreases quickly while fibers are disassembled, Figure E.22(b-c). The amount of DTT^- in solution plateaus after approximately 2 minutes at a non-zero value. At this time, the number of fibers in solutions plateaus at a low value, Figure E.22(b). This corresponds to experiments, where all or nearly all of the gel is consumed by the end of the reverse process.

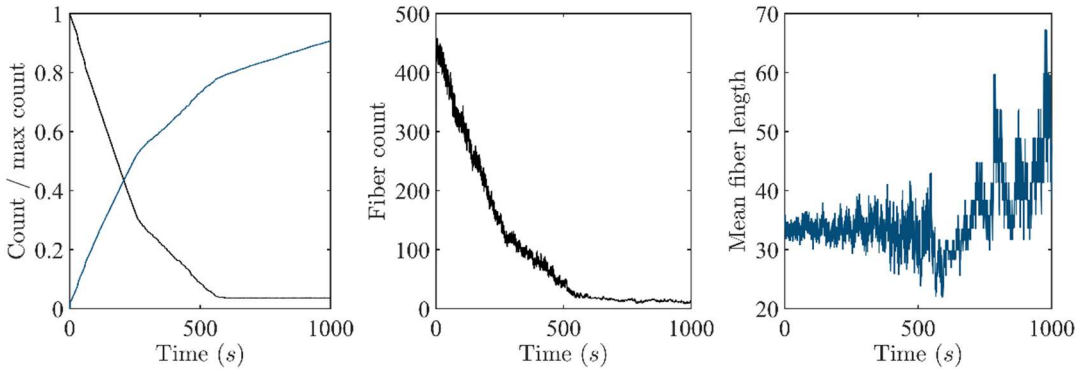

FigureE.22. (a) Normalized count of assembled subunits $CSSC_{fib}$ (black) and deactivated scavenging species DTT_{cyc} (blue) in time reported in $\Delta t = 0.1\ s$ time intervals. **(b)** Count of fibers in time reported in $\Delta t = 0.1\ s$ time intervals. **(c)** Mean length of fibers in time reported in $\Delta t = 0.1\ s$ time intervals.

The speed at which fibers are disassembled is controlled by how quickly subunits detach from fibers (through the rate constant k_{sp}) and how quickly DTT^- can scavenge

those subunits in solution (through the rate constant k_6). Both rate constants must be sufficiently large for fibers to disassembled and the reverse process to go forward. Both rate constants are determined through the means specified before.

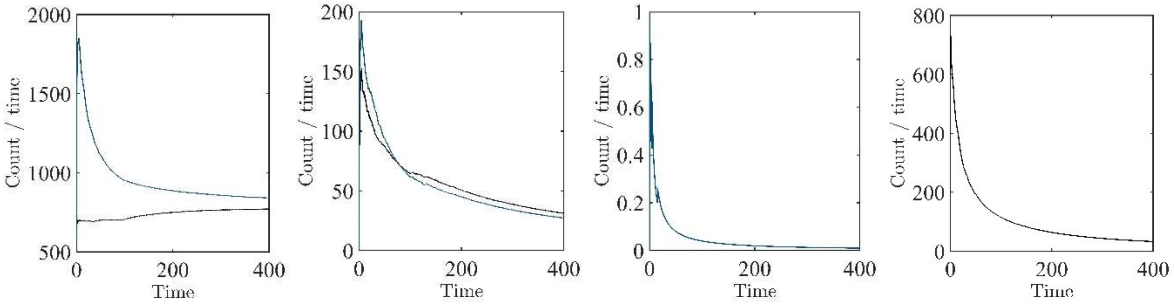

FigureS23. (a) Time series of count of occurrences of CSH deprotonation (black) and CS^- protonation (blue) per unit time, reported in $\Delta t = 0.1\ s$ increments. **(b)** Time series of count of occurrences of reaction 2 (black) and 3 (blue) to form CSSC per unit time, reported in $\Delta t = 0.1\ s$ increments. **(c)** Time series of count of occurrences of fiber birth (black, zero for all time) and CSSC addition to fibers (blue) per unit time, reported in $\Delta t = 0.1\ s$ increments. **(d)** Time series of count of occurrences of CSSC removal from fibers per unit time, reported in $\Delta t = 0.1\ s$ increments.

We can also track the count of occurrences of each reaction that is possible in the reverse process. Following introduction of DTT into solution, DTT is rapidly deprotonated, Figure S24(a, black). At the same time, subunits CSSC are incorporated into fibers and unincorporated from fibers, Figure S23(c-d). The DTT^- resulting from deprotonation of DTT in solution can then scavenge excess H_2O_2 remaining in solution from the forward process via reaction 9, CSOH remaining in solution (and, to a lesser extent, CSOH formed during the decay of fibers by excess hydrogen peroxide from the forward process) via reaction 7, and CSSC in solution via reaction 6 as subunits incorporate and unincorporate (reaction 4 forward and reverse) from fibers. Of these, CSSC is scavenged the most and hydrogen peroxide the least, Figure S24(b). The scavenging of hydrogen peroxide has a slower rate constant than hydrogen peroxide reacting with CS^- formed in the decomposition of fibers. This scavenging reaction therefore occurs the least. This process

rapidly decays the fibers. At the same time, a small amount of fiber growth reactions occur (Figure S23(c, blue)), though no new fibers are formed, Figure S23(c, black).

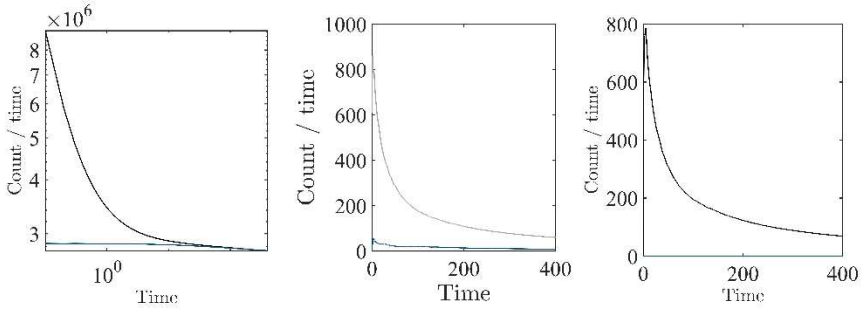

FigureS24. (a) Time series of count of occurrences per unit time of DTT deprotonation (black) and protonation of DTT^- (blue), lines overlap, reported in $\Delta t = 0.1\ s$ increments. **(b)** Times series of count of occurrences per unit time of DTT^- scavenging of hydrogen peroxide (black, zero for all time), CSOH (blue), and CSSC in solution (gray), reported in $\Delta t = 0.1\ s$ increments. **(c)** Time series of count of occurrences per unit time of decomposition of DTTSC (black) and DTTOH (blue, zero for all time), reported in $\Delta t = 0.1\ s$ increments.

Dissipative process

In the dissipative process, CSH, DTT, and H_2O_2 are initially all present in solution. Following the initial formation of subunits and fibers, the reactions associated with both the forward and reverse process can then proceed simultaneously. This process increases the number of fibers in solution and the length of those fibers for an extended time (until approx. 3000 s), Figure S25(b-c). During this time, fibers are being created and lengthened. While the fiber decay process does occur during this time, the consumption of hydrogen peroxide fuels fiber formation and growth. There are fluctuations in the number of fibers and the mean length of fibers associated with the simultaneous decay process. However, the overall trend we see during this time is fiber birth and growth.

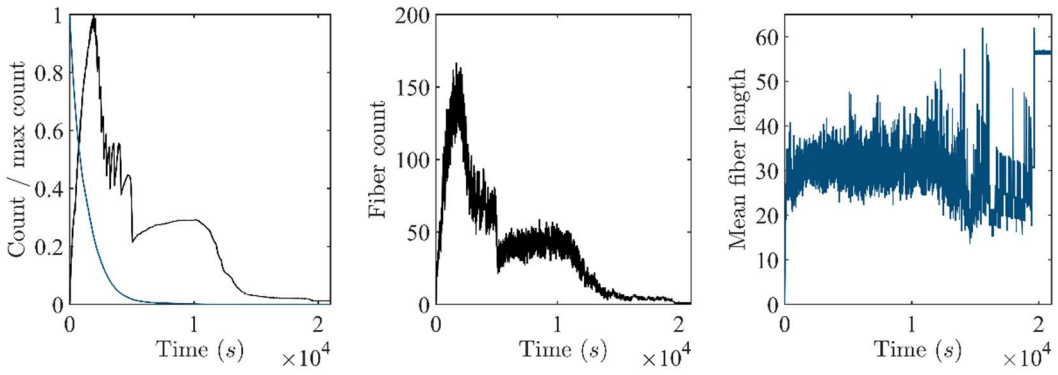

Figure E.25. (a) Normalized count of assembled subunits $CSSC_{fib}$ (black) and fuel H_2O_2 (blue) in time reported in $\Delta t = 0.1\ s$ time intervals. Dashed vertical line indicates time of peak amount of CSSC incorporated into fibers. **(b)** Count of fibers in time reported in $\Delta t = 0.1\ s$ time intervals. **(c)** Mean length of fibers in time reported in $\Delta t =$

After approximately 3000 s, the disassembly process dominates, Figure E.25(a-c). This occurs when the H_2O_2 in solution is largely depleted, Figure E.25(a, blue). However, the maximum in the fiber count as well as the maximum in the mean length of fibers occur before the hydrogen peroxide is fully consumed as the decreasing concentration of hydrogen peroxide at this time decreases the propensity of its reaction with CS^-, Figure E.25(a-b).

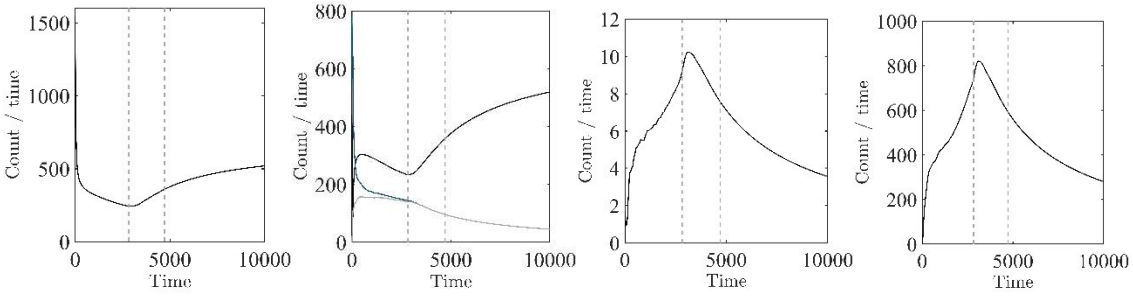

Figure E.26. (a) Time series of count of occurrences per unit time of CSH deprotonation reported in $\Delta t = 0.1\ s$ time intervals. **(b)** Time series of count of occurrences per unit time of CS^- protonation (black), CSOH formation (blue), and CSSC formation (gray) reported in $\Delta t = 0.1\ s$ time intervals. **(c)** Time series of count of occurrences per unit time of fiber births (black) reported in $\Delta t = 0.1\ s$ time intervals. **(d)** Time series of count of occurrences per unit time of subunit incorporation into fibers reported in $\Delta t = 0.1\ s$ time intervals.

The full consumption of H_2O_2 in solution (due to reaction with CS^- and DTT^-) prevents subunits CSSC to be reformed and reincorporated into fibers. This occurs near

3000 s in these data, as indicated by the plateau in the occurrence of the reaction for the formation of CSSC (Figure E.26(b, gray)), the maximum in the number of subunits incorporated into fibers (Figure E.25(a, black)), and the slowing to a plateau of the reaction incorporating subunits into fibers (Figure E.26(d)). This essentially stops the reassembly process and therefore the dissipative assembly as there is no more fuel to dissipate to perpetuate the process.

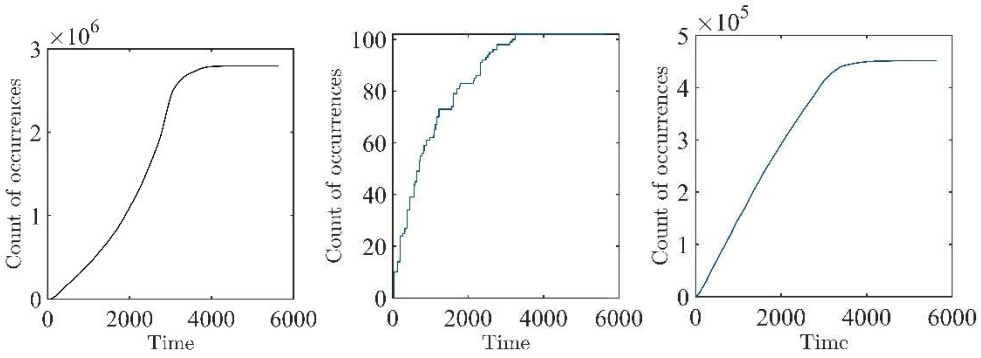

Figure E.27. (a) Time series of count of occurrences of DTT deprotonation reaction reported in $\Delta t = 0.1\ s$ time intervals. **(b)** Time series of count of occurrences of scavenging reactions of CSOH (black, nearly zero) and CSSC (blue) by DTT^- reported in $\Delta t = 0.1\ s$ time intervals. **(c)** Time series of count of occurrences of decomposition of DTTOH (black, nearly zero) and DTTSC (blue) reported in $\Delta t = 0.1\ s$ time intervals.

Following this time when the hydrogen peroxide fuel in solution is fully consumed, fibers are rapidly degraded. The scavenging reactions of DTT^- and subsequent decomposition of the product of scavenging continue until about 5000 s (Figure E.27(b-c)), by which point all or most of the CSSC, CSOH, and H_2O_2 in solution are consumed (Figure E.25(a)). As an excess amount of DTT is provided in solution, the remaining DTT and DTT^- in solution quickly reach their equilibrium concentrations. As the remaining CSSC and CSOH are being degraded, CSH and CS^- also go to their equilibrium concentrations.

A phase of short fibers stacking in parallel is observed in experiments for a (relatively) extended period of time in the dissipative process, for a brief period of time in

the reverse process, and not at all in the forward process. We surmise this is because fibers have time to grow to greater lengths and diffuse away from each other without also being simultaneously decayed when the process is carried out sequentially. The diffusion of fibers away from each other prevents there from being dense pockets of decaying fibers, as occurs in the dissipative process. There is then less entropic driving toward creating the stacked conformation in the sequential process. This can happen because fibers are not being decayed while they are simultaneously being built in the forward process. Allowing both of these processes to happen simultaneously (i.e., the dissipative process) prevents fibers from growing as long as they otherwise would in the sequential process. This decay in the dissipative process is also happening when fibers would otherwise be diffusing away from each other with very little decomposition in the sequential process. The occurrence of this stacked phase in the reverse process is also likely prolonged in the dissipative process due to the general lengthening of the timescale on which the dissipative process occurs. This lengthening is a direct result of the building and decaying of fibers being carried out simultaneously.

Cycle

From our simulations, the defining feature that distinguishes the dissipative process from the sequential process is a set of reactions that together constitute a “dissipative cycle”. This is a subset of reactions that leads to the repeated growth and decay of fibers. These reactions that form the dissipative cycle can be separated into those that lead to the growth of fibers and those that lead to the decay of fibers. The fiber growth reactions in this cycle are reactions 2 and 3, which together form the subunits for assembly CSSC. These reactions occur in all three processes. However, these reactions

occur much less frequently in the reverse process than the forward process and only as a result of H_2O_2 and CSOH remaining in solution from the forward process. The fiber decay reactions in this cycle are reactions 6 and 8, which involve the scavenging of free subunits CSSC by DTT and subsequent decay of the resulting DTTSC. These reactions are not possible in the forward process due to the lack of DTT in solution but occur in both the reverse and dissipative processes. Further, the decomposition of DTTSC produces CS^-, a reactant in both reactions 2 and 3, which form the other half of the cycle.

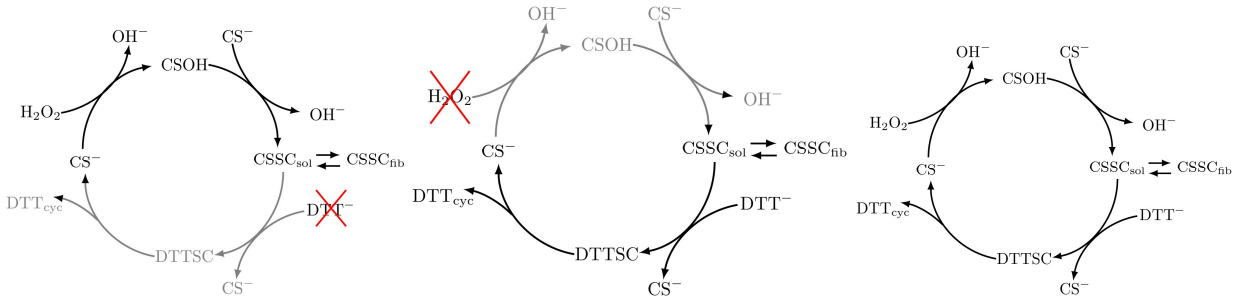

Figure E.28. (a)

To quantitatively measure the difference between the dissipative and sequential processes, we calculated the number of times the system goes through this cycle. We measured this here via the smallest count of reaction occurrences of the four reactions identified in the cycle—and only for simulations using our optimized rate constants. In the forward process, the system cannot undergo this cycle because half of the reactions constituting the cycle lack reactants. In the reverse process, this cycle can occur but only due to residual H_2O_2 and CSOH in the system. A limited number of cycle traversals are possible as a result (8,776 on average over 10 simulations). By comparison, the dissipative cycle has sufficient reactants to freely traverse this cycle many times (90,317 on average over 10 simulations). This prolongs the dis/assembly process by allowing both subunit production and scavenging to occur simultaneously. This cycle continues to be driven by the consumption of chemical fuel: hydrogen peroxide in solution, which is necessary to produce subunits.

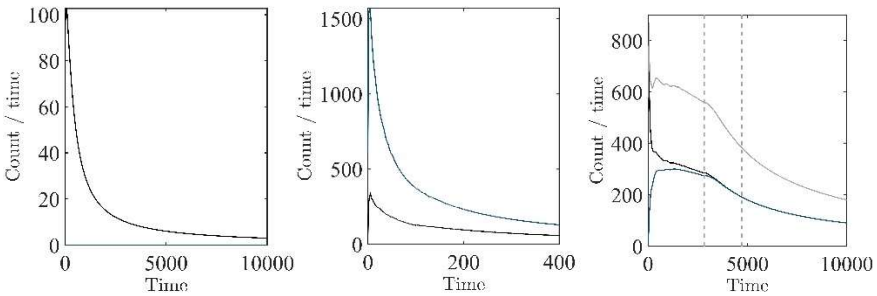

Figure E.29. (a) Sum of occurrences per unit time of reactions 2 and 3 (forward/production half of cycle) vs time reported in $\Delta t = 0.1\ s$ intervals for the forward process. No reactions for the reverse/destruction half of the cycle occur. **(b)** Sum of occurrences per unit time of reactions 2 and 3 (black) and reactions 6 and 8 (blue) vs time reported in $\Delta t = 0.1\ s$ intervals for the reverse process. **(c)** Sum of occurrences per unit time of reaction 2 and 3 (black), reactions 6 and 8 (blue), and reactions 2, 3, 6, and 8 (gray) vs time reported in $\Delta t = 0.1\ s$ intervals for the dissipative process with vertical lines marking the time of maximal number of fibers and time of final plateau.

The production half of this cycle occurs in all three processes but to differing amounts, Figure E.29(a-c). The reverse process has about 63% of the reaction occurrences of reactions 2 and 3 compared to the forward process, Figure E.29(b). This decrease is a result of only residual amounts of hydrogen peroxide and CSOH in solution from the forward process. Conversely, the dissipative process goes through 309% the occurrences of reactions 2 and 3 that the forward process does, Figure E.29(c). This is possible through the regeneration of CS^- through this cycle allowing new subunits to be formed until the hydrogen peroxide fuel is expended.

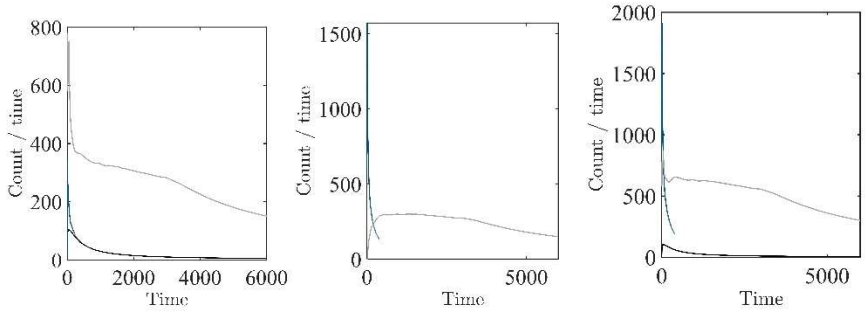

Figure E.30. (a) Sum of occurrences per unit time of reactions 2 and 3 (forward/production half of cycle) vs time reported in $\Delta t = 0.1\ s$ intervals for forward process (black), reverse process (blue), and dissipative process (gray). **(b)** Sum of occurrences per unit time of reactions 6 and 8 (reverse/destruction half of cycle) vs time reported in $\Delta t = 0.1\ s$ intervals for forward process (black, zero for all time), reverse process (blue), and dissipative process (gray). **(c)** Sum of occurrences per unit time of reactions 2, 3, 6, and 8 (all of cycle) vs time reported in $\Delta t = 0.1\ s$ intervals for forward process (black), reverse process (blue), and dissipative process (gray).

The destruction half of this cycle occurs only in the reverse and dissipative processes. The reverse process undergoes these reactions and quickly decomposes the

entire assembly. However, the dissipative system can regenerate reactants for the reproduction of subunits for assembly. As a result, the dissipative process has 309% the occurrence of reactions 6 and 8 that the reverse process has, Figure E.30(b-c).

Varying initial amount of hydrogen peroxide in the dissipative process

Given that hydrogen peroxide acts as a fuel for the dissipative cycle that occurs in the dissipative process, we hypothesize that the initial concentration of hydrogen peroxide will have some effect on the timing and yield of the fibrous material. To analyze this effect, we varied the initial concentration of hydrogen peroxide provided for the dissipative process with all other initial conditions the same as previously. We then observed several important points of time in the simulation data that mark changes in the behavior of the dissipative process: the positions in time and value of the maximal amount of CSSC incorporated into fibers, the maximal number of fibers, the start of the plateau in the number of CSSC incorporated into fibers at long times, the start of the plateau in the number of fibers at long times, the time at which the fuel is no longer consumed linearly in time, and the time at which the amount of fuel is so small in simulations as to be considered depleted.

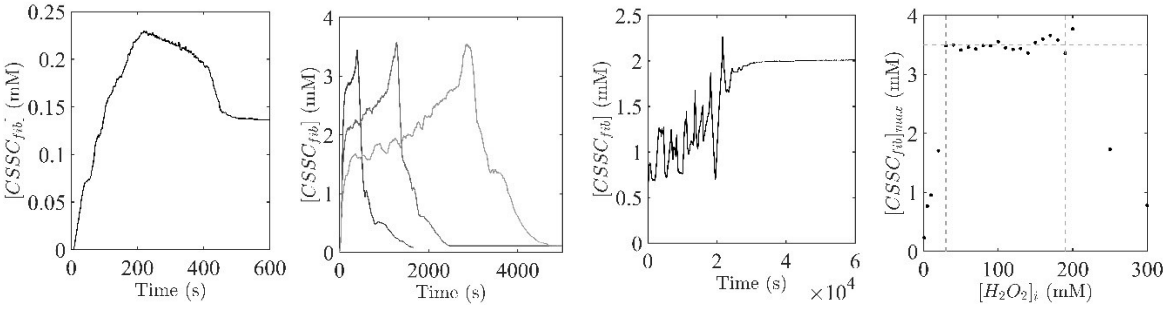

Figure E.31. (a) Concentration of subunits in fibers $[CSSC_{fib}]$ (mM) vs time (s) for starting concentration of hydrogen peroxide of $[H_2O_2]_i = 1\,mM$. **(b)** Concentration of subunits in fibers $[CSSC_{fib}]$ (mM) vs time (s) for starting concentration of hydrogen peroxide of $[H_2O_2]_i = 50, 100, 150\,mM$ (lighter color is increased concentration). **(c)** Concentration of subunits in fibers $[CSSC_{fib}]$ (mM) vs time (s) for starting concentration of hydrogen

peroxide of $[H_2O_2]_i = 240\,mM$. **(d)** Maximal concentration of subunits in fibers (mM) vs initial concentration of hydrogen peroxide (mM). Vertical lines denote minimal and maximal initial concentrations for dissipative process to proceed as previously detailed. Horizontal line denotes mean maximal concentration of subunits in fibers.

When we varied the initial amount of hydrogen peroxide supplied to the system between 0.1 mM and 1000 mM, we found that the maximal number of subunits incorporated into fibers, the number of fibers, the final plateau value in the amount of subunits incorporated into fibers, and the final plateau in the amount of fibers did not vary significantly with initial concentrations of hydrogen peroxide between 30 mM and 200 mM, Figures. E.31(d), E.31(a-b). Below this range, the amount of fuel provided was insufficient to sustain dissipative assembly for a prolonged time. Above this range, the among of fuel provided is enough to ensure that the total yield of subunits in fibers is maximal (all possible subunits are incorporated into fibers) and sustained. At such high concentrations of the fuel, fibers are not decayed to appreciable amounts, and the species profiles and fiber statistics resemble those of the forward process.

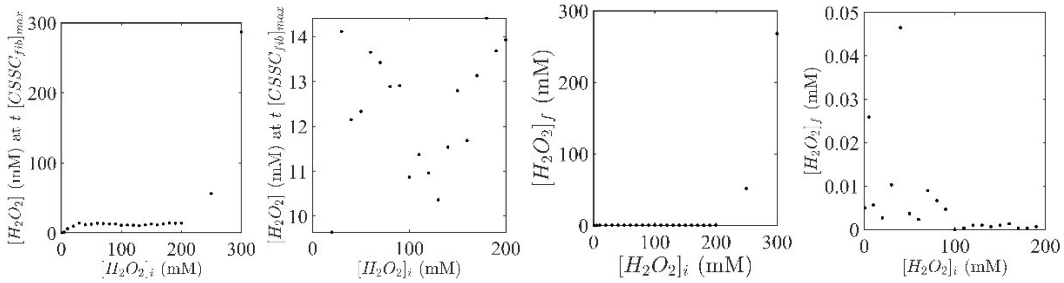

Figure E.32. (a) Concentration of hydrogen peroxide at the time of the maximal concentration of subunits in fibers vs. initial concentration of hydrogen peroxide. **(b)** Concentration of hydrogen peroxide at the time of the maximal concentration of subunits in fibers vs. initial concentration of hydrogen peroxide only within range of initial concentrations of hydrogen peroxide resulting in normal dissipative process. **(c)** Final concentration of hydrogen peroxide vs. initial concentration of hydrogen peroxide. **(d)** Final concentration of hydrogen peroxide vs. initial concentration of hydrogen peroxide only within range of initial concentrations of hydrogen peroxide resulting in normal dissipative process.

We also found that within the range of 30 mM to 200 mM of hydrogen peroxide initially provided, the amount of hydrogen peroxide remaining at the time when the

number of subunits incorporated into fibers is maximal also does not vary appreciably, Figure E.32(c-d). This finding suggests that for a given initial concentration of CSH and DTT, there is a threshold concentration of hydrogen peroxide in solution above which the process switches from being primarily characterized by fiber formation and growth to being primarily characterized by fiber decay and death.

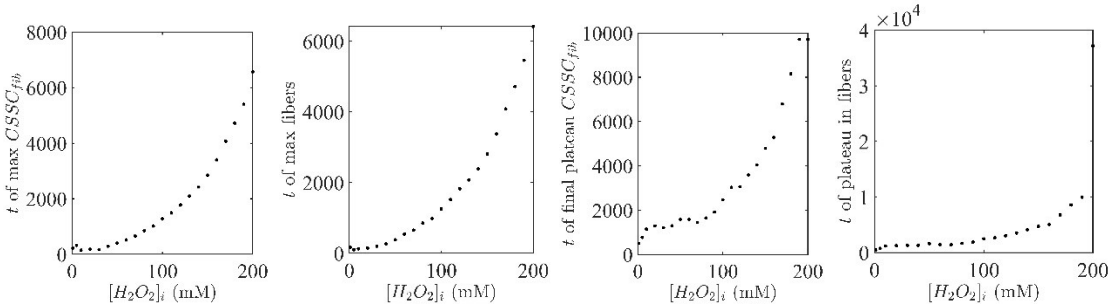

Figure E.33. (a) Time (s) of maximal subunits in fibers vs. initial concentration of hydrogen peroxide (mM). **(b)** Time (s) of maximal number of fibers vs. initial concentration of hydrogen peroxide (mM). **(c)** Time (s) of final plateau in number of subunits in fibers vs. initial concentration of hydrogen peroxide (mM). **(d)** Time (s) of final plateau in number of fibers vs. initial concentration of hydrogen peroxide (mM).

While the counts of species/fibers did not vary in a systematic way with the controlled variation in the initial concentration of hydrogen peroxide, the times at which these important changes in trends occurred did vary in a systematic fashion, Figure E.33. The time of maximal subunits in fibers and the time of maximal count of fibers are almost identical, Figure E.33(a-b). Both times vary systematically with the initial concentration of hydrogen peroxide in solution approximately via the equation $t\ (s) = 130 * \exp\left(0.0212 * [H_2O_2]_i\right)$. The other two pertinent times do not vary with as clean a trend, Figure E.32(c-d). We conclude from these data that the time to reach the peak number of subunits in fibers is a nonlinearly increasing function of the initial concentration of hydrogen peroxide.

Maintain fiber count by injection of hydrogen peroxide

From our simulations, a plausible design principle emerged: because of the nonlinear nature of the system, smaller amounts of fuel might be necessary to sustain the

fibers compared to the amount of fuel needed to create them initially. To test this hypothesis, we added small doses of fuel in the dissipative process to sustain the fiber population when the fiber population was nearly extinct. Using the simulation setup above, we attempted to maintain a specified count of fibers in the simulation by setting a desired threshold count of fibers below which a specified amount of hydrogen peroxide would be injected into the system. In these simulations, it was also important to set a limit on the frequency with which hydrogen peroxide can be injected into the system. If the frequency is too high, there is an abundance of hydrogen peroxide in solution rather than doping the system with small quantities of hydrogen peroxide.

With this constraint, the system proceeds as normal for the dissipative process until fibers begin to collapse, Figure E.34(a). In the time where fiber collapse dominates, injection of hydrogen peroxide proceeds when sufficient fibers have decayed to cross the threshold value. At this point, hydrogen peroxide is injected into the system. Each time hydrogen peroxide is injected, fibers grow for a short period of time before fibers collapse down to the threshold again. The system then oscillates between fiber growth just after an injection of hydrogen peroxide and fiber collapse following the depletion of that injected amount of hydrogen peroxide. These oscillations continue for an extended period of time (over 15,000 s). The amount of hydrogen peroxide injected into the system at any one time is significantly smaller than the initial amount of hydrogen peroxide in the system, Figure E.34(b, red).

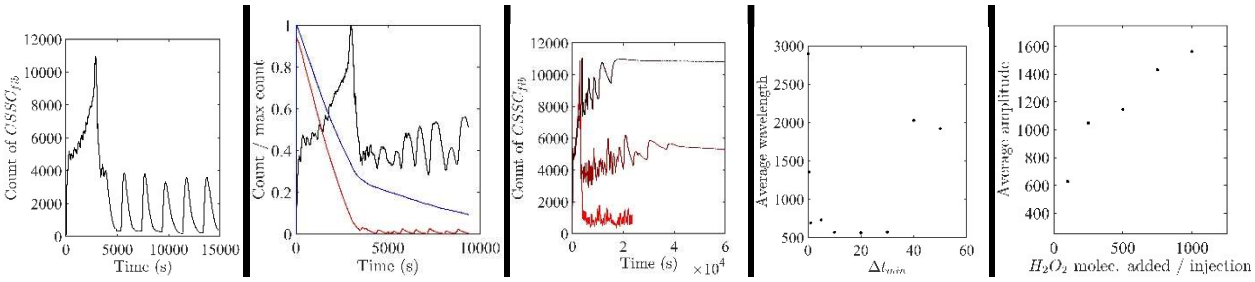

Figure E.34. (a) Count of subunits in fibers while injecting 500 molecules of hydrogen peroxide no more often than every 2,000 s if the number of fibers falls below 50. **(b)** Normalized time profile of count of subunits in fibers (black), hydrogen peroxide (red), and deprotonated DTT (blue) recorded in $\Delta t = 0.1\ s$ increments with a threshold of 50 fibers and injecting 500 molecules of hydrogen peroxide no more often than every 5 s. **(c)** Count of subunits in fibers while injecting 500 molecules of hydrogen peroxide no more than every 10 s if the number of fibers falls below 10 (bright red), 50 (dark red), and 100 (black). **(d)** Average wavelength of oscillations in subunits in fibers time series at late times for a given allowed frequency of injection $\Delta t \in \{0.1\ s, 0.5\ s, 1\ s, 5\ s, 10\ s, 20\ s, 30\ s, 40\ s, 50\ s\}$ for threshold number of fibers 50 and 500 molecules of hydrogen peroxide added per injection. **(e)** Average amplitude of oscillations in subunits in fibers time series at late times for a given number of molecules to add per injection (100, 250, 500, 750, 1000) for threshold number of fibers 50 and an allowed frequency of injection of $\Delta t = 10\ s$.

In this process, the frequency at which injections are allowed, the amount of hydrogen peroxide to inject at a time, and the threshold number of fibers below which to inject hydrogen peroxide can all be varied. We now explore each of these.

Frequency of injection. One might expect the frequency of injection to be closely related to the wavelength of oscillations. However, the wavelength of these oscillations is not the same as the allowed frequency of injection, Figure E.34(d). The period of time for a single wave of this oscillation is longer than the allowed frequency of injection of hydrogen peroxide. This suggests that the wavelength of these oscillations is indicative of the amount of time the system can use a given quantity of hydrogen peroxide to sustain fiber growth. The allowed frequency of injection can be small enough that the system becomes flooded with fuel. The DTT in the system is then quickly consumed, and the time profile for fibers and subunits in fibers resemble the forward process, Figure E.34(c, black). On the other hand, the allowed frequency of injection can be large enough that

the system uses up the injected amount of fuel in growing fibers before those fibers again collapse prior to the next allowed time of injection.

Amount injected. The amplitude of the oscillations is nearly linearly related to the amount of hydrogen peroxide injected, given the same allowed frequency of injection and threshold fiber count below which to inject hydrogen peroxide, Figure E.34(e). This is because a larger amount of fuel is able to sustain fiber growth for a longer period of time. This agrees with observations of varied initial concentrations of hydrogen peroxide.

Fiber threshold. The midpoint of the oscillations depends upon the threshold number of fibers to maintain. The larger the threshold in number of fibers, the higher the axis of oscillations, Figure E.34(c). This is because more subunits are required for a larger number of fibers to be sustained.

Efficiency. The amount of hydrogen peroxide injected in the course of this protocol is more than an order of magnitude less than the initial amount of hydrogen peroxide in solution. However, these small injections can sustain fiber growth significantly longer than the dissipative process alone. Measure the efficiency of this protocol, we define two measures of efficiency: the number of fibers present per count of hydrogen peroxide and the count of subunits in fibers per count of hydrogen peroxide. When we look at the profile of these efficiencies in time, they oscillate with significant amplitude at long times—longer times than when the normal dissipative process functions, Figure E.34 (a-b). This means that the efficiency of the injection process (as measured by either of these two quantities) is significantly greater than the efficiency of the initial dissipative assembly process.

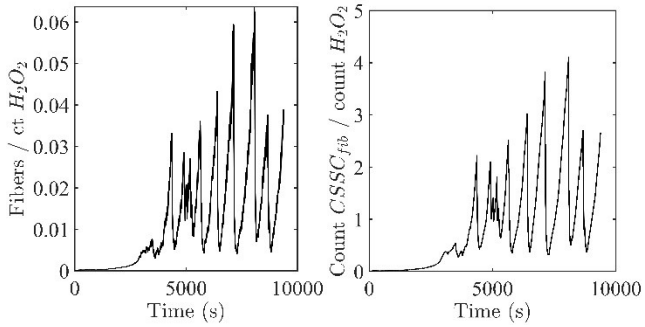

Figure E.35. (a) Time profile of number of fibers per count of hydrogen peroxide in simulations reported in $\Delta t = 0.1\ s$ increments with a threshold for injection of 50 fibers, an injection amount of 500 molecules of hydrogen peroxide, and an allowed frequency of injection of 5 s. **(b)** Time profile of count of subunits in fibers per count of hydrogen peroxide in simulations reported in $\Delta t = 0.1\ s$ increments with a threshold for injection of 50 fibers, an injection amount of 500 molecules of hydrogen peroxide, and an allowed frequency of injection of 5 s.

Inject hydrogen peroxide at regular intervals

From the above, we modified the protocol of injection so that rather than injecting with some allowed frequency *when there are sufficiently few fibers*, the hydrogen peroxide is injected at some rate defined by a frequency of injection and an amount to inject (i.e., the threshold condition is removed). In doing this, we found that the frequency of injection does not matter if the equivalent rate is the same (i.e., 100 molecules / 10 s is the same rate as 50 molecules / 5 s), Figure E.36(a). A smaller rate of injection in this protocol resulted in a longer period of fiber growth, Figure E.36(b). Further, the oscillations in both count of subunits in fibers and fiber counts at late times in the previous protocol are not present using this simplified injection protocol.

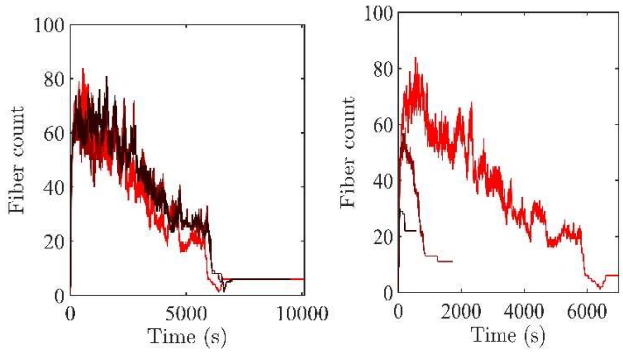

Figure E.36. (a) Fiber count over time for equivalent rate of 100 molecules/s injected with injection frequency of 1 s (red), 10 s (dark red), and 60 s (black), reported in $\Delta t = 0.1\ s$ increments. **(b)** Fiber count over time for an injection frequency of 1 s and an injection amount of 100 molecules (red), 1,000 molecules (dark red), and 10,000 molecules (black).

Maintain an amount of hydrogen peroxide in a simulation by injection of hydrogen peroxide

We next attempted to maintain a given amount of hydrogen peroxide fuel in to test the hypothesis that having excess fuel allows for prolonged fiber growth. When we do this, there are oscillations in the fiber growth for a period of time, Figure E.37. In this time, DTT^- is also available in solution to scavenge subunits and deactivate them. Once all of the DTT in solution has been deactivated to DTT_{cyc}, fibers grow until there are no more subunits available to add to fibers or create new fibers. There are then small fluctuations in the length of fibers and the number of subunits in those fibers. This is due to Reaction 4, which allows subunits to associate and dissociate from fibers and add to other fibers. However, no fiber collapse then occurs because there is no DTT available to facilitate this. Therefore, fuel alone is not sufficient to perpetuate fiber growth.

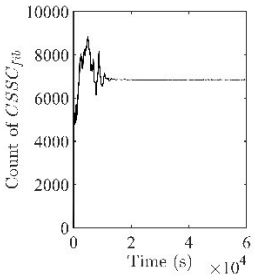

Figure E.37. Count of subunits incorporated into fibers in time reported in $\Delta t = 0.1\ s$ time increments looking to maintain 100,000 molecules of hydrogen peroxide in solution by injecting 100 molecules of hydrogen peroxide.

Diffusion limitation of k_6

Using the rate constants optimized for the forward and reverse processes resulted in simulation timescales of the dissipative process that were too short when compared to experimental timescales, suggesting a mechanism in the dissipative process not present in the isolated forward and reverse processes. We hypothesized that the mechanism causing this discrepancy was the speed of molecular diffusion when fibers are present in solution. To model this effect and match the timescale of experiments in the dissipative process, we modified the rate constant or the scavenging of subunits by DTT^- (k_6), decreasing its effective value based on the number of subunits in fibers at each time during the simulation. (We also attempted to account for this behavior using modifications to this rate constant based on the number of fibers in solution and the mean length of fibers in solution, but these did not appreciably change the timescale of the dissipative process.)

In the data reported for the dissipative process, we modified k_6 after each reaction based on count of $CSSC_{fib}$ in the simulation at that time:

$$k_6' = k_6\left(1 - \frac{1}{\left\lfloor\frac{CSH_i}{2}\right\rfloor + 1} \times [fiber\ count]\right)$$

Increasing the fiber count decreases the value of k_6'. This is normalized by the maximal amount of CSSC that can be in solution, which is given by the initial count of CSH molecules in the simulation integer divided by 2, plus 1 to ensure that the rate constant cannot have a value of zero. This formula ensures that the effective value of the rate constant is within the range $0 < k_6' \leq k_6$.

Using the above formula to modify k_6 after every reaction in the simulation, we again optimized the dissipative process to best match the timescale of experiments. The best matching simulations of the dissipative process to experiments in terms of time that did not sacrifice the matching of timescales for the forward and reverse processes extended the time of simulations of the dissipative process to 4320 s. This is about 1000 s longer than without this diffusion-based modification. However, this is still significantly shorter than the timescale of experiments (~10 hr).

Diffusion-limited bimolecular reaction rate constants

In the following section, we applied a limitation to the speed at which subunits could be scavenged from solution based upon the idea that the fiber content in solution limits the diffusion of species and thereby slowing reactions. This slowed the overall timescale of the dissipative process. However, the timescale resulting from the previous modification was insufficient to match the experimental timescale—the dissipative process still finished too quickly in simulations. Due to this, we add the same limitation on diffusion to all bimolecular reactions in the mechanism: Reactions 2, 3, 6, 7, and 9.

In order to modify these reactions in the same way as previously, we need to apply the same formula to the rate constants k_1, k_3, k_4, k_5, and k_6. Each of these rate constants was modified according to the formula (analogous to the previous):

$$k' = k\left(1 - \frac{1}{\left\lfloor \frac{CSH_i}{2} \right\rfloor + 1} \times [fiber\ count]\right)$$

This imposes an additional limitation on the dissipative system. Each bimolecular reaction in the mechanism is now limited by the amount of fiber content in the system at a given time due to the limitation on diffusion of having solid fibers in the system.

E.4. References

(1) Danino, D.; Talmon, Y.; Zana, R. Cryo-TEM of Thread-like Micelles: On-the-Grid Microstructural Transformations Induced during Specimen Preparation. *Colloids and Surfaces A: Physicochemical and Engineering Aspects* **2000**, *169* (1), 67–73. https://doi.org/10.1016/S0927-7757(00)00418-0.

(2) Nativ-Roth, E.; Regev, O.; Yerushalmi-Rozen, R. Shear-Induced Ordering of Micellar Arrays in the Presence of Single-Walled Carbon Nanotubes. *Chemical Communications* **2008**, *0* (17), 2037–2039. https://doi.org/10.1039/B718148E.

(3) De Yoreo, J. J.; Gilbert, P. U. P. A.; Sommerdijk, N. A. J. M.; Penn, R. L.; Whitelam, S.; Joester, D.; Zhang, H.; Rimer, J. D.; Navrotsky, A.; Banfield, J. F.; Wallace, A. F.; Michel, F. M.; Meldrum, F. C.; Cölfen, H.; Dove, P. M. Crystallization by Particle Attachment in Synthetic, Biogenic, and Geologic Environments. *Science* **2015**, *349* (6247), aaa6760. https://doi.org/10.1126/science.aaa6760.

(4) Pouget, E. M.; Bomans, P. H. H.; Goos, J. A. C. M.; Frederik, P. M.; de With, G.; Sommerdijk, N. A. J. M. The Initial Stages of Template-Controlled CaCO3 Formation Revealed by Cryo-TEM. *Science* **2009**, *323* (5920), 1455–1458. https://doi.org/10.1126/science.1169434.

(5) Nicholson, S. B.; Bone, R. A.; Green, J. R. Typical Stochastic Paths in the Transient Assembly of Fibrous Materials. *J. Phys. Chem. B* **2019**, *123* (22), 4792–4802. https://doi.org/10.1021/acs.jpcb.9b02811.

(6) Erban, R.; Chapman, J.; Maini, P. A Practical Guide to Stochastic Simulations of Reaction-Diffusion Processes. arXiv November 18, 2007. https://doi.org/10.48550/arXiv.0704.1908.

(7) Gillespie, D. T. Exact Stochastic Simulation of Coupled Chemical Reactions. *J. Phys. Chem.* **1977**, *81* (25), 2340–2361. https://doi.org/10.1021/j100540a008.

(8) Zwanzig, R. *Nonequilibrium Statistical Mechanics*; Oxford University Press, 2001.

Appendix F: Supplementary Information for Chapter 7

F.1. Supplementary Tables

Table F.1: Quantitative data for cell wall taken from cryoEM images

Teixobactin	# Images	# Bacteria	Cell Wall Degradation (%)[a]	Low Density Region (%)[a]	Cell Wall Hole(s) (%)[a]	Cell Wall Absent (%)[a]
0	44	85	19	12	7	0
4 µg/mL	104	169	69	6	53	10
1 mg/mL	81	146	100	0	4	96

Notes:
a: Cell wall degradation is a percentage of the bacteria present.

Table F.2: Quantitative data for bacterial fibrils taken from cryoEM images

Teixobactin	# Images	Fibrils Present (%)	Fibril Diameter (nm)	Fibril Diameter Standard Deviation (nm)	# Fibrils Measured [a]
0	44	86	10.9	0.8	55
4 µg/mL	104	94	11.0	0.8	55
1 mg/mL	81	96	10.9	0.7	55

Notes:
a: The number of fibrils measured does not represent the total number of fibrils in the sample.

Table F.3: Quantitative data for teixobactin sheets/cluster fibers

Teixobactin	Bacteria Present (Y/N)	# Images	Sheet Structure Count	(%) Images with Sheet Structure	Sheet Thickness (nm)	Sheet Thickness Standard Deviation (nm)	Fiber Thickness (nm)	Fiber Standard Deviation (nm)	# Fibers Measured [a]
4 µg/mL	Y	104	6	6	4.8	0.6	N/A	N/A	N/A
1 mg/mL	Y	81	128	67	4.5	0.7	7.2	0.7	67
1 mg/mL	N	29	216	100	4.6	0.9	N/A	N/A	N/A

Notes: a: The number of fibers measured does not represent the total number of fibers in the sample. The fibers were low contrast and overlapped as clusters making it difficult to determine the total amount in the sample.

F.2. Supplementary Figures

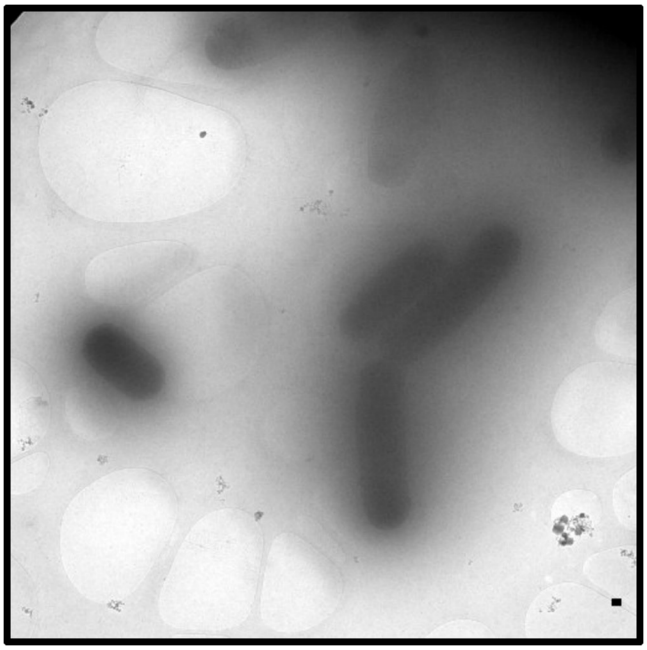

Figure F.1: Overview cryoEM image of *B. subtilis* showing thick densities around bacteria. Some bacteria are contained within thick ice layers making it difficult to see their internal structure.

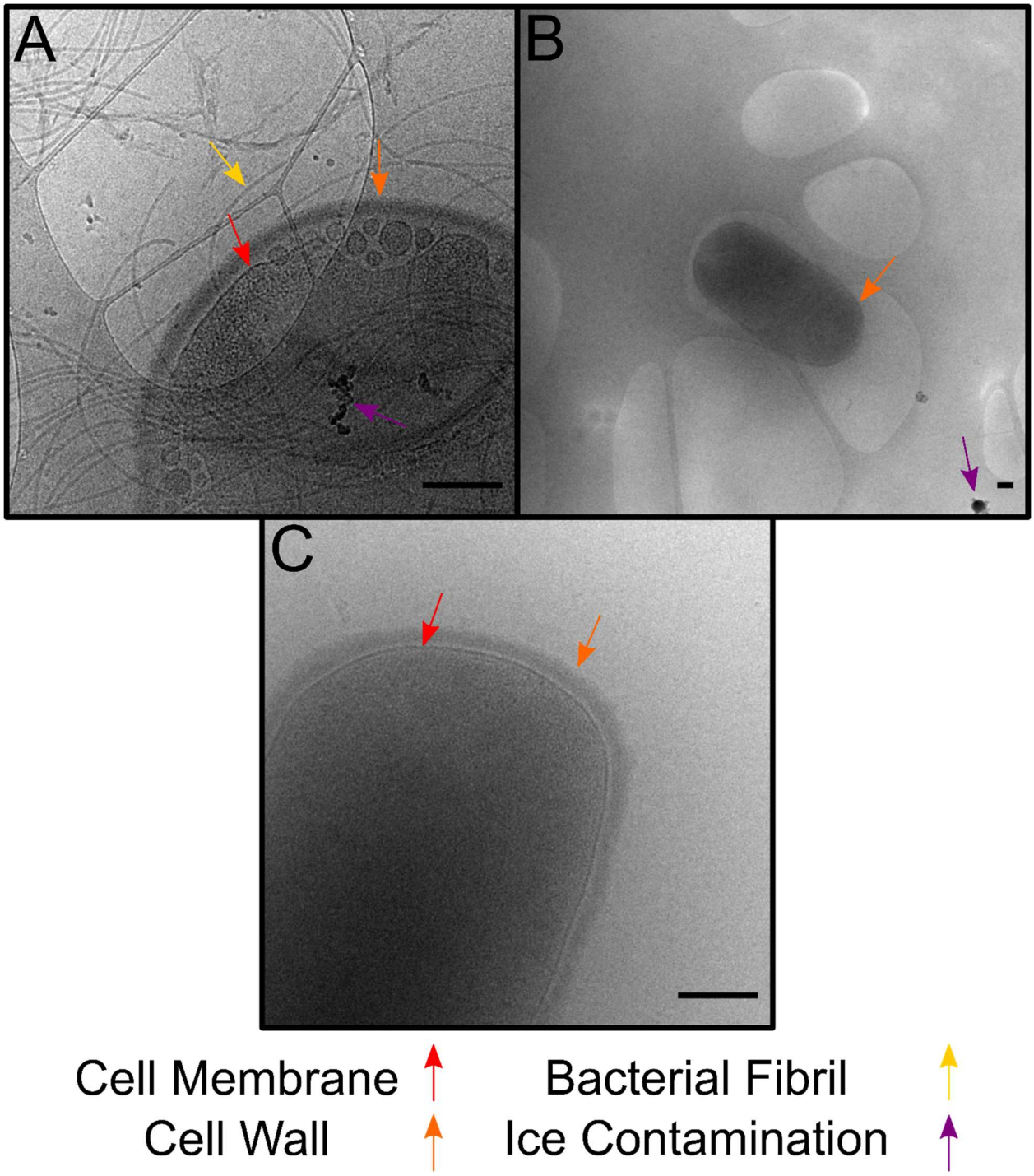

Figure F.2: CryoEM images of *B. subtilis* in PBS buffer and 5% DMSO. Scale bar is 200 nm. A) Image showing bacterial fibrils, and vesicles. B) Overview of bacterium. C). Thicker ice layer around a bacterium makes it harder to see the intracellular features but the cell wall is discernable.

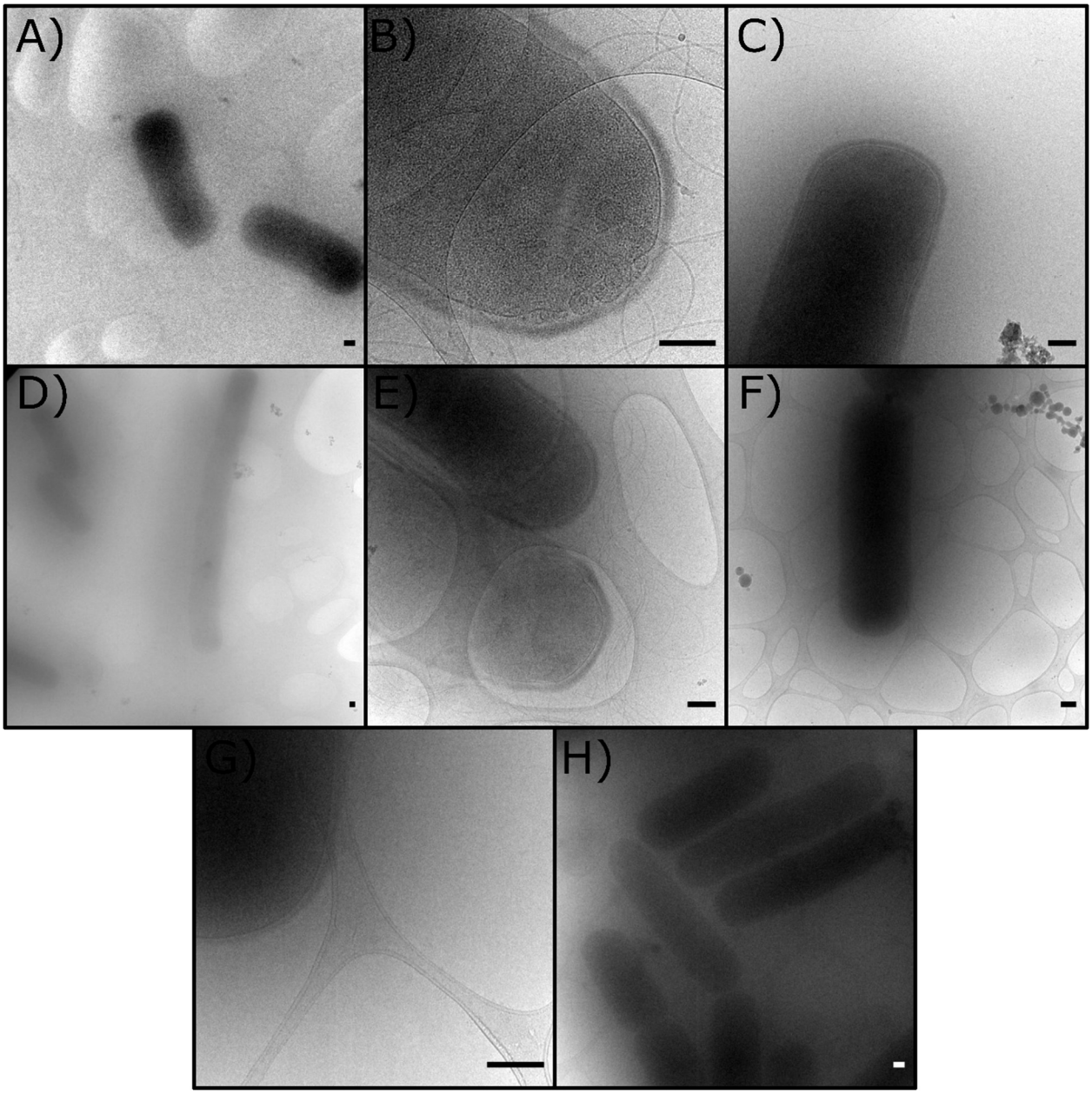

Figure F.3: Various cryoEM images of *B. subtilis* showing intact cell walls. Images A-E are from the *B. subtilis* sample without teixobactin. Images F-H are from the 4μg/mL teixobactin sample.

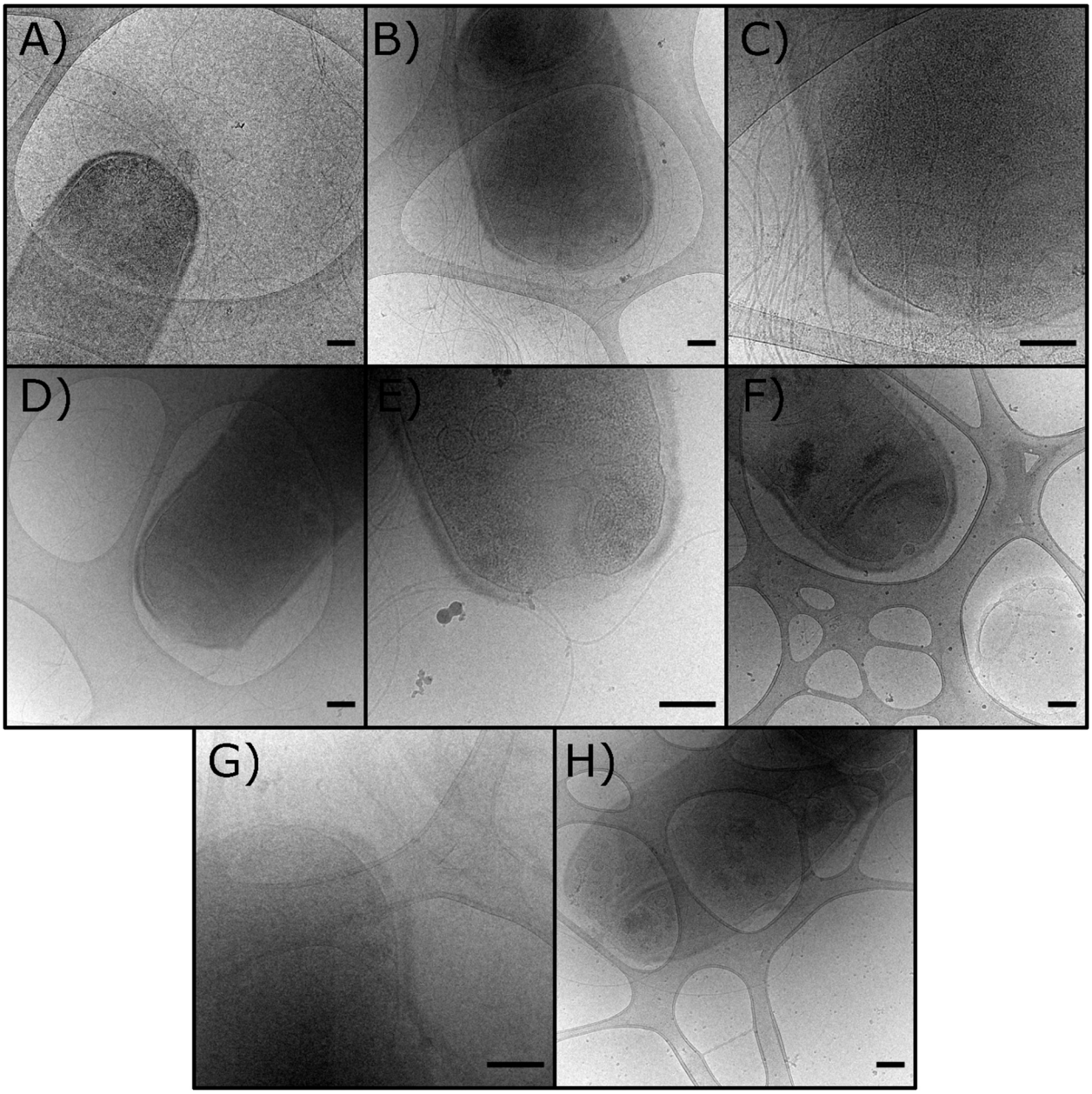

Figure F.4: Various cryoEM images of *B. subtilis* showing thinning or fading of the cell wall. Images A-E are from the *B. subtilis* sample without teixobactin. Images F-H are from the 4μg/mL teixobactin sample.

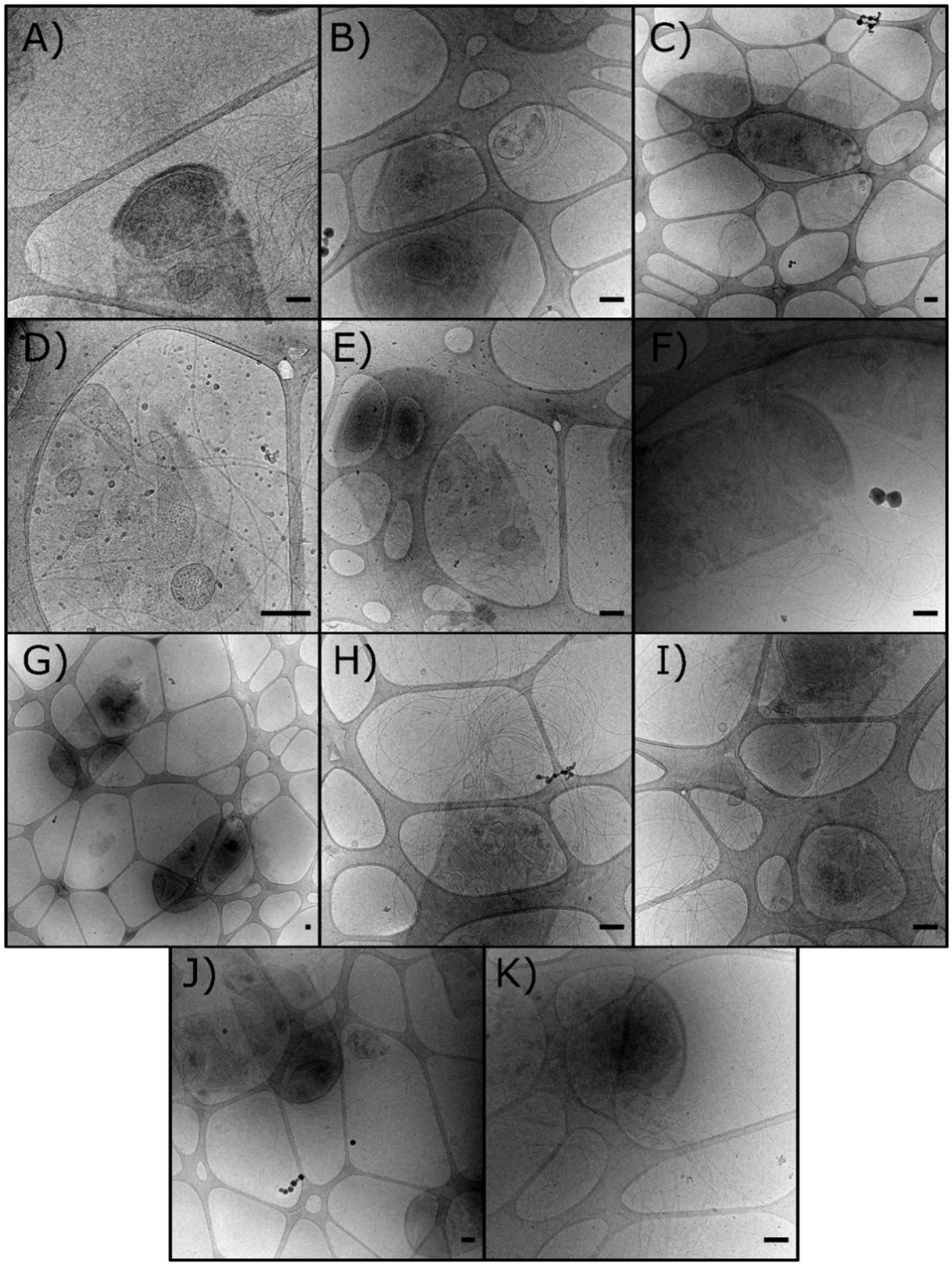

Figure F.5: Various cryoEM images of *B. subtilis* showing holes or breaks in the cell wall Images A is from the *B. subtilis* sample without teixobactin. Images B-J are from the 4µg/mL teixobactin sample. Image K is from the 1 mg/mL teixobactin sample.

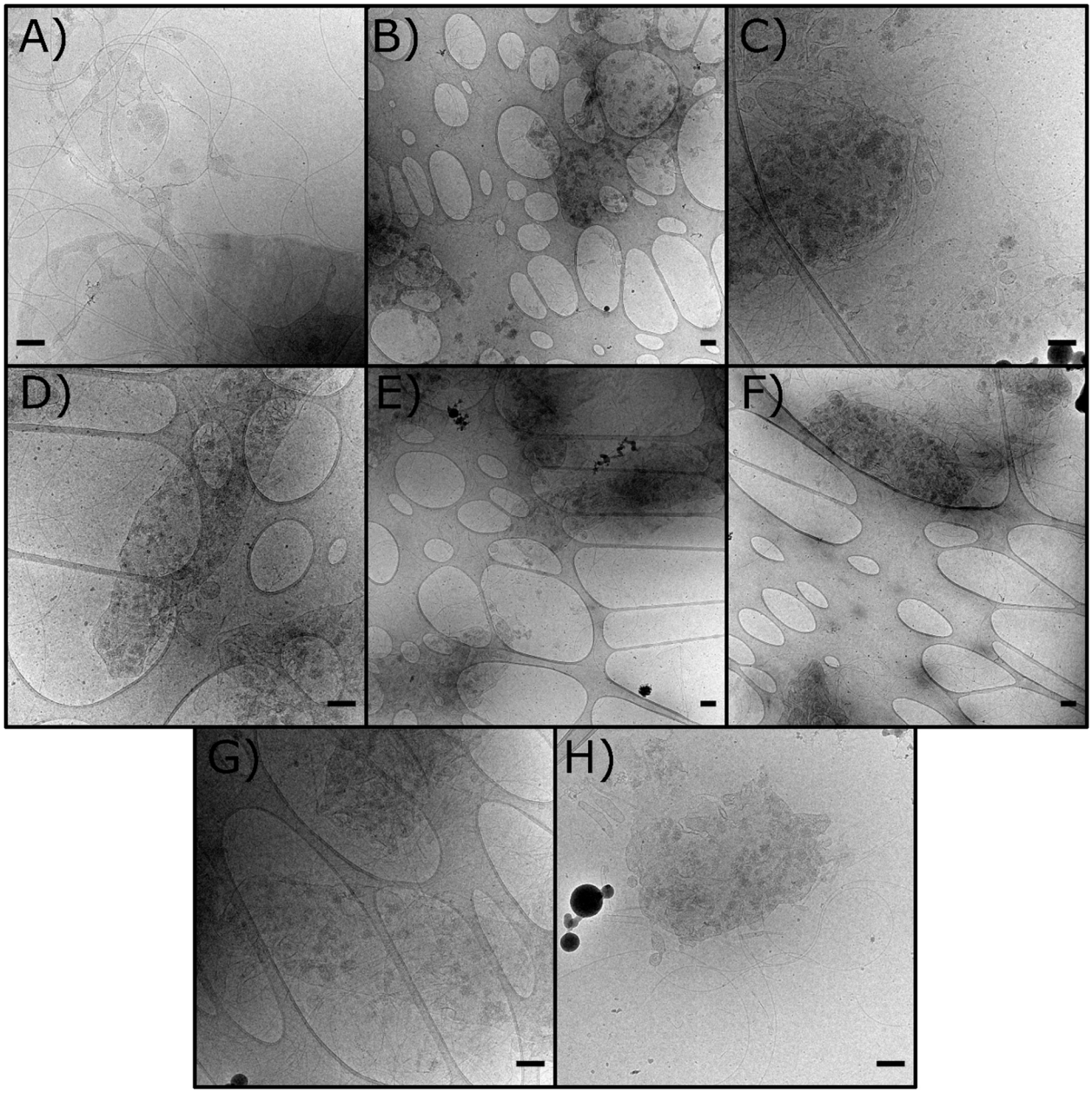

Figure F.6: Various cryoEM images of *B. subtilis* showing the absence of a cell wall. A is from the 4µg/mL teixobactin sample. Image B-H is from the 1 mg/mL teixobactin sample.

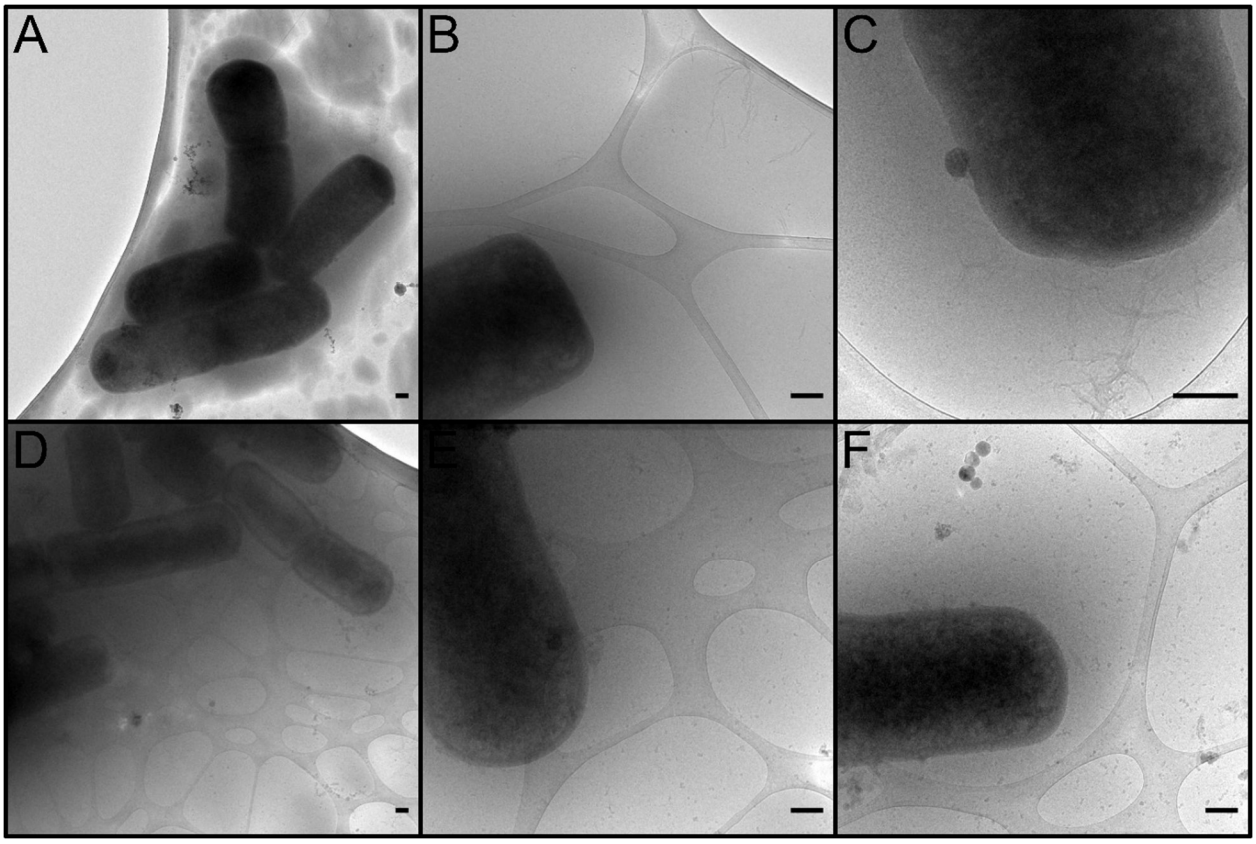

Figure F.7: CryoEM images of *B. subtilis* treated with formic acid. Scale bar is 200 nm. A-C) Treated with 1% formic acid. D-F) Treated with 10% formic acid. Biofilms of B. subtilis, composed of amyloid fibers, are known to impart a degree of antibiotic resistance.[104, 108] The introduction of formic acid in a solution of TasA has been shown to denature TasA fibers. Thus, to understand their origin, *B. subtilis* was treated with a 1% and 10% solution of formic acid and imaged them. No fibers were seen in either sample, providing evidence that the fibrils are TasA amyloid fibers. The formic acid has also deformed the remaining bacterial cells as they are markedly different from an untreated sample (See Figure 7.1 in the main text).

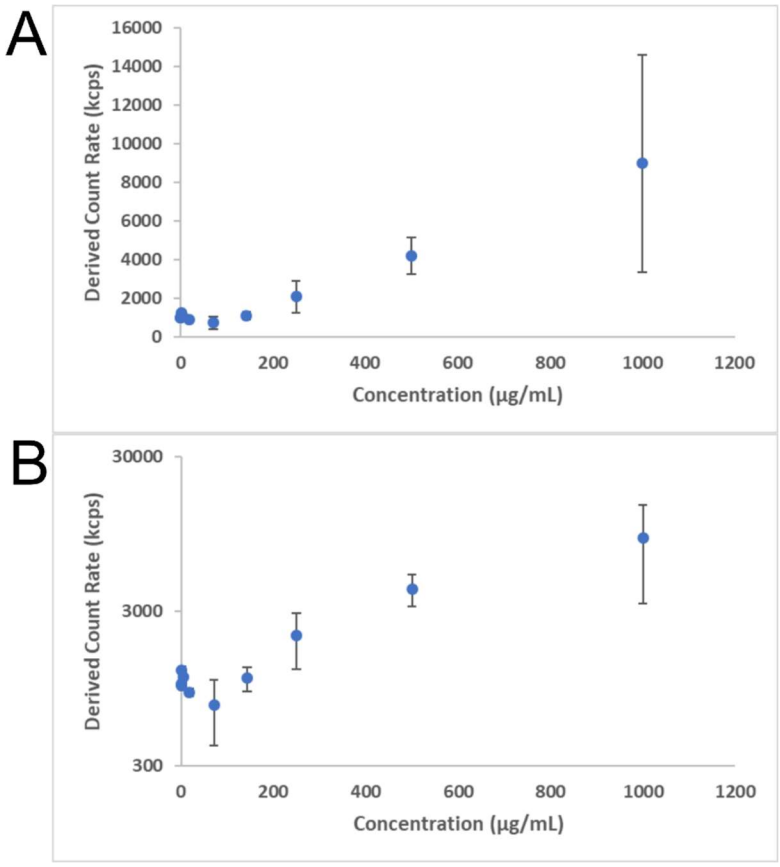

Figure F.8: Derived count rate from light scattering experiment for teixobactin aggregates taken in PBS and 5% DMSO. A) Linear scale. B) Logarithmic scale. Aggregation begins around a teixobactin concentration of 200 µg/mL.

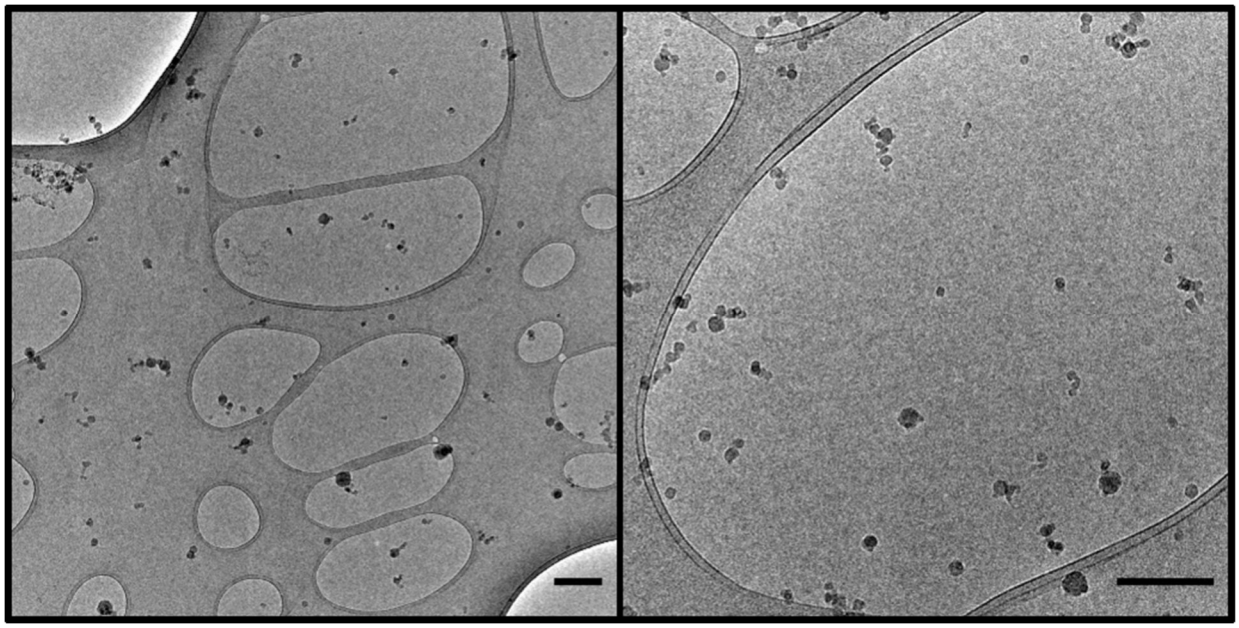

Figure F.9: CryoEM images of 4 µg/mL of teixobactin. Scale bar is 200 nm. Note the lack of assemblies or aggregates. The dark clusters are ice contamination.

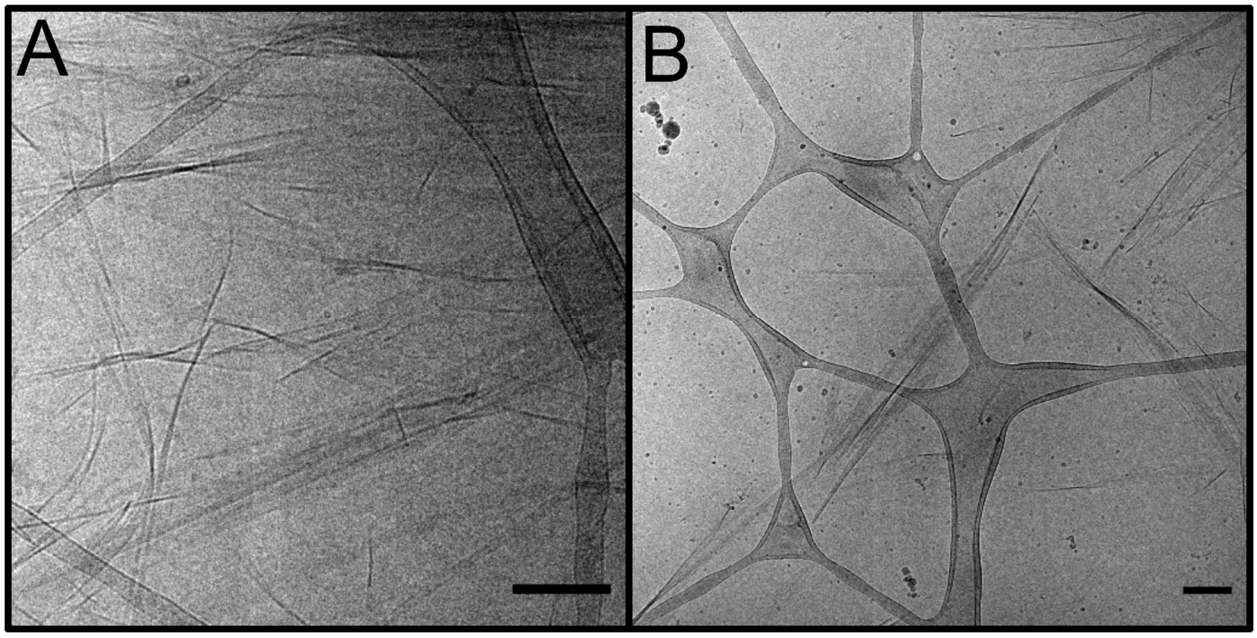

Figure F.10: CryoEM images of 1 mg/mL teixobactin in PBS buffer and 5% DMSO. Scale bar is 200 nm. A) Layer of teixobactin sheets with some sheets oriented perpendicular to the imaging plane giving a high contrast appearance. B) Teixobactin sheets with changing orientation revealing a larger sheetlike structure.

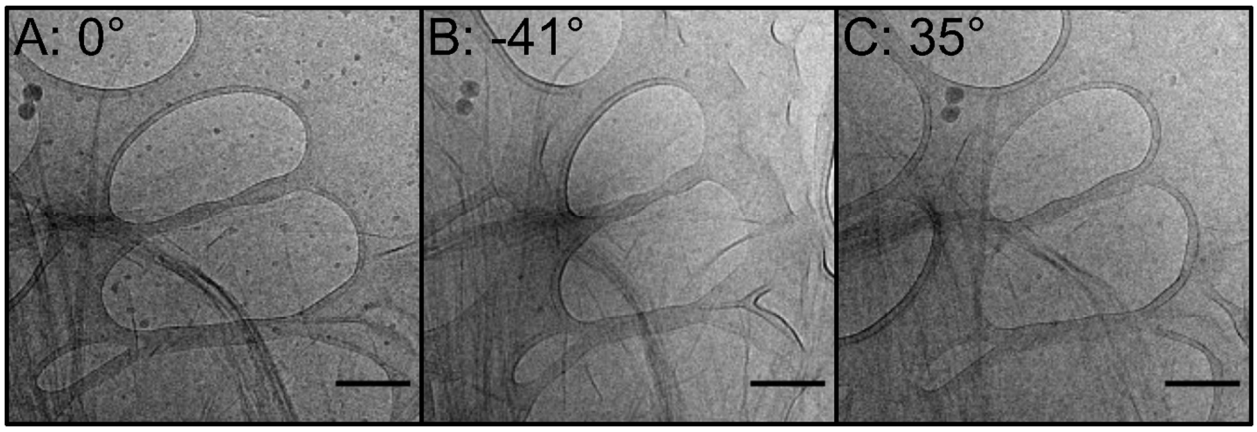

Figure F.11: CryoEM images of 1 mg/mL of teixobactin showing 3D nature of teixobactin sheets. Scale bar is 200 nm A) 0° showing what appears as a high-contrast rod. B) At -41° stage tilt the specimen appears more as a sheet. C) This is seen to a lesser extent at 35° stage tilt.

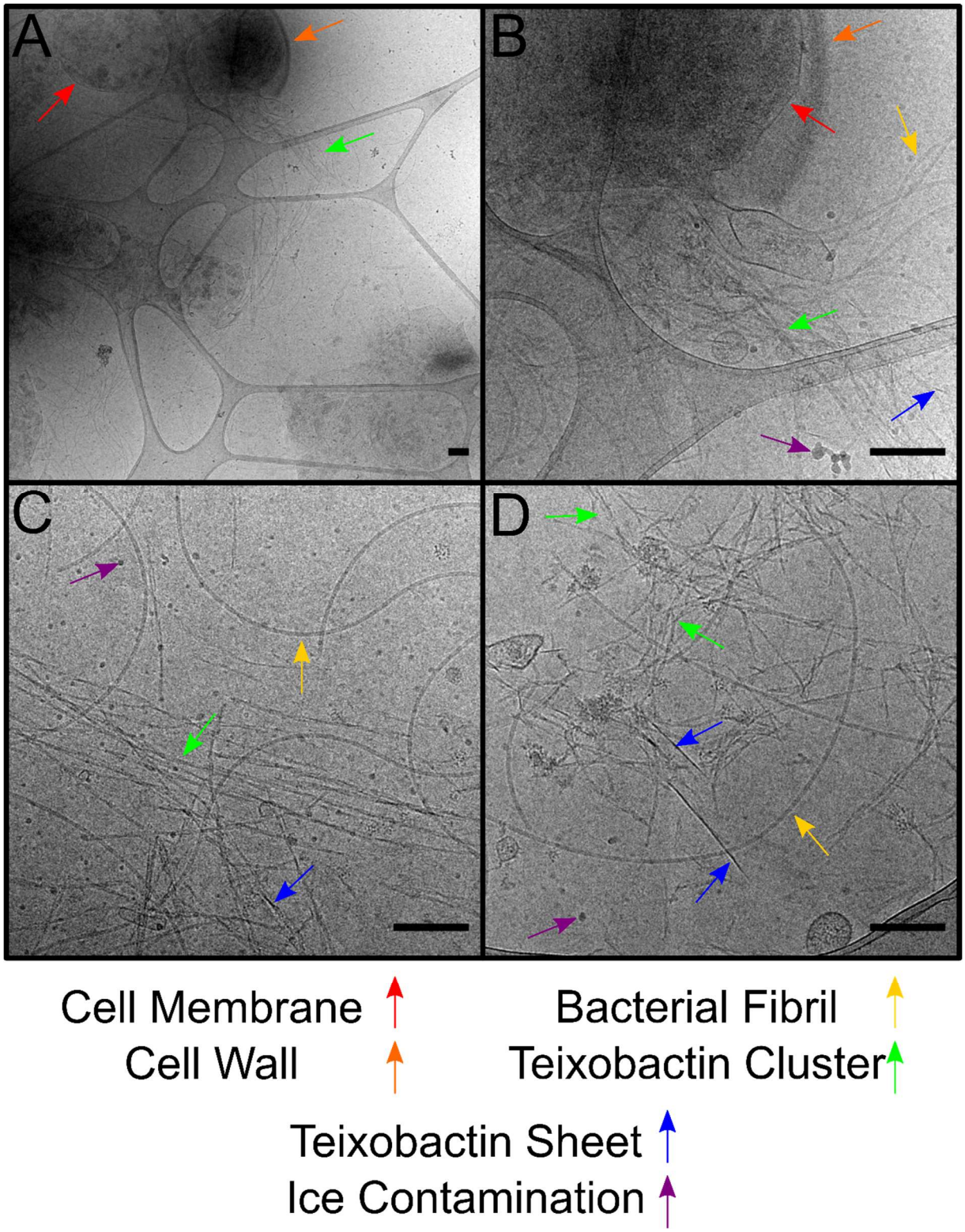

Figure F.12: CryoEM images of *B. subtilis* treated with 1 mg/mL teixobactin in PBS buffer and 5% DMSO. Scale bar is 200 nm. A) Overview of bacteria in sample. B-D) Images showing low-contrast teixobactin clusters, higher-contrast teixobactin sheets and bacterial remnants.

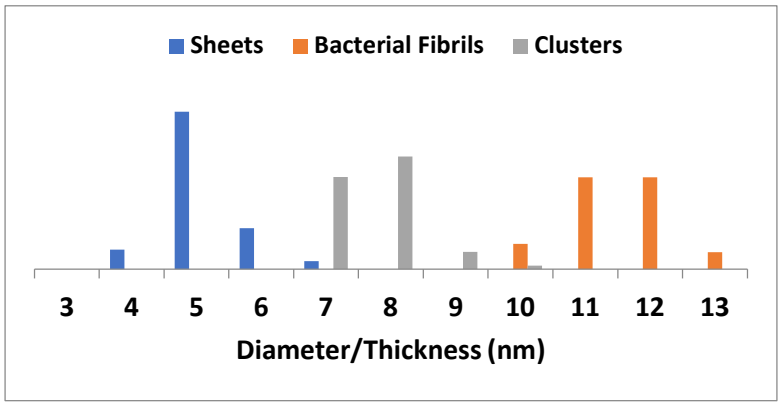

Figure F.13:Combined Histogram of all measured structures in the 1 mg/mL teixobactin bacteria samples. The histogram is normalized, giving the appearance that they all had an equal number of measurements. The teixobactin sheets are in blue. The bacterial fibrils are in orange. The teixobactin clusters containing rod/fiber-like structures are in gray. The histogram highlights the difference in the measured diameters/thickness between the three types of structures.

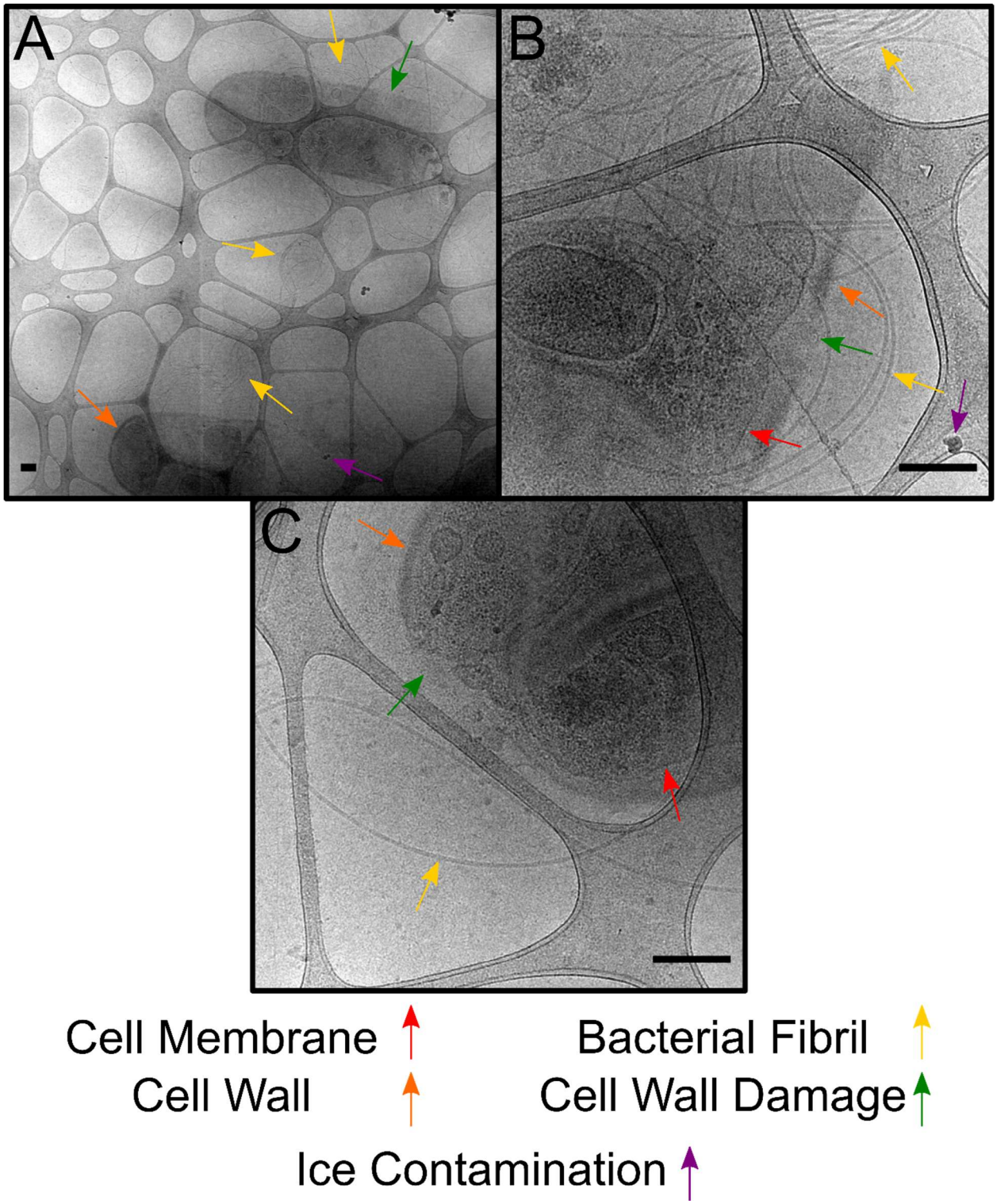

Figure F.14: CryoEM images of *B. subtilis* treated with 4 µg/mL teixobactin in PBS buffer and 5% DMSO. Scale bar is 200 nm. A) Overview of bacteria in sample. B-C) Images showing bacteria will cell wall damage.

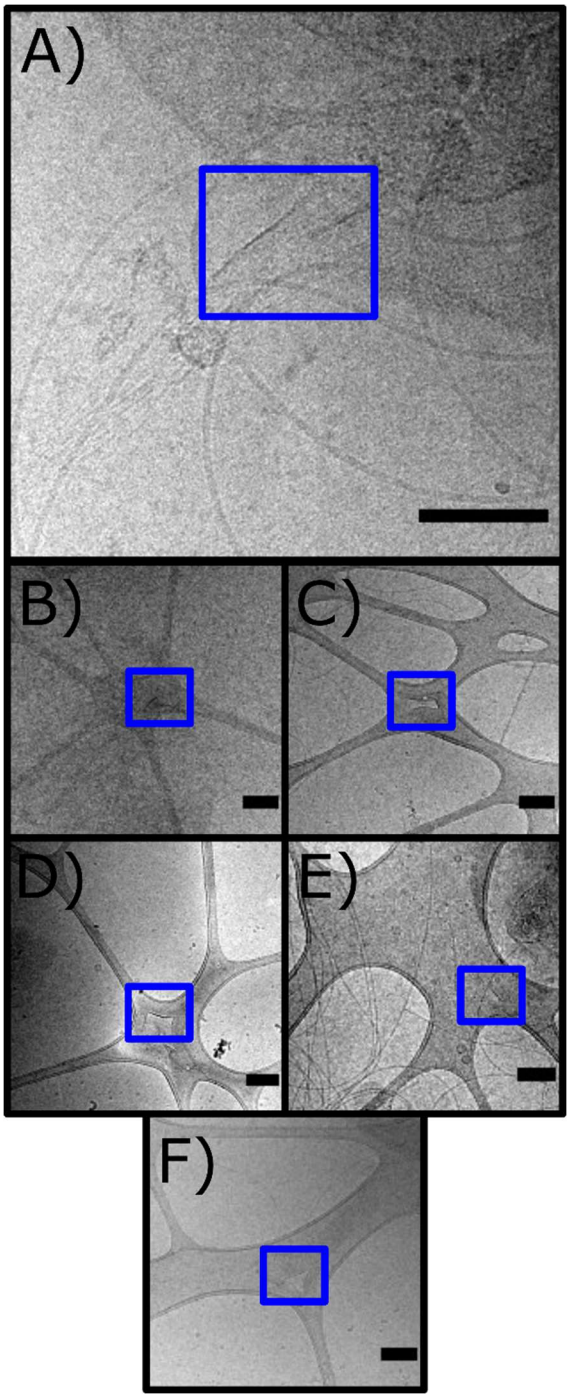

Figure F.15: Insets from CryoEM images of possible teixobactin sheets found in the 4 µg/mL teixobactin bacteria sample. Example A is found near the cell wall whereas B-F are all found in the sample grid away from the cell wall. As the structures in B-F are all over the carbon layer they could be damage to the grid, however they were not found in control experiments without teixobactin.

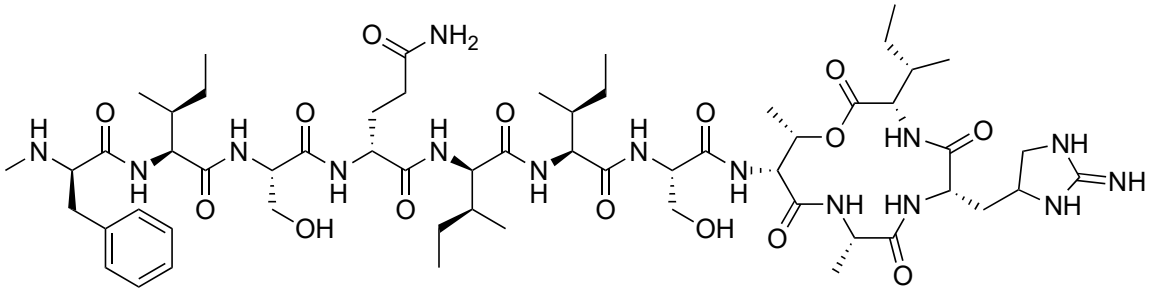

Figure F.16: Chemical structure of teixobactin (provided as a gift from Novobiotic Pharmaceuticals).

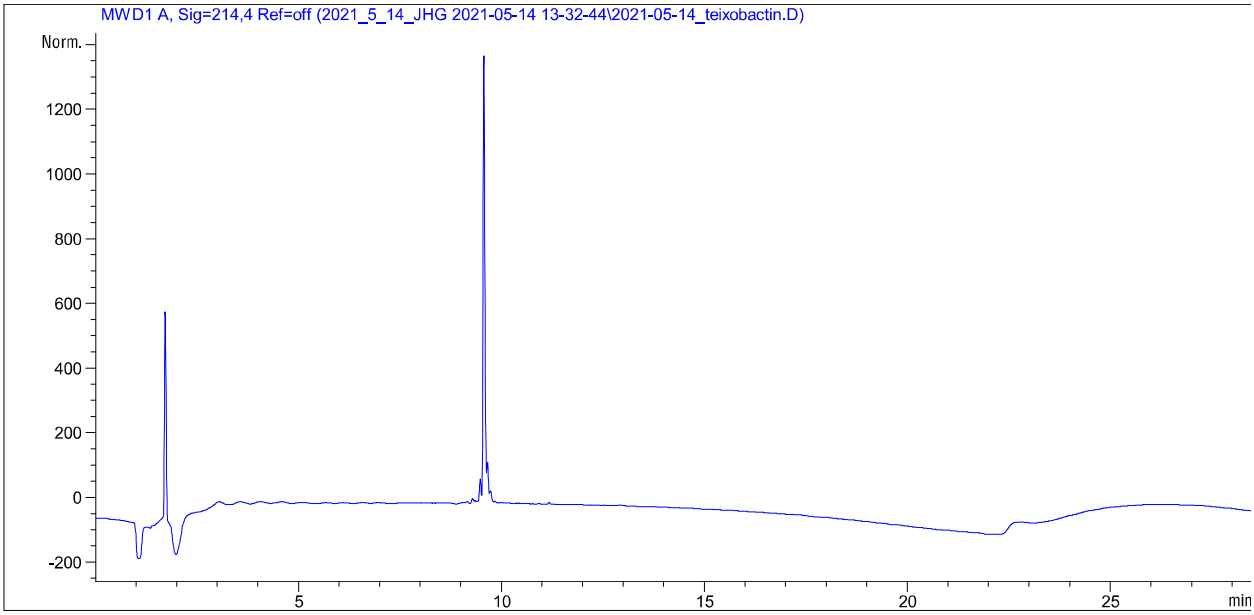

Figure F.17: Analytical HPLC trace: gradient elution of 5–100% acetonitrile over 20 min on an Aeris PEPTIDE 2.6u XB-C18 column (Phenomonex).

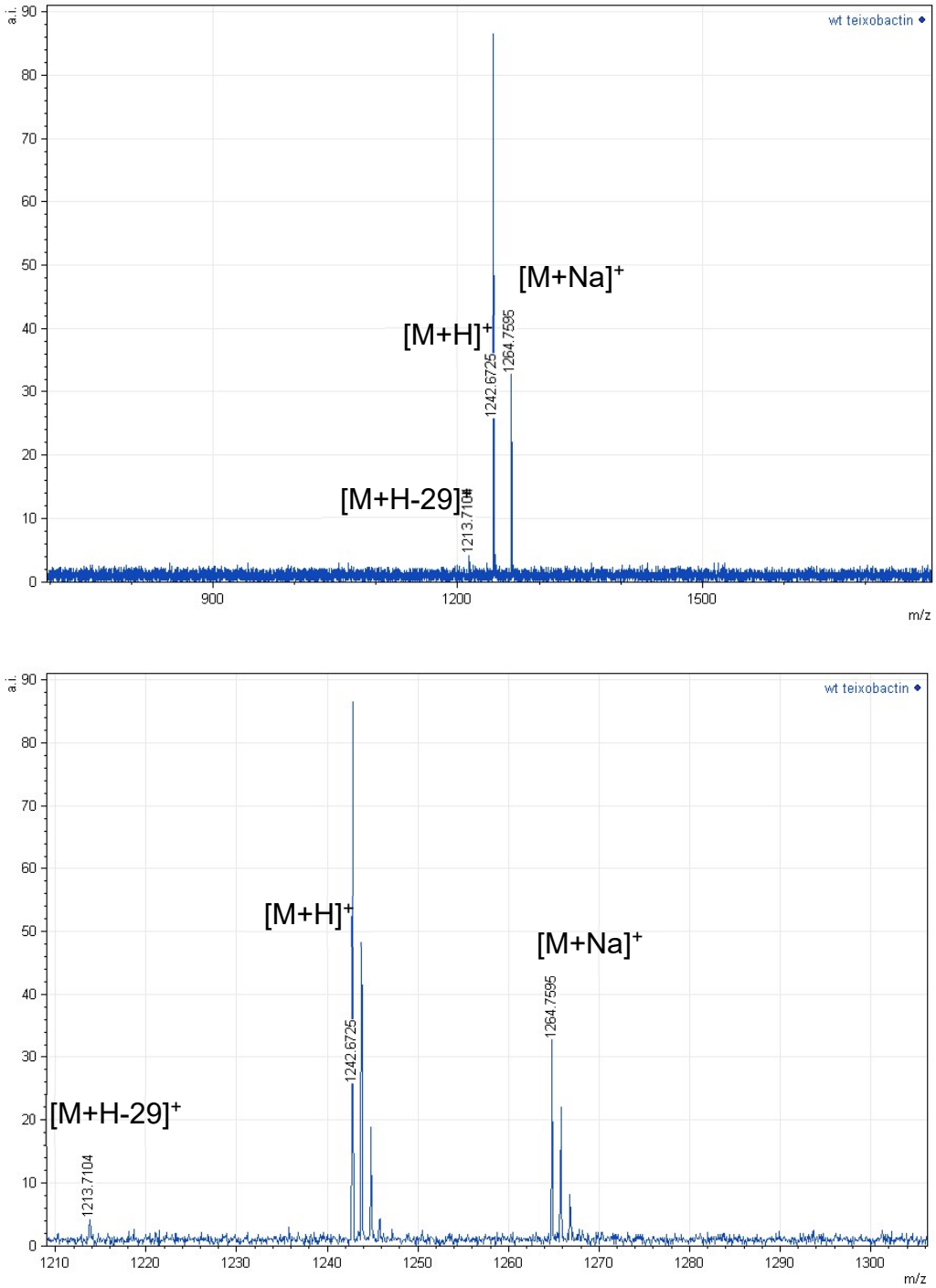

Figure F.18: MALDI mass spectrum of teixobactin.

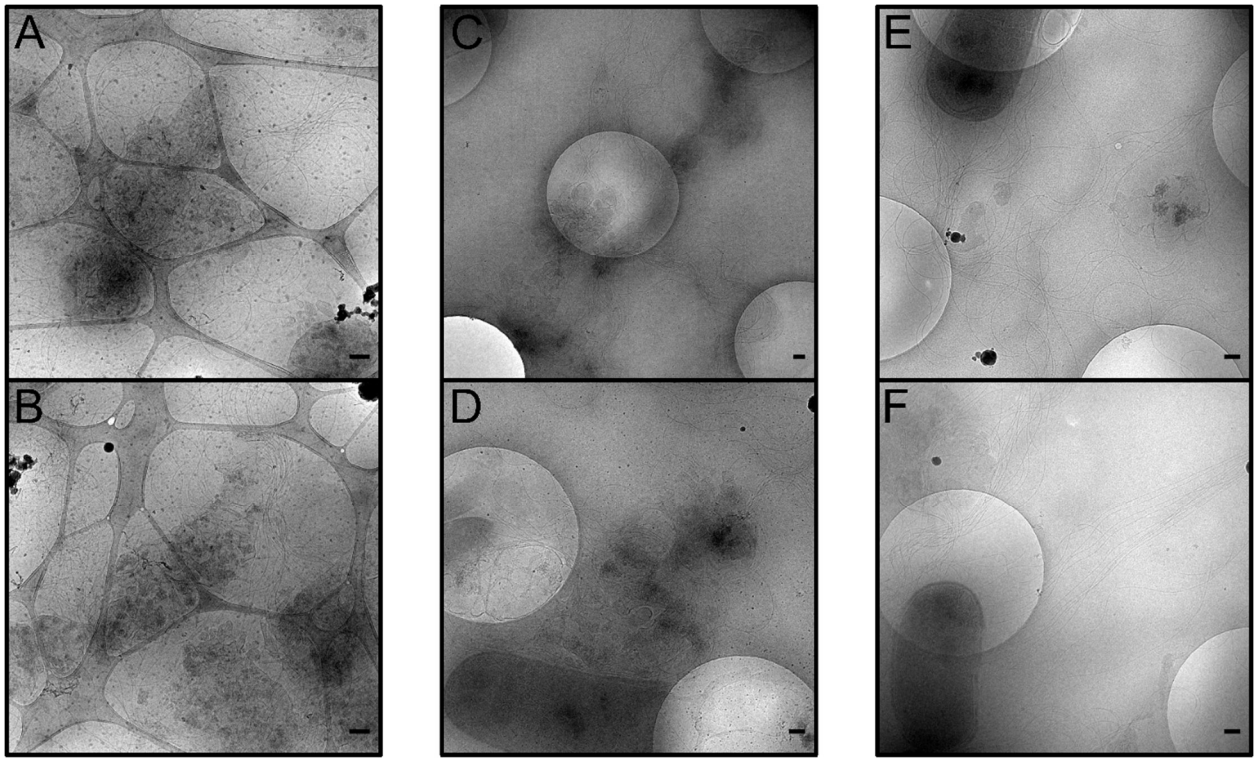

Figure F.19: Additional overview cryoEM images of bacteria & teixobactin images from different samples than those in main text. Samples are in PBS buffer and have some to no DMSO present. Scale bar is 200 nm. 1 mg/mL teixobactin, 5% DMSO (A-B), 4 µg/mL teixobactin, 0.2% DMSO (C-D) and no teixobactin, no DMSO (E-F) of *B. Subtilis* samples.

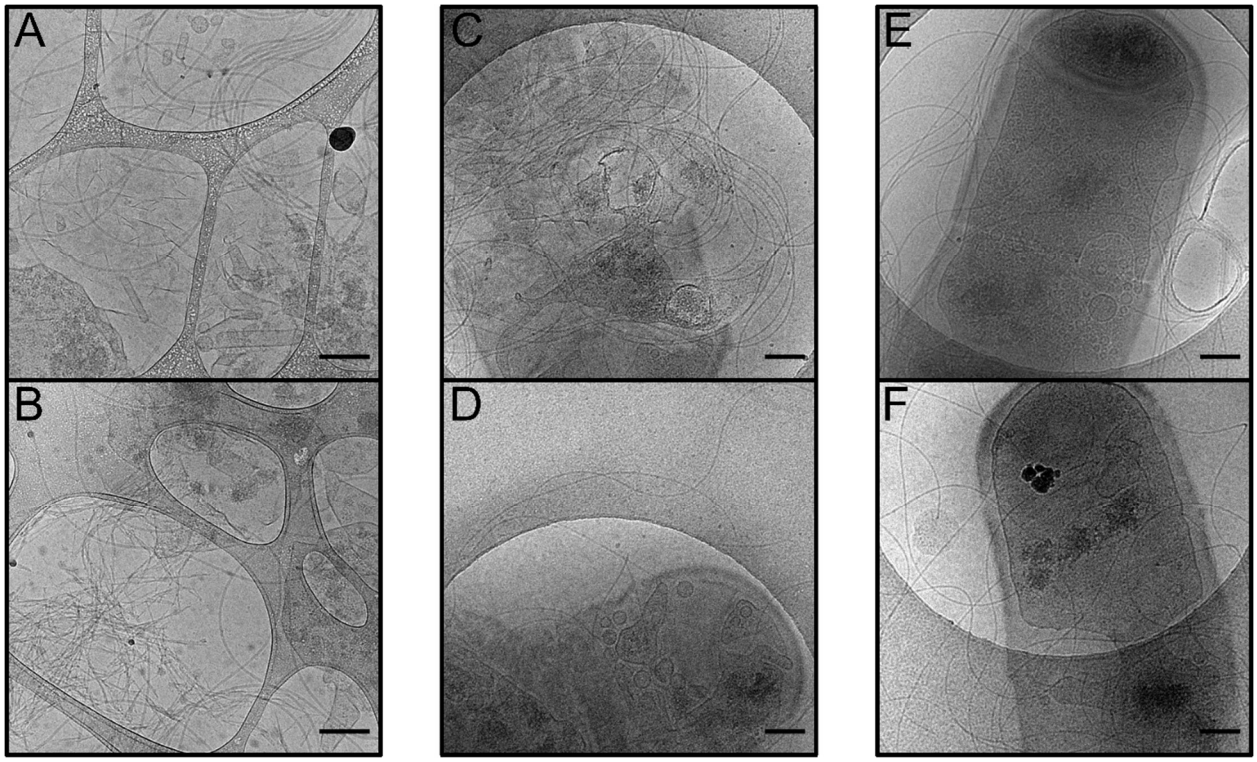

Figure F.20: Additional cryoEM images of bacteria & teixobactin images from different samples than those in main text. Samples are in PBS buffer and have some to no DMSO present. Scale bar is 200 nm. 1 mg/mL teixobactin, 5% DMSO (A-B), 4 µg/mL teixobactin, 0.2% DMSO (C-D) and no teixobactin, no DMSO (E-F) of *B. Subtilis* samples.

F.3. References

1. Romero, D.; Aguilar, C.; Losick, R.; Kolter, R. Amyloid fibers provide structural integrity to Bacillus subtilis biofilms. *Proc. Natl. Acad. Sci. U. S. A.* **2010,** *107* (5), 2230-2234.
2. Huang, J.; Liu, S.; Zhang, C.; Wang, X.; Pu, J.; Ba, F.; Xue, S.; Ye, H.; Zhao, T.; Li, K.; Wang, Y.; Zhang, J.; Wang, L.; Fan, C.; Lu, T. K.; Zhong, C. Programmable and printable Bacillus subtilis b